INNOVATIONS IN MODELING AND SIMULATION TO ADVANCE TRANSLATIONAL SCIENCE

EDITED BY: Melissa Knothe Tate, Leonardo Angelone, Christopher Basciano
and Markus Reiterer

PUBLISHED IN: Frontiers in Physiology and Frontiers in Medicine

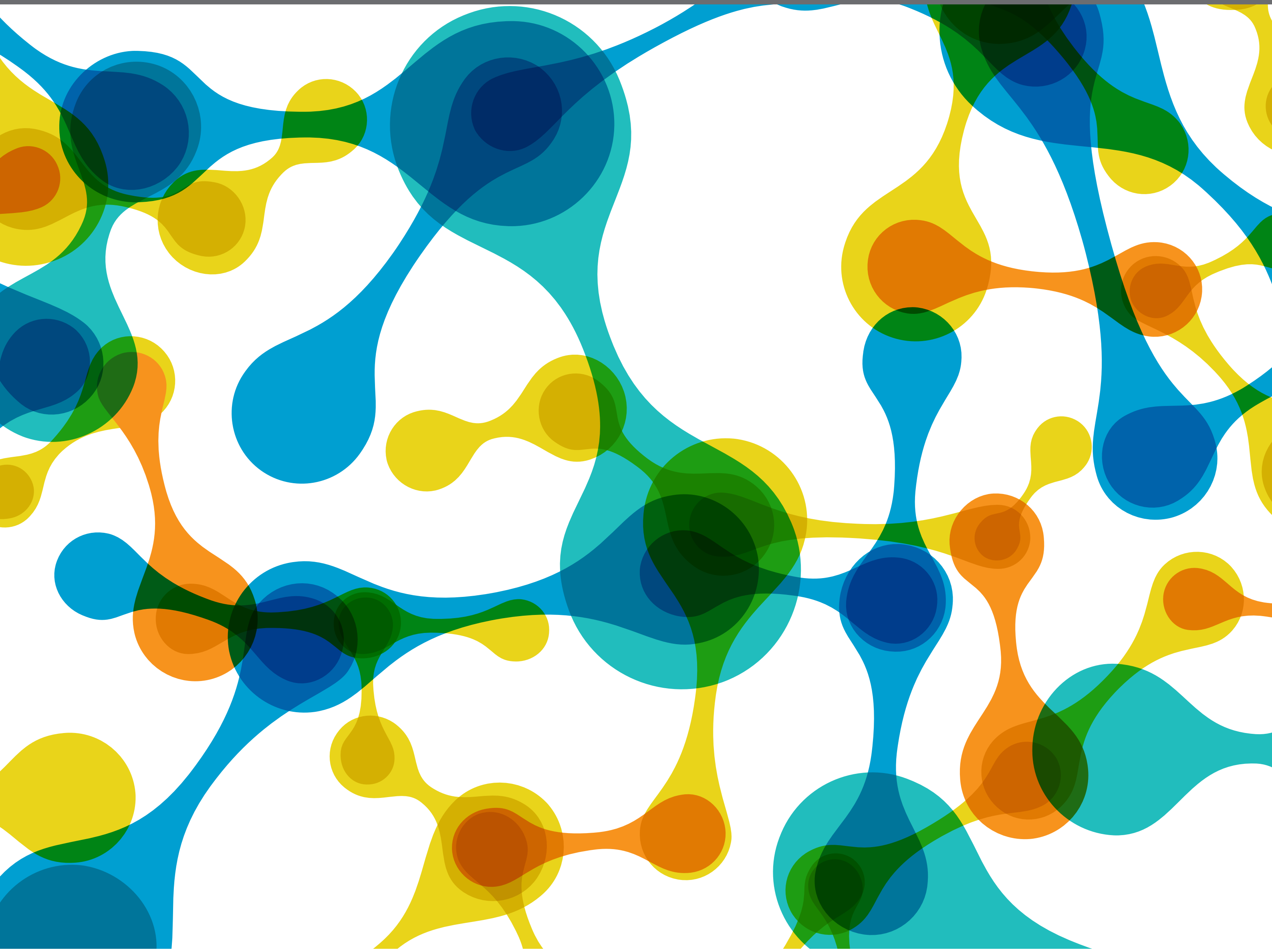

frontiers Research Topics

ISSN 1664-8714
ISBN 978-2-88966-225-8
DOI 10.3389/978-2-88966-225-8

About Frontiers

Frontiers is more than just an open-access publisher of scholarly articles: it is a pioneering approach to the world of academia, radically improving the way scholarly research is managed. The grand vision of Frontiers is a world where all people have an equal opportunity to seek, share and generate knowledge. Frontiers provides immediate and permanent online open access to all its publications, but this alone is not enough to realize our grand goals.

Frontiers Journal Series

The Frontiers Journal Series is a multi-tier and interdisciplinary set of open-access, online journals, promising a paradigm shift from the current review, selection and dissemination processes in academic publishing. All Frontiers journals are driven by researchers for researchers; therefore, they constitute a service to the scholarly community. At the same time, the Frontiers Journal Series operates on a revolutionary invention, the tiered publishing system, initially addressing specific communities of scholars, and gradually climbing up to broader public understanding, thus serving the interests of the lay society, too.

Dedication to Quality

Each Frontiers article is a landmark of the highest quality, thanks to genuinely collaborative interactions between authors and review editors, who include some of the world's best academicians. Research must be certified by peers before entering a stream of knowledge that may eventually reach the public - and shape society; therefore, Frontiers only applies the most rigorous and unbiased reviews.
Frontiers revolutionizes research publishing by freely delivering the most outstanding research, evaluated with no bias from both the academic and social point of view. By applying the most advanced information technologies, Frontiers is catapulting scholarly publishing into a new generation.

What are Frontiers Research Topics?

Frontiers Research Topics are very popular trademarks of the Frontiers Journals Series: they are collections of at least ten articles, all centered on a particular subject. With their unique mix of varied contributions from Original Research to Review Articles, Frontiers Research Topics unify the most influential researchers, the latest key findings and historical advances in a hot research area! Find out more on how to host your own Frontiers Research Topic or contribute to one as an author by contacting the Frontiers Editorial Office: researchtopics@frontiersin.org

INNOVATIONS IN MODELING AND SIMULATION TO ADVANCE TRANSLATIONAL SCIENCE

Topic Editors:
Melissa Knothe Tate, University of New South Wales, Australia
Leonardo Angelone, National Institute on Drug Abuse (NIDA), United States
Christopher Basciano, Becton Dickinson (United States), United States
Markus Reiterer, Medtronic (United States), United States

Citation: Tate, M. K., Angelone, L., Basciano, C., Reiterer, M., eds. (2020). Innovations in Modeling and Simulation to Advance Translational Science. Lausanne: Frontiers Media SA. doi: 10.3389/978-2-88966-225-8

Table of Contents

frontiers in Physiology

ORIGINAL RESEARCH
published: 02 July 2018
doi: 10.3389/fphys.2018.00723

Phenotype-Based and Self-Learning Inter-Individual Sleep Apnea Screening With a Level IV-Like Monitoring System

Hau-Tieng Wu[1,2,3†], Jhao-Cheng Wu[4†], Po-Chiun Huang[4], Ting-Yu Lin[5], Tsai-Yu Wang[5], Yuan-Hao Huang[6‡] and Yu-Lun Lo[5‡]*

[1] Department of Mathematics, Duke University, Durham, NC, United States, [2] Department of Statistical Science, Duke University, Durham, NC, United States, [3] Mathematics Division, National Center for Theoretical Sciences, Taipei, Taiwan, [4] Department of Electrical Engineering, National Tsing Hua University, Hsinchu, Taiwan, [5] Department of Thoracic Medicine, Chang Gung Memorial Hospital, School of Medicine, Chang Gung University, Taipei, Taiwan, [6] Department of Electrical Engineering, Institute of Communications Engineering, National Tsing Hua University, Hsinchu, Taiwan

Edited by:
Christopher Basciano,
Becton Dickinson, United States

Reviewed by:
Thomas Penzel,
Charité – Universitätsmedizin Berlin,
Germany
Paolo Castiglioni,
Fondazione Don Carlo Gnocchi Onlus
(IRCCS), Italy

***Correspondence:**
Yu-Lun Lo
loyulun@hotmail.com;
dr.loyulun@gmail.com

†These authors have contributed equally to this work as first authors.

‡These authors have contributed equally to this work as last authors.

Specialty section:
This article was submitted to
Computational Physiology
and Medicine,
a section of the journal
Frontiers in Physiology

Received: 12 March 2018
Accepted: 24 May 2018
Published: 02 July 2018

Citation:
Wu H-T, Wu J-C, Huang P-C, Lin T-Y, Wang T-Y, Huang Y-H and Lo Y-L (2018) Phenotype-Based and Self-Learning Inter-Individual Sleep Apnea Screening With a Level IV-Like Monitoring System. Front. Physiol. 9:723. doi: 10.3389/fphys.2018.00723

Purpose: We propose a phenotype-based artificial intelligence system that can self-learn and is accurate for screening purposes and test it on a Level IV-like monitoring system.

Methods: Based on the physiological knowledge, we hypothesize that the phenotype information will allow us to find subjects from a well-annotated database that share similar sleep apnea patterns. Therefore, for a new-arriving subject, we can establish a prediction model from the existing database that is adaptive to the subject. We test the proposed algorithm on a database consisting of 62 subjects with the signals recorded from a Level IV-like wearable device measuring the thoracic and abdominal movements and the SpO2.

Results: With the leave-one-subject-out cross validation, the accuracy of the proposed algorithm to screen subjects with an apnea-hypopnea index greater or equal to 15 is 93.6%, the positive likelihood ratio is 6.8, and the negative likelihood ratio is 0.03.

Conclusion: The results confirm the hypothesis and show that the proposed algorithm has potential to screen patients with SAS.

Keywords: sleep apnea screening, Level IV-like monitoring, self-learning AI system, phenotype metric, inter-individual prediction

INTRODUCTION

Sleep apnea syndrome (SAS) is a common sleep disorder that affects approximately 14% of adult men and 5% of adult women (Peppard et al., 2013). An even higher prevalence is reported in Swiss population (Heinzer et al., 2015) that the prevalence of moderate-to-severe SAS was 23.4% in women and 49.7% in men. SAS has been known to be related to different diseases, or even public tragedies (Yaggi et al., 2005; Canessa et al., 2011; Golbidi et al., 2012; Leger et al., 2012). Although SAS has received considerable attention, most patients with SAS are not aware of it and are untreated (Gibson, 2004; Young et al., 2009). Therefore, a screening tool, better designed for home screening, is urgently needed. This tool should be easy to install at home, cheap, comfortable, and not interfere sleep. Many sensors have been explored for this purpose, including those equipped in different items (Al-Mardini et al., 2014; Koyama et al., 2015), for example, the electrocardiogram (ECG) signal, oximeter signal, sound, nasal airflow measurement, respiration effort measurement, oximeter, and accelerometer. In addition to developing an easy-to-install, inexpensive, and accurate screening monitor, researchers have proposed several artificial intelligence (AI) systems for automatic annotation of the collected signal with high accuracy and, therefore, achieve the screening purpose (Alvarez-Estevez and Moret-Bonillo, 2015). However, the inevitable inter-individual variability issue is less considered in these computer-assisted screening techniques.

In addition to accurately annotating collected signals, an AI system should contain a *self-learning* ability like a sleep expert; that is, we are looking for a system that can perform better when there are more cases with good annotations. In practice, to make a diagnosis on a new-arriving patient, physicians automatically handle the inter-individual variability by taking various phenotypes into account, mainly based on his accumulated practicing experience; specifically, by reading available information, the underlying pathophysiological information is implicitly utilized. In this work, we take this wisdom into account, and propose a phenotype-based self-learning AI system for SAS screening. We test the proposed algorithm on a Level IV-like screening system (Ferber et al., 1994; Collop et al., 2007), which contains a pulse oximeter for SpO2 detection and two tri-axial accelerator (TAA) sensors for thoracic and abdominal movement, which are surrogates of the respiratory signal. For a new-arriving patient, based on the designed phenotype metric based on the clinical phenotypes [body mass index (BMI), age, gender, and comorbidity history] and SpO2 and respiratory signals, a prediction model is established from those subjects in the available annotated database that are most similar to the new-arriving subject. To evaluate the performance of the proposed phenotype-based self-learning AI, we compare the automatic annotations with expert labeled sleep records.

MATERIALS AND METHODS

The study was performed with at least 6 h of sleep recording time to confirm the presence or absence of OSA from the clinical subjects suspected of sleep apnea at the sleep center in Chang Gung Memorial Hospital (CGMH), Linkou, Taoyuan, Taiwan. The Level-1 monitoring system, polysomnography (PSG), Alice 5 data acquisition system (Philips Respironics, Murrysville, PA, United States), is carried out during the whole sleep as the ground truth. The Institutional Review Board of CGMH approved the study protocol (No. 101-4968A3). The written informed consent was obtained from the participants. The SpO2 is recorded by the Alice 5 data acquisition system sampled at 1 Hz. The thoracic and abdominal movements are simultaneously recorded at 226 Hz with the 8 bits resolution [The TAA sensors are ADXL335 (Analog device), and the micro-controller AT328P (Atmel) executes the data acquisition flow and then transfers the data to a server wirelessly by a Bluetooth channel], and the signals are synchronized with the SpO2 signal. We also collected the questionnaire from the subject, including age, gender, height, weight, medical history, and drug history. By reading the PSG data, an apnea event (obstructive, central or mixed) is identified when the airflow breathing amplitude decreases more than 90% for a duration ranging from 10 to 120 s, whereas a hypopnea event is identified when the airflow breathing amplitude decreases over 30% of the pre-event baseline with $\geq$3% oxygen desaturation or with an arousal (Berry et al., 2012).

Method

We designed a phenotype-base metric to determine the similarity between subjects. The flowchart of the algorithm is illustrated in **Figure 1**. We consider the commonly available phenotype information for each subject, including gender, age, and body-mass index (BMI) that are closely related to the sleep apnea pattern and severity (Liu et al., 2017). The similarity is designed based on the physician's clinical experience; that is, the closer the age and BMI are, the more similar two subjects are, and the similarity between two subjects with the same gender are weighted more. We call the designed similarity the *phenotype metric*. In clinics, the gender, BMI, and age are not the only considered parameters for the SAS. We further take the comorbidity of hypertension, diabetes, and hypothyroidism into account to better determine the similarity between subjects, which is called the *correction distance*. Two subjects with the same comorbidity are more similar. Following the clinical practice, if we want to find the K most similar subjects of the new-arriving subject, we first determine K + K' most similar subjects that are related to the phenotype metric and remove the K' subjects with the largest correction distance. If there are less than K' subjects that have the correction distance greater than 0, we remove subjects with the largest phenotype distance to determine the K most similar subjects. We call this a *modified K nearest neighbor (KNN) scheme*. The detailed description of the metric design can be found in the Supplementary Material.

For each subject, we extract two sets of features – the apnea-related features and the desaturation features. These features are extracted from 10-s-long segmented signals, with a 9.5 s overlap. For each segment of the recorded thoracic and abdominal movement signal, we extract the amplitude, frequency, and paradoxical movement as the apnea-related features that are introduced in Lin et al. (2016). For each segment of the SpO2 signal, the minimum, maximum, median, mean, variance of the first derivative, and difference between the median and minimum over a sliding 20-s window are selected as the desaturation features.

With the *modified KNN scheme* and selected features, the proposed phenotype-based self-learning AI system is carried out upon the available database with annotations provided by the sleep experts in the following way. For the new-arriving subject called Z, we find K most similar subjects by the modified KNN scheme. The kernel support vector machine (SVM) (Khandoker et al., 2009) based on the standard radial based function is applied to establish a prediction model from the features extracted from

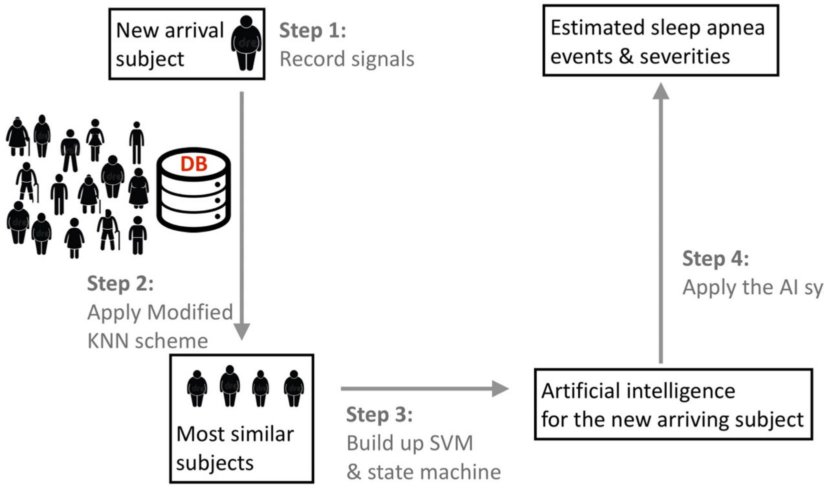

FIGURE 1 | The flowchart of the proposed phenotype-based self-learning artificial intelligence system, with the prototype of the sleep apnea screening instrument. In the clinical testing environment, a full-featured PSG system is also attached to record the ground truth. Two tri-axial accelerometers are attached on the backside of piezo belts. The oximeter probe is applied to the forefinger of right hand, which is not shown in this photo. DB indicates the existing database with experts' annotations and phenotype information.

those K most similar subjects. The established SVM classifier, combined with the paradoxical movement feature, is applied to design a state machine (Lin et al., 2016). The established state machine is applied to predict the sleep apnea stage of the new-arriving subject Z from the recorded SpO2 and thoracic and abdominal movement signals. Finally, for all epochs classified as normal, if there is a desaturation determined by the desaturation features, that epoch is corrected to an apnea event. With the final whole night sleep apnea annotation, we could estimate the AHI and, therefore, the severity of SAS. Since the sleep and awake information is not available, the AHI is estimated by the respiratory event index (REI), which is the average apnea events per hour over the recording period (the period from light off to light on). For reproducibility purposes, the detailed description of the feature extraction and state machine is shown in the Supplementary Material.

Assessment

To evaluate the proposed phenotype-based inter-individual classification performance, we apply the leave-one-subject-out cross validation (LOSOCV). Each subject was selected for the testing group and the remaining subjects were used for training. We up-sample the training dataset by uniformly duplicating the cases in the smaller subgroup to alleviate the imbalanced case numbers. For the selected subject, we find K most similar subjects from the up-sampled training dataset, and establish the prediction model. We then apply the prediction model on the selected subject. The results of all subjects were averaged to obtain inter-individual testing results. Note that this LOSOCV mimics the new-arriving subject in the real-world scenario.

We report two aspects of the performance – the event identification and the severity prediction. An accurate apnea events detection algorithm should identify those apnea events in the right location. It means that an identified apnea event should overlap an annotated apnea event provided by the sleep expert. Without this information, although the estimated events might still provide a reasonable AHI, the predicted events could not provide more information. A detected event is classified as true positive if it overlaps with an annotated event; if there is an annotated event but no event is detected, the detection result is classified as a false negative. We report the positive predictive value (PPV), or the precision, and the F1 score, which is the harmonic mean of recall (sensitivity) and PPV. We report the summary statistics by median ± median absolute deviation (MAD).

To report the performance of the severity prediction, including normal, mild, moderate, and severe, we report a 4-by-4 confusion matrix M. A summarized overall accuracy (AC), and sensitivities and PPV for each group are reported. For the purpose of screening subjects with severe sleep apnea, we divide subjects into two groups, one with subjects having an AHI greater than or equal to 15 and one less than 15, and report not only the sensitivity, specificity and AC, but also the positive likelihood ratio (LR+) and the negative likelihood ratio (LR−). The whole analysis is carried out in Matlab R2014b with the provided SVM module.

RESULTS

We enrolled 63 adult snoring subjects over 20-year-old from the outpatient clinic continuously from September 2015 to August 2016. The questionnaire of one subject was missing, so we excluded this case from the study. Two sleep experts identified, marked, and classified the overnight sleep records into normal (NOR), obstructive sleep apnea, central sleep apnea, mixed-type sleep apnea, and hypopnea. We do not distinguish between different types of apnea events, and view obstructive sleep apnea,

TABLE 1 | Demographic details of the enrolled 62 subjects.

	Gender (# of sub.)	AHI (#/h)	BMI (kg/m^2)	Age (y/o)	Recording time (h)	Sleep time (h)	# of CSA	# of MSA	# of OSA	# of HYP
Normal	All (10)	2.2 ± 1.4	22.4 ± 2.8	34.8 ± 16.3	6.3 ± 0.2	5.6 ± 0.6	2.1 ± 2.1	0.5 ± 0.7	1.0 ± 2.5	8.5 ± 6.4
	Male (4)	2.4 ± 1.0	22.1 ± 1.4	36.8 ± 17.0	6.3 ± 0.2	5.2 ± 0.8	1.3 ± 0.5	0.3 ± 0.5	0.5 ± 0.6	10.8 ± 5.3
	Female (6)	2.1 ± 1.8	22.6 ± 3.5	33.5 ± 17.2	6.3 ± 0.2	5.8 ± 0.3	2.7 ± 2.7	0.7 ± 0.8	1.3 ± 3.3	7.0 ± 7.1
Mild	All (11)	9.9 ± 2.7	25.0 ± 4.5	38.6 ± 15.5	6.3 ± 0.1	5.4 ± 0.5	3.1 ± 3.4	1.8 ± 1.8	14.9 ± 13.0	34.4 ± 11.8
	Male (7)	9.6 ± 3.3	23.5 ± 3.9	29.9 ± 8.1	6.3 ± 0.1	5.4 ± 0.5	3.9 ± 4.1	2.4 ± 2.0	18.0 ± 15.3	29.0 ± 7.3
	Female (4)	10.4 ± 1.4	27.5 ± 4.8	53.8 ± 13.8	6.1 ± 0.1	5.3 ± 0.4	1.8 ± 1.5	0.8 ± 0.5	9.5 ± 5.5	43.8 ± 13.1
Moderate	All (4)	24.9 ± 5.3	27.0 ± 1.6	49.8 ± 13.1	6.4 ± 0.3	5.1 ± 1.0	5.0 ± 10.0	3.3 ± 5.9	18.3 ± 16.6	96.0 ± 41.1
	Male (4)	24.9 ± 5.3	27.0 ± 1.6	49.8 ± 13.1	6.4 ± 0.3	5.1 ± 1.0	5.0 ± 10.0	3.3 ± 5.9	18.3 ± 16.6	96.0 ± 41.1
	Female (0)	–	–	–	–	–	–	–	–	–
Severe	All (37)	63.8 ± 23.4	27.8 ± 3.7	52.3 ± 13.8	6.3 ± 0.1	5.0 ± 0.8	9.1 ± 14.9	22.3 ± 32.7	179.6 ± 121.9	103.5 ± 71.7
	Male (34)	63.9 ± 23.6	27.6 ± 3.5	51.0 ± 13.6	6.3 ± 0.1	5.0 ± 0.8	9.6 ± 15.5	21.6 ± 32.7	181.4 ± 124.5	103.5 ± 74.7
	Female (3)	62.6 ± 24.9	29.6 ± 5.9	67.7 ± 1.2	6.2 ± 0.1	4.7 ± 0.2	4.3 ± 1.2	30.7 ± 39.4	159.3 ± 104.3	103.3 ± 23.9

central sleep apnea, mixed-type sleep apnea, and hypopnea as apnea (APN) in the whole analysis. Among 62 subjects, there are 49 males and 13 females, 10 normal subjects, and 11, 4, and 37 subjects with mild, moderate, and severe SAS, respectively. The age is 34.8 ± 16.3, 38.6 ± 15.5, 49.8 ± 13.1, and 52.3 ± 13.8 for the normal, mild, moderate, and severe group, respectively. More demographic detail information, including gender, AHI, BMI, age, recording time (the length of recording period), and sleep time (the length of intervals when the subject is in the sleep status during the period from light off to light on) is summarized in **Table 1**.

The event-by-event detection results are shown in **Table 2**. Overall, the PPV is 0.67 ± 0.23 and the F1 is 0.7 ± 0.22, and the algorithm is more accurate for subjects with moderate and severe SAS. For subjects with AHI less than 15, the PPV is 0.24 ± 0.24 and the F1 is 0.27±0.18; for subjects with AHI greater than 15, the PPV is 0.77 ± 0.12 and the F1 is 0.77 ± 0.11.

Table 3 shows the confusion matrix of the severity prediction results, based on the event-by-event prediction result, where the overall accuracy is 71% for four groups. The sensitivities are 60, 63.6, 75, and 75.7% for the normal, mild, moderate, and severe groups, respectively; the PPVs are 85.7, 58.3, 20, and 100%, respectively. If we take AHI 15 as the cutoff to determine if a subject has an urgent treatment need for his/her SAS, the sensitivity is 97.6%, the specificity is 85.7%, and the accuracy is 93.6%, with LR+ 6.8 and LR− 0.03.

TABLE 2 | Results of the event-by-event prediction of proposed phenotype-based inter-individual predictor.

PPV	Normal	0.10 ± 0.26
	Mild	0.38 ± 0.19
	Moderate	0.49 ± 0.07
	Severe	0.80 ± 0.11
	All	0.67 ± 0.23
F1	Normal	0.17 ± 0.16
	Mild	0.36 ± 0.16
	Moderate	0.56 ± 0.07
	Severe	0.81 ± 0.10
	All	0.70 ± 0.22

In the proposed algorithm, $K = 15$ and $K' = 5$. PPV, positive predictive value.

DISCUSSION

We propose a phenotype-based inter-individual SAS screening algorithm based on the proposed phenotype metric. For each new-arriving subject, we establish a predictor from the K most similar subjects in an existing database with annotations. The predictor is clearly adaptive to the new-arriving subject. We evaluate the algorithm on a database with a Level IV-like monitoring system equipped with TAA sensors capturing the thoracic and abdominal movements and an oximeter capturing the SpO2 and report the results. If we are concerned with classifying subjects into normal, mild, moderate, or severe subgroups, the proposed algorithm achieves 71% accuracy. If we are concerned with screening subjects with an urgent need for SAS treatment, which are those subjects with AHI greater than or equal to 15, the overall accuracy achieves 93.6% and LR− is as low as 0.03. The low LR− means that the proposed algorithm could efficiently rule out the possibility of moderate or severe SAS, and, therefore, accurately screen those patients with moderate or severe SAS based on the Level IV-like portable device. On the other hand, since LR+ is 6.8, which only moderately increases the post-test probability of disease, the proposed algorithm is less suitable for diagnostic purposes.

For the event-by-event detection result, overall the proposed algorithm could achieve PPV = 0.67±0.23 and F1 = 0.7±0.22, and the prediction accuracy is better when AHI is higher. When a subject is normal or has a mild SAS, the event-by-event prediction is not good. This is because, based on the metric, we find neighbors that have similar sleep apnea behavior, and there are limited sleep apnea events to train an efficient SVM classifier. On the other hand, we have a higher accuracy for the group with more severe patients, since more apnea events are available. The event-by-event detection is important for several clinical applications. For example, we need a real-time and accurate event-by-event predictor to establish an adaptive

TABLE 3 | Confusion matrix of the proposed phenotype-based inter-individual prediction algorithm.

		Expert label			
		Normal	**Mild**	**Moderate**	**Severe**
Prediction	Normal (AHI $\leq$ 5)	6	1	0	0
	Mild (5 < AHI $\leq$ 15)	4	7	1	0
	Moderate (15 < AHI $\leq$ 30)	0	3	3	9
	Severe (30 < AHI)	0	0	0	28
Accuracy		70.97%			

In the proposed algorithm, K = 15 and K' = 5.

continuous positive airway pressure (CPAP) machine. Since the proposed algorithm performs better for subjects with AHI greater than 15, we could expect its clinical potential to improve the CPAP compliance of those patients who urgently need a treatment.

Note that we determine the SAS severity by evaluating REI from the Level IV-like equipment, since the wake-sleep status information is not available from the signals. Compared with the standard AHI determined from PSG, REI determined from PSG tends to underestimate the SAS severity since it reflects the average apnea events per hour during the whole recording period, instead of the sleep time. In **Table 1**, it is shown that the recording time is in general longer than the sleep time. In our case, REI is evaluated based on the event-by-event detection over the whole recording period, so the false positive detected events during the awake stage are included in the analysis. Despite this fact, based on the results, we have shown the potential of taking REI evaluated from the Level IV-like equipment based on the proposed algorithm as a screening tool.

The main obstacle toward a self-evolving capability of a system is the inevitable variation among individuals, and our solution is encoding the physicians' decision-making process and clinical experience into the AI system. To the best of our knowledge, this phenotype-based approach to handle inter-individual variability was never considered in the existing computer-assisted SAS screening techniques. See, for example, (Álvarez et al., 2017; Shokoueinejad et al., 2017), and the literature cited therein, for the recent systematic review of computer-assisted SAS screening techniques. The SAS is a reflection of the complicated interaction between different underlying physiological systems and the environment. The interaction varies from subject to subject, so the signals we collect also vary from subject to subject. Due to this inter-individual variation, the model established from the *whole* database might be blurred. For example, two subjects of different genders might express their SAS patterns differently in the collected signals, and the model established from males might not accurately predict the SAS severity of a female. This "blurring effect" deteriorates the performance of the AI system, and the larger the database is, the more severe the "blurring effect" caused by the inter-individual variability will be. As a result, no matter how large the database is, the accumulated knowledge might be limited. Therefore, finding a way to "compare" individuals and to select a suitable subset from the database to establish the prediction model for the new-arriving subject becomes a critical problem. This problem could be understood as the "metric design" problem in the machine learning field, which is the main component of our work. With the designed phenotype metric, the "blurring effect" could be alleviated and hence the self-evolving system is possible. The metric is designed based on the physician's experience and interpretation in order to alleviate the influence of the inter-individual variability. This fact has been shown in the reported result – the modified KNN scheme helps us to select subjects sharing similar features, which improves the prediction accuracy. In general, if we have more complete electrical health records, more phenotype information can be taken into account to design the desired metric.

According to 2007 JCSM guideline (Collop et al., 2007), the equipment we consider to prove the concept of the proposed self-learning system technically does not fall in the category of Level 4 devices while it does not fall in the category of Level 3 neither, since we have less than 4 channels. However, since the sensors we consider collect two types of information – respiratory effort and oxygen saturation, it is closer to a Level 4 device in 2007 JCSM guideline. Therefore, we call it "Level 4-like" device. Regarding the term "phenotype-based approach," in clinics, when we discuss phenotype-based diagnosis, it is the pathophysiological origin of sleep apnea, like the chemoreceptor driver, the collapsibility of upper airway, or so on, that is considered, instead of the quantities we discuss here. Ideally, finding these pathophysiological would give us the best diagnosis accuracy. However, in general we do not have these information; instead, we only have other information about the subjects that are related to the underlying pathophysiological status. The existence of relationship allows us to take underlying pathophysiological status into account, and hence improve the diagnosis accuracy of sleep apnea. We thus call our approach "phenotype-based."

There are several technical details regarding the algorithm that must be discussed. We emphasize that although we could run a greedy optimization to determine the optimal weight for each phenotype parameter for the phenotype distance, we do not do it to avoid over-fitting, due to the case number limitation. Second, while the selected features and SVM overall performs well, it is widely accepted that when the database is large, the multi-layer neural network might perform better. In the future large scale study, we could consider designing a multi-layer neural network to replace SVM. Third, to purely study the potential of the algorithm, we do not consider the signal quality effect. All recorded signals are taken into account for the analysis. For a practical application, we could consider distinguishing between signals with high and low qualities. Designing a signal quality index for the TAA signal is a research topic of its own interest but is out of the scope of this paper. It will be carried out in the future research, and in general this could improve the result.

Despite the strength of the proposed algorithm, we acknowledge several limitations. First, the case number is small and there is a subgroup (female with moderate SAS) that is empty. Based on this preliminary study, a large scale prospective study is needed. With a larger database, we could further take more physicians' wisdom into account. For example, it is known that menopause females have an increased prevalence of SAS. The metric design should take this into account. Second, while the proposed event-by-event detection algorithm has the potential for the clinical application, like improving the CPAP machine, its accuracy could be further improved. Third, the subjects all slept in the lab (not at home) for only one night. Therefore, the first night effect (Tamaki et al., 2016) is inevitable. A prospective study designed for a home care scenario is also needed.

CONCLUSION

We confirm that the proposed novel phenotype-based inter-individual SAS prediction algorithm based on a Level IV-like monitoring system has potential as a self-learning AI system for homecare screening.

ETHICS STATEMENT

All procedures performed in studies involving human participants were in accordance with the ethical standards of the institutional and/or national research committee and with the 1964 Helsinki declaration and its later amendments or comparable ethical standards.

AUTHOR CONTRIBUTIONS

H-TW, Y-HH, T-YL, T-YW, and Y-LL designed the experiment, carried out the study, and prepared the manuscript. H-TW, J-CW, and Y-HH carried out the data analysis. P-CH handled the hardware preparation and data collection. All authors contributed to the final manuscript proofreading.

FUNDING

This work is supported by Chang Gung University and National Tsing Hua University Joint Project under grant number CMRPG3H0251 (Chang Gung University) and 107Q2516E1 (National Tsing Hua University)

SUPPLEMENTARY MATERIAL

The Supplementary Material for this article can be found online at: https://www.frontiersin.org/articles/10.3389/fphys.2018.00723/full#supplementary-material

REFERENCES

Al-Mardini, M., Aloul, F., Sagahyroon, A., and Al-Husseini, L. (2014). Classifying obstructive sleep apnea using smartphones. *J. Biomed. Inform.* 52, 251–259. doi: 10.1016/j.jbi.2014.07.004

Álvarez, D., Cerezo-hernández, A., Lopez-Muniz, G., Alvaro-De Castro, T., Ruiz-Albi, T., Hornero, R., et al. (2017). *Usefulness of Artificial Neural Networks in the Diagnosis and Treatment of Sleep Apnea-Hypopnea Syndrome. Sleep Apnea Mayank Vats*. Rijeka: Intech Open, 33–68. doi: 10.5772/66570

Alvarez-Estevez, D., and Moret-Bonillo, V. (2015). Computer-assisted diagnosis of the sleep apnea-hypopnea syndrome: a review. *Sleep Disord.* 2015:237878. doi: 10.1155/2015/237878

Berry, R. B., Budhiraja, R., Gottlieb, D. J., Gozal, D., Iber, C., Kapur, V. K., et al., (2012). Rules for scoring respiratory events in sleep: update of the 2007 AASM manual for the scoring of sleep and associated events. *J. Clin. Sleep Med.* 8, 597–619. doi: 10.5664/jcsm.2172

Canessa, N., Castronovo, V., Cappa, S. F., Aloia, M. S., Marelli, S., Falini, A., et al. (2011). Obstructive sleep apnea: brain structural changes and neurocognitive function before and after treatment. *Am. J. Respir. Crit. Care Med.* 183, 1419–1426. doi: 10.1164/rccm.201005-0693OC

Collop, N. A., Anderson, W. M., Boehlecke, B., Claman, D., Goldberg, R., Gottlieb, D. J., et al. (2007). Clinical guidelines for the use of unattended portable monitors in the diagnosis of obstructive sleep apnea in adult patients. *J. Clin. Sleep Med.* 3, 737–747.

Ferber, R., Millman, R., Coppola, M., Fleetham, J., Murray, C. F., Iber, C., et al. (1994). Portable recording in the assessment of obstructive sleep apnea. ASDA standards of practice. *Sleep* 17, 378–392. doi: 10.1093/sleep/17.4.378

Gibson, G. J. (2004). Obstructive sleep apnoea syndrome: underestimated and undertreated. *Br Med Bull.* 72, 49–65. doi: 10.1093/bmb/ldh044

Golbidi, S., Badran, M., Ayas, N., and Laher, I. (2012). Cardiovascular consequences of sleep apnea. *Lung* 190, 113–132. doi: 10.1007/s00408-011-9340-1

Heinzer, R., Vat, S., Marques-Vidal, P., Marti-Soler, H., Andries, D., Tobback, N., et al. (2015). Prevalence of sleep-disordered breathing in the general population: the HypnoLaus study. *Lancet Respir. Med.* 3, 310–318. doi: 10.1016/S2213-2600(15)00043-0

Khandoker, A. H., Palaniswami, M., and Karmakar, C. K. (2009). Support vector machines for automated recognition of obstructive sleep apnea syndrome from ECG recordings. *IEEE Trans. Inf. Technol. Biomed.* 13, 37–48. doi: 10.1109/TITB.2008.2004495

Koyama, T., Sato, S., Kanbayashi, T., Kondo, H., Watanabe, H., Nishino, S., et al. (2015). Apnea during Cheyne-Stokes-like breathing detected by a piezoelectric sensor for screening of sleep disordered breathing. *Sleep Biol. Rhythms* 13, 57–67. doi: 10.1111/sbr.12097

Leger, D., Bayon, V., Laaban, J. P., and Philip, P. (2012). Impact of sleep apnea on economics. *Sleep Med. Rev.* 16, 455–462. doi: 10.1016/j.smrv.2011.10.001

Lin, Y. Y., Wu, H. T., Hsu, C. A., Huang, P. C., Huang, Y. H., and Lo, Y. L. (2016). Sleep apnea detection based on thoracic and abdominal movement signals of wearable piezo-electric bands. *IEEE J. Biomed. Health Inform.* 21, 1533–1545. doi: 10.1109/JBHI.2016.2636778

Liu, W. T., Wu, H. T., Juang, J. N., Wisniewski, A., Lee, H. C., Wu, D., et al. (2017). Prediction of the severity of obstructive sleep apnea by anthropometric features via support vector machine. *PLoS One* 12:e0176991. doi: 10.1371/journal.pone.0176991

Peppard, P. E., Young, T., Barnet, J. H., Palta, M., Hagen, E. W., and Hla, K. M. (2013). Increased prevalence of sleep-disordered breathing in adults. *Am. J. Epidemiol.* 177, 1006–1014. doi: 10.1093/aje/kws342

Shokoueinejad, M., Fernandez, C., Carroll, E., Wang, F., Levin, J., Rusk, S., et al. (2017). Sleep apnea: a review of diagnostic sensors, algorithms, and therapies. *Physiol. Meas.* 38, R204–R252. doi: 10.1088/1361-6579/aa6ec6

Tamaki, M., Bang, J. W., Watanabe, T., and Sasaki, Y. (2016). Night watch in one brain hemisphere during sleep associated with the first-night effect in humans. *Curr. Biol.* 26, 1190–1194. doi: 10.1016/j.cub.2016.02.063

Yaggi, H. K., Concato, J., Kernan, W. N., Lichtman, J. H., Brass, L. M., and Mohsenin, V. (2005). Obstructive sleep apnea as a risk factor for stroke and death. *N. Engl. J. Med.* 353, 2034–2041. doi: 10.1056/NEJMoa043104

Young, T., Palta, M., Dempsey, J., Peppard, P. E., Nieto, F. J., and Hla, K. M. (2009). Burden of sleep apnea: rationale, design, and major findings of the Wisconsin Sleep Cohort study. *WMJ* 108, 246–249.

Conflict of Interest Statement: The authors declare that the research was conducted in the absence of any commercial or financial relationships that could be construed as a potential conflict of interest.

frontiers in Physiology

TECHNOLOGY REPORT
published: 27 July 2018
doi: 10.3389/fphys.2018.00724

Solenoidal Micromagnetic Stimulation Enables Activation of Axons With Specific Orientation

Laleh Golestanirad[1,2†], John T. Gale[3†], Nauman F. Manzoor[4,5], Hyun-Joo Park[4], Lyall Glait[4,5], Frederick Haer[6], James A. Kaltenbach[4] and Giorgio Bonmassar[1,2*]

[1] Athinoula A. Martinos Center, Massachusetts General Hospital, Charlestown, MA, United States, [2] Harvard Medical School, Boston, MA, United States, [3] Department of Neurosurgery, Emory University, Atlanta, GA, United States, [4] Department of Neurosciences, Cleveland Clinic Lerner Research Institute, Cleveland, OH, United States, [5] Ear, Nose and Throat Institute, University Hospitals Cleveland Medical Center, Case Western Reserve University, Cleveland, OH, United States, [6] Frederick Haer Corporation, Bowdoin, ME, United States

OPEN ACCESS

Edited by:
Christopher Basciano,
Becton Dickinson, United States

Reviewed by:
Yael Yaniv,
Technion – Israel Institute of Technology, Israel
Arun V. Holden,
University of Leeds, United Kingdom

Correspondence:
Giorgio Bonmassar
giorgio@nmr.mgh.harvard.edu

†These authors have contributed equally to this work.

Specialty section:
This article was submitted to Computational Physiology and Medicine, a section of the journal Frontiers in Physiology

Received: *13 March 2018*
Accepted: *24 May 2018*
Published: *27 July 2018*

Citation:
Golestanirad L, Gale JT, Manzoor NF, Park H-J, Glait L, Haer F, Kaltenbach JA and Bonmassar G (2018) Solenoidal Micromagnetic Stimulation Enables Activation of Axons With Specific Orientation. Front. Physiol. 9:724. doi: 10.3389/fphys.2018.00724

Electrical stimulation of the central and peripheral nervous systems - such as deep brain stimulation, spinal cord stimulation, and epidural cortical stimulation are common therapeutic options increasingly used to treat a large variety of neurological and psychiatric conditions. Despite their remarkable success, there are limitations which if overcome, could enhance outcomes and potentially reduce common side-effects. Micromagnetic stimulation (μMS) was introduced to address some of these limitations. One of the most remarkable properties is that μMS is theoretically capable of activating neurons with specific axonal orientations. Here, we used computational electromagnetic models of the μMS coils adjacent to neuronal tissue combined with axon cable models to investigate μMS orientation-specific properties. We found a 20-fold reduction in the stimulation threshold of the preferred axonal orientation compared to the orthogonal direction. We also studied the directional specificity of μMS coils by recording the responses evoked in the inferior colliculus of rodents when a pulsed magnetic stimulus was applied to the surface of the dorsal cochlear nucleus. The results confirmed that the neuronal responses were highly sensitive to changes in the μMS coil orientation. Accordingly, our results suggest that μMS has the potential of stimulating target nuclei in the brain without affecting the surrounding white matter tracts.

Keywords: eddy currents, TMS, finite element method, microcoils, inductive stimulation, numerical modeling, neurostimulation

INTRODUCTION

Implanted medical devices based on electrical stimulation such as cardioverter-defibrillators and pacemakers (Ellenbogen and Wood, 2008), spinal cord stimulation (Kreis and Fishman, 2009), and deep brain stimulation (DBS) (Montgomery, 2010) devices have become well-accepted therapeutic options to treat a wide variety of medical conditions. Electrical stimulation has considerable clinical impact in alleviating symptoms of an increasingly diverse range of neurological and psychiatric disorders including for example, cochlear (Gifford, 2013) and auditory brainstem implants for restoring hearing (Møller, 2006), DBS to treat symptoms of Parkinsonism (Benabid, 2003; Deuschl et al., 2006), cortical stimulation for epilepsy and depression (Howland, 2008; Morace et al., 2016; Williams et al., 2016), spinal cord stimulation for neuropathic pain (Lopez et al., 2016), and vagus nerve stimulation for epilepsy (Panayiotopoulos, 2011) and depression (O'Reardon et al., 2006; United States Congress Senate Committee on Finance, 2006), just to mention a few. More recently, electrical stimulation has also shown promise for the restoration of function of retinal implants to restore vision in the blind (Humayun et al., 2012; Shepherd et al., 2013; Zrenner, 2013; Ayton et al., 2014; Stingl et al., 2015).

Although electrical techniques for neuronal stimulation have proven quite useful, they have several limitations that can be overcome by micro magnetic stimulation (μMS) which uses sub-millimeter coils. For example, for an electrode pair to generate currents it needs to be placed in contact with a conductive media (e.g., excitable tissue). Electric currents that are delivered by these electrodes diffuse and can spread to undesired areas adjacent to the structures being targeted, leading to unintended side-effects (Histed et al., 2009; Behrend et al., 2011; Licari et al., 2011; Weitz et al., 2015). A magnetic coil, on the other hand, can induce electric currents in the tissue from a distance (i.e., through an insulation layer). In nature these currents are closed-loop circular currents with a higher spatial focality (**Figure 1**). Furthermore, the fact that μMS coils can deliver stimulation while being insulated from the tissue increases their biocompatibility and compatibility with magnetic resonance imaging (considering no ferromagnetic material is present). Finally, as μMS coils can be positioned within or immediately adjacent to the neural tissue, the power needed to evoke neuronal activities is significantly reduced compared to techniques such as transcranial magnetic stimulation (TMS) which are designed to generate strong magnetic fields that pass through the skull and deliver stimulation to the cortical tissue.

Our group recently demonstrated the feasibility of using μMS to elicit neuronal activation *in vitro* (Bonmassar et al., 2012), as well as the activation of neuronal circuitry on the system level *in vivo* (Park et al., 2013). As μMS is a novel technology, its mechanism(s) of nerve activation, induced field characteristics, and optimum topological features are yet to be explored. In this work, we performed numerical simulations to provide an insight into spatial distribution of μMS-induced electric fields, which in turn dictate the dynamics of nerve stimulation threshold changes with different axonal directionalities. Electromagnetic simulations were performed to estimate the magnetic flux $\vec{B}$ and the electric field $\vec{E}$ and its spatial gradient at different distances from the coil. These simulations were based on the actual coil prototypes built (**Figure 2**) and utilized in our animal experiments (**Figure 3**). The estimated $\vec{E}$ fields were then used in conjunction with the NEURON cable model to investigate the directional sensitivity of μMS (**Figures 4**, **5**). Finally, we performed *in vivo* experiments where we studied responses evoked in the inferior colliculus (IC) of rodents by applying μMS stimuli to the surface of animal's dorsal cochlear nucleus (DCN). Specifically, we examined the IC responses to different coil orientations (**Figure 6**).

METHODS

Electromagnetic Simulations

Numerical modeling has been long used to understand the phenomenology of field-tissue interaction in a wide variety of medical and diagnostic applications. Examples include use of electrostatic finite element modeling to predict the volume of activated tissue in electrical brain stimulation (McIntyre and Grill, 2001; Butson and McIntyre, 2006; Golestanirad et al., 2012b), eddy current modeling to assess the distribution of cortical currents in magnetic brain stimulation (Wagner T. et al., 2004; Wagner T.A. et al., 2004; Golestanirad et al., 2010, 2012c), and analysis of body exposure to low frequency magnetic fields and safety hazards due to motion of medical implants in magnetic fields (Condon and Hadley, 2000; Golestani-Rad et al., 2007; Golestanirad et al., 2012a). Recently, the role of numerical modeling has also been emphasized in safety assessment of MRI in patients with conductive implants (Clare McElcheran and Graham, 2014; Golestanirad et al., 2017a,b; McElcheran et al., 2017). The use of computational modeling to predict the response of neurons to external electric fields has been pioneered by eminent works of McIntyre and Grill (2001) and McIntyre et al. (2002, 2004) and followed by others (Wei and Grill, 2005; Woock et al., 2010; Golestanirad et al., 2012b, 2013). Electromagnetic simulations have also been successfully applied to quantify induced currents and assess the safety of transcranial magnetic brain stimulation (Wagner T.A. et al., 2004; Golestanirad et al., 2010, 2012c; Deng et al., 2013). In this work, we used ANSYS Maxwell (ANSYS, Canonsburg, PA, United States) which solves a modified $\mathrm{T}-\Omega$ formulation of Maxwell's Equations expressively designed for low-frequency calculations (Ren, 2002) using the finite element method (FEM). Simulations were performed with solenoidal μMS coils (500 μm diameter, 600 μm height, 21 turns, wire diameter 7 μm, carrying ~20 amperes for a total current per turn = 420 AT). Coils were placed 20 μm above the surface of the tissue and were excited with a 70-kHz sinusoidal current. The tissue was modeled as a 10 mm × 10 mm × 1 mm slab of conductive material ($\sigma = 0.13$S/m). The ensemble of the coil-tissue system was enclosed in a 14 mm × 14 mm × 6 mm air box with Neumann boundary conditions applied to its outer faces which ensured that magnetic field was tangential to the boundary and flux did not cross it. ANSYS Maxwell was set up to follow an adaptive mesh scheme. A high-resolution initial tetrahedral mesh (60 μm) was seeded inside the tissue close to the coil. Maxwell generated a field solution using the specified mesh. It then analyzed the accuracy of the solution by calculating an energy value based on the error in the solution. The exact mechanism for evaluating the error varies by solution type. For eddy current solution, Maxwell uses $\nabla \times \vec{H}$ to find current density and then subtracts all input currents and other sources. For a perfect solution, the result would be zero, whereas for a real finite mesh the

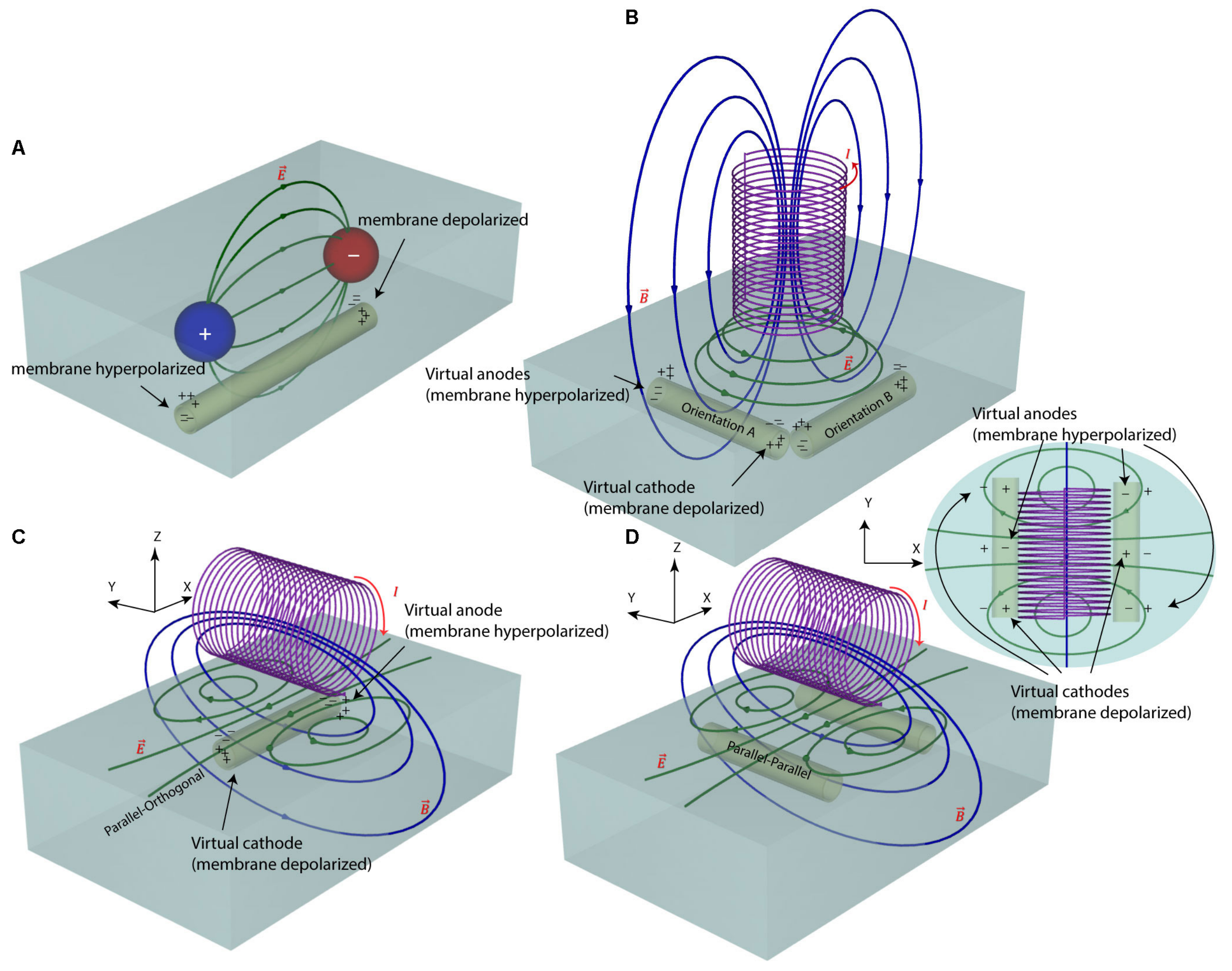

FIGURE 1 | Electric and magnetic nerve stimulation mechanisms. **(A)** In electric nerve stimulation conductive electrodes are positioned in direct galvanic contact with the tissue. A DC (as in tDCS) or pulsed (as in DBS) voltage is applied between two electrode contacts to induce electric currents in the tissue. These currents follow a diffuse path from anode to cathode, hyperpolarizing neuron's membrane under the anode and depolarizing it under the cathode. The current path, however, is diffuse and hard to control. **(B,C)** In magnetic nerve stimulation a time-varying electric current is passed through a coil, generating a time-varying magnetic field around the coil (as in TMS). According to Faraday's law of induction, these time-varying magnetic fields induce a time-varying circular electric field in the tissue. The direction of this magnetically induced electric field depends on the orientation of the magnetic coil and thus, its stimulating effect on neurons can be better controlled. **(D)** For axons running with an orientation parallel to the axis of the coil, there will be no hyperpolarizing/depolarizing membrane net effect.

result would include some amount of residual current density. An energy value calculated from this residual current density is then used as the criteria to refine the mesh. An iterative process then will follow, which refines the mesh in each step until the energy error is below a user-specified value (1% in our case). The final solution had ~630,000 mesh elements with edge length varying from 9 μm inside the tissue to 2 mm at the outer boundary the air box. The simulations converged after two adaptive passes which completed in 17 h on a Dell PowerEdge R730 with 16x32GB = 512GB of RAM, an NVIDIA K80 GPU and 28 cores (2xIntel Xeon CPU with each 14 cores) running 64-bit Windows Server 2012. Electric field values were then exported to MATLAB (The Mathworks, Inc., Natick, MA, United States) for smoothing and were used to simulate the response of neurons with different orientations below the coil.

μMS Coil Orientations

In our previous work (Bonmassar et al., 2012) we showed that response of ganglion cells to μMS could be altered by changing the coil's orientation. Specifically, we demonstrated that when the long axis of a solenoidal μMS coil was perpendicular to the surface of the excitable tissue (corresponding to **Figure 1B**), weaker neuronal responses were evoked compared to the case where the coil's long axis was parallel to the surface of the tissue. Our surgical setup at the time, however, did not allow further examination of μMS directionality when the coil was parallel to the surface of the tissue. Theoretically, the

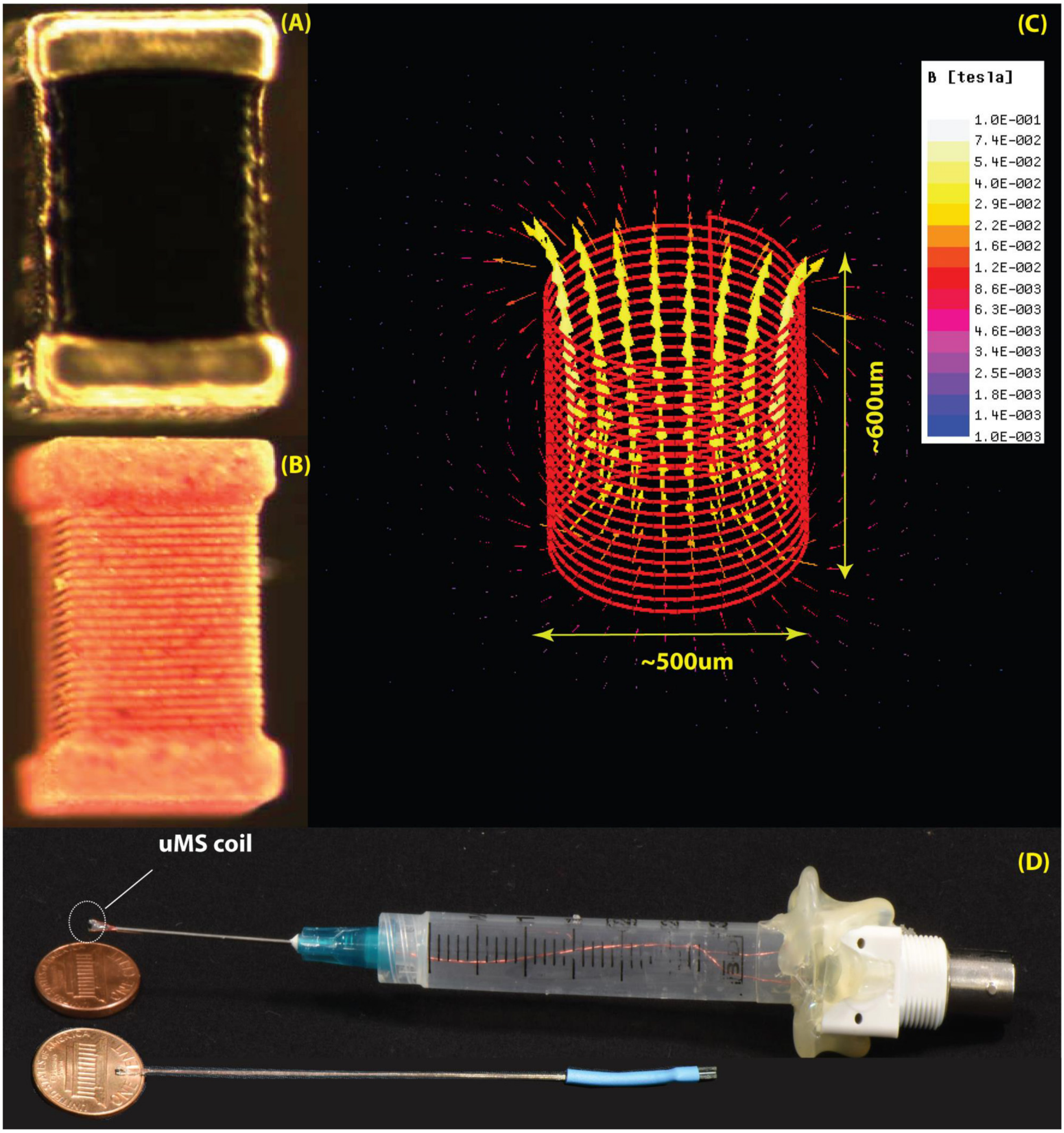

FIGURE 2 | The μMS coils. **(A)** Image of the microcoil used in the experiments. **(B)** The outer layer of the conductor was chemically removed to expose the structure of the underlying solenoid. **(C)** Model of the coil with 21 turns of 6 μm gold microwire implemented in ANSYS Maxwell 18.0. The generated magnetic field is shown for a unit current of 1 A passing through the coil. **(D)** Top: the origin used in the experiments with the microcoil mounted on a syringe connected to a BNC connector. Bottom: a more compact model recently developed.

μMS coil in a perpendicular orientation generates symmetric electric fields in the tissue underneath the coil, affecting axons with different orientations alike (see **Figure 1B**, axons with orthogonal orientations A and B experience similar electric field). This symmetry breaks down when the long axis of the coil is parallel to the surface of the tissue. In theory, the parallel μMS coil highly depolarizes axons that are located under its center and are orthogonal to its long axis (**Figure 1C**). We refer to this relative coil–axon orientation as the parallel–orthogonal orientation. In contrast,

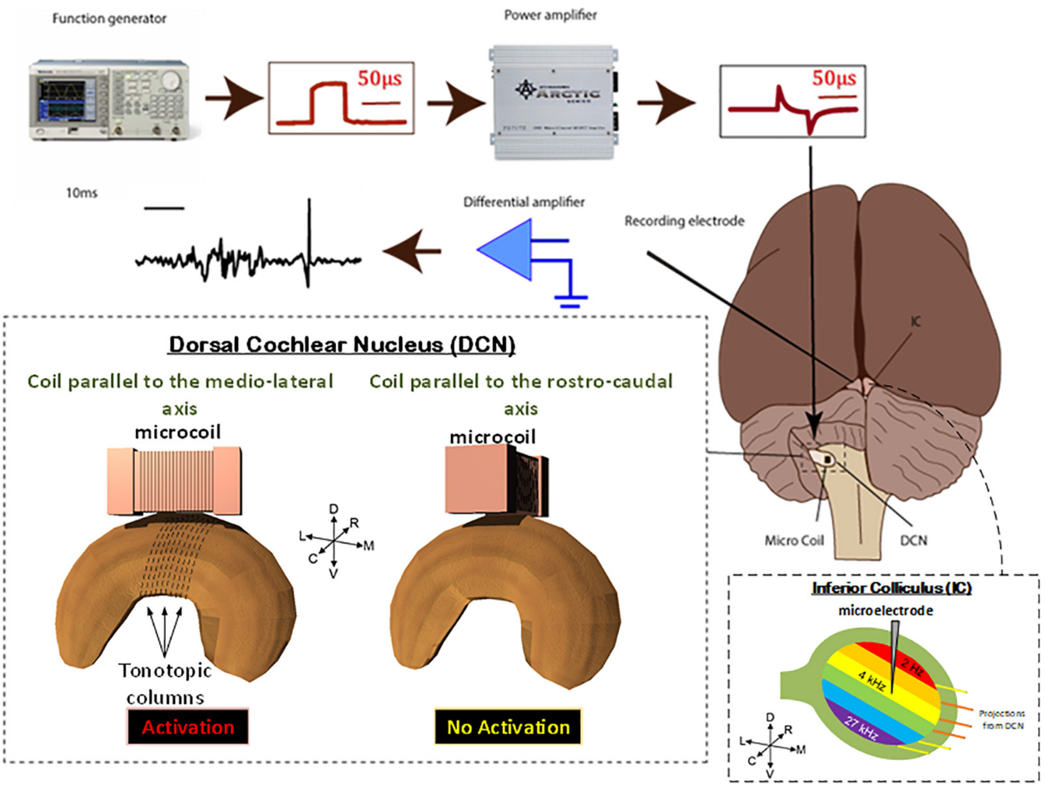

FIGURE 3 | Animal preparation. Animals were anesthetized and the DCS and IC were surgically exposed. A recording electrode was placed into the IC and a μMS coil was positioned over the DCN. Stimulation was then applied to the coils, using a function generator and amplifier as electrophysiological data were simultaneously recorded from the IC. For each animal, the coil was first oriented along the medial–lateral axis of the DCN which evoked a strong response in the IC. The coil was then pulled up, rotated 90°, and positioned back on the same spot above the DCN. The latter rostrocaudal orientation of the coil evoked a much weaker response in the IC. To assure that the changes observed in the response were not due to disconnection of coil's internal circuit during the rotation manipulation, we rotated the coil back to the medial–lateral orientation which again evoked a strong response from the IC. The stimuli were delivered to the DCN from microscopic stimulators with different orientations with respect to the long axis of the DCN: coil parallel to the medial–lateral axis will stimulate fibers in the rostrocaudal orientation (red).

axons that are oriented parallel to the long axis of the coil (parallel–parallel orientation, **Figure 1D**) experience a reduced tangential electric field along with their length and should be minimally excited. We tested this hypothesis in NEURON simulations and in rodent experiments as described below.

Neuron Modeling

A computational model of axons was built for simulation of neuronal activation for the three-dimensional electric fields obtained in the previous section. The parallel fiber axon model was assumed to have a diameter of 2 μm (Tolbert et al., 2004). Since the detailed information about the ion channels was not available, the ion channel properties were adopted from the double cable axon model of globus pallidus efferent axons (McIntyre et al., 2002; Johnson and McIntyre, 2008). In electrical or magnetic stimulation, the defining factor of axonal firing is the trans-membrane current at the nodes of Ranvier. When the transmembrane current is large enough to depolarize the membrane, an action potential initiates at the node and propagates both in the orthodromic and antidromic directions. Typically, the first node of activation is the node closest to the cathode in electrical stimulation or the coil in magnetic stimulation. In our neuronal simulation, the outgoing transmembrane current was calculated by the summation of the axonal current from the adjacent compartments in the compartmental model (Nagarajan et al., 1993; McIntyre et al., 2002; Carnevale and Hines, 2006). The axonal directional current density in each compartment is calculated by the multiplication of the axonal conductivity and the induced electric field in the axonal direction. Since the compartmental size of the double cable axon model is so small, the induced electric field in each compartment was assumed to be constant. The axons were assumed to be in a transverse plane 20 μm below the coil. The induced electric field at each compartment along the axon was obtained using bilinear interpolation of the electric field obtained in the previous section. A total of 41 axons were tested where the distance between each adjacent axon was set to 100 μm. Each axon was assumed to have 41 nodes of Ranvier, and the intermodal distance was set to 200 μm, and the center node was positioned at random distances from the coil. Regarding the orientation of the coil, we tested both the configurations where the axonal direction is parallel and orthogonal to the long axis of the coil. The software package NEURON was used to study the

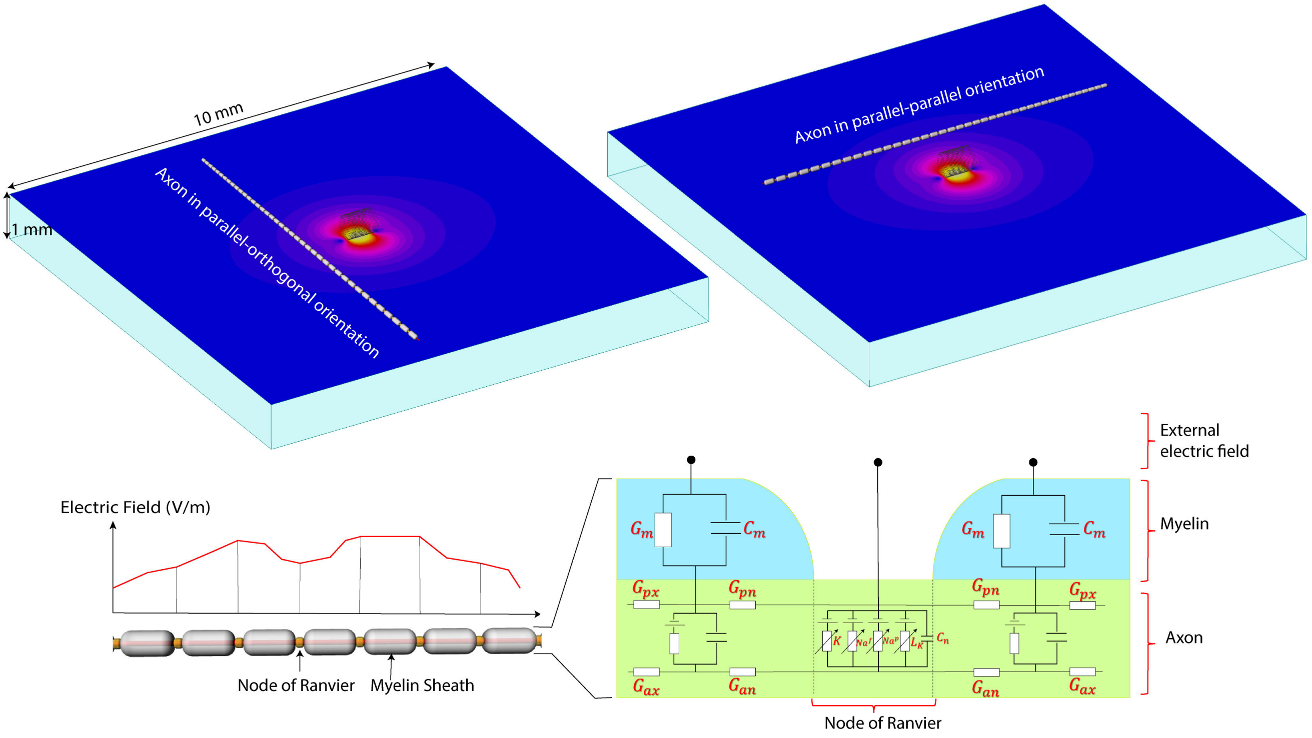

FIGURE 4 | The NEURON model. **(Top)** A computational model of the micromagnetic coil suspended over a 10 mm × 10 mm × 1 mm slab of tissue. Electric and magnetic fields are calculated inside the whole volume of tissue. Field values on a transverse plane located 20 μm below the surface of the coil were exported to simulate the behavior of neurons. **(Bottom)** Model of the axon used in NEURON simulations. The parameters for the axonal conductance (Gax), the transmembrane conductance (Gm) and capacitance (Cm), the voltage-gated ion channel membrane conductance at the Node of Ranvier was adopted from Johnson and McIntyre (2008).

neuronal responses to the induced electric fields (Carnevale and Hines, 2006).

Microcoil Construction

All microcoils were constructed to keep overall resistances below 5 Ω and inductances below 150 nH (4263B, Keysight Technologies, Santa Rosa, CA, United States) in order to ensure high stimulation efficacy. A multilayer inductor (ELJ-RFR10JFB, Panasonic Electronic Devices Corporation of America, Knoxville, TN, United States) was attached by soldering to two 34-AWG copper wires (Philmore Mfg., Rockford, IL, United States) with polyimide enamel inner coat and polyurethane overcoat. To insulate the tissue from the voltage applied and to protect against moisture, the microcoils were coated with an acrylic conformal coating (419C, MG = Chemicals, Burlington, ON, Canada) that offered high dielectric strength. The 419C Technical Data Sheet reports a thickness of 25 μm with an estimated variability of the dielectric thickness to be ± 5 μm. After curing (24 h), the insulation of the microcoil was tested by immersing the coils in a saline solution (0.9% of NaCl) and verifying that the resistance between the microcoil and an EGG electrode also dipped in the saline solution was greater than 5 MΩ (TX3, Tektronix, Inc., Beaverton, OR, United States). The microscopic stimulator was placed on the tip of a 23 AWG needle (Becton Dickinson, Franklin Lakes, NJ, United States) and the two wires inserted in the shaft/hub of the needle, and through the tip and barrel of a 3 ml syringe with the plunger that was removed and the flange end piece of the syringe was attached to a BNC connector by means of a glue gun, and electrically connected.

Magnetic Stimulation

Two adult male Syrian golden hamsters were studied in this work. All procedures performed were approved by the Institutional Animal Care and Use Committee of the Cleveland Clinic, which adheres to the NIH Guide for the Care and Use of Laboratory Animals. In each experiment, μMS coils was mounted to a micromanipulator and manually positioned so that the coil was located just above the dorsal surface of the DCN, as described by Park et al. (2013). In our *in vivo* animal experiments, the μMS coils were driven by a generator (AFG3021B, Tektronix, Inc., Beaverton, OR, United States) connected to a 1,000-W audio amplifier (PB717X, Pyramid, Inc., Brooklyn, NY, United States) with a frequency band up to 70 kHz. The output of the amplifier was connected to a BNC splitter so that the signal sent to the μMS coil was monitored with an oscilloscope (DPO3012, Tektronix, Inc., Beaverton, OR, United States). Monophasic rectangular stimulation pulses with different pulse-widths and amplitudes were triggered by an analog A/D card (NI PCIe-6251, National Instruments), with an average rate of 2 Hz. The input pulse to the power amplifier and the corresponding output waveform of

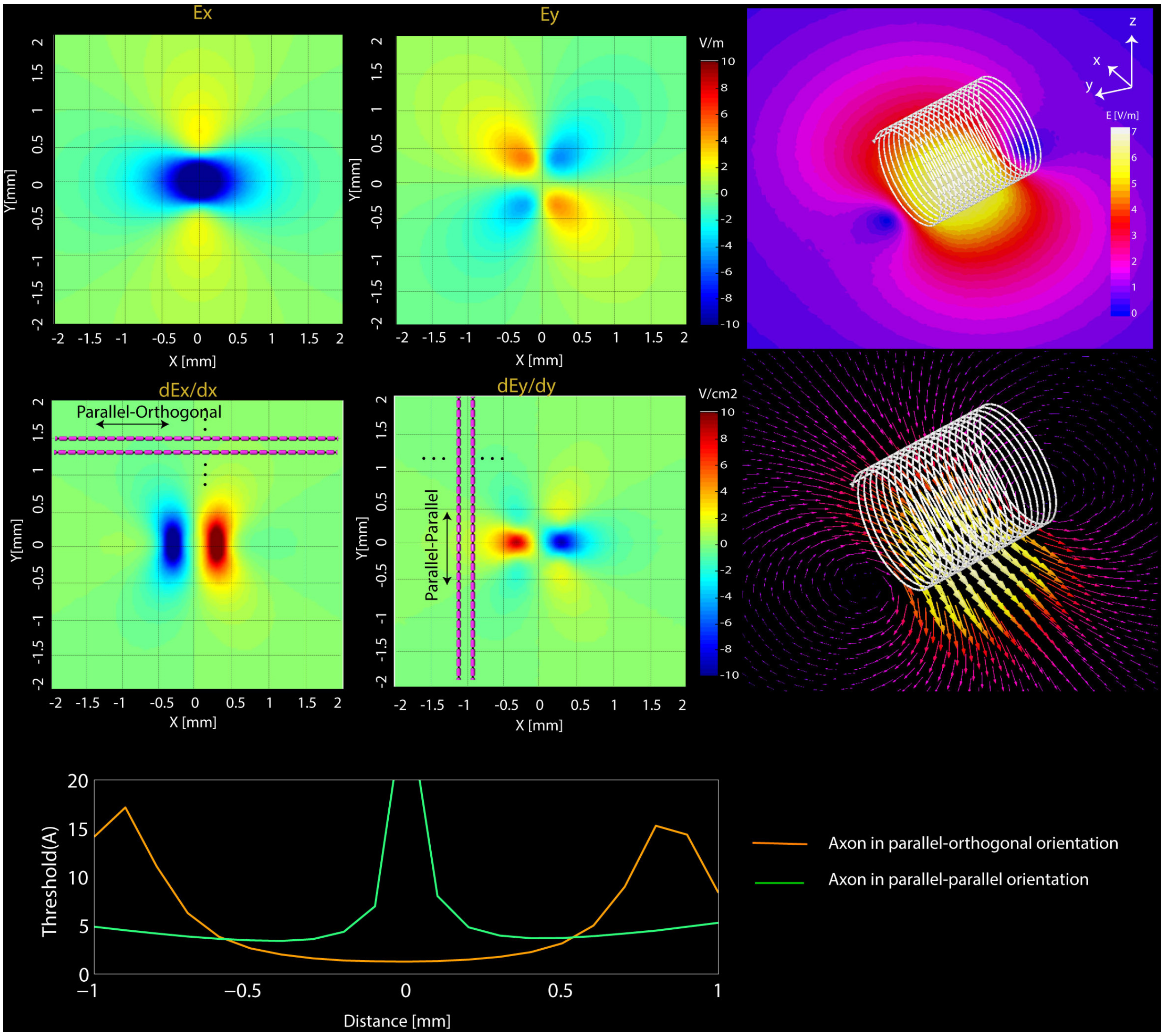

FIGURE 5 | Simulations results. **(Top)** Computational results of the magnitude of Ex and Ey and their spatial derivatives (dEx/dx, dEy/dy) on transverse planes located at 20 μm below the surface of microcoil. **(Bottom)** NEURON estimated current threshold levels for the two orientations (orange-mediolateral and blue-rostrocaudal) at various distances from the axon.

the power amplifier are shown in **Figure 3**. When referencing 'stimulus amplitude' in this paper, we indicate only the input pulse amplitude to the power amplifier. To prevent the carrying over effect from the previous trial, the order of the stimulation parameters (pulse amplitude and pulse-width) was randomized for each animal in addition to allowing 30 s resting periods between each 60 s.

Electrophysiology

Recordings were conducted at multiple sites along the tonotopic axis of the central nucleus of the contralateral IC. This region was recognized by its sharp tuning properties and by the progression from high to low-frequency selectivities as the electrode was moved along the dorsoventral axis. Methods for recording and analyzing multiunit signals were similar to those described in previous studies (Manzoor et al., 2012, 2013). Signals were filtered and amplified using an Alpha Omega (SNR, Alpha Omega, Inc., Nazareth, Israel) preamplifier. Neural signals were digitized and read off the electrode channels using a National Instruments data acquisition board and customized software written in MATLAB Software was used to synchronize data collection with acoustic stimulus delivery for tuning curve and rate vs. tone level testing and with magnetic stimulus delivery. The software also allowed selection of stimulus parameters to test stimulus–response relationships.

Acoustic Stimulation

Acoustic stimuli were needed for the dual purposes of characterizing the frequency tuning properties of recorded neurons to determine tonotopic coordinates of the IC recording

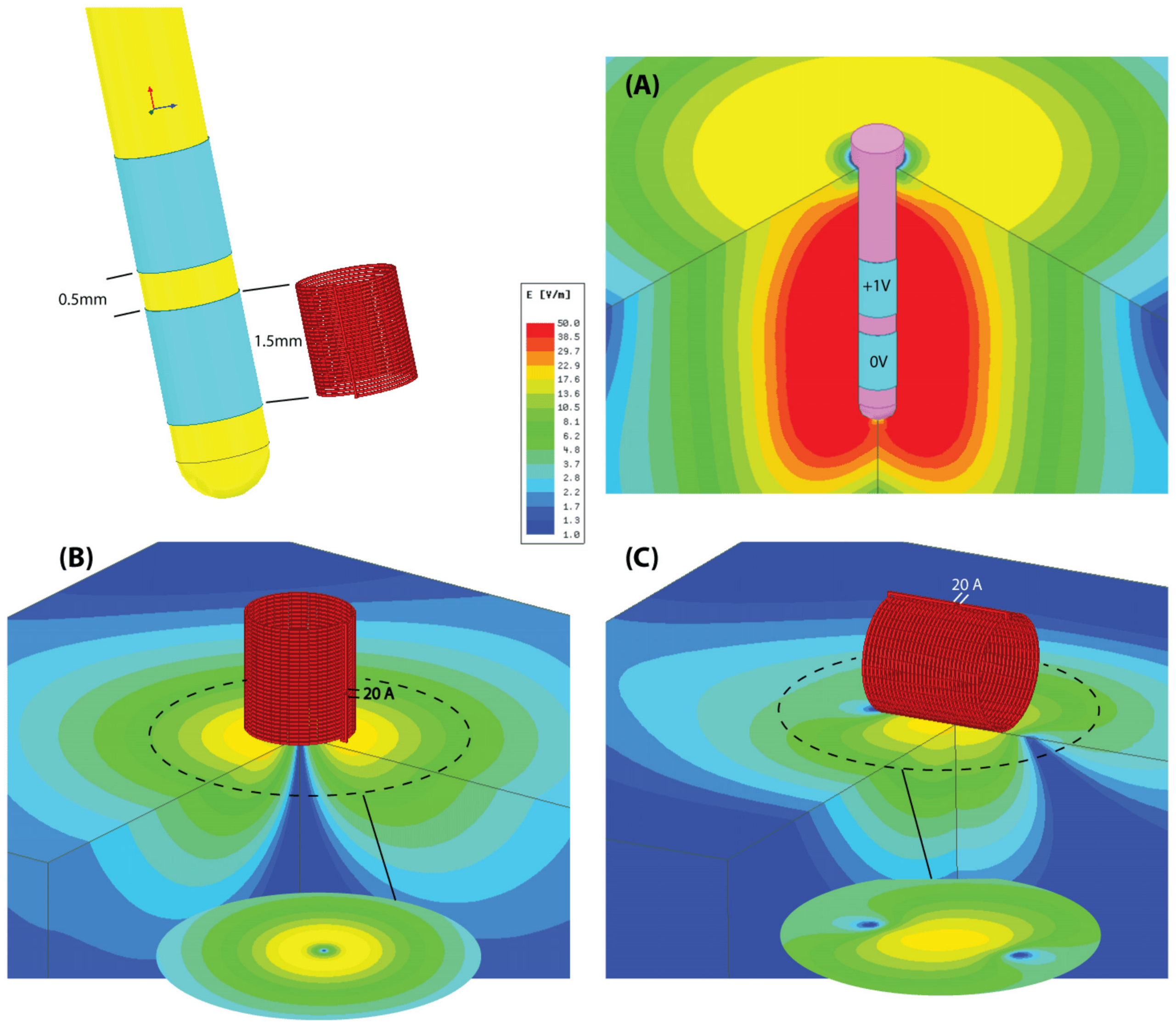

FIGURE 6 | Simulation results. Schematic comparison of the distribution of electric field produced during electric and magnetic nerve stimulation. **(A)** A conventional DBS electrode pair in bipolar configuration (electrode length, diameter, and spacing mimics the Medtronic Lead 3389). The differential voltage between anode and cathode is set to be at the lowest limit of typical values (ranging from 1 to 5 V). **(B)** A μMS coil with dimensions matching the DBS electrode. The coil is fed with 20A similar to those used in our experiments and is perpendicular to the surface of the tissue. The electric field is symmetrical, but is confined to an annulus region under the coil. **(C)** A μMS parallel to the surface of the tissue. The electric field is mostly confined to a region beneath the coil and it's asymmetric, leading to different neural activation thresholds depending on neurons' axonal direction.

electrodes, and also to examine effects of changing the acoustic stimulus conditions on IC responses. For both measures, we used 40 ms tone bursts (5 ms rise/fall times, 40 ms interstimulus intervals). For testing the tuning properties, we used a battery of 800 tone bursts varied in frequency from 3 to 32 kHz and in intensity from 6 to 96 dB SPL as previously described (Finlayson and Kaltenbach, 2009).

Data Analysis

Samples of activity recorded from IC neurons were obtained from 100 to 150 repetitive stimuli and plotted as a function of time. The resulting time sweeps were used to compare responses during and following stimulation with the activity level recorded during the prestimulus period and to derive measures of several response characteristics, such as amplitude and magnetic coil orientation. Each of these measures was obtained for each of the parameters of stimulation that were tested and were compared with responses to baseline activities stimulation. Specifically, for each stimulation parameter (Amplitude and Orientation) baseline activities (15 ms before each stimulation pulse) were compared to stimulation response (15 ms following stimulation artifact; 17–32 ms). To facilitate comparisons, the absolute value of raw electrophysiological activities were summed for the baseline and stimulus–response periods for each stimulus delivered. Significant differences in responses for each parameter were compared using parametric ANOVA with Bonferroni corrections. In each analysis, responses were compared to their baseline activities and then tested relative to each amplitude or orientation.

RESULTS

We have explored the effects of coil orientation on the resulting stimulation capabilities both with numerical simulations and with animal studies.

Numerical Simulations

The use of magnetic fields to induce electric fields or currents in the tissue from a distance is extremely inefficient from an energy standpoint. We hypothesize that much smaller energy than TMS may be required for neural stimulation at a microscopic level. One important difference between $\vec{E}$ and $\vec{H}$ is that the magnitude of the latter is well-known to fall much more rapidly in space (e.g., quadratic vs. cubic law for an electric vs. magnetic dipole in empty space). Our hypothesis is based on the prediction by various activation models (Warman et al., 1992) that the gradient of the E field, is primarily responsible for neural stimulation. The FEM simulations confirm that the electric field gradient (i.e., 10^5 V/m^2) induced by a peak voltage of 35 V driven μMS in the physiological solution at the distances of 20 μm below the microcoil is comparable to the electric field gradient (i.e., 7.6×10^5 V/m^2) generated by a stimulation peak voltage of 5 V driven DBS electrode set (Astrom et al., 2015). In contrast, the electric field gradient sensitivity threshold for peripheral nerve stimulation in MRI (Koshtoiants Kh, 1957; Schaefer et al., 2000; Bencsik et al., 2007) is much smaller (Blake et al., 2014) (i.e., 150 V/m^2) and can become near zero in quasi-uniform electric field modes such as in TMS (Barker et al., 1985; Bikson et al., 2013), given distance between the coil and the stimulated target region, which is referred to as the electric "farfield." This farfield is hypothesized to produce stimulation through bends of the axon's trajectory (Sheĭkh-Zade et al., 1987). Thus, the neuronal stimulation mode based on electric field gradient or "nearfield" is dominant for μMS, albeit farfield or combination of these two modes may also play a role for neurons further away.

The FEM simulations also predict that solenoidal μMS coils placed parallel to the surface of the tissue are capable of differentially activating neurons based on their axonal direction. It is established that neural activation function is proportional to the spatial derivative of the electric field along the axon's axis (Roth and Basser, 1990). Our electromagnetic simulations predicted that the spatial derivative of electric field reached values up to three times higher for axons orientated in parallel–orthogonal orientation than for those oriented in parallel–parallel position (**Figure 5**, top). Similarly, NEURON simulations predicted that the axons whose direction is perpendicular to the long axis of the coil have a lower threshold compared to the axons parallel to the coil (**Figure 5**, bottom). The reason for lower threshold underneath the microcoil is that when the axons are parallel to the induced electric field the axonal activation is maximized since the activating function of an axon is the spatial derivate of the induced electric field along the axon. On the contrary, when the axonal direction is perpendicular to the induced electric field, the gradient of the electric field along the axonal direction becomes very small. Therefore, perpendicular coil orientation requires a much higher current threshold for the axonal activation underneath the coil. However, on the edges of the microcoil, there is a sudden change in the induced electric field due to its small size resulting in the increased activating function.

Importantly, and as demonstrated here, μMS provides a unique opportunity over electrical stimulation techniques in that neural interfaces can be constructed that take advantage of the orientation properties provided by magnetic stimulation. Namely, the construction of brain stimulation leads that maximally active the target tissue while mitigating the activation of fibers in the passage would have a significant advantage in DBS therapies, as the activation of fibers of passage represents the greatest side-effects for patients. Likewise, μMS coils could be used to provide more spatial resolution over existing electrical stimulation strategies, by designing interfaces that account for the orientation of the coils relative to the target tissue to be activated. This can be better appreciated from **Figure 6**, illustrating the schematic of the electric field distribution produced by (A) a conventional DBS electrode pair in bipolar configuration and (B,C) same-sized μMS coils in perpendicular and parallel positions. It can be observed from the figure that even for a DBS voltage as low as 1 V (typical values range from 1 to 5 V) the electric field produced by the electrode pair covers a large symmetric area containing both electrode contacts. The electric field of the μMS coil on the other hand, is more confined to the edges at the periphery of the coil when the coil is perpendicular to the tissue, and to the center of the solenoid when the coil is parallel to the tissue. Specifically, when the coil is in parallel position the induced electric field is asymmetric, indicating different sensitivity for neuron activation depending on their axonal direction. Moreover, we speculate that our modeling also brings up the notion that the mechanisms of action of magnetic stimulation may be fundamentally different from that of electrical stimulation. Specifically, the ionic movement of charge that ultimately results in neuronal activation operates differently between magnetic and electrical stimulation. In electrical stimulation, the current flow from pole to pole of the electrical stimulator while in magnetic stimulation the induced current flows as eddy currents relative to the magnetic fields. Electrical stimulation activates neural elements by operating on the electric potential of the extracellular matrix and manipulating the transmembrane potentials. In contrast, eddy currents act not only upon the extracellular matrix but also on the intracellular matrix as the magnetic stimulation fields penetrate the cellular compartments.

In general, μMS operates similarly to TMS generating time-varying magnetic fields and inducing electric fields in the brain, which can stimulate surrounding cortical or subcortical neurons (Walsh and Cowey, 2000), albeit at a microscopic scale. As TMS, which is presently the method of choice to investigate causal functional interactions across macroscopic brain regions, μMS can be used to investigate microscopic neuronal interactions at a cell level and as such can further the aim of developing innovative technologies to understand the human brain and treat its disorders.

Animal Experiments

Recently it has been demonstrated that μMS is capable of eliciting neuronal activation in both retinal ganglion cells *in vitro* (Bonmassar et al., 2012) and IC neurons *in vivo* (Park et al., 2013). In the *in vitro* experiments, performed in a retinal cell preparation, it was demonstrated that neuron action potentials could be elicited by μMS. It was also demonstrated that neuronal activation was amplitude dependent, where higher amplitudes of simulation resulted in greater activation. Also, the orientation of the coils relative to the neural substrate resulted in a different activation pattern, where perpendicular orientations of the coil resulted in minimal activation and parallel orientations resulted in maximal activation. In the *in vivo* experiments, it was demonstrated that μMS of the DCN resulted in the generation of neuronal activities in the IC and in the cochlea. The *in vivo* experiments have recently been extended to the feline cochlea (Lee and Fried, 2017). Hence, μMS can elicit neuronal activation within an interconnected neural circuit and is not restricted to modulation of only local circuitry. Despite these results, some key issues need to be addressed before μMS can be further translated to chronic neuromodulation therapies, including the effect of coil orientation *in vivo* experiments.

The microcoil prototypes we tested in this study reproducibly activated the brain, *in vivo*, in a tissue-appropriate manner consistent with the known microcircuitry of the DCN and projection patterns that link the DCN to the IC. Two adult male Syrian golden hamsters were studied, and all surgical procedures used to expose the DCN and IC were the same as previously described (Manzoor et al., 2012, 2013). The microcoils produced responses that were typically manifested in the contralateral IC as bursts or barrages of spike-like waveforms in the first 15–20 ms of the post-stimulus period (**Figure 7**). The responses to the microcoils placed just above but not in contact with the DCN surface produced well-defined activity that resembled the spike-like multiunit responses observed during sound stimulation (Kaltenbach and McCaslin, 1996; Kaltenbach and Afman, 2000).

In a set of experiments, we examined the effect of coil orientation on neuronal activation properties. Two different orientations of the microcoils were studied, one with the long axis of the μMS parallel to the long (medial–lateral or tonotopic) axis of the DCN (**Figure 3**, bottom), and the other with the long axis of the μMS coil parallel to the rostrocaudal axis of the DCN (i.e., parallel to the isofrequency bands) (**Figure 3**, bottom). Strong IC responses were observed for microcoil orientations parallel to the medial–lateral axis of the DCN, while weaker or absent responses for the orthogonal orientations (**Figure 7**, top). In animal 2 (**Figure 7**, bottom), both the medial–lateral orientations were different from the rostral–caudal orientation but were not different from animal 1.

An important aspect of our results that was unexpected was the dependence of the strength of the IC response on the rotational angle of the microcoil above the DCN. IC responses were vigorous when the long axis of the microcoil was parallel to the medial–lateral axis of the DCN but weak for micro-stimulator orientations parallel to the rostrocaudal axis. This difference implies contrasting levels of efficacy in stimulus–response coupling between the different micro-stimulator orientations. The simplest mechanism to explain this results is that micro-stimulator orientations parallel to the medial–lateral axis of the DCN more effectively excite the main output neurons of the DCN, the fusiform cells, which project to the contralateral IC (Beyerl, 1978; Ryugo and Willard, 1985; Cant and Benson, 2003). This greater effectiveness of activation may occur because any stimulation that fusiform cells receive may receive input directly from the fibers running along the tonotopic columns of the DCN that are activated by the microcoil in the medial–lateral axis orientation (Mugnaini et al., 1980; Blackstad et al., 1984; Manis, 1989; Kanold and Young, 2001) and potentiate the responses of fusiform cells to other inputs (Fujino and Oertel, 2003; Tzounopoulos et al., 2007). Activation of fibers running along the tonotopic column would be expected to be greater when the axis of the micro-stimulator is perpendicular to the axes of the tonotopic column, thus parallel to the medial–lateral axis, as shown by our numerical simulations results. At the present juncture, we have not yet elucidated precise targets of the stimulation of the DCN circuitry. Multiple neural populations in the ventral cochlear nucleus (VCN) also project to the IC and interact with the DCN circuitry as well. These polysynaptic pathways are potential targets and possibly underlie the generation of late-onset responses in the IC.

DISCUSSION

There are some limitations that currently limit the efficacy and safety of electrical stimulation. First, electric currents delivered by microelectrodes can spread to undesired areas adjacent to the targeted structures, leading to unintended side effects (Histed et al., 2009; Behrend et al., 2011; Licari et al., 2011; Weitz et al., 2015). For example, imprecise targeting of the subthalamic nucleus (STN) due to current spread to neighboring white matter tracts during DBS in Parkinson's patients can lead to undesirable motor and sensory responses (Li et al., 2016). In this work, we show that unlike electrical stimulation μMS has the potential of being able to stimulate target nuclei in the brain without affecting the surrounding white matter tracts. Neuronal processes such as axons parallel to the direction of the electric current density $\vec{J}$ are depolarized or hyperpolarized depending on the direction and strength of $\vec{J}$, but the processes transverse to the $\vec{J}$ are not affected (Beurrier et al., 2001). Thus, the magnetic stimulation via μMS is capable of synaptically activating or inhibiting neurons in a spatially oriented manner. One aspect of the directionality of μMS was shown *in vitro* (Serano et al., 2015), where depending on the direction of the magnetic field flux the axon of the ganglion cell beneath the coil showed the generation of action potentials recorded by the patch clamping technique. In this work, we also expand this finding to our *in vivo* rodent model, showing for the first time, our ability to stimulate the brain stem of a rodent with a net sensitivity

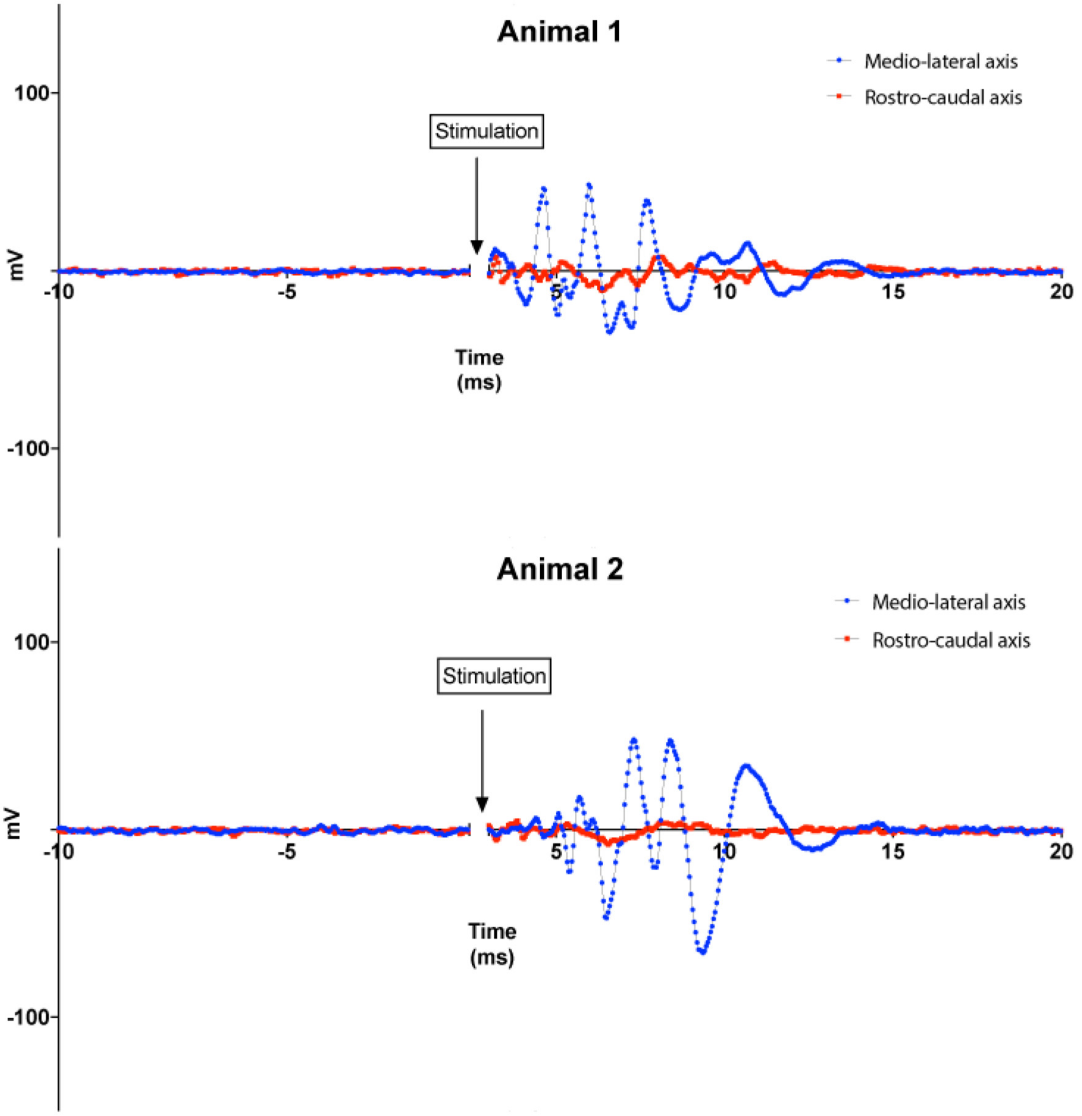

FIGURE 7 | Animal experiments results. Top: responses of the IC to magnetic stimuli delivered to the DCN from microscopic stimulators with different orientations with respect to the long axis of the DCN. Blue lines: microcoil oriented parallel to the medial–lateral (tonotopic) axis of the DCN. Red lines: microcoil oriented perpendicular to the medial–lateral axis of the DCN. Recordings from two animals are shown for each orientation. Each curve represents the average of 100 trials performed for each coil orientation on each animal.

to the directionality of the magnetic flux. A similar μMS-orientation sensitivity was shown (Lee and Fried, 2017) in layer V pyramidal neurons (PNs) and the asymmetric fields arising from such microcoils did not simultaneously activate horizontally oriented axon Furthermore, μMS was shown to stimulate in confined narrow regions (<60 μm) cortical pyramidal neurons in brain slices *in vitro*, which helped to avoid the simultaneous activation of passing axons (Mehta and Oxenham, 2017). μMS coils were also surgically introduced 8–10 mm into the cochlea of anesthetized deafened felines (Lee and Fried, 2017), thus unresponsive to acoustic stimuli, and auditory responses were then recorded during magnetic stimulation. These experiments were aimed at showing that magnetic field steerability of μMS may solve the low-resolution stimulation shortcomings of the state-of-the-art cochlear implants that are limited by their ability to reproduce accurately pitch in music and speech in the presence of background noise, which instead may require as much as four times the number of channels currently available (Mehta and Oxenham, 2017). In the cochlea (Macherey and Carlyon, 2014) as well as in cortex (Matteucci et al., 2016) stimulation resolution is limited by the channel to channel cross-talk rather than electrode sub-millimeter size and spacing. μMS has shown the ability to selectively activate neurons by different orientations, thus a μMS coil in a single position can activate different neurons by rotation, thus increasing the spatial resolution.

Second, unlike electrical stimulation, μMS does not require direct galvanic contact with the tissue. For an electrode pair (**Figure 1A**) to generate current, it needs to be placed in direct contact with a conductive media (e.g., excitable tissue). In a bipolar electrode pair, the 'anode' or source (**Figure 1A**, plus sign) injects a current and hyperpolarizes the neuronal membrane toward more negative potential which can arrest the neural action, whereas the 'cathode' acts as a sink and depolarizes the axon membrane which could trigger an action potential (**Figure 1A**, minus sign). However, the metal electrode implanted in the tissue may lead to oxidation–reduction reaction at the electrode-tissue interface changing the pH of surrounding tissue which may provoke an immune response. Histopathology analysis has shown gliosis and spongiosis around the stimulation electrode track (Caparros-Lefebvre et al., 1994), which formed an encapsulation layer referred to as the "glial scar." With μMS however, the solenoidal coil (**Figures 1B–D**) can induce a current from a distance, without placing a metal in direct contact with the tissue and new materials may allow for soft coils development (Wang et al., 2000). The pulsed current passing through the coil generates a time-varying magnetic field $\vec{B}$ inside and in the space surrounding the coil. In the conductive tissue, this time-varying magnetic field $\vec{B}$, in turn, generates an orthogonal current density $\vec{J}$ capable of evoking neuronal action potentials (**Figures 1B–D**), according to Faraday's Law [i.e., $\frac{1}{\sigma}\nabla \times \vec{J} = -\frac{\partial \vec{B}}{\partial t}$ in homogeneous isotropic medium where $\nabla\times$ is the curl operator and σ is, the tissue conductivity, albeit the brain has tissues with anisotropic conductivities (Tuch et al., 1999)]. A number of studies have shown that the magnetically induced currents can directly excite axons as long as the spatial gradient of the induced electric field is strong enough to generate a transmembrane potential above the threshold (Roth and Basser, 1990; Basser and Roth, 1991; Pashut et al., 2011). The exact threshold depends on the axon's geometry such as the diameter and its geometrical shape (Pashut et al., 2011), the pulse width (Basser and Roth, 1991), size and shape of the electrodes, etc. Furthermore, even though electric stimulation affects the myelinated neurons in the nodes of Ranvier, μMS can theoretically stimulate a myelinated axon anywhere within its length. Modulation of neuronal activation or inhibition can also be potentially achieved in μMS by driving specific waveforms (e.g., sharp rising edges followed by slowly falling dips, and vice versa), producing asymmetric induced current pulses in the tissue.

Finally, unlike electrical stimulation μMS does not require a charge-balanced stimulation waveform. In electrical stimulation, charge balancing is necessary to avoid excessive charge accumulation at the neural interface, and thus undesired stimulation and electroporation (Nduka et al., 2017). Electroporation occurs when the external electric field of the membrane potential of the cell exceeds a 0.2–1 V threshold, which leads to a change in the molecular structure of the membrane, and a subsequent membrane perforation with pore formation increasing the membrane permeability to ions, and molecules (Chen et al., 2006). Electroporation with a transmembrane potential of approximately 1 V could cause necrosis, due to membrane rupture and the subsequent cytoplasmic contents leakage (Sale and Hamilton, 1968; Neumann and Rosenheck, 1972; Crowley, 1973). In μMS, no net charge is transferred from the electrode into tissue since neither sinks nor sources are present when a current density $\vec{J}$ is induced by the time-varying magnetic field. The current density in the tissue $\vec{J}$ is a rotating field that mirrors the current direction in the coil (**Figure 1B**). Because the induced electric field is a solenoidal or incompressible vector field in three dimensions, μMS does not suffer from charge buildup (Bonmassar et al., 2012).

Despite these specific limitations, electrically based DBS has been tremendously successful. However, the application of μMS could mitigate some of the challenges of these limitations. Theoretically, and supported by limited data (Bonmassar et al., 2012), it is possible that specific orientations of magnetic fields relative to different neural substrates may result in differential neuronal response patterns. If demonstrated to be a valid property of magnetic stimulation, this would open the possibility of custom designing μMS coils in a way to maximize the stimulation of the intended target and minimizing the activation of unintended targets. In the case of DBS for movement disorders, the primary cause of side-effects is the unintended activation of fibers of passage. Namely, with STN stimulation the activation of the internal capsule, adjacent and lateral to the STN, or activation of the medial lemniscus fibers, medial to the STN, can cause muscle contracts or paresthesia respectively. Even if therapeutic efficacy is seen in a patient, it is possible that activation of these fibers of passage can limit the ultimate therapeutic effect, as the threshold of the side-effect may be less than the threshold for therapeutic benefit. The unintended activation of fibers of the passage is not unique to STN stimulation, as the unintended activation of the internal capsule is also seen with DBS of the ventral intermediate nucleus of the thalamus and globus pallidus internus, which are the other primary targets for DBS therapy for Parkinson's disease. Hence, if it is demonstrated that orientation of magnetic fields has differential effects on the activation of axonal fibers, one can propose to custom design μMS coils to take advantage of this unique property. As this property is not directly achievable with electrical stimulation based technologies, it would provide a new avenue to improve outcomes and mitigate side-effects beyond the other limitation previously discussed between electrical and magnetic stimulation based approaches.

CONCLUSION

Microscopic magnetic stimulation (μMS) could potentially become the pacemaker and brain stimulator of the future with their contactless ability to deliver the neuronal stimulation needed for therapeutic efficacy in patients with Parkinson's disease, epilepsy, in need of implantable cardioverter-defibrillators or pacemakers, and so forth. Due to recent advancements in micro-machining technologies, we can now utilize manufactured inductors (or coils) constructed on the sub-millimeter scale to produce magnetic fields. Such coils would offer several advantages over classical electrical and TMS techniques. Unlike TMS coils, the coils are sub-millimeter in size and can be placed within or near a neuronal substrate, increasing spatial resolution and reducing the power needed to evoke neuronal activity. Moreover, because the coils are not in direct contact with the tissue and no current is directly injected into the tissue, they may overcome the inflammatory tissue encapsulation and mitigate charge buildup issues inherent in traditional electrical stimulation technologies. Our data indicate that these microcoils can activate neuronal activity with high degrees of spatial and temporal resolution and that the orientation of the coils relative to the tissue activated can be used to activate specific elements optimally and to avoid the activation of others. Future work will concentrate on developing specific neural models of the target structures to quantify the parameters of μMS for directional stimulation, and include more animal models to establish the statistical features of the neural response.

ETHICS STATEMENT

This study was carried out in accordance with the recommendations of Public Health Service (PHS) Policy on Humane Care and Use of Laboratory Animals and the Animal Welfare Act. The protocol was approved by the institutional animal care and use committee (IACUC) Committee of the Cleveland Clinic.

AUTHOR CONTRIBUTIONS

LaG, JG, JK, and GB conceptualized the study; provided support and guidance with data interpretation. H-JP designed and performed the NEURON analyses with support from LaG and JK. NM and LyG designed and performed the animal experiments with support from JK and H-JP. LaG and GB contributed electromagnetic data analysis and visualization software. FH built the μMS coils. LaG wrote the manuscript, with contributions from GB and comments from all other authors.

FUNDING

This work was supported by the US National Institutes of Health (NIH) grants R43MH107037 (FH, JG, GB, and JK), R01MH111875 (GB), and K99EB021320 (LaG).

REFERENCES

Astrom, M., Diczfalusy, E., Martens, H., and Wardell, K. (2015). Relationship between neural activation and electric field distribution during deep brain stimulation. *IEEE Trans. Biomed. Eng.* 62, 664–672. doi: 10.1109/TBME.2014.2363494

Ayton, L. N., Blamey, P. J., Guymer, R. H., Luu, C. D., Nayagam, D. A., Sinclair, N. C., et al. (2014). First-in-human trial of a novel suprachoroidal retinal prosthesis. *PLoS One* 9:e115239. doi: 10.1371/journal.pone.0115239

Barker, A. T., Jalinous, R., and Freeston, I. L. (1985). Non-invasive magnetic stimulation of human motor cortex. *Lancet* 1, 1106–1107. doi: 10.1016/S0140-6736(85)92413-4

Basser, P. J., and Roth, B. J. (1991). Stimulation of a myelinated nerve axon by electromagnetic induction. *Med. Biol. Eng. Comput.* 29, 261–268. doi: 10.1007/BF02446708

Behrend, M. R., Ahuja, A. K., Humayun, M. S., Chow, R. H., and Weiland, J. D. (2011). Resolution of the epiretinal prosthesis is not limited by electrode size. *IEEE Trans. Neural Syst. Rehabil. Eng.* 19, 436–442. doi: 10.1109/TNSRE.2011.2140132

Benabid, A. L. (2003). Deep brain stimulation for Parkinson's disease. *Curr. Opin. Neurobiol.* 13, 696–706. doi: 10.1016/j.conb.2003.11.001

Bencsik, M., Bowtell, R., and Bowley, R. (2007). Electric fields induced in the human body by time-varying magnetic field gradients in MRI: numerical calculations and correlation analysis. *Phys. Med. Biol.* 52, 2337–2353. doi: 10.1088/0031-9155/52/9/001

Beurrier, C., Bioulac, B., Audin, J., and Hammond, C. (2001). High-frequency stimulation produces a transient blockade of voltage-gated currents in subthalamic neurons. *J. Neurophysiol.* 85, 1351–1356. doi: 10.1152/jn.2001.85.4.1351

Beyerl, B. D. (1978). Afferent projections to the central nucleus of the inferior colliculus in the rat. *Brain Res.* 145, 209–223. doi: 10.1016/0006-8993(78)90858-2

Bikson, M., Dmochowski, J., and Rahman, A. (2013). The "quasi-uniform" assumption in animal and computational models of non-invasive electrical stimulation. *Brain Stimul.* 6, 704–705. doi: 10.1016/j.brs.2012.11.005

Blackstad, T. W., Osen, K. K., and Mugnaini, E. (1984). Pyramidal neurones of the dorsal cochlear nucleus: a Golgi and computer reconstruction study in cat. *Neuroscience* 13, 827–854. doi: 10.1016/0306-4522(84)90099-X

Blake, D. T., Bhatti, P. T., Beek-King, J. V., Crawford, J., and McKinnon, B. (2014). "Micro magnetic stimulation of the feline cochlea," in *Proceedings of the 13th International Conference on Cochlear Implants and Other Implantable Auditory Technologies*, Munich, S4–S8.

Bonmassar, G., Lee, S. W., Freeman, D. K., Polasek, M., Fried, S. I., and Gale, J. T. (2012). Microscopic magnetic stimulation of neural tissue. *Nat. Commun.* 3:921. doi: 10.1038/ncomms1914

Butson, C. R., and McIntyre, C. C. (2006). Role of electrode design on the volume of tissue activated during deep brain stimulation. *J. Neural Eng.* 3, 1–8. doi: 10.1088/1741-2560/3/1/001

Cant, N. B., and Benson, C. G. (2003). Parallel auditory pathways: projection patterns of the different neuronal populations in the dorsal and ventral cochlear nuclei. *Brain Res. Bull.* 60, 457–474. doi: 10.1016/S0361-9230(03)00050-9

Caparros-Lefebvre, D., Ruchoux, M. M., Blond, S., Petit, H., and Percheron, G. (1994). Long-term thalamic stimulation in Parkinson's disease: postmortem anatomoclinical study. *Neurology* 44, 1856–1860. doi: 10.1212/WNL.44.10.1856

Carnevale, N. T., and Hines, M. L. (2006). *The Neuron Book*. Cambridge: Cambridge University Press. doi: 10.1017/CBO9780511541612

Chen, C., Smye, S. W., Robinson, M. P., and Evans, J. A. (2006). Membrane electroporation theories: a review. *Med. Biol. Eng. Comput.* 44, 5–14. doi: 10.1007/s11517-005-0020-2

Clare McElcheran, L. G., and Graham, S. (2014). "Reduced heating of implanted electrical conductors using parallel radiofrequency transmission," in *Proceedings of the Joint Annual Meeting of the International Society of Magnetic Resonance in Medicine (ISMRM)*, Milan.

Condon, B., and Hadley, D. M. (2000). Potential MR hazard to patients with metallic heart valves: the Lenz effect. *J. Magn. Reson. Imaging* 12, 171–176. doi: 10.1002/1522-2586(200007)12:1<171::AID-JMRI19>3.0.CO;2-W

Crowley, J. M. (1973). Electrical breakdown of bimolecular lipid membranes as an electromechanical instability. *Biophys. J.* 13, 711–724. doi: 10.1016/S0006-3495(73)86017-5

Deng, Z.-D., Lisanby, S. H., and Peterchev, A. V. (2013). Electric field depth–focality tradeoff in transcranial magnetic stimulation: simulation comparison of 50 coil designs. *Brain Stimul.* 6, 1–13. doi: 10.1016/j.brs.2012.02.005

Deuschl, G., Schade-Brittinger, C., Krack, P., Volkmann, J., Schäfer, H., Bötzel, K., et al. (2006). A randomized trial of deep-brain stimulation for Parkinson's disease. *N. Engl. J. Med.* 355, 896–908. doi: 10.1056/NEJMoa060281

Ellenbogen, K. A., and Wood, M. A. (2008). *Cardiac Pacing and ICDs*, 5th Edn, Vol. IX. Hoboken, NJ: Blackwell Publishing, 558.

Finlayson, P. G., and Kaltenbach, J. A. (2009). Alterations in the spontaneous discharge patterns of single units in the dorsal cochlear nucleus following intense sound exposure. *Hear. Res.* 256, 104–117. doi: 10.1016/j.heares.2009.07.006

Fujino, K., and Oertel, D. (2003). Bidirectional synaptic plasticity in the cerebellum-like mammalian dorsal cochlear nucleus. *Proc. Natl. Acad. Sci. U.S.A.* 100, 265–270. doi: 10.1073/pnas.0135345100

Gifford, R. H. (2013). *Cochlear Implant Patient Assessment: Evaluation of Candidacy, Performance, and Outcomes. Core Clinical Concepts in Audiology*. San Diego, CA: Plural Publishing, 144.

Golestani-Rad, L., Elahi, B., and Rashed-Mohassel, J. (2007). Investigating the effects of external fields polarization on the coupling of pure magnetic waves in the human body in very low frequencies. *Biomagn. Res. Technol.* 5:3. doi: 10.1186/1477-044X-5-3

Golestanirad, L., Dlala, E., Wright, G., Mosig, J. R., and Graham, S. J. (2012a). Comprehensive analysis of Lenz Effect on the artificial heart valves during magnetic resonance imaging. *Prog. Electromagn. Res.* 128, 1–17. doi: 10.2528/PIER12031505

Golestanirad, L., Elahi, B., Molina, A., Mosig, J. R., Pollo, C., Chen, R., et al. (2013). Analysis of fractal electrodes for efficient neural stimulation. *Front. Neuroeng.* 6:3. doi: 10.3389/fneng.2013.00003

Golestanirad, L., Iacono, M. I., Keil, B., Angelone, L. M., Bonmassar, G., Fox, M. D., et al. (2017a). Construction and modeling of a reconfigurable MRI coil for lowering SAR in patients with deep brain stimulation implants. *Neuroimage* 147, 577–588. doi: 10.1016/j.neuroimage.2016.12.056

Golestanirad, L., Izquierdo, A. P., Graham, S. J., Mosig, J. R., and Pollo, C. (2012b). Effect of realistic modeling of deep brain stimulation on the prediction of volume of activated tissue. *Prog. Electromagn. Res.* 126, 1–16. doi: 10.2528/PIER12013108

Golestanirad, L., Keil, B., Angelone, L. M., Bonmassar, G., Mareyam, A., and Wald, L. L. (2017b). Feasibility of using linearly polarized rotating birdcage transmitters and close-fitting receive arrays in MRI to reduce SAR in the vicinity of deep brain simulation implants. *Magn. Reson. Med.* 77, 1701–1712. doi: 10.1002/mrm.26220

Golestanirad, L., Mattes, M., Mosig, J. R., and Pollo, C. (2010). Effect of model accuracy on the result of computed current densities in the simulation of transcranial magnetic stimulation. *IEEE Trans. Magn.* 46, 4046–4051. doi: 10.1109/TMAG.2010.2082556

Golestanirad, L., Rouhani, H., Elahi, B., Shahim, K., Chen, R., Mosig, J. R., et al. (2012c). Combined use of transcranial magnetic stimulation and metal electrode implants: a theoretical assessment of safety considerations. *Phys. Med. Biol.* 57:7813. doi: 10.1088/0031-9155/57/23/7813

Histed, M. H., Bonin, V., and Reid, R. C. (2009). Direct activation of sparse, distributed populations of cortical neurons by electrical microstimulation. *Neuron* 63, 508–522. doi: 10.1016/j.neuron.2009.07.016

Howland, R. H. (2008). Neurosurgical approaches to therapeutic brain stimulation for treatment-resistant depression. *J. Psychosoc. Nurs. Ment. Health Serv.* 46, 15–19.

Humayun, M. S., Dorn, J. D., da, Cruz L, Dagnelie, G., Sahel, J. A., Stanga, P. E., et al. (2012). Interim results from the international trial of Second Sight's visual prosthesis. *Ophthalmology* 119, 779–788. doi: 10.1016/j.ophtha.2011.09.028

Johnson, M. D., and McIntyre, C. C. (2008). Quantifying the neural elements activated and inhibited by globus pallidus deep brain stimulation. *J. Neurophysiol.* 100, 2549–2563. doi: 10.1152/jn.90372.2008

Kaltenbach, J. A., and Afman, C. E. (2000). Hyperactivity in the dorsal cochlear nucleus after intense sound exposure and its resemblance to tone-evoked activity: a physiological model for tinnitus. *Hear. Res.* 140, 165–172. doi: 10.1016/S0378-5955(99)00197-5

Kaltenbach, J. A., and McCaslin, D. L. (1996). Increases in spontaneous activity in the dorsal cochlear nucleus following exposure to high intensity sound: a possible neural correlate of tinnitus. *Audit. Neurosci.* 3, 57–78.

Kanold, P. O., and Young, E. D. (2001). Proprioceptive information from the pinna provides somatosensory input to cat dorsal cochlear nucleus. *J. Neurosci.* 21, 7848–7858. doi: 10.1523/JNEUROSCI.21-19-07848.2001

Koshtoiants Kh, S. (1957). Enzymo-chemical principles of the action of the vagus nerve on the heart (role of potassium). *Fiziol. Zh. SSSR Im. I M Sechenova* 43, 681–684.

Kreis, P., and Fishman, S. (2009). *Spinal Cord Stimulation Implantation Percutaneous Implantation Techniques*. Oxford: Oxford Press.

Lee, S. W., and Fried, S. I. (2017). Enhanced control of cortical pyramidal neurons with micromagnetic stimulation. *IEEE Trans. Neural Syst. Rehabil. Eng.* 25, 1375–1386. doi: 10.1109/TNSRE.2016.2631446

Li, Z., Zhang, J. G., Ye, Y., and Li, X. (2016). Review on factors affecting targeting accuracy of deep brain stimulation electrode implantation between 2001 and 2015. *Stereotact. Funct. Neurosurg.* 94, 351–362. doi: 10.1159/000449206

Licari, F. G., Shkoukani, M., and Kaltenbach, J. A. (2011). Stimulus-dependent changes in optical responses of the dorsal cochlear nucleus using voltage-sensitive dye. *J. Neurophysiol.* 106, 421–436. doi: 10.1152/jn.00982.2010

Lopez, W. O., Barbosa, D. C., Teixera, M. J., Paiz, M., Moura, L., Monaco, B. A., et al. (2016). Pain relief in CRPS-II after spinal cord and motor cortex simultaneous dual stimulation. *Pain Phys.* 19, E631–E635.

Macherey, O., and Carlyon, R. P. (2014). Cochlear implants. *Curr. Biol.* 24, R878–R884. doi: 10.1016/j.cub.2014.06.053

Manis, P. B. (1989). Responses to parallel fiber stimulation in the guinea pig dorsal cochlear nucleus in vitro. *J. Neurophysiol.* 61, 149–161. doi: 10.1152/jn.1989.61.1.149

Manzoor, N. F., Gao, Y., Licari, F., and Kaltenbach, J. A. (2013). Comparison and contrast of noise-induced hyperactivity in the dorsal cochlear nucleus and inferior colliculus. *Hear. Res.* 295, 114–123. doi: 10.1016/j.heares.2012.04.003

Manzoor, N. F., Licari, F. G., Klapchar, M., Elkin, R. L., Gao, Y., Chen, G., et al. (2012). Noise-induced hyperactivity in the inferior colliculus: its relationship with hyperactivity in the dorsal cochlear nucleus. *J. Neurophysiol.* 108, 976–988. doi: 10.1152/jn.00833.2011

Matteucci, P. B., Barriga-Rivera, A., Eiber, C. D., Lovell, N. H., Morley, J. W., and Suaning, G. J. (2016). The effect of electric cross-talk in retinal neurostimulation. *Invest. Ophthalmol. Vis. Sci.* 57, 1031–1037. doi: 10.1167/iovs.15-18400

McElcheran, C. E., Yang, B., Anderson, K. J. T., Golestanirad, L., and Graham, S. J. (2017). Parallel radiofrequency transmission at 3 tesla to improve safety in bilateral implanted wires in a heterogeneous model. *Magn. Reson. Med.* 78, 2406–2415. doi: 10.1002/mrm.26622

McIntyre, C. C., and Grill, W. M. (2001). Finite element analysis of the current-density and electric field generated by metal microelectrodes. *Ann. Biomed. Eng.* 29, 227–235. doi: 10.1114/1.1352640

McIntyre, C. C., Mori, S., Sherman, D. L., Thakor, N. V., and Vitek, J. L. (2004). Electric field and stimulating influence generated by deep brain stimulation of the subthalamic nucleus. *Clin. Neurophysiol.* 115, 589–595. doi: 10.1016/j.clinph.2003.10.033

McIntyre, C. C., Richardson, A. G., and Grill, W. M. (2002). Modeling the excitability of mammalian nerve fibers: influence of afterpotentials on the recovery cycle. *J. Neurophysiol.* 87, 995–1006. doi: 10.1152/jn.00353.2001

Mehta, A. H., and Oxenham, A. J. (2017). Vocoder simulations explain complex pitch perception limitations experienced by cochlear implant users. *J. Assoc. Res. Otolaryngol.* 18, 789–802. doi: 10.1007/s10162-017-0632-x

Møller, A. R. (2006). *Cochlear and Brainstem Implants. Advances in Oto-Rhino-Laryngology*, Vol. VIII. New York, NY: Karger, 228. doi: 10.1159/isbn.978-3-318-01380-1

Montgomery, E. B. (2010). *Deep Brain Stimulation Programming: Principles and Practice*, Vol. XVII. Oxford: Oxford University Press, 179.

Morace, R., Di Gennaro, G., Quarato, P., D'Aniello, A., Amascia, A., Grammaldo, L., et al. (2016). Deep brain stimulation for intractabile epilepsy. *J. Neurosurg. Sci.* 60, 189–198.

Mugnaini, E., Warr, W. B., and Osen, K. K. (1980). Distribution and light microscopic features of granule cells in the cochlear nuclei of cat, rat, and mouse. *J. Comp. Neurol.* 191, 581–606. doi: 10.1002/cne.901910406

Nagarajan, S. S., Durand, D. M., and Warman, E. N. (1993). Effects of induced electric fields on finite neuronal structures: a simulation study. *IEEE Trans. Biomed. Eng.* 40, 1175–1188. doi: 10.1109/10.245636

Nduka, C. C., Poland, N., Kennedy, M., Dye, J., and Darzi, A. (2017). The cutting mechanism of the electrosurgical scalpel. *J. Phys. D Appl. Phys.* 50:025401.

Neumann, E., and Rosenheck, K. (1972). Permeability changes induced by electric impulses in vesicular membranes. *J. Membr. Biol.* 10, 279–290. doi: 10.1007/BF01867861

O'Reardon, J. P., Cristancho, P., and Peshek, A. D. (2006). Vagus nerve stimulation (VNS) and treatment of depression: to the brainstem and beyond. *Psychiatry* 3, 54–63.

Panayiotopoulos, C. P. (2011). *Principles of Therapy in the Epilepsies*, Vol. VIII. New York, NY: Springer, 99. doi: 10.1007/978-0-85729-009-0

Park, H. J., Bonmassar, G., Kaltenbach, J. A., Machado, A. G., Manzoor, N. F., and Gale, J. T. (2013). Activation of the central nervous system induced by micro-magnetic stimulation. *Nat. Commun.* 4:2463. doi: 10.1038/ncomms3463

Pashut, T., Wolfus, S., Friedman, A., Lavidor, M., Bar-Gad, I., Yeshurun, Y., et al. (2011). Mechanisms of magnetic stimulation of central nervous system neurons. *PLoS Comput. Biol.* 7:e1002022. doi: 10.1371/journal.pcbi.1002022

Ren, Z. (2002). T-Omega formulation for eddy-current problems in multiply connected regions. *IEEE Trans. Magn.* 38, 557–560. doi: 10.1109/20.996146

Roth, B. J., and Basser, P. J. (1990). A model of the stimulation of a nerve fiber by electromagnetic induction. *IEEE Trans. Biomed. Eng.* 37, 588–597. doi: 10.1109/10.55662

Ryugo, D. K., and Willard, F. H. (1985). The dorsal cochlear nucleus of the mouse: a light microscopic analysis of neurons that project to the inferior colliculus. *J. Comp. Neurol.* 242, 381–396. doi: 10.1002/cne.902420307

Sale, A. J., and Hamilton, W. A. (1968). Effects of high electric fields on microorganisms. 3. Lysis of erythrocytes and protoplasts. *Biochim. Biophys. Acta* 163, 37–43. doi: 10.1016/0005-2736(68)90030-8

Schaefer, D., Bourland, J., and Nyenhuis, J. (2000). Review of patient safety in time-varying gradient fields. *J. Magn. Reson. Imaging* 12, 20–29. doi: 10.1002/1522-2586(200007)12:1<20::AID-JMRI3>3.0.CO;2-Y

Serano, P., Angelone, L. M., Katnani, H., Eskandar, E., and Bonmassar, G. (2015). A novel brain stimulation technology provides compatibility with MRI. *Sci. Rep.* 5:9805. doi: 10.1038/srep09805

Sheĭkh-Zade, I. R., Kruchinin, V. M., Sukach, L. I., Pokrovskiĭ, M. V., and Urmancheva, T. G. (1987). General principles of heart rate control during burst stimulation of the vagus nerve in various animals. *Fiziol. Zh. SSSR Im. I M Sechenova* 73, 1325–1330.

Shepherd, R. K., Shivdasani, M. N., Nayagam, D. A., Williams, C. E., and Blamey, P. J. (2013). Visual prostheses for the blind. *Trends Biotechnol.* 31, 562–571. doi: 10.1016/j.tibtech.2013.07.001

Stingl, K., Bartz-Schmidt, K. U., Besch, D., Chee, C. K., Cottriall, C. L., Gekeler, F., et al. (2015). Subretinal visual implant alpha IMS–clinical trial interim report. *Vision Res.* 111(Pt B), 149–160. doi: 10.1016/j.visres.2015.03.001

Tolbert, D. L., Conoyer, B., and Ariel, M. (2004). Quantitative analysis of granule cell axons and climbing fiber afferents in the turtle cerebellar cortex. *Anat. Embryol.* 209, 49–58. doi: 10.1007/s00429-004-0423-0

Tuch, D. S., Wedeen, V. J., Dale, A. M., George, J. S., and Belliveau, J. W. (1999). Conductivity mapping of biological tissue using diffusion MRI. *Ann. N. Y. Acad. Sci.* 888, 314–316. doi: 10.1111/j.1749-6632.1999.tb07965.x

Tzounopoulos, T., Rubio, M. E., Keen, J. E., and Trussell, L. O. (2007). Coactivation of pre- and postsynaptic signaling mechanisms determines cell-specific spike-timing-dependent plasticity. *Neuron* 54, 291–301. doi: 10.1016/j.neuron.2007.03.026

United States Congress Senate Committee on Finance (2006). *Committee Staff Report to the Chairman and Ranking Member: Review of the FDA's Approval Process for the Vagus Nerve Stimulation Therapy System for Treatment-Resistant Depression. S. Prt*, Vol. IV. Washington, DC: U.S. Government Printing Office, 386.

Wagner, T., Gangitano, M., Romero, R., Théoret, H., Kobayashi, M., Anschel, D., et al. (2004). Intracranial measurement of current densities induced by transcranial magnetic stimulation in the human brain. *Neurosci. Lett.* 354, 91–94. doi: 10.1016/S0304-3940(03)00861-9

Wagner, T. A., Zahn, M., Grodzinsky, A. J., and Pascual-Leone, A. (2004). Three-dimensional head model simulation of transcranial magnetic stimulation. *IEEE Trans. Biomed. Eng.* 51, 1586–1598. doi: 10.1109/TBME.2004.827925

Walsh, V., and Cowey, A. (2000). Transcranial magnetic stimulation and cognitive neuroscience. *Nat. Rev. Neurosci.* 1, 73–79. doi: 10.1038/35036239

Wang, S. X., Sun, N. X., Yamaguchi, M., and Yabukami, S. (2000). Properties of a new soft magnetic material. *Nature* 407, 150–151. doi: 10.1038/35025142

Warman, E. N., Grill, W. M., and Durand, D. (1992). Modeling the effects of electric fields on nerve fibers: determination of excitation thresholds. *IEEE Trans. Biomed. Eng.* 39, 1244–1254. doi: 10.1109/10.184700

Wei, X. F., and Grill, W. M. (2005). Current density distributions, field distributions and impedance analysis of segmented deep brain stimulation electrodes. *J. Neural Eng.* 2, 139–147. doi: 10.1088/1741-2560/2/4/010

Weitz, A. C., Nanduri, D., Behrend, M. R., Gonzalez-Calle, A., Greenberg, R. J., Humayun, M. S., et al. (2015). Improving the spatial resolution of epiretinal implants by increasing stimulus pulse duration. *Sci. Transl. Med.* 7:318ra203. doi: 10.1126/scitranslmed.aac4877

Williams, N. R., Short, E. B., Hopkins, T., Bentzley, B. S., Sahlem, G. L., Pannu, J., et al. (2016). Five-year follow-up of bilateral epidural prefrontal cortical stimulation for treatment-resistant depression. *Brain Stimul.* 9, 897–904. doi: 10.1016/j.brs.2016.06.054

Woock, J. P., Yoo, P. B., and Grill, W. M. (2010). Finite element modeling and in vivo analysis of electrode configurations for selective stimulation of pudendal afferent fibers. *BMC Urol.* 10:11. doi: 10.1186/1471-2490-10-11

Zrenner, E. (2013). Fighting blindness with microelectronics. *Sci. Transl. Med.* 5:210s16. doi: 10.1126/scitranslmed.3007399

Conflict of Interest Statement: JG provided consulting services for Alpha Omega Co. USA, Inc. and author FH was employed by the company FHC, Inc.

The remaining authors declare that the research was conducted in the absence of any commercial or financial relationships that could be construed as a potential conflict of interest.

frontiers in Physiology

MINI REVIEW
published: 13 August 2018
doi: 10.3389/fphys.2018.01107

Predictive Physiological Modeling of Percutaneous Coronary Intervention – Is Virtual Treatment Planning the Future?

Rebecca C. Gosling[1,2,3*†], Paul D. Morris[1,2,3†], Patricia V. Lawford[1,3], D. Rodney Hose[1,3,4] and Julian P. Gunn[1,2,3]

[1] Department of Infection, Immunity and Cardiovascular Disease, University of Sheffield, Sheffield, United Kingdom, [2] Department of Cardiology, Sheffield Teaching Hospitals NHS Foundation Trust, Northern General Hospital, Sheffield, United Kingdom, [3] INSIGNEO Institute for in Silico Medicine, Sheffield, United Kingdom, [4] Department of Circulation and Medical Imaging, Norwegian University of Science and Technology, Trondheim, Norway

Computational modeling has been used routinely in the pre-clinical development of medical devices such as coronary artery stents. The ability to simulate and predict physiological and structural parameters such as flow disturbance, wall shear-stress, and mechanical strain patterns is beneficial to stent manufacturers. These methods are now emerging as useful clinical tools, used by physicians in the assessment and management of patients. Computational models, which can predict the physiological response to intervention, offer clinicians the ability to evaluate a number of different treatment strategies *in silico* prior to treating the patient in the cardiac catheter laboratory. For the first time clinicians can perform a patient-specific assessment prior to making treatment decisions. This could be advantageous in patients with complex disease patterns where the optimal treatment strategy is not clear. This article reviews the key advances and the potential barriers to clinical adoption and translation of these virtual treatment planning models.

Keywords: computational modeling, coronary artery disease, percutaneous coronary intervention, coronary physiology, predictive modeling

Edited by:
Markus Reiterer,
Medtronic, United States

Reviewed by:
Steve McKeever,
Uppsala University, Sweden
Marc Horner,
Ansys, United States

***Correspondence:**
Rebecca C. Gosling
r.gosling@sheffield.ac.uk

†These authors have contributed equally to this work and are joint first authors

Specialty section:
This article was submitted to Computational Physiology and Medicine, a section of the journal Frontiers in Physiology

Received: 13 April 2018
Accepted: 23 July 2018
Published: 13 August 2018

Citation:
Gosling RC, Morris PD, Lawford PV, Hose DR and Gunn JP (2018) Predictive Physiological Modeling of Percutaneous Coronary Intervention – Is Virtual Treatment Planning the Future? Front. Physiol. 9:1107. doi: 10.3389/fphys.2018.01107

INTRODUCTION

Computational modeling techniques are employed routinely in the pre-clinical development of medical devices. In this context, modeling allows rapid prototyping, which is both time- and cost-effective. Yet, few models have entered the clinical domain as either diagnostic or predictive treatment-planning tools. *In silico* models of the cardiovascular system are amongst the most advanced. The recent adoption of CT-FFR into the major clinical guidelines represents a major breakthrough (Koo et al., 2011; NICE, 2016). However, this has not been universally adopted by healthcare professionals (Schoenhagen and Desai, 2015; Davies and Cook, 2017). The emergence of such tools has been hampered by difficulties with validation, regulatory approval, and lengthy processing times (Morris et al., 2015).

Abbreviations: 3-D, three dimensional; CAD, coronary artery disease; CFD, computational fluid dynamics; CTCA, computed tomography coronary angiography; CT-FFR, computed tomography fractional flow reserve; FDA, Food and Drug Administration; FEM, finite element modeling; FFR, fractional flow reserve; ISR, in-stent re-stenosis; IVUS, intravascular ultrasound; MACE, major adverse cardiac events; NPV, negative predictive value; OCT, optical coherence tomography; PCI, percutaneous coronary intervention; PPV, positive predictive value; VCI, virtual coronary intervention; vFFR, virtual fractional flow reserve; WSS, wall shear stress.

The nature of predictive computational modeling is appropriate for virtual treatment planning, especially in the context of structural cardiovascular intervention. Clinicians frequently make treatment decisions based upon data pooled from randomized controlled trials, which can be problematic. First, these population-level data are extrapolated and applied to individuals. Second, randomized trials frequently recruit younger, otherwise well patients, and therefore under-represent the "average" patient who is typically older, with multiple comorbidities. Medicine requires an approach more tailored to the individual patient, based upon patient-specific characteristics. As one example, existing computer models created for the purpose of device design can be adapted to permit virtual treatment planning with the addition of patient specific geometries and personalized parameterization. In CAD, there is an opportunity to improve treatment planning. PCI treatment planning is often subjective. Decisions regarding the number, size, and position of stent(s) required to treat a coronary artery lesion(s) are made by the operator based upon a visual interpretation of the angiogram, a method which is frequently flawed due to the difficulty inferring the physiological impact of atherosclerotic lesions, and indeed their likely response to treatment, from 2D anatomical imaging (White et al., 1984). The development of virtual stenting tools may allow predictive treatment planning. This is emerging as an area of increasing clinical interest. This article reviews the rationale and developing methodology behind virtual PCI tools, the current state of the art, and what barriers need to be overcome before this patient-specific approach can be fully translated and incorporated into routine medical practice.

What Is Computational Modeling, and How Can It Be Applied to CAD?

Computational models simulate the behavior of systems combining mathematics, physics, and computer science. Computational modeling techniques have been used for decades in engineering applications, and some of these techniques are particularly applicable in the study of CAD, namely CFD and FEM. CFD is a numerical technique that predicts and analyses mechanical responses of fluids to external (and other) forces allowing the quantification of physiological parameters such as blood flow velocity and pressure. Furthermore, the use of FEM can provide full and detailed quantitative stress and strain analysis, which can be applied to the vessel wall (Morris et al., 2016). These models can be manipulated to simulate states of disease and are especially relevant in the study of CAD where the clinical importance of physiology has been recognized in recent years.

A number of invasively measured physiological parameters have been developed that can be used to guide treatment decisions (Pijls et al., 1993; Meuwissen et al., 2002; Sen et al., 2012; van de Hoef et al., 2012, 2016). These can describe the effect of a coronary lesion on blood flow, pressure, and the relationship between the two. FFR, the pressure drop measured across a lesion at maximal hyperaemia, is now considered the gold standard measure to determine coronary artery lesion significance (NICE, 2016). Using FFR to guide PCI is associated with improved clinical outcomes (De Bruyne et al., 2012). Furthermore, other physiological indices, that cannot be measured invasively, such as WSS are increasingly being recognized as factors that influence outcomes such as the rate of development of ISR (Tahir et al., 2011). With the application of CFD and FEM modeling, it is possible to predict the effect of stenting on these parameters, which can be useful in both stent design and patient-specific treatment planning.

Modeling Coronary Artery Stents

Computational methods are routinely used in designing stents and in predicting their performance and fatigue. They can also be used to model the effect of the stent upon blood flow in a diseased artery at the strut level, where disturbed flow can be a causative factor in the development of in-stent thrombosis, restenosis, and neo-atherosclerosis. Modeling is particularly applicable to study these phenomena, which are beyond the level of resolution of clinical measurements of flow (Van der Heiden et al., 2013). Neointimal thickening after stenting is related to altered local fluid dynamics (low and oscillating WSS provoked by the presence of the stent within the coronary artery) (Timmins et al., 2011). A number of models of ISR have been developed, and a relationship between stent design parameters such as strut thickness and the shape and depth of strut deployment within the vessel wall on the severity of ISR is well established (Tahir et al., 2011). Such models can be used to assist with stent design and to predict local hemodynamic effects of stenting and have been reviewed elsewhere (Martin and Boyle, 2011). The advancement of these models has received significant support from industry, and the technology is well developed. Applying the same technology to patient-specific geometries allows virtual treatment planning and is a growing area of interest. The two main thrusts of being in bifurcation modeling and modeling FFR.

TREATMENT PLANNING IN BIFURCATION DISEASE

Percutaneous coronary intervention of bifurcation lesions is beset by poorer results than non-bifurcation lesions (Lassen et al., 2014; Sawaya et al., 2016). Multiple technical strategies have been proposed, and the optimal strategies are still an area of debate (Lassen et al., 2016; Sawaya et al., 2016). Computational simulations offer key information on the biomechanical effects of stenting. Such simulations enable virtual testing of various strategies and can assist in evaluating outcomes.

What Is Special About Bifurcations?

Bifurcations are more prone to atherosclerosis due to the development of adverse flow patterns leading to regions of low WSS developing opposite the side branch and down the lateral wall of the branch itself. PCI to the main vessel is complicated by the risk of side branch occlusion due to plaque shift. Often multiple stent strategies are employed, which increases the risk of vascular damage and ISR. A number of studies have successfully utilized computational models to examine the impact of different stent designs and techniques on local hemodynamic factors (Williams et al., 1985; Gastaldi et al., 2010; Morlacchi et al., 2011, 2014; Mortier et al., 2015). Such models have advanced in terms of sophistication over the past 5–10 years. These studies have assisted with advancements in the modeling of stent insertion and have provided valuable insights into the relationships between stent design, WSS, and ISR. However, only with patient-specific models can accurate patient-specific treatment planning be achieved.

Anatomical Representation of Bifurcations

The first challenge in modeling bifurcations using patient-specific models is in the segmentation (reconstruction) of the patient anatomy. This is complex due to the necessity for precision of the cross-sectional area, branch diameter, and branching angle. The more realistic the models, the more insightful the investigations. Because of the difficulty faced reconstructing a complex bifurcation anatomy from invasive coronary angiography alone, many of these models utilize information from invasive imaging such as IVUS and OCT. Various methods are complementary and many hybrid combinations have been tested (Morlacchi et al., 2011; Mortier et al., 2015; Wang et al., 2015; Chiastra et al., 2016). The addition of numerical simulations of mechanical stresses and fluid flow in patient-derived geometries can contribute to translational experimentation. Modeling can also compare the expected results with different stent designs and strategies.

Complementary Imaging to Assist Bifurcation Modeling

Mortier et al. (2015) used CTCA and IVUS pullbacks to create a patient-specific virtual 3-D model. Using FEM, they generated stent and balloon models, accurate in terms of geometry and mechanical behavior, allowing them to perform and evaluate different stenting strategies. Transient CFD analysis was performed to produce velocity patterns and examine WSS along the arterial wall after stent deployment. Stents could be repositioned to investigate the impact upon WSS distributions, the optimal position being associated with minimal area of low WSS (Mortier et al., 2015) (**Figure 1**). Similar work has been achieved combining CTCA with OCT. Chiastra et al. (2016) reconstructed patient-specific models of coronary bifurcations from CT-OCT . They demonstrated good qualitative geometrical correlation between post-operative lumen area after virtual stent expansion and that from hybrid CT-OCT. They demonstrated the ability to determine the best stent position to minimize the percentage of mal-opposed struts (Chiastra et al., 2016). Wang et al. (2015) created a patient-specific bifurcation model from angiographic images alone. As well as using FEM analysis to identify areas of low WSS associated with four different stenting approaches, they also used 3-D printing to create an *in vitro* model. Using microfabrication, microfluidic chips implanted with real stents were used to mimic PCI with real time visualization. The results from their 3-D models were highly consistent with simulated results. This model has the advantage of allowing the testing of positioning effects of real stents experimentally. This approach may be more translational as it is subject to the same difficulties of such precise stent positioning faced *in vivo*.

Limitations of Bifurcation Modeling

One problem is that the above methods considerably add to the complexity of a PCI procedure. Most bifurcations can be treated reasonably well with 2-D angiographic guidance. However, in select patients with complex anatomy, these techniques could allow detailed treatment planning to occur prior to PCI. Demonstrating clinical benefit would also be challenging as the results of conventional angiographically guided PCI are generally good, masking particular benefit to be derived by a minority of patients with complex 3-D anatomy. Moreover, replicating exact stent positioning recommended by the model in the catheterization laboratory would be challenging and this could be a major barrier to clinical translation. At present, significant processing time is required as these models incorporate FEM technologies. This limits the option of "live" modeling in the cardiac catheter laboratory. These models may be able to assist in demonstrating the benefit of one strategy over another, but using them to guide exact stent positioning may be unrealistic without further advances.

MODELING THE EFFECT OF STENTING UPON FFR

In recent years, there has been a renewed interest in coronary physiology. FFR, a physiological parameter, is now considered the gold standard for assessing coronary artery lesion significance. FFR is measured during invasive angiography using a pressure-sensitive wire that is placed distal to the lesion. FFR is defined as the ratio of pressure distal to the lesion to the proximal pressure at maximal hyperemia. Attainment of maximal hyperemia is a requirement for accurate FFR assessment and is most commonly achieved with the infusion of intravenous adenosine, a vasodilatory drug. The resultant vasodilatation of the coronary microvasculature reduces the distal resistance, maximizing the flow rate of blood through the vessel. A threshold of 0.80 is applied to determine physiological lesion significance. If the FFR is <0.80, revascularization is recommended whereas if the FFR is >0.80, there is no indication for revascularization.

Using FFR to determine when PCI is required, is associated with improved clinical outcomes (De Bruyne et al., 2012). Computing coronary physiology, eliminating the need for invasive instrumentation, is an area of great interest. Several groups have developed methods to compute vFFR with varied success (Koo et al., 2011; Morris et al., 2013; Tu et al., 2014). Virtual stenting can be applied to these models, allowing a prediction of the likely improvement in physiology that can be achieved with stenting. Any desired width or length of stent can be modeled. For this, the details of the stent structure are not required, because we do not require details of flow disturbance at the stent/artery interface, reducing the complexity of the modeling.

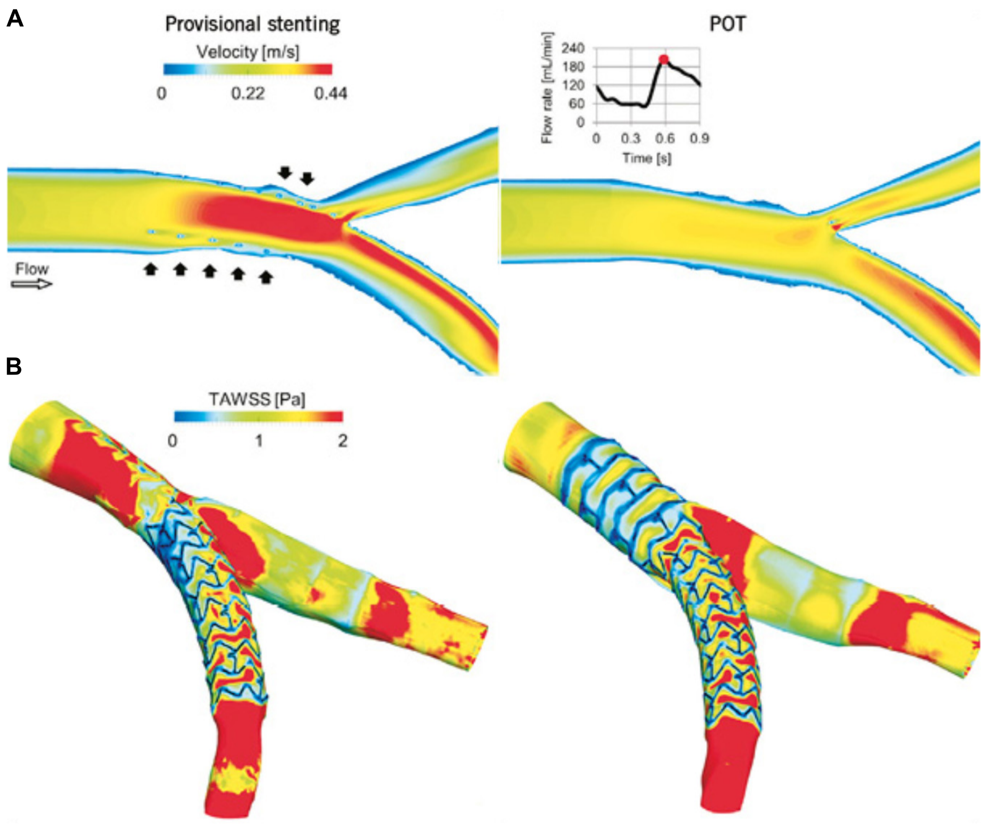

FIGURE 1 | Computational replication of bifurcation stenting. Mortier et al. (2015) compared flow velocity patterns and WSS following virtual provisional stenting (left) and proximal optimization technique (right). **(A)** Velocity contour maps on an internal plane of the bifurcation at peak flow rate. In the provisional stenting, where the malapposed struts are clearly visible (black arrows), higher velocities are present as the stent behaves as a cylindrical hurdle in the flow stream. Indeed, in the proximal optimization technique (POT), struts are well opposed to the wall and do not obstruct the blood stream. **(B)** Time-averaged WSS (TAWSS) contour maps. Low WSS are generated next to the stent struts. A wide area with low WSS is present in the bifurcation region in the provisional stenting model and in the proximal part of the stent in the POT model. Reprinted from Mortier et al. (2015). Copyright (2015), with permission from Europa Digital & Publishing.

Inserting a "Virtual" Stent Using CT Imaging

Simulating the insertion of a virtual, cylindrical, stented segment into a modeled coronary vessel with recalculation of blood flow permits treatment planning. This allows operators to predict the physiological and anatomical response to treatment with different stent sizes in different locations, to plan the optimal solution before any treatment is delivered. This technique has recently been demonstrated with CTCA imaging (Kim et al., 2014). The investigators identified 44 patients with functionally significant lesions who underwent invasive angiography with FFR measurement. CTCA was performed prior to angiography and 3-D models of the coronary tree were reconstructed. Data on coronary flow and pressure were simulated using CFD. The pre-stent model was then marked for the location of stent used to treat the patient and a virtual stent was inserted to replicate the *in vivo* procedure. Subsequent FFR was computed following virtual stent implantation. The diagnostic accuracy to predict ischemia after PCI was 96%. The mean difference between vFFR and measured FFR after PCI was 0.024 (95% level of agreement −0.08 to 0.13). However, CTCA is still limited in its availability, most of these patients will still proceed to invasive angiography, and CTCA images can be limited by movement artifacts, poor heart rate control, and inaccuracy in calcific disease.

Modeling Stenting Based Upon Invasive Angiography

More recently, modeling the effect of stenting on FFR has been demonstrated by our group using invasive angiographic imaging (Gosling et al., 2018). This has the advantage of not using complementary imaging, so no co-registration of another modality to the angiogram is necessary, and the whole process is kept simple and readily interpretable by a conventional, angiogram-guided PCI. VCI was carried out in 54 patients (59 arteries) who underwent elective PCI. A 3-D reconstruction of the arterial geometry was created from the angiographic images. To validate the process, the size and position of stent(s) used *in vivo* was replicated using dedicated software (**Figure 2**). The authors demonstrated good accuracy in predicting the physiological response to stenting. Mean FFR post-PCI was 0.90 and mean vFFR post VCI was 0.92. The mean difference between vFFR after VCI and measured FFR after PCI was 0.01 ± 0.03.

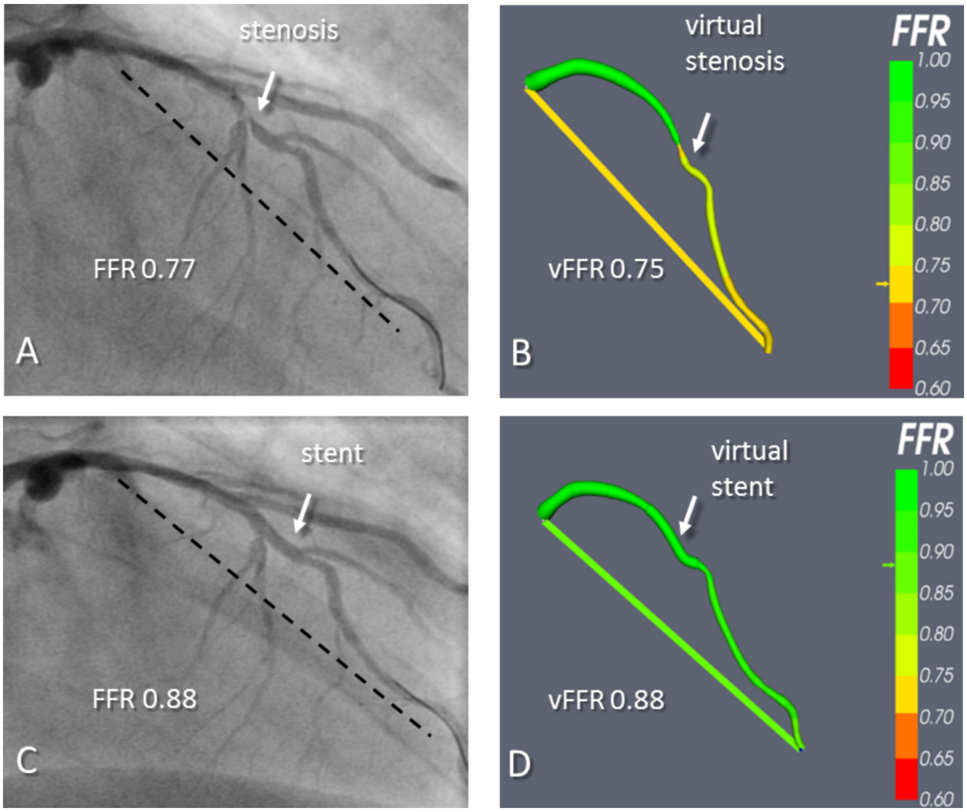

FIGURE 2 | An example of virtual coronary intervention. Angiography revealed a severe mid vessel stenosis in the LAD (arrow). The mFFR between the proximal and distal points marked with the dashed line was 0.77. **(B)** The angiograms were used to model the vFFR using the VIRTUheart system, which was calculated to be 0.75 over the same segment. This is displayed as a straight yellow line connecting the same two points between which the vFFR was calculated, exactly matching the two spots marked by the dashed line in **(A)**. **(C)** After implantation of a 2.75 mm × 18 mm stent at the stenosis, the mFFR was 0.88 over the same segment. **(D)** VCI using the VIRTUheart system was then used to implant a "virtual" 2.75 mm × 18 mm stent, and the recalculated vFFR was 0.88, corresponding to a green color in the line connecting the two points. Reproduced from JACC: Cardiovascular imaging under creative commons license CC BY 4.0 (Gosling et al., 2018).

Importantly, the average computational time was just 2 min per case. Applying a VCI tool to invasive angiography will allow treatment planning to occur in the cardiac catheterization laboratory.

What Is the Value of Virtual Treatment Planning?

A simple case with an isolated lesion may not require VCI. Interest will be concentrated on complex disease, such as arteries with serial lesions, diffuse disease, and bifurcations. Some outcome data suggests that patients who have a post-treatment FFR < 0.90 have increased risk of MACE at follow up (Pijls et al., 2002). The ability to predict the post treatment FFR for a particular stenting approach would potentially allow the operator to optimize the strategy prior to intervention, therefore improving both the post treatment FFR and clinical outcomes. Importantly, it can also allow the identification of patients unlikely to achieve significant improvement in FFR following PCI. This could help prevent unnecessary/futile procedures. VCI can also allow a more personalized assessment of a patient's physiology. In the presence of serial stenoses, it is not possible to accurately measure the impact of one lesion upon the measured FFR across all the lesions due to the complex interplay of flow between them. Even FFR pullback is misleading. Therefore, deciding which lesion(s) to stent is challenging and often leads to unnecessary stenting (Pijls et al., 2000). Only by removing a stenosis (invasively by stenting it, which may not be necessary, or now "virtually" by computational modeling) is it possible to assess the effect of hyperemic flow across an individual stenosis among several.

IMMEDIATE NEXT STEPS

Although the potential for virtual stenting is clear, further work is required to validate treatment planning tools in patients with complex disease. The FFR-based tools may be more applicable than the models that employ complex WSS analysis. The technology is simpler and therefore the computational power required is significantly less. Rather than advising on exact positioning, they can provide a simpler recommendation of number and size of stent(s) which may be more translational. Moreover, the processing time is only a few minutes per case (Morris et al., 2017), with just slight improvements, "live" results are possible. This would be attractive to the interventionalist, who with the patient on the table, could get an immediate read out of optimal stent size and predicted response to their proposed strategy. This is important for clinical translation. In most cases, operators would not want to wait for overnight processing and then have to bring the patient back for their PCI procedure once the results are available.

Future of PCI Treatment Planning Tools

Despite apparent success in the research domain, there are a number of challenges to be faced before PCI treatment planning tools can be incorporated into routine clinical practice. One of these is the computational power and time required to perform these analyses, in particular when FEM is used. Accuracy is key to success, but defining this is difficult, especially when there is no *in vivo* measure available to allow validation. All of the models are based upon a number of assumptions, which can affect their accuracy. The two key factors determining the accuracy of these models are the geometrical reconstruction and parameterization. Many of the models to date use reconstructions based upon CTCA, and although the accuracy of CTCA has improved in recent years, there are still a number of drawbacks including the translation of findings to those seen at invasive coronary angiography. The evolution of tools based upon the angiographic images may be a key advance. Accurate parameterization perhaps represents a more significant challenge. In many cases, much of the data required is readily available. However, predicting or calculating parameters that are not easily obtainable clinically, such as microvascular resistance, represents a major challenge and is perhaps the most significant factor hampering the accuracy of these models. Ultimately, demonstrating clinical success is vital and prospective randomized clinical trials will be required. There are also commercial considerations regarding accuracy and reliability of validation of such tools. The United States FDA is addressing this through a benchmarking initiative that aims to advance the application of CFD technology within the regulatory context and they have identified "developing computer modeling technologies" as a regulatory science priority (U.S Food and Drug Administration, 2017). Furthermore, the American Society of Mechanical Engineering (ASME) has produced standards for the verification and validation of computation fluid dynamics models (ASME, 2006, 2009). To allow widespread adoption of these tools, these, or similar approaches need to be extended to Europe. The final and perhaps most significant challenge is achieving acceptance within the clinical community. With modeling becoming a rapidly growing area, clinicians are increasingly encountering modeling-based technologies. The most recent example is the introduction of CT-FFR into national guidance (NICE, 2017). Yet, there is still some skepticism among many clinicians surrounding these technologies. Data from outcome studies will assist with this, but only with increased exposure over time, and a perseverance from the modeling community will wide spread acceptance be achieved.

CONCLUSION

Computational modeling is routinely applied to assist with stent design, and there has been significant success in this area. More recently, the same technologies have been adapted to permit patient-specific virtual treatment planning. Complex models assessing WSS in bifurcation stenting can provide interesting insights into the relationships between stent design and stenting strategies on factors such as ISR. However, it is hard to see how they will impact clinical practice without significant simplification. Perhaps closer to clinical translation are models of FFR. These models permit prediction of post treatment FFR, a validated clinical measure, associated with different stenting strategies. Post PCI FFR is already established to be associated with clinical outcomes therefore the clinical benefit is clear. Moreover, the technology is simpler and therefore the processing time is substantially quicker. These models may not be too far from the clinical domain, but only time will tell.

AUTHOR CONTRIBUTIONS

RG and PM conceived the idea and wrote the first draft. All authors critically reviewed the paper and approved the final manuscript for submission.

FUNDING

RG was funded as part of a clinical research training fellowship awarded by the British Heart Foundation (FS/16/48/32306).

REFERENCES

ASME (2006). *Guide for Verification and Validation in Computational Solid Mechanics*. Available at: https://www.asme.org/products/codes-standards/v-v-10-2006-guide-verification-validation

ASME (2009). *Standard for Verification and Validation in Computational Fluid Dynamics and Heat Transfer*. Available at: https://www.asme.org/products/codes-standards/v-v-20-2009-standard-verification-validation

Chiastra, C., Wu, W., Dickerhoff, B., Aleiou, A., Dubini, G., Otake, H., et al. (2016). Computational replication of the patient-specific stenting procedure for coronary artery bifurcations: from OCT and CT imaging to structural and hemodynamics analyses. *J. Biomech.* 49, 2102–2111. doi: 10.1016/j.jbiomech.2015.11.024

Davies, J. E., and Cook, C. M. (2017). Is FFRCT ready to assume the crown jewels of invasive FFR? *JACC Cardiovasc. Imaging* 10, 434–436. doi: 10.1016/j.jcmg.2016.06.016

De Bruyne, B., Pijls, N. H., Kalesan, B., Barbato, E., Tonino, P. A., Piroth, Z., et al. (2012). Fractional flow reserve-guided PCI versus medical therapy in stable coronary disease. *N. Engl. J. Med.* 367, 991–1001. doi: 10.1056/NEJMoa1205361

Gastaldi, D., Morlacchi, S., Nichetti, R., Capelli, C., Dubini, G., Petrini, L., et al. (2010). Modelling of the provisional side-branch stenting approach for the treatment of atherosclerotic coronary bifurcations: effects of stent positioning. *Biomech. Model. Mechanobiol.* 9, 551–561. doi: 10.1007/s10237-010-0196-8

Gosling, R. C., Morris, P. D., Silva Soto, D. A., Lawford, P. V., Hose, D. R., and Gunn, J. P. (2018). Virtual coronary intervention: a treatment planning tool based upon the angiogram. *JACC Cardiovasc. Imaging* doi: 10.1016/j.jcmg.2018.01.019 [Epub ahead of print].

Kim, K. H., Doh, J. H., Koo, B. K., Min, J. K., Erglis, A., Yang, H. M., et al. (2014). A novel noninvasive technology for treatment planning using virtual coronary stenting and computed tomography-derived computed fractional flow reserve. *JACC Cardiovasc. Interv.* 7, 72–78. doi: 10.1016/j.jcin.2013.05.024

Koo, B. K., Erglis, A., Doh, J. H., Daniels, D. V., Jegere, S., Kim, H. S., et al. (2011). Diagnosis of ischemia-causing coronary stenoses by noninvasive fractional flow reserve computed from coronary computed tomographic angiograms. Results from the prospective multicenter DISCOVER-FLOW (Diagnosis of Ischemia-Causing Stenoses Obtained Via Noninvasive Fractional Flow Reserve) study. *J. Am. Coll. Cardiol.* 58, 1989–1997. doi: 10.1016/j.jacc.2011.06.066

Lassen, J. F., Holm, N. R., Banning, A., Burzotta, F., Lefevre, T., Chieffo, A., et al. (2016). Percutaneous coronary intervention for coronary bifurcation disease: 11th consensus document from the European Bifurcation Club. *EuroIntervention* 12, 38–46. doi: 10.4244/EIJV12I1A7

Lassen, J. F., Holm, N. R., Stankovic, G., Lefevre, T., Chieffo, A., Hildick-Smith, D., et al. (2014). Percutaneous coronary intervention for coronary bifurcation disease: consensus from the first 10 years of the European Bifurcation Club meetings. *EuroIntervention* 10, 545–560. doi: 10.4244/EIJV10I5A97

Martin, D., and Boyle, F. J. (2011). Computational structural modelling of coronary stent deployment: a review. *Comput. Methods Biomech. Biomed. Eng.* 14, 331–348. doi: 10.1080/10255841003766845

Meuwissen, M., Siebes, M., Chamuleau, S. A., van Eck-Smit, B. L., Koch, K. T., de Winter, R. J., et al. (2002). Hyperemic stenosis resistance index for evaluation of functional coronary lesion severity. *Circulation* 106, 441–446. doi: 10.1161/01.CIR.0000023041.26199.29

Morlacchi, S., Chiastra, C., Cutri, E., Zunino, P., Burzotta, F., Formaggia, L., et al. (2014). Stent deformation, physical stress, and drug elution obtained with provisional stenting, conventional culotte and Tryton-based culotte to treat bifurcations: a virtual simulation study. *EuroIntervention* 9, 1441–1453. doi: 10.4244/EIJV9I12A242

Morlacchi, S., Chiastra, C., Gastaldi, D., Pennati, G., Dubini, G., and Migliavacca, F. (2011). Sequential structural and fluid dynamic numerical simulations of a stented bifurcated coronary artery. *J. Biomech. Eng.* 133:121010. doi: 10.1115/1.4005476

Morris, P. D., Narracott, A., von Tengg-Kobligk, H., Silva Soto, D. A., Hsiao, S., Lungu, A., et al. (2016). Computational fluid dynamics modelling in cardiovascular medicine. *Heart* 102, 18–28. doi: 10.1136/heartjnl-2015-308044

Morris, P. D., Ryan, D., Morton, A. C., Lycett, R., Lawford, P. V., Hose, D. R., et al. (2013). Virtual fractional flow reserve from coronary angiography: modeling the significance of coronary lesions: results from the VIRTU-1 (VIRTUal Fractional Flow Reserve From Coronary Angiography) study. *JACC Cardiovasc. Interv.* 6, 149–157. doi: 10.1016/j.jcin.2012.08.024

Morris, P. D., Silva Soto, D. A., Feher, J. F. A., Rafiroiu, D., Lungu, A., Varma, S., et al. (2017). Fast virtual fractional flow reserve based upon steady-state computational fluid dynamics analysis: results from the VIRTU-fast study. *JACC Basic Transl. Sci.* 2, 434–446. doi: 10.1016/j.jacbts.2017.04.003

Morris, P. D., van de Vosse, F. N., Lawford, P. V., Hose, D. R., and Gunn, J. P. (2015). "Virtual" (Computed) fractional flow reserve: current challenges and limitations. *JACC Cardiovasc. Interv.* 8, 1009–1017. doi: 10.1016/j.jcin.2015.04.006

Mortier, P., Wentzel, J. J., De Santis, G., Chiastra, C., Migliavacca, F., De Beule, M., et al. (2015). Patient-specific computer modelling of coronary bifurcation stenting: the John Doe programme. *Eurointervention* 11(Suppl. V), V35–V39. doi: 10.4244/EIJV11SVA8

NICE (2016). *Chest Pain of Recent Onset: Assessment and Diagnosis of Recent Onset Chest Pain or Discomfort of Suspected Cardiac Origin. Clinical Guideline CG95.* London: NICE.

NICE (2017). *HeartFlow FFRCT for Estimating Fractional Flow Reserve from Coronary CT Angiography*. Available at: nice.org.uk/guidance/mtg32/chapter/1-Recommendations

Pijls, N. H., De Bruyne, B., Bech, G. J., Liistro, F., Heyndrickx, G. R., Bonnier, H. J., et al. (2000). Coronary pressure measurement to assess the hemodynamic significance of serial stenoses within one coronary artery: validation in humans. *Circulation* 102, 2371–2377. doi: 10.1161/01.CIR.102.19.2371

Pijls, N. H., Klauss, V., Siebert, U., Powers, E., Takazawa, K., Fearon, W. F., et al. (2002). Coronary pressure measurement after stenting predicts adverse events at follow-up: a multicenter registry. *Circulation* 105, 2950–2954. doi: 10.1161/01.CIR.0000020547.92091.76

Pijls, N. H., van Son, J. A., Kirkeeide, R. L., De Bruyne, B., and Gould, K. L. (1993). Experimental basis of determining maximum coronary, myocardial, and collateral blood flow by pressure measurements for assessing functional stenosis severity before and after percutaneous transluminal coronary angioplasty. *Circulation* 87, 1354–1367. doi: 10.1161/01.CIR.87.4.1354

Sawaya, F. J., Lefevre, T., Chevalier, B., Garot, P., Hovasse, T., Morice, M. C., et al. (2016). Contemporary approach to coronary bifurcation lesion treatment. *JACC Cardiovasc. Interv.* 9, 1861–1878. doi: 10.1016/j.jcin.2016.06.056

Schoenhagen, P., and Desai, M. Y. (2015). Computed tomography-based fractional flow reserve (FFR-CT) - an attractive concept, but still lacking proof of clinical utility. *Circ. J.* 79, 300–302. doi: 10.1253/circj.CJ-14-1306

Sen, S., Escaned, J., Malik, I. S., Mikhail, G. W., Foale, R. A., Mila, R., et al. (2012). Development and validation of a new adenosine-independent index of stenosis severity from coronary wave-intensity analysis: results of the ADVISE (Adenosine Vasodilator Independent Stenosis Evaluation) study. *J. Am. Coll. Cardiol.* 59, 1392–1402. doi: 10.1016/j.jacc.2011.11.003

Tahir, H., Hoekstra, A. G., Lorenz, E., Lawford, P. V., Hose, D. R., Gunn, J., et al. (2011). Multi-scale simulations of the dynamics of in-stent restenosis: impact of stent deployment and design. *Interface Focus* 1, 365–373. doi: 10.1098/rsfs.2010.0024

Timmins, L. H., Miller, M. W., Clubb, F. J. Jr., and Moore, J. E. Jr. (2011). Increased artery wall stress post-stenting leads to greater intimal thickening. *Lab. Invest.* 91, 955–967. doi: 10.1038/labinvest.2011.57

Tu, S., Barbato, E., Koszegi, Z., Yang, J., Sun, Z., Holm, N. R., et al. (2014). Fractional flow reserve calculation from 3-dimensional quantitative coronary angiography and TIMI frame count: a fast computer model to quantify the functional significance of moderately obstructed coronary arteries. *JACC Cardiovasc. Interv.* 7, 768–777. doi: 10.1016/j.jcin.2014.03.004

U.S Food and Drug Administration (2017). *Regulatory Science Priorities*. Available at: https://www.fda.gov/downloads/MedicalDevices/ScienceandResearch/UCM521503.pdf

van de Hoef, T. P., Nolte, F., Damman, P., Delewi, R., Bax, M., Chamuleau, S. A., et al. (2012). Diagnostic accuracy of combined intracoronary pressure and flow velocity information during baseline conditions: adenosine-free assessment of functional coronary lesion severity. *Circ. Cardiovasc. Interv.* 5, 508–514. doi: 10.1161/CIRCINTERVENTIONS.111.965707

van de Hoef, T. P., Petraco, R., van Lavieren, M. A., Nijjer, S., Nolte, F., Sen, S., et al. (2016). Basal stenosis resistance index derived from simultaneous pressure and flow velocity measurements. *Eurointervention* 12, e199–e207. doi: 10.4244/EIJV12I2A33

Van der Heiden, K., Gijsen, F. J., Narracott, A., Hsiao, S., Halliday, I., Gunn, J., et al. (2013). The effects of stenting on shear stress: relevance to endothelial injury and repair. *Cardiovasc. Res.* 99, 269–275. doi: 10.1093/cvr/cvt090

Wang, H., Liu, J., Zheng, X., Rong, X., Zheng, X., Peng, H., et al. (2015). Three-dimensional virtual surgery models for percutaneous coronary intervention (PCI) optimization strategies. *Sci. Rep.* 5:10945. doi: 10.1038/srep10945

White, C. W., Wright, C. B., Doty, D. B., Hiratza, L. F., Eastham, C. L., Harrison, D. G., et al. (1984). Does visual interpretation of the coronary arteriogram predict the physiologic importance of a coronary stenosis? *N. Engl. J. Med.* 310, 819–824. doi: 10.1056/NEJM198403293101304

Williams, A. R., Koo, B. K., Gundert, T. J., Fitzgerald, P. J., and LaDisa, J. F. Jr. (1985). Local hemodynamic changes caused by main branch stent implantation and subsequent virtual side branch balloon angioplasty in a representative coronary bifurcation. *J. Appl. Physiol.* 109, 532–540. doi: 10.1152/japplphysiol.00086.2010

Conflict of Interest Statement: The authors declare that the research was conducted in the absence of any commercial or financial relationships that could be construed as a potential conflict of interest.

frontiers in Physiology

ORIGINAL RESEARCH
published: 17 August 2018
doi: 10.3389/fphys.2018.01106

Non-invasive Stenotic Renal Artery Haemodynamics by *in silico* Medicine

Aikaterini Mandaltsi*[1,2]*, Andrii Grytsan*[1,2]*, Aghogho Odudu*[3,4]*, Jacek Kadziela*[5]*,
Paul D. Morris*[1,6,7]*, Adam Witkowski*[5]*, Timothy Ellam*[6]*, Philip Kalra*[3,4] *and
Alberto Marzo*[1,2]**

[1] INSIGNEO Institute for in silico Medicine, University of Sheffield, Sheffield, United Kingdom, [2] Mechanical Engineering Department, University of Sheffield, Sheffield, United Kingdom, [3] Division of Cardiovascular Sciences, University of Manchester, Manchester, United Kingdom, [4] Salford Royal Hospital NHS Foundation Trust, Salford, United Kingdom, [5] Department of Interventional Cardiology and Angiology, Institute of Cardiology, Warsaw, Poland, [6] Department of Infection, Immunity and Cardiovascular Disease, University of Sheffield, Sheffield, United Kingdom, [7] Department of Cardiology, Sheffield Teaching Hospitals NHS Foundation Trust, Sheffield, United Kingdom

Edited by:
Markus Reiterer,
Medtronic, United States

Reviewed by:
Paolo Di Achille,
IBM Research, United States
Radu Iliescu,
Grigore T. Popa University of Medicine and Pharmacy, Romania

****Correspondence:***
Alberto Marzo
a.marzo@sheffield.ac.uk

Specialty section:
This article was submitted to Computational Physiology and Medicine, a section of the journal Frontiers in Physiology

Received: *28 February 2018*
Accepted: *23 July 2018*
Published: *17 August 2018*

Citation:
Mandaltsi A, Grytsan A, Odudu A, Kadziela J, Morris PD, Witkowski A, Ellam T, Kalra P and Marzo A (2018) Non-invasive Stenotic Renal Artery Haemodynamics by in silico Medicine. Front. Physiol. 9:1106. doi: 10.3389/fphys.2018.01106

Background: Measuring the extent to which renal artery stenosis (RAS) alters renal haemodynamics may permit precision medicine by physiologically guided revascularization. This currently requires invasive intra-arterial pressure measurement with associated risks and is rarely performed. The present proof-of-concept study investigates an *in silico* approach that uses computational fluid dynamic (CFD) modeling to non-invasively estimate renal artery haemodynamics from routine anatomical computed tomography (CT) imaging of RAS.

Methods: We evaluated 10 patients with RAS by CT angiography. Intra-arterial renal haemodynamics were invasively measured by a transducing catheter under resting and hyperaemic conditions, calculating the translesional ratio of distal to proximal pressure (Pd/Pa). The diagnostic and quantitative accuracy of the CFD-derived virtual Pd/Pa ratio (vPd/Pa) was evaluated against the invasively measured Pd/Pa ratio (mPd/Pa).

Results: Hyperaemic haemodynamics was infeasible and CT angiography in 4 patients had insufficient image resolution. Resting flow data is thus reported for 7 stenosed arteries from 6 patients (one patient had bilateral RAS). The comparison showed a mean difference of 0.015 (95% confidence intervals of ± 0.08), mean absolute error of 0.064, and a Pearson correlation coefficient of 0.6, with diagnostic accuracy for a physiologically significant Pd/Pa of ≤ 0.9 at 86%.

Conclusion: We describe the first *in silico* estimation of renal artery haemodynamics from CT angiography in patients with RAS, showing it is feasible and diagnostically accurate. This provides a methodological framework for larger prospective studies to ultimately develop non-invasive precision medicine approaches for studies and interventions of RAS and resistant hypertension.

Keywords: computational fluid dynamics, fractional flow reserve, precision medicine, cardiovascular modeling, non-invasive diagnosis, renal artery haemodynamics, *in silico* medicine

INTRODUCTION

Renovascular disease is characterized by unilateral or bilateral renal artery stenosis (RAS). In Western populations 90% of RAS is caused by atherosclerotic renal artery stenosis (ARAS), and 10% by fibromuscular dysplasia (FMD) (Textor, 2017). ARAS affects 7% of North Americans aged over 65 years (Hansen et al., 2002), and the incidence is rising due to aging, obesity, diabetes, and hypertension (Kalra et al., 2005). FMD affects 0.4% of the population and is seen in younger patients (Slovut and Olin, 2004). Reduced renal perfusion causes progressive chronic kidney disease (CKD) and drives neurohormonal activation with subsequent resistant hypertension, end-stage kidney disease, and death (Textor, 2017). Major trials testing efficacy of reperfusion by angioplasty and stenting demonstrated no benefit beyond drug therapy (antihypertensives and statins) (Wheatley et al., 2009; Riaz et al., 2014). However, those trials recruited patients with physiologically mild ARAS and less severe CKD. This group are less likely to derive benefit from revascularisation compared with those with more severe ARAA and CKD (Hagemann et al., 2017). There is therefore a need for less invasive method to determine the physiological significance of ARAS. Moreover, neutral outcomes might have been exemplified due to patients with: median stenoses of no less than 70%, preserved renal function, and low annual mortality (Ritchie et al., 2014). It is acknowledged that a visually measured RAS diameter for the assessment of the lesion's severity has a poor correlation to quantitative methods (Kadziela et al., 2016). Moreover, multiplanar angiographic assessment has a poor correlation with physiological assessment of the pressure and flow dynamics (Drieghe et al., 2008). The dissociation is attributed to two-dimensional angiographic views that ignore: complex vessel geometry, lesion length, radiolucent atherosclerotic plaques, collateral circulation, microvascular remodeling, and renal parenchymal injury both distal to the stenosis and in the contralateral kidney (Johnson et al., 2013).

The Cardiovascular Outcomes in Renal Atherosclerotic Lesions (CORAL) trial was initially designed to select haemodynamically severe ARAS cases, but eligibility criteria were expanded due to slow recruitment (Clinical Trials Identifier: NCT0081731[1]). This was related to the added complexity, risk, and cost of invasive haemodynamic measurements in ARAS which are not routine clinical practice. Recent subgroup analysis of the CORAL trial found no benefit of revascularization amongst those with more haemodynamically severe ARAS (Murphy et al., 2015). Hence the potential of RAS haemodynamics to permit precision medicine through physiologically guided trials of revascularization remains uncertain and further studies are hampered by the need for invasive measurements with associated risks.

The same haemodynamic and clinical considerations are apparent in the context of coronary artery disease. In 2007, the landmark COURAGE trial failed to demonstrate prognostic benefit from percutaneous coronary intervention (PCI) in stable coronary artery disease (Boden et al., 2007), whereas subsequent studies did demonstrate prognostic benefit when patients with demonstrable ischaemia, i.e., physiologically significant lesions were specifically targeted (Shaw et al., 2008). More recently, a number of studies have demonstrated the superiority of physiological over anatomical assessment of CAD (De Bruyne et al., 2014).

In silico medicine describes the use of computational simulations in the diagnosis, treatment or prevention of disease. A robust *in silico* technique for the non-invasive assessment of the haemodynamic severity of RAS would enable targeted trial recruitment and therapeutic intervention, to those most likely to derive benefit. Better characterisation of RAS lesion severity could also reduce the sample size required for trials of novel interventions. An *in silico* application, called VIRTUheart, has been developed at the University of Sheffield to compute the physiological significance of coronary artery disease from angiography using CFD modeling (Morris et al., 2013). The aim of this proof-of-concept study was to develop and validate a similar CFD model to predict RAS haemodynamics from computed tomography (CT) imaging.

MATERIALS AND METHODS

Patients

Demographic, imaging and haemodynamic data from 10 patients with 11 stenoses (one patient had bilateral RAS) were provided by the Department of Interventional Cardiology and Angiology (Warsaw, Poland). The patients were both female and male, aged between 40 and 79 years of age. **Table 1** presents the clinical profiles for the anonymised patient data set. Ethics approval for sharing and analyzing retrospective anonymised patient data was obtained from the local Bioethics Committee at the Institute of Cardiology in Warsaw. Patient data was fully anonymised prior to data sharing and analysis. We collected CT and invasive angiographic imaging data from consenting patients with hypertension and RAS. Patients with prior contrast nephropathy, severe valvular disease, New York Heart Association (NYHA) III-IV heart failure or estimated Glomerular Filtration Rate (eGFR) below 30 mL/min were excluded. Serum creatinine was measured and eGFR was calculated by the modification of diet in renal disease (MDRD) 4-variable equation for each patient (Levey et al., 2006). eGFR reflects kidney function and may also reflect distal vascular resistance which is important for the computational model.

CT Renal Angiography

Computed tomography renal angiography was performed with a 64-detector CT scanner (Somatom Sensation Cardiac 64; Siemens, Erlangen, Germany). ARAS patients had CT images acquired as a part of the PREFFER study (Kadziela et al., 2011). The two FMD patients underwent imaging as per standard clinical practice. A minimum of 100 CT slices in axial, coronal, and sagittal orientations were acquired with in-plane resolution by pixel spacing of 0.59 to 0.83 mm. A typical example is shown in **Figure 1**.

---

[1] https://clinicaltrials.gov/

TABLE 1 | Patient Characteristics.

Patient no.	Age (yrs)	Gender	Stenotic Side	Condition	Diameter stenosis (%)	eGFR (mL/min/1.73m^2)
1	74	Female	Left	ARAS	72	62
2	65	Female	Left	ARAS	46	46
3	64	Male	Left	ARAS	72	72
4	79	Male	Right	ARAS	20	43
5	58	Male	Left	ARAS	42	86
6	57	Female	Right	FMD	43	87
7	49	Female	Left	ARAS	53	125
8	74	Male	Left	ARAS	76	33
9	72	Female	Right	ARAS	67	65
10	40	Female	Both	FMD	n.a.	102

*Age was at the time of the CT image acquisition. ARAS, atherosclerotic renal artery stenosis; FMD, fibromuscular dysplasia; eGFR, estimated Glomerular Filtration Rate. Diameter stenosis values were calculated using the formula DS = 100-(MLD/RLD)*100, where DS is diameter stenosis, MLD is minimum lumen diameter, RLD is reference lumen diameter.*

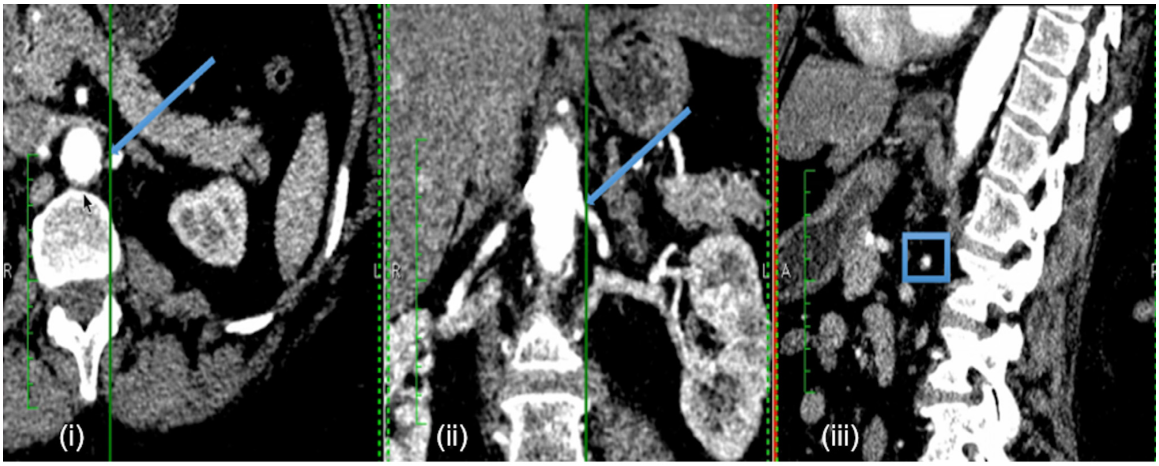

FIGURE 1 | Example of patient-specific CT images. Example CT images of each anatomical orientation for Patient 2: axial **(i)**, coronal **(ii)**, and sagittal **(iii)**. The arrows in the axial and coronal slices, and the box in the sagittal slice indicate the approximate location of the renal stenosis for the specific case.

Invasive Haemodynamic Measurements

Heparin (4000–5000 IU) was administered to maintain adequate anticoagulation during the procedure. Distal pressure (Pd) was measured with a 0.014″ Pressure Wire 5 (Radi Medical Systems, Sweden) and proximal pressure (Pa) was measured from the guiding catheter tip. During pressure measurements, the tip was disengaged from the ostium to avoid pressure damping. The translesional ratio Pd/Pa was calculated as the ratio of mean Pd to mean Pa. This *in vivo* measured Pd/Pa ratio (mPd/Pa) is a standard measure to evaluate the haemodynamic significance of an arterial stenosis (Subramanian et al., 2005). The hyperaemic renal Fractional Flow Reserve (rFFR) was calculated in the same way after the administration of 30 mg of papaverine into the renal artery distal to the stenosis via a 3F multifunctional catheter.

COMPUTATIONAL WORKFLOW

Our computational workflow segmented and reconstructed the patient-specific three-dimensional arterial geometries from the CT images. CFD analysis was used to simulate the translesional haemodynamics. The computed results were used to calculate the 'virtual' Pd/Pa (vPd/Pa) which was validated against the invasively measured Pd/Pa (mPd/Pa).

Volume Segmentation

The workflow's first step involved segmenting a volume from the available CT images. For that purpose the non-parametric geodesic active regions (GAR) method was implemented, following the algorithm presented in (Hernandez and Frangi, 2007). This segmentation model was tested and made available through the application @neufuse, initially developed as part of the '@neurIST project'[2].

Computational Fluid Dynamics

CFD was implemented on the ANSYS®-CFX^{TM} (ANSYS Canonsburg, United States) simulation software: a volumetric mesh was created, the flow's boundary conditions were set,

---

[2] http://www.aneurist.org//index.php

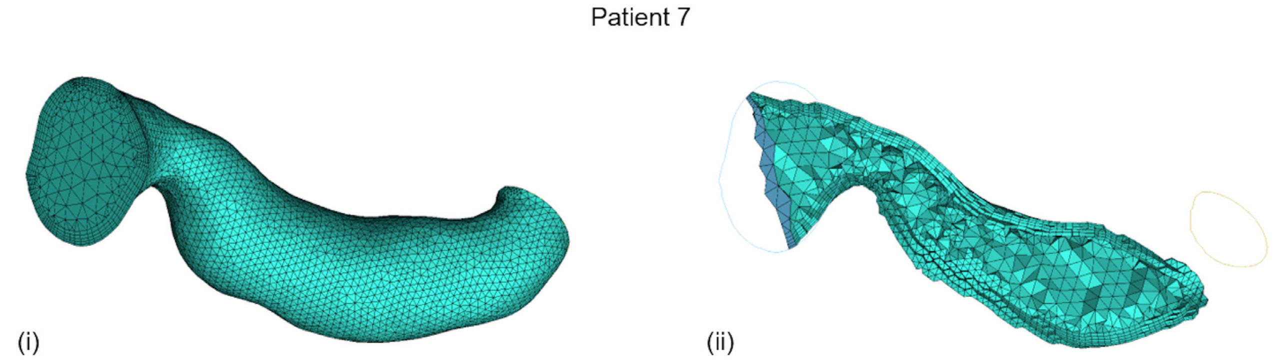

FIGURE 2 | Typical volume mesh for the CFD simulations: **(i)** the mesh elements on the wall and on the inlet cross-section, and **(ii)** the tetrahedral elements inside the volume and the prismatic layers near the wall on a cut plane can be observed.

the flow was solved on a Navier–Stokes-based solver, and the flow solution was post-processed for the vPd/Pa estimation. The method from Marzo et al. (2009) was adopted for the creation of the volumetric mesh: an octree approach was implemented with finer grids at the wall, tetrahedral elements inside the volume, and five layers of prismatic elements adjacent to the wall (for better accuracy of the velocity gradient). An average mesh density of approximately 200 elements per cubed millimeter was chosen. An example volume mesh cross-section is presented in **Figure 2**.

Typical renal boundary flow conditions were chosen for the CFD on the renal arterial segments. The 1D model of the systemic arterial tree by Reymond et al. (2011) was utilized, which provides pressure and flow values (at rest) over a heart cycle for various points within the renal vasculature, based on the healthy state. Based on these data, an inlet velocity (with a plug flow velocity profile) and an outlet peripheral resistance were set. Peripheral resistance is defined as the ratio of the pressure drop from the point of measurement to the capillary level along that branch to the flow passing through the point of measurement. It describes the resistance encountered by the blood as it flows through the systemic arterial system and represents the effect of downstream microcirculation (of smallest arteries and arterioles) (Bott, 2014). For the steady flow simulations of the current study we calculated an average from Reymond's values over the heart cycle for the pressure and flow boundary conditions in the renal arteries. The ultimate vPd/Pa calculation is thus a time-averaged parameter extracted from the time-dependent boundary data. It should be noted that, under the aforementioned boundary conditions, hyperaemic haemodynamics was infeasible and the study focuses on resting flow conditions.

Additionally, we compared the vPd/Pa estimations when the geometry included the aortic and contralateral renal geometry, and when it did not. Reymond's boundary conditions are not representative of our patient data set, consisting of old and diseased subjects. When the geometry only includes the renal arterial segment, a realistic flow is imposed by the inlet boundary condition and therefore this limitation is overcome. However, when the inlet velocity boundary condition is set on the aorta, Reymond's measurements underestimate the resistance of renal artery with stenosis, resulting in much higher resistance to blood flow entering the renal artery, which in turn results in insufficient blood flow into the renal artery.

Therefore, for the purposes of this comparative part of our study (patient 7 and 10), we fine-tuned the outlet pressure in order for the blood flow into the renal artery to reach expected generic levels. A direct comparison between the two geometric segments was then possible by setting the boundary flow conditions, as follows: (i) for the cases including the aorta, a generic inlet aortic velocity boundary, and adjusted outlet stenotic renal, contralateral renal and downstream aortic pressure were defined, and (ii) for the cases excluding the aorta, a generic inlet renal velocity and the same adjusted outlet renal stenotic pressure as with case (i) were defined. The boundary flow conditions for the comparative study and for the aforementioned simulations on the complete data set are illustrated in **Figure 3**.

The program solves the steady incompressible Navier–Stokes momentum equations in combination with the continuity equation. The flow solution follows the implicit finite volume discretisation method for the numerical approach. The blood flow is modeled as a Newtonian fluid of viscosity at $\mu = 0.0035$ Pa s and constant density $\rho = 1066$ kg m^{-3}, and the arterial wall is assumed to be rigid (Ferziger and Peric, 2002). The computer used for the simulations was an Intel(R) Xeon(R) X5690 CPU @ 3.47 GHz x 12, 24.0 GB RAM, 64-bit OS (Windows 7). The steady flow simulations took on average 2 min to solve. The general clinical protocol indicated that the proximal pressure was measured furthest from the stenosis and close to the opening to the aorta, whereas the distal pressure was measured 10–20 mm downstream of the stenosis. We defined three downstream cross-sectional areas within this range and calculated the average pressure across each of them. Downstream pressure was then simply defined as the arithmetic average of the three. For the upstream pressure, an additional cross-sectional area was carefully chosen to exclude pressure extremes resulting from the Bernoulli effect due to the proximity of the stenosis to the inlet boundary, and the average pressure across it was calculated. vPd/Pa was then estimated as the ratio of downstream to upstream pressure (**Figure 4**).

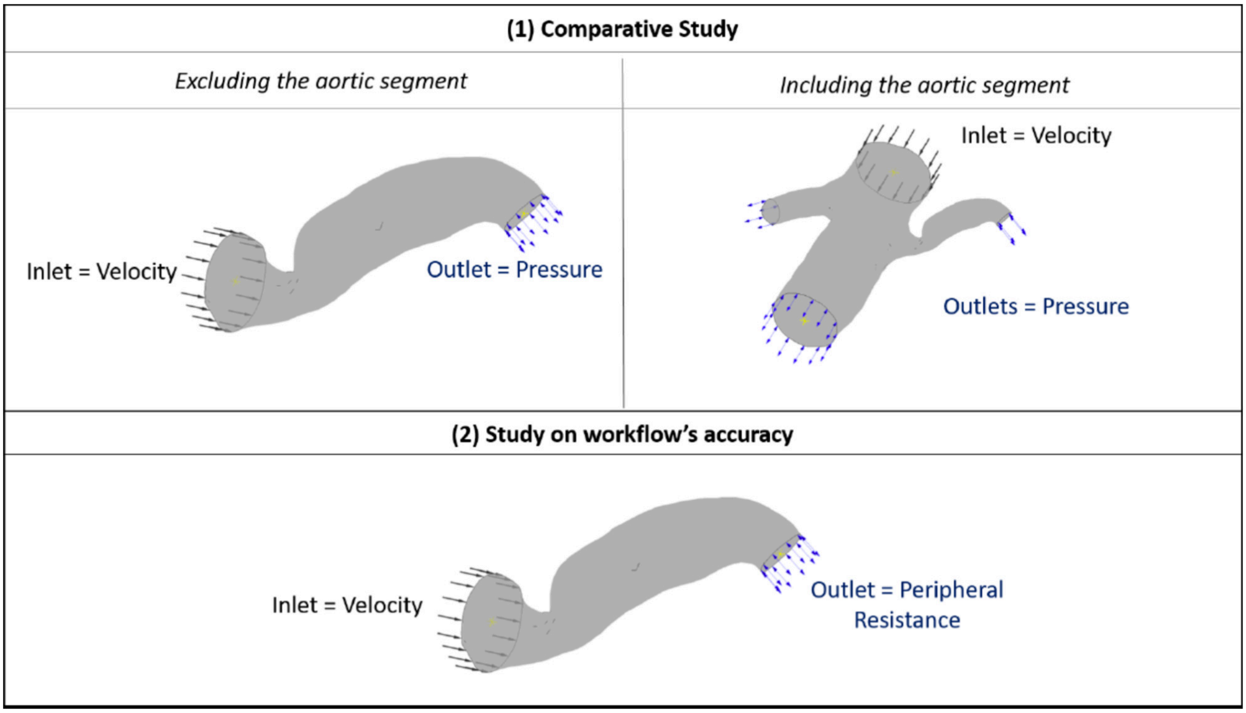

FIGURE 3 | Boundary flow conditions for the set of simulations. The image summarizes the boundary flow conditions applied on the computational simulations: **(1)** for the comparative study between including and excluding the aortic segment (top row) and **(2)** for testing the accuracy of the workflow (bottom row) across the patient data set. The case of Patient 7 is used here for illustration purposes.

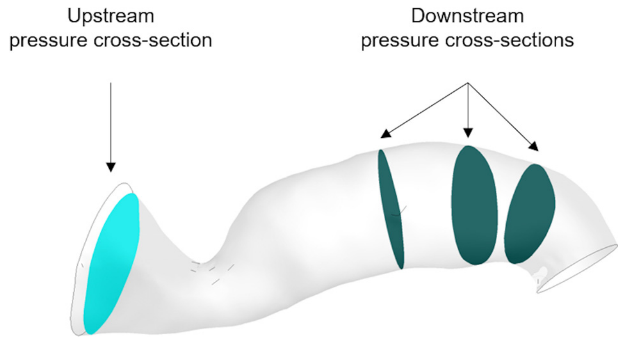

FIGURE 4 | Downstream and upstream pressure monitoring cross-sections.

Statistical Analysis

We follow the statistical analysis of (Morris et al., 2013) for the diagnostic and quantitative accuracy of our workflow. Consensus guidelines for RAS stenting (Parikh et al., 2014) and research on the criteria for renovascular hypertension due to RAS (De Bruyne et al., 2006) indicate a Pd/Pa of ≤ 0.9 as physiologically significant. On that basis, the diagnostic accuracy was evaluated by calculating the sensitivity, specificity, positive predictive value (PPV), negative predictive value (NPV) and overall accuracy for our results, with the binomial test's 95% confidence intervals (CIs). The correlation between mPd/Pa and vPd/Pa data was visualized and assessed through a diagram plot. Additionally, agreement was measured by the mean difference and absolute error between measured and virtual values, and the standard deviation of the differences were computed in order to illustrate the quantitative accuracy of the workflow in a Bland–Altman plot.

RESULTS

Volume Segmentation

Figure 5 presents the reconstructed geometries, following a process of manual correction whereby the region of interest was separated from local tissue artifact. Three of the CT scans were of insufficient quality for vessel reconstruction (indicated by a red frame in **Figure 5**) and were therefore excluded from analysis. For an additional case, the number of CT slices were insufficient in order for the segmentation tool to process them. The successfully segmented stenosed renal arteries include the descending aorta and the contralateral renal artery. Patients whose renal arteries show multiple stenoses, for example Patient 10, were suffering from FMD.

Simulations

The following sections present the results from our study, including a quantitative comparison to assess the accuracy of the vPd/PA against the mPd/Pa from the simulations in the complete dataset of 7 RASs.

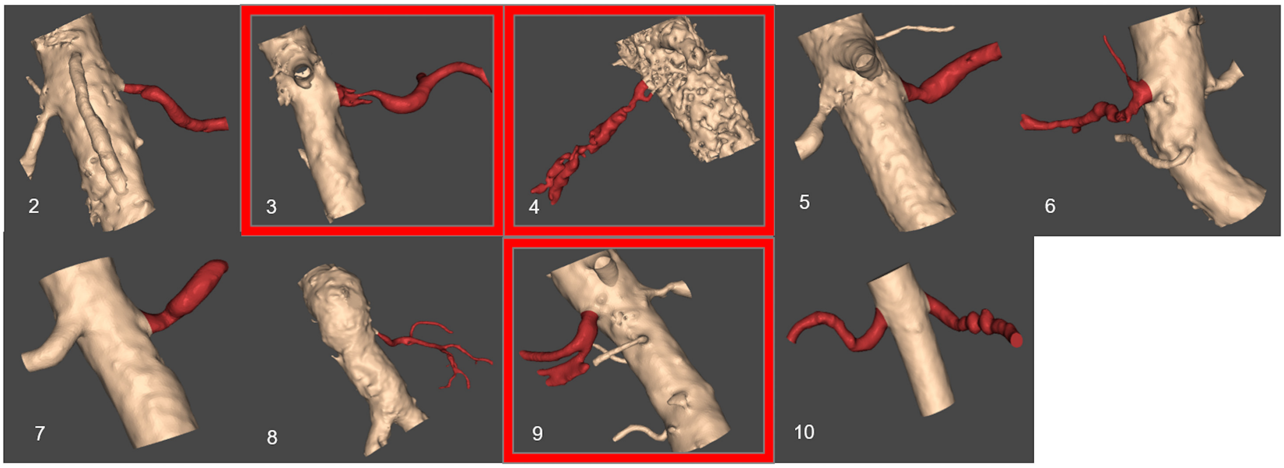

FIGURE 5 | Resulting segmented patient renal geometries. Segmented volumes of renal arteries: unsuccessful segmentation examples based on the provided CT images are indicated by a red frame. The number for each image corresponds to patient number in **Table 1**.

Comparative Study With and Without the Aorta

Table 2 shows the calculations of vPd/Pa for the two patients of our comparative study: Patient 7 (one stenosis), and Patient 10 (double stenosis). A percentile differences in vPd/Pa is estimated between the computations when the aortic geometry is included and when it is not, demonstrating a maximum difference of 1.28% for the left RAS of Patient 10. The remaining two cases present a difference of less than 1%. **Table 2** (last column) also shows the variability in the values of downstream pressure extracted from the three different post-stenotic locations, showing a direct correlation between pressure variability and anatomical complexity (**Figure 5**).

Quantitative Accuracy

The results of mPd/Pa and vPd/Pa are presented in parallel in the bar plot diagram of **Figure 6**. This bar plot illustrates mPd/Pa side-by-side with vPd/Pa for each patient, indicated by their number (Patient 10's RAS on both renal arteries is distinguished with R for the right, and L for the left RAS).

TABLE 2 | Comparative study between including and excluding the aortic geometry in CFD.

Patient no.	vPd/Pa (incl. aorta)	vPd/Pa (excl. aorta)	difference [%]	Pd [Pa]
7	0.847	0.865	2.1	13374 ± 69
10 (Right)	0.829	0.862	3.8	12806 ± 8
10 (Left)	0.852	0.853	0.1	13037 ± 169

Quantitative differences of vPd/Pa when implementing CFD with geometries that include and exclude the aortic segment, for Patients 7 and 10 (Patient 10 presents a renal stenosis on both the right and the left renal artery). The last column reports the arithmetic average and standard deviation (SD) of the downstream pressure (Pd) calculated at three different locations for the case without the aorta only.

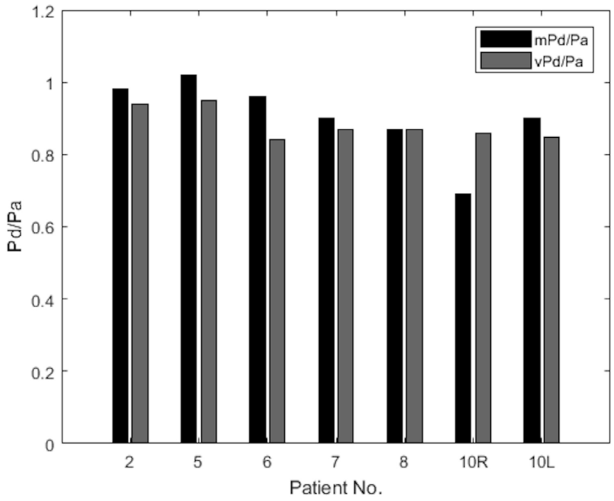

FIGURE 6 | Measured versus virtual Pd/Pa.

Table 3 summarizes the measures of accuracy of our vPd/Pa estimations against mPd/Pa: the mean difference between mPd/Pa and vPd/Pa was ± 0.015, with an average absolute error of ± 0.064, representing a percentage error of 8.1%. Those quantitative measures are used to illustrate the accuracy of our computations, seen in the Bland Altman plot of **Figure 7**. The correlation between measured and virtual values (Pearson correlation coefficient $r = 0.604$) is illustrated in **Figure 8**.

Diagnostic Accuracy

Table 4 overviews the accuracy of our virtual simulations in identifying a physiologically significant RAS. Relative to mPd/Pa, the sensitivity, specificity, PPV and NPV of vPd/Pa was 1.0 (95% CI 0.4–1.0), 0.67 (0.13–0.98), 0.8 (0.3–0.99) and 1.0 (0.2–1.0). Overall diagnostic accuracy was 86%.

TABLE 3 | Quantitative accuracy of vPd/Pa.

Patient no.	mPd/Pa	vPd/Pa	Diameter stenosis (%)
2	0.981	0.954	46
5	1.016	0.954	42
6	0.958	0.862	43
7	0.903	0.865	53
8	0.872	0.865	76
10R	0.690	0.862	n.a.
10L	0.900	0.853	n.a.

Measures of accuracy	
Mean difference	± 0.015
Standard deviation	0.087
Mean absolute error	± 0.064
Mean absolute error (%)	8.1
Pearson's coefficient (r)	0.604

Quantitative comparison between mPd/Pa and vPd/Pa for our patient-specific data set, evaluating the mean difference between mPd/Pa and vPd/Pa, standard deviation, average absolute error, and Pearson's correlation coefficient.

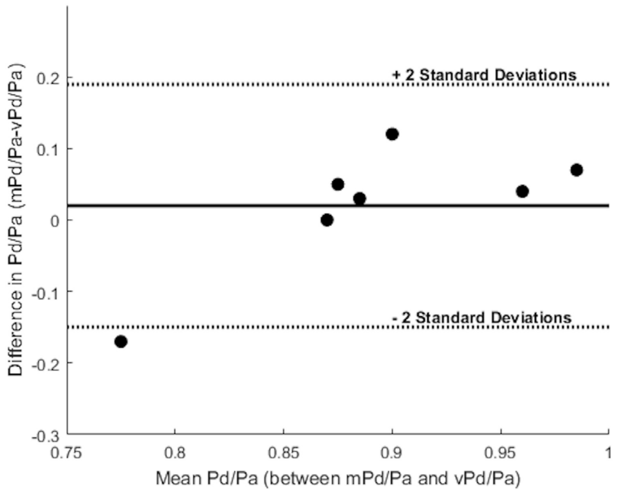

FIGURE 7 | Bland Altman plot. The solid line represents the mean value of the difference between mPd/Pa and vPd/Pa, and the dotted lines create boundaries for ± 2 standard deviations from the mean difference. Each dot represents a stenosis and combines the knowledge for the difference and the mean value between the measured and the virtual calculations.

DISCUSSION

This proof-of-concept study investigates a novel *in silico* approach that uses CFD modeling to non-invasively estimate renal artery haemodynamics from routine CT imaging of RAS. Our results demonstrate that this approach is feasible and diagnostically accurate. This may have great value in reducing the need for invasive haemodynamic assessment. In this feasibility study, several challenges and limitations were encountered. Although the range of mPd/Pa reflects the expected clinical range, the sample size was modest. There were limited available data around 0.9 threshold and only one case was less than 0.8. It is likely that clinically and statistically more conclusive results might be achieved with a larger sample size.

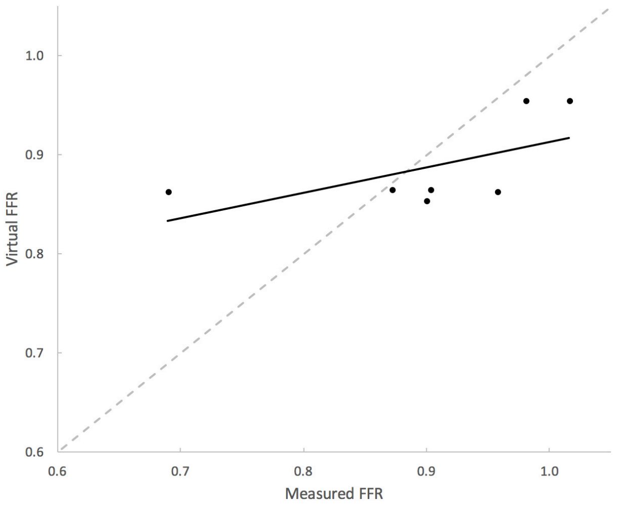

FIGURE 8 | Correlation between mPd/Pa and vPd/Pa. The diagram plots mPd/Pa against vPd/Pa for each stenosis, where the segmented line in gray represents the points of exact agreement between measured and virtual calculations, while the solid line represent the data trendline of best-fit.

TABLE 4 | Diagnostic accuracy of vPd/Pa.

Patient no.	Test outcome
2	True negative
5	True negative
6	False negative
7	True positive
8	True positive
10R	True positive
10L	True positive

Diagnostic accuracy of vPd/Pa for our patient-specific data set on the basis of identifying a physiologically significant RAS.

The anatomy and geometry of the stenosed segments (**Figure 5**) are highly variable but some anatomic generalizations could be made: the arteries are tortuous, they emerge perpendicular to the aorta, and most of the stenoses are detected very close to the ostium of the renal artery, an observation which is clinically supported for ARASs (Kaatee et al., 1996). These anatomic observations also posed a challenge for the *in silico* simulations. The velocity field at the inlet of the renal artery will be influenced by these sharp bifurcating angles and there will be a difference when considering or not the aortic part. This different flow field might result in a different pressure distribution at these bifurcations that might influence adversely our vPd/Pa prediction across the stenosis. As part of this study we investigated the effect of including the aorta or not on the accuracy of vPd/Pa. We found that the difference in the vPd/Pa estimations was too small ($< 3.8\%$) to justify the use of the aortic segment. Considering the added requirements on computational time, and boundary conditions that are largely unknown or will have to be invasively measured, it was decided that the workflow should use only the stenosed arterial geometry in the vPd/Pa calculations.

Executing the simulation including the aorta also contributed to an improved understanding of the expected velocity profile at the inlet of the renal artery. In our simulations, we assumed plug flow, i.e., the velocity was constant across the inlet cross-section (this is demonstrated in a cross-sectional area near the inlet in **Figure 9**(i) for the case excluding the aortic geometry). For the same cross-section in the case when the aortic geometry is included [**Figure 9**(ii)], the velocity profile upon entry to the renal artery, although not presenting plug flow, does not exactly represent a parabolic velocity profile either. At a later stage, a more complex velocity profile might be more suitable, supported by *in vivo* measurements.

For a subset of datasets (patient 7, patient 10L, patient 10R) we reported the potential impact of uncertainty in the location of data extraction on the predicted values of downstream pressure (**Table 2**). This showed only marginal effect on clinical significance but a direct correlation between data variability (standard deviation) and anatomical complexity, highlighting the importance for more precise protocols for more quantitative comparisons and analyses.

Even though patient-specific arterial geometries were used in the CFD calculations, the applied boundary flow conditions were generic (defined for healthy and young individuals) for renal flows, which might have compromised the precision of vPd/Pa. The potentially unrealistic high flow rates due to the generic boundary flow conditions might have led to the observed overestimation of vPd/Pa for all but one presented cases (**Figure 8**). However, echo Doppler measurements of maximum velocity at the stenoses were available, and these data were used and compared with velocity at the same locations, to validate the approach of using typical renal artery flows.

Despite the sample size and the generic boundary conditions, vPd/Pa for the present data set, showed a good agreement with

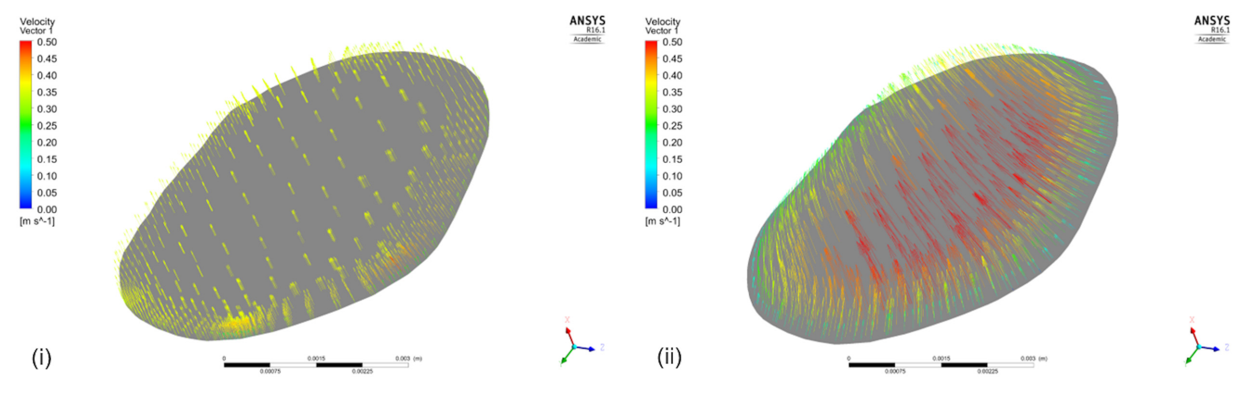

FIGURE 9 | Velocity Vectors including and excluding the aorta. The figure shows the velocity vectors on a cross-sectional area of the renal artery close to the aorta for the simulation **(i)** that does not include the aortic geometry, and **(ii)** that does.

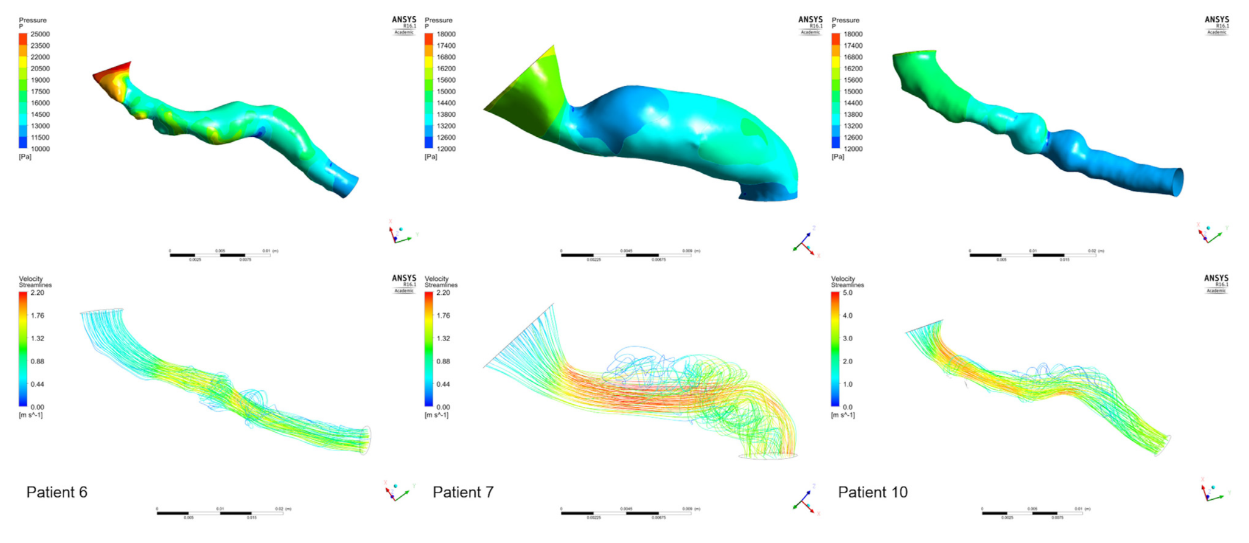

FIGURE 10 | Examples from the CFD analysis. Pressure distributions (top row) and velocity streamlines (bottom row) are presented for the stenoses of three patients: 6 (left column), 7 (middle column), 10 (Right RAS, right column).

the values of mPd/Pa (only Patient's 10 Right RAS was evaluated just outside the 2 standard deviation boundaries, shown in **Figure 7**). This vPd/Pa underestimation for Patient 10 possibly indicates the importance of patient-specific boundary conditions, especially for cases of severe stenosis. Nonetheless, contrary to previous CFD studies (Morris et al., 2017), we can argue that the influence of geometry in our workflow seems more important than boundary conditions. It should also be noted that based on the estimated diagnostic accuracy, and in comparison with the standard anatomical criteria in **Table 1**, our workflow managed to evaluate only one false result in identifying a physiologically significant RAS (**Table 4**), demonstrating a very encouraging result for RAS diagnosis using physiology based metrics.

The aim of these computational simulations is achieving accuracy in calculating vPd/Pa but computational time and memory are also of importance. It should be noted that, alongside the presented steady simulations, finer mesh simulations and transient simulations over the heart cycle for the dataset were run, that rendered quantitatively insignificant differences in the resultant vPd/Pa.

Figure 10 presents the pressure distribution (top row) and velocity streamlines (bottom row) for three of our cases. Considering the complex geometries, the flow, as is evident in the figure, is also complex. Vortices are observed and areas of both high and low pressures can be identified. Estimating a Reynolds number for our data set is thus important. Reynolds number in the presented results ranged between 813 and 940, with two cases at 1463 and 1965. According to the theoretical Reynolds definition for internal flow in straight pipes, that indicates laminar flow. However, most of the presented geometries are far from an assumed straight cylinder which may induce turbulence at lower Reynolds number values. Therefore, consideration of turbulent effects in stenosed renal arteries might be further considered in the next research stage to achieve further accuracy.

Given the observations made in this study, there is a clear direction for the next stage of research. A larger clinical cohort, with a clinically representative range of mPd/Pa values will increase statistical confidence of the hypothesized correlations we demonstrated in this proof-of-concept study. Standardization and automisation of the workflow will be required in order to deal with a larger number of clinical cases. A further limitation was the use of retrospective CT angiographic and invasive haemodynamic data not specifically collected for the purposes of this study. Future studies are planned that will prospectively collect more detailed information of invasive haemodynamics and optimize CT or magnetic resonance image acquisition protocols. This will permit: (1) the standardization of image resolution for increased feasibility of volume segmentation, (2) the enhancement of *in silico* predictions by complementary non-invasive measures of renal artery blood flow using Doppler sonography (Li et al., 2008; Kaya, 2012), and (3) the more direct comparison of *in silico* with *in vivo* predictions by more precisely specifying the location of pressure measurements.

Information on the functionality of the post-stenosis tissue is important for the clinical diagnosis of RAS, but can also affect our computational simulations, as it is reflected on the value of peripheral resistance. eGFR which was measured in this study can provide such an assessment and although most of the provided cases presented normal levels of eGFR, biomarkers for kidney function could inform our *in silico* simulations in the future. Bearing in mind that there is no consensus in the medical community on a quantitative measure for the health of each individual kidney, creatinine clearance rates, kidney size, resistant hypertension, and velocity measurements comparing the stenosed artery with the aorta and the contralateral renal artery, have been previously examined to create an informed profile on stenosis severity (Zeller et al., 2008; Noory et al., 2016; Staub et al., 2016). There has also been recent research on the use of MRI for the assessment of kidney perfusion (Odudu et al., 2012). Consequently, knowledge on the functionality of the stenosed kidney provided clinically at a later study, combined with a statistically significant data set size, could contribute to the investigation of a correlation between peripheral resistance and renal function clinical indicators.

This study demonstrated the potential value of *in silico* assessment of renal haemodynamics for the purposes of RAS diagnosis, implementing a fast segmentation of high standard, and calculating reliable values of vPd/Pa. The next stage of research, based on the presented analysis, will largely contribute to reliably illustrating the importance of non-invasive renal haemodynamics on diagnosis.

CONCLUSION

This is the first *in silico* assessment of renal artery haemodynamics from CT angiography. This approach is feasible and diagnostically accurate. Non-invasive renal artery haemodynamic assessment may facilitate precision medicine in patients with RAS and resistant hypertension.

AUTHOR CONTRIBUTIONS

AiM, AM, and PM conceived and designed the study. AO, JK, PK, AiM, and AM acquired and analyzed the clinical data. All authors analyzed and interpreted the study results and critically revised the article. AiM drafted the article. AM supervised the study.

FUNDING

We acknowledge Sheffield Hospitals Charity and the Insigneo Bursary for Clinical Translation for funding this research.

ACKNOWLEDGMENTS

We acknowledge the valuable contribution of Dr. Maria-Cruz Villa-Uriol, for her expert advice on image segmentation, and Dani Silva Soto, for his advice in the computational tool-chain.

REFERENCES

Boden, W. E., O'Rourke, R. A., Teo, K. K., Hartigan, P. M., Maron, D. J., Kostuk, W. J., et al. (2007). Optimal medical therapy with or without PCI for stable coronary disease. *N. Engl. J. Med.* 356, 1503–1516. doi: 10.1056/NEJMoa070829

Bott, R. (2014). *Guyton and Hall Textbook of Medical Physiology*, 13th Edn. New York, NY: Elsevier, doi: 10.1007/s13398-014-0173-7.2

De Bruyne, B., Manoharan, G., Pijls, N. H., Verhamme, K., Madaric, J., Bartunek, J., et al. (2006). Assessment of renal artery stenosis severity by pressure gradient measurements. *J. Am. Coll. Cardiol.* 48, 1851–1855. doi: 10.1016/j.jacc.2006.05.074

De Bruyne, B., Pijls, N. H., Kalesan, B., Barbato, E., Tonino, P. A., Piroth, Z., et al. (2014). Fractional flow reserve–guided pci for stable coronary artery disease. *N. Engl. J. Med.* 371, 1208–1217. doi: 10.1056/NEJMoa1408758

Drieghe, B., Madaric, J., Sarno, G., Manoharan, G., Bartunek, J., Heyndrickx, G. R., et al. (2008). Assessment of renal artery stenosis: side-by-side comparison of angiography and duplex ultrasound with pressure gradient measurements. *Eur. Heart J.* 29, 517–524. doi: 10.1093/eurheartj/ehm631

Ferziger, J. H., and Peric, M. (2002). *Computational Methods for Fluid Dynamics*. New York, NY: Springer-Verlag Berlin Heidelberg, doi: 10.1016/S0898-1221(03)90046-0

Hagemann, R., Dos Santos Silva, V., Cardoso Carvalho, F., Barretti, P., Martin, L. C., Vassallo, D., et al. (2017). Attenuation of renal functional decline following angioplasty and stenting in atherosclerotic renovascular disease. *Nephron* 135, 15–22. doi: 10.1159/000447753

Hansen, K. J., Edwards, M. S., Craven, T. E., Cherr, G. S., Jackson, S. A., Appel, R. G., et al. (2002). Prevalence of renovascular disease in the elderly: a population-based study. *J. Vasc. Surg.* 36, 443–451. doi: 10.1067/mva.2002.127351

Hernandez, M., and Frangi, A. F. (2007). Non-parametric geodesic active regions: method and evaluation for cerebral aneurysms segmentation in 3DRA and CTA. *Med. Image Anal.* 11, 224–241. doi: 10.1016/j.media.2007.01.002

Johnson, N. P., Kirkeeide, R. L., and Gould, K. L. (2013). Coronary anatomy to predict physiology fundamental limits. *Circ. Cardiovasc. Imaging* 6, 817–832. doi: 10.1161/CIRCIMAGING.113.000373

Kaatee, R., Beek, F. J., Verschuyl, E. J., vd Ven, P. J., Beutler, J. J., van Schaik, J. P., et al. (1996). Atherosclerotic renal artery stenosis: ostial or truncal? *Radiology* 199, 637–640.

Kadziela, J., Michalowska, I., Pregowski, J., Janaszek-Sitkowska, H., Lech, K., Kabat, M., et al. (2016). Stent sizing strategies in renal artery stenting: the comparison of conventional invasive renal angiography with renal computed tomographic angiography. *Postepy Kardiol. Interwencyjnej* 12, 116–121. doi: 10.5114/aic.2016.59361

Kadziela, J., Witkowski, A., Januszewicz, A., Cedro, K., Michałowska, I., Januszewicz, M., et al. (2011). Assessment of renal artery stenosis using both resting pressures ratio and fractional flow reserve: relationship to angiography and ultrasonography. *Blood Press.* 20, 211–217. doi: 10.3109/08037051.2011.558332

Kalra, P. A., Guo, H., Kausz, A. T., Gilbertson, D. T., Liu, J., Chen, S. C., et al. (2005). Atherosclerotic renovascular disease in United States patients aged 67 years or older: risk factors, revascularization, and prognosis. *Kidney Int.* 68, 293–301. doi: 10.1111/j.1523-1755.2005.00406.x

Kaya, M. (2012). "The evaluation of renal hemodynamics with doppler ultrasonography," in *Hemodynamics-New Diagnostic and Therapeutic Approaches*, (Erzurum: Atatürk University), 1–31. doi: 10.5772/2113

Levey, A. S., Coresh, J., Greene, T., Stevens, L. A., Zhang, Y. L., Hendriksen, S., et al. (2006). Using standardized serum creatinine values in the modification of diet in renal disease study equation for estimating glomerular filtration rate. *Ann. Intern. Med.* 145, 247–254. doi: 10.7326/0003-4819-145-4-200608150-00004

Li, J.-C., Jiang, Y. X., Zhang, S. Y., Wang, L., Ouyang, Y. S., and Qi, Z. H. (2008). Evaluation of renal artery stenosis with hemodynamic parameters of doppler sonography. *J. Vasc. Surg.* 48, 323–328. doi: 10.1016/j.jvs.2008.03.048

Marzo, A., Singh, P., Reymond, P., Stergiopulos, N., Patel, U., and Hose, R. (2009). Influence of inlet boundary conditions on the local haemodynamics of intracranial aneurysms. *Comput. Methods Biomech. Biomed. Engin.* 12, 431–444. doi: 10.1080/10255840802654335

Morris, D. P., Ryan, D., Morton, A. C., Lycett, R., Lawford, P. V., Hose, D. R., et al. (2013). Virtual fractional flow reserve from coronary angiography: modeling the significance of coronary lesions. *JACC Cardiovasc. Interv.* 6, 149–157. doi: 10.1016/j.jcin.2012.08.024

Morris, P. D., Silva Soto, D. A., Feher, J. F. A., Rafiroiu, D., Lungu, A., Varma, S., et al. (2017). Fast virtual fractional flow reserve based upon steady-state computational fluid dynamics analysis: results from the VIRTU-fast study. *JACC Basic Transl. Sci.* 2, 434–446. doi: 10.1016/j.jacbts.2017.04.003

Murphy, T. P., Cooper, C. J., Matsumoto, A. H., Cutlip, D. E., Pencina, K. M., Jamerson, K., et al. (2015). Renal artery stent outcomes effect of baseline blood pressure, stenosis severity, and translesion pressure gradient. *J. Am. Coll. Cardiol.* 66, 2487–2494. doi: 10.1016/j.jacc.2015.09.073

Noory, E., Rastan, A., Beschorner, U., Macharzina, R., and Zeller, T. (2016). Duplex derived intrarenal resistance index correlates with invasive pressure gradient measurements in detecting relevant unilateral renal artery stenosis. *Vasa* 45, 175–180. doi: 10.1024/0301-1526/a000513

Odudu, A., Francis, S. T., and McIntyre, C. W. (2012). MRI for the assessment of organ perfusion in patients with chronic kidney disease. *Curr. Opin. Nephrol. Hypertens.* 21, 647–654. doi: 10.1097/MNH.0b013e328358d582

Parikh, S. A., Shishehbor, M. H., Gray, B. H., White, C. J., and Jaff, M. R. (2014). SCAI expert consensus statement for renal artery stenting appropriate use. *Catheter. Cardiovasc. Interv.* 84, 1163–1171. doi: 10.1002/ccd.25559

Reymond, P., Bohraus, Y., Perren, F., Lazeyras, F., and Stergiopulos, N. (2011). Validation of a patient-specific one-dimensional model of the systemic arterial tree. *Am. J. Physiol. Heart Circ. Physiol.* 301, H1173–H1182. doi: 10.1152/ajpheart.00821.2010

Riaz, I. B., Husnain, M., Riaz, H., Asawaeer, M., Bilal, J., Pandit, A., et al. (2014). Meta-analysis of revascularization versus medical therapy for atherosclerotic renal artery stenosis. *Am. J. Cardiol.* 114, 1116–1123. doi: 10.1016/j.amjcard.2014.06.033

Ritchie, J., Green, D., Chrysochou, C., Chalmers, N., Foley, R. N., and Kalra, P. A. (2014). High-risk clinical presentations in atherosclerotic renovascular disease: prognosis and response to renal artery revascularization. *Am. J. Kidney Dis.* 63, 186–197. doi: 10.1053/j.ajkd.2013.07.020

Shaw, L. J., Berman, D. S., Maron, D. J., Mancini, G. B., Hayes, S. W., Hartigan, P. M., et al. (2008). Optimal medical therapy with or without percutaneous coronary intervention to reduce ischemic burden: results from the clinical outcomes utilizing revascularization and aggressive drug evaluation (courage) trial nuclear substudy. *Circulation* 117, 1283–1291. doi: 10.1161/CIRCULATIONAHA.107.743963

Slovut, D. P., and Olin, J. W. (2004). Fibromuscular dysplasia. *N. Engl. J. Med.* 350, 1862–1871. doi: 10.1056/NEJMra032393

Staub, D., Partovi, S., Zeller, T., Breidthardt, T., Kaech, M., Boeddinghaus, J., et al. (2016). Multimarker assessment for the prediction of renal function improvement after percutaneous revascularization for renal artery stenosis. *Cardiovasc. Diagn. Ther.* 6, 221–233. doi: 10.21037/cdt.2016.03.01

Subramanian, R., White, C. J., Rosenfield, K., Bashir, R., Almagor, Y., Meerkin, D., et al. (2005). Renal fractional flow reserve: a hemodynamic evaluation of moderate renal artery stenoses. *Catheter. Cardiovasc. Interv.* 64, 480–486. doi: 10.1002/ccd.20318

Textor, S. C. (2017). Renal arterial disease and hypertension. *Med. Clin. North Am.* 101, 65–79. doi: 10.1016/j.mcna.2016.08.010

Wheatley, K., Ives, N., Gray, R., Kalra, P. A., Moss, J. G., Baigent, C., et al. (2009). Revascularization versus medical therapy for renal-artery stenosis. *N. Engl. J. Med.* 361, 1953–1962. doi: 10.1056/NEJMoa0905368

Zeller, T., Bonvini, R. F., and Sixt, S. (2008). Color-coded duplex ultrasound for diagnosis of renal artery stenosis and as follow-up examination after revascularization. *Catheter. Cardiovasc. Interv.* 71, 995–999. doi: 10.1002/ccd.21525

Conflict of Interest Statement: The authors declare that the research was conducted in the absence of any commercial or financial relationships that could be construed as a potential conflict of interest.

frontiers
in Physiology

ORIGINAL RESEARCH
published: 21 August 2018
doi: 10.3389/fphys.2018.01116

Impact of Modeling Assumptions on Stability Predictions in Reverse Total Shoulder Arthroplasty

***Mehul A. Dharia*[1]*, *Jeffrey E. Bischoff*[1] *and David Schneider*[2]**

[1] Computational Biomechanics, Corporate Research, Zimmer Biomet, Warsaw, IN, United States, [2] Shoulder & Elbow Institute, Panorama Orthopedics & Spine Center, Golden, CO, United States

Reverse total shoulder arthroplasty (rTSA) is commonly used in the shoulder replacement surgeries for the relief of pain and to restore function, in patients with grossly deficient rotator cuff. Primary instability due to glenoid loosening is one of the critical complications of rTSA; the implants are designed and implanted such that the motion between the glenoid baseplate and underlying bone is minimized to facilitate adequate primary fixation. Finite element analysis (FEA) is commonly used to simulate the test setup per ASTM F2028-14 for comparing micromotion between designs or configurations to study the pre-clinical indications for stability. The FEA results can be influenced by the underlying modeling assumptions. It is a common practice to simplify the screw shafts by modeling them as cylinders and modeling the screw-bone interface using bonded contact, to evaluate micromotion in rTSA components. The goal of this study was to evaluate the effect of three different assumptions for modeling the screw-bone interface on micromotion predictions. The credibility of these modeling assumptions was examined by comparing the micromotion rank order predicted among three different modular configurations with similar information from the literature. Eight configurations were modeled using different number of screws, glenosphere offset, and baseplate sizes. An axial compression and shear load was applied through the glenosphere and micromotion at the baseplate-bone interface was measured. Three modeling assumptions pertaining to modeling of the screw-bone interface were used and micromotion results were compared to study the effect of number of peripheral screws, eccentricities, and baseplate diameter. The relative comparison of micromotion between configurations using two versus four peripheral screws remained unchanged irrespective of the three modeling assumptions. However, the relative comparison between two inferior offsets and baseplate sizes changed depending on the modeling assumptions used for the screw-bone interface. The finding from this study challenges the generally believed hypothesis that FEA models can be used to make relative comparison of micromotion in rTSA designs as long as the same modeling assumptions are used across all models. The comparisons with previously published work matched the finding from this study in some cases, whereas the comparison was contradicting in other cases. It is essential to validate the computer modeling approach with an experiment using similar designs and methods to increase the confidence in the predictions to make design decisions.

Keywords: micromotion, stability, initial fixation, reverse shoulder arthroplasty, finite element analysis, screw modeling

Edited by:
Leonardo Angelone,
USFDA and Center for Devices and Radiological Health, United States

Reviewed by:
Andrew Baumann,
USFDA and Center for Devices and Radiological Health, United States
Christopher Basciano,
Becton Dickinson, United States

****Correspondence:***
Mehul A. Dharia
mehul.dharia@zimmerbiomet.com

Specialty section:
This article was submitted to Computational Physiology and Medicine, a section of the journal Frontiers in Physiology

Received: *13 April 2018*
Accepted: *25 July 2018*
Published: *21 August 2018*

Citation:
Dharia MA, Bischoff JE and Schneider D (2018) Impact of Modeling Assumptions on Stability Predictions in Reverse Total Shoulder Arthroplasty. Front. Physiol. 9:1116. doi: 10.3389/fphys.2018.01116

INTRODUCTION

Since 1972, total shoulder arthroplasty (TSA) has been used for treatment of osteoarthritis, fracture, and other shoulder non-inflammatory issues. Anatomic total shoulder arthroplasty (aTSA) and reverse total shoulder arthroplasty (rTSA) are commonly used in the shoulder replacement surgeries for the relief of pain and to restore function. Both aTSA and rTSA are considered as successful procedures with similar patient outcomes (Kiet et al., 2015). Surgeons make the decision to use aTSA or rTSA based on the condition of the joint as well as past TSA history of the patient. TSA procedures are commonly used in patients with arthritis in the joint between scapula and humeral bones, with intact rotator cuff. aTSA typically entails a stem component implanted in the humeral canal with a metal head component assembled on the superior side of the stem, articulating against a plastic socket component implanted in the scapula. Significant rotator cuff muscle damage in patients may prove inadequate to provide joint stability to the aTSA components. The component positions can be reversed in such cases (rTSA) by implanting a socket type component in the humeral bone and a metallic hemisphere component in the glenoid bone. **Figure 1** presents an example of an rTSA implant. rTSA is commonly used as a primary procedure for patients whose shoulder joint has a grossly deficient rotator cuff with severe arthropathy, and also as a revision procedure for a failed aTSA due to reduced bone stock in the humerus and scapula with deficient rotator cuff. The complication rate for rTSA has been reported as three times higher when used as revision for failed aTSA, in comparison to a primary rTSA (Boileau, 2016).

There are several complications associated with rTSA including joint instability, periprosthetic fracture, infection, and component loosening. Bohsali et al. (2017) studied complications of rTSA in 78 studies published between 2006 and 2015, including a total of 4,124 shoulders, and found that 7.2% of all complications were attributed to glenoid loosening. A literature review comprising 782 rTSA found radiographic lucent lines in the glenoid in 4.3% of the cases with postoperative problems and glenoid loosening in 5% of cases with complications (Zumstein et al., 2011). Boileau (2016) reported their experience with 825 rTSA performed between 1996 and 2013 and found the rate of glenoid loosening as a reason for reintervention at 9%.

It is essential to minimize the motion between the baseplate and the underlying glenoid bone to promote osseous integration at the bone-baseplate interface in uncemented designs and therefore achieve adequate primary fixation. However, the service loads experienced by rTSA components challenge the fixation at the interface between the bone and the baseplate. Additionally, the glenosphere can be lateralized in many systems in order to improve range of motion without impingement, which further challenges the fixation by increasing the moment arm at the bone-implant interface (Berliner et al., 2015). An increased torque of 44 and 69% at the baseplate-bone interface has been reported with increased lateral offsets of 23 and 27 mm, respectively (Harman et al., 2005). Implant designs offer a variety of mechanisms to achieve fixation stability such as various numbers of screws, screw types, screw lengths, and screw angles, as well as use of a porous material substrate to increase friction with the bone and to facilitate bony ingrowth. A narrative review cited initial baseplate screw fixation has been reported as the most important factor leading to long-term fixation through osseous integration (Berliner et al., 2015).

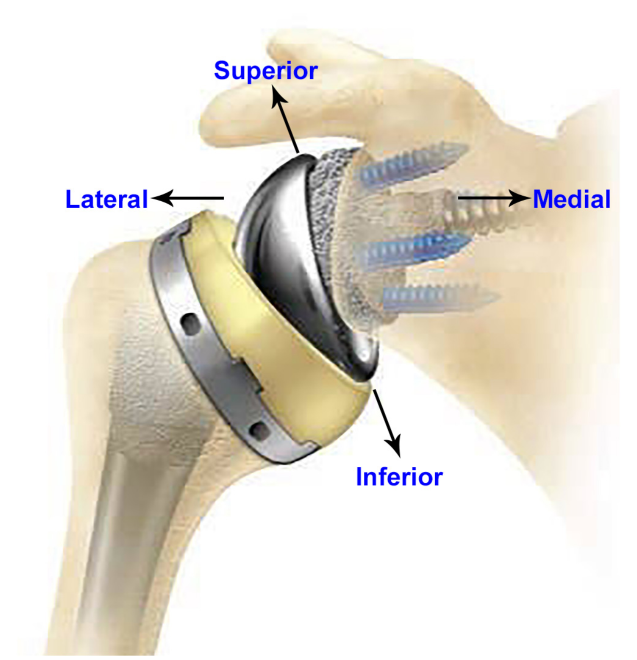

FIGURE 1 | A typical rTSA system (anterior–posterior view).

Micromotion between baseplate and bone is commonly used as a pre-clinical indicator for stability. ASTM F2028-14 provides a standard test method *in vitro* for evaluating glenoid loosening or disassociation by measuring displacement of the glenoid baseplate in response to axial compression and shear loading (ASTM F2028-14, 2017). This test method has been utilized to demonstrate significant differences in displacement between different screw configurations, medialized/lateralized center of rotation, and different densities of bone substrates (Roche et al., 2008, 2011; Stroud et al., 2013). Testing various configurations is complicated and time consuming. Additionally, the measurements are obtained at the edges of the baseplate or glenoid component, not representing interfacial micromotion and could be misleading (Favre et al., 2011).

Finite element analysis (FEA) simulations are often used for replicating the test setup per ASTM F2028-14, to determine worst case configuration for physical testing or to make comparisons among different designs or configurations. Several FEA studies have been performed to study the effect of implant designs, lateralization, inferior tilt of glenoid, and degree of joint conformity on glenoid baseplate-bone micromotion (Hopkins et al., 2008; Virani et al., 2008; Hopkins and Hansen, 2009; Suárez et al., 2012; Chae et al., 2016; Denard et al., 2017;

Elwell et al., 2017; Geraldes et al., 2017). The complexity of the FEA models has increased with time due to improvements in computing power and software technologies. However, it is a common practice to simplify the FEA models for increasing efficiency of solution times by reducing model size. For this purpose, small features that are deemed irrelevant or are located away from an area of interest are often ignored. However, results from FEA can be critically dependent on the modeling assumptions. In particular, one commonly used simplification in rTSA modeling studies is de-featuring of the screw threads from the screw shafts and the screw holes in the bone (Hopkins et al., 2008; Virani et al., 2008; Hopkins and Hansen, 2009; Suárez et al., 2012; Chae et al., 2016; Denard et al., 2017; Elwell et al., 2017; Geraldes et al., 2017). The screw shafts are modeled as cylinders, virtually implanted in the cylindrical holes created in the bone. Further, in most cases, the interfaces between the screw shafts and the respective holes in the bone are modeled using bonded or tied contact. Similar modeling assumptions are found in studies involving modeling of screws in other joints as well (Alonso-Vázquez et al., 2004a,b). A study by Inzana et al. (2016) used a single screw-in-bone model to demonstrate that the relative comparisons of implant stability of a fracture plate in the proximal humerus remained unaffected by de-featuring the threads in the screw shaft and the holes in the bone. However, principal strains were used as a measure of stability and the measurements were in the proximity of the screw-bone interface itself. Most of the previous modeling studies have implicitly hypothesized that models can be used for one-to-one comparisons as long as the same modeling assumptions are used in all models. To the authors' knowledge, no previous study has investigated the effects of these modeling assumptions on the resulting micromotion at the baseplate-bone interface in the rTSA components.

The aim of this study is to evaluate the impact of key modeling assumptions related to screw-bone interactions on the predicted relative motion (micromotion) between the glenoid baseplate and the bone in various rTSA configurations. Specifically, three research questions were examined to study the effect of number of screws, eccentricity, and baseplate size, on micromotion by using three different modeling assumptions to model the screw-bone interface. Further, the credibility of these modeling assumptions was examined by comparing the predicted answers for three research questions with similar information from the literature.

MATERIALS AND METHODS

rTSA Components

Figure 2 provides the description of various components. rTSA components with two glenoid baseplate diameter sizes were selected; 25 mm and 28 mm. The underside of the baseplates has porous plasma spray (PPS®) coating to facilitate osseous integration. The baseplate designs have a short central boss housing to accommodate a central screw for rigid compression into the glenoid vault. While the central boss itself can provide resistance to shear loading, the central screw used in conjunction with the central boss can improve the compression between the baseplate and the bone to reduce micromotion at the bony interface. Additionally, the baseplate can accommodate four peripheral screws which can be inserted at variable angles. Overall, the combination of 5 screws, central boss and PPS coating offers stability for osseous integration in the months immediately following surgery. An adapter component is placed between the baseplate and the glenosphere. The adapter can be rotated to create a glenosphere offset in any direction (superior–inferior, anterior–posterior) to provide component positioning specific to patients and also avoid scapular notching while maintaining optimal range of motion.

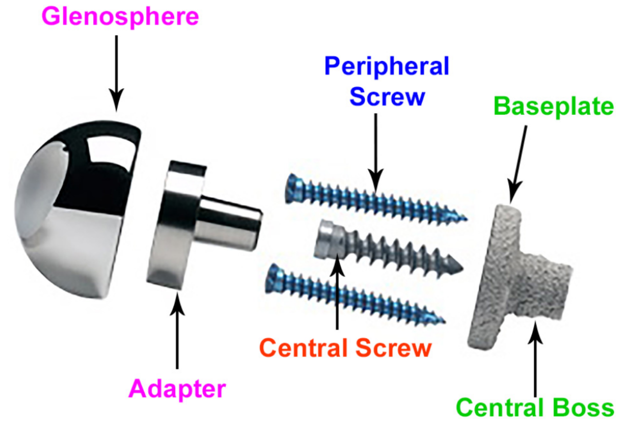

FIGURE 2 | Description of rTSA components.

Study Configurations

With the modularity of implantation options described above, infinite combinations are available to the surgeons. Several combinations were selected for this study using variables in four main categories: screw-bone interface condition, number of peripheral screws, offset of the glenosphere in the superior-inferior direction, and baseplate diameter size. Configurations in all four categories are described in detail in the following sub-sections. With two combinations for number of peripheral screws, two inferior offset combinations, and two baseplate sizes, a total of 8 combinations were possible. Each of these eight combinations was studied with three different approaches for modeling the screw-bone interface. Thus, a total of 24 configurations were studied. **Table 1** presents the configurations considered in this study.

Screw-Bone Interface

Three configurations were considered representing different ways to model the interface between screws and the bone. (1) Screw shafts were modeled as cylinders without threads. The interface between screws and the bone was modeled using rigidly bonded contact. This configuration will be referred to as **cyl-b**. The outer thread diameter was used to model the cylinders representing screw shafts. (2) Screw threads were modeled on the screw shafts and corresponding thread geometries were modeled in the bone. The screw-bone interface was modeled using rigidly bonded contact. This configuration will be referred to as **thr-b**. (3) Similar to configuration 2, but the screw-bone interface was modeled using sliding friction with coefficient of friction 0.3 (Inzana et al., 2016). This configuration will be referred to as **thr-f**. **Figure 3** illustrates the three modeling assumptions between the screw shafts and the bone.

Number of Peripheral Screws

As described before, this implant allows the surgeon to use up to four peripheral screws based on the quality of the bone and the amount of fixation deemed necessary for a specific patient. In this study, two of many possible combinations were selected. (1) Two peripheral screws; one each on the inferior and superior sides. (2) Four peripheral screws; one each on the inferior and superior sides, and one each on the anterior and posterior sides.

Eccentricity

While infinite combinations of eccentricities in anterior-posterior and inferior–superior directions are available by allowable glenosphere rotations through use of an adapter, two combinations of offsets in inferior-superior directions were selected, (1) Minimum inferior superior offset and (2) Maximum inferior offset. A minimum offset of 0.5 mm and 1.5 mm was used for the 28 mm and 25 mm baseplate, respectively, based on the glenosphere compatibility. For both baseplates, a maximum offset of 3.5 mm was used.

Baseplate Size

Two baseplate diameter sizes were considered, (1) 25 mm and (2) 28 mm, combined with a size 36 and 41 mm glenosphere, respectively.

TABLE 1 | Combinations considered in this study.

Combinations	Baseplate size (mm)	Number of peripheral screws	Inferior offset		Screw-bone block interface
			Type	mm	
1	28	2	Minimum	0.5	
2	28	2	Maximum	3.5	**cyl-b**
3	28	4	Minimum	0.5	OR
4	28	4	Maximum	3.5	**thr-b**
5	25	2	Minimum	1.5	OR
6	25	2	Maximum	3.5	**thr-f**
7	25	4	Minimum	1.5	
8	25	4	Maximum	3.5	

Research Questions

This study performed FEA on the above described configurations to answer three questions pertaining to micromotion at the interface between the glenoid baseplate and the bone.

(1) Which number of peripheral screws (2 or 4) results in lower micromotion?
(2) Which eccentricity in inferior-superior direction (minimum inferior superior offset or maximum inferior offset) results in lower micromotion?
(3) Which baseplate size (25 or 28 mm) results in lower micromotion?

Finally, the main question was whether the approach for modeling the screw-bone interface affects the answers to the above three questions.

Test Method

The experimental setup, per ASTM F2028-14, measures the initial glenoid baseplate fixation to the bone before cyclic loading. Fixation is measured as an axial load of 430N is applied approximately through the center of rotation, perpendicular to the glenoid plane, and as a shear load of 350N is applied parallel to the glenoid plane. The resulting displacement of the baseplate in the direction of applied axial compression and shear loads is

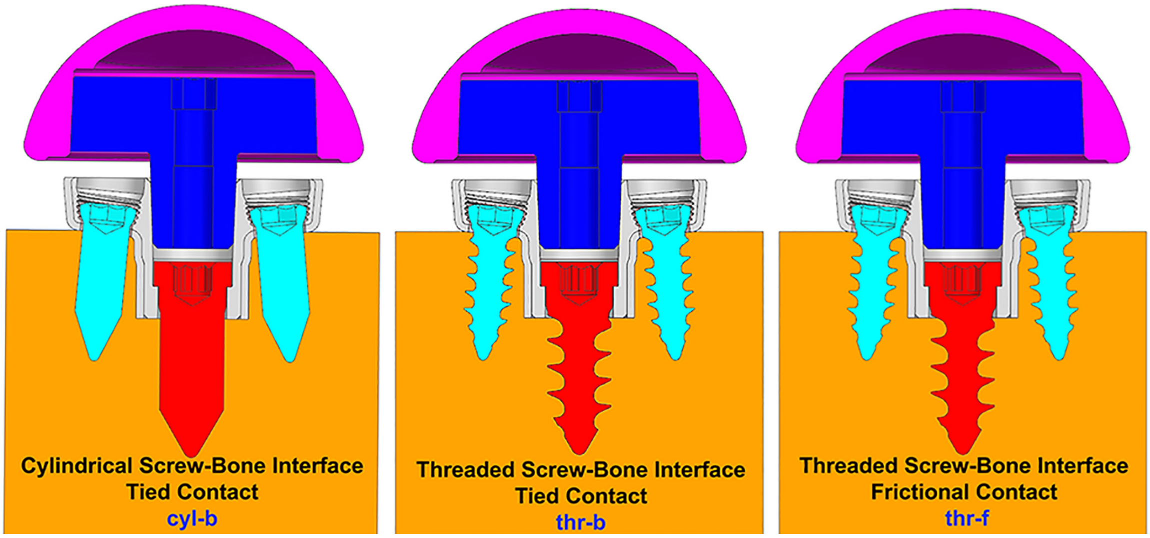

FIGURE 3 | Three modeling assumptions between the screw shafts and the bone (cross-sectional view in sagittal plane).

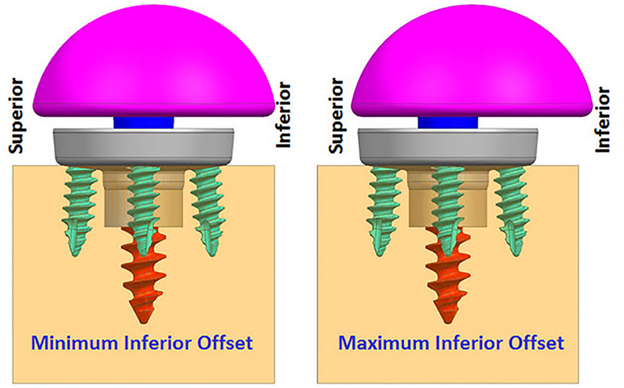

FIGURE 4 | Finite element analysis (FEA) models with two offset conditions (anterior–posterior view).

measured as a fixation response. Then, the glenoid components are rotated about the humeral liner for a fixed number of cycles as an axial compressive load of 750N is applied through the humeral liner to the glenoid component, to load the assembly in a physiologically relevant manner. After the cyclic loading is completed, glenoid baseplate fixation to the bone is measured again in both directions as described previously.

Finite element analysis models were created to simulate the experimental setup described above without considering the cyclic loading aspect. rTSA glenoid components were virtually implanted using the screw solids into a block of material representing the idealized bone, as prescribed by the surgical technique. A load of 756N, representing one body weight, was applied through the glenosphere at the center of rotation in axial compression direction perpendicular to the glenoid baseplate. An additional load of 756N was also applied in the shear direction, parallel to the glenoid baseplate plane, creating a resultant load of 1070N. This load magnitude was derived in a previous study as high-impact daily loading by reviewing a series of shoulder motion analyses (Anglin and Wyss, 2000), and is more rigorous than that prescribed by ASTM F2028-14. This technique of applying axial compression and shear load creates eccentric loading conditions similar to the rocking-horse loosening mechanism and is consistent with what has been used in previously reported physical testing as well as FEA studies (Anglin et al., 2000; Harman et al., 2005; Hopkins et al., 2008; Mroczkowski, 2008; Virani et al., 2008; Hopkins and Hansen, 2009; Bergmann et al., 2011; Chae et al., 2016) to evaluate micromotion at the interface between the bone and the baseplate. **Figure 5** presents a representative laboratory test setup replicated by the FEA models.

Finite Element Model

System Configuration

Finite element analysis models included components described in Section "rTSA Components." Three dimensional computer aided design models were created at nominal dimensions using NX version 8.5 (Siemens PLM Software, Plano, TX, United States).

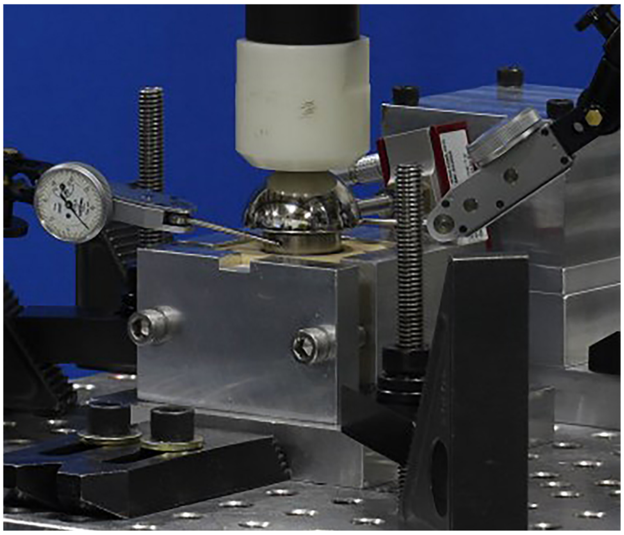

FIGURE 5 | A representative laboratory test setup showing axial compression and shear load cells.

All FEA models were created by importing the CAD models into ANSYS (Workbench 16.2, Ansys, Inc., Canonsburg, PA, United States).

System Properties

All the components were modeled using linear elastic material properties. It was assumed that deformation of the components is small under this test condition and therefore, modeling the non-linear material response of the system was not deemed necessary. For all models, the predicted stress response of the critical components was below the yield strength, justifying this assumption.

The baseplate, adapter, and screws were modeled using Titanium Ti-6Al-4V material (E = 1.1e5 MPa, nu = 0.3) (Boampong et al., 2003). The glenosphere was modeled using Cobalt-Chromium-Molybdenum material properties (E = 2.2e5MPa, nu = 0.3) (ASTM F75, 2000). The solid polyurethane foam used as a bone substitute is not intended to replicate the mechanical properties of the human bone, however, it does provide consistent and uniform material with properties in the range of human cancellous bone. The bone block was modeled using bone foam properties (E = 193 MPa, nu = 0.3) (ASTM F1839-08, 2016).

System Conditions

Loading and support conditions

A small patch was defined at the center of the proximal glenosphere dome to apply load. An axial compression load of 756 N was applied through that load patch in the direction perpendicular to the baseplate. An additional 756 N load was applied in the shear direction through the same load patch, parallel to the baseplate. The distal surface and the side faces of the rectangular bone block were constrained against motion in all degrees of freedom.

Interactions

The central and peripheral screw heads were connected to the baseplate holes using tied contact. The connection between the glenosphere and the adapter, as well as the connection between the adapter and the baseplate was modeled using tied or bonded contact. The contact between the baseplate and PPS coating was also modeled using bonded contact to capture the PPS coating bonded to the baseplate. The interface between the PPS coating with the bone block was modeled using a coefficient of friction of 0.64 (Biemond et al., 2011). The interface between screws and bone block were modeled as described in Section "Screw-Bone Interface."

System Discretization

All components were meshed using 10-node tetrahedron elements with consistent mesh density among specific components in all the models. To ensure that the results were not affected by the mesh size selection, a mesh refinement study was performed upfront using two models; one each with two and four peripheral screws; configurations 1 and 3 in **Table 1**. Starting with 1mm mesh size, the mesh at the interface between baseplate and the bone was refined by cutting the mesh size into half until the relative difference in micromotion predictions between iterations was within 5% of each other, an acceptable threshold for comparative device evaluations (ASTM F2996-13, 2013). Using a mesh size of 0.5 mm at the baseplate-bone interface, the % difference in predicted peak micromotion was within 5 and 3% for the configurations 1 and 3, respectively, compared to the respective models using 1 mm mesh size. With further mesh refinement using 0.25 mm mesh size at the baseplate-bone interface, the predicted peak micromotion was within 3% of the previous iteration for both configurations. Therefore, the mesh size of 0.5 mm at the baseplate-bone interface was considered as the converged mesh size and was used for all the other configurations in **Table 1**. Thus, micromotion results in any two models which are within 5% of each other were considered equal.

Numerical Implementation

All analyses were performed using ANSYS version 16.2 FEA software. Non-linear static analyses were performed using an implicit solver. The default convergence criteria and iteration methods were used. FEA were performed in two steps. In the first step, 750N axial compression load was applied, followed by the 750N shear load application in the second step.

Results Postprocessing

The peak micromotion predicted at the interface between the baseplate and the bone was recorded for all the configurations. The relative motion of the baseplate with the bone includes two tangential components [inferior–superior (IS) and anterior–posterior (AP)], as well as the normal medial-lateral (ML) component. Most experimental implementations of F2028-14 measure only selected components of the micromotion, and also only at the outside edge of the baseplate. Thus, the overall micromotion across the baseplate-bone interface may be poorly characterized. FEA models can provide greater insight into the micromotion response by quantifying all components of micromotion across the entire interface. The relative displacement between glenoid baseplate and the interfacing bone block was computed as a vector composition of the tangential and normal micromotion (Viceconti et al., 2006; Favre and Henderson, 2016).

RESULTS

Table 2 presents the micromotion results predicted for all eight combinations, using all three screw-bone modeling assumptions. Among all 24 combinations, the highest micromotion value was predicted for the combination that used the 25 mm baseplate implanted with two peripheral screws and 1.5 mm inferior offset. **Figure 6** presents the model setup resulting in rocking motion of the baseplate with respect to the bone and resulting interfacial micromotion plot for this configuration. Micromotion results for all the combinations were normalized against this highest micromotion value.

Overall Micromotion

The overall peak micromotion at the baseplate-bone interface was contributed by the relative motion in both the tangential (superior–inferior) as well as normal (medial-lateral) directions. The peak micromotion was located toward the inferior edge. On average, the contribution by inferior-superior tangential motion was 20–30% higher than that of the normal motion at the inferior

TABLE 2 | Normalized micromotion results.

Combinations	Baseplate size (mm)	Number of peripheral screws	Inferior offset		Screw-bone block micromotion		
			Type	mm	cyl-b	thr-b	thr-f
1	28	2	Minimum	0.5	0.698	0.665	0.890
2	28	2	Maximum	3.5	0.628	0.564	0.793
3	28	4	Minimum	0.5	0.625	0.582	0.826
4	28	4	Maximum	3.5	0.549	0.512	0.738
5	25	2	Minimum	1.5	0.570	0.677	1.000
6	25	2	Maximum	3.5	0.652	0.616	0.902
7	25	4	Minimum	1.5	0.454	0.564	0.866
8	25	4	Maximum	3.5	0.558	0.509	0.823

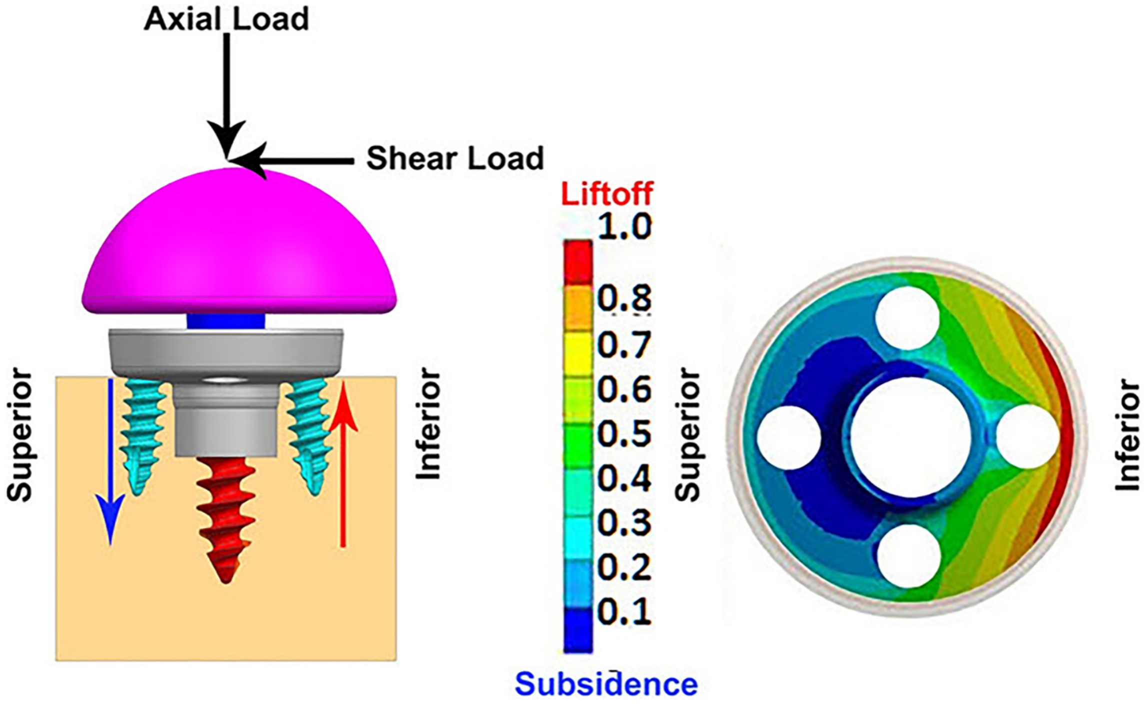

FIGURE 6 | (Left) FEA model of 25 mm baseplate implanted using 2 peripheral screws (view in sagittal plane); red and blue arrows showing resulting rocking motion. **(Right)** Interfacial normalized micromotion plot in distal view (results shown for configuration using thr-f screw-bone interface).

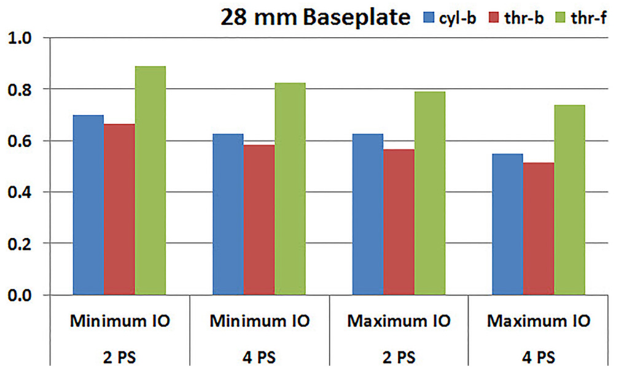

FIGURE 7 | Interfacial micromotion results of 28 mm diameter baseplate using two and four peripheral screws (2PS and 4PS); Minimum and Maximum inferior offset (Minimum IO and Maximum IO).

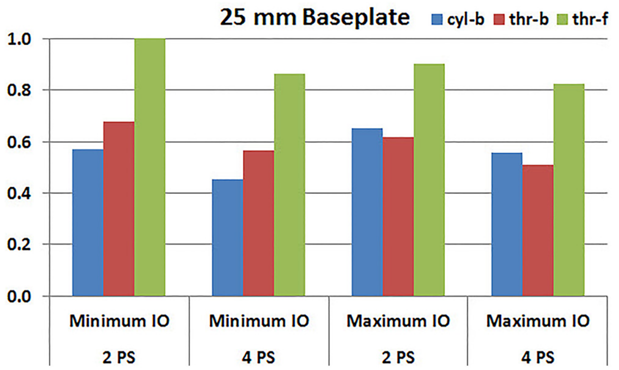

FIGURE 8 | Interfacial micromotion results of 25 mm diameter baseplate using two and four peripheral screws (2PS and 4PS); Minimum and Maximum inferior offset (Minimum IO and Maximum IO).

edge. For all eight combinations, models using thr-f screws-bone interface predicted significantly higher micromotion; 26–91% higher compared to models using cyl-b interface, 34–62% higher compared to thr-b interface. Among models using bonded contact at the screw-baseplate interface, models using cyl-b interface predicted marginally higher micromotion (5–11% higher) compared to those using thr-b interface. However, for two models using 25 mm baseplates with minimum inferior offset, this trend was reversed, resulting in 16–19% decreased micromotion in models using cyl-b interface with 2 and 4 peripheral screws, respectively. Following paragraphs evaluate the three specific Research questions listed in Section “Eccentricity.”

Number of Peripheral Screws

Figures 7, **8** plot the interfacial micromotion results showing the effect of implanting different number of peripheral screws on predicted micromotion using 28 and 25 mm diameter baselates, respectively. Irrespective of the screw-bone interface used, the combination using four peripheral screws resulted in

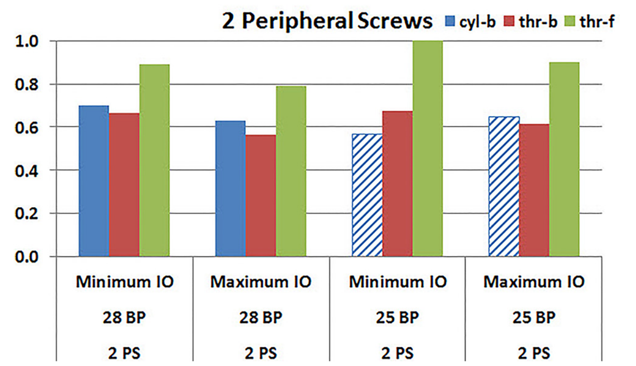

FIGURE 9 | Interfacial micromotion results using Minimum and Maximum inferior offset (Minimum IO and Maximum IO); and 28 mm and 25 mm baseplates (28 BP and 25 BP), with two peripheral screws. *The patterned bars represent the predictions where the primary trend (maximum inferior offset resulted in reduced micromotion) was reversed.*

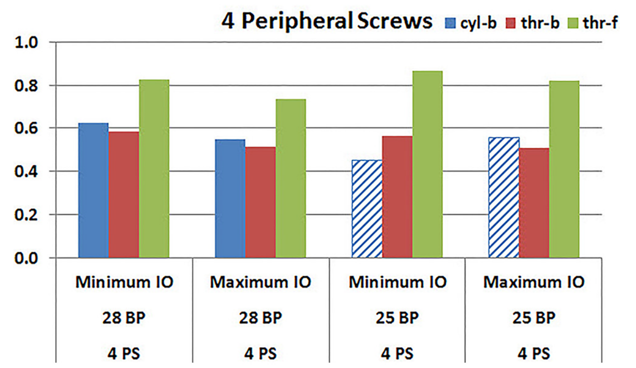

FIGURE 10 | Interfacial micromotion results using Minimum and Maximum inferior offset (Minimum IO and Maximum IO); 28 mm and 25 mm baseplates (28 BP and 25 BP), with four peripheral screws. *The patterned bars represent the predictions where the primary trend (maximum inferior offset resulted in reduced micromotion) was reversed.*

less micromotion than the respective combination using two peripheral screws. The rates of reduction were less pronounced when thr-f interface was used, compared to cyl-b (31–45% lower) and thr-b (20–49% lower) interfaces.

Eccentricity

Figures 9, **10** plot the micromotion results showing the effect of implanting two different offsets in superior-inferior direction on predicted micromotion using 2 and 4 peripheral screws, respectively. For all three screw-bone interface assumptions, maximum inferior offset resulted in lower micromotion than the minimum inferior offset in models using 28 mm baseplate. This trend was independent of the number of peripheral screws implanted. While the same trend was mostly predicted in models using 25 mm baseplate as well, the trend was reversed when screw-bone interface was modeled using cyl-b configuration; where 14 and 23% increase in micromotion was demonstrated using 2 and 4 peripheral screws, respectively. The patterned bars in the **Figures 9**, **10** represent the predictions where the primary trend (maximum inferior offset resulted in reduced micromotion) was reversed.

Baseplate Size

Figures 11, **12** plot the micromotion results showing the effect of baseplate size on micromotion using maximum and minimum inferior offset, respectively. Models with the larger 28 mm baseplate resulted in lower micromotion than the smaller 25 mm baseplate, when implanted with maximum inferior offset, irrespective of the screw-bone interface assumption. However, when implanted using minimum inferior offset with 4 peripheral screws, this trend was reversed for the cyl-b and thr-b modeling assumptions at the screw-bone interface. A similar trend reversal was also shown for cyl-b modeling assumption for the minimum inferior offset implanted with 2 peripheral screws. The patterned bars in the **Figure 12** represent the predictions where the primary trend (smaller baseplate resulted in increased micromotion) was reversed.

DISCUSSION

The objective of this study was to evaluate whether the method in which the screw-bone interface is modeled within FEA studies of rTSA baseplate stability affects the resulting micromotion predictions, by answering three specific research questions relevant to implant design and intra-operative decision making:

(1) Does the use of more peripheral screws increase the stability of the baseplate?
(2) Does increased inferior eccentricity of components result in increased or decreased baseplate micromotion?
(3) Is a smaller or larger baseplate more stable?

This was examined by looking at model predictions for two and four peripheral screws; two differing amounts of inferior offset; and two different baseplate sizes.

Configurations with two peripheral screws resulted in higher predicted micromotion than the respective configurations using four peripheral screws, for all three methods of modeling the screw-bone interface; the modeling assumption used to model the screw-bone interface had no impact on these predictions. This consistency was not seen, however, when addressing baseplate eccentricity (superior-inferior offset) and baseplate size. Specifically, for the smaller baseplate diameter and four peripheral screws (**Figure 10**), the defeatured screw-bone interface resulted in an increase of micromotion with maximum inferior offset. For those same configurations, when using the fully featured screw geometry (with bonded or frictional contact), maximum inferior offset led to decreased micromotion. Similarly, for the minimum inferior offset configurations, the impact of baseplate size on predicted micromotion was dependent on the screw-bone interface model. As a specific example, when using four peripheral screws and a minimum inferior offset (**Figure 12**), higher micromotion was predicted for the 28 mm baseplate than for the 25 mm baseplate when the screw was bonded to the bone (whether or not the threads were explicitly modeled); whereas the

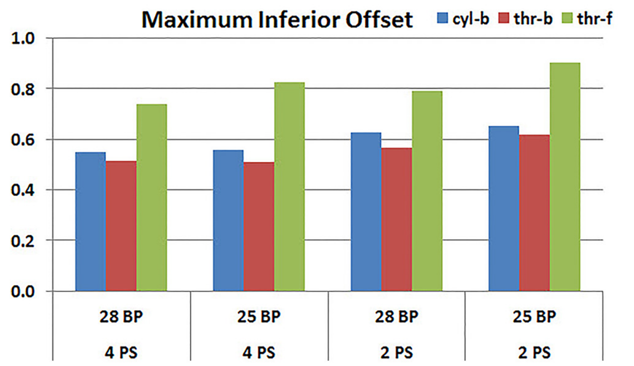

FIGURE 11 | Interfacial micromotion results using 28 and 25 mm baseplates (28 BP and 25 BP) and four and two peripheral screws (4PS and 2PS), with maximum inferior offset.

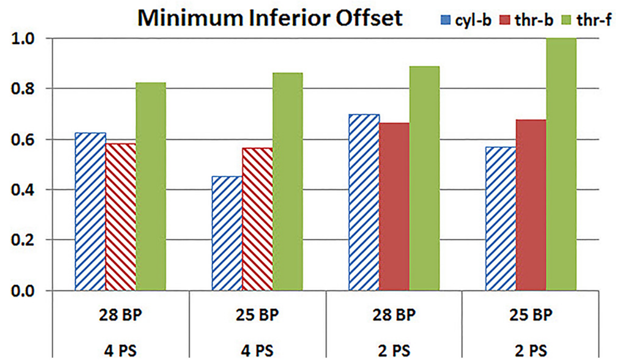

FIGURE 12 | Interfacial micromotion results using 28 and 25 mm baseplates (28 BP and 25 BP) and four and two peripheral screws (4PS and 2PS), with minimum inferior offset. *The patterned bars represent the predictions where the primary trend (smaller baseplate resulted in increased micromotion) was reversed.*

opposite trend was predicted when using fully featured screws with frictional contact.

Out of the three research questions considered in the present study, therefore, the answer to only one question (do more peripheral screws result in increased stability?) was insensitive to how the screw-bone interface was modeled. For the other two questions, however, for selected configurations (e.g., the specific number of peripheral screws, inferior offset, and baseplate diameter), the predicted basic trends were *reversed* based on the way in which the screw-bone interface was modeled. This directly highlights the criticality of the modeling assumptions, even for a direct relative comparison across reasonably comparable system configurations. Further, it motivates careful scrutiny based on the *mechanical basis* of the findings from these modeling approaches, in order to ensure that predicted trending is a reasonable representation of reality.

Mechanical Basis

For each of the eight configurations (in terms of the number of peripheral screws, inferior offset, and baseplate diameter), increased micromotion was consistently predicted when using fully featured screws in frictional contact with the bone (thr-f). This is attributed to the increased compliance of the system that is associated with frictional contact, rather than bonded contact. Further, for most configurations, minimum micromotion was predicted when using fully featured screws with bonded contact (thr-b), as compared to defeatured screws with bonded contact (cyl-b). This may be attributed to fully featured screws having a larger area between the screw and the bone in bonded contact, and therefore adding rigidity to the system as compared to the defeatured (cylindrical) screws. However, this trend was not consistent across all configurations. Further, the extent to which this trend would be impacted by modeling the cylinders using the average thread diameter, or the inner thread diameter, as opposed to the outer thread diameter as used in the current study, is unknown.

At this point, the limit to effectively judge the credibility of modeling assumptions has been reached regarding the extent to which model predictions can be trusted to draw conclusions on device performance. To ensure that correct trending is predicted requires *model validation*, even for evaluating relative performance.

Model Validation

Various experimental studies documented in the literature have set out to address the influence of peripheral screws, eccentricity, and baseplate size on micromotion in rTSA (Humphrey et al., 2008; Hoenig et al., 2010; Poon et al., 2010; James et al., 2013; Chae et al., 2014; Formaini et al., 2017), and potentially could be used to deduce which, if any, of the three approaches considered here for modeling the screw-bone interface is accurate.

Peripheral Screws

Hoenig et al. (2010) reported a decrease in micromotion with the use of a higher number of peripheral screws, using loading conditions that closely match the current simulation study, and thus seemingly reinforcing the conclusions here. However, James et al. (2013) showed no significant impact of the number of peripheral screws on micromotion. This latter study used a different combination of loading than the current simulation study, as well as different metrics for assessing micromotion and a different base implant design. Further, the authors hypothesized that the lack of measurable difference in motion between two and four peripheral screws in their study may be due to variations in reaming of the glenoid due to differences in bone erosion and initial drill location, as well as due to variations in impaction of the baseplate which could permit a gap between the baseplate and the bone, none of which were incorporated in the current study.

Eccentricity

While a glenosphere with inferior eccentricity has been shown to have good clinical outcomes (De Biase et al., 2013) mainly due to improvement in glenoid notching, an increased baseplate micromotion has been reported in a dynamic *in vitro* test (Poon et al., 2010), which is contrary to the finding from the current study. While the increase in micromotion reported by Poon et al. (2010) was small, their study also had other variables such as design differences, lateral offsets which could have contributed to the micromotion and the difference in micromotion between each design cannot be attributed to the eccentricity alone. The micromotion measurement itself was obtained by measuring differences in motion between one point on glenosphere and three points on the glenoid bone; which could be misleading the micromotion assessment compared to recommendations for accurate interface micromotion (Favre et al., 2011) used in this FEA study. The micromotion measurement in the *in vitro* test seem to have measured tangential motion, whereas the predictions from FEA study also included the motion in medial-lateral (lift-off) direction, which was one of the main contributor to the overall peak micromotion at the inferior edge of the baseplate. Further, the FEA setup in current study has the load vector located laterally on the glenoid, which uses a shear load vector directed from inferior to superior direction along with axial compression load, creating a resultant load vector that is passing through the baseplate more inferiorly with maximum inferior offset than minimum inferior offset, which explains the reduced micromotion prediction at the inferior edges of the baseplate with maximum inferior offset. The loading used in the mechanical testing study (Poon et al., 2010) used cyclic loading and the orientation of the eccentricity used may not be matching the one used in this study.

Baseplate Diameter

A previous study used biomechanical testing on cadaveric specimens to study the effect of baseplate size on micromotion at the baseplate-bone interface (Chae et al., 2014). In that study, a larger 29 mm baseplate size resulted in larger surface area at the micromotion site at the baseplate-bone interface than the smaller 25 mm baseplate, resulting in an increased micromotion. This finding is contrary to the determination in the current FEA study for the maximum inferior offset configurations, as well as to the findings of another study by Hopkins and Hansen (2009) which suggested that a larger implant surface area should provide a greater resistance to interfacial micromotion than a smaller implant. However, in the biomechanical testing study (Chae et al., 2014), due to insufficient bone stock of the small glenoid for the fixation of the larger 29 mm baseplate, shorter length peripheral screws were used than the ones used to fix the 25 mm baseplate, which could potentially influence the increase in micromotion in the larger 29 mm baseplate. In the present study, higher micromotion was predicted in the smaller size baseplate for some configurations with minimum inferior offset using cyl-b and thr-b modeling assumptions, matching the findings of the biomechanical study.

The discussion here follows a common practice found in the modeling literature, namely to speak to the validity of the model using experimental data from independent laboratories. However, as seen above, rarely are such studies conducted using equivalent test conditions, in terms of system geometries, loading parameters, etc. When there are differences between model and test setup, it is then difficult to judge whether apparently complementary or apparently conflicting test results are most appropriate for assessing the validity of the model (Pathmanathan et al., 2017). It was beyond the scope of this study to formally validate this modeling approach either by comparing to the literature studies or by conducting an independent validation study. As such, it is not possible here to state unequivocally which of the three modeling assumptions used in this study gives the correct answer. Rather, the goal was to highlight the importance of basic modeling assumptions on basic modeling results; and provide guidance on key points that, if followed, can improve the utilization of computational models for rTSA stability.

Significance

The results from this study highlight two key points that can guide the development, utilization, and interpretation of modeling studies to evaluate micromotion performance in rTSA.

Quantitative Device Performance

One trend consistent in all the configurations examined here is that modeling of fully featured screws, with frictional contact between the screw and the bone, results in the largest quantitative predictions of baseplate micromotion. This is the most expensive simulation considered here; and is the one that consistently resulted in the highest predictions of micromotion. It is thus an important finding for researchers who may want to employ FEA studies to calculate absolute values of micromotion for a given design or configuration, in order to make a design safety decision relative to an acceptable threshold of micromotion conducive for primary stability. Reducing the complexity of the screw-bone interface (cyl-b and thr-b) results in lower predicted values for micromotion, and therefore may lead to a false sense of confidence in the stability of the device.

Direct Model Validation

When comparing different configurations within a single device family, as was done here, basic performance questions were directly and meaningfully impacted by the method in which the screw-bone interface was modeled. This would be exacerbated further when comparing across different devices, in which additional parameters held constant here (frictional coefficient; effective screw diameter; etc) would vary across the models. Experimental studies documented in the literature, in many cases, are poor surrogates for direct model validation; the level of agreement, whether finally judged to be adequate or inadequate based on the purposes of the study, may be a consequence of good modeling fortune rather than engineering insight. Rigorous hierarchical model validation may not always be required; but careful consideration to model validity, even in cases of comparing across configurations, is warranted.

Limitations

There are several limitations in this study. The actual screw preloads were not incorporated in the model, which would compress the baseplate against the bone, potentially reducing the micromotion. The findings were not confirmed with additional sensitivity studies such as different load vector orientations, screw diameters, screw lengths, bone material properties, coefficient of friction at the micromotion interface etc; many of which have been shown to have an impact on micromotion at the implant-bone interface (Hopkins et al., 2008; Hopkins and Hansen, 2009; Favre et al., 2011). The axial compression and shear loading was applied in two sequential steps. If both the loads were simultaneously applied, its effect on micromotion could have been different. The de-featured screw shafts in the configurations using cyl-b screw-bone modeling assumptions were modeled using outside thread diameters. The effect of modeling them at inner or average thread diameter was not studied. While an infinite number of combinations are possible for implantation due to modularity of various components, only eight combinations were explored in this study to investigate the impact of three modeling assumptions. However, the differences in results have already shown that the modeling assumption can impact the relative comparisons among these eight combinations.

Finally, this FEA modeling approach has not been validated against an appropriate test or set of tests, as the appropriate model validation was outside the scope of this study. While it may not be pragmatic to conduct a large number of physical tests for the purposes of model validation, a subset of the configurations analyzed here could be directly tested to ensure consistency between the parametric sensitivities predicted here and those measured experimentally. Such validation experiments likely would necessitate use of alternative micromotion metrics, as the full-field interfacial micromotions predicted here generally cannot be accessed experimentally. With such data, the appropriate set of modeling assumptions could be identified, or additional variations of the existing model (including further sensitivities identified in the preceding paragraph) could be implemented to achieve the desired accuracy.

CONCLUSION

Three levels of model fidelity were tested for modeling the screw-bone interface with increased modeling complexity, model size and solution time, differentiated by whether the screw thread was explicitly geometrically modeled and by whether the screw was bonded to the bone. Using each modeling assumption, three specific questions of interest were examined within a single baseplate system based on the relative comparison of implant-bone micromotion predictions. The rank order among eight different configurations was not impacted for one of those three questions of interest; effect of number of screws. However the modeling assumptions resulted in a different rank order among eight configurations for the other two questions; effect of eccentricity in superior-inferior direction and baseplate size. If a design safety decision regarding primary stability is made solely based on absolute values of micromotion predicted by computational models, modeling simplifications at the screw-bone interface may result in lower micromotion values, and therefore may lead to an incorrect decision. Moreover, these findings demonstrate the importance of carefully evaluating the underlying modeling assumptions used to evaluate differential performance of interfacial micromotion between different rTSA configurations and designs. It further promotes an argument for performing sufficient model validation even for comparative analyses.

AUTHOR CONTRIBUTIONS

MD and JB conceived of the presented idea. MD carried out the implementation including developing FEA models, performing simulations, interpreting the results, and working on the manuscript. JB verified the analytical methods, results interpretation, and worked on the manuscript. DS encouraged MD and JB to investigate the topic and provided critical feedback from a practicing surgeon's viewpoint. All authors discussed the results and contributed to the final manuscript.

FUNDING

This study was funded by Zimmer Biomet.

ACKNOWLEDGMENTS

We would like to acknowledge the help of Yang Son of Zimmer Biomet who guided us in creating various configurations of three dimensional computer models.

REFERENCES

Alonso-Vázquez, A., Lauge-Pedersen, H., Lidgren, L., and Taylor, M. (2004a). Initial stability of ankle arthrodesis with three-screw fixation. A finite element analysis. *Clin. Biomech.* 19, 751–759.

Alonso-Vázquez, A., Lauge-Pedersen, H., Lidgren, L., and Taylor, M. (2004b). The effect of bone quality on the stability of ankle arthrodesis. A finite element study. *Foot Ankle Int.* 25, 840–850.

Anglin, C., and Wyss, U. P. (2000). Review of arm motion analyses. *Proc. Inst. Mech. Eng.* 214, 541–555. doi: 10.1243/0954411001535570

Anglin, C., Wyss, U. P., and Pichora, D. R. (2000). Glenohumeral contact forces. *Proc. Inst. Mech. Eng.* 214, 637–644. doi: 10.1243/0954411001535660

ASTM F1839-08 (2016). *Standard Specification for Rigid Polyurethane Foam for Use as a Standard Material for Testing Orthopaedic Devices and Instruments*. West Conshohocken, PA: ASTM International.

ASTM F2028-14 (2017). *Standard Test Methods for Dynamic Evaluation of Glenoid Loosening or Disassociation*. West Conshohocken, PA: ASTM International.

ASTM F2996-13 (2013). *Standard Practice for Finite Element Analysis (FEA) of Non-Modular Metallic Orthopaedic Hip Femoral Stems*. West Conshohocken, PA: ASTM International.

ASTM F75 (2000). "Carbide hardness data on file at biomet, "introduction to cobalt and cobalt alloys," in *Nickel, Cobalt and Their Alloys*, ed. J. R. Davis (Bangalore: ASM).

Bergmann, G., Graichen, F., Bender, A., Rohlmann, A., Halder, A., Beier, A., et al. (2011). In vivo gleno-humeral joint loads during forward flexion and abduction. *J. Biomech.* 44, 1543–1552. doi: 10.1016/j.jbiomech.2011.02.142

Berliner, J. L., Regalado-Magdos, A., Ma, C. B., and Feeley, B. T. (2015). Biomechanics of reverse total shoulder arthroplasty. *J. Shoulder Elbow Surg.* 24, 150–160. doi: 10.1016/j.jse.2014.08.003

Biemond, J. E., Aquarius, R., Verdonschot, N., and Buma, P. (2011). Frictional and bone ingrowth properties of engineered surface topographies produced by electron beam technology. *Arch. Orthop. Trauma Surg.* 131, 711–718. doi: 10.1007/s00402-010-1218-9

Boampong, D. K., Green, S. M., and Unsworth, A. (2003). N+ ion implantation of Ti6Al4V alloy and UHMWPE for total Joint replacement application. *J. Appl. Biomater. Biomech.* 1, 164–171.

Bohsali, K. I., Bois, A. J., and Wirth, M. A. (2017). Complications of shoulder arthroplasty. *J. Bone Joint Surg. Am.* 99, 256–269. doi: 10.2106/JBJS.16.00935

Boileau, P. (2016). Complications and revision of reverse total shoulder arthroplasty. *Orthop. Traumatol. Surg. Res.* 102(1 Suppl.), S33–S43. doi: 10.1016/j.otsr.2015.06.031

Chae, S.-W., Kim, S.-Y., Lee, H., Yon, J.-R., Lee, J., and Han, S.-H. (2014). Effect of baseplate size on primary glenoid stability and impingement-free range of motion in reverse shoulder arthroplasty. *BMC Musculoskelet. Disord.* 15:417. doi: 10.1186/1471-2474-15-417

Chae, S.-W., Lee, H., Kim, S. M., Lee, J., Han, S.-H., and Kim, S.-Y. (2016). Primary stability of inferior tilt fixation of the glenoid component in reverse total shoulder arthroplasty: a finite element study. *J. Orthop. Res.* 34, 1061–1068. doi: 10.1002/jor.23115

De Biase, C. F., Ziveri, G., Delcogliano, M., de Caro, F., Gumina, S., Borroni, M., et al. (2013). The use of an eccentric glenosphere compared with a concentric glenosphere in reverse total shoulder arthroplasty: two-year minimum follow-up results. *Int. Orthop.* 37, 1949–1955. doi: 10.1007/s00264-013-1947-9

Denard, P. J., Lederman, E., Parsons, B. O., and Romeo, A. A. (2017). Finite element analysis of glenoid-sided lateralization in reverse shoulder arthroplasty. *J. Orthop. Res.* 35, 1548–1555. doi: 10.1002/jor.23394

Elwell, J., Choi, J., and Willing, R. (2017). Quantifying the competing relationship between adduction range of motion and baseplate micromotion with lateralization of reverse total shoulder arthroplasty. *J. Biomech.* 52, 24–30. doi: 10.1016/j.jbiomech.2016.11.053

Favre, P., and Henderson, A. D. (2016). Prediction of stemless humeral implant micromotion during upper limb activities. *Clin. Biomech.* 36, 46–51. doi: 10.1016/j.clinbiomech.2016.05.003

Favre, P., Perala, S., Vogel, P., Fucentese, S. F., Goff, J. R., Gerber, C., et al. (2011). In vitro assessments of reverse glenoid stability using displacement gages are misleading - recommendations for accurate measurements of interface micromotion. *Clin. Biomech.* 26, 917–922. doi: 10.1016/j.clinbiomech.2011.05.002

Formaini, N. T., Everding, N. G., Levy, J. C., Santoni, B. G., Nayak, A. N., and Wilson, C. (2017). Glenoid baseplate fixation using hybrid configurations of locked and unlocked peripheral screws. *J. Orthop. Traumatol.* 18, 221–228. doi: 10.1007/s10195-016-0438-3

Geraldes, D. M., Hansen, U., and Amis, A. A. (2017). Parametric analysis of glenoid implant design and fixation type. *J. Orthop. Res.* 35, 775–784. doi: 10.1002/jor.23309

Harman, M., Frankle, M., Vasey, M., and Banks, S. (2005). Initial glenoid component fixation in 'reverse' total shoulder arthroplasty: a biomechanical evaluation. *J. Shoulder Elbow Surg.* 14(1 Suppl. S), 162S–167S. doi: 10.1016/j.jse.2004.09.030

Hoenig, M. P., Loeffler, B., Brown, S., Peindl, R., Fleischli, J., Connor, P., et al. (2010). Reverse glenoid component fixation: is a posterior screw necessary? *J. Shoulder Elbow Surg.* 19, 544–549. doi: 10.1016/j.jse.2009.10.006

Hopkins, A. R., and Hansen, U. N. (2009). Primary stability in reversed-anatomy glenoid components. *Proc. Inst. Mech. Eng.* 223, 805–812. doi: 10.1243/09544119JEIM557

Hopkins, A. R., Hansen, U. N., Bull, A. M. J., Emery, R., and Amis, A. A. (2008). Fixation of the reversed shoulder prosthesis. *J. Shoulder Elbow Surg.* 17, 974–980. doi: 10.1016/j.jse.2008.04.012

Humphrey, C. S., Kelly, J. D., and Norris, T. R. (2008). Optimizing glenosphere position and fixation in reverse shoulder arthroplasty, Part Two: the three-column concept. *J. Shoulder Elbow Surg.* 17, 595–601. doi: 10.1016/j.jse.2008.05.038

Inzana, J. A., Varga, P., and Windolf, M. (2016). Implicit modeling of screw threads for efficient finite element analysis of complex bone-implant systems. *J. Biomech.* 49, 1836–1844. doi: 10.1016/j.jbiomech.2016.04.021

James, J., Allison, M. A., Werner, F. W., McBride, D. E., Basu, N. N., Sutton, L. G., et al. (2013). Reverse shoulder arthroplasty glenoid fixation: is there a benefit in using four instead of two screws? *J. Shoulder Elbow Surg.* 22, 1030–1036. doi: 10.1016/j.jse.2012.11.006

Kiet, T. K., Feeley, B. T., Naimark, M., Gajiu, T., Hall, S. L., Chung, T. T., et al. (2015). Outcomes after shoulder replacement: comparison between reverse and anatomic total shoulder arthroplasty. *J. Shoulder Elbow Surg.* 24, 179–185. doi: 10.1016/j.jse.2014.06.039

Mroczkowski, M. (2008). *Initial Fixation Of The Trabecular Metal Reverse Shoulder Glenoid Baseplate Implant*. Warsaw, IN: Zimmer Biomet.

Pathmanathan, P., Gray, R., Romero, V., and Morrison, T. (2017). Applicability analysis of validation evidence for biomedical computational models. *J. Verif. Valid. Uncertain. Quantif.* 2:021005. doi: 10.1115/1.4037671

Poon, P. C., Chou, J., Young, D., Sharif, M., and Anderson, I. A. (2010). Biomechanical evaluation of different designs of glenospheres in the SMR reverse shoulder prosthesis: micromotion of the baseplate and risk of loosening. *Shoulder Elb.* 2, 94–99. doi: 10.1111/j.1758-5740.2010.00059.x

Roche, C. P., Flurin, P.-H., Wright, T., Crosby, L., Hutchinson, D., and Zuckerman, J. (2008). "Effect of varying screw configuration and bone density on reverse shoulder glenoid fixation following cyclic loading," in *54th Annual Meeting of the Orthopaedic Research Society*, (Gainesville, FL: University of Florida), 1553.

Roche, C. P., Steffens, J., Flurin, P., Wright, T., Crosby, L., and Zuckerman, J. (2011). "Reverse shoulder glenoid loosening test method: an analysis of fixation between two different offset glenospheres," in *57th Annual Meeting of the Orthopaedic Research Society*, (Gainesville, FL: University of Florida), 563.

Stroud, N. J., DiPaola, M. J., Martin, B. L., Steiler, C. A., Flurin, P. H., Wright, T. W., et al. (2013). Initial glenoid fixation using two different reverse shoulder designs with an equivalent center of rotation in a low-density and high-density bone substitute. *J. Shoulder Elbow Surg.* 22, 1573–1579. doi: 10.1016/j.jse.2013.01.037

Suárez, D. R., Nerkens, W., Valstar, E. R., Rozing, P. M., and van Keulen, F. (2012). Interface micromotions increase with less-conforming cementless glenoid components. *J. Shoulder Elbow Surg.* 21, 474–482. doi: 10.1016/j.jse.2011.03.008

Viceconti, M., Brusi, G., Pancanti, A., and Cristofolini, L. (2006). Primary stability of an anatomical cementless hip stem: a statistical analysis. *J. Biomech.* 39, 1169–1179. doi: 10.1016/j.jbiomech.2005.03.024

Virani, N. A., Harman, M., Li, K., Levy, J., Pupello, D. R., and Frankle, M. A. (2008). In vitro and finite element analysis of glenoid bone/baseplate interaction in the reverse shoulder design. *J. Shoulder Elbow Surg.* 17, 509–521. doi: 10.1016/j.jse.2007.11.003

Zumstein, M. A., Pinedo, M., Old, J., and Boileau, P. (2011). Problems, complications, reoperations, and revisions in reverse total shoulder arthroplasty: a systematic review. *J. Shoulder Elbow Surg.* 20, 146–157. doi: 10.1016/j.jse.2010.08.001

Conflict of Interest Statement: MD and JB are paid employees of Zimmer Biomet. DS is a paid consultant of Zimmer Biomet.

The reviewer AB and handling Editor declared their shared affiliation at the time of review.

frontiers in Physiology

ORIGINAL RESEARCH
published: 04 September 2018
doi: 10.3389/fphys.2018.00974

The Resting Potential and K^+ Currents in Primary Human Articular Chondrocytes

Mary M. Maleckar[1,2], **Robert B. Clark**[3], **Bartholomew Votta**[4] and **Wayne R. Giles**[5]*

[1] Simula Research Laboratory, Center for Biomedical Computing and Center for Cardiological Innovation, Oslo, Norway, [2] Allen Institute for Cell Science, Seattle, WA, United States, [3] Faculty of Kinesiology, University of Calgary, Calgary, AB, Canada, [4] Glaxo Smith Kline, Collegeville, PA, United States, [5] Faculties of Kinesiology and Medicine, University of Calgary, Calgary, AB, Canada

Human transplant programs provide significant opportunities for detailed *in vitro* assessments of physiological properties of selected tissues and cell types. We present a semi-quantitative study of the fundamental electrophysiological/biophysical characteristics of human chondrocytes, focused on K^+ transport mechanisms, and their ability to regulate to the resting membrane potential, E_m. Patch clamp studies on these enzymatically isolated human chondrocytes reveal consistent expression of at least three functionally distinct K^+ currents, as well as transient receptor potential (TRP) currents. The small size of these cells and their exceptionally low current densities present significant technical challenges for electrophysiological recordings. These limitations have been addressed by parallel development of a mathematical model of these K^+ and TRP channel ion transfer mechanisms in an attempt to reveal their contributions to E_m. In combination, these experimental results and simulations yield new insights into: (i) the ionic basis for E_m and its expected range of values; (ii) modulation of E_m by the unique articular joint extracellular milieu; (iii) some aspects of TRP channel mediated depolarization-secretion coupling; (iv) some of the essential biophysical principles that regulate K^+ channel function in "chondrons." The chondron denotes the chondrocyte and its immediate extracellular compartment. The presence of discrete localized surface charges and associated zeta potentials at the chondrocyte surface are regulated by cell metabolism and can modulate interactions of chondrocytes with the extracellular matrix. Semi-quantitative analysis of these factors in chondrocyte/chondron function may yield insights into progressive osteoarthritis.

Keywords: human chondrocyte, patch clamp recordings, K^+ currents, TRP channels, mathematical model, resting membrane potential, depolarization-secretion coupling

Edited by:
Leonardo Angelone,
United States Food and Drug Administration, United States

Reviewed by:
Richard Gray,
State Food and Drug Administration, China
Ali Mobasheri,
University of Surrey, United Kingdom

***Correspondence:**
Wayne R. Giles
wgiles@ucalgary.ca

Specialty section:
This article was submitted to Computational Physiology and Medicine, a section of the journal Frontiers in Physiology

Received: *13 April 2018*
Accepted: *03 July 2018*
Published: *04 September 2018*

Citation:
Maleckar MM, Clark RB, Votta B and Giles WR (2018) The Resting Potential and K^+ Currents in Primary Human Articular Chondrocytes. Front. Physiol. 9:974. doi: 10.3389/fphys.2018.00974

INTRODUCTION

Articular cartilage is a major component of the flexible connective tissue that covers the opposed ends of articular joints. It is essential for the stability and low friction movement of the associated long bones (Huber et al., 2000). This tissue is populated predominately by only one type of cell—the *chondrocyte,* and it lacks any significant vascular, or lymphatic elements. Each chondrocyte, together with its immediate pericellular coat or glycocalyx, forms a functional unit that has been named a "chondron" (Poole, 1997; Guilak et al., 2006; Nguyen et al., 2010; McLane et al., 2013). Under physiological circumstances, cyclical mechanical forces within the joint capsule create a dynamic environment that modulates cellular metabolism and maintains overall health (Wu and Chen, 2000; Guilak et al., 2006; Chen et al., 2013).

Although chondrocytes occupy only ∼1–10% of the total volume of mammalian articular cartilage (Hall et al., 1996; Archer and Francis-West, 2003), they play essential roles in the homeostasis of the extracellular matrix (ECM). In part, this is because these cells synthesize and secrete most of the essential lubricants within the joint, including hyaluronan and lubricin (Ogawa et al., 2014). The ECM is composed of: (i) collagen fibers that give the tissue the ability to resist tension, (ii) negatively charged gel-like proteoglycans that are trapped within the collagen mesh and allow the tissue to bear compression, and (iii) synovial fluid which acts as a lubricant, thus ensuring low friction movement of the bones. The primary role of the chondrocyte is to maintain viable cartilage by regulating macromolecular synthesis and breakdown of its essential constituents and to produce lubricants (Huber et al., 2000; Guilak et al., 2006; Ogawa et al., 2014).

In a variety of progressive chronic diseases, or as a consequence of injury, there is chondrocyte damage and related dysfunction (Bush et al., 2003; Martin and Buckwalter, 2003; Bush and Hall, 2005; Mobasheri et al., 2015). In these situations, the dynamic balance between matrix synthesis and degradation is altered and the low friction environment within the joint may also be reduced (Urban et al., 1993). Frequently, there also is an inflammatory response within the articular joint (Pelletier et al., 2001). These factors can increase the early development of osteoarthritis, and attendant thinning of the cartilage layer, thus resulting in painful, bone-against-bone friction (Bush et al., 2003; Mobasheri et al., 2015). The progression of osteoarthritis and the reduced ability of chondrocyte ion transport systems to respond to perturbations in the extracellular environment (Pelletier et al., 2001) have also been associated with deficiencies in volume regulation (Urban et al., 1993; Lewis et al., 2011). It is known that damage to cartilage is more prominent in the setting of co-incident changes in osmolarity in the chondron. In part, this may be because these volume changes are linked to an abnormal resting membrane potential in chondrocytes (Lewis et al., 2011) caused by altered ion transport, e.g., changes in K^+ and/or Cl^- channel activity. However, uncertainty and some disagreements remain concerning the fundamental ionic mechanisms for this progressive loss of function of the affected chondrocytes in chronic disease settings.

Detailed experimental investigations that address possible functional relationships between chondrocyte electrophysiology and pathophysiology are technically challenging. This is mainly due to the very small size of a mature chondrocyte and the associated limitations of *in vitro* electrophysiological/biophysical studies. In fact, it is not certain that conventional patch pipette methods (Lewis et al., 2011) can accurately determine the resting potential of isolated single chondrocytes (Ince et al., 1986; Mason et al., 2005; Wilson et al., 2011). Partly for this reason, and also to allow us to integrate our patch clamp results with other experimental data we have developed a mathematical model based on the fundamental components responsible for K^+ transport in the human chondrocyte. This model is based mainly on experimental data obtained from human chondrocyte preparations.

The goals of this paper are: (i) to identify the main K^+ currents that contribute to the resting membrane potential (ii) to develop the first mathematical model of essential electrophysiological principles exhibited by human chondrocytes, (iii) to illustrate the utility of this model by simulating the dependence of the chondrocyte resting membrane potential on identified electrolytes and osmolarity in synovial fluid (iv) to put our findings in the context of depolarization-secretion coupling in the chondrocyte based on data from recordings of TRP channel-mediated cation (Na^+ and Ca^{2+}) influx in chondrocytes (cf. Lewis et al., 2013; O'Conor et al., 2014).

METHODS

Mammalian chondrocytes express a number of different voltage- and ligand-gated ion channels, together with ion-selective pumps and exchangers as well as intercellular coupling proteins (cf. Barrett-Jolley et al., 2010; Asmar et al., 2016). In this study, we have extended this published data set using two different experimental preparations for recordings of ion selective currents in unstimulated chondrocytes. We have also complemented and extended these findings with the development of a mathematical model to account for regulation of the resting membrane potential, E_m, in human chondrocytes. The new data sets presented in this paper are based mainly on patch clamp experiments which were done using enzymatically isolated individual human chondrocytes obtained from a knee replacement program (The Southern Alberta Transplant Service). These cells, held in 2D culture for 1–3 days, were not passaged and are therefore classified as "primary."

Experimental Conditions

In the experimental conditions employed in this study, isolated human chondrocytes had E_m values ranging from −30 to −60 mV when superfused with normal Tyrode's solution and studied using standard whole-cell patch clamp methods (Clark et al., 2011). This range of resting membrane potential values may reflect the intrinsic heterogeneous physiological states of these cells. However, as we have reported previously, some of this variability is very likely to result from the fact that in these very small, approximately spherical cells (diameter, ∼7 microns; capacitance, ∼6–12 pF), the patch pipette recording method is being applied very near its maximal technical capabilities (Wilson et al., 2011). That is, the input resistance of the chondrocyte is very large (5–10 GΩ), and the maximum seal resistance between the surface membrane of the chondrocytes and the polished surface of the glass pipette is comparable to 5–15 GΩ. The consequence is that the actual chondrocyte membrane potential may be underestimated due to the current flow through the seal resistance. In most circumstances this results in a depolarization, as noted in our previous work (Wilson et al., 2011).

Electrophysiological Studies

For these electrophysiological studies, selected populations of chondrocytes were first plated on pieces of glass coverslips, which were then transferred from the culture dishes to our superfusion chamber at the start of each experiment. Only single isolated cells with a smooth surface rounded appearance were selected for these recordings using standard patch-clamp methods (Clark et al., 2011).

Patch pipettes were fabricated from non-heparinized hematocrit capillaries. Patch pipette-filling solutions were either (i) K^+-rich (KCl) or (ii) Cs^+-rich (CsCl), depending on the protocol. In most experiments, free Ca^{2+} concentration in the pipette solutions was buffered to very low levels ($<10\,nM$) by 10 mM EGTA, without added Ca^{2+}. The D.C. resistance of the pipettes when filled with internal solutions was in the range ∼2–4 MΩ. The seal resistance before breaking into the chondrocyte to begin whole-cell recording ranged from 4.8 to 72.3 GΩ (mean ± s.e.m.; 16.1 ± 1.5 GΩ, $n = 66$). Successful seals formed very rapidly (∼1–2 s), and the subsequent break-in to the cells for whole-cell recording was "clean"; access resistance was generally about twice the value of the pipette resistance. (cf. Clark et al., 2011).

All electrophysiological measurements were made with a Multi-Clamp 700 A patch clamp amplifier (Molecular Devices). Membrane currents and potentials were digitized with a 1,322 A data acquisition system, stored on a microcomputer and analyzed off-line with PClamp (version 8). The "standard" voltage-clamp protocols consisted of (i) 1 s voltage ramp from −100 to +100 mV (holding potential generally −80 mV), repeated at a frequency of 0.2–0.5 Hz, and (ii) a "step" protocol, consisting of 500 ms steps from a holding potential of −80 mV membrane to potentials between −100 and +100 mV. In some experiments, a "P/n" protocol was used to correct "step" currents for linear leakage and capacity transient currents. Since the ramp and step protocols gave very similar current-voltage (I–V) relationships, the ramp protocol was used to obtain rapid, repetitive measurement of the I–V, e.g., during drug applications.

Transmembrane current values were normalized to cell capacitance, which was measured from the area under the capacitative current transient produced by a +5 mV step in membrane potential. Capacitance was recorded before and after break-in to the cell; the capacitance of each single chondrocyte was taken as the difference in these capacitance values. Drugs were delivered to cells with a multi-barreled local superfusion device that changed the solution around a cell within <1 s. All experiments were carried out at room temperature (20–22°C).

In the second experimental part of this study, after obtaining the data that characterized the predominant K^+ currents in enzymatically isolated human chondrocytes, we analyzed TRP channel mediated currents (**Figures 8**, **9**) using a different source human articular chondrocytes. These cells were from a chondrocyte preparation made available by Glaxo Smith Kline Ltd (GSK) (Balakrishna et al., 2014). GSK cells that were cultured from frozen samples of primary cells (batches #1060, #1274). The culture medium was DMEM/F12, supplemented with 10% fetal calf serum, 2 mM L-glutamine and penicillin/streptomycin (1:10). These chondrocytes were used up to a maximum of 6 days after plating and were not passaged. TRP channels were activated or blocked using proprietary compounds that were obtained from Glaxo Smith Kline; GSK Ltd. (Thorneloe et al., 2008; Hilfiker et al., 2013).

The Atypical Microenvironment of the Chondrocyte

In adult mammals, the chondrocyte cell population is in a physiological environment, the articular joint fluid that differs significantly from that of most other cells in healthy human tissues. A number of these important differences are listed in **Table 1**. Note that the extracellular fluid within the articular joint is hypertonic (∼320 mOsm vs. blood plasma, ∼280 mOsm). In addition, the extracellular pH, i.e., that of the synovial fluid that bathes the chondrocyte is somewhat acidic, pH 7.2; and the extracellular $[K^+]_o$ levels are significantly elevated measuring ∼10–15 mM, as opposed to 4.0–5.4 mM $[K^+]_o$ in normal mammalian plasma (Huber et al., 2000; Wilkins et al., 2000a). Nevertheless, the main large transmembrane electrochemical gradients for Na^+, K^+, and Cl^- in chondrocytes are quite similar to those in other mammalian cells. Establishment and maintenance of these gradients leads to the requirement for an ATP-dependent Na^+/K^+ pump mechanism (assumed to be electrogenic). This maintains ionic homeostasis and stabilizes cell volume. Evidence for expression of a Na^+/K^+ ATPase has been obtained in bovine articular chondrocytes (Mobasheri et al., 1997). It is also known that glucose is the major energy substrate for articular chondrocytes and that these cells express Glut1 and Glut3 glucose transporter (Phillips et al., 2005). The Mobasheri Group (Mobasheri et al., 2008) have also reported that the expression, distribution and function of these facilitative glucose transporters are regulated significantly by hypoxia, inflammation, or altered complements of articular joint growth factors.

The fixed negative charges on proteoglycans of the extracellular matrix are in the immediate vicinity of the chondrocyte and can attract cations (e.g., Na^+), while also excluding anions. As a result, localized cation accumulation occurs (**Table 1**), and for this reason there is a significant osmotically driven water influx (Urban et al., 1993; Wilkins et al., 2000a; Lewis et al., 2011). In addition, intrinsic characteristics of the "pericellular matrix" on the immediate surface of each

TABLE 1 | Ion concentrations in compartments within the mammalian knee joint (see Ref. Hall et al., 1996) (adapted from Table 1 in Wilkins et al., 2000a).

Electrolyte concentrations (mM)	Cytoplasm	Matrix	Sinovial fluid
$[Na^+]$	40	240–350	140
$[K^+]$	120–140	7–12	5
$[Ca^{2+}]$	$1\text{-}5 \times 10^{-5}$	6–15	1.5
$[Cl^-]$	60–90	60–100	140
$[HCO_3^-]$	20	15	23
$[SO_4^{2-}]$	0.17	0.30	0.81
pH	7.1–7.2	6.6–6.9	7.4
Osmolarity (mOsm)	–	350–450	300

chondrocyte can serve as a significant diffusion barrier, as demonstrated recently with the use of optical trap methods (McLane et al., 2013). It is also important to note that the literature now suggests that the relevant functional unit of the chondrocyte is the chondron. It includes the cell (chondrocyte) and its glycocalyx or pericellular coat (Muir, 1995; Poole, 1997; Guilak et al., 2006).

The articular joint receives only very limited blood supply. Accordingly, the synovial fluid must supply adult articular cartilage with the required (small amounts of) nutrients, as well as sufficient oxygen to maintain Na^+/K^+ pump activity and ensure intracellular Ca^{2+}, $[Ca^{2+}]_i$, homeostasis (Mobasheri et al., 1997; Mobasheri, 1998; Chao et al., 2006). Metabolic byproducts are removed mainly by diffusion (Urban et al., 1993; Wilkins et al., 2000b). An important consequence of the "avascular" nature of this articular joint tissue is that chondrocytes generate ATP by substrate-level phosphorylation during anaerobic respiration (Guilak et al., 1997). This generates H^+ ions as a byproduct, and this tends to acidify the pH in this micro-environment. The dynamic changes in mechanical loading within the knee joint during activity also expose chondrocytes to very significant fluctuations in vector and shear forces. The resulting mechanical changes can activate mechano-or shear-sensitive ion channels (Hall et al., 1996; Lane Smith et al., 2000; Mouw et al., 2006).

MODEL DEVELOPMENT

We have developed a new, first generation mathematical model for the resting membrane potential, E_m, of the chondrocyte, based partly on the experimental data obtained and described in section Electrophysiological Studies. This includes (a) K^+ currents, (b) time-independent currents, (c) pump and exchanger currents, and (d) intracellular Ca^{2+} buffering. These components are illustrated in **Figure 1** and are described in detail in following sections. The transmembrane ion transport processes include: I_{K-DR}, a voltage-dependent delayed rectifier K^+ channel; I_{K-Ca}, voltage and internal Ca^{2+}-dependent K^+ channel; I_{K-2p}, a two-pore K^+ channel; I_{K-ATP}, ATP-dependent K^+ channel; $I_{Na,b}$, a time-independent "background" Na^+ channel; $I_{K,b}$, a time-independent "background" K^+ channel; $I_{Cl,b}$, a time-independent "background" Cl^- channel; I_{NaK}, ATP-dependent electrogenic Na^+-K^+ pump; I_{NaCa}, electrogenic Na^+-Ca^{2+} exchanger; I_{NaH}, the transmembrane Na^+ flux of the electroneutral Na^+-H^+ antiporter; $I_{Ca,ATP}$, electroneutral ATP-dependent Ca pump; and I_{TRPV4}, cation permeable TRPV4 ion channel. In this model, intracellular Ca^{2+} is buffered by binding to calmodulin.

The equation governing the transmembrane potential, V, of the chondrocyte is

$$C_m \frac{dV}{dt} = -(I_{K-DR} + I_{K-Ca} + I_{K-2p} + I_{K-ATP} + I_{Na,b} + I_{K,b} + I_{Cl,b} + I_{NaK} + I_{NaCa} + I_{TRPV4}) \quad (1)$$

where C_m is chondrocyte capacitance (8 pF). This equation includes all transport processes that are electrogenic i.e., generate net transmembrane current(s).

The intracellular concentrations of Na^+, $[Na^+]_i$ and K^+, $[K^+]_i$, are governed by two transport equations, namely,

$$\frac{d[Na^+]_i}{dt} = \frac{-(I_{Na,b} + 3I_{NaK} + 3I_{NaCa} - I_{NaH})}{vol_i\, F} \quad (2)$$

and

$$\frac{d[K^+]_i}{dt} = \frac{-(I_{K,b} - 2I_{NaK} + I_{K-DR} + I_{K-2p} + I_{K-Ca} + I_{K-ATP})}{vol_i\, F} \quad (3)$$

where vol_i is the internal volume of the chondrocyte (calculated to be 0.005884 mL), and F is the Faraday constant, 96,485 C/mol. Note that Equation (1) does not include I_{NaH}, since this is the Na^+ flux generated by the electroneutral Na^+-H^+ antiporter, but this term is included in the Na^+ homeostasis Equation (2). Equations (2) and (3) specify how the intracellular concentrations of Na^+ and K^+ evolve with time, and also how the Nernst potentials for Na^+, and for K^+, change with time. $R = 8.314$ J K^{-1} mol^{-1} is the universal gas constant, $T = 310.15$ is body temperature in deg. Kelvin, and $z_{Na} = 1$ and $z_K = 1$ are ionic valances for Na^+ and K^+, respectively. The extracellular concentrations of Na^+, $[Na^+]_o$, and K^+, $[K^+]_o$, are held constant during each simulation. However, some simulations were done after changing these values to those that are more representative of the physiological milieu of the chondrocyte, (shown in **Table 1**), rather than those set by our experimental superfusate for the patch-clamp experiments.

Intracellular Ca^{2+} concentration, $[Ca^{2+}]_i$, also changes with time, due to transmembrane transport of Ca^{2+} by the Na^+-Ca^{2+} exchanger and ATP-dependent Ca^{2+} pump, and intracellular calmodulin binding, according to the equation:

$$\frac{d\left[Ca^{2+}\right]_i}{dt} = \frac{(I_{NaCa} - I_{Ca,\,ATP})}{vol_i\, F} - 0.045\,\frac{d\boldsymbol{O_c}}{dt} \quad (4)$$

where $\boldsymbol{O_c}$ is the fraction of intracellular calmodulin bound to Ca^{2+} (see Equation 39).

Differential equations (1–4) and those for $I_{K,Ca}$ and calmodulin buffering were solved numerically. All data simulations and processing was performed off-line using both noncommercial and commercial software packages (Radhakrishnan and Hindmarsh, 1993; Maleckar et al., 2009; Eaton et al., 2014), as well as custom, in-house scripts. The software that is the basis of our model of the chondrocyte resting membrane potential is available on request.

RESULTS

Ion-Selective Transmembrane Currents

Potassium Currents

We have identified and partially characterized three different K^+ currents in mammalian chondrocytes. In principle, each of these can contribute to the resting membrane potential, E_m, either at baseline or following selective activation/enhancement by physiological stimuli or pathophysiological conditions. These K^+ currents are: (i) a time-and voltage dependent delayed rectifier K^+ current, I_{K-DR}; (ii) a K^+ current due to 2-pore

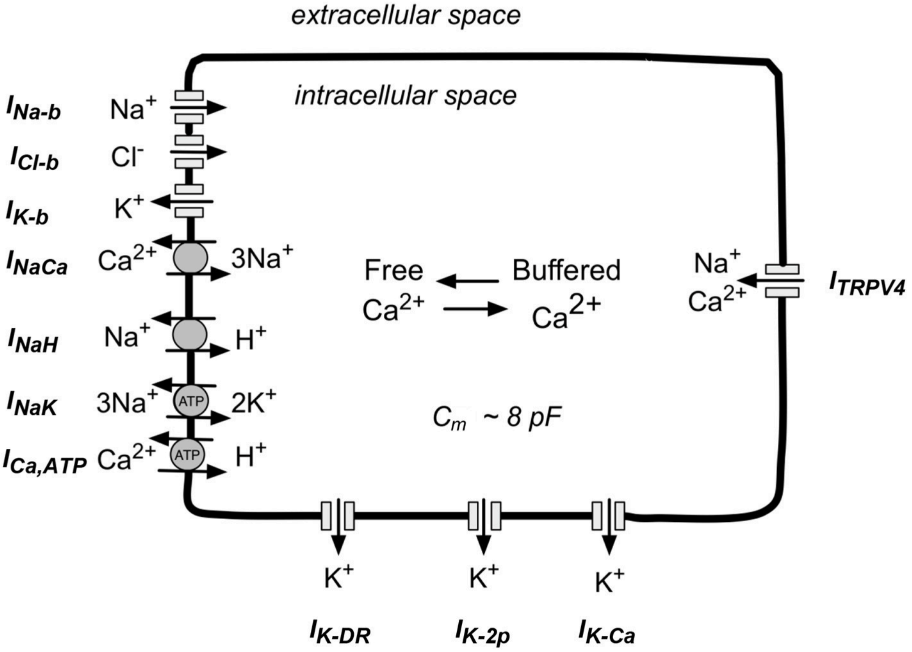

FIGURE 1 | Schematic illustration of the main ion selective channels, ion exchange proteins, and ATP-dependent ion pumps that are known to be expressed in human chondrocytes. This information forms the basis for our mathematical model of chondrocyte K^+ transport and resting potential, E_m. The three ion selective channels labeled at the top left of this diagram are so-called background channels; these currents show no time dependence. The three types of ion channels shown on the bottom are the focus of this paper. These K^+-selective channels in human chondrocytes, have been studied in detail in our Laboratory and by other groups (see section Results). The ion-selective pumps and exchangers shown at the bottom left are necessary to maintain volume, and contribute to electrolyte homeostasis in the human chondrocyte. The TRPV4 channels shown on the right can allow Na^+ and $Ca^{2}+$ influx. In addition, (see section Discussion) chondrocytes can exhibit cell-to-cell coupling via connexin-mediated ion and metabolite transfer, and/or "hemichannel behavior" (see section Discussion).

K^+ channels, I_{K-2p}; and (iii) a large conductance voltage and Ca^{2+}-activated K^+ current, I_{K-Ca}, have been studied in some detail in our laboratory (Wilson et al., 2004; Clark et al., 2010, 2011, respectively) and also by other groups (for reviews, see Grandolfo et al., 1992; Mobasheri et al., 2007, 2012; Barrett-Jolley et al., 2010; Asmar et al., 2016). An ATP-dependent K^+ current (I_{K-ATP}) has also been identified in patch clamp studies published by other investigators (cf. Mobasheri et al., 2007).

A typical pattern of K^+ currents from our patch clamp recordings using single isolated human articular chondrocytes (denoted HAC) is illustrated in **Figure 2A**. This chondrocyte first held at −80 mV, and then the membrane potential was stepped to selected levels between −100 and +110 mV, in 10 mV increments at a rate of 0.2 Hz. Three consistent features are noteworthy: (i) over much of this membrane potential range, the currents showed no obvious time- and voltage dependence, (ii) after being activated, these currents became much greater in amplitude and showed larger fluctuations with increasingly depolarized membrane voltages; (iii) large, very noisy outward currents began to appear at about +60 mV.

Figure 2B consists of an averaged isochronal current-voltage (I–V) relationship based on data obtained from 13 human chondrocytes, each studied after 1 day in cell culture. The magnitude of these K^+ currents was normalized to the capacitance of each cell in order to compensate for differences in cell size. Note that this I–V relationship is approximately linear at membrane potentials negative to about −50 mV but becomes non-linear at more depolarized voltages. The solid red trace shows the best-fit straight line for the data between −50 and −100 mV, extrapolated over the entire potential range of the I–V plot. The nonlinearity at depolarized membrane potentials is mainly due to increases in the noisy outward current. This feature is very evident at membrane potentials positive to about +60 mV. Note also that there is a small non-linearity in the I–V between ∼−40 and +50 mV. This suggests that another component of outward current might be present in these single HAC preparations.

Delayed rectifier K^+ current: $I_{K\text{-}DR}$

A conventional time- and voltage-dependent delayed rectifier K^+ current has been identified in mouse, canine, rabbit, and human articular chondrocytes under primary culture conditions (Wilson et al., 2004; Barrett-Jolley et al., 2010; Clark et al., 2010). Our previous analysis of ion selectivity, as judged by reversal potential measurements, has shown that this current, denoted I_{K-DR}, is carried mainly by K^+ (Wilson et al., 2004; Clark et al., 2010). Moreover, the biophysical properties of this current and its pharmacological blockade suggested that it is generated by a well-known Kv1.x conductance family, perhaps Kv1.5 or Kv1.6.

The presence of this small time- and voltage-dependent current in these human chondrocyte (HAC) preparations was

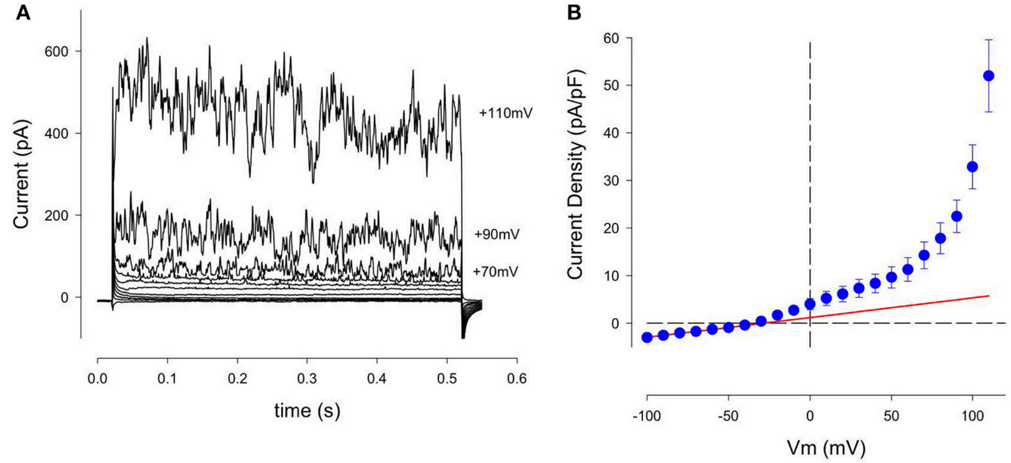

FIGURE 2 | Family of K^+ currents recorded from an isolated human chondrocyte maintained in primary 2D culture conditions. **(A)** These currents were recorded from a chondrocyte that was held at −80 mV, and then stepped to membrane potentials between −100 and +110 mV, in 10 mV increments. Current records are shown between −90 and +100 mV, (in 20 mV increments). This chondrocyte had been in culture for 3 days; its capacitance, C_m, was 7.3 pF. Panel **(B)** is an averaged current-voltage (I–V) relation for 13 cells, (1 day in culture). Currents recorded from each cell were normalized to cell capacitance before averaging. Solid red trace is the best-fit straight line between −100 and −50 mV. Its slope is 0.042 nS/pF. Mean ± s.e.m. C_m of 13 cells was 7.4 ± 0.8 pF.

revealed more clearly when the linear leak and capacity currents were removed from the raw current records (see Methods section). An example of current records from one HAC preparation in which these correction procedures were used is shown in **Figure 3**. The records in **Figure 3A** clearly reveal the time- and voltage-dependent properties of the relatively small component of outward current that is activated at membrane potentials positive to ∼-40 mV. The rate of activation of this current increases significantly with progressively larger depolarizations. Note, however, these K^+ currents showed no inactivation during the 500 ms voltage-clamp steps. In summary, the properties of this current resembled the "delayed rectifier" K^+ current, I_{K-DR} that we and others have reported previously from studies in chondrocytes from other species (Wilson et al., 2004; Clark et al., 2010). Not all isolated human chondrocytes expressed this type of "delayed-rectifier" K^+ current. As an example, in one group of 13 HAC studied after 1 day in culture, only 8 cells expressed a detectable I_{K-DR}. In a second group of 12 HAC studied after 3 days in culture, only 4 cells expressed I_{K-DR}. These findings suggest that there is intrinsic variability in the expression of this K^+ current; and/or that its expression may decrease with time in culture (see section Discussion). **Figure 3B** shows a plot of I_{K-DR} conductance vs. membrane voltage, E_m, for 16 cells. The I_{K-DR} conductance values were obtained by dividing peak I_{K-DR} by the electrochemical driving force. (EMF), which is defined as the membrane potential, V, minus the Nernst potential for K^+, E_k (∼−83 mV under the experimental recording conditions). The best-fit Boltzmann relationship (red line) in **Figure 3B** yields a descriptor of the voltage dependent activation of this K^+ current. I_{K-DR} was described by the following expression, as we have published previously (Maleckar et al., 2009);

$$I_{K-DR} = g_{K-DR}\,\alpha_{KDr}(V - E_K) \tag{5}$$

where

g_{K-DR} is the maximal I_{K-DR} conductance, namely 0.0289 nS/pF from **Figure 3B**, and

α_{KDr} is a voltage-dependent activation factor, given by the expression

$$\alpha_{KDr} = \frac{1.0}{(1.0 + e^{\frac{-(V+26.7)}{4.1}}} \tag{6}$$

Note that the extracellular potassium concentration, $[K^+]_o$, was initially set to 5.4 mM under "typical" physiological conditions. In fact, however, $[K^+]_o$ is likely to be in the 5–15 mM range in the microenvironment of the chondrocyte *in situ* (see **Table 1**). Intracellular K^+ concentration was initially set to 140 mM in this parameterization of the model, but evolves through time, governed by Equation (3).

Ca^{2+}-activated K^+ current: I_{K-Ca}

The prominent fluctuations in outward current traces recorded from all human chondrocytes at strongly depolarized membrane potentials suggested the expression of this "large" variant of Ca^{2+}-activated K^+ channels ("BK," KCa1.1). It is well-known that the voltage dependent gating of these BK channels is strongly modulated by the intracellular Ca^{2+} concentration, $[Ca^{2+}]_i$ (cf. Horrigan and Aldrich, 2002; Magleby, 2003; Berkefeld et al., 2006, 2010; Barrett-Jolley et al., 2010; Mobasheri et al., 2012; Asmar et al., 2016). In the experimental results in **Figure 2** $[Ca^{2+}]_i$ was held very low (<10 nM) by using a patch pipette solution containing no added Ca^{2+}, combined with a strong Ca^{2+} buffer (10 mM EGTA). In the presence of this very low $[Ca^{2+}]_i$, these BK channels can be activated only by very strong voltage clamp depolarizations (e.g., > +40 mV).

To more clearly reveal the functionally important properties of this BK current, additional experiments were carried out

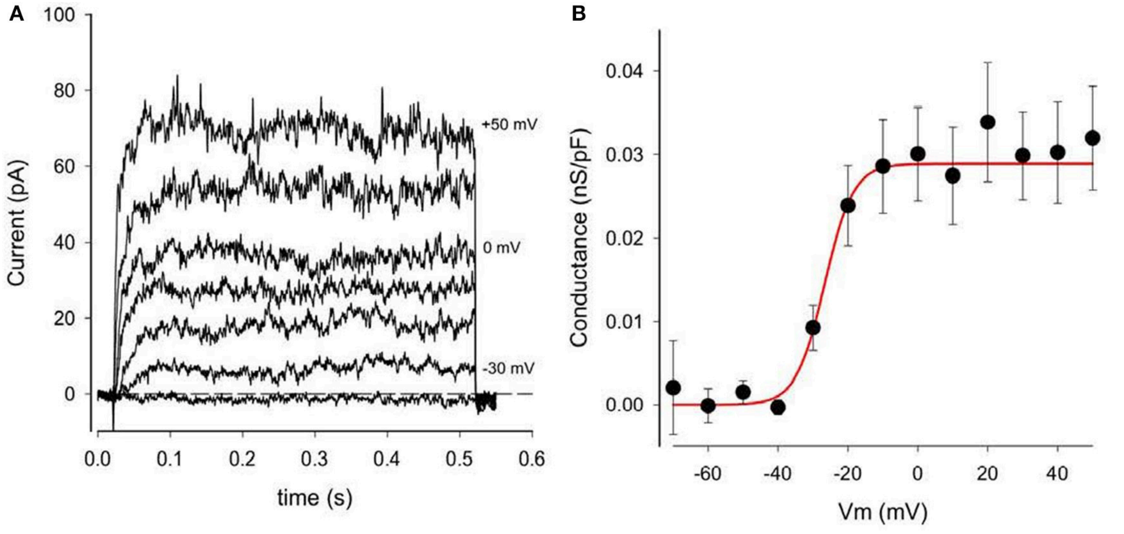

FIGURE 3 | Delayed rectifier K$^+$ currents, I_{K-DR}, in a human chondrocyte. **(A)** Examples of I_{K-DR} activated by voltage-clamp steps from holding potential of −80 mV to membrane potentials of −40, −30, −20, −10, 0, +20, and +50 mV. Records have been corrected for capacity and linear leak currents. **(B)** Plot of I_{K-DR} peak conductance (per pF) vs. membrane voltage, V. Conductance was obtained by dividing peak I_{K-DR} by (V-E_K), where E_K is K$^+$ Nernst potential (−83 mV). Data from 16 cells (mean ± SEM). The best-fit Boltzmann relationship (red line) is the factor αK-DR (Equation 2).

using a pipette solution containing 3 mM Ca^{2+} and 10 mM EGTA, which yielded a nominal free Ca^{2+} concentration of ∼175 nM. Data from these experiments are summarized in **Figure 4**. Currents from two groups of HAC's, one with "low" internal Ca^{2+} solution, and one with "high" Ca^{2+}, are shown in **Figures 4A,B**, respectively. It is clear that the "noisy" outward currents were much larger in the presence of "high" $[Ca^{2+}]_i$ compared with "low." **Figure 4C** compares pooled I–V data from subsets of HAC preparations perfused internally with either "low" or "high" internal $[Ca^{2+}]_i$. All of these chondrocytes were from the same batch, and recordings were made after 1 day in conventional 2D cell culture. As expected for currents generated by BK channels the large, fluctuating outward currents recorded from chondrocytes with "high" $[Ca^{2+}]_i$ were activated at considerably more negative membrane potentials than from chondrocytes with "low" $[Ca^{2+}]_i$ (Horrigan and Aldrich, 2002; Berkefeld et al., 2010). Moreover, the maximum current (measured at +100 mV) was several times larger in the "high" $[Ca^{2+}]_i$ chondrocytes. These results strongly suggest that a Ca^{2+}-activated current I_{K-Ca}, produced by the so-called BK channels, is an important component of K$^+$ current in these cultured HAC cells (Magleby, 2003; cf. Sun et al., 2009).

It is well-known that the molecular properties and biophysical characteristics of the extensive Ca^{2+} activated K$^+$ channel family can be used to divide them into three sub-groups (Berkefeld et al., 2010). Defining characteristics include: (i) the specific biophysical properties of the current (e.g., its voltage dependence), (ii) their pharmacological profile (e.g., sensitivity to block by apamin or tetraethylammonium, TEA), or (iii) the single channel conductance. In the case of human chondrocytes (as shown in **Figures 2**, **3**) the pronounced current fluctuations (noise) strongly suggest the presence of the variant of Ca^{2+} activated K$^+$ channels known as the large conductance subtype, BK. The major properties of this current (cf. Horrigan and Aldrich, 2002) have been incorporated into a detailed mathematical model developed by Sun et al. (2009).

The mathematical description for this Ca^{2+}-activated K$^+$ current is a 10-state kinetic Markov-type model, including four calcium-binding steps, with all the voltage dependence assigned to the transitions between closed and open states, i.e., the C-O equilibrium:

$$\frac{d\mathbf{C}_O}{dt} = \beta_O\mathbf{O}_o - \alpha_O\mathbf{C}_o + K_c\mathbf{C}_1 - 4Ca\mathbf{C}_o \tag{7}$$

$$\frac{d\mathbf{C}_1}{dt} = \beta_1\mathbf{O}_1 - \alpha_1\mathbf{C}_1 - K_c\mathbf{C}_1 + 4Ca\mathbf{C}_o - 3Ca\mathbf{C}_1 + 2K_c\mathbf{C}_2 \tag{8}$$

$$\frac{d\mathbf{C}_2}{dt} = \beta_2\mathbf{O}_2 - \alpha_2\mathbf{C}_2 - 2K_c\mathbf{C}_2 + 3Ca\mathbf{C}_1 - 2Ca\mathbf{C}_2 + 3K_c\mathbf{C}_3 \tag{9}$$

$$\frac{d\mathbf{C}_3}{dt} = \beta_3\mathbf{O}_3 - \alpha_3\mathbf{C}_3 - 3K_c\mathbf{C}_3 + 2Ca\mathbf{C}_2 - Ca\mathbf{C}_3 + 4K_c\mathbf{C}_4 \tag{10}$$

$$\frac{d\mathbf{C}_4}{dt} = \beta_4\mathbf{O}_4 - \alpha_4\mathbf{C}_4 - 4K_c\mathbf{C}_4 + Ca\mathbf{C}_3 \tag{11}$$

$$\frac{d\mathbf{O}_0}{dt} = -\beta_0\mathbf{O}_0 + \alpha_0\mathbf{C}_0 + K_0\mathbf{O}_1 - 4Ca\mathbf{O}_0 \tag{12}$$

$$\frac{d\mathbf{O}_1}{dt} = -\beta_1\mathbf{O}_1 + \alpha_1\mathbf{C}_1 - K_o\mathbf{O}_1 + 4Ca\mathbf{O}_o - 3Ca\mathbf{O}_1 + 2K_o\mathbf{O}_2 \tag{13}$$

$$\frac{d\mathbf{O}_1}{dt} = -\beta_2\mathbf{O}_2 + \alpha_2\mathbf{C}_2 - 2K_o\mathbf{O}_2 + 3Ca\mathbf{O}_1 - 2Ca\mathbf{O}_2 + 2K_o\mathbf{O}_3 \tag{14}$$

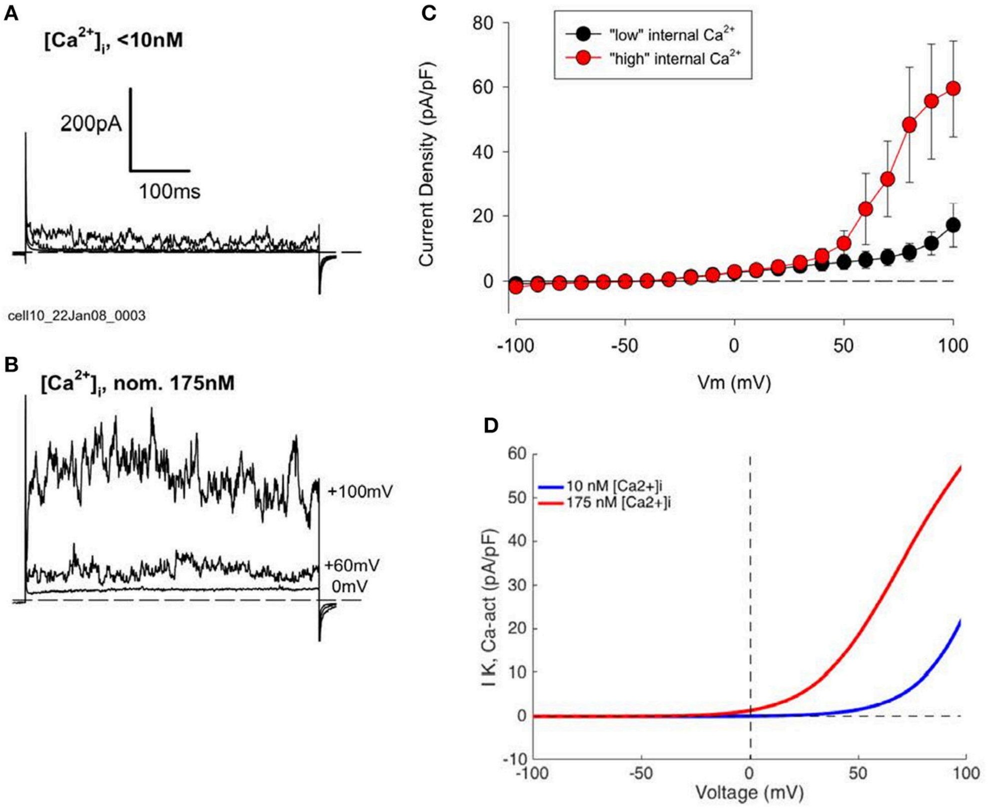

FIGURE 4 | Effect of changes in intracellular Ca^{2+}, $[Ca^{2+}]_i$, concentration on K^+ currents in human articular chondrocytes. **(A)** Example of currents from a HAC with "low" internal $[Ca^{2+}]_i$ (0 $[Ca^{2+}]_i$, 10 mM EGTA). Currents produced by voltage steps to 0, +60, and +100 mV from a holding potential of −80 mV are shown. $C_m = 9.72$ pF. **(B)** Currents from a cell with "high" internal $[Ca^{2+}]_i$ (3 mM added Ca^{2+}, 10 mM EGTA; nominal Ca^{2+} concentration = 175 nM). Voltage-clamp steps were to 0, +60, and +100 mV. $C_m = 6.24$ pF. Currents in **(A,B)** were not leak or capacity current corrected. **(C)** I–V relations for groups of HAC with "low" (n = 5, blue) and "high" (n = 4, red) $[Ca^{2+}]_i$ patch-clamp solution. These chondrocytes were all from same batch, 1 day in culture. **(D)** Model I–Vs for I_{K-Ca}, with different internal $[Ca^{2+}]$ levels (from Equation 4).

$$\frac{d\boldsymbol{O}_3}{dt} = -\beta_3\boldsymbol{O}_3 + \alpha_3\boldsymbol{C}_3 - 3K_o\boldsymbol{O}_3 + 2Ca\boldsymbol{O}_2 - Ca\boldsymbol{O}_3 + 4K_o\boldsymbol{O}_4 \tag{15}$$

$$\frac{d\boldsymbol{O}_4}{dt} = -\beta_4\boldsymbol{O}_4 + \alpha_4\boldsymbol{C}_4 - 4K_o\boldsymbol{O}_4 + Ca\boldsymbol{O}_3 \tag{16}$$

where $\boldsymbol{C}_{n=0,1,2,3,4}$ and $\boldsymbol{O}_{n=0,1,2,3,4}$ are closed and open states 1 through 4, respectively, with the total open probability corresponding to the sum of the open states, **O;** $\alpha_{n=0,1,2,3,4}$ represent rates corresponding to transition from a closed to an open state and $\beta_{n=0,1,2,3,4}$ represent rates corresponding to transition from an open to a closed state; K_o and K_c are off-rates from open and closed states, respectively, and *Ca* is the calcium on-rate, where

$$\alpha_n = A_n\, e^{\frac{z_{CO}VF}{RT}} \tag{17}$$

$$\beta_n = B_n\, e^{\frac{z_{OC}VF}{RT}} \tag{18}$$

$A_0 = 0.659, A_1 = 3.955, A_2 = 25.05, A_3 = 129.2, A_4 = 261.1;$ $B_0 = 2651.7, B_1 = 1767.8, B_2 = 1244.0, B_3 = 713.0, B_4 = 160.0;$ $z_{CO} = 0.718, z_{OC} = 0.646, K_c = 13.5, K_O = 1.5,$ and the Ca^{2+} on-rates per site are $10^9\ M^{-1}s^{-1}$, Ca^{2+} off-rates from C_n per binding site are $10^9\ K_C$ (13,500 s^{-1}) and Ca^{2+} off-rates from O_n per binding site are $10^9\ K_O$ (1,500 s^{-1}), and *R* is the universal gas constant, =8.314 J K^{-1} mol^{-1} and $T = 310.15$ is body temperature in Kelvin.

I_{K-Ca} is then defined by:

$$\boldsymbol{I}_{K-Ca} = g_{K-Ca}\mathbf{O}(V - E_K) \tag{19}$$

where g_{K-Ca} is the maximal conductance of the channel, equal to 2.50 nS/pF, **O** is the total open probability as given above, V is the transmembrane potential, and E_K is the Nernst potential for potassium.

We have used this mathematical formalism to compute I–V relationships for BK currents that can assumed to have been recorded from isolated human chondrocytes under conditions in which the composition of the pipette solution was adjusted (buffered) so that the $[Ca^{2+}]_i$ was $\sim 10^{-8}$ M. In this situation, this K^+ current can be activated at only very positive membrane potentials. In contrast, when $[Ca^{2+}]_i$ was increased to ∼175 nM this Ca^{2+}-activated K^+ current activates at much less strongly depolarized membrane potentials, as shown by the computations summarized in **Figure 4D**.

Further information regarding the functional properties of this BK channel-mediated current was obtained using conventional pharmacological approaches. As shown in **Figure 5** this K^+ current can be blocked completely by concentrations of TEA that are known to quite selectively inhibit these BK channels. This pattern of results provides further evidence for the consistent and potentially prominent expression of this K^+ current in human articular chondrocytes.

Although, I_{K-Ca} is a major outward current in human chondrocytes, it apparently does not contribute substantially to the resting potential under our conditions. This is because of the following: the input resistance of the human chondrocyte is very high (∼5–10 GΩ); and under this circumstance, activation of a small number of these Ca^{2+} activated K^+ channels would give rise to a resting potential that would be characterized by significant fluctuations in membrane voltage. Activation of these large conductance K^+ channels is not consistent with recordings of resting membrane potential in the region of −40 mV (see Discussion section).

2-Pore K^+ current: I_{K-2p}

Our previous work (Clark et al., 2011) defined recording conditions under which a K^+ current generated by the TASK family of two-pore K^+ channels could be identified consistently in single chondrocytes. This apparently very small current, that we denote I_{K-2p}, exhibits no detectable time dependence (Goldstein et al., 2001). It is known that certain 2-pore K^+ currents (including the TASK variants) are augmented by an increase in pH (alkalinization) of the extracellular medium (Patel and Honoré, 2001; Cid et al., 2013) and can be blocked by some local anesthetics (Kindler and Yost, 2005; Webb and Ghosh, 2009).

We have recorded this K^+ current under high $[K^+]_o$ conditions, to ensure that the current changes are relatively large, so that their biophysical properties can be resolved. However, before these results can be put into a functional context, or incorporated into a mathematical model of human chondrocyte electrophysiology, they need to be corrected (scaled) to physiological conditions (i.e., normal $[K^+]_o$ levels). This can be done based on the Eisenman principle (cf. Hille, 2001): the conductance of an ion-selective channel scales according to the

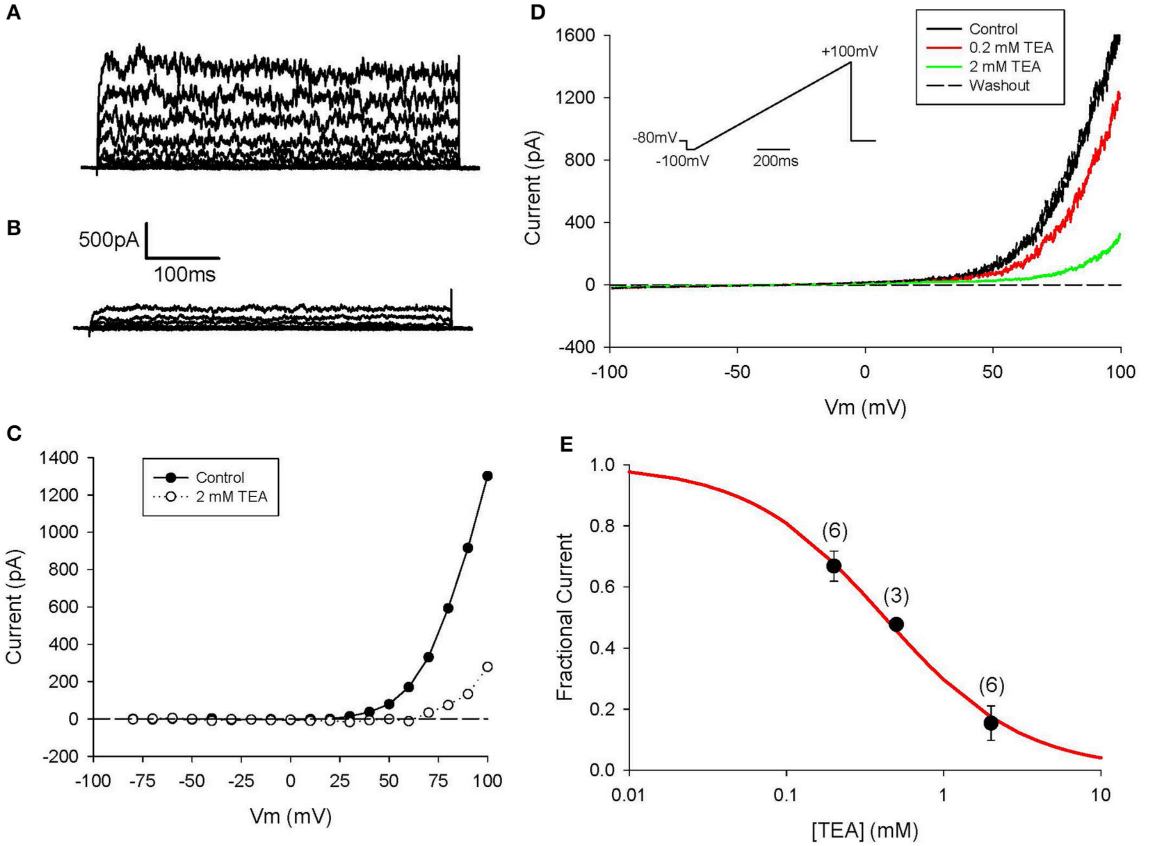

FIGURE 5 | Block of I_{K-Ca} in human chondrocyte by TEA. **(A)** Control currents. The voltage-clamp protocol consisted of 500 ms steps from h.p. −80 to +100 mV. Linear leak and capacitive currents were removed using a P/3 protocol. **(B)** Currents in presence of 2 mM TEA. **(C)** I–V relations for control and TEA currents in **(A,B)**. **(D)** Currents in response to a ramp protocol (inset), in control and in presence of 0.2 and 2 mM TEA. Same cell as **(A,B)**. Cell capacitance was 12.0 pF; 3 days in culture. **(E)** Dose-response for TEA pooled from 3 to 6 cells (indicated above each data point). Each current amplitude was measured at +100 mV. Solid line is best-fit binding equation, with $K_m = 0.42$ mM.

square root of the extracellular concentration of the permeant ion. Accordingly, I_{K-2p} is described by the classical Goldman-Hodgkin-Katz equation for a single ion species, with a square-root scaling factor to account for $[K^+]_o$:

$$I_{K-2p} = \frac{P_k z^2 V F^2}{RT}\,\frac{\left([K^+]_i - [K^+]_o\, e^{\frac{-zVF}{RT}}\right)}{\left(1 - e^{\frac{-zVF}{RT}}\right)} \qquad (20)$$

where P_K is a $[K^+]$-dependent scaling factor that describes the permeability (conductance) for this K^+ current, namely $3.1\text{x}10^{-6}\sqrt{([K^+]_i/[K^+]_o)}$, and $z = 1$ is the ionic valence for potassium.

The I–V relationship in **Figure 6A** shows that our primary data (Wilson et al., 2004) recorded in isotonic $[K^+]$ (∼145 mM), has the expected reversal potential (of 0 mV). The I–V relationship based on Equation (20) was fitted to the data. This fit determined the magnitude of P_K. **Figure 6B** shows the model I–V when $[K^+]_o$ is an assumed normal $[K^+]_o$ of 5.4 mM, with a corresponding reversal potential of ∼−83 mV.

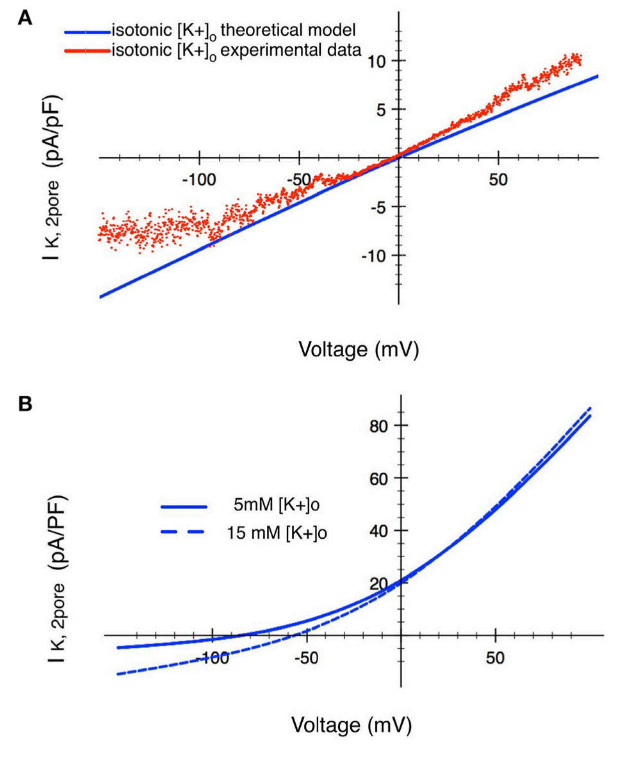

FIGURE 6 | Analysis of the ion transfer function (I–V relationship) for a 2-pore K^+ current in human chondrocytes. **(A)** Raw experimental data plotted as an I–V curve together with a superimposed I–V relationship (red trace) based on the mathematical formulation given in the text. These results were obtained in isotonic $[K^+]$o conditions. The two traces in **(B)** show corresponding I–V relationships derived using the Eisenman Principle, so that this K^+ current can be studied in conditions ($[K^+]$o of 5 mM and 15 mM) that are in the physiological range. The blue trace shows the I–V relationship for this 2-pore K^+ channel when $[K^+]$o is 15 mM. The black trace shows the change in this ion transfer relationship when $[K^+]$o is decreased to 5 mM. (see **Table 1** and section Discussion).

As illustrated in **Table 1**, the extracellular milieu of the chondrocyte is somewhat unusual, since it has been reported to have a $[K^+]_o$ level of ∼7–12 mM. Accordingly, a I–V curve for the 2-pore or TASK K^+ current was also calculated assuming a $[K^+]_o$ of 15 mM, as shown by the broken trajectory in **Figure 6B**. We have previously reported (Wilson et al., 2004) that this K^+ current is strongly inhibited by the anesthetic bupivacaine; and that an effective concentration of bupivacaine resulted in a significant depolarization of the resting potential (see section Discussion and Kindler and Yost, 2005; Webb and Ghosh, 2009).

ATP-sensitive K^+ current: I_{K-ATP}

An ATP-sensitive K^+ current I_{K-ATP} has been identified in chondrocytes that were isolated from the knee joint of a number of different mammalian species (Barrett-Jolley et al., 2010; Mobasheri et al., 2012; Asmar et al., 2016). Our previous experimental work in human articular chondrocytes (Clark et al., 2011) did *not* reveal any significant I_{K-ATP}. A likely reason for this is that the intracellular ATP/ADP ratio is set by the "internal pipette solution" in these electrophysiological experiments, and these conditions are such that I_{K-ATP} is unlikely to be activated. However, a relatively low ATP/ADP ratio that is prevalent in the somewhat hypoxic environment of the chondrocyte in articular joints makes it likely that I_{K-ATP} in fact will be activated during physiological biomechanical activity. Thus, a validated but general mathematical expression for this time-independent current (I_{K-ATP}) has been included in our mathematical model of the chondrocyte resting potential. This expression scaled to the I_{K-ATP} experimental data published by Mobasheri et al. (2007, 2012). An ATP-dependent K^+ current simulated using to Equation (21) below is illustrated in **Figure S1**.

$$\boldsymbol{I_{K-,ATP}} = \boldsymbol{\sigma g_o p_o f_{ATP}}(\mathbf{V} - \mathbf{E_K}) \qquad (21)$$

where $\boldsymbol{\sigma} = 0.6$ is the channel density, $\boldsymbol{g_o}$ is the unitary channel conductance, $\boldsymbol{p_o} = 0.91$ is the maximum open channel probability, and $\boldsymbol{f_{ATP}}$ is the fraction of activated channels, given by:

$$f_{ATP} = \frac{1.0}{1.0 + \left[\frac{ATP_i}{K_m}\right]^H} \qquad (22)$$

$$H = 1.3 + 0.74e^{-H_{K_{ATP}} ADP_i} \qquad (23)$$

$$K_m = 35.8 + 17.9ADP_i^{K_{m,ATP}} \qquad (24)$$

$$\mathrm{ADP_i} = \mathrm{C_A} - \mathrm{ATP_i} \qquad (25)$$

where $C_A = 8$ mM is the total concentration of adenine nucleotides, ADP_i and ATP_i are the intracellular concentrations of adenosine diphosphate, (ADP) and adenosine triphosphate, (ATP) respectively, $H_{K,ATP} = -0.001$, and $K_{m,ATP} = 0.56$.

Note that this ATP-sensitive K^+ current is *not* utilized in our initial description of the ionic basis for the HAC resting potential. That is, its channel density, $\boldsymbol{\sigma}$, has been set to zero in our initial or first order model parameterization.

Time-Independent or Background Ionic Currents

Three distinct time-independent background (or leakage) conductances corresponding to "resting" Na$^+$, K$^+$, and Cl$^-$ fluxes, have been included in this model. Simple mathematical descriptors for each conductance have been formulated, and each yields a linear I–V relationship.

The background (inward) Na$^+$ and (outward) K$^+$ currents, are described by.

$$\begin{aligned} \boldsymbol{I_{Na,b}} &= \boldsymbol{G_{Na,b}}(\mathbf{V} - \mathbf{E_{Na}}) \qquad (26) \\ \boldsymbol{I_{K,b}} &= \boldsymbol{G_{K,b}}(\mathbf{V} - \mathbf{E_{K}}) \qquad (27) \end{aligned}$$

where $\boldsymbol{G_{Na,b}} = 0.1$ nS/pF is the maximum conductance for the background sodium channel, and $\boldsymbol{G_{K,b}} = 0.07$ nS/pF is the maximum conductance for the background potassium channel. $[Na^+]_o$ was initially set to 130 mM under "typical" physiological conditions, but in the environs of the chondrocyte may be in the range shown in **Table 1**. $[Na^+]_i$, was initially set to 8 mM in this parameterization of the model, and evolves through time, governed by Equation (2), hence E_{Na} also changes with time. Similarly, $[K^+]_o$ was set to "typical" physiological conditions, 5.4 mM, but is likely to be higher in the chondrocyte's environment (**Table 1**). $[K^+]_i$ was initially set to 140 mM, but this concentration evolved according to Equation (3), thus also changing E_K.

In mammalian chondrocytes from a number of different species, a significant background Cl$^-$ conductance has also been identified (cf. Tsuga et al., 2002; Barrett-Jolley et al., 2010; Funabashi et al., 2010a; Kurita et al., 2015). We have incorporated this type of Cl$^-$ current by formulating it as a linear time-independent current, specified by the equations below:

$$I_{Cl,b} = \boldsymbol{G_{Cl,b}}(V - E_{\mathrm{Cl}}) \qquad (28)$$

where $\boldsymbol{G_{Cl,b}} = 0.05$ pS/pF is the maximum conductance for the background Cl$^-$ channel, and where the reversal potential, is −65 mV. The I–V relationships for these three background currents are shown in **Figure S2**.

Ion Pump and Exchanger Currents

Electrogenic Na$^+$/K$^+$ pump: I_{NaK}

Active (ATP requiring) extrusion of Na$^+$ from chondrocytes is assumed to be achieved by the combined expression level and turnover rate of a conventional electrogenic Na$^+$/K$^+$ pump. Mobasheri et al. (1997, 1998) have characterized some of the functional properties of an electrogenic Na$^+$/K$^+$ pump in bovine articular chondrocytes. Our model makes use of the Na$^+$/K$^+$ pump formulation from Nygren et al. (1998):

$$I_{NaK} = \bar{I}_{NaK}\left(\frac{[K^+]_o}{[K^+]_o + k_{NaK_K}}\right)\left(\frac{[Na^+]_i^{1.5}}{[Na^+]_i^{1.5} + k_{NaK_{Na}}^{1.5}}\right)\left(\frac{V+150}{V+200}\right) \qquad (29)$$

where $\bar{I}_{NaK}$ is the maximal current density 1.58 pA/pF $[K^+]_o$ is the extracellular potassium concentration. It has been initially set to 140 mM for "typical" values; **Table 1**), $[Na^+]_i$ is the intracellular sodium concentration, as defined previously, and given by equation (2), $k_{NaK,K}$ is the half-maximum K$^+$ binding concentration, and $k_{NaK,Na}$ is half-maximum Na$^+$ binding concentration, with values of 1.0 and 11.0 mmol/L, respectively.

This Na$^+$/K$^+$ pump activity (the product of expression density and turnover rate) generates a small outward electrogenic current. In this simplified model (cf. Trujillo et al., 1999) this Na$^+$/K$^+$ pump magnitude has been scaled to achieve a steady-state $[Na^+]_i$ of 10–12 mM. Representative ion transfer relationships for this I_{Nak} are shown in **Figure 7A**.

Na$^+$/Ca^2+ Exchanger: I_{NaCa}

The activity of the Na$^+$/Ca^{2+} exchanger plays a key role in Ca^{2+} homeostasis in articular chondrocytes (Sánchez et al., 2006) as it does in most other cell types. We have modeled this electrogenic exchange process using a mathematical expression that we have developed from our work on human atrial myocytes. Its overall

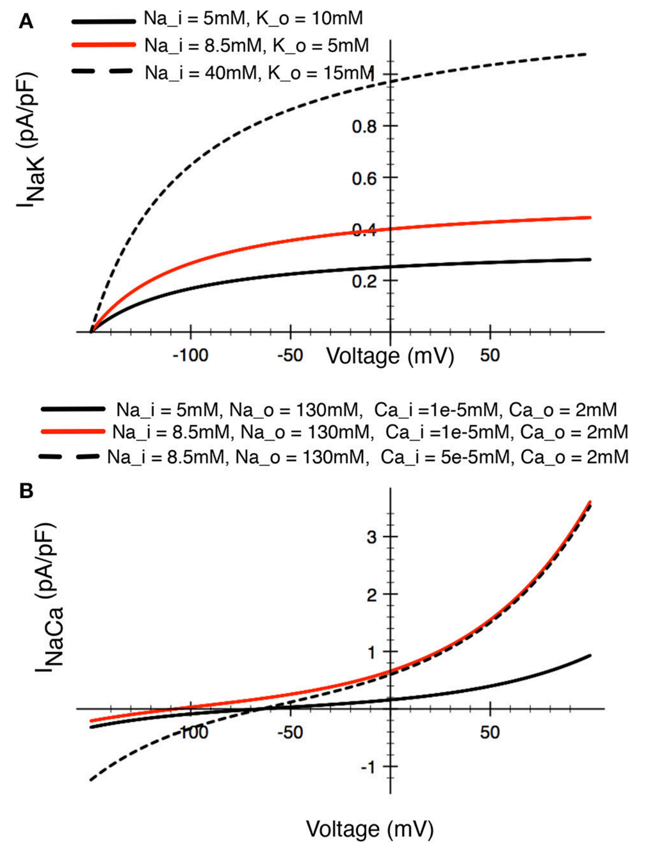

FIGURE 7 | Illustrations of the relative sizes of net currents produced by **(A)** the Na$^+$/K$^+$ pump, and **(B)** the Na$^+$/Ca^{2+} exchanger in a human chondrocyte. The three superimposed I–V curves for the Na$^+$/K$^+$ pump illustrated in **(A)** bracket the [Na$^+$] and [K$^+$] levels that have been reported in the literature (see **Table 1**). The red trace would approximately correspond to baseline conditions for [Na$^+$] and [K$^+$] in other mammalian cells. The three superimposed I–V curves for the Na$^+$/Ca^{2+} exchanger in **(B)** illustrated the relative magnitudes for this current, with the red trace again approximating the resting or baseline I_{Na-Ca} current in most other mammalian cells.

properties (ion transfer characteristics, dependence on $[Na^+]_i$ and $[Ca^{2+}]_i$ have been validated previously (Nygren et al., 1998):

$$I_{NaCa} = k_{NaCa}\frac{\left[Na^+\right]_i^3 [Ca^{2+}]_o e^{\frac{\gamma VF}{RT}} - \left[Na^+\right]_o^3 [Ca^{2+}]_i e^{\frac{(\gamma-1.0)VF}{RT}}}{1.0 + d_{NaCa}\{\left[Na^+\right]_o^3 [Ca^{2+}]_i + \left[Na^+\right]_i^3 [Ca^{2+}]_o\}} \tag{30}$$

Where k_{NaCa} is a scaling factor for this current, set to 0.0374842 pA/(mmol/L)^4, γ is the position of the energy barrier that modulates the voltage dependence of I_{NaCa}, set to 0.45, and d_{NaCa} is the denominator constant for the current, set to 0.0003 (mmol/L)$^{-4.}$, $[Na^+]_o$ is the extracellular Na$^+$ concentration; $[Na^+]_i$ is the intracellular Na$^+$ concentration as given by Equation (2), $[Ca^{2+}]_o$ is extracellular Ca^{2+} concentration (1.8 mM in a "typical" parameterization; see **Table 1**), and $[Ca^{2+}]_i$ is the evolving intracellular calcium concentration given by Equation (4).

This electrogenic ion exchange mechanism has been scaled based on a baseline or resting $[Na^+]_i$ of 12 mM, and $[Ca^{2+}]_i$ of 3 x 10^{-8} M (see **Table 1** and section Discussion). The resulting I–V relationship under these conditions is shown in **Figure 7B**.

Na$^+$/H$^+$ exchanger: I_{NaH}

Chondrocytes express a Na$^+$/H$^+$ antiporter (Trujillo et al., 1999; Barrett-Jolley et al., 2010) that contributes importantly to pH regulation. By analogy with its role in many other cells and tissues, this antiporter is responsible for establishing and maintaining the transcellular pH gradient that is essential for maintaining baseline $[Na^+]_i$ levels and optimizing several different intracellular enzyme activities. In addition, intracellular pH indirectly regulates a number of the ion channels that are expressed (e.g., 2-pore K$^+$ channels). pH can modulate essential enzymatic processes (e.g., Na$^+$/K$^+$ pump) in both physiological and pathophysiological settings.

We have used the equations originally developed by Crampin and Smith (2006) to model this electroneutral antiporter:

$$I_{NaH} = N_{NaH} I_{NaH_{mod}} I_{NaH_{exch}} \tag{31}$$

$$I_{NaHmod} = \frac{1}{1 + (K_i^{n_H} / \left[H^+\right]_i^{n_H}} \tag{32}$$

$$I_{NaH_{exch}} = \frac{t_1 t_2 - t_3 t_4}{t_1 + t_2 + t_3 + t_4} \tag{33}$$

$$t_1 = \frac{k_1^+ \left[Na^+\right]_o / K_{Na}^o}{1 + \frac{[Na^+]_o}{K_{Na}^o} + \frac{[H^+]_o}{K_H^o}} \tag{34}$$

$$t_2 = \frac{k_2^+ \left[H^+\right]_i / K_H^i}{1 + \frac{[Na^+]_i}{K_{Na}^i} + \frac{[H^+]_i}{K_H^i}} \tag{35}$$

$$t_3 = \frac{k_1^- \left[Na^+\right]_i / K_{Na}^i}{1 + \frac{[Na^+]_i}{K_{Na}^i} + \frac{[H^+]_i}{K_H^i}} \tag{36}$$

$$t_4 = \frac{k_2^- \left[H^+\right]_o / K_H^o}{1 + \frac{[Na^+]_o}{K_{Na}^o} + \frac{[H^+]_o}{K_H^o}} \tag{37}$$

where, $N_{NaH} = 4899$, $k_1^+ = 10.5$, $k_1^- = 0.201$, $k_2^+ = 15.8$, $k_2^- = 183$, $K_{H,mod}^i = 3.07\text{e-}5$, $K_{H,mod}^\circ = 4.8\text{e-}7$, $K_{Na}^i = 16.2$, $K_{Na}^\circ = 195$, $K_H^i = 6.05\text{e-}4$, $K_H^\circ = 1.62\text{e-}3$, $n_H = 1$, $m_H = 3$, $[Na^+]_i$ and $[Na^+]_o$ are the intracellular and extracellular Na$^+$ concentrations as given by Equation (2) respectively. $[H^+]_i$ and $[H^+]_o$ are the intracellular and extracellular proton concentrations. $[H^+]_i$ is an evolving concentration, initialized at pH 7.2. In any given simulation $[H^+]_o$ is selected and then held at this but constant value, typically set to pH 7.4.

Intracellular $[Ca^{2+}]_i$ Homeostasis: ATP-Dependent Ca Pump: $I_{Ca,ATP}$

In human chondrocytes, $[Ca^{2+}]_i$ is regulated by a combination of ion transporters, ion pumps, and intrinsic intracellular Ca^{2+} buffering mechanisms. As noted, there is evidence that Na$^+$/Ca^{2+} exchanger is functionally expressed in mammalian chondrocytes (Sánchez et al., 2006). Accordingly, Equation (4) in our model that accounts for overall $[Ca^{2+}]_i$ dynamics includes this antiporter mechanism: an electroneutral, sarcolemmal ATP-requiring Ca^{2+} pump (Nygren et al., 1998), as well as intracellular Ca^{2+} buffering.

The Ca^{2+} pump ion transporter is electroneutral as a consequence of its ability to allow two H$^+$ ions to move into the cell for each Ca^{2+} ion that is extruded per transport cycle. We have assumed that the major Ca^{2+} buffer in the cytosol (both in terms of its Ca^{2+} binding capacity and its kinetics) is calmodulin. The cytosolic calmodulin concentration has been adapted from our previous work (Nygren et al., 1998) adjusted for the much smaller intracellular volume of the human chondrocyte. The relevant equations for this electroneutral Ca^{2+} pump and for Ca^{2+} buffering by calmodulin are given by:

$$I_{Ca,ATP} = \boldsymbol{Imax}_{Ca,ATP}\frac{[Ca^{2+}]_i}{[Ca^{2+}]_i + k_{Ca,ATP}} \tag{38}$$

and

$$\frac{d\boldsymbol{O}_C}{dt} = 2x10^5 [Ca^{2+}]_i (1 - \boldsymbol{O}_C) - 476\ \boldsymbol{O}_C \tag{39}$$

where $\boldsymbol{Imax}_{Ca,ATP} = 0.6349$ pA/pF is the maximal Ca^{2+} pump current density, $k_{Ca,ATP}$ is the half-maximum Ca^{2+} binding concentration, (0.0002 mmol/L), $[Ca^{2+}]_i$ is the intracellular calcium concentration as described by Equation (4), and $\boldsymbol{O}_C$ is the fractional occupancy of the calmodulin buffer by Ca^{2+}.

Transient Receptor Potential (TRP) Current: I_{TRPV4}

A fundamental question concerning the electrophysiology of non-excitable cells is: how do they sense the external environment and what ion flux mechanism(s) are responsible for this "trigger/transducer" signal? Ligand-gated cation-selective channels that have properties very similar to those exhibited by some members of the transient receptor potential or TRP family of ion channels (Nilius and Oswianik, 2011; Kaneko and Szallasi, 2014) are expressed in mammalian chondrocytes (cf. Gavenis et al., 2009; Phan et al., 2009; Clark et al., 2010; Asmar et al., 2016). Specifically, TRPV4 is prominently expressed in mouse (Clark et al., 2010) and porcine (Phan et al., 2009) chondrocytes. Previous work on endothelial cells suggests that this type of conductance is the basis for the small Ca^{2+} influx that then "triggers" a much larger release of Ca^{2+} from intracellular stores (the endoplasmic reticulum, Sonkusare et al., 2012) and thus can even produce "Ca^{2+} waves" (Guilak et al., 1999; Han et al., 2012). This important chain of events can initiate dynamic Ca^{2+}-dependent intracellular signaling pathways, as well as modulating much longer-term processes such as transcription (Berridge, 1997; Dolmetsch et al., 1997; Berridge et al., 2000; Parekh and Muallem, 2011). Some of these initial sensing/signaling pathways rely on specific integrin isoforms (Wright et al., 1997; Millward-Sadler et al., 2000; Mobasheri et al., 2002; Han et al., 2012).

We have identified significant TRP currents in human articular chondrocyte (HAC) preparations after superfusion with novel "TRPV4 activator" compounds synthesized by Glaxo Smith Kline (GSK) (Thorneloe et al., 2008; Hilfiker et al., 2013). These experimental results and related mathematical analysis/simulations are shown in **Figures 8**, **9**. Based on this and a variety of other published results we have formulated the working hypothesis that, in the human chondrocyte, there is a multicomponent signaling complex that includes: TRP channels, Ca^{2+}-activated K^+ channels, connexins/pannexins, and purinergic receptors (Loeser et al., 2000; Millward-Sadler et al., 2004; Elliott et al., 2009; Knight et al., 2009; Chekeni et al., 2010; Garcia and Knight, 2010). By analogy with a number of other non-excitable cells this may form the basis for some of the ligand and stretch-sensitive responses in chondrocytes, including the initiation and modulation of intra- and intercellular Ca^{2+} waves.

GSK SB488-induced currents in voltage-clamped human chondrocytes

The GSK compound SB488 is a potent agonist for TRPV4 channels (Nilius and Oswianik, 2011; Hilfiker et al., 2013). Our preliminary work has shown that SB488 (1 μM) can induce large non-selective cation currents in primary mouse articular chondrocytes (Giles and Clark, unpublished). Since the inward current due to TRPV4 channels is carried by Ca^{2+} and Na^+ ions (Nilius and Oswianik, 2011) these non-selective cation channels could constitute one of the essential triggers for intracellular Ca^{2+} release and Ca^{2+}-dependent signal transduction in HAC

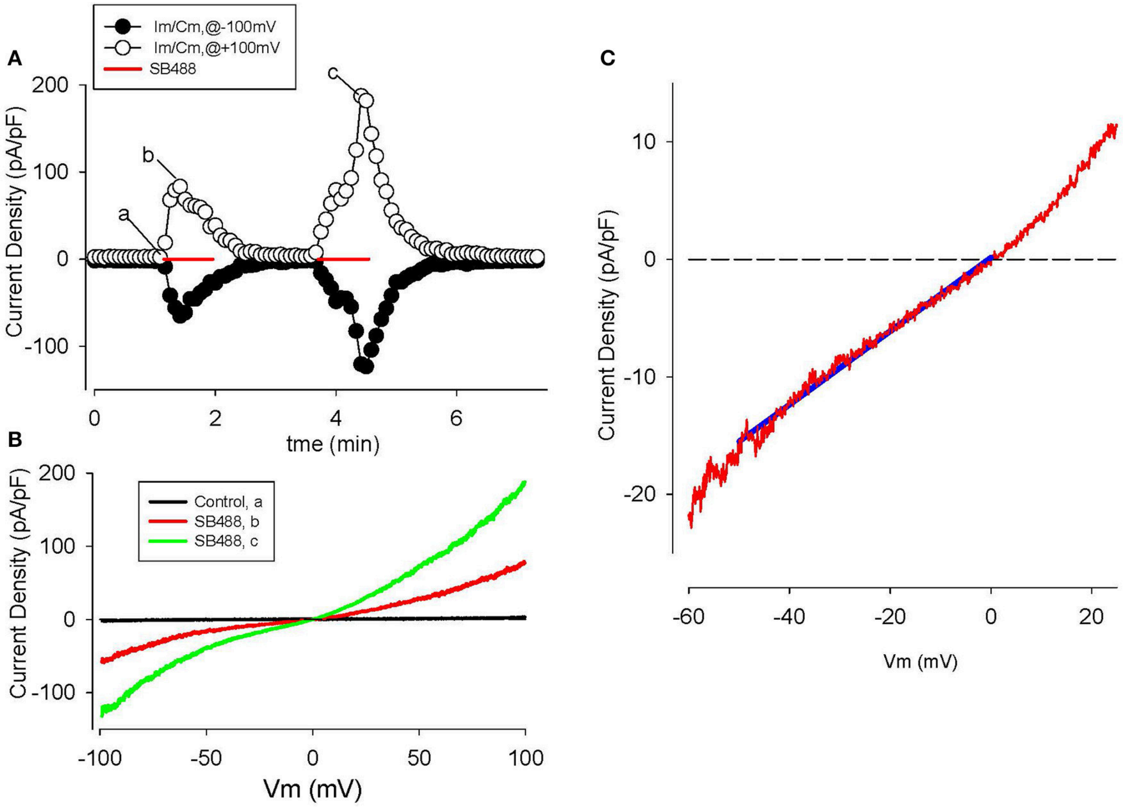

FIGURE 8 | Activation of TRPV4 channel currents by the GSK agonist, SB488, in human articular chondrocytes. **(A)** Time course of membrane current density changes at +100 (open circles) and −100 mV (closed circles) during repeated ramp voltage-clamp protocols. Red bars indicate the application of 1 μM SB488. **(B)** I–V relations before (trace "a," black) and during application of SB488 (b,c) as illustrated in **(A)**. **(C)** I–V for SB488 induced current on reduced membrane voltage and current scales i.e., in the voltage range of the chondrocyte resting membrane potential. The solid blue line is a linear fit to the I–V over the potential range from 0 to −50 mV.

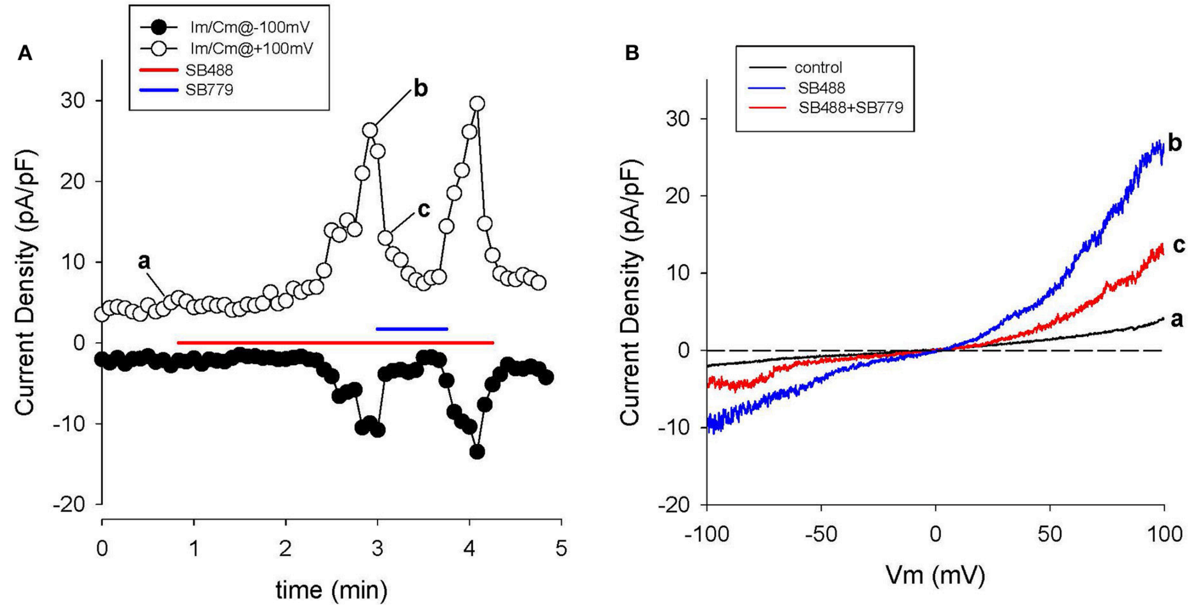

FIGURE 9 | Block of SB488-induced currents through TRPV4 channels by SB779. **(A)** Time course of membrane current changes at +100 (open circles) and −100 mV (closed circles) during repeated ramp voltage-clamp protocols. Colored bars indicate application of 1 μM SB488 (red), or SB488 +1 μM SB779 (blue). Note the nearly complete inhibition of SB488-induced current by SB779. I-V relations before (a), during SB488 (b) and during SB488 + SB779 (c). Panel **(B)** shows 3 superimposed I-V curves: (a) baseline, (b) in the agonist (SB488), and (c) in the combined presence of SB488 and SB779.

preparations. **Figure 8** shows a representative example of the time course and I-V relationships of the SB488-induced currents in a voltage-clamped HAC. **Figure 8A** consists of a plot of these membrane currents measured at +100 and −100 mV, in response to a ramp voltage-clamp protocol (see Methods section). SB488 (1 μM) application activated a quasi linear current that exhibited both transient and maintained components and declined very slowly after removal of this compound (taking ∼1.5 min to return to control levels).

Examples of HAC I-V relations recorded before and during SB488 application are shown in **Figure 8B**. The baseline or control current was very small and its I–V was essentially linear over the entire potential range that was tested. However, the pipette solution was CsCl-rich, so K^+ currents were completely blocked. In contrast, after SB488 application a relatively large transmembrane current developed. These two I–V curves intersect very near 0 mV, as shown in the inset. The mean (± s.e.m.) of this reversal potential value for SB488-induced currents in 13 different HAC preparations was 1.8 ± 0.4 mV consistent with the known properties of the TRPV4 family of ion channels.

A different GSK compound, SB779, (Hilfiker et al., 2013) can potently block the currents induced by SB488. It was also studied in our HAC preparations. The data in **Figure 9** confirm that SB 799 is an effective blocker of the SB488-induced currents. **Figure 9A** shows the time course of membrane current at +100 and −100 mV in response to a multiple ramp voltage-clamp protocol. In this HAC, application of SB488 (1 μM) resulted in a slow increase in current i.e., taking about 1 min before currents increased significantly above control levels. This SB488-induced current was quickly blocked by application of SB779 (even in the presence of SB488). This marked reduction of the SB488-induced current by SB779 is consistent with either block of a SB488 "receptor," or direct, potential-independent block of the SB488-activated ion channels by SB779. **Figure 9B** illustrates I–V relations recorded at base line, during SB488 alone, and in the presence of SB488 and SB779. The similarity of these I–V relationships and reversal potentials suggest that these compounds do in fact act as selective TRPV4 agonists and antagonists in these HAC preparations.

DISCUSSION

The Resting Membrane Potential in Human Chondrocytes

The new electrophysiological data and first order mathematical model provided by this study add significantly to the previously published papers on fundamental mechanisms of human chondrocyte biology and pathophysiology (cf. Barrett-Jolley et al., 2010; Mobasheri et al., 2012; Asmar et al., 2016). Our main goal was to define the ionic basis for the resting membrane potential, E_m. Detailed knowledge of the basis for E_m of the chondrocyte is especially important since it is a non-excitable cell. In these preparations e.g., endothelial cells, glia, it is known that even very small changes in E_m can strongly modulate $[Ca^{2+}]_i$ (Bouchard et al., 1993; Baczkó et al., 2003; Poon et al., 2014). Either transient or maintained changes in $[Ca^{2+}]_i$ can modulate Ca^{2+}-dependent signaling, as well as the related homeostatic and gene transcription mechanisms (Chao et al., 2006; Lin et al., 2008). In chondrocytes there is also evidence that relatively small alterations in E_m can contribute to dynamic regulation of cell volume (Barrett-Jolley et al., 2010; Lewis et al., 2011).

Given the technical difficulty of making accurate, reproducible recordings of transmembrane ionic currents in small cells that have large input resistances, our mathematical model provides an additional basis for understanding the physiological roles of each of the distinct K^+ currents that have been characterized in human chondrocytes. It is evident from the results in **Figures 2–6** that any one, or a combination, of these K^+ currents could: (i) significantly hyperpolarize the resting potential, and/or (ii) repolarize the chondrocyte after it had been depolarized (Funabashi et al., 2010b). It is also apparent that significant, cyclic depolarization can result from the effects of mechanical activity (stretch or shear), as well as via ligand-gated conductances, (e.g., ATP) or activation of TRP channels.

At this stage of model development our simulations do *not* fully reveal the ionic basis for E_m in isolated human chondrocytes. However, they provide further insight into the consistent finding that a range of membrane potential values (-30 to -50 mV) are obtained in single cell patch clamp experiments on human chondrocytes, even after ensuring that 'multi-GΩ' seal resistances are obtained. This is because the net outward current that sets the resting membrane potential at steady-state is very small as shown in **Figures 2**, **7**; and is expected from the very large (5–10 GΩ) input resistance (cf. Wilson et al., 2011). Improvement on the work reported here will require extensive additional experimental data, perhaps recorded at physiological temperatures. Additional data analyses and model development will also need to consider alternate approaches for accounting for the interactions among Na^+/K^+ pump activity, background Cl^- fluxes, and overall cellular osmotic homeostasis (Armstrong, 2003).

The Physiological Milieu of the Chondrocyte

Classical knowledge of unusual physiologic milieu (see **Table 1**) within the articular joint yields the expectation that these conditions would be expected to regulate the E_m, e.g., by altering the conductance or gating properties of intrinsic K^+ currents that expressed at baseline; through modulation ligand-gated currents; or by changing cell metabolism. For example, the extracellular synovial fluid is somewhat hypertonic (320–340 mOsM vs. approximately 280 mOsM in most mammalian tissues). The effects of osmolarity on voltage gated K^+ currents have been studied quite extensively, and chondrocytes also express volume-sensitive K^+ and Cl^- currents (Lewis et al., 2011).

We were very interested in an additional mechanism through which changes in the osmolarity of the superfusate or extracellular solution may manifest themselves. It is well-known that changes in osmolarity can alter the "screening or shielding" of discrete membrane surface charges on the plasma membrane and that such changes can regulate channel gating displacement or shifting by altering the voltage-dependence of gating. The main effect of this has been identified as a shift in the voltage-dependence of gating variables, due to altered surface charge or zeta potential (Kell and DeFelice, 1988; Hille, 2001). It is also known that divalent or trivalent cations, (as well as charged osmolytes) can effectively reduce the zeta potential component of the overall membrane potential (Hille, 2001). Although surface potential cannot be measured directly by conventional transmembrane potential recordings, changes in it can be mimicked *in silico* (as shown in **Figure 10**). Accordingly, in our final set of computations we have shifted the activation curve for I_{K-DR} by 10 mV in either the depolarizing or hyperpolarizing direction (**Figure 10A**). As expected, this maneuver alters the size of this K^+ current by changing the fraction that is "available" within the membrane potential range that is near the estimated HAC resting potential (**Figure 10B**). In the case of the human chondrocyte (as shown in **Table 1**), surface charge screening resulting from increased osmolarity, would be expected to shift the activation curve to the right (in the depolarized direction), therefore decreasing I_{K-DR} at membrane potentials near E_m. An important functional consequence would be a tendency to depolarize the resting potential of the chondrocyte (**Figure 10C**).

Perhaps the strongest evidence that *in situ* the chondrocyte can exhibit significant surface membrane delimited zeta potentials (and restricted diffusion profiles) has been provided by both classical and recent studies that have defined important properties of the chondrocyte pericellular matrix (Poole et al., 1987; Pfander and Gelse, 2007). As mentioned previously, these papers argue in favor of the chondrocyte and its pericellular matrix being defined as an integral functional unit denoted the chondron (Poole et al., 1987; Nguyen et al., 2010; Wilusz et al., 2014). The microanatomy of the chondron, specifically its likelihood for promoting restricted diffusion of e.g., K^+ and metabolites is likely to be significant factors regulating the chondrocyte "microenvironment." Within this functional space emerging knowledge of glucose transport (and hence cellular energetics), as well as paracrine and inflammatory factor profiles, will need to be further defined and accounted for (c.f. Mobasheri et al., 1998).

As noted in the Introduction, the pH in the extracellular matrix can be somewhat acidic, ~6.9 as opposed to 7.2 (see **Table 1**). Changes in $[H^+]_o$ measured in terms of pH alteration can also have "surface change effects" similar to those described above (cf. Hille, 2001). Specifically, lowering pH_o (acidification) would result in a decrease in I_{KDR} and therefore an independent and additional tendency to depolarize the chondrocyte resting membrane potential.

Other conditions that characterize the milieu mammalian articular chondrocyte would also be expected to have very significant electrophysiological consequences, mainly by altering E_m. Perhaps the main one of these in chondrocytes is the significant elevation of intracellular $[Na^+]_i$ levels to (perhaps) as much as 20 mM as opposed to values of 8–10 mM in most other mammalian cells. This elevated $[Na^+]_i$ may partly explain the somewhat atypical pH_i values, since intrinsic Na^+/H^+ exchange activity and thus pH regulation would be altered. What is likely more important, $[Na^+]_i$ levels in the 15–30 mM range would strongly regulate (activate) the electrogenic Na^+/K^+ pump. The resulting increase in outward electrogenic pump current (see **Figure 7A**) would provide a significant hyperpolarizing influence to the chondrocyte E_m. This possibility is illustrated

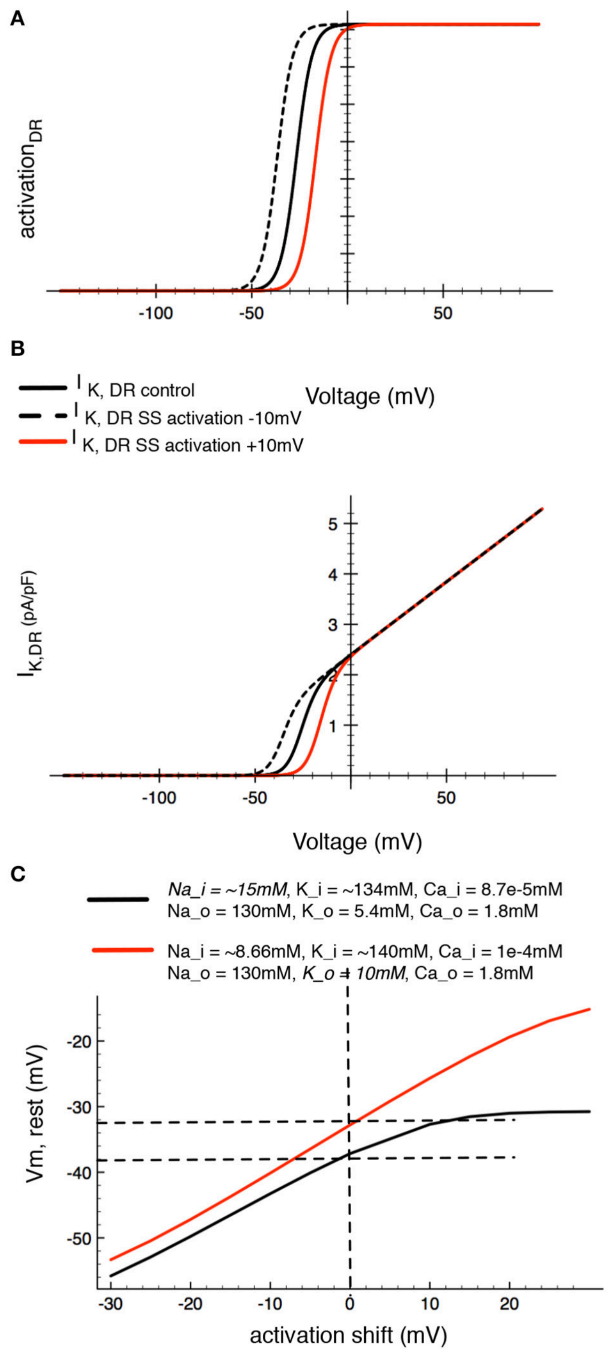

FIGURE 10 | Demonstration of the effects of *in silico* changes in the voltage-dependence for activation of the delayed rectifier K^+ current, I_{K-DR}, Panels **(A,B)**, illustrate the altered activation curves and I-V relationships, respectively. Panel **(A)** shows the derived activation curve for I_{K-DR} (black line) at baseline and after shifting its midpoint ±10 mV to begin an analysis of the effects of changes in surface potential on chondrocyte E_m. Panel **(B)** shows the (black line computed chondrocyte I–V curves for I_{K-DR} at baseline and after the activation of I_{K-DR} is shifted ±10 mV. Panel **(C)** shows the corresponding changes in resting membrane potential in the baseline model and after $[Na^+]_i$. The red line in **(C)** was computed assuming that intracellular $[Na^+]_i$ is 15 mM. The resulting augmentation/stimulation of the Na^+/K^+ pump provides an electrogenic outward current that can significantly hyperpolarize E_m (see Discussion section) at all membrane potentials.

by the black traces in **Figure 10C**. Note that when $[Na^+]_i$ is increased (8.6 to 15 mM) the extra outward Na^+/K^+ pump current can significantly hyperpolarize the chondrocyte E_m. After key principles of chondrocyte Ca^{2+} transport are further understood, it may be possible to revise and improve related aspects of our chondrocyte model as has been done for the PC 12 cell (Duman et al., 2008). One reason for working toward these changes/improvements is the possibility of gaining new insights into $[Ca^{2+}]_i$ regulated apoptosis and autophagy (Harr and Distelhorst, 2010) as well as senescence (Mobasheri et al., 1998).

Ca^{2+}-Influx and Ca^{2+}-Dependent Currents

As noted, activation of TRPV4 channels would be expected to result in a significant influx of Ca^{2+} and Na^+, and a related depolarization, when the chondrocyte membrane potential is negative to approximately −20 mV, the reversal potential (see **Figures 8**, **9**) for ion flux through these channels. However, any such TRP channel-induced depolarization would be transient, and relatively small. This is because depolarization and/ or Ca^{2+} influx would be expected to be quickly followed by a K^+ efflux. This would result in repolarization back to E_m or even beyond (a hyperpolarization). This K^+ efflux/outward current would be due to a combination of: (i) the depolarization-induced activation of the delayed rectifier K^+ currents, I_{K-DR}, and/or (ii) turning on of the BK and/or other Ca^{2+}-activated K^+ current (cf. Horrigan and Aldrich, 2002; Magleby, 2003; Sun et al., 2009). In other nonexcitable cells, even a very small Ca^{2+} influx can trigger a large Ca^{2+} release from the ER, thus producing a significant increase in intracellular Ca^{2+}, $[Ca^{2+}]_i$. Moreover, the extent to which $[Ca^{2+}]_i$ in the ER changes can trigger a secondary but significant net Ca^{2+} influx mediated by I_{CRAC} channels expressed in the surface membrane (c.f. Shaw et al., 2013). In a human chondrocyte-derived cell line, Funabashi et al. (2010b) have shown that histamine can strongly enhance a Ca^{2+}-activated K^+ current, and thus hyperpolarize the chondrocyte membrane potential. This relatively hyperpolarized transmembrane voltage, E_m, is maintained until $[Ca^{2+}]_i$ and/or Ca^{2+}-dependent signaling mechanisms reset to "resting" values. This Ca^{2+} dependent hyperpolarization may also contribute to chondrocyte differentiation (Muramatsu et al., 2007).

Connexin-Mediated Current Flow and Electrotonic Interactions

As mentioned in the Introduction, chondrocytes in articular joints from adult humans function as isolated, single cells. Interestingly, however, Cell Physiological data from early adolescent articular joint preparations suggest that the growth plate of articular joints includes small groups of closely opposed chondrocytes. In these preparations, expression of selected members of the connexin family of intercellular communication proteins (e.g., Cx43) has been detected using standard immunohistochemical approaches (Chi et al., 2004; Mayan et al., 2013a,b; Asmar et al., 2016).

We also note that is Cx43 increased expression in isolated adult chondrocytes can result in release ATP in response to e.g. mechanical perturbations (Millward-Sadler et al., 2004; Knight et al., 2009; Garcia and Knight, 2010). One plausible mechanism for this, is the occurrence of transient openings of these "hemichannels" that consist of either pannexin or connexin subunits (Saez et al., 2003; Garcia and Knight, 2010; Penuela et al., 2013). Given this important functionality, our mathematical model also includes a connexin-mediated conductance (**Figure 4**). However, since this initial model development was focused on simulating adult chondrocyte behavior under a restricted set of physiological conditions, these connexin single-cell channels were shut off (assigned a conductance value of 0 pS) in all simulations that form the basis of this paper. We acknowledge that this choice does **not** allow this model to account for any of the interesting function properties that arise from the so-called connexon-43 hemichannel behavior in chondrocytes (Knight et al., 2009). This "hemichannel activity" in chondrocytes can also be mediated by the pannexin family of integral membrane proteins (Bond et al., 2011; Matta et al., 2015).

Limitations of the Mathematical Model of the Human Chondrocyte Resting Membrane Potential

The mathematical model that we have developed is an important advance. However, we recognize that it has significant limitations. These include:

a) It is apparent that Ca^{2+} is an essential signaling molecule in the chondrocyte. Expression of L-type Ca^{2+} channels has been reported in growth plate chondrocytes (Sugimoto et al., 1996; Zuscik et al., 1997), but not in other single cell adult chondrocyte preparations. In the future, more detailed consideration of the details of (i) Ca^{2+} channels (ii) TRP channels (iii) CRAC channels (iv) the Na^+/Ca^{2+} exchanger and (v) the Ca^{2+} pumps in both the endoplasmic reticulum and the surface membrane must be included in the model. In fact systematic experimental and modeling studies of each functional element in chondrocyte $[Ca^{2+}]$ homeostasis are needed, perhaps with an emphasis on the so-called Ca^{2+} signalosome with emphasis on the Ca^{2+} pump in the endoplasmic reticulum, (Kranias and Hajjar, 2012).

b) Mathematical expressions that would allow simulations of what has been termed "the AM and FM modes of Ca^{2+} signaling" (Berridge, 1997; Berridge et al., 2000), will require consideration of $[Ca^{2+}]_i$-dependent phosphorylation and dephosphorylation reactions, the involvement of IP-3 in Ca^{2+} release, (Mak and Foskett, 2015) as well as accounting for the Ca^{2+}-dependence involved in transcriptional regulation of ion channel, antiporter and pump target molecules.

c) There is evidence that cell culture conditions can alter both chondrocyte phenotype and gene expression profiles (Spitzer et al., 2000; Chen et al., 2012; but see Asmar et al., 2016). These patterns of changes will need to be taken into account for attempting to either interpolate or extrapolate findings from this model. This limitation can be addressed when new data sets are available from isolated chondrocytes that have been isolated from defined 'zone' (Berridge, 2007; Amanatullah et al., 2014) cultures in 3-D scaffold or substrates with known stiffness (Chen et al., 2012).

SUMMARY

This mathematical model of chondrocyte electrophysiology provides a reliable platform for integrating and evaluating both recent and well-established experimental data that is relevant to the generation of the resting potential. At a minimum, given that the chondrocyte is in a unique but relatively inaccessible, environment, our model provides new insights into: the biophysical effects of alterations in ionic strength of synovial fluid on ion channel voltage-dependent gating (zeta potential effects). Key elements of the zeta potential working hypothesis can be tested if recent advances in voltage-dependent dye methods are implemented to provide a means of separating the various components of the signal that underlies the "transmembrane potential" in small nonexcitable cells (Cohen and Venkatachalam, 2014). It will also be necessary to account for the effects of cyclic stretch on chondrocyte ion channels by defining the main strain dependent alterations in channel gating voltage dependence or kinetics (cf. Hille, 2001; Maleckar et al., 2009). Approaches for detecting and determining the limitations of present patch clamp methods that can bias key electrophysiological data sets and influence their interpretation must continue to be utilized and refined. However, even in its present form this first-order model will continue to be useful for rationalizing and bringing together genomic data from microarray expression profiles, and understanding ion channel/antiporter drug target initiatives.

AUTHOR CONTRIBUTIONS

RBC carried out all of the experimental work in this paper, and provided valuable input into the development and validation of the mathematical model. MM when supervising Dr. H. Narayanan at Simula Research Inc in Oslo, Norway lead the mathematical modeling component of this study. BV, a Senior Scientist at Glaxo Smith Kline, Philadelphia, USA provided valuable input into experimental design and facilitated transfer of the GSK properiarty cell lines and pro-drugs. WRG lead the project and wrote the manuscript. All authors have read and revised the manuscript, and are in agreement with its main findings and conclusions.

ACKNOWLEDGMENTS

An Alberta Innovates—Health Solutions (AI-HS) Scientist Award (WRG), an AI-HS Starter Grant, and a Canadian Institutes of Health Research Grant were combined to support this experimental work and related model development in the Giles laboratory at the University of Calgary. We are grateful to the Southern Alberta Tissue Transplant Facility (Dr. R. Krawetz) for supply of human articular joint (knee) tissue. Ms. Colleen Kondo prepared and maintained the human chondrocyte cultures and was responsible for project management in the Giles laboratory. Postdoctoral Fellowship funding for Dr. Harish Narayanan from both the Simula Research Laboratory, Oslo, Norway and the AI-HS is gratefully acknowledged. Dr. Narayanan provided input into early aspects of the computational work in this paper. Glaxo Smith Kline Laboratories in Philadelphia, Pennsylvania supplied the human chondrocyte cell line and TRPV4 agonists/antagonists that were used to generate some of the data.

REFERENCES

Amanatullah, D. F., Yamane, S., and Reddi, A. H. (2014). Distinct patterns of gene expression in the superficial, middle and deep zones of bovine articular cartilage. *J. Tiss. Eng. Regen. Med.* 8, 505–514. doi: 10.1002/term.1543

Archer, C. W., and Francis-West, P. (2003). The chondrocyte. *Int. J. Biochem. Cell Biol.* 35, 401–404. doi: 10.1016/S1357-2725(02)00301-1

Armstrong, C. M. (2003). The Na/K pump, Cl ion, and osmotic stabilization of cells. *Proc. Natl. Acad. Sci. U.S.A.* 100, 6257–6262. doi: 10.1073/pnas.0931278100

Asmar, A., Barrett-Jolley, R., Werner, A., Kelly, R. Jr, and Stacey, M. (2016). Membrane channel gene expression in human costal and articular chondrocytes. *Organogenesis* 12, 94–107. doi: 10.1080/15476278.2016.1181238

Baczkó, I., Giles, W. R., and Light, P. E. (2003). Resting membrane potential regulates Na^+-Ca^{2+} exchange-mediated Ca^{2+} overload during hypoxia-reoxygenation in rat ventricular myocytes. *J. Physiol.* 550, 889–898. doi: 10.1113/jphysiol.2003.043372

Balakrishna, S., Song, W., Achanta, S., Doran, S. F., Liu, B., Kaelberer, M. M. (2014). TRPV4 inhibition counteracts edema and inflammation and improves pulmonary function and oxygen saturation in chemically induced acute lung injury. *Am. J. Physiol. Lung Cell. Mol. Physiol.* 307, L158–L172. doi: 10.1152/ajplung.00065.2014

Barrett-Jolley, R., Lewis, R., Fallman, R., and Mobasheri, A. (2010). The emerging chondrocyte channelome. *Front. Physiol.* 223:135. doi: 10.3389/fphys.2010.00135

Berkefeld, H., Falker, B., and Schulte, U. (2010). Ca^{2+}+-activated K^+ channels: from protein complexes to function. *Physiol. Rev.* 90, 1437–1459. doi: 10.1152/physrev.00049.2009

Berkefeld, H., Sailer, C. A., Bildi, W., Rohde, V., Thumfart, J. O., Eble, S., et al. (2006). BKCa-Cav channel complexes mediate rapid and localized Ca^{2+}-activated K^+ signaling. *Science* 314, 615–620. doi: 10.1126/science.1132915

Berridge, M. J. (1997). The AM and FM of calcium signalling. *Nature* 386, 759–760. doi: 10.1038/386759a0

Berridge, M. J. (2007). Inositol triphosphate and calcium osciallations. *Biochem. Soc. Symp.* 74, 1–7. doi: 10.1042/BSS2007c01

Berridge, M. J., Lipp, P., and Bootman, M. D. (2000). The versatility and universitality of calcium signalling. *Nat. Rev. Mol. Cell Biol.* 1, 11–21. doi: 10.1038/35036035

Bond, S. R., Lau, A., Penuela, S., Sampaio, A. V., Underhill, T. M., Laird, D. W., et al. (2011). Pannexin 3 is a novel target for Runx2 expressed by osteoblasts and mature growth plate chondrocytes. *J. Bone Miner. Res.* 26, 2911–2922. doi: 10.1002/jbmr.509

Bouchard, R. A., Clark, R. B., and Giles, W. R. (1993). Regulation of unloaded cell shortening by sarcolemmal sodium-calcium exchange in isolated rat ventricular myocytes. *J. Physiol.* 469, 583–599. doi: 10.1113/jphysiol.1993.sp019831

Bush, P. G., and Hall, A. C. (2005). Passive osmotic properties of *in situ* human articular chondrocytes within non-degenerate and degenerate cartilage. *J. Cell. Physiol.* 204, 309–319. doi: 10.1002/jcp.20294

Bush, P. G., Huntley, J. S., Brenkel, I. J., and Hall, A. C. (2003). The shape of things to come: chondrocytes and osteoarthritis. *Clin. Invest. Med.* 26, 249–251.

Chao, P. H., West, A. C., and Hung, C. T. (2006). Chondrocyte intracellular calcium, cytoskeletal organization, and gene expression responses to dynamic osmotic loading. *Am. J. Physiol. Cell Physiol.* 291, C718–C725. doi: 10.1152/ajpcell.00127.2005

Chekeni, F. B., Elliott, M. R., Sandilos, J. K., Walk, S. F., Kinchen, J. M., Lazarowski, E. R., et al. (2010). Pannexin 1 channels mediate 'find-me' signals ATP release and membrane permeability during apoptosis. *Nature* 467, 863–867. doi: 10.1038/nature09413

SUPPLEMENTARY MATERIAL

The Supplementary Material for this article can be found online at: https://www.frontiersin.org/articles/10.3389/fphys.2018.00974/full#supplementary-material

Chen, C., Tambe, D. T., Deng, L., and Yang, L. (2013). Biomechanical properties and mechanobiology of the articular chondrocyte. *Am. J. Physiol. Cell Physiol.* 305, C1202–C1208. doi: 10.1152/ajpcell.00242.2013

Chen, J., Irianto, J., Inamdar, S., Pravincumar, P., Lee, D. A., Bader, D. L., et al. (2012). Cell mechanics, structure, and function are regulated by the stiffness of the three-dimensional microenvironment. *Biophys. J.* 103, 1188–11997. doi: 10.1016/j.bpj.2012.07.054

Chi, S. S., Rattner, J. B., and Matyas, J. R. (2004). Communication between paired chondrocytes in the superficial zone of articular cartilage. *J. Anat.* 205, 363–370. doi: 10.1111/j.0021-8782.2004.00350.x

Cid, L. P., Roa-Rojas, H. A., Niemeyer, M. I., González, W., Araki, M., and Sepúlveda, K. F. V. (2013). TASK-2: a K_{2P} K^+ channel with complex regulation and diverse physiological functions. *Front. Physiol.* 4:198. doi: 10.3389/fphys.2013.00198

Clark, A. L., Votta, B. J., Kumar, S., Liedtke, W., and Guilak, F. (2010). Chondroprotective role of the osmotically sensitive ion channel transient receptor potential vanilloid 4: age- and sex-dependent progression of osteoarthritis in TRPV 4-deficient mice. *Arthritis Rheumatol.* 62, 2973–2983. doi: 10.1002/art.27624

Clark, R. B., Kondo, C., and Giles, W. R. (2011). Two-pore K^+ channels contribute to membrane potential of isolated human articular chondrocytes. *J. Physiol.* 589, 5071–5089. doi: 10.1113/jphysiol.2011.210757

Cohen, A. E., and Venkatachalam, V. (2014). Bringing bioelectricity to light. *Annu. Rev. Biophys.* 43, 211–232. doi: 10.1146/annurev-biophys-051013-022717

Crampin, E. J., and Smith, N. P. (2006). A dynamic model of excitation-contraction coupling during acidosis in cardiac ventricular myocytes. *Biophys. J.* 90, 3074–3090. doi: 10.1529/biophysj.105.070557

Dolmetsch, R. E., Lewis, R. S., Goodnow, C. C., and Healy, J. I. (1997). Differential activation of transcription factors induced by Ca^{2+} response amplitude and duration. *Nature* 386, 855–858. doi: 10.1038/386855a0

Duman, J. G., Chen, L., and Hille, B. (2008). Calcium transport mechanisms of PC12 cells. *J. Gen. Physiol.* 131, 307–323. doi: 10.1085/jgp.200709915

Eaton, J. W., Bateman, D., Hauberg, S., and Wehbring, R. (2014). GNU *Octave Version 3.8.1 Manual: A High-Level Interactive Language for Numerical Computations.* CreateSpace Independent Publishing Platform. Available online at: http://www.gnu.org/software/octave/doc/interpreter/

Elliott, M. R., Chekeni, F. B., Trampont, P. C., Lazarowski, E. R., Kadl, A., Walk, S. F., et al. (2009). Nucleotides released by apoptotic cells act as a find-me signal to promote phagocytic clearance. *Nature* 461, 282–286. doi: 10.1038/nature08296

Funabashi, K., Fujii, M., Yamamura, H., Ohya, S., and Imaizumi, Y. (2010a). Contribution of chloride channel conductance to the regulation of resting membrane potential in chondrocytes. *J. Pharmacol. Sci.* 113, 94–99. doi: 10.1254/jphs.10026SC

Funabashi, K., Ohya, S., Yamamura, H., Hatano, N., Muraki, K., and Giles, W. R. (2010b). Accelerated Ca^{2+} entry by membrane hyperpolarization due to Ca^{2+}-activated K^+ channel activation in response to histamine in chondrocytes. *Am. J. Physiol. Cell Physiol.* 298, C786–C797. doi: 10.1152/ajpcell.00469.2009

Garcia, M., and Knight, M. M. (2010). Cyclic loading opens hemichannels to release ATP as part of a chondrocyte mechanotransduction pathway. *J. Orthop. Res.* 28, 510–515. doi: 10.1002/jor.21025

Gavenis, K., Schumacher, C., Schneider, U., Eisfeld, J., Mollenhauer, J., and Schmidt-Rohlfing, B. (2009). Expression of ion channels of the TRP family in articular chondrocytes from osteoarthritic patients: changes between native and *in vitro* propagated chondrocytes. *Mol. Cell. Biochem.* 321, 135–143. doi: 10.1007/s11010-008-9927-x

Goldstein, S. A. N., Bockenhauer, D., and Zilberberg, N. (2001). Potassium leak channels and the KCNK family of two-P-domain subunits. *Nat. Rev. Neurosci.* 2, 175–184. doi: 10.1038/35058574

Grandolfo, M., D'Andrea, P., Martina, M., Ruzzier, F., and Vittur, F. (1992). Calcium-activated potassium channels in chondrocytes. *Biochem. Biophys. Res. Commun.* 182, 1429–1434. doi: 10.1016/0006-291X(92)91893-U

Guilak, F., Alexopoulos, L. G., Upton, M. L., Youn, I., Choi, J. B., Cao, L., et al. (2006). The pericellular matrix as a transducer of biomechanical and biochemical signals in articular cartilage. *Ann. N.Y. Acad. Sci.* 1068, 498–512. doi: 10.1196/annals.1346.011

Guilak, F., Sah, R. L., and Setton, L. A. (1997). "Physical regulation of cartilage metabolism," in *Basic Orthopaedic Biomechanics*, eds V. C. Mow and W. C. Hayes (Philadelphia, PA: Lippincott-Raven), 179–207.

Guilak, F., Zell, R. A., Erickson, G. R., Grande, D. A., Rubin, C. T., McLeod, K. J. (1999). Mechanically induced calcium waves in articular chondrocytes are inhibited by gadolinium and amiloride. *J. Orthop. Res.* 17, 421–429. doi: 10.1002/jor.1100170319

Hall, A., Horwitz, E. R., and Wilkins, R. J. (1996). The cellular physiology of articular cartilage. *Exp. Physiol.* 81, 535–545. doi: 10.1113/expphysiol.1996.sp003956

Han, S. K., Wouters, W., Clark, A., and Herzog, W. (2012). Mechanically induced calcium signaling in chondrocytes in situ. *J. Orthop. Res*. 30, 475–481. doi: 10.1002/jor.21536

Harr, M. W., and Distelhorst, C. W. (2010). Apoptosis and autophagy: decoding calcium signals that mediate life or death. *Cold Spring Harb. Perspect. Biol.* 2, 1–18. doi: 10.1101/cshperspect.a005579

Hilfiker, M. A., Hoang, T. H., Cornil, J., Eidam, H. S., Matasic, D. S., Roethke, T. J. (2013). Optimization of a novel series of TRPV4 antagonists with *in vivo* activity in a model of pulmonary edema. *ACS Med. Chem. Lett.* 4, 293–296. doi: 10.1021/ml300449k

Hille, B. (2001). *Ion Channels of Excitable Membranes*. Sunderland, MA: Sinauer Associates.

Horrigan, F. T., and Aldrich, R. W. (2002). Coupling between voltage sensor activation, Ca^{2+} binding and channel opening in large conductance (BK) potassium channels. *J. Gen. Physiol*. 120, 267–305. doi: 10.1085/jgp.20028605

Huber, M., Trattnig, S., and Lintner, F. (2000). Anatomy, biochemistry and physiology of articular cartilage. *Invest. Radiol.* 35, 573–580. doi: 10.1097/00004424-200010000-00003

Ince, C., van Bavel, E., van Duijn, B., Donkersloot, K., Coremans, A., Ypey, D. L. (1986). Intracellular microelectrode measurements in small cells evaluated with the patch clamp technique. *Biophys. J.* 50, 1203–1209. doi: 10.1016/S0006-3495(86)83563-9

Kaneko, Y., and Szallasi, A. (2014). Transient receptor potential (TRP) channels: a clinical perspective. *Br. J. Pharmacol.* 171, 2474–2507. doi: 10.1111/bph.12414

Kell, M. J., and DeFelice, L. J. (1988). Surface charge near the cardiac inward-rectifier channel measured from single-channel conductance. *J. Membr. Biol.* 102, 1–10. doi: 10.1007/BF01875348

Kindler, C. H., and Yost, C. S. (2005). Two-pore domain potassium channels: new sites of local anesthetic action and toxicity. *Reg. Anesth. Pain Med.* 30, 260–274. doi: 10.1016/j.rapm.2004.12.001

Knight, M. M., McGlashan, S. R., Garcia, M., Jensen, C. G., and Poole, C. A. (2009). Articular chondrocytes express connexin 43 hemichannels and P2 receptors - a putative mechanoreceptor complex involving the primary cilium? *J. Anat.* 214, 275–283. doi: 10.1111/j.1469-7580.2008.01021

Kranias, E. G., and Hajjar, R. J. (2012). Modulation of cardiac contractility by the phopholamban/SERCA2a regulatome. *Circ. Res.* 110, 1646–1660. doi: 10.1161/CIRCRESAHA.111.259754

Kurita, T., Yamamura, H., Suziki, Y., Giles, W. R., and Imaizumi, Y. (2015). The ClC-7 chloride channel is down regulated by hypo-osmotic stress in human chondrocytes. *Mol. Pharmacol.* 1, 113–120. doi: 10.1124/mol.115.098160

Lane Smith, R., Trindade, M. C., Ikenoue, T., Mohtai, M., Das, P., Carter, D. R., et al. (2000). Effects of shear stress on articular chondrocyte metabolism. *Biorheology* 37, 95–107.

Lewis, R., Asplin, K. E., Bruce, G., Dart, C., Mobasheri, A., and Barrett-Jolley, R. (2011). The role of the membrane potential in chondrocyte volume regulation. *J. Cell. Physiol.* 226, 2979–2986. doi: 10.1002/jcp.22646

Lewis, R., May, H., Mobasheri, A., and Barrett-Jolley, R. (2013). Chondrocyte channel transcriptomics: do microarray data fit with expression and functional data? *Channels* 7, 459–467. doi: 10.4161/chan.26071

Lin, Z., Fitzgerald, J. B., Xu, J., Willers, C., Wood, D., Grodzinsky, A. J., et al. (2008). Gene expression profiles of human chondrocytes during passaged monolayer cultivation. *J. Orthop. Res.* 26, 1230–1237. doi: 10.1002/jor.20523

Loeser, R. F., Sadiev, S., Tan, L., and Goldring, M. B. (2000). Integrin expression by primary and immortalized human chondrocytes: evidence of a differential role for α1β1 and α2β1 integrins in mediating chondrocyte adhesion to types II and VI collagen. *Osteoarthr. Cartil.* 8, 96–105. doi: 10.1053/joca.1999.0277

Magleby, K. L. (2003). Gating mechanism of BK (Slo1) channels: so near, yet so far. *J. Gen. Physiol.* 121, 81–96. doi: 10.1085/jgp.20028721

Mak, D. O., and Foskett, J. K. (2015). Inositol 1,4,5-trisphosphate receptors in the endoplasmic reticulum: a single-channel point of view. *Cell Calcium* 58, 67–78. doi: 10.1016/j.ceca.2014.12.008

Maleckar, M. M., Greenstein, J. L., Giles, W. R., and Trayanova, N. A. (2009). K^+ current changes account for the rate dependence of the action potential in the human atrial myocyte. *Am. J. Physiol. Heart Circ. Physiol.* 297, 1398–1410. doi: 10.1152/ajpheart.00411.2009

Martin, J. A., and Buckwalter, J. A. (2003). The role of chondrocyte senescence in the pathogenesis of osteoarthritis and in limiting cartilage repair. *J. Bone Joint Surg. Am.* 85, 106–110. doi: 10.2106/00004623-200300002-00014

Mason, M. J., Simpson, A. K., Mahaut-Smith, M. P., and Robinson, H. P. C. (2005). The interpretation of current-clamp recordings in the cell-attached patch-clamp configuration. *Biophys. J.* 88, 739–750. doi: 10.1529/biophysj.104.049866

Matta, C., Fodor, J., Miosge, N., Takacs, R., Juhasz, T., Rybaltovszki, H., et al. (2015). Purinergic signaling is required for calcium oscillations in migratory chondrogenic progenitor cells. *Pflugers Arch. Eur. J. Physiol.* 467, 429–442. doi: 10.1007/s00424-014-1529-8

Mayan, M. D., Carpintero-Fernandez, P., Gago-Fuentes, R., Fernandez-Puente, P., and Filguiera-Fernandez, P. (2013a). Articular chondrocytes are physically connected through a cellular network that is responsible of the metabolic coupling between chondroctifs located in different layers of the tissue. *Osteoarthr. Cartil.* 21, S18–S19. doi: 10.1016/j.joca.2013.02.060

Mayan, M. D., Carpintero-Fernandez, P., Gago-Fuentes, R., Martinez-de-Ilarduya, O., Wang, H. Z., Valiunas, V., et al. (2013b). Human articular chondrocytes express multiple gap junction proteins differential expression of connexins in normal and osteoarthritic cartilage. *Am. J. Pathol.* 182, 137–1346. doi: 10.1016/j.ajpath.2012.12.018

McLane, L. T., Chang, P., Granquist, A., Boehm, H., Kramer, A., Scrimgeour, J., et al. (2013). Spatial organization and mechanical properties of the pericellular matrix on chondrocytes. *Biophys. J.* 104, 986–996. doi: 10.1016/j.bpj.2013.01.028

Millward-Sadler, S. J., Wright, M. O., Flatman, P. W., and Salter, D. M. (2004). ATP in the mechanotransduction pathway of normal human chondrocytes. *Biorheology* 41, 567–575.

Millward-Sadler, S. J., Wright, M. O., Lee, H. S., Caldwell, H., Nuki, G., and Salter, D. M. (2000). Altered electrophysiological responses to mechanical stimulation and abnormal signaling through alpha 5 beta 1 integrin in chondrocytes from osteoarthritic cartilage. *Osteoarthr. Cartil.* 8, 272–278. doi: 10.1053/joca.1999.0301

Mobasheri, A. (1998). Correlation between $[Na^+]$, glycosaminoglycan and Na^+/K^+ pump density in the extracellular matrix of bovine articular cartilage. *Physiol. Res.* 47, 47–52.

Mobasheri, A., Bondy, C. A., Moley, K., Mendes, A. F., Rosa, S. C., and Richardson, S. M. (2008). Facilitative glucose transporters in articular chondrocytes. Expression, distribution and functional regulation of GLUT isoforms by hypoxia, hypoxia mimetics, growth factors and proinflammatory cytokines. *Adv. Anat. Embryol. Cell Biol.* 200, 1–84. doi: 10.1007/978-3-540-78899-7

Mobasheri, A., Carter, S. D., Martín-Vasallo, P., Shakibaei, M. (2002). Integrins and stretch activated ion channels; putative components of functional cell surface mechanoreceptors in articular chondrocytes. *Cell Biol*. 26, 1–18. doi: 10.1006/cbir.2001.0826

Mobasheri, A., Errington, R. J., Golding, S., Hall, A. C., Urban, J. P. G. (1997). Characterization of the Na^+K^+-ATPase in isolated bovine articular chondrocytes; molecular evidence for multiple α and β isoforms. *Cell Biol. Int.* 21, 201–212. doi: 10.1006/cbir.1997.0137

Mobasheri, A., Gent, T. C., Nash, A. I., Womack, M. D., Moskaluk, C. A., and Barrett-Jolley, R. (2007). Evidence for functional ATP-sensitive (K_{ATP})

potassium channels in human and equine articular chondrocytes. *Osteoarthr. Cartil.* 15, 1–8. doi: 10.1016/j.joca.2006.06.017

Mobasheri, A., Lewsi, R., Ferreira-Mendes, A., Rufino, A., Dart, C., and Barrett-Jolley, R. (2012). Potassium channels in articular chondrocytes. *Channels* 6, 416–425. doi: 10.4161/chan.22340

Mobasheri, A., Matta, C., Zakany, R., and Musumeci, G. (2015). Chondrosenescence: definition, hallmarks and potential role in the pathogenesis of osteoarthritis. *Maturitas* 80, 237–244. doi: 10.1016/j.maturitas.2014.12.003

Mobasheri, A. R., Mobasheri, M. J. O., Francis, E., Trujillo, D., Alvarez de la Rosa, D., and Martin-Vasallo, P. (1998). Ion transport in chondrocytes: membrane transporters involved in intracellular ion homeostasis and the regulation of cell volume, free [Ca^{2+}] and pH. *Histol. Histopathol.* 13, 893–910. doi: 10.14670/HH-13.893

Mouw, J. K., Imler, S. M., and Levenston, M. E. (2006). Ion-channel regulation of chondrocyte matrix synthesis in 3D culture under static and dynamic compression. *Biomech. Model. Mechanobiol.* 6, 33–41. doi: 10.1007/s10237-006-0034-1

Muir, H. (1995). The chondrocyte, architect of cartilage. Biomechanics, structure, function and molecular biology of cartilage matrix macromolecules. *Bioessays* 17, 1039–1048. doi: 10.1002/bies.950171208

Muramatsu, S., Wakabayashi, M., Ohno, T., Amano, K., Ooishi, R., and Sugahara, T. (2007). Functional gene screening system identified TRPV4 as a regulator of chondrogenic differentiation. *J. Biol. Chem.* 282, 32158–32167. doi: 10.1074/jbc.M706158200

Nguyen, B. V., Wang, Q. G., Kuiper, N. J., El Haj, A. J., Thomas, C. R., and Zhang, Z. (2010). Biomechanical properties of single chondrocytes and chondrons determined by micromanipulation and finite-element modeling. *J. Rheumat. Soc. Interface* 7, 1723–1733. doi: 10.1098/rsif.2010.0207

Nilius, B., and Oswianik, G. (2011). The transient receptor potential family of ion channels. *Genome Biol.* 12, 218–224. doi: 10.1186/gb-2011-12-3-218

Nygren, A., Fiset, C., Firek, L., Clark, W., Lindblad, D. S., Clark, R. B., et al. (1998). Mathematical model of an adult human atrial cell: the role of K^+ currents in repolarization. *Circ. Res.* 82, 63–81. doi: 10.1161/01.RES.82.1.63

O'Conor, C. J., Leddy, H. A., Benefield, H. C., Liedtke, W. B., and Guilak, F. (2014). TRPV4-mediated mechanotransduction regulates the metabolic response of chondrocytes to dynamic loading. *Proc. Natl. Acad. Sci. U.S.A.* 111, 1316–1321. doi: 10.1073/pnas.1319569111

Ogawa, H., Kozhemyakina, E., Hung, H. H., Grodzinsky, A. J., and Lassar, A. B. (2014). Mechanical motion promotes expression of Prg4 in articular cartilage via multiple CREB-dependent, fluid flow shear stress-induced signaling pathways. *Genes Dev*. 28, 127–139. doi: 10.1101/gad.231969.113

Parekh, A. B., and Muallem, S. (2011). Ca^{2+} signaling and gene regulation. *Cell Calcium* 49:279. doi: 10.1016/j.ceca.2011.01.002

Patel, A. J., and Honoré, E. (2001). Properties and modulation of mammalian 2P domain K^+ channels. *Trends Neurosci*. 24, 339–346. doi: 10.1016/S0166-2236(00)01810-5

Pelletier, J. P., Martel-Pelletier, J., and Abramson, S. B. (2001). Osteoarthritis, an inflammatory disease: potential implication for the selection of new therapeutic targets. *Arthrit. Rheumatol*. 44, 1237–1247. doi: 10.1002/1529-0131(200106)44:6<1237::AID-ART214>3.0.CO;2-F

Penuela, S., Gehi, R., and Laird, D. W. (2013). The biochemistry and function of pannexin channels. *Biochim. Biophys. Acta* 1828, 15–22. doi: 10.1016/j.bbamem.2012.01.017

Pfander, D., and Gelse, K. (2007). Hypoxia and osteoarthritis: how chondrocytes survive hypoxic environments. *Curr. Opin. Rheumatol.* 19, 457–462. doi: 10.1097/BOR.0b013e3282ba5693

Phan, M. N., Leddy, H. A., Votta, B. J., Kumar, S., Levy, D. S., Lipshutz, D. B., et al. (2009). Functional characterization of TRPV4 as an osmotically sensitive ion channel in porcine articular chondrocytes. *Arthritis Rheumatol*. 60, 3028–3037. doi: 10.1002/art.24799

Phillips, T., Ferraz, I., Bell, S., Clegg, P. D., Carter, D., and Mobasheri, A. (2005). Differential regulation of the GLUT1 and GLUT3 glucose transporters by growth factors and pro-inflammatory cytokines in equine articular chondrocytes. *Vet. J.* 169, 216–222. doi: 10.1016/j.tvjl.2004.01.026

Poole, A. C., Flint, M. H., and Beaumont, B. W. (1987). Chondrons in cartilage: ultrastructural analysis of the pericellular microenvironment in adult human articular cartilages. *J. Orthop. Res.* 5, 509–522. doi: 10.1002/jor.1100050406

Poole, C. A. (1997). Articular cartilage chondrons: form, function and failure. *J. Anat.* 191, 1–13. doi: 10.1046/j.1469-7580.1997.19110001.x

Poon, I. K., Chiu, Y. H., Armstrong, A. J., Kinchen, J. M., Juncadella, I. J., Bayliss, D. A., et al. (2014). Unexpected link between an antibiotic, pannexin channels and apoptosis. *Nature* 507, 329–334. doi: 10.1038/nature13147

Radhakrishnan, K., and Hindmarsh, A. C. (1993). *Description and Use of LSODE, the Livermore Solver for Ordinary Differential Equations*. NASA, Office of Management, Scientific and Technical Information Program. UCRL-ID-113855.

Saez, J. C., Berthoud, V. M., Brañes, M. C., Martínez, A. D., and Beyer, E. C. (2003). Plasma membrane channels formed by connexins: their regulation and functions. *Physiol. Rev.* 83, 1359–1400. doi: 10.1152/physrev.00007.2003

Sánchez, J. C., Powell, T., Staines, H. M., and Wilkins, R. J. (2006). Electrophysiological demonstration of Na^+/Ca^{2+} exchange in bovine articular chondrocytes. *Biorheology* 43, 83–94.

Shaw, P. J., Qu, B., Hoth, M., and Feske, S. (2013). Molecular regulation of CRAC channels and their role in lymphocyte function. *Cell Mol. Life Sci.* 70, 2637–2656. doi: 10.1007/s00018-012-1175-2

Sonkusare, S. K., Bonev, A. D., Ledoux, J., Liedtke, W., Kotlikoff, M. I., Heppner, T. J., et al. (2012). Elementary Ca^{2+} signals through endothelial TRPV4 channels regulate vascular function. *Science* 336, 597–601. doi: 10.1126/science.1216283

Spitzer, N. C., Lautermilch, N. J., Smith, R. D., and Gomez, T. M. (2000). Coding of neuronal differentiation by calcium transients. *Bioessays* 22, 811–817. doi: 10.1002/1521-1878(200009)22:9<811::AID-BIES6>3.0.CO;2-G

Sugimoto, T., Yoshino, M., Nagao, M., Ishii, S., and Yabu, H. (1996). Voltage-gated ionic channels in cultured rabbit articular chondrocytes. *Comp. Biochem. Physiol.* 115, 223–232. doi: 10.1016/S0742-8413(96)00091-6

Sun, L., Xiong, Y., Zeng, X., Wu, Y., Pan, N., Lingle, C. J., et al. (2009). Differential regulation of action potentials by inactivating and nonactivating BK channels in rat adrenal chromaffin cells. *Biophys. J.* 97, 1832–1842. doi: 10.1016/j.bpj.2009.06.042

Thorneloe, K. S., Sulpizio, A. C., and Westfall, T. D. (2008). N-((1S)-1-{[4-((2S)-2-{[2,4-Dichlorophenyl)sulfonyl]amino}-3-hydroxypropanoyl)-1-piperazinyl]carbonyl}-3-methylbutyl)-1-benzothiophene-2-carboxamide (GSK1016790A), a novel and potent transient receptor potential vanilloid 4 channel agonist induces urinary bladder contraction and hyperactivity: part 1. *J. Pharm. Exp. Ther.* 326, 432–442. doi: 10.1124/jpet.108.139295

Trujillo, E., Alvarez de la Rosa, D., Mobasheri, A., Gonzalez, T., Canessa, C. M., and Martín-Vasallo, P. (1999). Sodium transport systems in human chondrocytes II. Expression of ENaC, Na^+/K^+ $/2Cl^-$ cotransporter and Na^+/H^+ exchangers in healthy and arthritic chondrocytes. *Histol. Histopathol.* 14, 1023–1031.

Tsuga, K., Tohse, N., Yoshino, M., Sugimoto, T., Yamashita, T., Ishii, S., et al. (2002). Chloride conductance determining membrane potential of rabbit articular chondrocytes. *J. Membr. Biol.* 185, 75–81. doi: 10.1007/s00232-001-0112-3

Urban, J. P., Hall, A. C., and Gehl, K. A. (1993). Regulation of matrix synthesis rates by the ionic and osmotic environment of articular chondrycytes. *J. Cell. Physiol*. 154, 262–270. doi: 10.1002/jcp.1041540208

Webb, S. T., and Ghosh, S. (2009). Intra-articular bupivacaine: potentially chondrotoxic? *Br. J. Anaes*. 102, 439–441. doi: 10.1093/bja/aep036

Wilkins, R. J., Browning, J. A., and Ellory, J. C. (2000a). Surviving in a matrix: membrane transport in articular chondrocytes. *J. Membr. Biol.* 177, 95–108. doi: 10.1007/s002320001103

Wilkins, R. J., Browning, J. A., and Urban, J. P. (2000b). Chondrocyte regulation by mechanical load. *Biorheology* 37, 67–74.

Wilson, J. R., Clark, R. B., Banderali, U., and Giles, W. R. (2011). Measurement of the membrane potential in small cells using patch clamp methods. *Channels* 5, 530–537. doi: 10.4161/chan.5.6.17484

Wilson, J. R., Duncan, N. A., Giles, W. R., and Clark, R. B. (2004). A voltage-dependent K^+ current contributes to membrane potential of acutely isolated canine articular chondrocytes. *J. Physiol.* 557, 93–104. doi: 10.1113/jphysiol.2003.058883

Wilusz, R. E., Sanchez-Adams, J., and Guilak, F. (2014). The structure and function of the pericellular matrix of articular cartilage. *Matrix Biol.* 39, 25–32. doi: 10.1016/j.matbio.2014.08.009

Wright, M. O., Nishida, K., Bavington, C., Godolphin, J. L., Dunne, E., Walmsley, S., et al. (1997). Hyperpolarisation of cultured human chondrocytes following cyclical pressure-induced strain: evidence of a role for alpha 5 beta 1 integrin as a chondrocyte mechanoreceptor. *J. Orthop. Res.* 15, 742–747. doi: 10.1002/jor.1100150517

Wu, Q. Q., and Chen, Q. (2000). Mechanoregulation of chondrocyte proliferation, maturation, and hypertrophy: ion-channel dependent transduction of matrix deformation signals. *Exp. Cell Res.* 256, 383–391. doi: 10.1006/excr.2000.4847

Zuscik, M. J., Gunter, T. E., Puzas, J. E., Rosier, R. N. (1997). Characterization of voltage-sensitive calcium channels in growth plate chondrocytes. *Biochem. Biophys. Res. Commun.* 234, 432–438. doi: 10.1006/bbrc.1997.6661

Conflict of Interest Statement: The authors declare that the research was conducted in the absence of any commercial or financial relationships that could be construed as a potential conflict of interest.

frontiers in Physiology

ORIGINAL RESEARCH
published: 11 September 2018
doi: 10.3389/fphys.2018.01259

A Multiphysics Biventricular Cardiac Model: Simulations With a Left-Ventricular Assist Device

***Azam Ahmad Bakir*[1]*, *Amr Al Abed*[1], *Michael C. Stevens*[1,2], *Nigel H. Lovell*[1] and *Socrates Dokos*[1]**

[1] Graduate School of Biomedical Engineering, University of New South Wales, Kensington, NSW, Australia, [2] Innovative Cardiovascular Engineering and Technology Laboratory, Critical Care Research Group, The Prince Charles Hospital, Brisbane, QLD, Australia

Computational models have become essential in predicting medical device efficacy prior to clinical studies. To investigate the performance of a left-ventricular assist device (LVAD), a fully-coupled cardiac fluid-electromechanics finite element model was developed, incorporating electrical activation, passive and active myocardial mechanics, as well as blood hemodynamics solved simultaneously in an idealized biventricular geometry. Electrical activation was initiated using a simplified Purkinje network with one-way coupling to the surrounding myocardium. Phenomenological action potential and excitation-contraction equations were adapted to trigger myocardial contraction. Action potential propagation was formulated within a material frame to emulate gap junction-controlled propagation, such that the activation sequence was independent of myocardial deformation. Passive cardiac mechanics were governed by a transverse isotropic hyperelastic constitutive formulation. Blood velocity and pressure were determined by the incompressible Navier-Stokes formulations with a closed-loop Windkessel circuit governing the circulatory load. To investigate heart-LVAD interaction, we reduced the left ventricular (LV) contraction stress to mimic a failing heart, and inserted a LVAD cannula at the LV apex with continuous flow governing the outflow rate. A proportional controller was implemented to determine the pump motor voltage whilst maintaining pump motor speed. Following LVAD insertion, the model revealed a change in the LV pressure-volume loop shape from rectangular to triangular. At higher pump speeds, aortic ejection ceased and the LV decompressed to smaller end diastolic volumes. After multiple cycles, the LV cavity gradually collapsed along with a drop in pump motor current. The model was therefore able to predict ventricular collapse, indicating its utility for future development of control algorithms and pre-clinical testing of LVADs to avoid LV collapse in recipients.

Keywords: computational modeling, multiphysics modeling, heart, LVAD, cardiac, physiome, electromechanics, fluid-structure interaction

OPEN ACCESS

Edited by:
Christopher Basciano,
Becton Dickinson, United States

Reviewed by:
Ethan Kung,
Clemson University, United States
Joakim Sundnes,
Simula Research Laboratory, Norway

****Correspondence:***
Azam Ahmad Bakir
a.ahmadbakir@unsw.edu.au

Specialty section:
This article was submitted to Computational Physiology and Medicine,
a section of the journal Frontiers in Physiology

Received: *30 April 2018*
Accepted: *21 August 2018*
Published: *11 September 2018*

Citation:
Ahmad Bakir A, Al Abed A, Stevens MC, Lovell NH and Dokos S (2018) A Multiphysics Biventricular Cardiac Model: Simulations With a Left-Ventricular Assist Device. Front. Physiol. 9:1259. doi: 10.3389/fphys.2018.01259

1. INTRODUCTION

The optimal function of the heart relies on multiphysics phenomena, comprised of electrical activation, as well as myocardial contraction and blood hemodynamics. A deficiency in any of these physics will impact the others. As such, development of cardiac medical devices has to consider these multiphysics interactions during both pre-clinical and clinical studies. Multiphysics cardiac computational models can be a test-bed for early ideas to assess how therapeutic interventions could impact the diseased heart. This is especially beneficial to reduce the risk to patients with rare medical conditions, where the number of subjects that can be recruited for device clinical trials is limited. Results from computational simulations could be used to generate more plausible hypotheses for future testing; thus, helping to reduce development and technology transfer costs and potential clinical adverse reactions.

Numerous studies have modeled the electromechanical interactions in the myocardium with varying levels of complexity (Usyk et al., 2002; Gurev et al., 2011; Quarteroni et al., 2017). Most were coupled to Windkessel-type models to mimic the systemic circulation (Usyk et al., 2002; Gurev et al., 2011). Instead of modeling the spatially varying fluid dynamics, a uniform endocardial pressure load was calculated to constrain the volume during the isovolumic phases. Whilst such an approach may be sufficient to model most cardiac electromechanics phenomena, it limits model usability: for example, to simulate cardiac interaction with intra-cavity implants. In cases with large intraventricular pressure gradients, such as in hypertrophic obstructive cardiomyopathy (Geske et al., 2011), fluid loading on the endocardium may be spatially heterogeneous. This could render the spatially uniform pressure load constraint inaccurate. Furthermore, formation of vortices, a potential measure of cardiac health index (Hong et al., 2008), cannot be simulated in such models.

Fluid-structure interaction (FSI) models of the ventricles are important in studying fluid loading on the myocardium as well as the heart's blood pumping efficiency. For the sake of simplicity, the contribution of electrical activation on wall mechanics was not considered in many ventricular FSI models. Instead, a temporal activation function was used to govern contraction uniformly across the entire left ventricle (LV) (Nordsletten et al., 2011). Therefore, the effect of spatially heterogeneous activation on fluid behavior cannot be investigated in such models. Several studies have performed simulations of cardiac electrophysiology coupled with FSI (Watanabe et al., 2004; Choi et al., 2015). Nevertheless, their approach only utilized one-way coupling for some of the modeled physics, limiting the scope of physics interactions. A fully coupled fluid-electromechanics model can provide added advantages in terms of predictive power and future-expansion capability to test devices and drugs, or to be applied as a surgery planning tool to predict the heart's motion and blood flow profile post-surgery. The review by Quarteroni et al. (2017) provides a detailed summary of various approaches of modeling cardiac electromechanics as well as fluid-structure interactions.

A potential application of cardiac multiphysics models is to study heart-implant interactions such as the left ventricular assist device (LVAD), classified as a Class III device by the United States' Food and Drug Administration (FDA). As it may pose a high risk to patients, the device needs to be rigorously tested prior to marketing approval. Whilst the LVAD works well for patients with the most severe heart disease, excessively high pump flow rate relative to ventricular filling rate can cause the ventricles to collapse. This phenomenon is known as ventricular suction and it represents a common complication (Vollkron et al., 2007). Moreover, increased arrhythmic tendency has been noted among LVAD recipients, which may reduce right ventricular (RV) output resulting in reduced LVAD preload, worsening the suction (Robertson et al., 2017). Furthermore, several LVAD recipients also suffer from post-implantation RV dysfunction and commonly require an additional RV assist device (Neyer et al., 2016). Positioning and design of the LVAD cannula can also affect its performance (Ong et al., 2013). Therefore, LVAD complications are inherently multiphysics in nature and not only fluid-structure interactions, but also ventricular electromechanics as well as adjacent ventricular function. If any of these issues can be predicted beforehand, a strategy can be developed to lessen the risk.

In this study, we develop a multiphysics modeling framework for simulating biventricular electrophysiological behavior along with myocardial mechanics and two-way blood-myocardium interaction. The framework is implemented in an idealized biventricular structure that embeds a Purkinje fiber network to trigger myocardial electrical activation. We present computational simulations of a healthy heart as well as LVAD intervention in a dilated heart, including the impact of pump speed on both the pump and ventricles, as well as LV collapse in mitral stenosis case. We utilized commercial computational modeling software for easy replication and future model expansion.

2. METHODS

We first present our standard framework for formulating a healthy biventricular model based on our preliminary work presented in Bakir et al. (2017). **Figure 1A** summarizes all physics included along with their coupling. We then describe the implementation of heart-LVAD interaction by introducing a failing dilated heart and adding a LVAD model to the standard framework. Unless otherwise stated, descriptions and parameter values are listed in the **Supplementary Material**.

2.1. Standard Biventricular Model Formulations

2.1.1. Gross Geometry and Microstructure

The geometry was constructed using two truncated ellipsoids merged at the interventricular sulci, as shown in **Figure 2A**. The aortic and mitral valve boundaries were generated using circular and semilunar shapes, respectively, whilst the pulmonary and tricuspid valve boundaries were created using circular and elliptical shapes, respectively.

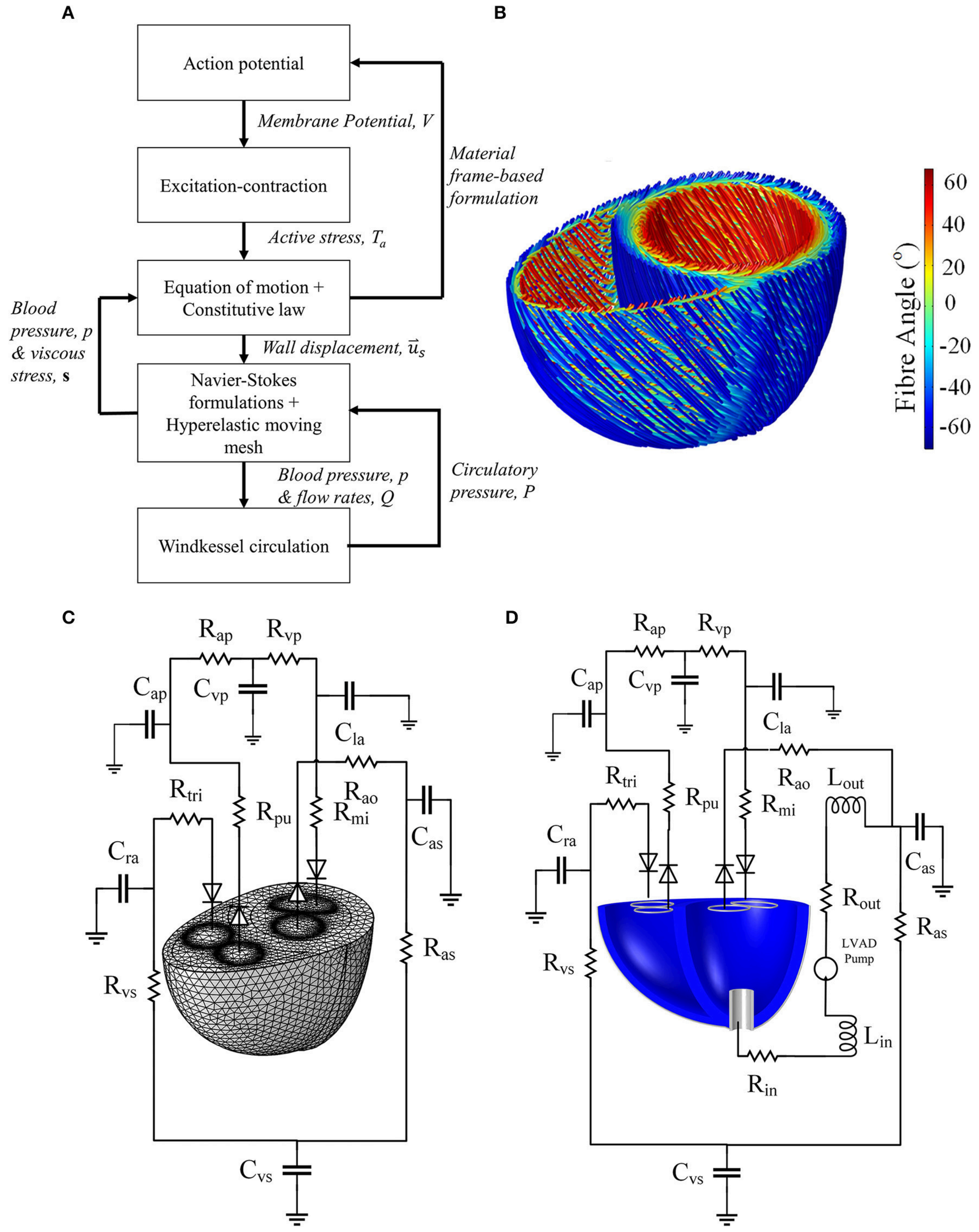

FIGURE 1 | (A) Schematic summarizing the physics modeled, as well as the interphysics couplings. **(B)** Fiber direction streamlines for the standard model geometry of **Figures 2A,B**. It should be noted that the fibers are not implemented as geometrical structures but a numerical representation of the anisotropic direction of material properties. **(C)** The Windkessel circulation coupled with the normal mesh of the standard biventricular model, and **(D)** Windkessel modification for the LVAD model as well as the cannula structure implanted in the dilated heart geometry.

To obtain a realistic activation sequence, an idealized Purkinje fiber tree structure (**Figures 2C,D**) was constructed within the myocardium to mimic the gross anatomy of the Purkinje network (Vigmond and Stuyvers, 2015) without restricting meshing requirements. The Purkinje structure begins at the septal base with two major bundles: the left and right bundle branches. The

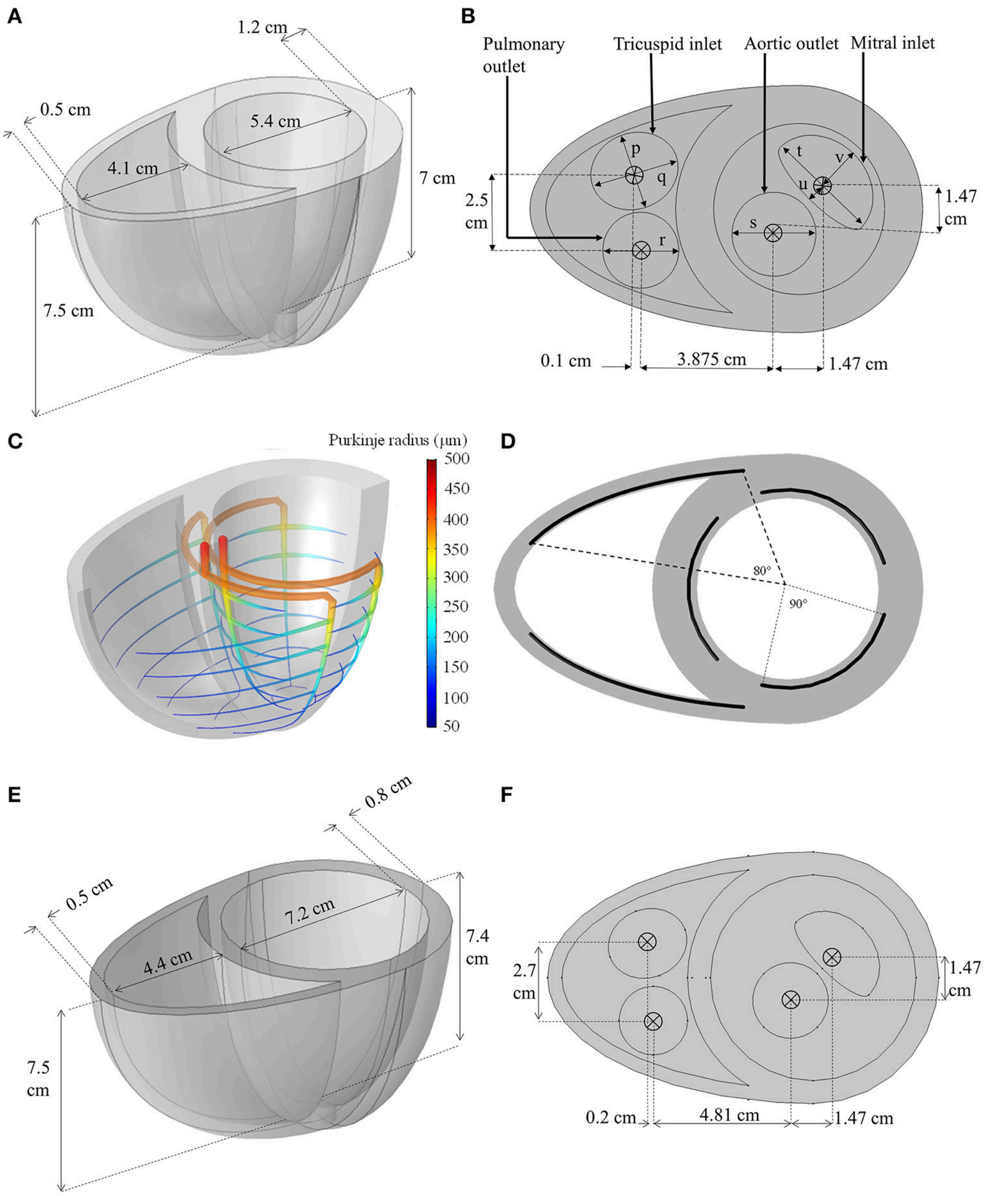

FIGURE 2 | (A,B) Dimensions of the idealized biventricular geometry of the standard model. (p = 2.4 cm, q = 2.8 cm, r = 2.4 cm, s = 2.65 cm, t = 3.6 cm, u = 0.5 cm, v = 1.5 cm) **(C)** The Purkinje fiber network illustrating the change in fiber radius. **(D)** The angle span of each Purkinje-myocyte branch. **(E,F)** The dimension of the dilated heart used for LVAD modeling.

left bundle branch was further divided into three minor bundles near the basal septal entry, whilst the right bundle branched into anterior and posterior minor bundles. These minor bundles further branched out circumferentially, every 1 cm between the apex and base, forming the Purkinje-myocyte junctions (PMJ). The Purkinje fibers were represented in the geometry as 1D edges embedded in 3D space: and were numerically assigned a radius, r, that was set to decrease linearly from 500 μm at the basal origin to 50 μm at the endpoints of the PMJs based on the measurements by James (1961).

The myocardial microstructure is governed by the fiber, sheet and normal-to-sheet orientations (LeGrice et al., 1997). For simplicity, the following settings and assumptions were implemented:

1. The fiber was assumed to be $-60°$ with respect to the circumferential plane at the epicardium, and $60°$ at the endocardium (LeGrice et al., 1997). The fiber angle changed linearly transmurally as shown in **Figure 1**.
2. The microstructural sheets were assumed to lie perpendicular to the epicardial and endocardial surfaces.

3. As the apical microstructure is difficult to measure experimentally (LeGrice et al., 1997), and adaptation of above principles could result in a singularity, the microstructure of the apex region, defined by a 1 cm diameter cylinder, was assumed to be isotropic (Nordsletten et al., 2011).

2.1.2. Electrophysiology and Gap Junction-based Propagation

Myocardial action potential (AP) formulations Equations (1)–(5) were based on the phenomenological Nash and Panfilov (2004) model, modified to incorporate units into the originally dimensionless form. Variables V_m and V_p represent myocardial and Purkinje membrane potentials respectively, whilst R is an auxiliary recovery variable for both myocardium and Purkinje fiber. Parameter a in Equations (3) and (5) was chosen to vary linearly such that a_{epi} is 0.12 and a_{endo} is 0.07 to allow the myocardium to relax in the opposite direction of its activation (Glukhov et al., 2010).

$$\beta_{sv}\left(C_m\frac{\partial V_m}{\partial t}+i_{ion}+i_{pr}\right)=\nabla_X\cdot(\boldsymbol{\sigma}\nabla_X V_m) \tag{1}$$

$$r\left(C_m\frac{\partial V_p}{\partial t}+i_{ion}\right)=\nabla_X\cdot\left(\frac{r^2}{2\rho_i}\nabla_X V_p\right) \tag{2}$$

$$\begin{aligned} i_{ion} = {} & k_1k_2(V_m-B)\left(\left[\frac{V_m-B}{A}\right]-a\right)(V_m-1)\\ & +k_2R(V_m-B) \end{aligned} \tag{3}$$

$$i_{pr}=R_{pmj}(V_m-V_p) \tag{4}$$

$$\begin{aligned} \frac{\partial R}{\partial t} = {} & \left(\varepsilon_0+\frac{\mu_1 R}{\left[\frac{V_m-B}{A}\right]+\mu_2}\right)\\ & \times\left(-R-k_1\left[\frac{V_m-B}{A}\right]\left(\left[\frac{V_m-B}{A}\right]-a-1\right)\right) \end{aligned} \tag{5}$$

Membrane potential dynamics and AP propagation within the myocardium were governed by Equation (1), and within the Purkinje fibers by Equation (2), based on the modified cable equation developed by Alqahtani et al. (2017) to take into account the effect of varying fiber radius. Equation (3) represents the transmembrane ionic current flow while Equation (5) governs AP recovery in both the myocardium and Purkinje fiber domains. For the Purkinje fibers, parameters a and k_2 were adjusted to achieve a three-fold increase in conduction velocity and a 2-fold increase in AP upstroke velocity relative to their respective values in the myocardium (Vigmond and Stuyvers, 2015). The Purkinje current source, i_{pr}, was supplied to the myocardium only at the the PMJs to trigger myocardial activation (Equation 4).

The ∇_X operator in Equations (1) and (2) is defined within the material frame (X, Y, Z) such that $\nabla_X = (\frac{\partial}{\partial X}, \frac{\partial}{\partial Y}, \frac{\partial}{\partial Z})^T$, corresponding to a gap junction-based constitutive formulation described in an earlier study (Bakir and Dokos, 2015). Except at the apex, the electrical conductivity tensor, $\boldsymbol{\sigma}$, was set to exhibit an anisotropy ratio of 4:2:1 along the fiber, $\hat{F}$, sheet, $\hat{S}$, and normal-to-sheet, $\hat{N}$ directions respectively, in accordance with Hooks et al. (2007). The conductivity tensor, $\boldsymbol{\sigma}$, was determined from conductivities defined in the local fiber (σ_f), sheet (σ_s) and normal-to-sheet (σ_n) directions according to:

$$\boldsymbol{\sigma}=\sigma_f(\hat{F}\otimes\hat{F})+\sigma_s(\hat{S}\otimes\hat{S})+\sigma_n(\hat{N}\otimes\hat{N}) \tag{6}$$

The value of σ_f was set such that the epicardial activation time matched reported *ex vivo* experimental findings in human heart (Durrer et al., 1970). The electrical conductivity of the isotropic apex was assumed to be σ_f. Zero flux boundary conditions were implemented for all myocardial boundaries unless otherwise noted.

2.1.3. Active Stress

The simplified form of active stress proposed by Nash and Panfilov (2004), and further modified by Göktepe and Kuhl (2010), was chosen to generate mechanical contraction triggered by the AP. Active stress, T_a, was represented by the following phenomenological ordinary differential equation (ODE):

$$\frac{\partial T_a}{\partial t}=\epsilon(V_m)\left(k_{Ta}\left[\frac{V_m-B}{A}\right]-T_a\right) \tag{7}$$

where k_{Ta} controls the maximum magnitude of T_a. A, and B are fixed parameters introduced here to give units to the originally dimensionless formulation. The delay function, $\epsilon(V_m)$, was given by Göktepe and Kuhl (2010) as follows:

$$\epsilon(V_m)=\epsilon_0+(\epsilon_\infty-\epsilon_0)\exp(-\exp(-\xi(V_m-V_{threshold}))) \tag{8}$$

where ϵ_0, ϵ_∞, ξ and $V_{threshold}$ are also fixed parameters. The active stress was set such that the myocardial membrane potential, but not the Purkinje fiber, triggers active stress generation.

2.1.4. Myocardial Mechanics

The myocardium was represented by the transverse isotropic myocardial hyperelastic formulation of Holzapfel and Ogden (2009), as detailed in Equations (9)–(11), which can simulate the myocardial biaxial tension response with four parameters. A nearly-incompressible constraint was enforced through the adaptation of a volumetric strain energy function, ψ_{vol} in Equation (12), based on the formulation of Doll and Schweizerhof (1999):

$$\psi=\psi_{isotropic}+\psi_{fiber}+\psi_{vol} \tag{9}$$

$$\psi_{isotropic}=\frac{a_i}{2b_i}\exp(b(I_1-3)) \tag{10}$$

$$\psi_{fiber}=\frac{a_f}{2b_f}\exp(b_f(I_{4f}-1)^2-1) \tag{11}$$

$$\psi_{vol}=\frac{\kappa(J-1)ln(J)}{2} \tag{12}$$

I_1 in Equation (10) denotes the first invariant of the isochoric elastic right Cauchy-Green tensor, $\mathbf{C}$, whilst $I_{4f} = \hat{F} \cdot (\mathbf{C}\hat{F})$. J in Equation (12) represents the determinant of the deformation gradient tensor, $\mathbf{F}$. In order to ensure material stability, I_{4f} was set to zero when $I_{4f} < 0$, assuming that myocardial fibers do not contribute significantly to passive mechanics during compression (Holzapfel and Ogden, 2009). The apical strain energy function was solely given by $\psi_{isotropic}$ due to the isotropic apex assumption.

The equation of motion governing myocardial deformation is given by Equation (13):

$$\rho_s \frac{\partial^2 \vec{u_s}}{\partial t^2} + \alpha \rho_s \frac{\partial \vec{u_s}}{\partial t} = \nabla_X \cdot \left(\mathbf{FT} + \beta \frac{\partial \mathbf{FT}}{\partial t} \right) \tag{13}$$

where $\vec{u_s}$ is the myocardial displacement. Equation (13) also contains Rayleigh damping, represented by the first order time derivative of displacement and stress, to eliminate unphysiological oscillations during fluid loading. Rayleigh damping parameters were adapted from Fritz et al. (2014) such that $\alpha = 100\ s^{-1}$ and $\beta = 0.01\ s$.

In order to couple the electrical and mechanical formulations, T_a was added to the 2nd Piola Kirchhoff stress, $\mathbf{T}$, along the fiber, sheet, and normal-to-sheet directions, as shown in Equation (14) such that the magnitude of active stress in the sheet and normal-to-sheet directions was 40% of its value along the fiber direction (Usyk et al., 2002). In the isotropic apex, an isotropic active stress of T_a was assumed.

$$\mathbf{T} = \frac{\partial \psi}{\partial \mathbf{E}} + T_a(\hat{F} \otimes \hat{F}) + 0.4\ T_a(\hat{S} \otimes \hat{S}) + 0.4\ T_a(\hat{N} \otimes \hat{N}) \tag{14}$$

$\mathbf{E}$ in Equation (14) is the Green-Lagrange strain tensor whilst ψ is the myocardial strain-energy function.

For simplicity, the ventricular base, including the valves, was assumed to be fixed to avoid translation and rotation. The endocardial boundary was also subjected to pressure and viscous stress from the blood fluid, discussed further below. The remaining myocardial boundaries were allowed to move freely.

2.1.5. Blood Hemodynamics and Circulation

The fluid velocity, $\vec{v_f}$, and pressure, p, in the blood cavity were determined using the incompressible Newtonian Navier-Stokes formulation (Equation 15) and the continuity equation (Equation 16).

$$\rho_f \frac{\partial \vec{v_f}}{\partial t} + \rho_f (\vec{v_f} \cdot \nabla_x)\vec{v_f} = \nabla_x \cdot (-p\mathbf{I} + \mu_f(\nabla_x \vec{v_f} + (\nabla_x \vec{v_f})^T)) \tag{15}$$

$$\nabla_x \cdot \vec{v_f} = 0 \tag{16}$$

∇_x in Equations (15) and (16) describes the spatial derivative in the spatial frame such that $\nabla_x = (\frac{\partial}{\partial x}, \frac{\partial}{\partial y}, \frac{\partial}{\partial z})^T$.

No-slip boundary conditions were applied at the ventricular base surface except at the inlets and outlets. FSI was implemented as a strongly coupled two-way framework where (1) the fluid velocity at the endocardium was set to be equal to the endocardial surface velocity (Equation 17), and (2) the fluid total stress, $\mathbf{s}$, a sum of pressure and viscous stress, was applied along the normal of the endocardial surface (Equation 18):

$$\vec{v_f}\Big|_{endo} = \frac{\partial \vec{u_s}}{\partial t}\Big|_{endo} \tag{17}$$

$$\mathbf{s} = \hat{n}\Big|_{endo} \cdot (-p\mathbf{I} + \mu_f(\nabla_x \vec{v_f} + (\nabla_x \vec{v_f})^T)) \tag{18}$$

To couple $\mathbf{s}$ to the solid formulation in Equation (13), a transformation from the spatial frame (i.e. the deformed frame where the Navier-Stokes equations are solved) to the material frame (i.e. the reference or material frame where the solid mechanics are solved) is needed, as shown in Equation (19), where dv and dV are mesh element scale factors in the spatial and material frame respectively.

$$\mathbf{S} = \mathbf{s} \cdot \frac{dv}{dV} \tag{19}$$

Here, $\mathbf{S}$ denotes the traction from the fluid applied to the endocardial wall in material frame coordinates. The scale factors simply scale the local mesh element coordinates to the spatial and material frame coordinates.

The fluid boundary deformation was governed by the myocardial structural deformation, $\vec{u_s}$, whilst deformation of the mesh within the fluid domain was governed by a mesh smoothing formulation (Equation 20). The hyperelastic mesh smoothing algorithm in Equation (20) was solved to determine the minimum mesh deformation energy, $\psi_{\mathbf{mesh}}$, within the blood domain, Ω_f:

$$\psi_{mesh} = \frac{1}{2} \int_{\Omega_f} C_1(I_{1,mesh} - 3) + C_2(I_{1,mesh} - 3)^2 + \kappa_{mesh}(J_{mesh} - 1)^2\, dV_{\Omega_f} \tag{20}$$

The invariants, J_{mesh} and $I_{1,mesh}$, were given by Equations (21) and (22):

$$J_{mesh} = det(\nabla_X \mathbf{x}) \tag{21}$$

$$I_{1,mesh} = (J_{mesh})^{-2/3}\ \mathrm{tr}((\nabla_X \mathbf{x})^T \nabla_X \mathbf{x}) \tag{22}$$

where C_1 and κ_{mesh} are artificial shear and bulk moduli, both set to a value of 1, whilst $\nabla_X \mathbf{x} = \frac{\partial \mathbf{x}}{\partial \mathbf{X}}$, where $\mathbf{x}$ represents the spatial frame coordinates and $\mathbf{X}$ the material frame coordinates. The non-linear stiffening parameter C_2 was set to 0 for the healthy simulation and 100 for the LVAD simulations to cope with greater mesh deformation subsequent to cannula inclusion. Boundary conditions for Equation (20) were set to equal the displacement of the endocardial wall, $\vec{u_s}$, and held fixed at the ventricular base.

The finite element model was coupled to a closed-loop Windkessel circulation (**Figures 1C,D**), based on the Kerckhoffs et al. (2007) circuit, modified to include an unstressed volume parameter in the capacitances, and to reflect healthy human circulation. Laminar flow rate conditions were implemented at the inlet and outlet boundaries. Each flow rate was determined from the difference between the average boundary pressure, taken at each of the inlet and outlet boundary of the finite element model, and the Windkessel circulatory pressure. The flow rate variables, described in the **Supplementary Material**, were applied as follows: Q_{mi} was applied to the mitral inlet, Q_{ao} to the aortic outlet, Q_{tri} to the tricuspid inlet, and Q_{pa} to the pulmonary artery outlet.

These laminar inflow and outflow boundary conditions were implemented by appending a fictitious tube to each boundary, and applying:

$$L_{ext}\nabla_{x,t}\cdot[-p\boldsymbol{I}+\mu(\nabla_{x,t}\vec{v_f}+(\nabla_{x,t}\vec{v_f})^T)]=-p_{ext}\vec{n} \tag{23}$$

where $\nabla_{x,t}$ is the tangential derivative in spatial frame at the inlet or outlet surfaces. This equation essentially determines the velocity applied at the boundary, assuming the inlet and outlet boundaries are connected to a tube of L_{ext} external length. A constraint, p_{ext}, was applied to ensure that the flow rate through the tube matched the assigned flow rate from the above. To ensure a laminar profile and prevent back-flow when the valve is closed, L_{ext} needs to be sufficiently large to eliminate numerical backflow was set to 20 m in our model. It should be noted that the L_{ext} does not represent an actual physical tube length, but a value chosen to satisfy the conditions.

2.1.6. Simulation Protocol

1. To begin, the Windkessel circuit was decoupled from the heart and the LV and RV chambers were inflated until they reached their end diastolic volumes, $V_{lv,\infty}$ and $V_{rv,\infty}$, respectively. The filling rate for each ventricle was calculated using Equation (24) based on a proportional controller:

$$Q_{fill}=-k_{flow}(V_{lv}-V_{lv,\infty}) \tag{24}$$

   where k_{flow} is a fixed parameter set to 200,000 s^{-1}.
2. Using the filled ventricle, the Windkessel circuit was connected and the model was solved using the initial Windkessel volumes listed in the **Supplementary Material**, which were tuned to be near their steady-state cycle' volumes. The model was run for three steady cycles. A pulse stimulus of 2 ms duration at 60 beats per minute (bpm) was applied at the basal entry of both left and right bundles of the Purkinje network.

2.2. LVAD Simulations

A left ventricular assist device (LVAD) model was attached to the biventricular model via a cannula.

2.2.1. Heart Failure Modifications

Prior to adding the LVAD, the biventricular model was modified to reflect dilated cardiomyopathy (DCM), a common etiology of LVAD recipients. The geometry was modified by increasing the LV short axis and reducing its wall thickness as shown in **Figures 2E,F** (Mohiaddin, 1995; Dandel et al., 2008). This increased the LV chamber size whilst the RV chamber size was minimally affected. The heart rate was increased to 80 bpm (Mohiaddin, 1995; Dandel et al., 2008) and the LV contraction strength was reduced by setting the k_{Ta} parameter of the standard model to half its value, in accordance with isometric twitch measurements in isolated epicardial tissue obtained from DCM patients (Hasenfuss et al., 1992). Other settings described in the standard model were left unchanged.

2.2.2. LVAD Model

The LVAD was represented by an ODE model that relates the hydraulic state experienced by the pump and pump motor current. The LVAD model, developed by Lim et al. (2010), consists of three components:

1. Motor windings electrical equation, describing the current, I, needed to maintain the pump motor speed, ω:

$$V_{pump}=-2k_e\,\omega+R_{pump}\,I+L\frac{dI}{dt} \tag{25}$$

   The voltage, V_{pump}, was controlled using a proportional controller, which maintains the pump speed at the desired speed, ω_{set}:

$$V_{pump}=k_{pump}\,(\omega-\omega_{set}) \tag{26}$$

2. Electromagnetic torque transfer equation, relating the electromagnetic torque, T_e, produced by the pump to the input flow rate, Q (L min^{-1}):

$$T_e=3k_e\,I=J\frac{d\omega}{dt}+a_p\,Q^2\,\omega+b_p\,Q\,\omega^2+c_p\,\omega+d_p\,\omega^3 \tag{27}$$

3. Pump hydraulic equation, relating the differential pressure, ΔP, produced by the pump to the input flow rate and pump speed:

$$\Delta P=e_p+f_p\,Q^3+g_p\,\omega^2 \tag{28}$$

   Pump inflow rate was obtained via the equation:

$$\frac{dQ}{dt}=\frac{\Delta P-(P_{as}-P_{lv,cannula})-(R_{in}+R_{out})\,Q}{L_{in}+L_{out}} \tag{29}$$

Variable inflow and outflow resistances, R_{in} and R_{out}, were set to be proportional to the pump flow rate to account for the turbulence effect in the pump (Lim et al., 2010), and are given by

$$R_{in}+R_{out}=k_r\,Q \tag{30}$$

The LVAD equations were linked to the ventricular model via the numerical difference between LV pressure averaged at the cannula outlet boundary, $P_{lv,cannula}$, and the systemic arterial pressure, P_{as} of the Windkessel circulation as shown in Equation (29). This difference is the pressure head of the pump, ΔP, minus the pressure loss across the cannula. Equations (25)–(29) describe the relationships that determines the overall pump flow rate, Q, using this pressure difference.

2.2.3. Cannula Design

A cylindrical generic pump cannula, 1.6 cm inner diameter and 0.2 cm wall thickness, was inserted at the LV apex of the biventricular geometry as shown in **Figure 1C**. The cannula extends only a quarter of the LV apicobasal distance as suggested by Ong et al. (2013). The cannula was set to be a linear elastic silicon material ($E = 170$ GPa, $\nu = 0.28$, $\rho_s = 2{,}329$ kg m^{-3}), was held fixed in space at its external parts outside the LV.

Contact modeling between the LV endocardium and the cannula is necessary to prevent mesh collapse when surface contact occurs. In essence, the contact formulation applies loads that are inversely proportional to the distance between contacting surfaces when the surfaces move closer than a certain threshold. A wall distance formulation (Fares and Schröder, 2002), described in the **Supplementary Material**, was applied to calculate the distance between the endocardial surface and contact destination surfaces (cannula and ventricular base). The ventricular base of the fluid domain was included as a contact destination, due to the possibility of the collapsing wall contacting the basal surface, inducing mesh collapse.

A boundary load $P_{contact}$, given by Equation (31), was applied along the normal direction of the endocardial surface to counter its movement toward the contact destination surfaces:

$$P_{contact} = \begin{cases} k_{contact}(G_{contact} - G_{contact,lim}) & G_{contact,lim} \le G_{contact} \\ 0 & \text{otherwise} \end{cases} \tag{31}$$

$G_{contact}$ is the reciprocal of distance between surfaces, whilst $G_{contact,lim}$ is the set threshold (150 m^{-1}). $k_{contact}$ was set to 10^3 N mm^{-1}, which was sufficient to prevent the wall contact. To enhance the blood domain mesh deformation with the added cannula, parameter C_2 in Equation (20) was set to 100, introducing a non-linear stiffening to the mesh smoothing formulation.

2.2.4. Simulation Protocol

1. The dilated heart model was run for three cycles without the LVAD cannula added.
2. The LVAD was connected to the dilated heart model at the low-end speed of 2,100 RPM and run for three stable cycles.
3. The model was run for half a cycle (systolic) at 2,100 RPM, followed by a 300 ms duration where the pump speed was linearly ramped up to 150% of its original speed (3,150 RPM). This speed was held for three cycles, and the impact of this increased speed on the heart was observed. This was performed to determine whether aortic ejection ceased at high speed, as observed by Lim et al. in their simulation and animal experiments Lim et al. (2010).
4. To simulate suction or ventricular collapse, the LV preload was reduced significantly. Starting from the fourth cycle at 3,150 RPM pump speed, mitral stenosis was induced by increasing mitral resistance, R_{mi} by 25-fold and then running the model for three more cycles.

2.3. Mesh Settings

The mesh was constructed using a combination of tetrahedral, pyramidal and prism elements. A fluid boundary layer of two elements was placed at the fluid domain side of the fluid-structure interface. The outlet and inlet surface meshes were refined by setting their edges to an average element size of 0.1 cm. The resulting normal mesh is shown in **Figure 1C**. Mesh element size was determined as the length of the element's largest edge. The average mesh size for the myocardium was 0.52 cm whilst in the fluid domain it was 0.4 cm, which resulted in 22661 myocardial mesh elements and 44078 blood domain elements. A mesh convergence analysis was conducted on the standard model by reducing the average element size to 0.35 and 0.31 cm for the myocardium and fluid domains respectively, defined as the finer mesh setting from here on. The LVAD simulation was computed using a similar setting to the normal mesh to the standard healthy heart simulation, but with an average element size of 0.21 cm within the cannula. This resulted in 28005 myocardial mesh elements and 103569 blood domain elements.

Mesh convergence analysis was performed for the biventricular model using the following quantities:

1. Characteristic quantities, C_q

$$C_q = \frac{1}{N}\sum_{n=1}^{N}\frac{1}{M}\left(\sum_{m=1}^{M}\zeta_{mn}\right) \tag{32}$$

2. Relative root mean square, $\%\overline{RMS}$

$$\%\overline{RMS} = 100\left(\frac{\sqrt{\frac{1}{M}\sum_{m=1}^{M}(\zeta_{m,normalmesh} - \zeta_{m,refinedmesh})^2}}{\sqrt{\frac{1}{M}\sum_{m=1}^{M}(\zeta_{m,refinedmesh})^2}}\right) \tag{33}$$

where the ζ_{mn} quantities represent the local electrical activation time, myocardial displacement and fluid pressure at the times of peak LV ejection and peak LV filling rate at a set of 40x40x40 material datapoints generated across the biventricular structure. The magnitudes of the first derivatives of V_m, $\vec{u}_s$, $\vec{v}_f$ and p were extracted, and electrical activation time was determined by finding the time of maximum first derivative of V_m at each point.

2.4. Solver Settings

The physics involved in the model are summarized in **Figure 1A**. In brief, the myocardial AP (Equation 1) was triggered by the Purkinje current (Equation 2). AP activation triggers the generation of active stress in Equation (7). This active stress was in turn coupled to the transverse isotropic hyperelastic myocardial formulation by directly adding the active stress tensor (Equation 14) into the 2nd Piola-Kirchoff stress in Equation (14). The latter was determined from the derivative of the strain energy function with respect to the strain components, as indicated in Equation (14). The electromechanics formulations (Equations 1–14) are implemented only in the myocardial domain and solved in the material frame, to consider for gap junction-controlled AP propagation as described in Bakir and Dokos (2015).

The fluid physics (Equations 15–16) was solved in the spatial frame within a moving mesh. The fluid-solid coupling occurs at the endocardial surfaces (Equations 17–19), with the fluid velocity set to the endocardial wall velocity and fluid total stress, **S**, applied as a boundary load for the myocardial mechanics. Deformation of the mesh in the blood domain was governed by the hyperelastic formulation (Equation 20), with boundary conditions given by the endocardial displacement (Equation 13) while the basal plane was held fixed.

We utilized COMSOL Multiphysics 5.2a (COMSOL A.B., Sweden) for generating the geometry and mesh as well as solving all formulations. Fully-coupled PARDISO direct linear solver with an automatic damped Newton method were implemented, where all formulations were assembled in a single matrix and solved simultaneously together with preordering algorithm set to nested dissection multithreaded. Streamline diffusion and crosswind diffusion artificial stabilizations of the Navier-Stokes equations were applied, which enabled same-order velocity-pressure numerical integration and eased the requirement for a very fine fluid domain mesh. We adopted P1-P1 linear Lagrange elements for the Navier-Stokes equations and quadratic Lagrange elements for the membrane potential potential and recovery, *R*, variable as well as for all the solid mechanics formulations. All formulations were solved simultaneously and all variables were updated at each time step using a second order Backward Differentiation Formula (BDF) adaptive time-stepping method with an event detection algorithm implemented to ensure the BDF solver did not miss the stimulus events. Simulation results were output at 2 ms time steps.

3. RESULTS

3.1. Standard Biventricle Model

3.1.1. Overall Multiphysics Behavior

Electric activation, myocardial motion, and blood velocity vector streamlines are shown in the snapshots of model behavior in **Figure 3** and in the **Supplementary Animation 1**. The snapshots were taken at various phases in the third cycle of the steady cycle model.

The model started from the end-diastolic volume (EDV) phase, where vortices from the previous filling phase still persist in both ventricles. The stimulus began at the basal entries of the Purkinje fibers. As the myocardium began to electrically activate, a torsional motion was noted. The blood flow vortices began to diminish and the flow was gradually directed toward the outlets until ejection was initiated. As the heart reached total electrical activation, blood flow streamlines were oriented toward the outlets in near straight lines. The apex also moved toward the base during contraction. The straight streamlines gradually diminished as the heart entered isovolumic relaxation.

AP relaxation first occurred in the epicardium, whilst the endocardium repolarized last: the opposite of the activation direction. The filling was initiated even before the heart contraction fully relaxed. As the ventricles were being filled, blood vortices formed near the inlets. The vortices grew larger and moved apically. LV vortex shape was somewhat symmetrical whilst the RV displayed a more elongated and crescent-like shape due to the RV geometry. At the end of the cycle, the ventricles returned back to their starting EDV shape with larger vortex presents within the central region of the ventricular cavities. Smaller vortices can also be noted in the lateral regions nearing the myocardial wall, near the inlets.

3.1.2. Electrical Activation

Following external stimulation of the basal entries of the Purkinje network, the AP propagated through the branching fibers toward the apex. The Purkinje fiber network took 34 ms to be wholly activated. As the AP traveled through the PMJ edges the myocardium was excited. The site of first myocardial activation occurred at the septal region 20 ms after the Purkinje base was stimulated.

LV activation was initiated at three endocardial sites that merged into a single wavefront, which propagated radially toward the epicardium before finally reaching the base (**Figures 4A,B**). Epicardial breakthrough occurred first in the anterior and posterior interventricular sulci. These breakthroughs formed two wavefronts that propagated toward the unactivated regions in the RV. These wavefronts moved in a near tangential fashion at the free wall of the RV toward the base. Overall, it took 94 ms for the whole structure to be activated, with the RV free wall base the last activated region. On the other hand, the repolarization sequence was the opposite of the activation sequence such that it was initiated at the epicardium rather than the endocardium.

The action potential and active stress profiles are displayed in **Figures 4C–H**. The APD90 measured at the endocardium and epicardium was 324 and 266 ms, respectively. The presence of this APD gradient was sufficient to generate a recovery sequence opposite to that of the activation sequence. The Purkinje AP morphology exhibited an upstroke velocity twice that of the myocardium and the APD was longer (**Figure 4D**). At the Purkinje-myocyte junction (PMJ), the myocardial AP appeared similar to the Purkinje AP morphology. The time to peak active stress was 192 and 222 ms whilst the time to half relaxation was 142 and 156 ms in the epicardium and endocardium, respectively. These measures were extracted from three material points, located mid-apicobasal distance of the LV free wall, septum and RV free wall.

3.1.3. Mechanical Variables

The fiber, sheet, and normal-to-sheet components of the 2nd Piola-Kirchoff stress and Green-Lagrange strain tensors were extracted from three material points, located at the epicardium of the LV free wall, septum and RV free wall. These points were taken at midway between the base and apex.

To assess regional work, stress-strain loops were generated (**Figure 5**) as in Russell et al. (2012). The fiber direction was the dominant direction of deformation and stress. The LV free wall stress-strain loop was the largest compared to the those measured at the septum or RV free wall, indicating greater regional work in the LV free wall relative to the other regions. The stress strain loops for the sheet and normal-to-sheet components showed more skewed and distorted loops.

Torsional motion was assessed at three points in the myocardium: LV free wall, septum and RV free wall. These material points were positioned near the apical region at three quarters of the apicobasal distance. All points were placed at the epicardial surfaces. Torsion was mostly predominant in the LV free wall, with 16.5° counterclockwise motion when viewed upward from the apex, as shown in **Figure 6**. The torsion was substantially less in the RV free wall and septal region with magnitude of 5°. During the cardiac cycle, an apicobasal displacement of 1.2 cm was also noted in the model.

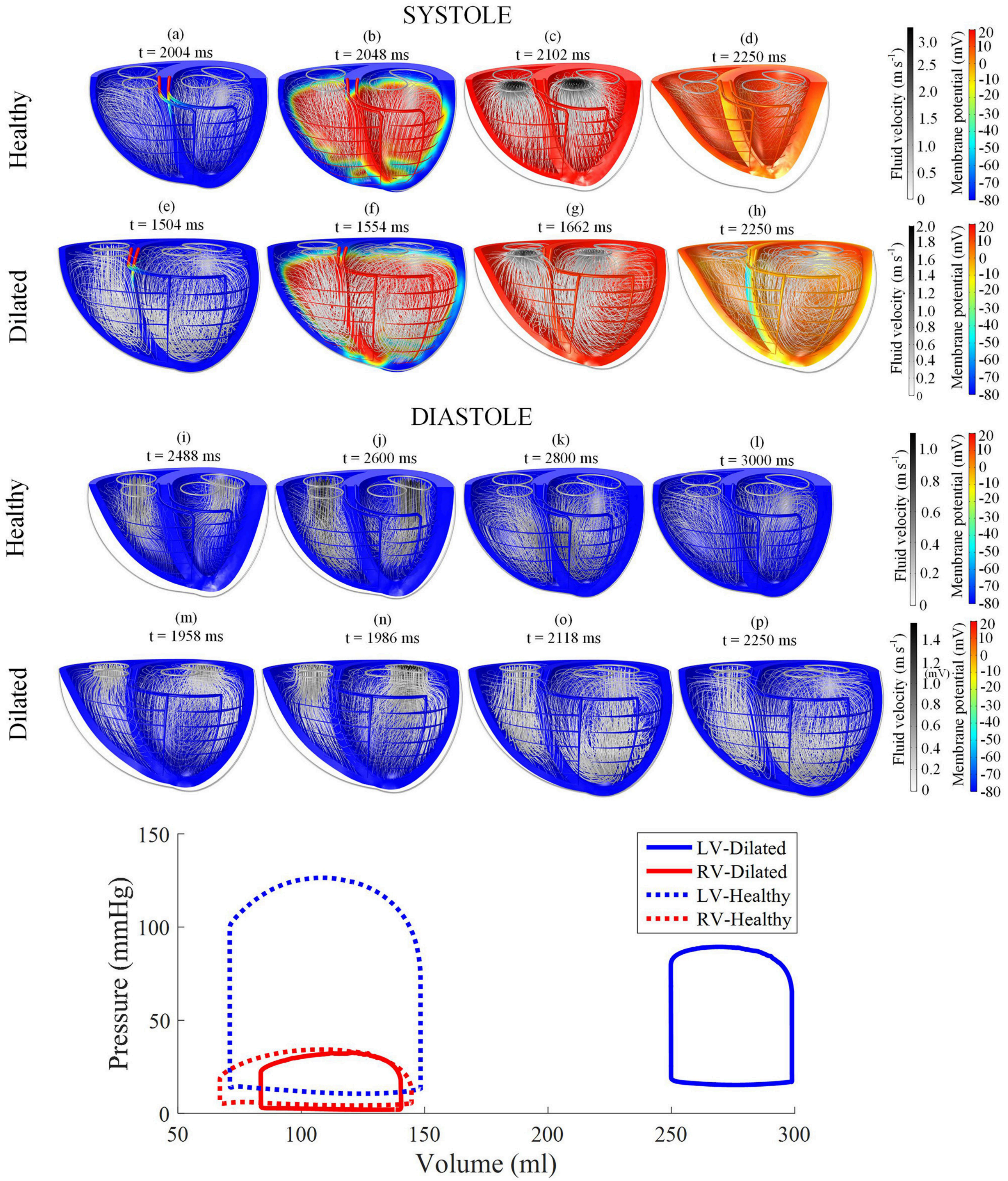

FIGURE 3 | Snapshots of the biventricular multiphysics model depicting the myocardial membrane potential, myocardial movement and fluid velocity streamlines taken at various time points during systole and diastole. **(a–d,i–l)** were taken from the healthy heart model. **(e–h,m–p)** were from the dilated heart model. The stimulus was applied at *t* = 2,002 ms for the healthy model and *t* = 1,502 ms for the dilated model. The pressure-volume relations are displayed at the bottom of the figure. Streamline tube radius is proportional to the blood velocity magnitude. The animations of healthy model and dilated heart model are available in **Supplementary Animations 1**, **2** respectively.

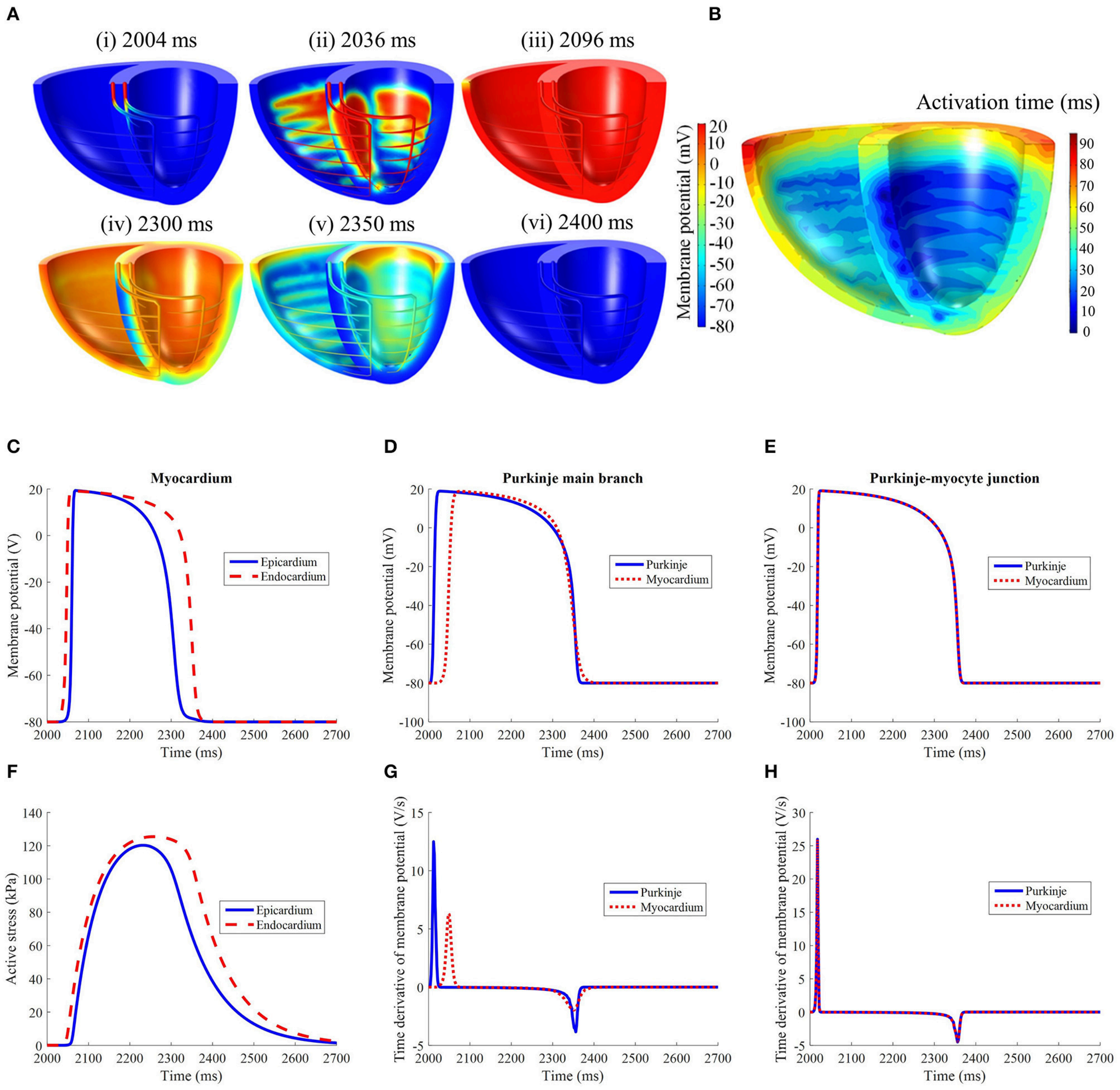

FIGURE 4 | **(A)** Electrical activation in the standard model following initiation at t = 2,002 ms. It should be noted that the recovery spreads in the opposite direction of activation. **(B)** Electrical activation time map in the standard model. Comparison of **(C)** LV free wall myocardium endocardial and epicardial, **(D)** Purkinje fiber, and **(E)** Purkinje-myocyte junction action potential profiles. **(F)** Active stress profile of the myocardium taken at the same location as **(C)**. The time derivative of membrane potential of the **(G)** Purkinje fiber and **(H)** Purkinje-myocyte junction, taken at the same locations as in **(D,E)**.

3.1.4. Hemodynamics

Table 1 lists the hemodynamic quantities measured at the third cycle of the biventricular model, compared against the normal range of healthy humans.

The pressure-volume (PV) loop plots in **Figure 3** depict the commonly observed rectangular shape for these loops. This indicates that the four cardiac cycle phases were simulated: isovolumic contraction, ejection, isovolumic relaxation, and filling. As the model reached stable cycles, the stroke volume of both ventricles equalized, as shown in the PV loop and **Table 1**. At maximum ejection rate, aortic velocity was 3.18 m s^{-1}, whilst the pulmonary velocity was 2.94 m s^{-1}, as shown in **Figure 3**. The mitral velocity was 1.04 m s^{-1} during peak filling rate, whereas the tricuspid inlet velocity was 1.07 m s^{-1}.

During peak ejection rate, a pressure gradient existed predominantly at the outlets (**Figure 7**). The pressure difference

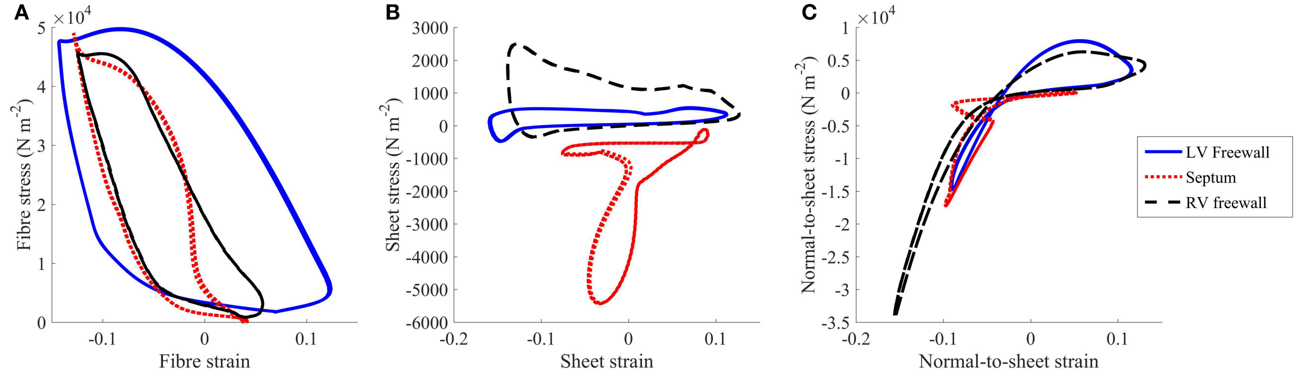

FIGURE 5 | Stress vs. strain plots taken from the **(A)** fiber, **(B)** sheet, and **(C)** normal-to-sheet components of the 2nd Piola-Kirchoff stress and Green-Lagrange strain tensors. The results are taken from the standard healthy model at the third cycle (t = 2,000–3,000 ms).

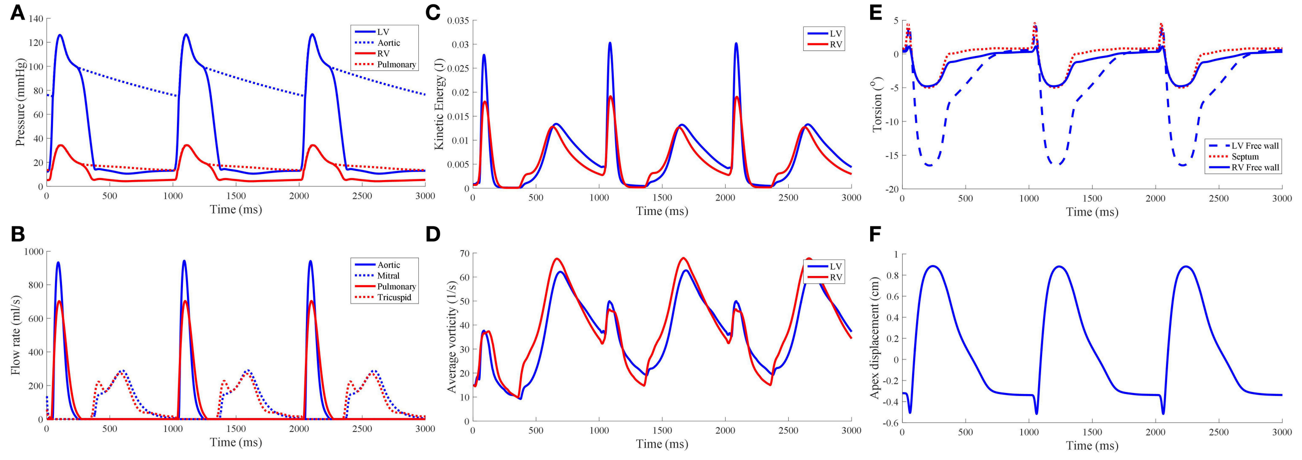

FIGURE 6 | Hemodynamic measures from the standard model, namely **(A)** pressure waveforms, **(B)** inlet and outlet flow rates, **(C)** blood kinetic energy, and **(D)** average vorticity. Global mechanical measures of ventricular torsion and apex displacement are displayed in **(E,F)**, respectively.

between the outlet and the inner cavity region were 31.3 mmHg and 28.9 mmHg in the LV and RV, respectively. During the filling phase, LV and RV pressure distributions showed more dispersed patterns, with the lowest pressure at the vortex centers. The LV, RV, aortic and pulmonary arterial pressure waveforms rose and dropped at nearly the same time (**Figure 6**). The time to peak pressure for the LV and RV also appeared to occur at a similar time, indicating a synchronous behavior. Similarly, peak filling rates occurred in near synchrony, where the time of ejection start and end occurred at the roughly the same time (outflow rates plot **Figure 6**).

The mean kinetic energy ($\overline{KE}$) of blood in the ventricles was computed using a similar method to Carlsson et al. (2012):

$$\overline{KE} = \rho_f \int |\vec{v}_f|^2 \, dV_{\Omega_f} \tag{34}$$

where ρ_f is the blood density, v_f blood velocity, and dV_{Ω_f} the ventricular fluid cavity. $\overline{KE}$ of both ventricles is shown in **Figure 6C**. $\overline{KE}$ was near zero prior to the start of the first contraction as the blood velocity magnitude was near zero, and was largest during the ejection phase of the cardiac cycle with the LV showing the larger magnitude of $\overline{KE}$. During isovolumic relaxation, $\overline{KE}$ dropped and rose again during the subsequent filling phase. As filling phase ceased, $\overline{KE}$ gradually declined but never dropped to near zero. Consequently, the maximum $\overline{KE}$ of the subsequent cycle's ejection phase was higher than the first cycle's.

The average vorticity, $|\overline{\omega}|$, was also measured by averaging the vorticity magnitude across the entire ventricular cavities. Vorticity, $\vec{\omega}$ was obtained via the the curl operator on the blood velocity vectors:

$$\vec{\omega} = \nabla \times \vec{v_f} \tag{35}$$

The $|\overline{\omega}|$ waveform showed two main peaks in both LV and RV (**Figure 6D**): (1) during the ejection phase and (2) during the filling phase. The filling phase exhibited a larger magnitude of $|\overline{\omega}|$, which is also qualitatively visible in the snapshots of **Figure 3** with the blood swirling motion.

TABLE 1 | Hemodynamics quantities obtained from the standard healthy model and clinical values from normal human. (Syst. - Systolic, Diast. - Diastolic).

Quantity	Standard model	Normal human range (mean ± standard deviation)	References
LV End diast.volume	148.39 ml	150 ± 31 ml, range 82–218 ml	Hudsmith et al., 2005
LV End syst. volume	71.02 ml	47 ± 15 ml, range 18–82 ml	Hudsmith et al., 2005
LV Ejection fraction	52.14%	69 ± 6 %, range 57–81%	Hudsmith et al., 2005
		57 ± 6%	Di Donato et al., 2006
LV stroke volume	77.38 ml	104 ± 21 ml, range 57–150 ml	Hudsmith et al., 2005
RV End diast. volume	144.70 ml	173 ± 39 ml, range 78–256 ml	Hudsmith et al., 2005
RV End syst. volume	67.05 ml	69 ± 22 ml, range 20–118 ml	Hudsmith et al., 2005
RV Ejection fraction	53.7%	61 ± 6 %, range 47–73%	Hudsmith et al., 2005
RV stroke volume	77.65 ml	104 ± 21 ml, range 52–128 ml	Hudsmith et al., 2005
Syst. aortic pressure	126.71 mmHg	113 ± 18 mmHg	Tandri et al., 2006
Diast. aortic pressure	75.15 mmHg	65 ± 9 mmHg	Tandri et al., 2006
Syst. pulmonary pressure	34.46 mmHg	28 ± 7 mmHg	Lankhaar et al., 2006
Diast. pulmonary pressure	13.44 mmHg	10 ± 3 mmHg	Lankhaar et al., 2006
LV End diast. pressure	10.57 mmHg	5–12 mmHg	Braunwald et al., 1961
RV End diast. pressure	4.23 mmHg	0–5 mmHg	Braunwald et al., 1961

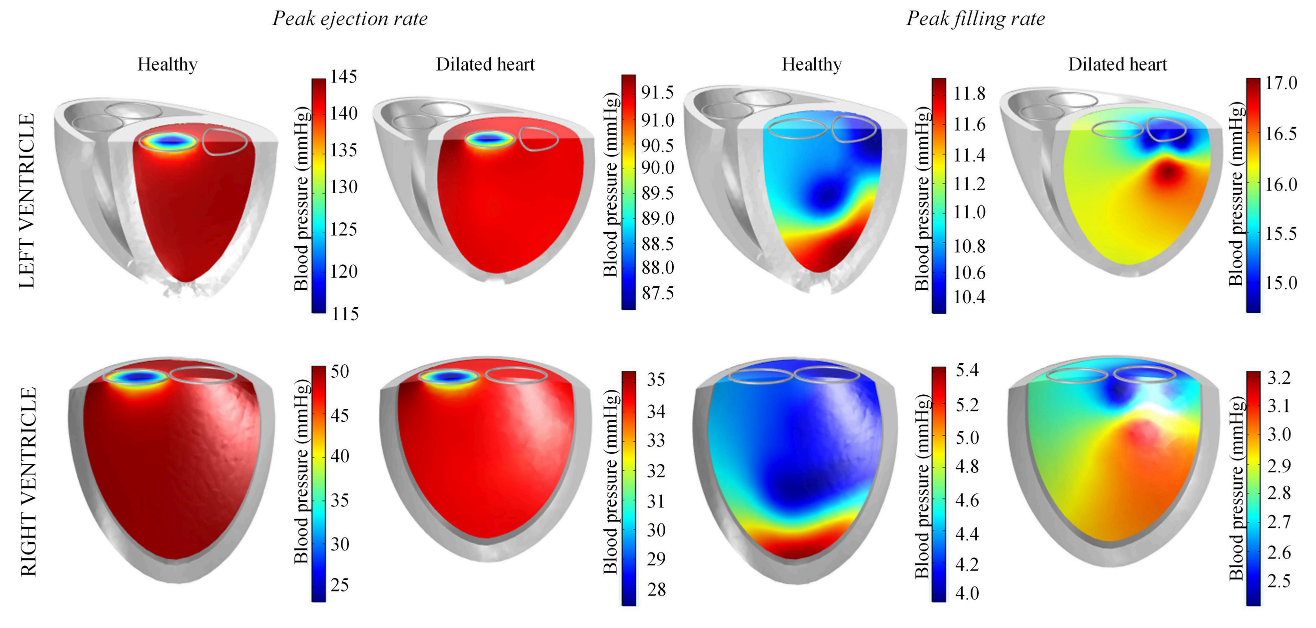

FIGURE 7 | Blood pressure distribution in the left and right ventricles of the standard healthy and dilated heart models taken at timepoints of peak ejection and filling rates.

TABLE 2 | Mesh convergence analysis: comparison of characteristics quantities and $\%\overline{RMS}$ comparing normal and finer meshes.

Metric	% Difference of characteristics quantities, C_q, between normal and finer mesh
Myocardial displacement (cm)	0.292
Fluid velocity (m/s)	1.636
Fluid pressure (mmHg)	0.0959
Metric	$\%\overline{RMS}$
Electrical activation time	3.47
Myocardial displacement at time of peak ejection rate	4.64
Myocardial displacement at time of peak filling rate	4.48
Fluid velocity at time of peak ejection rate	3.98
Fluid velocity at time of peak filling rate	7.25
Fluid pressure at time of peak ejection rate	0.012
Fluid pressure at time of peak filling rate	0.067

Following ventricular contraction, $|\overline{\omega}|$ increased momentarily before dropping significantly, but then increased again during the filling phase. Overall, the RV and LV $|\overline{\omega}|$ showed comparable magnitudes and waveform phases throughout the cardiac cycle, indicating synchronized behavior.

3.2. Mesh Convergence

Mesh sensitivity analysis showed good convergence ($< 5\%$) for global characteristic quantities, C_q, of the mechanical and fluid dynamics, as summarized in **Table 2**. A more local measure, $\%\overline{RMS}$ comparing normal and finer meshes, revealed a good convergence ($< 5\%$) for local electrical activation time, myocardial displacement, and fluid pressure at the time of peak LV ejection and peak LV filling rate. Whilst the fluid velocity showed a good $\%\overline{RMS}$ convergence at the time of peak LV ejection between the two meshes, the same measure was slightly higher at the time of LV filling rate.

3.3. LVAD Simulations

The model simulated the general impact of LVAD on the failing heart as well as, the impact of pump speed, reproducing ventricular collapse, when mitral stenosis was introduced.

3.3.1. Heart Failure Without LVAD

By reducing LV contractility and inducing heart dilation, the LV ejection fraction (EF) dropped to 16.5% and the LV end-diastolic volume (EDV) increased to 299 ml. EF was also reduced in the healthy RV to 40%. The LV pressure, along with aortic pressure, dropped to a peak systolic pressure of merely 89 mmHg, whilst the RV peak systolic pressure reached 32 mmHg.

The qualitative behavior is shown in the snapshots of **Figure 3** and the **Supplementary Animation**. Overall, minimal change was noted in the electrical activation sequence. The most obvious LV changes are a weaker contraction, blood vortices persisting even during systole, and a slower peak aortic ejection. On the other hand, the RV showed minimal changes relative to the standard model.

3.3.2. Low LVAD Pump Speed

Snapshots of the fluid streamlines in **Figure 8** during systole show that the aortic ejection persisted with the LVAD, albeit at lower velocity magnitude. Due to the presence of two outlets during systole, a low speed vortex region was observed in the LV free wall region. The smallest LV volume occurred at about the same time as the initiation of ventricular filling. As the LV was being filled, a fluid vortex formed at the LV free wall region and traveled toward the apex. Toward the end of the filling phase, the vortex separated into two main vortices: one near the basal LV free wall and one near the cannula. The RV showed typical systolic and diastolic streamlines as was seen in the healthy model. Throughout the cycles, the LV endocardium was well out of contact with the cannula.

Throughout the three cycles, the PV loops overlapped, indicating stability (**Figure 9A**). It can be seen that aortic ejection was preserved at this pump speed, although lower than the pre-LVAD setting. The aortic pressure peaked at 95 mmHg and reached a minimum of 86 mmHg, displaying less pulsatility (**Figure 10**). The LV pressure waveform observed at the LV base and the pressure waveform at the cannula showed synchronous characteristics, and were nearly identical. This was also illustrated in the LV pressure distribution of **Figure 11** where the LV pressure is lowest at the cannula. The LV pressure gradients were highest during the systolic phase ($\approx$ 9 mmHg) and lowest at diastole ($\approx$ 2 mmHg).

The LVAD model also provides measures of pump electrical current, pump flow rate and speed. With the proportional controller applied, the pump speed was nearly constant with very insignificant ($< 1\%$) drops during systolic contraction. The pump motor current showed a bump to 0.57 A from a baseline of 0.35 A, coinciding with increased pump flow rate to a peak of 6.2 L min^{-1} from a baseline of 2.2 L min^{-1}. Qualitatively, it can be seen that the pump motor current and flow rate waveforms coincided with the LV pressure waveform due to direct correlation with ΔP in Equations (25)–(28).

3.3.3. Sudden Increment of Pump Speed

A sudden increase of pump speed to 3,150 RPM immediately resulted in an increased aortic pressure, causing a cessation of aortic ejection in the subsequent cycles (**Figure 10**). Both peak LV and RV pressures also gradually dropped from cycle to cycle as the high pump speed was maintained. Moreover, LV pressure gradient between the cannula and ventricular base increased, as illustrated in the pressure snapshots of **Figure 11**. At the end of the third cycle, the pressure became negative in the cannula region (**Figure 11**).

As shown in **Figure 10**, the increase in speed was accompanied by an immediate increase in the pump flow rate from the previous baseline of 2.2 L min^{-1} to a new baseline of 7 L min^{-1}. During systole, the pump flow rate peaked at $\approx$9 L min^{-1} as opposed to 6.2 L min^{-1} at the lower, 2,100 RPM, speed. Consequently, the

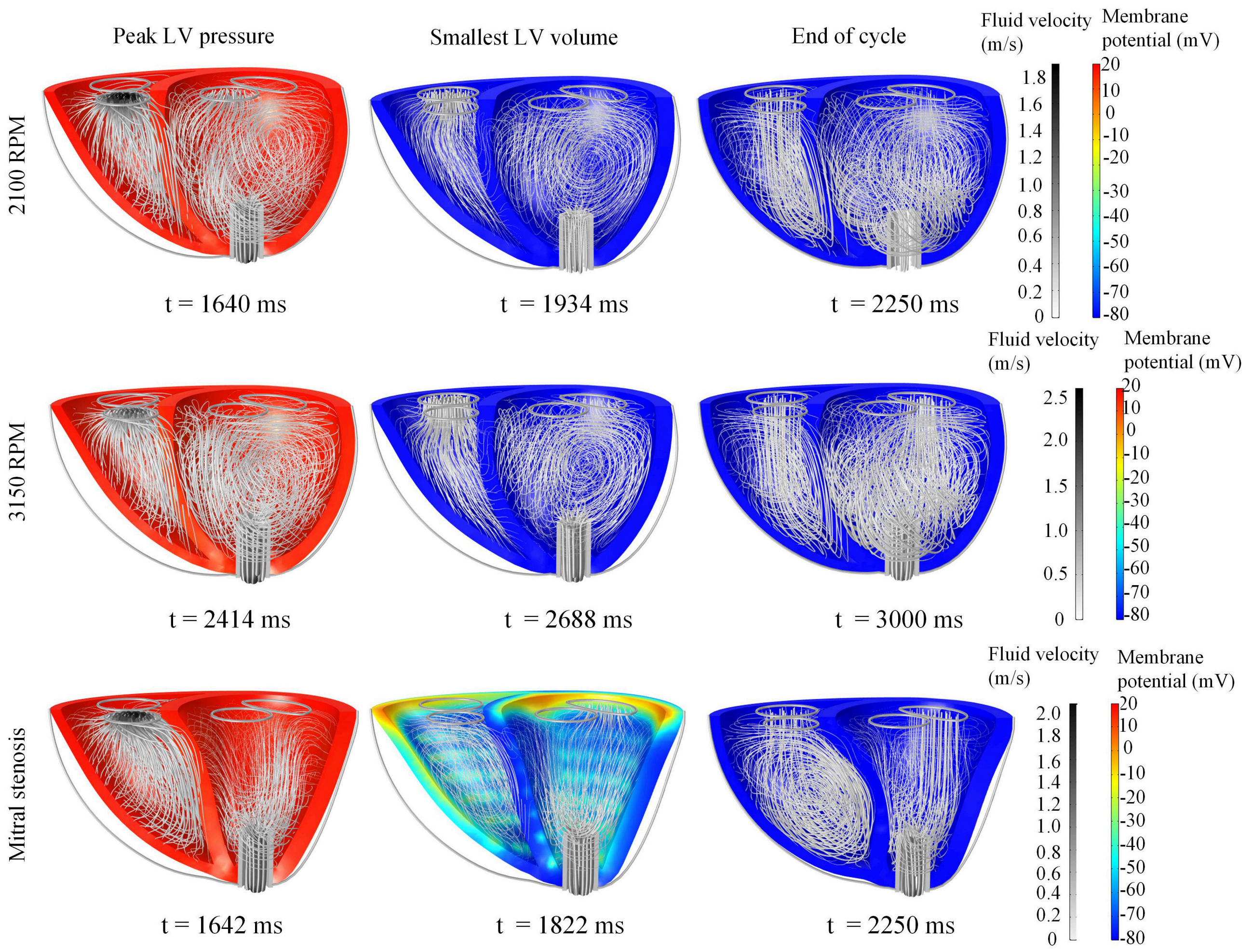

FIGURE 8 | Snapshots of the biventricular model with LVAD, depicting the membrane potential, myocardial movement and fluid velocity streamlines at the times of peak LV pressure, smallest LV volume, and end-diastole. The snapshots are taken at the third cycle of stable 2,100 RPM pump speed **(Top)**, fourth cycle following speed increment to 3,150 RPM **(Middle)**, and third cycle of mitral stenosis **(Bottom)**. Streamline density is proportional to the blood velocity magnitude. The animations of these snapshots are available in **Supplementary Animation 3** for the 2,100 RPM setting, **Supplementary Animation 4** for speed increment setting and **Supplementary Animation 5** for mitral stenosis case.

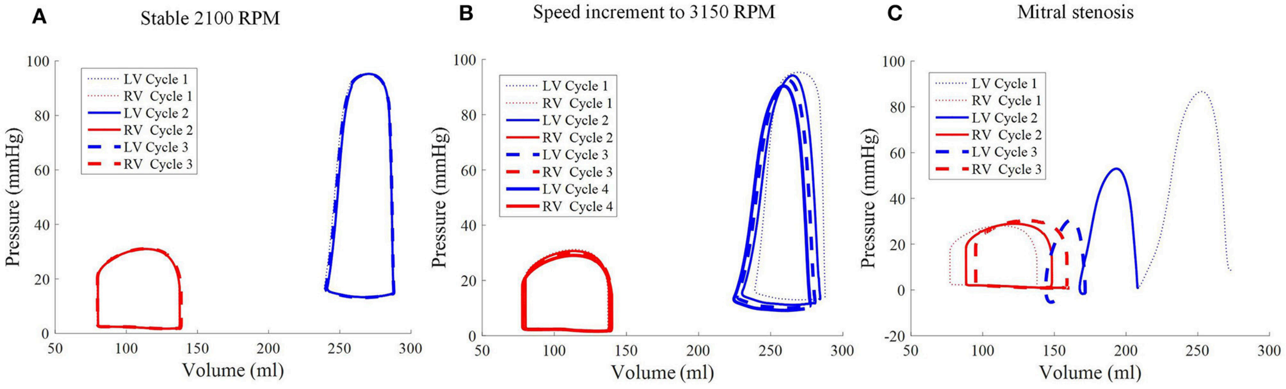

FIGURE 9 | Pressure-volume loops of the biventricular model with LVAD taken at stable 2,100 RPM pump speed **(A)**, speed increment to 3,150 RPM **(B)**, and mitral stenosis **(C)**. The loop shape transformed following the speed increase (cycle 2 onwards of middle figure) and introduction of mitral stenosis **(C)** from cycle to cycle.

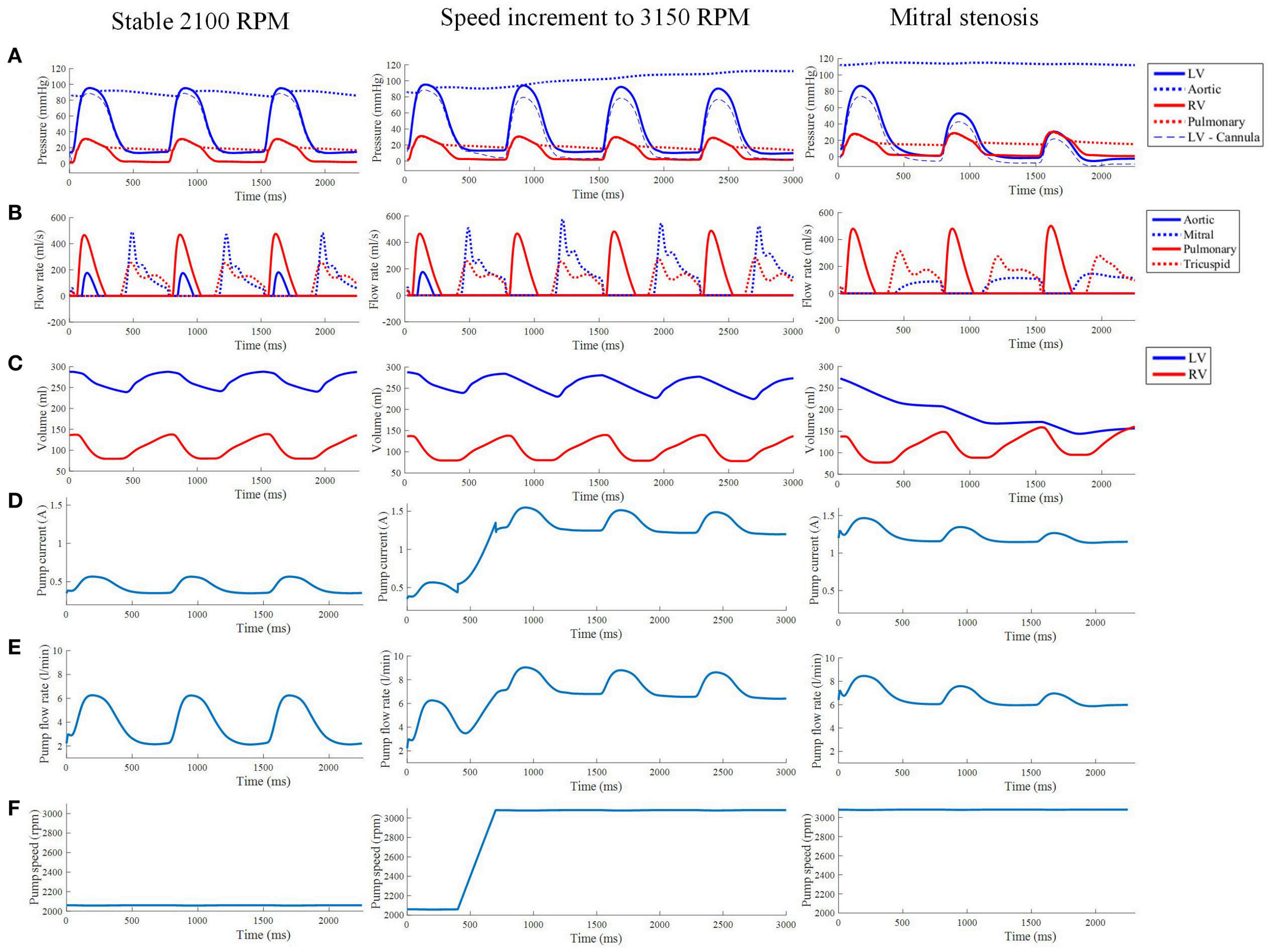

FIGURE 10 | (A) The LV, aortic, RV and pulmonary arterial pressure waveforms from the third cycle of stable 2,100 RPM pump speed, speed increment to 3,150 RPM, and mitral stenosis. **(B,C)** The aortic, mitral, pulmonary and tricuspid flow rate waveforms **(B)** along with ventricular volume waveforms **(C)** with similar LVAD settings as the top row. The pump current **(D)**, pump flow rate **(E)**, and pump speed **(F)** waveforms from the third cycle of stable 2,100 RPM pump speed, speed increment to 3,150 RPM, and mitral stenosis.

pump current also elevated to a baseline of 1.2 A with a maximum current of 1.5 A.

With the cessation of aortic ejection, the blood flow streamlines during systole were directed toward the cannula at a higher velocity, as shown in the snapshots in **Figure 8**. Slight swirling was also observed in the region surrounding the cannula. Similar to the low speed setting, the smallest LV volume occurred at about the same time as the mitral filling phase. At end-diastole, both ventricles exhibited fluid vortices. The cannula and the LV endocardium were not in contact throughout the simulation (**Figure 8**).

As the cycles went on, the LV pressure-volume loops gradually became more triangular (**Figure 9B**). The LV EDV also gradually reduced, along with overall LV blood pressure characteristics. The increased speed also appeared to improve RV function, with enhanced ejection fraction and lower peak RV pressure. The decongested LV also resulted in a small, yet gradual, wall collapse as quantified by the decrease in distance between the LV free wall and septum (**Figure 12**).

The stress-strain loops measured at the epicardial sites along the mid-apicobasal distance, LV and RV free walls and septum, suggest a potential change in regional work in the ventricles. The fiber components of the stress-strain loop showed a gradual shift to the left as the speed increased, especially for the LV free wall (**Figure 13**). On the contrary, minimal change was noted in the RV stress-strain loops.

3.3.4. Mitral Stenosis With LVAD

In the first cycle with mitral stenosis, the systolic measures did not appear to be affected by the stenosis. During diastole, the introduction of mitral stenosis severely impeded the inflow into the LV, resulting in an immediate imbalance between the pump flow rate and input flow rate into the pump. As such, the LV collapsed as the cycles continued.

The major impact of mitral stenosis appeared from the second cycle onwards, in which the ejected blood was not replenished in the LV for the subsequent cycles, resulting in a lower LV EDV in subsequent cycles. Consequently, the LV pressure generated from

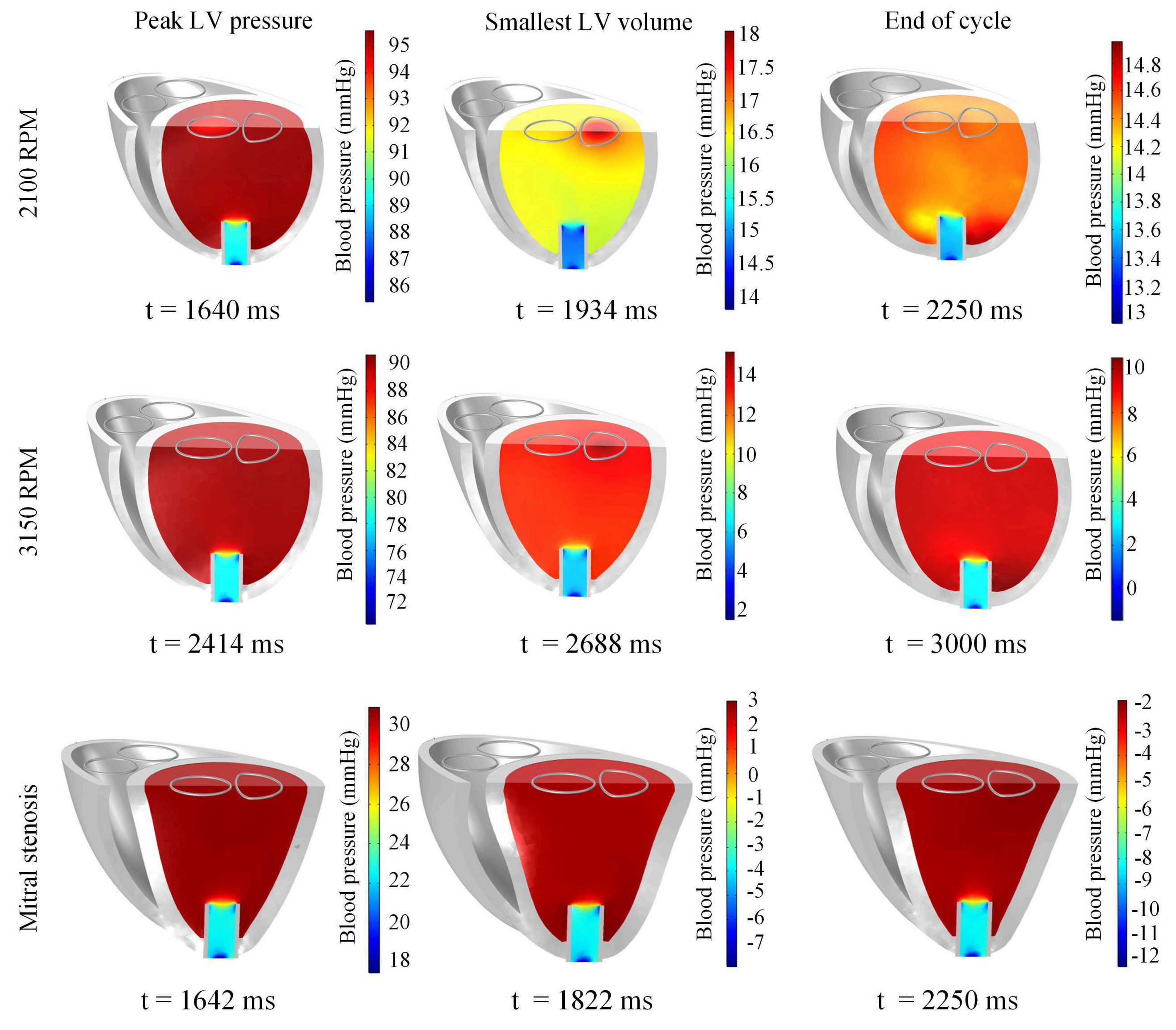

FIGURE 11 | Snapshots of the biventricular model with LVAD depicting the LV blood pressure distribution at the times of peak LV pressure, smallest LV volume, and end-diastole. The snapshots are taken at the third cycle of stable 2,100 RPM pump speed **(Top)**, fourth cycle following speed increment to 3,150 RPM **(Middle)**, and third cycle of mitral stenosis **(Bottom)**.

the second cycle onwards was significantly lower (52.9 mmHg) than prior to mitral stenosis (86.6 mmHg). The LV pressure dropped even further in the third cycle to 30 mmHg, nearly similar to the RV pressure, as shown in **Figure 9C**.

The collapsing LV also resulted in the LV PV loop to be smaller than the RV (**Figure 9**). The LV PV loop also shifted downwards and leftward toward the negative pressure region. The RV PV loop was also affected, as it shifted to the right, since the RV started to dilate with a slight increase in peak RV pressure. In addition, the fiber direction stress-strain loop, exhibited in **Figure 13**, also shrank significantly for the LV free wall and septum across all strain and stress tensor components.

The snapshots in **Figure 8** showed an obvious shift in the septum orientation toward the LV. Mitral flow was noted to initiate earlier, and last for a longer duration (**Figure 10**). The smallest LV volume occurred at an earlier phase of the cardiac cycle, compared to previous settings. During end-diastole, the fluid vortices were notably absent in the LV, and only present in the RV. The snapshots of LV blood pressure distribution in **Figure 11** also revealed greater negative pressure, with the filling phase showing an entirely negative pressure throughout the whole chamber. With the ventricular wall collapsing into the LV, it can be seen that the endocardium was in contact with the cannula throughout the cardiac cycles. The distance between LV free wall and septum was reduced significantly in the presence of mitral stenosis (**Figure 12**).

The reduction in LV pressure also manifested in a reduced peak pump flow rate and pump current (**Figure 10**).

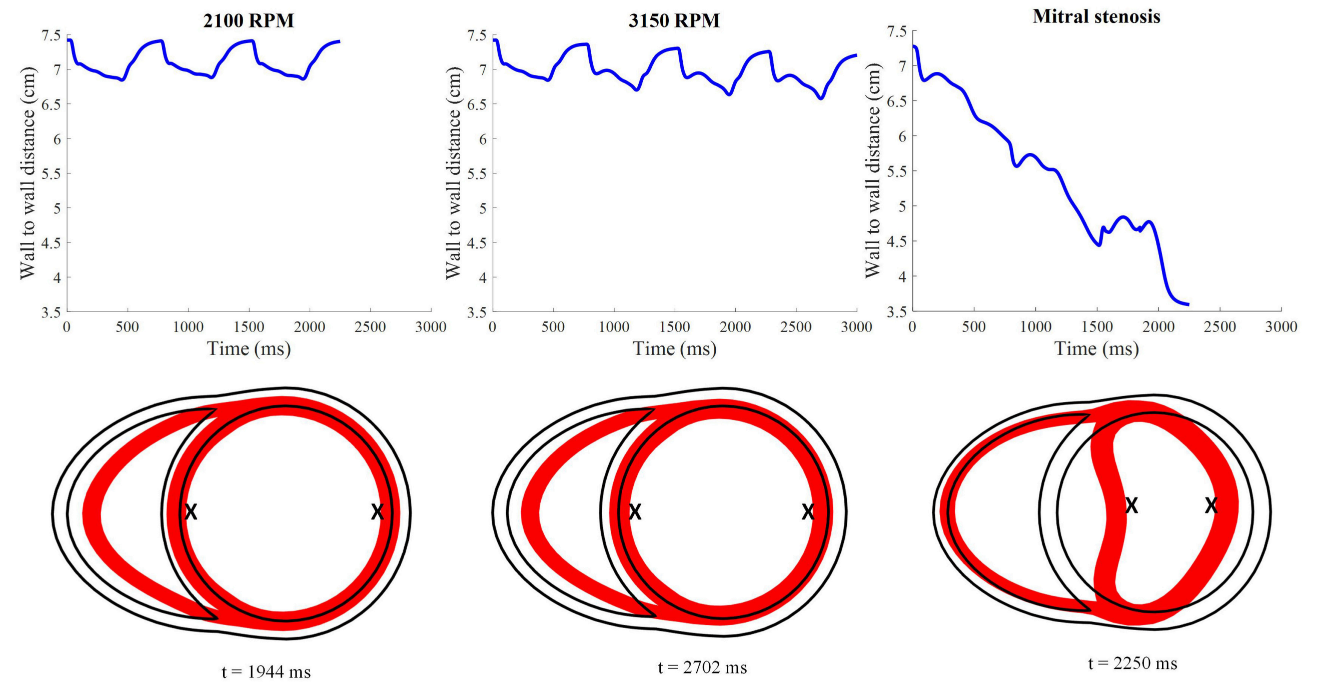

FIGURE 12 | Distance between the LV free wall endocardium and LV septal endocardium midway between the apex and the base. The lower 2D plots depict the cross-section of the ventricles taken at midlevel along the apicobasal direction for all LVAD simulation settings. The red surface indicates the myocardial cross-section at time of smallest LV whilst the black outline indicates the myocardial cross-section at time *t* = 0. "X"; denotes the two points used to calculate the wall to wall distance.

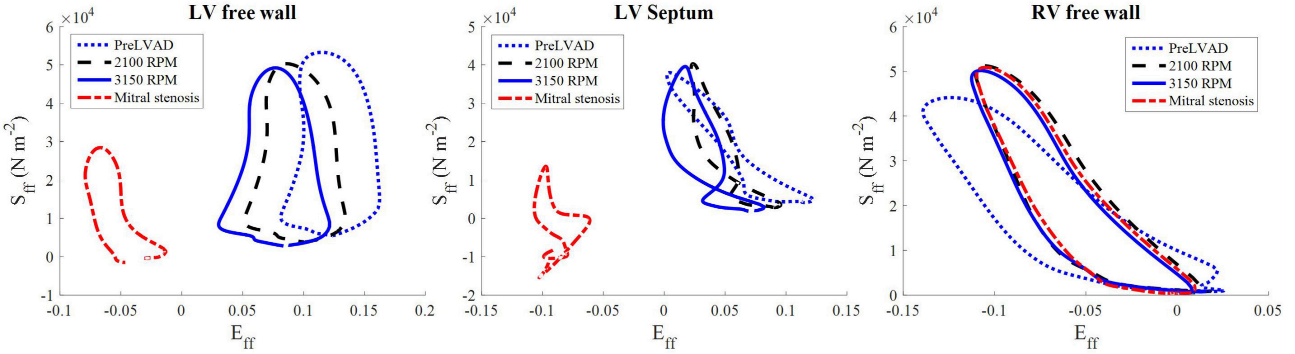

FIGURE 13 | The stress-strain loops of the LVAD simulations at the third cycle (*t* = 1,500–2,250 ms) of stable 2,100 RPM pump speed **(Left)**, speed increment to 3,150 RPM **(Middle)** at (*t* = 2,250–3,000 ms), and mitral stenosis (*t* = 1,500–2,250 ms) **(Right)**. S_{ff} is the 2nd Piola-Kirchoff stress and E_{ff} is the Green-Lagrange strain tensor components along the fiber direction.

Nevertheless, the baseline pump flow rate and current were maintained at approximately 6 L min^{-1} and 1.3 A, respectively. The waveforms also became less pulsatile with the onset of ventricular collapse.

4. DISCUSSION

In this study, we developed a cardiac multiphysics modeling framework for biventricular electrical, mechanical and fluid dynamics physics in a healthy heart. The modeling framework was then applied to simulate a failing heart with LVAD support. This framework can be applied in future pre-clinical investigations of device performance under various pathological conditions.

4.1. Standard Biventricular Model

4.1.1. Electrical Characteristics

The simulated LV activation pattern is nearly radial and the RV activation pattern is nearly tangential ending at the basal region, whilst the interventricular septum is predominantly activated in a left to right sequence. The first epicardial breakthrough occurred in the RV due to its thinner wall structure. As such, the model's electrical activation reproduced normal human electrical activation sequence (Durrer et al., 1970). Furthermore, the total duration of electrical activation, 94 ms, falls within the range of the QRS duration in healthy humans (80-120 ms), which corresponds to the ventricular activation time (Guyton and Hall, 2006). The model also reproduced the transmural APD gradient observed in the healthy myocardium. In addition, AP repolarization began from the epicardium and ended at the endocardium, the opposite direction to the activation. Such behavior has been recorded in ventricular tissue strips from rejected donor hearts by Glukhov et al. (2010).

The Purkinje fiber network implementation enabled simulation of a healthy activation sequence, and can be applied in future studies to simulate diseased activation such as bundle branch block by simply disabling select branches of the Purkinje tree. The Purkinje fiber APD is longer than that of the nearby contractile myocardium to prevent retrograde activation (Vigmond and Stuyvers, 2015). Although current flow from the myocardium to the Purkinje fibers was not included in this study, retrograde activation can be considered in the future. For example to simulate ectopic beat re-entry, an additional current could be added to the Purkinje AP model of Equation (2) (Vigmond and Stuyvers, 2015).

AP propagation physics was formulated in the material frame to emulate gap junction controlled propagation as described in our previous work (Bakir and Dokos, 2015). Since the resistivity of the gap junctions is higher than the intracellular space of cardiomyocytes, the myocardial substrate can be treated as network of interconnected resistors whose total electrical resistance remains unchanged as the structure deforms. This phenomenon has been experimentally observed in a number of animal species by Penefsky and Hoffman (1963), who measured papillary muscle conduction velocity while they were stretched. For this reason, formulating the electrical propagation in the material frame represents a more suitable approach. Although, the use of material frame-based formulation may have an insignificant effect on rhythmic activation patterns, we have shown that in more complex electrical activation scenarios, such as arrhythmias, the effect is prominent (Bakir and Dokos, 2015).

4.1.2. Mechanical Variables

The predicted apex to base shortening of 1.2 cm is within the range measured in healthy humans (Alam et al., 1990). The torsion was predominantly within the LV due to its larger muscle mass, as opposed to the RV. The LV wall torsion magnitude was within the range reported by Henson et al. (2000). On the other hand, RV torsion measures have been under-reported in the literature. Nonetheless, it is expected that the RV exhibits lesser twist as its thinner wall accommodates lesser circumferential fibers and more oblique fibers (Pettersen et al., 2007). The RV also restricted the septal motion generating lesser torsion in the septum as opposed to the LV free wall. Thus, the common healthy ventricular mechanics were observed in our biventricular model.

Stress-strain loops are indicators of regional ventricular work, which may be correlated to myocardial oxygen consumption and potential structural remodeling (Russell et al., 2012). Our model predicted a relatively large and box-shaped loop for the LV free wall, indicating a greater work load on this section of the myocardium to eject blood, compared to those at the LV septum. This is in agreement with a clinical study that reported regional work is larger in the LV free wall compared to LV septum (Russell et al., 2012). The predicted RV free wall stress-strain loop was smaller than the LV free wall. This is due to the lower afterload pressure imposed on the RV, even though both ventricles produced a similar cardiac output.

4.1.3. Hemodynamics

Global hemodynamics measures predicted by our model were similar to normal quantities reported in healthy humans. The simulated LV ejection fraction and stroke volume were on the lower end of normal ranges, possibly due to the smaller amount of myocardial thickening exhibited by our model. We speculate that this in turn was due to our assumption of transverse isotropy. A multiscale model by Washio et al. (2013) includes tissue level structure in its myocardial mechanics formulations, enabling modeling of cleavage planes. This facilitates sheet sliding, which helps to eject an additional 7.5 ml of blood compared to modeling without this level of detail. However, inclusion of realistic microstructure will hugely increase computational workload. Our fixed constraint at the base and lack of geometrical outflow tract may also impede further motion of the ventricles, thus rendering a lesser amount of myocardium usable for volume displacement, and therefore blood ejection.

Our simulations predicted a slightly higher pressure gradient within the LV ($\approx$ 31 mmHg) than typical values reported for healthy humans ($<$ 30 mmHg), even though the outlet boundary area is within the healthy human range (Westaby et al., 1984; Geske et al., 2011). Nevertheless, our predicted value does not exceed the severe obstruction threshold of 50 mmHg defined by Geske et al. (2011). As a consequence, the predicted peak velocity of inlet and outlet flows are also higher than normal (Mowat et al., 1983). We hypothesize that this disparity is due to our simplified generic structure with a flat ventricular base, whilst in reality the structure is slightly angled and funnel-like, which may help direct the flow (Greenbaum et al., 1981). This issue could be resolved when the framework introduced here is applied to an anatomically realistic structure for future patient-specific simulations.

The filling phase FSI has been of considerable interest in cardiac mechanics research, particularly the formation of a vortex ring and its possible link to cardiac efficiency (Hong et al., 2008). In our healthy simulation, a vortex ring formed in each of the ventricles during the early filling phase, growing in size as they approached the apex. As the filling ceased, the vortex ring moved to the basal region near the outlets. This simulated LV behavior matched the description reported in the echocardiographic study of Hong et al. (2008), which attributed the vortex to the occurrence of a shear layer between the high speed mitral jet and the low speed blood movement in the cavity, causing the mitral jet to roll up, forming a vortex. These investigators reasoned that the vortex helps to maintain kinetic energy of the blood prior to ejection.

Blood $\overline{KE}$ and $|\overline{\omega}|$ have been proposed as potential markers for predicting cardiac dysfunction (Carlsson et al., 2012). The systolic and diastolic peaks of $\overline{KE}$ have been calculated clinically from 4D flow MRI data (Carlsson et al., 2012). Whilst our model's RV $\overline{KE}$ is similar in behavior to that reported by Carlsson et al. (2012), this is not the case for the LV. The clinical measurement revealed the LV $\overline{KE}$ is larger during diastole than during systole, which is not seen in our simulations. Carlsson et al. (2012) argues that two mechanisms contribute to the diastolic $\overline{KE}$: elastic recoil of the myocardium and the displacement of the ventricular base into the position previously occupied by the atria. Since the atrial structure is not incorporated in our model, this latter effect cannot be simulated.

The $\overline{KE}$ never dropped to zero, which can be attributed to the vortex present in the chambers during diastole. The vortex has been suggested to aid energy and momentum transfer in the fluid, and the vorticity magnitude has been proposed as a measure to predict LV diastolic dysfunction caused by ventricular interdependency in cases of RV failure (Schäfer et al., 2016). Both RV and LV $|\overline{\omega}|$ magnitude was largest during the filling phase as expected, due to the presence of rotating flow observed in **Figure 6**. A slight bump was observed during systole, which can be caused by the fluid being pushed against the flat fixed basal boundaries. It should be noted that the atrial contraction will generate an additional vortex, affecting $|\overline{\omega}|$ (Schäfer et al., 2016).

In comparison to the passive filling vorticity measured by Schäfer et al. (2016) in healthy human LVs ($\approx$ 30 1/s), LV $|\overline{\omega}|$ simulated by the standard model was higher. We hypothesize that this discrepancy is due to filtering out the larger vorticity magnitude ($>$ 70 1/s) during clinical image analysis, in addition to the lack of internal ventricular structures such as valves and papillary muscles in our model geometry, which could affect the vortex strength. Although both $\overline{KE}$ and $|\overline{\omega}|$ did not entirely replicate realistic measurements, the details presented here could provide basic insights on how disease states affect blood energetics. More accurate measures would be obtained should a more realistic structure be implemented.

4.2. LVAD Simulation

We simulated the success of the LVAD in restoring the aortic pressure in a failing heart. An immediate reduction in the native aortic flow rate was also observed. Moreover, our computational simulations demonstrated that an imbalance of pump flow rate and LV filling rate can result in ventricular collapse, a phenomenon known as suction, which can impede the pump's performance. As such, our modeling framework can be applied as a simulation tool to optimize LVAD design, as well as predict and investigate any clinical risks for various heart conditions prior to clinical studies, considering LVAD is designated as high risk (Class III) device by the US FDA.

By simply adjusting the geometry and myocardial contractile strength parameter, k_{Ta}, the standard model was modified to simulate typical characteristics of LVAD recipients. The diseased heart model's LV EF (16.5%), LV internal diameter (7.4 cm) and LV EDV (299 ml) are within the ranges observed in severe dilated heart failure patients (Dandel et al., 2008). Therefore, the standard model can be easily modified to simulate behaviors of relevant diseases.

4.2.1. Impact of LVAD on Hemodynamics

Computational electrical-FSI simulations offer advantages over most imaging modalities to investigate fluid velocity profiles in the presence of LVADs. This is due to their superior resolution and no risk of image artifacts brought by the metallic implants (Carr et al., 2010). Analysis of the fluid streamlines can be beneficial to determine risk of thrombosis associated with cannula design and placement, as was performed in the 2D modeling study of Ong et al. (2013).

Following LVAD placement, our model displayed an immediate increase in aortic pressure due to the additional input on the systemic circulation by the LVAD outflow. As such, higher LV pressure was needed to enable opening of the aortic outlet. However, with a weaker contractility, the LV was not capable of generating sufficient pressure to overcome the restored aortic pressure. This explains the reduction in the aortic flow rate and aortic ejection duration. With further increase in pump speed, the aortic pressure rose more, resulting in a complete cessation of aortic ejection. Aortic valve closure is a known complication in many LVAD recipients as it may result in valve fusion, thus requiring speed adjustment as a prevention (Rose et al., 2000). Therefore, using computational simulations under patient-specific settings, it is possible to determine whether a safe window of pump speed operation exists for a certain ventricular state prior to clinical implantation.

Our simulations predicted separation of pressure waveforms measured at the LV base and cannula as the pump was maintained at a higher pump speed. Such behavior has been observed in a canine experiment where separation of pressure waveforms was associated with suction or overpumping characteristics (Salamonsen et al., 2015). Following implantation, the normally rectangular LV pressure-volume loop transformed into a more triangular shape. This was due to the loss of isovolumic phases, since the LVAD model is based on a continuous flow pump. The triangular shape became more prominent at a higher pump speed as the LV pressure generation capability was negated by the stronger LVAD flow rate.

Under reduced LV filling induced by mitral stenosis, the LV pressure-volume loop was severely depressed because the pump flow rate was larger than the inflow rate supplied by the left atrium. Therefore, the LVAD emptied the LV, causing it to collapse. Consequently, native heart pumping capability was impaired, as predicted by the end-systolic pressure volume relation (ESPVR), which linearly relates the maximum pressure that can be generated with the LV volume. During LV collapse following mitral occlusion, the LV is held at an extremely low volume, so, according to the ESPVR it is expected that the generated LV pressure is low (Guyton and Hall, 2006).

Increasing the LVAD pump speed appeared to result in diminished diastolic vortex formation, as shown by the fluid streamlines in **Figure 8**. This is further aggravated in the collapsed LV induced by mitral stenosis. We speculate that this change can be attributed to the LV geometry becoming less ellipsoidal, which could reduce space for the vortex to form. This effect is especially exaggerated in the collapsed LV.

4.2.2. Impact of LVAD on Myocardial Mechanics

Following the increase in LVAD pump speed, our simulations revealed that the stress level experienced by the LV wall gradually dropped from cycle to cycle. The stress-strain loops assessed along the fiber direction exhibited a leftward trend, and the local strain was reduced, which are the result of LV decongestion by the LVAD.

On the contrary, our model predicted only a small drop in RV stress level following LVAD intervention, whilst the RV strain components were unchanged. This is similar to predictions by the modeling study of Sack et al. (2016) that RV stresses remain unaltered following LVAD intervention. The improvement in the RV PV loop under LVAD support, shown by our simulation, may only be due to the alteration in septal stresses and strains due to the unloaded LV. As such, only a slight PV improvement was noted and the RV free wall mechanical work remained unchanged.

When LVAD support was simulated in the presence of mitral stenosis, the LV was substantially drained and all LV stress-strain tensor components reduced significantly, indicating a severe reduction of LV mechanical regional work. The LV chamber lost its ellipsoidal geometry and its diameter was reduced significantly. At the apex, mechanical contact was observed between the endocardium and the cannula. If such a suction event is not alleviated, myocardial injury may occur and could trigger arrhythmia (Vollkron et al., 2007).

4.2.3. Behavior of LVAD Variables

In our simulations, pump motor current and flow rate waveforms approximately followed the LV pressure waveform. During contraction, pump flow rate increases due to reduced pressure difference between the aorta and the LV that needs to be overcome by the pump. The increase in pump flow results from the increased hydraulic loading on the pump impeller, as noted by the torque transfer formulation in Equation (27) (Lim et al., 2010). Therefore, the pump motor current has to increase as well to generate more torque to overcome the increased hydraulic loading.

At higher pump speed, the simulation predicted loss of pulsatility (**Figure 10**), which coincided with the loss of peak ventricular pressure. Since the pump produces stronger torque at higher speed, the increased hydraulic loading can be easily overcome by the pump without requiring an extensive increase in pump current during systole. The collapsed LV imposed greater resistance to the pump flow rate, causing the pump flow pulsatility to be severely weakened.

Pump current waveforms have been used as a measure to detect suction events in the heart under LVAD support (Yuhki et al., 1999). As the pump current waveform shows good agreement with the LV pressure waveform, this measure can be used to detect suction events, heart rate and aortic valve closure. The pump current is a non-invasive measure that is readily available in the pump. Furthermore, it does not suffer baseline drifting, typically experienced by pressure sensors (Troughton et al., 2011). Our biventricular model can be applied as a simulation tool to aid design and test better controllers capable of detecting these events and providing counter measures, such as lowering the pump speed or alerting medical personnel (Stevens et al., 2014; Robertson et al., 2017), before the patient situation gets worse.

Overall, we observed a stable pump speed throughout the simulation, with the pump speed was nearly similar to the target speed, ω_{set} as shown in **Figure 10F**. Whilst Lim et al. (2010) employed a proportional-integral (PI) controller to maintain the speed, we did not model the integral component. Nevertheless, we did not observe any major discrepancy in the pump speed relative to ω_{set}, indicating a sufficient controller function for the simulation.

4.2.4. Impact of LVAD on the RV

Our simulations predicted a small improvement in the RV function with LVAD support, in particular a stroke volume increase and a drop in peak RV pressure to a healthy level. Further improvements were observed with an increase in pump speed. These improvements may be attributed to increased RV filling subsequent to LVAD-enhanced LV output, as well as the direct result of reduced afterload (Morgan et al., 2013). As the LV decompressed, LV filling improved and subsequently reduced the pulmonary arterial pressure. With reduced afterload, RV ejection fraction is expected to improve according to the end-systolic pressure volume relation (Maughan et al., 1984).

On the contrary, when mitral stenosis was induced in the simulation, RV dilation and increased peak RV pressure reappeared. The mitral stenosis essentially increased RV afterload, preventing more blood from leaving the pulmonary circulation. As such, RV pressure increased to counter the increased afterload. With the baseline pump flow rate barely changed and the increased afterload impeding RV outflow, the RV began to dilate. This helped push the septum further into the LV chamber as the LV collapsed.

Clinically there is considerable interest in the impact of LVADs on the RV due to the significant pool of LVAD recipients developing RV failure (Neyer et al., 2016). Nonetheless, a clinical observation by Morgan et al. (2013) noted that LVAD actually improved RV function in some patients. RV failure may be caused by an undetected RV disease that is masked by more significant LV failure. LVAD support improves the venous return to the RV; however this may aggravate the undetected RV disease as a weaker RV will be unable to cope with the improved preload. This could be investigated in future with this model to optimize LVAD settings prior to implantation.

To our knowledge, previous finite element models of heart-LVAD interaction did not consider the biventricular interaction. For example, the study by McCormick et al. (2013) expands the LV FSI model of Nordsletten et al. (2011) by adding an immersed cannula structure, but does not implement any electrophysiology physics. Other studies by Sack et al. (2016) and Heikhmakhtiar et al. (2017) simply modeled the LVAD contribution by adding a constant flow from the heart and into the aortic circuit of the four-chamber Living Heart Model (Baillargeon et al., 2014) and the Gurev et al. (2011) biventricular model, respectively.

Nevertheless, the cannula itself and the fluid dynamics were not modeled in these studies.

The framework presented here offers a number of advantages over previous heart-LVAD models. In particular the capability to simulate

1. the impact of abnormal electrical activation on LVAD pump performance. As noted by Robertson et al. (2017), LVAD recipients have high arrhythmic tendency that may result in RV dysfunction and suction events.
2. pump current behavior throughout the cardiac cycle. Pump current provides a minimally invasive measure that can be utilized in future pump controller designs to predict the present state of the heart.
3. LVAD impact on the RV. This allows study of various metrics to predict vulnerability of LVAD-induced RV failure in future. Criteria could be developed based on these metrics to support the clinical decision whether an LVAD or biventricular assist device (BiVAD) should be implanted in a patient to ensure optimal management.
4. the impact of cannula shape and positioning on LVAD performance. Non-optimal cannula placement can reduce pump performance and has been suggested to induce thrombosis (Ong et al., 2013; Neyer et al., 2016).

Considering the LVAD is classified as high risk class III medical device by the FDA, we believe computational modeling via the framework introduced here can help improve device safety and efficacy prior to pre-clinical studies and clinical testing in patients with severe heart disease. Furthermore, some devices, such as the pediatric Berlin Heart LVAD, have also been approved for rare medical cases through the Humanitarian Device Exemption (HDE) rule, which relaxes the clinical efficacy requirement due to the lack of test subjects (Almond et al., 2011). Computational simulations can help fill this gap and provide a higher degree of confidence among clinicians and regulatory bodies to approve the usage of this high risk device in this cohort of patients.

With all major cardiac physics present in this model, simulations can be easily expanded for other treatments and diseases. The inclusion of basic fluid hemodynamics allows the model to simulate internal flow characteristics of the heart with various implants such as artificial valves, which cannot be presented in electromechanical simulations such as Kerckhoffs et al. (2009). On the other hand, FSI simulations with spatially-uniform contraction stress, such as Krittian et al. (2010), cannot be extended to include electrical abnormalities. Inclusion of a closed-loop circulation and biventricular structure also provide the capability to study biventricular interaction, which cannot be simulated in the previous LV fluid-electromechanics studies (Watanabe et al., 2004). As such, the model presented here provides a framework for more intensive and extensive cardiac simulations.

4.3. Limitations of Current Modeling Framework

A morphologically-realistic geometry was not implemented as the main aim of this study was to demonstrate the model's capability to simulate cardiac multiphysics phenomena. An idealized geometry eases the computational load, making it more suitable for framework development. We consider this study a stepping stone for future simulations based on patient-specific anatomies, extracted from imaging modalities such as computed tomography (CT).

In terms of electrophysiology, the model presently does not include several mechanofeedback components such as the stretch-activated currents and stretch effect on the cellular membrane's caveolae. Stretch-activated channels have been proposed to be capable of triggering electrical activation via mechanical stretch alone (Sachs, 2010). However, more characterization needs to be performed to better understand the channel kinetics. The effect of stretch-activated channels can be easily added to the source term in Equation (1) in the future. Stretch may also reduce the number of caveolae structures, leading to a reduction in membrane area and hence reduced membrane capacitance. This effect has been found to slow electric conduction in the cardiac myocyte (Pfeiffer et al., 2014). Thus, this suggests that the membrane capacitance must be made stretch-dependent if such characteristics are to be modeled. Nevertheless, it should be noted that the addition of these stretch-dependencies may increase the non-linearity of the electrical physics. It is likely that these additions may not alter the predictions of most organ-level simulations as the electrical to mechanical interaction is the more crucial coupling.

The use of phenomenological AP and active stress formulations provided considerable simplification, since it reduced the number of variables required to be solved relative to biophysically-based models. This also enabled the use of larger time step steps, for more efficient computation. Mechanical dependencies of the contraction strength may be necessary for specific future studies to simulate the Frank-Starling mechanism, which was not considered in the present model. The mechanism enables the heart to pump at a greater ejection fraction should it be filled with a larger amount of blood (Guyton and Hall, 2006). Nevertheless in failing heart, the Frank-Starling mechanism is known to be absent (Schwinger et al., 1994). With mechanical dependencies, numerical instability may arise especially if a segregated-type solver is implemented (Niederer and Smith, 2008). While a fully coupled-type solvers as adapted here and elsewhere (Göktepe and Kuhl, 2010)are more robust, they tend to require larger computer processing power and memory. As such, additional tuning of the solver settings may be necessary.

Passive myocardial mechanical properties were simply assumed to be a transverse isotropic hyperelastic, whilst in reality, the myocardium exhibits orthotrophic properties (Dokos et al., 2002). Nonetheless, the transverse isotropic hyperelastic material should be able to replicate the uniaxial and biaxial mechanical testing by Demer and Yin (1983). However, if realistic shear characteristics are desired, the orthotrophic terms of Holzapfel and Ogden (2009) can be simply added to the existing strain-energy function.

Viscoelasticity is a common property of myocardial tissue, contributed by the collagenous structure and intercellular fluids, helping to damp out vibration, due to the blood flow (Cansiz et al., 2017; Quarteroni et al., 2017). In the model presented here, a Rayleigh damping component was added to damp out oscillations, where the Rayleigh damping parameters were set proportional to the mass and stiffness terms in the equation of motion. In future, incorporation of the viscoelastic components would be a more accurate way to damp out such oscillation without the need for Rayleigh damping.

Active atrial contribution to the filling phase was not considered in the present study. The atrial contraction is expected to produce an additional peak in the filling flow rate waveform, which forms the "A" wave commonly observed in Doppler imaging of the flow waveforms (Sohn et al., 1997). This atrial contraction will form an additional vortex following the early passive filling (E-wave), and will thus affect the blood kinetic energy and average vorticity plots Hong et al. (2008). The "A" waveform could be simulated by adding an active atrial function in the Windkessel atrial compliances to simulate their physiological pressure-volume relations. In addition, filling kinetic energy is dependent on the basal displacement into the spatial location, previously occupied by the atria (Carlsson et al., 2012). However, incorporating this effect into the simulation would require structural modeling of the atria as well.

Valve structure will influence the intra-ventricular blood flow profile. Furthermore, the angled position of the valves may also ease flow resistance during filling and ejection. Among LVAD recipients, tricuspid regurgitation has also been noted, in particular in those who developed RV failure, since the RV may not be able to cope with the restored systemic venous return (Hayek et al., 2014). Furthermore, aortic valve fusion is a known issue, experienced among LVAD recipients (Rose et al., 2000). Consequently, incorporating the valve structure mechanics into the multiphysics models may be necessary in future due to the high prevalence of valve failure in many ventricular diseases. Inclusion of valvular structure will likely require contact modeling, as was performed between the endocardium and cannula, as well as employing a re-meshing algorithm to overcome severe mesh distortion. Although we used laminar Navier-Stokes formulations, the turbulent form may need to be considered in future, especially in the presence of structural valves. Turbulence models have rarely been considered in multiphysics simulations, since they are more computationally expensive, mainly applied in pure fluid simulation studies (Chnafa et al., 2015).

The model mesh we have used was selected as a compromise between global convergence and computational cost. Fluid dynamics, especially during the diastolic phase, can involve more complex flow patterns, due to vortex formation and the presence of low velocity regions; these may require a finer mesh to be accurately modeled. With the present mesh setting, a converged solution was obtained for blood flow systolic characteristics, but the convergence slightly worsens during the isovolumic phases and diastolic filling. Nevertheless, qualitative and global measures such as vortex shape and flow waveforms can be sufficiently obtained with present mesh settings. In addition, changes to action potential parameters such as σ and k_2, resulting in increased conduction velocity, will require finer meshing to achieve a converged conduction velocity and to prevent numerical convergence failure at large element size. Therefore, future mesh settings need to be tailored to the requirements of the study.

5. CONCLUSION

The cardiac multiphysics framework developed was applied in a biventricular structure with an idealized Purkinje fiber network utilizing a modified form of the standard cable equation, taking into account the change in Purkinje fiber radius. The Windkessel circulation was expanded by including a closed-loop circulation which linked both ventricular chambers. The model managed to simulate healthy LV and RV electrical activation sequences, mechanical behavior as well as global hemodynamics. This highlights the model's capability for future biventricular modeling work. The model was also tested to simulate LVAD support and impact of the pump on ventricular function. The model was shown to be capable of predicting changes in pump variables following changes in the state of the heart, possibly aiding pump controller design in future. The fluid-electromechanics model enables study of the link between electrical activation, myocardial mechanics and blood hemodynamics characteristics, allowing holistic simulations of new therapeutic approaches in their ideation stage, aiding to speed up technology transfer to pre-clinical and clinical trial stages.

AUTHOR CONTRIBUTIONS

AAB carried out the computational modeling. AAB, AA, and SD developed the framework for the standard model. AAB and AA drafted the manuscript. AAB, AA, MS, NL, and SD developed the framework for LVAD simulations, conceived of and coordinated the study, reviewed the manuscript and gave final approval for publication.

FUNDING

AAB is funded by a University of New South Wales (UNSW Sydney) Postgraduate Research Scholarship.

ACKNOWLEDGMENTS

This research was undertaken with the assistance of resources and services from the National Computational Infrastructure (NCI), which is supported by the Australian Government. We would also like to thank the High Performance Computing unit at UNSW for providing computational resources and assistance.

SUPPLEMENTARY MATERIAL

The Supplementary Material for this article can be found online at: https://www.frontiersin.org/articles/10.3389/fphys.2018.01259/full#supplementary-material

REFERENCES

Alam, M., Höglund, C., Thorstrand, C., and Philip, A. (1990). Atrioventricular plane displacement in severe congestive heart failure following dilated cardiomyopathy or myocardial infarction. *J. Int. Med.* 228, 569–575. doi: 10.1111/j.1365-2796.1990.tb00281.x

Almond, C. S., Buchholz, H., Massicotte, P., Ichord, R., Rosenthal, D. N., Uzark, K., et al. (2011). Berlin heart EXCOR pediatric ventricular assist device investigational device exemption study: study design and rationale. *Am. Heart J.* 162, 425–435.e6. doi: 10.1016/j.ahj.2011.05.026

Alqahtani, A., Al Abed, A., Guo, T., Lovell, N. H., and Dokos, S. (2017). "A continuum model of electrical stimulation of multi-compartmental retinal ganglion cells," in *2017 39th Annual International Conference of the IEEE Engineering in Medicine and Biology Society (EMBC)* (Seogwipo), 2716–2719.

Baillargeon, B., Rebelo, N., Fox, D. D., Taylor, R. L., and Kuhl, E. (2014). The living heart project: a robust and integrative simulator for human heart function. *Eur. J. Mechan. A Solids* 48, 38–47. doi: 10.1016/j.euromechsol.2014.04.001

Bakir, A. A., Al Abed, A., Lovell, N. H., and Dokos, S. (2017). "A generic cardiac biventricular fluid-electromechanics model," in *2017 39th Annual International Conference of the IEEE, Engineering in Medicine and Biology Society (EMBC)* (IEEE), 3680–3683.

Bakir, A. A. and Dokos, S. (2015). "A gap junction-based cardiac electromechanics model," in *2015 37th Annual International Conference of the IEEE Engineering in Medicine and Biology Society (EMBC)* (Milan), 25–28.

Braunwald, E., Brockenbrough, E. C., Frahm, C. J., and Ross, J. (1961). Left atrial and left ventricular pressures in subjects without cardiovascular disease: observations in eighteen patients studied by transseptal left heart catheterization. *Circulation* 24, 267–269. doi: 10.1161/01.CIR.24.2.267

Cansiz, B., Dal, H., and Kaliske, M. (2017). Computational cardiology: a modified hill model to describe the electro-visco-elasticity of the myocardium. *Comput. Methods Appl. Mechan. Eng.* 315(Suppl. C), 434–466. doi: 10.1016/j.cma.2016.10.009

Carlsson, M., Heiberg, E., Toger, J., and Arheden, H. (2012). Quantification of left and right ventricular kinetic energy using four-dimensional intracardiac magnetic resonance imaging flow measurements. *Am. J. Physiol. Heart Circ. Physiol.* 302, H893–H900. doi: 10.1152/ajpheart.00942.2011

Carr, C. M., Jacob, J., Park, S. J., Karon, B. L., Williamson, E. E., and Araoz, P. A. (2010). CT of left ventricular assist devices. *Radiographics* 30, 429–444. doi: 10.1148/rg.302095734

Chnafa, C., Mendez, S., Moreno, R., and Nicoud, F. (2015). *Using Image-based CFD to Investigate the Intracardiac Turbulence*. Cham: Springer International Publishing.

Choi, Y. J., Constantino, J., Vedula, V., Trayanova, N., and Mittal, R. (2015). A new MRI-based model of heart function with coupled hemodynamics and application to normal and diseased canine left ventricles. *Front. Bioeng. Biotechnol.* 3:140. doi: 10.3389/fbioe.2015.00140

Dandel, M., Weng, Y., Siniawski, H., Potapov, E., Drews, T., Lehmkuhl, H. B., et al. (2008). Prediction of cardiac stability after weaning from left ventricular assist devices in patients with idiopathic dilated cardiomyopathy. *Circulation* 118(14 Suppl. 1), S94–S105. doi: 10.1161/circulationaha.107.755983

Demer, L. L., and Yin, F. C. (1983). Passive biaxial mechanical properties of isolated canine myocardium. *J. Physiol.* 339, 615–630. doi: 10.1113/jphysiol.1983.sp014738

Di Donato, M., Dabic, P., Castelvecchio, S., Santambrogio, C., Brankovic, J., Collarini, L., et al. (2006). Left ventricular geometry in normal and post-anterior myocardial infarction patients: sphericity index and 'new' conicity index comparisons. *Eur. J. Cardio Thorac. Surg.* 29(Suppl. 1), S225–S230. doi: 10.1016/j.ejcts.2006.03.002

Dokos, S., Smaill, B. H., Young, A. A., and LeGrice, I. J. (2002). Shear properties of passive ventricular myocardium. *Am. J. Physiol. Heart Circ Physiol.* 283, H2650–H2659. doi: 10.1152/ajpheart.00111.2002

Doll, S., and Schweizerhof, K. (1999). On the development of volumetric strain energy functions. *J. Appl. Mech.* 67, 17–21. doi: 10.1115/1.321146

Durrer, D., Van Dam, R. T., Freud, G. E., Janse, M. J., Meijler, F. L., and Arzbaecher, R. C. (1970). Total excitation of the isolated human heart. *Circulation* 41, 899–912. doi: 10.1161/01.CIR.41.6.899

Fares, E., and Schröder, W. (2002). A differential equation for approximate wall distance. *Int. J. Numerical Methods Fluids* 39, 743–762. doi: 10.1002/fld.348

Fritz, T., Wieners, C., Seemann, G., Steen, H., and Dössel, O. (2014). Simulation of the contraction of the ventricles in a human heart model including atria and pericardium. *Biomech. Model. Mechanobiol.* 13, 627–641. doi: 10.1007/s10237-013-0523-y

Geske, J. B., Sorajja, P., Ommen, S. R., and Nishimura, R. A. (2011). Variability of left ventricular outflow tract gradient during cardiac catheterization in patients with hypertrophic cardiomyopathy. *J. Am. Coll. Cardiol.* 4, 704–709. doi: 10.1016/j.jcin.2011.02.014

Glukhov, A. V., Fedorov, V. V., Lou, Q., Ravikumar, V. K., Kalish, P. W., Schuessler, R. B., et al. (2010). Transmural dispersion of repolarization in failing and nonfailing human ventricle. *Circ. Res.* 106, 981–991. doi: 10.1161/CIRCRESAHA.109.204891

Göktepe, S., and Kuhl, E. (2010). Electromechanics of the heart: a unified approach to the strongly coupled excitation-contraction problem. *Comput. Mech.* 45, 227–243. doi: 10.1007/s00466-009-0434-z

Greenbaum, R. A., Ho, S. Y., Gibson, D. G., Becker, A. E., and Anderson, R. H. (1981). Left ventricular fibre architecture in man. *Br. Heart J.* 45, 248–263. doi: 10.1136/hrt.45.3.248

Gurev, V., Lee, T., Constantino, J., Arevalo, H., and Trayanova, N. A. (2011). Models of cardiac electromechanics based on individual hearts imaging data. *Biomech. Model. Mechanobiol.* 10, 295–306. doi: 10.1007/s10237-010-0235-5

Guyton, A., and Hall, J. (2006). *Textbook of Medical Physiology*. Philadelphia, PA: Elsevier Saunders.

Hasenfuss, G., Mulieri, L. A., Leavitt, B. J., Allen, P. D., Haeberle, J. R., and Alpert, N. R. (1992). Alteration of contractile function and excitation-contraction coupling in dilated cardiomyopathy. *Circ. Res.* 70, 1225–32. doi: 10.1161/01.RES.70.6.1225

Hayek, S., Sims, D. B., Markham, D. W., Butler, J., and Kalogeropoulos, A. P. (2014). Assessment of right ventricular function in left ventricular assist device candidates. *Circ. Cardiovasc. Imaging* 7, 379–389. doi: 10.1161/CIRCIMAGING.113.001127

Heikhmakhtiar, A. K., Ryu, A. J., Shim, E. B., Song, K. S., Trayanova, N. A., and Lim, K. M. (2017). Influence of LVAD function on mechanical unloading and electromechanical delay: a simulation study. *Med. Biol. Eng. Comput.* 56, 911–921. doi: 10.1007/s11517-017-1730-y

Henson, R. E., Song, S. K., Pastorek, J. S., Ackerman, J. J., and Lorenz, C. H. (2000). Left ventricular torsion is equal in mice and humans. *Am. J. Physiol. Heart Circ. Physiol.* 278, H1117–H1123. doi: 10.1152/ajpheart.2000.278.4.H1117

Holzapfel, G. A., and Ogden, R. W. (2009). Constitutive modelling of passive myocardium: a structurally based framework for material characterization. *Philos. Trans. R. Soc. A Math. Phys. Eng. Sci.* 367, 3445–3475. doi: 10.1098/rsta.2009.0091

Hong, G. R., Pedrizzetti, G., Tonti, G., Li, P., Wei, Z., Kim, J. K., et al. (2008). Characterization and quantification of vortex flow in the human left ventricle by contrast echocardiography using vector particle image velocimetry. *J. Am. Coll. Cardiol. Cardiovasc. Imaging* 1, 705–717. doi: 10.1016/j.jcmg.2008.06.008

Hooks, D. A., Trew, M. L., Caldwell, B. J., Sands, G. B., LeGrice, I. J., and Smaill, B. H. (2007). Laminar arrangement of ventricular myocytes influences electrical behavior of the heart. *Circ. Res.* 101, e103–e112. doi: 10.1161/CIRCRESAHA.107.161075

Hudsmith, L. E., Petersen, S. E., Francis, J. M., Robson, M. D., and Neubauer, S. (2005). Normal human left and right ventricular and left atrial dimensions using steady state free precession magnetic resonance imaging. *J. Cardiovasc. Magn. Reson.* 7, 775–782. doi: 10.1080/10976640500295516

James, T. N. (1961). Morphology of the human atrioventricular node, with remarks pertinent to its electrophysiology. *Am. Heart J.* 62, 756–771. doi: 10.1016/0002-8703(61)90664-0

Kerckhoffs, R. C., McCulloch, A. D., Omens, J. H., and Mulligan, L. J. (2009). Effects of biventricular pacing and scar size in a computational model of the failing heart with left bundle branch block. *Med. Image Anal.* 13, 362–369. doi: 10.1016/j.media.2008.06.013

Kerckhoffs, R. P., Neal, M., Gu, Q., Bassingthwaighte, J., Omens, J., and McCulloch, A. (2007). Coupling of a 3D finite element model of cardiac ventricular mechanics to lumped systems models of the systemic and pulmonic circulation. *Ann. Biomed. Eng.* 35, 1–18. doi: 10.1007/s10439-006-9212-7

Krittian, S., Janoske, U., Oertel, H., and Böhlke, T. (2010). Partitioned fluid–solid coupling for cardiovascular blood flow. *Ann. Biomed. Eng.* 38, 1426–1441. doi: 10.1007/s10439-009-9895-7

Lankhaar, J. W., Westerhof, N., Faes, T. J., Marques, K. M., Marcus, J. T., Postmus, P. E., et al. (2006). Quantification of right ventricular afterload in patients with and without pulmonary hypertension. *Am. J. Physiol. Heart Circ. Physiol.* 291, H1731–H1737. doi: 10.1152/ajpheart.00336.2006

LeGrice, I. J., Hunter, P. J., and Smaill, B. H. (1997). Laminar structure of the heart: a mathematical model. *Am. J. Physiol. Heart Circ. Physiol.* 272, H2466–H2476. doi: 10.1152/ajpheart.1997.272.5.H2466

Lim, E., Dokos, S., Cloherty, S. L., Salamonsen, R. F., Mason, D. G., Reizes, J. A., et al. (2010). Parameter-optimized model of cardiovascular:rotary blood pump interactions. *IEEE Trans. Biomed. Eng.* 57, 254–266. doi: 10.1109/TBME.2009.2031629

Maughan, W. L., Sunagawa, K., Burkhoff, D., and Sagawa, K. (1984). Effect of arterial impedance changes on the end-systolic pressure-volume relation. *Circ. Res.* 54, 595–602. doi: 10.1161/01.RES.54.5.595

McCormick, M., Nordsletten, D. A., Kay, D., and Smith, N. P. (2013). Simulating left ventricular fluid-solid mechanics through the cardiac cycle under LVAD support. *J. Comput. Phys.* 244, 80–96. doi: 10.1016/j.jcp.2012.08.008

Mohiaddin, R. H. (1995). Flow patterns in the dilated ischemic left ventricle studied by MR imaging with velocity vector mapping. *J. Magn. Reson. Imaging* 5, 493–498. doi: 10.1002/jmri.1880050503

Morgan, J. A., Paone, G., Nemeh, H. W., Murthy, R., Williams, C. T., Lanfear, D. E., et al. (2013). Impact of continuous-flow left ventricular assist device support on right ventricular function. *J. Heart Lung Transplant.* 32, 398–403. doi: 10.1016/j.healun.2012.12.018

Mowat, D. H., Haites, N. E., and Rawles, J. M. (1983). Aortic blood velocity measurement in healthy adults using a simple ultrasound technique. *Cardiovasc. Res.* 17, 75–80. doi: 10.1093/cvr/17.2.75

Nash, M. P., and Panfilov, A. V. (2004). Electromechanical model of excitable tissue to study reentrant cardiac arrhythmias. *Progr. Biophys. Mol. Biol.* 85, 501–522. doi: 10.1016/j.pbiomolbio.2004.01.016

Neyer, J., Arsanjani, R., Moriguchi, J., Siegel, R., and Kobashigawa, J. (2016). Echocardiographic parameters associated with right ventricular failure after left ventricular assist device: a review. *J. Heart Lung Transplant.* 35, 283–293. doi: 10.1016/j.healun.2015.12.018

Niederer, S. A., and Smith, N. P. (2008). An improved numerical method for strong coupling of excitation and contraction models in the heart. *Progr. Biophys. Mol. Biol.* 96, 90–111. doi: 10.1016/j.pbiomolbio.2007.08.001

Nordsletten, D., McCormick, M., Kilner, P., Hunter, P., Kay, D., and Smith, N. (2011). Fluid-solid coupling for the investigation of diastolic and systolic human left ventricular function. *Int. J. Num. Methods Biomed. Eng.* 27, 1017–1039. doi: 10.1002/cnm.1405

Ong, C., Dokos, S., Chan, B., Lim, E., Al Abed, A., Osman, N., et al. (2013). Numerical investigation of the effect of cannula placement on thrombosis. *Theor. Biol. Med. Model.* 10:35. doi: 10.1186/1742-4682-10-35

Penefsky, Z., and Hoffman, B. F. (1963). Effects of stretch on mechanical and electrical properties of cardiac muscle. *Am. J. Physiol.* 204, 433–438. doi: 10.1152/ajplegacy.1963.204.3.433

Pettersen, E., Helle-Valle, T., Edvardsen, T., Lindberg, H., Smith, H. J., Smevik, B., et al. (2007). Contraction pattern of the systemic right ventricle: shift from longitudinal to circumferential shortening and absent global ventricular torsion. *J. Am. Coll. Cardiol.* 49, 2450–2456. doi: 10.1016/j.jacc.2007.02.062

Pfeiffer, E. R., Wright, A. T., Edwards, A. G., Stowe, J. C., McNall, K., Tan, J., et al. (2014). Caveolae in ventricular myocytes are required for stretch-dependent conduction slowing. *J. Mol. Cell. Cardiol.* 76, 265–274. doi: 10.1016/j.yjmcc.2014.09.014

Quarteroni, A., Lassila, T., Rossi, S., and Ruiz-Baier, R. (2017). Integrated heart—coupling multiscale and multiphysics models for the simulation of the cardiac function. *Comput. Methods Appl. Mech. Eng.* 314, 345–407. doi: 10.1016/j.cma.2016.05.031

Robertson, J., Long, B., and Koyfman, A. (2017). The emergency management of ventricular assist devices. *Am. J. Emerg. Med.* 34, 1294–1301. doi: 10.1016/j.ajem.2016.04.033

Rose, A. G., Park, S. J., Bank, A. J., and Miller, L. W. (2000). Partial aortic valve fusion induced by left ventricular assist device. *Ann. Thorac. Surg.* 70, 1270–1274. doi: 10.1016/S0003-4975(00)01929-9

Russell, K., Eriksen, M., Aaberge, L., Wilhelmsen, N., Skulstad, H., Remme, E. W., et al. (2012). A novel clinical method for quantification of regional left ventricular pressure–strain loop area: a non-invasive index of myocardial work. *Eur. Heart J.* 33, 724–733. doi: 10.1093/eurheartj/ehs016

Sachs, F. (2010). Stretch-activated ion channels: what are they? *Physiology* 25, 50–56. doi: 10.1152/physiol.00042.2009

Sack, K. L., Baillargeon, B., Acevedo-Bolton, G., Genet, M., Rebelo, N., Kuhl, E., et al. (2016). Partial LVAD restores ventricular outputs and normalizes LV but not RV stress distributions in the acutely failing heart *in silico*. *Int. J. Artif. Organs* 39, 421–430. doi: 10.5301/ijao.5000520

Salamonsen, R. F., Lim, E., Moloney, J., Lovell, N. H., and Rosenfeldt, F. L. (2015). Anatomy and physiology of left ventricular suction induced by rotary blood pumps. *Artif. Organs* 39, 681–690. doi: 10.1111/aor.12550

Schäfer, M., Browning, J., Schroeder, J. D., Shandas, R., Kheyfets, V. O., Buckner, J. K., et al. (2016). Vorticity is a marker of diastolic ventricular interdependency in pulmonary hypertension. *Pulmon. Circ.* 6, 46–54. doi: 10.1086/685052

Schwinger, R. H., Böhm, M., Koch, A., Schmidt, U., Morano, I., Eissner, H. J. (1994). The failing human heart is unable to use the frank-starling mechanism. *Circ. Res.* 74, 959–969. doi: 10.1161/01.RES.74.5.959

Sohn, D. W., Chai, I. H., Lee, D. J., Kim, H. C., Kim, H. S., Oh, B. H., et al. (1997). Assessment of mitral annulus velocity by doppler tissue imaging in the evaluation of left ventricular diastolic function. *J. Am. Coll. Cardiol.* 30, 474–480. doi: 10.1016/S0735-1097(97)88335-0

Stevens, M. C., Wilson, S., Bradley, A., Fraser, J., and Timms, D. (2014). Physiological control of dual rotary pumps as a biventricular assist device using a master/slave approach. *Artif. Organs* 38, 766–774. doi: 10.1111/aor.12303

Tandri, H., Daya, S. K., Nasir, K., Bomma, C., Lima, J. A., Calkins, H., et al. (2006). Normal reference values for the adult right ventricle by magnetic resonance imaging. *Am. J. Cardiol.* 98, 1660–1664. doi: 10.1016/j.amjcard.2006.07.049

Troughton, R. W., Ritzema, J., Eigler, N. L., Melton, I. C., Krum, H., Adamson, P. B., et al. (2011). Direct left atrial pressure monitoring in severe heart failure: long-term sensor performance. *J. Cardiovasc. Transl. Res.* 4, 3–13. doi: 10.1007/s12265-010-9229-z

Usyk, T. P., LeGrice, I. J., and McCulloch, A. D. (2002). Computational model of three-dimensional cardiac electromechanics. *Comput. Visual. Sci.* 4, 249–257. doi: 10.1007/s00791-002-0081-9

Vigmond, E. J., and Stuyvers, B. D. (2015). Modeling our understanding of the His-Purkinje system. *Progr. Biophys. Mol. Biol.* 120, 179–188. doi: 10.1016/j.pbiomolbio.2015.12.013

Vollkron, M., Voitl, P., Ta, J., Wieselthaler, G., and Schima, H. (2007). Suction events during left ventricular support and ventricular arrhythmias. *J. Heart Lung Transplant.* 26, 819–825. doi: 10.1016/j.healun.2007.05.011

Washio, T., Okada, J., Takahashi, A., Yoneda, K., Kadooka, Y., Sugiura, S., et al. (2013). Multiscale heart simulation with cooperative stochastic cross-bridge dynamics and cellular structures. *Multi. Model. Simulat.* 11, 965–999. doi: 10.1137/120892866

Watanabe, H., Sugiura, S., Kafuku, H., and Hisada, T. (2004). Multiphysics simulation of left ventricular filling dynamics using fluid-structure interaction finite element method. *Biophys. J.* 87, 2074–2085. doi: 10.1529/biophysj.103.035840

Westaby, S., Karp, R. B., Blackstone, E. H., and Bishop, S. P. (1984). Adult human valve dimensions and their surgical significance. *Am. J. Cardiol.* 53, 552–556. doi: 10.1016/0002-9149(84)90029-8

Yuhki, A., Hatoh, E., Nogawa, M., Miura, M., Shimazaki, Y., and Takatani, S. (1999). Detection of suction and regurgitation of the implantable centrifugal pump based on the motor current waveform analysis and its application to optimization of pump flow. *Artif. Organs* 23, 532–537.

Conflict of Interest Statement: The authors declare that the research was conducted in the absence of any commercial or financial relationships that could be construed as a potential conflict of interest.

frontiers in Medicine

PERSPECTIVE
published: 25 September 2018
doi: 10.3389/fmed.2018.00241

Advancing Regulatory Science With Computational Modeling for Medical Devices at the FDA's Office of Science and Engineering Laboratories

Tina M. Morrison, Pras Pathmanathan, Mariam Adwan and Edward Margerrison*

Office of Science and Engineering Laboratories, Center for Devices and Radiological Health, U.S. Food and Drug Administration, Silver Spring, MD, United States

OPEN ACCESS

Edited by:
Markus Reiterer,
Medtronic, United States

Reviewed by:
Marco Viceconti,
Insigneo Institute of in silico Medicine,
United Kingdom
Adam Himes,
Medtronic, United States

***Correspondence:**
Tina M. Morrison
tina.morrison@fda.hhs.gov

Specialty section:
This article was submitted to
Translational Medicine,
a section of the journal
Frontiers in Medicine

Received: 30 April 2018
Accepted: 08 August 2018
Published: 25 September 2018

Citation:
Morrison TM, Pathmanathan P, Adwan M and Margerrison E (2018) Advancing Regulatory Science With Computational Modeling for Medical Devices at the FDA's Office of Science and Engineering Laboratories.
Front. Med. 5:241.
doi: 10.3389/fmed.2018.00241

Protecting and promoting public health is the mission of the U.S. Food and Drug Administration (FDA). FDA's Center for Devices and Radiological Health (CDRH), which regulates medical devices marketed in the U.S., envisions itself as the world's leader in medical device innovation and regulatory science–the development of new methods, standards, and approaches to assess the safety, efficacy, quality, and performance of medical devices. Traditionally, bench testing, animal studies, and clinical trials have been the main sources of evidence for getting medical devices on the market in the U.S. In recent years, however, computational modeling has become an increasingly powerful tool for evaluating medical devices, complementing bench, animal and clinical methods. Moreover, computational modeling methods are increasingly being used within software platforms, serving as clinical decision support tools, and are being embedded in medical devices. Because of its reach and huge potential, computational modeling has been identified as a priority by CDRH, and indeed by FDA's leadership. Therefore, the Office of Science and Engineering Laboratories (OSEL)—the research arm of CDRH—has committed significant resources to transforming computational modeling from a valuable scientific tool to a valuable regulatory tool, and developing mechanisms to rely more on digital evidence in place of other evidence. This article introduces the role of computational modeling for medical devices, describes OSEL's ongoing research, and overviews how evidence from computational modeling (i.e., digital evidence) has been used in regulatory submissions by industry to CDRH in recent years. It concludes by discussing the potential future role for computational modeling and digital evidence in medical devices.

Keywords: medical devices, computational modeling, regulatory science, virtual patients, virtual clinical trials, FDA

INTRODUCTION

The mission of the U. S. Food and Drug Administration (FDA) is to protect and promote public health, and it does so by ensuring the safety, effectiveness and security of FDA-regulated products[1] These products include, but are not limited to, medical devices, drugs for humans and animals, and biological products such as vaccines and the blood supply, each of which are managed by separate Centers within the Agency. The FDA accomplishes its mission by performing pre-market clearance, approval and post-market monitoring of the performance and safety of products, enforcing, and ensuring compliance to manufacturing processes and quality control, and conducting regulatory science research. The latter, although less well-known in the scientific community, is fundamental to support science-based regulatory decision-making by FDA. Regulatory science encompasses the development of new methods, standards, and approaches to assess the safety, efficacy, quality, and performance of FDA-regulated products and products under development. Each Center in the FDA is committed to advancing these efforts, which have accelerated the product development pathway and regulatory review cycle so that new, innovative products can be made available to the American public.

The FDA faces many challenges (1), such as new and evolving public health threats; rapid scientific breakthroughs and emerging technologies resulting in novel products that may raise unique testing and safety issues; globalization of public health, science, manufacturing and supply chains; and providing timely, accurate and useful consumer information in an age of information overload. To enable the Agency to meet today's public health needs and to be fully prepared for the challenges and opportunities of tomorrow, FDA leadership developed a strategic plan identifying nine target areas, stating that investment in these areas is essential to mission success[2] Of those nine, four priority areas identified an important role for computational modeling[3], see **Table 1**. These priorities also have relevant aspects related to medical devices[4]. regulated by the Center for Devices and Radiological Health (CDRH)[5], as mentioned by the FDA Commissioner in a blog posted in July 2017[6].

CDRH's mission goes beyond protecting and public health; with a vision to be the world's leader in medical device innovation, they provide consumers, patients, their caregivers, and providers with understandable and accessible science-based information about the products it oversees, and facilitate innovation by advancing regulatory science. Science-based regulatory decisions are made with evidence collected from four different models: animal, bench, computational[7], and human (i.e., clinical trials), see **Figure 1A**. While each model has its advantages and limitations for evaluating different aspects of medical device performance (3), computational modeling is a promising one for supporting the future of medical devices and healthcare. FDA's Office of Science and Engineering Laboratories (OSEL) has committed significant resources for transforming computational modeling from a valuable scientific tool to a valuable regulatory tool because of its potential for significant cost-savings in evaluating medical devices, simulating performance under scenarios that may not be possible with human use or that could more effectively be evaluated with simulation.

OSEL has a unique role in medical device regulation serving as the research arm for CDRH. OSEL's expertise spans a variety of scientific, engineering, and mathematical disciplines[8], with a diverse group of 130 full time scientists and engineers (supported by numerous post-doctoral fellows and interns) that provide expert support internally to the regulatory teams and externally to industry, clinical and the scientific communities. They conduct cutting-edge research, ensure readiness for emerging and innovative medical technologies, develop evaluation strategies and testing standards, create accessible and understandable public health information, deliver timely decisions for products across their life cycle, and readily share data and engage with stakeholders to advance regulatory science. The growing area of computational modeling is fully supported by OSEL and CDRH through research and development of methods and tools, serving as expert consultants by reviewing and assessing computational modeling submitted by medical device companies, i.e., sponsors, in regulatory submissions, and publicly sharing computational modeling that supports regulatory decision-making. Moreover, OSEL houses a high-performance computing center which supports scientific computing needs for CDRH and other Centers across FDA[9]

Because OSEL scientists have different roles to support CDRH, we designed and conducted a 35-question survey to better understand computational modeling in research and regulatory domains, including goals and objectives on the use of computational modeling in research, reliance of evidence from computational modeling and simulation (i.e., digital evidence) in regulatory submissions, and opportunities for the future with computational modeling and simulation. Thirty-six OSEL scientists with direct involvement in computational modeling projects and initiatives were

---

[1] https://www.fda.gov

[2] http://www.fda.gov/ScienceResearch/SpecialTopics/RegulatoryScience/

[3] Computational modeling is the process of representing a real-world system by means of a computer and then running the simulation by implementing a numerical scheme.

[4] The FDA definition of medical devices excludes drugs, which achieve their effects through chemical action within or on the body. The vast majority of medical device manufacturers are classified by the U.S. Department of Commerce in five industries: x-ray and electromedical equipment, surgical and medical instruments, surgical appliances and supplies, dental equipment, and ophthalmic goods (2)

[5] https://www.fda.gov/AboutFDA/CentersOffices/OfficeofMedicalProductsandTobacco/CDRH/CDRHReports/ucm274152.htm

[6] https://blogs.fda.gov/FDAvoice/index.php, post July 7, 2017.

[7] Evidence from algorithms, and computer-based modeling and simulation will be referred to as digital evidence.

[8] https://www.fda.gov/AboutFDA/CentersOffices/OfficeofMedicalProductsandTobacco/CDRH/CDRHOffices/ucm115989.htm

[9] https://scl-wiki-01.fda.gov/wiki/index.php/Main_Page

TABLE 1 | In 2011, FDA identified an important role for computational modeling in its strategic priorities.

The four strategic areas with a specific call for computational modeling	Relevance to medical devices	Proposed computational modeling methods and approaches
1. Modernize Toxicology to Enhance Safety	Improving medical device safety; analyzing medical device performance	• (Q)SAR[a] models to predict the risk to human due to exposure to molecules
2. Stimulate Innovation in Clinical Evaluations and Personalized Medicine to Improve Product Development and Patient Outcomes	Improving health of pediatric and other special populations; identifying new sources of evidence for clinical evaluation	• Computer models of cells, organs, and systems to better predict product safety and efficacy
3. Ensure FDA Readiness to Evaluate Innovative Emerging Technologies	Advancing innovation and evaluating new and emerging technologies	• Virtual physiological patients for testing medical products
4. Harness Diverse Data through Information Sciences to Improve Health Outcomes	Developing novel ways to use clinical data in evaluating medical devices	• Clinical trial simulations that reveal interactions between therapeutic effects, patient characteristics, and disease variables • Knowledge building tools: data mining, machine and deep learning, visualization, knowledge bases, high throughput methods • Mechanism for sharing and reuse of data, models, and algorithms.

FDA's Center for Devices and Radiological Health also published a special report on regulatory science[5] to align with these efforts. The table highlights the priority areas on the left, the medical device relevance in the middle, and the proposed methods and approaches on the right.

[a] Note that (Q)SAR models are classification models that relate the structure of a chemical to its activity, i.e., quantitative structure activity relationship.

interviewed, their responses were transcribed in a database and then shared with the scientists for fact checking. This perspective will present the results from that survey and highlight the different roles that computational modeling has and can play in medical devices, and discuss the potential future for digital evidence and simulation in medical devices.

OVERVIEW OF COMPUTATIONAL MODELING FOR MEDICAL DEVICES

Computational modeling can be used to simulate and better understand medical devices in several ways, as depicted in **Figure 1B**. Starting with the upper row, the simplest and most common implementation of computational modeling for medical devices is simply to simulate the device under a variety of conditions that mimic some aspect of the clinical or use environment to investigate some aspect of the device's performance. Computational modeling applications also include simulating the anatomy or serving as computational human phantoms for medical imaging systems or as a platform for assessing implanted devices; simulating physiology, such as electrophysiology during arrhythmias in the heart, or of pancreatic function; simulating chemical toxicology (using (Q)SAR models), which can support our ability to understand whether or not compounds released from medical devices, such as from dyes and coatings, are harmful; simulating the additive manufacturing process to optimize a 3D-printed product or simulating the substrate on which a 3D-printed product will be manufactured. The applications in the upper row of **Figure 1B** typically support design or evaluation of a physical, medical device. Other applications, depicted in the lower row, include computational algorithms embedded in a medical device or serving as the medical device, i.e., software as a medical device (4). An example of the former is embedded control algorithms in glucose monitors, which have the potential for advancing modern artificial pancreas systems[10] used in glucose regulation for patients with diabetes (5). The models for the artificial pancreas have been used to replace *in vivo* animal studies to initiate clinical studies for these closed-loop devices (6). An example of computational modeling as a medical device is the use of personalized simulation to indicate whether a patient is a candidate for a medical device or a pharmaceutical, for example, to simulate an invasive clinical procedure or dosage effect to predict an outcome before the therapy is selected.

Computational modeling can also be used to simulate treatment outcomes. Statistical models have long been used to simulate clinical trial design and interpret results. An evolving concept is that of "virtual patients," and new statistical models to augment clinical trial design with virtual patients to predict treatment outcomes (7, 8). It is important to note that a "virtual patient" is not necessarily a digitized patient; it is an approach that allows previously collected evidence (such as digital evidence or other historical clinical evidence typically referred to as "external evidence") to inform the collection of *new* evidence from a clinical trial using Bayesian methodologies. Thus, computational modeling can enable a pathway to expose fewer patients to experimental therapies by relying on other sources of evidence. It can offer an opportunity to address questions that we cannot address clinically due to financial or ethical considerations, and investigate aspects of device performance in many more clinically-relevant cases (hundreds of

---

[10] https://www.fda.gov/MedicalDevices/ProductsandMedicalProcedures/HomeHealthandConsumer/ConsumerProducts/ArtificialPancreas/default.htm

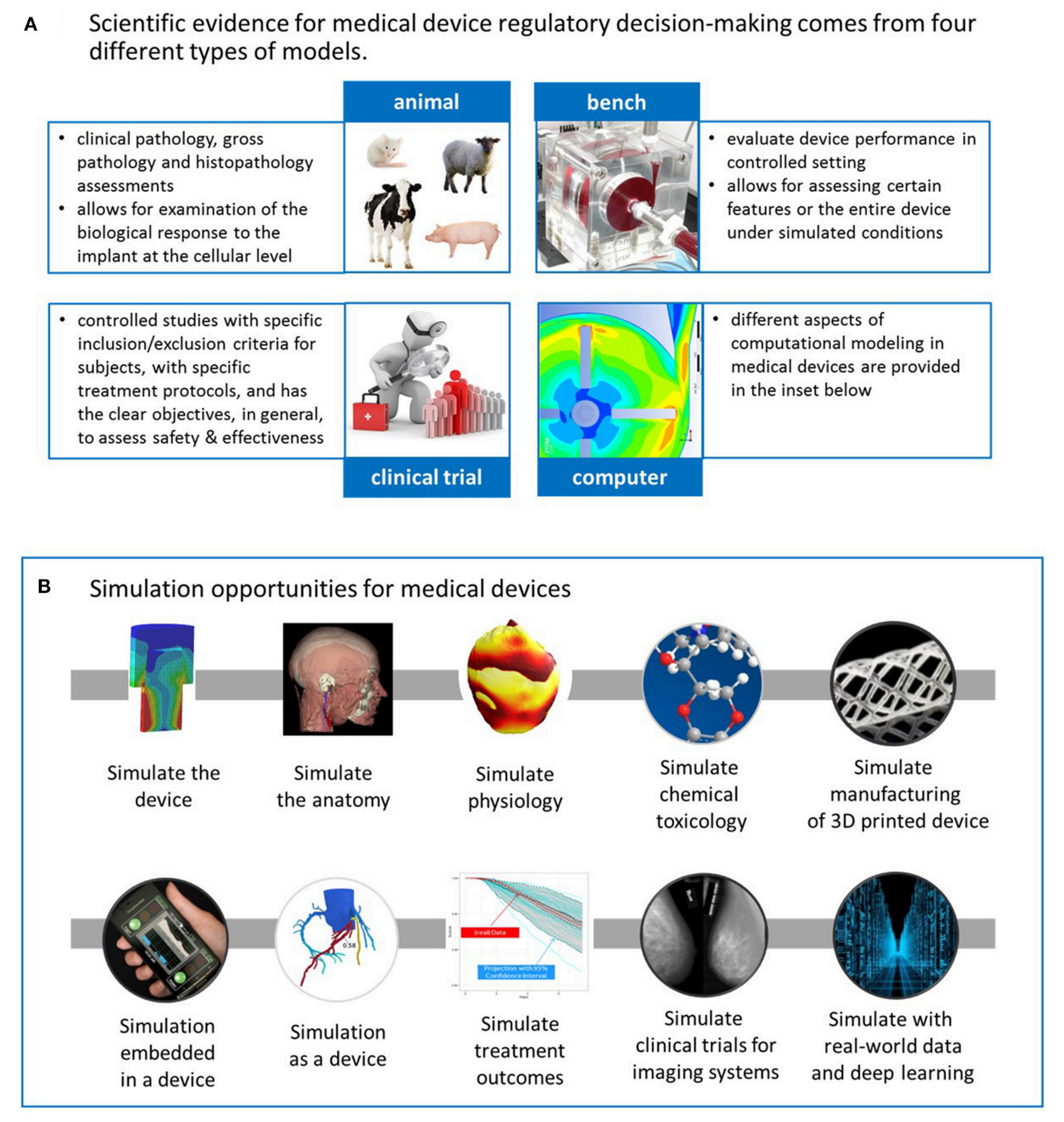

Scientific evidence for medical device regulatory decision-making comes from four different types of models.

- clinical pathology, gross pathology and histopathology assessments
- allows for examination of the biological response to the implant at the cellular level

- evaluate device performance in controlled setting
- allows for assessing certain features or the entire device under simulated conditions

- controlled studies with specific inclusion/exclusion criteria for subjects, with specific treatment protocols, and has the clear objectives, in general, to assess safety & effectiveness

- different aspects of computational modeling in medical devices are provided in the inset below

Simulation opportunities for medical devices

FIGURE 1 | (A) CDRH's science-based regulatory decisions about medical devices are made with evidence collected from four different models: animal, bench, computational, and human (i.e., clinical trials). **(B)** Computational modeling has the potential to transform medical device design and evaluation in several ways. The upper row consists of applications that typically support the design or evaluation of the physical device. The lower row represents other applications, such as those embedded in a device or simulation as a medical device. Moreover, computational modeling can also simulate treatment outcomes or simulate the clinical trial for imaging systems. Lastly, it can play a critical role in the development of data-driven models from real-world data. See the text for more details.

thousands as compared to hundreds). Computational modeling can facilitate the exploration of using a medical device in populations that cannot be investigated clinically, such as in patients with rare diseases or pediatric patients, without harm. Computational modeling has also enabled the complete "*in silico*" simulation of clinical trials for medical imaging systems. By this we mean the implementation of different computational models to simulate the *entire* clinical evaluation of an imaging system, creating a "virtual clinical trial," where no patients are physically exposed to the imaging system–more on this later. Lastly, knowledge-base tools can be harnessed to develop data-driven models from big data sources, such as real-world data, and employ deep learning methods to gain relevant insights about medical device use and performance. Computational modeling for medical devices has a broad scope impacting many facets of the product lifecycle, and scientists from OSEL are leading or closely collaborating with leaders in the field in each of the aforementioned categories.

COMPUTATIONAL MODELING RESEARCH

The research conducted in OSEL is directly motivated by regulatory needs, scientific questions arising from the review of regulatory submissions and anticipating future direction of industry needs through technology forecasting. Moreover, the vision of CDRH is to ensure patients in the U.S. have access to innovative medical devices first in the world, and computational modeling is one tool to support faster more efficient regulatory approvals without sacrificing patient safety or the confidence in regulatory decisions. Some companies have stated that the cost for clinical trials may soon outpace revenue (9), and industry will therefore need other relevant and reliable data sources for demonstrating safety and effectiveness of medical devices; computational modeling is a practical and viable method for gathering clinical information to augment clinical trials (10). More details on this are provided in the closing section.

There is a broad range of modeling disciplines that OSEL scientists are using in their medical device-driven research, including photon transport, fluid dynamics, heat transfer, electromagnetism, solid mechanics, acoustics and optics, along with anatomical, physiological, and mechanistic modeling. Other include (Q)SAR models for assessing molecular carcinogenicity (11), deep learning methods and artificial intelligence for analyzing and synthesizing real-world data. Within this diverse range, OSEL has been advancing different areas of computational modeling for medical devices. The following examples provide a glimpse of the many computational modeling applications in OSEL.

Scientists have developed *computational models of medical devices* for investigating a specific approach or consideration about the medical device. It is important to emphasize that the computational studies below are not of a specific manufacturer's device, but of generic devices where the study results have broad impact in that device domain and are translatable to other domains. These models include implantable cardiovascular stents for assessing different methods to calculate fatigue safety factor (12); heart valves implanted with non-circular configurations (13) to assess the impact on stresses and strains; inferior vena cava filters to demonstrate a new method for computing embolus transport (14); hip implants for evaluating the impact of the design on contact mechanics (15); radiofrequency coils for MRI systems (16, 17) to investigate the design parameters on the electromagnetic field; surgical facemasks (18) for evaluating aerosol leakage of different designs; blood pump (19) for assessing the ability to predict hemolysis using computational fluid dynamics; and electrical stimulation of implanted lead wires (20) to investigate local heating. They have also developed new methods for simulating photon transport of x-ray emitters (21) and compressive sensing for imaging systems (22). Another computational effort was the development of a complex constitutive models for absorbable polymers used in medical implants (23).

Computational models of anatomy or physiology include improved drug delivery in the cornea with ultrasound energy (24); physiological models of heart cells (25), renal circulation (26), hemodynamic responses to blood volume perturbations (27), left bundle branch block (28), gas dynamics in the retina (29), coupled electrical and mechanical activity in the heart (30); energy absorption in patients with deep-brain stimulators (31–34), breast tissue expanders (35), in pregnant women and fetus during MRI exams (36); subthalamic nucleus (37), the breast (38), cancellous bone (39), the head (40) and whole body models (41, 42).

A part of OSEL's mission is to improve CDRH's ability to evaluate medical devices and support the regulatory approval of innovative medical devices more efficiently without sacrificing safety. Therefore, some of the research efforts involve demonstrating through examples that the output from *computational modeling is a viable source of regulatory-grade evidence*, i.e., sufficiently-credible digital evidence that can support regulatory applications (43–45); developing frameworks (46, 47) and metrics (48) for assessing the trustworthiness of models, and studying workflows for creating reproducible models[11] (49), and identifying considerations for computational patient models for autonomous medical devices (50).

Other *computational tools to assess specific aspects of device performance* or safety that industry can employ include a simulator for high-intensity focused ultrasound (HIFU) beams and heating effects (51, 52), benchmarks models for computational fluid dynamics (19), patient-specific workflows for assessing clot trapping efficiency in IVC filters (53), surrogate models for predicting device-specific and species-specific hemolysis (Craven et al., under review), optical-thermal light-tissue interactions for photoacoustic breast imaging (54), and an online app for assessing the safety of color additives (55).

Additional efforts are pushing the *state of the art of simulation for medical devices*, including fluid-structure-interaction of deformable blood clots, computational human phantoms for active implants (37), lesion insertion and image reconstruction (56), computational patient models for closed-loop control devices (27), whole-heart modeling for electrophysiology devices (30), computational modeling for determining hemolysis levels in patients supported by blood-circulating medical devices (57), evaluating exposure risk from nickel leaching devices (58) and risk assessment for framing policy and deciding on the stockpile of personal protective equipment for wide-spread outbreaks or virus epidemics (59).

Lastly, as previously mentioned, one team is developing and validating a framework for streamlining the market entry of imaging systems relying solely on *simulation in place of clinical trials*. The VICTRE project (virtual imaging of clinical trials for regulatory evaluation) approach involves simulating the anatomical structure of the breast (with or without a neoplastic lesion), the radiological transmission (i.e., imaging

---

[11] NIBIB. R01EB024573, https://simtk.org/projects/kneehub

system) and reconstructed images, and the clinical reader studies. By simulating each component of the clinical trial process, there is the potential for minimizing the need for clinical trials and thus the regulatory review of imaging systems (60). Note that the VICTRE project uses statistical analysis tools that evaluate the diagnostic performance of radiologists (virtual or human). An important aspect of the statistical analyses is that they account for radiologist variability and case variability. Such analyses are not trivial and have been developed by OSEL scientists (61–64) with validation based on sophisticated simulation tools (65).

OSEL scientists share their models and data with the public to facilitate the use and broader adoption of these computational tools and approaches. For example, anatomical models of the head (the MIDA model) and whole body models (the Virtual Family) can be downloaded from the IT'IS Foundation's website[12, 13] The experimental and computational data from an FDA-led multi-laboratory study for fluid dynamics on generic medical devices can be found here;[14] the simulation and statistical tools for the VICTRE project are here[15] and here (66, 67); the HIFU simulator here[16] Other software applications are being shared through Github[17], such as the design of a generic inferior vena cava filter[18] and a risk assessment tool for assessing color additives[19]

COMPUTATIONAL MODELING IN REGULATORY SUBMISSIONS

The OSEL scientists also serve as expert consultants on regulatory submissions. The review and decision about a medical device regulatory application requires a team of experts led by the regulatory offices in CDRH. OSEL scientists serve as specialized, technical experts on the regulatory teams. More than 2500 consulting reviews were completed by all scientists in OSEL in 2017, and about 500 were completed by the 36 scientists interviewed for this perspective. Of the 500 consults performed by the scientists surveyed, 220 (44%) included computational modeling and digital evidence in the submission. (Note that therefore 9% of *all* expert consults performed by OSEL for the regulatory offices in 2017 involved computational modeling). Of these 220, the submission-type breakdown is as follows: 36% were for premarket 510(k) notifications (for moderate risk devices), 25% for clinical trial applications, 24% for pre-submissions, 13% for premarket approval applications (for high risk devices), with only a handful for other submission types. With respect to medical areas, the largest number of consults in 2017 were for neurological devices, followed by cardiovascular and orthopedic devices, imaging systems, and surgical devices.

The survey results indicated that the primary use of computational modeling in regulatory submissions was to identify the appropriate bench testing configurations, such as worst-case or clinically challenging conditions, for cardiovascular, orthopedic, and surgical implants. The second most common use of computational modeling was to provide evidence supporting the safety assessment of patients with and without implanted devices when exposed to the radiofrequency (RF) fields of an MR system. A noteworthy example of the latter is the recent clearance[20] of the first 7 Tesla MRI system (Siemens Magnetom)[21], where the Virtual Family (41) and the MIDA head model (40) were used to predict aspects of safety and effectiveness of the new system. Examples of the former include RF safety evaluation for patients with implanted electrically passive (e.g., joint replacement, stents) or electrically active devices (e.g., neurostimulators, pacemakers, cochlear implants). Other modeling examples include therapeutic ultrasound systems where simulation results of the ultrasound energy delivered to *in vivo* locations have been used in regulatory submissions as justification for system parameters, or the recent clearance of Compressed Sensing GRASP-VIBE® to support high-resolution dynamic abdominal imaging under free-breathing. From the 510(k) summary[22], "A comparison of the functionality was performed between the new feature and the device feature by detailed simulations with a numerical [computational] phantom".

In general, computational modeling can be part of a regulatory submission in two ways. The first is when simulation results serve as supporting (digital) evidence in a marketing application for a medical device. The second is when simulation is a medical device, such as for clinical decision support; this is "software as a medical device." Virtually all consults regarding computational modeling were of the former; the latter, with just a handful of submissions, is a new growth area for CDRH, especially with the release of the FDA guidance that describes the clinical evaluation for these software application, and the new program area on Digital Health Technologies[23] Two examples of software as a medical device that have received FDA clearance used patient-specific computational models generated from CT imaging data to non-invasively predict clinically-relevant quantities for treatment selection. Heartflow® generates a personalized 3D model of the patient's coronary arteries and simulates blood flow to predict fractional flow reserve[24] The CardioInsight® Mapping System generates a personalized model of the patient's heart and torso, then simulates the electrical activity on the

---

[12] The MIDA Model: https://www.itis.ethz.ch/virtual-population/regional-human-models/mida-model/,

[13] The Virtual Family: https://www.itis.ethz.ch/virtual-population/virtual-population/overview/

[14] https://nciphub.org/wiki/FDA_CFD

[15] https://github.com/didsr/victre

[16] https://www.mathworks.com/matlabcentral/fileexchange/30886-high-intensity-focused-ultrasound-simulator.

[17] https://github.com/didsr

[18] https://github.com/kenaycock/Generic-IVC-Filter

[19] https://dsaylor.github.io/CHRIS/

[20] 510(k) Summary: https://www.accessdata.fda.gov/cdrh_docs/pdf17/K170840.pdf

[21] https://usa.healthcare.siemens.com/news/magnetomterrafdaclearance.html

[22] 510(k) Summary: https://www.accessdata.fda.gov/cdrh_docs/pdf17/K173617.pdf

[23] https://www.fda.gov/medicaldevices/digitalhealth/

[24] https://www.accessdata.fda.gov/cdrh_docs/pdf15/K152733.pdf

heart surface from body surface potential recordings[25] For more information on these and other patient-specific cardiovascular models see (68).

As indicated by the relatively large number of pre-submissions (approximately five dozen) that contain computational modeling, many sponsors are using this mechanism to discuss with FDA how their computational approaches will be used in different regulatory pathways. The pre-submission[26] process enables interaction between companies and FDA to discuss issues (e.g., outstanding regulatory deficiencies) or present new technology or regulatory approaches. Pre-submissions might include details describing how computational modeling might support device performance, augment clinical trials, or be a part of a software as a medical device, but might also include the introduction of innovative devices for informational purposes or for strategic regulatory planning. The mechanism for early interaction is called the *Information Meeting*, found on page 22 of the guidance.

In this section, we have presented some success stories of computational modeling being used to support medical device regulatory review. However, there remain hurdles for broader adoption of computational modeling. FDA is using its leadership role to help overcome some of these hurdles; one in particular is on communication. The regulatory review process is typically dominated by the review of tens (sometime hundreds) of test reports. CDRH reviewers do not conduct or run simulations for specific regulatory submissions, and consequently rely on the details of a report to understand what was accomplished. Detailed and comprehensive reporting of computational modeling can thus substantively improve the acceptance of digital evidence submitted to CDRH. In 2016, FDA published a guidance document (69) on the details that should be provided to CDRH if computational modeling is used in a regulatory application. The scope of this guidance document, however, does not address the *adequacy* of the evidence, and therefore adherence to the guidance may not always result in a sufficiently credible digital evidence to support the device safety and/or effectiveness claims. Reasons for this failure include the lack of appropriate scope of use for the computational model or that the verification and validation (V&V) results provided do not support using the model for the specified use. Industry has communicated to FDA that what remains unclear is the V&V evidentiary bar and lack of standards for computational modeling studies. Therefore, FDA has been working closely with the ASME V&V40 Standards Subcommittee on a new standard (44) that will be published in Summer 2018. It presents a risk-informed credibility assessment framework that will help decision-makers determine the V&V evidence needed to support using a computational model for a specific context of use. Other device-specific modeling standards are being developed through ASTM and IEEE. Moreover, FDA actively engages with stakeholders about computational modeling efforts by hosting yearly workshops and conferences with co-sponsors such as the NIH & NSF[27] and the Biomedical Engineering Society (70), recorded webinars[28, 29, 30] and training seminars (71) on these documents. The use of simulation and digital evidence is rapidly evolving so FDA hopes industry will connect early and often through the pre-submission process to discuss potential opportunities for their computational modeling approaches.

FUTURE OF COMPUTATIONAL MODELING IN MEDICAL DEVICES

The rapid advance of technology has drastically changed the power and availability of computational modeling tools. Increased storage capacity via the cloud, the acceleration of the graphics processing unit (GPU), parallelization, multicore machines, and high performance computing have transformed and facilitated the building of higher fidelity models and models with more complexity through multiscale and multiphysics applications, and improved the resolution and capability for enhanced visualization. With this increased capability and power, evidence from computational modeling has the potential to replace traditional, more burdensome data collection from other models. Notable are the simulations of radiofrequency energy absorption that have replaced confirmatory clinical trials for the MR safety assessment of implants previously discussed (10). Wanting to find more opportunities to minimize the burden of animal and human studies, CDRH will continue to promote the use of computational modeling in medical device development, applications and regulatory submissions and is committed to ensuring the appropriate research, methodologies and expertise is available to make such advances. For example, the FDA has been exploring the use of computational modeling as a possible way to facilitate better reprocessing for reusable medical devices[31] Computational fluid dynamics models have the capability to isolate high risk regions in new device designs and can provide appropriate cleaning protocols to eliminate the risk of infection in reusable devices (72).

Another demonstrative example of FDA's commitment to facilitating innovation in medical devices is the collaboration between CDRH and industry through the Medical Device Innovation Consortium (MDIC) using the mechanism of a "mock submission" to demonstrate the regulatory process and evidence collection that could be submitted to FDA when using a new framework to augment clinical trials with virtual patients[32].

---

[25] https://www.accessdata.fda.gov/cdrh_docs/pdf16/k162440.pdf

[26] FDA Final Guidance, Software as a Medical Device (SAMD): Clinical Evaluation. (2017). Available from: https://www.fda.gov/downloads/medicaldevices/deviceregulationandguidance/guidancedocuments/ucm311176.pdf

[27] https://www.fda.gov/ucm/groups/fdagov-public/@fdagov-meddev-gen/documents/document/ucm364603.pdf

[28] ORS Webinar: FDA - Modeling and Simulation Initiatives at CDRH on Vimeo (2017): https://vimeo.com/194712010,

[29] ORS Webinar: FDA - Assessing the Predictive Capability of Computational Modeling for Medical Device Submissions on Vimeo (2017): https://vimeo.com/221479130,

[30] Xtalks Webinar (2018) FDA Perspectives on Computer Simulations in the Evaluation of Medical Devices, https://xtalks.com/webinars/fda-perspectives-on-computer-simulations-in-the-evaluation-of-medical-devices/

[31] https://www.fda.gov/MedicalDevices/DeviceRegulationandGuidance/ReprocessingofReusableMedicalDevices/ucm252952.htm

[32] Virtual Patient Website, http://mdic.org/computer-modeling/virtual-patients/

The mock submission approach has been a successful means to gather input from industry and FDA about new and innovative approaches for medical device evaluation (73). The MDIC, a non-profit in the U.S., was established to advance medical device regulatory science for patient benefit. The "Clinical Trials Informed by Bench and Simulation" working group included members from industry and FDA; their main objective was to establish and implement a framework, called the virtual patient discount model (VPDM), for incorporating virtual patients from simulation with real patient data from a clinical study through statistical simulations. Due to its novelty, the members of the working group formed a "sponsor team," with members from industry and FDA, and prepared the mock submission proposing to initiate a clinical trial with a reduced number of actual patients by harnessing virtual patients; the goal was to present and evaluate the VPDM. The VPDM (74) harnesses Bayesian methods in conjunction with FDA guidance (75) on the use of Bayesian statistics in medical device clinical trials. The mock submission highlighted two key themes. First, early communication between the sponsor and regulatory teams is important to identify areas for detailed discussion, education, or that raise issues of concern, particularly due to the intersection of clinical statistics and engineering simulation. Second, model credibility, suitability, and context of use should be integral to the model development work, as they will heavily influence the success of the approach. All mock submission documents and FDA's formal response are publicly available on the MDIC website for the Virtual Patient Project.

The aforementioned VICTRE project for imaging systems also exemplifies other advances FDA is considering for augmenting clinical trials. The power of this approach lies in the ability to replace expensive and lengthy clinical trials for new imaging systems with completely *in silico* trials. The physics for these systems are well-known and all aspects of the evaluation cycle can be simulated with sufficient confidence to replace each step with simulation. The main objective of this approach is to achieve the *same* regulatory conclusion with the virtual clinical trial as with a large 600-patient clinical trial (76). The success of this approach relies on statistical models, deep learning and artificial intelligence (AI); these advanced analysis and statistical methods, which are comparable with mechanistic, predictive engineering tools, have the potential to dramatically transform medical devices (77). In fact, CDRH just permitted the marketing of the first medical device with AI[33]. The device uses deep learning algorithms (78) to analyze images of the eye taken with a retinal camera for detecting diabetic retinopathy.

In other industries, computational modeling has long been recognized as a crucial scientific tool for getting innovative products into the hands of consumers[34] (79) and facilitating design excellence through product lifecycle management (PLM). "PLM is a business solution which aims to streamline the flow of information about the product and related processes throughout the product's lifecycle such that the right information in the right context at the right time can be made available (80)". If the medical device industry were to embrace PLM, they could more fully harness the power of simulation in each phase of the product's lifecycle and utilize AI tools to implement knowledge gained from real-world data to enhance their understanding of performance, support continuous improvement, and inform new designs and therapies. FDA also believes that computational modeling is poised to become a critical tool for accelerating regulatory decision-making. Continued adoption will be essential for advancing FDA's mission, improving our ability to evaluate medical devices more efficiently, reducing regulatory burden for sponsors, and accelerating the introduction of innovative technologies to the U.S. market for the benefit of patients.

AUTHOR CONTRIBUTIONS

TM led this study, designed the survey with PP and MA, analyzed results, organized and gathered references, drafted perspective article, organized multiple reviews and connected with authors cited in the article ensure accuracy. MA conducted the survey and interviews, collated responses in a database, and analyzed results. PP co-designed the survey, analyzed results, provided input and edited article. EM provided input on survey, analyzed results, provided input and edited article.

ACKNOWLEDGMENTS

We thank OSEL colleagues Leonardo Angelone, Genevieve McRae and Donna Lochner for reviewing this article; we value their perspective and input. We would also like to acknowledge Ms. Lochner for her support of advancing computational modeling as a regulatory tool, and for serving as a focal point for bringing academic, government and industry stakeholders together to tackle important issues during her tenure at the FDA.

---

[33] https://www.fda.gov/newsevents/newsroom/pressannouncements/ucm604357.htm

[34] UL Science news: https://newscience.ul.com/articles/computational-modeling-of-lithium-ion-batteries

REFERENCES

1. Hamburg MA. Advancing regulatory science. *Science* (2011) 331:987. doi: 10.1126/science.1204432
2. Institute of Medicine. *Assessing Medical Technologies*. Washington, DC: The National Academies Press (1985).
3. Morrison TM, Dreher ML, Nagaraja S, Angelone LM, Kainz W. The role of computational modeling and simulation in the total product life cycle of peripheral vascular devices. *J Med Devices* (2017) 11:024503. doi: 10.1115/1.4035866
4. International Medical Device Regulators Forum. *Final Guidance, Software as a Medical Device, IMDRF/SaMD WG/N10 FINAL*. Available online at: http://www.imdrf.org/docs/imdrf/final/technical/imdrf-tech-131209-samd-key-definitions-140901.pdf (2013)
5. Zavitsanou S, Chakrabarty A, Dassau E, Doyle FJ III. Embedded control in wearable medical devices: application to the artificial pancreas. *Processes* (2016) 4:35. doi: 10.3390/pr4040035
6. Cobelli C, Renard E, Kovatchev B. Artificial pancreas: past, present, future. *Diabetes* (2011) 60:2672–82. doi: 10.2337/db11-0654

7. Viceconti M, Cobelli C, Haddad T, Himes A, Kovatchev B, Palmer M. *In silico* assessment of biomedical products: The conundrum of rare but not so rare events in two case studies. *Proc Inst Mech Eng H*. (2017) 231:455–66. doi: 10.1177/0954411917702931
8. Himes A, Haddad T, Bardot D. Augmenting a clinical study with virtual patient models: food and drug administration and industry collaboration. *J Med Devices* (2016) 10:030947. doi: 10.1115/1.4033870
9. Kramer JM, Schulman KA. *Institute of Medicine (US). Envisioning a Transformed Clinical Trials Enterprise in the United States: Establishing an Agenda for 2020: Workshop Summary*. Washington (DC): National Academies Press (US) (2012). Appendix, F., Discussion Paper: Transforming the Economics of Clinical Trials. Available online at: https://www.ncbi.nlm.nih.gov/books/NBK114653/
10. Faris O, Shuren J. An FDA viewpoint on unique considerations for medical-device clinical trials. *NEJM* (2017) 376:1350–7. doi: 10.1056/NEJMra1512592
11. Brown R, White S, Goode J, Pradeep P, Merrill, S. Use of QSAR modeling to predict the carcinogenicity of color additives. In: *ASME 2013 Conference on Frontiers in Medical Devices: Applications of Computer Modeling and Simulation* (2013). p. 2. doi: 10.1115/FMD2013-16161
12. Marrey R, Baillargeon B, Dreher M, Weaver JD, Nagaraja S, Rebelo N, et al. Validating Fatigue safety factor calculation methods for cardiovascular stents. *J Biomech. Eng.* (2018) 140:9. doi: 10.1115/1.4039173
13. Duraiswamy N, Weaver JD, Ekrami Y, Retta SM, Wu C. A parametric computational study of the impact of non-circular configurations on bioprosthetic heart valve leaflet deformations and stresses: possible implications for transcatheter heart valves. *Cardiovasc Eng Technol* (2016) 7:126–38. doi: 10.1007/s13239-016-0259-9
14. Aycock KI, Campbell RL, Manning KB, Craven BA. A resolved two-way coupled CFD/6-DOF approach for predicting embolus transport and the embolus-trapping efficiency of IVC filters. *Biomech Model Mechanobiol.* (2017) 16:851–69. doi: 10.1007/s10237-016-0857-3
15. Donaldson FE, Nyman EJr, Coburn JC. Prediction of contact mechanics in metal-on-metal Total Hip Replacement for parametrically comprehensive designs and loads. *J Biomech.* (2015) 48:1828–35. doi: 10.1016/j.jbiomech.2015.04.037
16. Lucano E, Liberti M, Lloyd T, Apollonio F, Wedan S, Kainz W, et al. A numerical investigation on the effect of RF coil feed variability on global and local electromagnetic field exposure in human body models at 64 MHz. *Magn Reson Med*. (2018) 79:1135–44. doi: 10.1002/mrm.26703
17. Lucano E, Liberti M, Mendoza G, Lloyd T, Iacono MI, Apollonio F, et al. Assessing the electromagnetic field generated by a radiofrequency body coil at 64 MHz: defeaturing vs. accuracy. *IEEE Trans Biomed Eng.* (2016) 63:1591–601. doi: 10.1109/TBME.2015.2506680
18. Guha S, McCaffrey B, Hariharan P, Myers MR. Quantification of leakage of sub-micron aerosols through surgical masks and facemasks for pediatric use. *J Occup Environ Hyg.* (2017) 14:214–23. doi: 10.1080/15459624.2016.1237029
19. Malinauskas RA, Hariharan P, Day SW, Herbertson LH, Buesen M, Steinseifer U, et al. FDA benchmark medical device flow models for CFD validation. *ASAIO J.* (2017) 63:150–60. doi: 10.1097/MAT.0000000000000499
20. Bassen HI, Angelone LM. Evaluation of unintended electrical stimulation from MR gradient fields: simplified computational models vs. experimental measurements for an implanted lead wire in a human tissue-equivalent phantom. *Front Biosci E* (2012) 4:1731–42. doi: 10.2741/e494
21. Badal A, Badano A. Accelerating Monte Carlo simulations of photon transport in a voxelized geometry using a massively parallel graphics processing unit. *Med Phys.* (2009) 36:4878–80. doi: 10.1118/1.3231824
22. Graff CG, Sidky EY. Compressive sensing in medical imaging. *Appl Optics* (2015) 54:C23–44. doi: 10.1364/AO.54.000C23
23. Dreher ML, Nagaraja S, Bergstrom J, Hayman D. Development of a flow evolution network model for the stress-strain behavior of poly(L-lactide). *J Biomech Eng*. 139:091002. doi: 10.1115/1.4037071
24. Hariharan P, Gouza GD, Horner M, Morrison TM, Malinauskas RA, Myers MR. Use of the FDA nozzle model to illustrate validation techniques in computational fluid dynamics (CFD) simulations. *PloS ONE* (2017) 12:e0178749. doi: 10.1371/journal.pone.0178749
25. Gray RA, Pathmanathan PP. A Parsimonious model of the rabbit action potential elucidates the minimal physiological requirements for alternans and spiral wave breakup. *PLoS Comput Biol*. (2016) 12:e1005087. doi: 10.1371/journal.pcbi.1005087
26. Scully CG, Mitrou N, Braam B, Cupples WA, Chon KH. Detecting interactions between the renal autoregulation mechanisms in time and space. *IEEE Trans Biomed Eng*. (2017) 64:690–8. doi: 10.1109/TBME.2016.2569453
27. Bighamian R, Parvinian B, Scully CG, Kramer G, Hahn JO. Control-oriented physiological modeling of hemodynamic responses to blood volume perturbation. *Control Eng Practice* (2018) 73:149–60. doi: 10.1016/j.conengprac.2018.01.008
28. Galeotti L, van Dam PM, Loring Z. Evaluating strict and conventional left bundle branch block criteria using electrocardiographic simulations. *Europace* (2013) 15:1816–21 doi: 10.1093/europace/eut132
29. Hall SK, Williamson TH, Guillemaut JY, Goddard T, Baumann AP, Hutter JC. Modeling the dynamics of tamponade multicomponent gases during retina reattachment surgery. *AIChE J.* (2017) 9:3651–62. doi: 10.1002/aic.15739
30. Gurev V, Pathmanathan P, Fattebert JL, Wen HF, Magerlein J, Gray RA, et al. A high-resolution computational model of the deforming human heart. *Biomech Model Mechanobiol*. (2015) 14:829–49. doi: 10.1007/s10237-014-0639-8
31. Serano P, Angelone LM, Katnani H, Eskandar E, Bonmassar G. A novel brain stimulation technology provides compatibility with MRI. *Sci Rep*. (2015) 5:9805. doi: 10.1038/srep09805
32. Guerin B, Serano P, Iacono MI, Herrington TM, Widge AS, Dougherty DD, et al. Realistic modeling of deep brain stimulation implants for accurate electromagnetic MRI safety studies. *Phys Med Biol.* (2018) 63: 095015. doi: 10.1088/1361-6560/aabd50
33. Golestanirad L, Angelone LM, Iacono MI, Liang L, Katnani H, Wald LL, et al. Local SAR near deep brain stimulation (DBS) electrodes for realistic vs. simplified lead trajectories in patient-specific human head models. *Magn Reson Med*. (2017) 78:1558–1565. doi: 10.1002/mrm.26535
34. Golestanirad L, Iacono MI, Keil B, Angelone LM, Bonmassar G, Fox M, et al. Construction and modeling of a reconfigurable MRI coil for lowering SAR in patients with deep brain stimulation implants. *Neuroimage* (2017) 147:577–88. doi: 10.1016/j.neuroimage.2016.12.056
35. Park BS, Razjouyan A, Angelone LM, McCright B, Rajan SS. RF safety evaluation of a breast tissue expander device for mri: numerical simulation and experiment. *IEEE Trans Electromagn Compat.* (2017) 59:1390–9. doi: 10.1109/TEMC.2017.2678201
36. Razjouyan A, Park BS, Rajan SS, Kainz W, McCright B, Angelone LM. MRI in Pregnant Women: A Systematic Analysis of Radiofrequency Safety Assurance depending on Landmark Positions at 64/128 MHz. *Phys Med Biol.* (2018) 77: 2048–56. doi: 10.1002/mrm.26268
37. Iacono MI, Neufeld E, Bonmassar G, Akinnagbe E, Jakab A, Cohen E, et al. A computational model for bipolar deep brain stimulation of the subthalamic nucleus. In: *2014 36th Annual International Conference of the IEEE Engineering in Medicine and Biology Society*. Chicago, IL (2014). p. 6258–61. doi: 10.1109/EMBC.2014.6945059
38. Graff CG. A new, open-source, multi-modality digital breast phantom. *Phys Med Imaging* (2016) 9783:978309. doi: 10.1117/12.2216312
39. Wear KA, Nagaraja S, Dreher ML, Sadoughi S, Zhu S, Keaveny TM. Relationships among ultrasonic and mechanical properties of cancellous bone in human calcaneus *in vitro*. *Bone* (2017) 103:93–101. doi: 10.1016/j.bone.2017.06.021
40. Iacono MI, Neufeld E, Akinnagbe E, Wolf J, Oikonomidis IV, Sharma D, et al. MIDA: a multimodal imaging-based detailed anatomical model of the human head and neck. *PLoS ONE* (2015) 10:e0124126. doi: 10.1371/journal.pone.0124126

41. Christ A, Kainz W, Hahn EG, Honegger K, Zefferer M, Neufeld E, et al. The Virtual Family–development of surface-based anatomical models of two adults and two children for dosimetric simulations. *Phys Med Biol.* (2010) 55:N23–38. doi: 10.1088/0031-9155/55/2/N01
42. Gosselin MC, Neufeld E, Moser H, Huber E, Farcito S, Gerber L, et al. Development of a new generation of high-resolution anatomical models for medical device evaluation: the Virtual Population 3.0. *Phys Med Biol.* (2014) 59:5287–303. doi: 10.1088/0031-9155/59/18/5287
43. Aycock KI, Rebelo N, Craven C. Code verification for solid mechanics problems including superelastic nitinol. In: *ASME 2018 V&V Symposium* (2018).
44. ASME V and V40. *ANSI Standard, Assessing the Credibility of Computational Models for Medical Devices*. Available online at: http://go.asme.org/VnV40Committee (2018).
45. Morrison TM, Aycock KI, Weaver JD, Craven B. A mock submission to initiate a clinical trial in the U.S. with modeling and simulation. In: *Proceedings Virtual Physiological Human Institute Conference*. (Zaragosa) (2018).
46. Pathmanathan P, Gray RA, Romero VJ, Morrison TM. Applicability analysis of validation evidence for biomedical computational models. *J. Verif. Valid. Uncert.* (2017) 2:021005-021005-11. doi: 10.1115/1.4037671
47. Pathmanathan P, Gray RA. Validation and trustworthiness of multiscale models of cardiac electrophysiology. *Front Physiol.* (2018) 9:106. doi: 10.3389/fphys.2018.00106
48. Hariharan P, Nabili M, Guan A, Zderic V, Myers M. Model for porosity changes occurring during ultrasound-enhanced transcorneal drug delivery. *Ultrasound Med Biol.* (2017) 43:1223–36. doi: 10.1016/j.ultrasmedbio.2017.01.013
49. Halloran JP, Besier TF, Imhauser CW, Laz P, Morrison TM, Shelburne K, et al. A collaborative strategy to establish reproducibility in simulation-based prediction of natural knee mechanics. In: *Proceedings Virtual Physiological Human Institute Conference 2018.* (Zaragosa) (2018).
50. Parvinian B, Scully C, Wiyor H, Kumar A, Weininger S. Regulatory considerations for physiological closed-loop controlled medical devices used for automated critical care: food and drug administration workshop discussion topics. *Anesth Analg.* (2017) 126:1916–25. doi: 10.1213/ANE.0000000000002329
51. Soneson J. A user-friendly software package for hifu simulation. *AIP Conf Proc.* (2009) 1113:165. doi: 10.1063/1.3131405
52. Soneson JE. Extending the utility of the parabolic approximation in medical ultrasound using wide-angle diffracztion modeling. *IEEE Trans Ultrason Ferroelectr Freq Control.* (2017) 64:679–87. doi: 10.1109/TUFFC.2017.2654125
53. Aycock KI, Campbell RL, Lynch FC, Manning KB, Craven BA. Computational predictions of the embolus-trapping performance of an IVC filter in patient-specific and idealized IVC geometries. *Biomech Model Mechanobiol.* (2017) 16:1957–69. doi: 10.1007/s10237-017-0931-5
54. Gould T, Wang Q, Pfefer TJ. Optical-thermal light-tissue interactions during photoacoustic breast imaging. *Biomedical Opt Express* (2014) 5:832–47. doi: 10.1364/B.O.E.5.000832
55. Chandrasekar V, Janes DW, Forrey C, Saylor DM, Bajaj A. et al. Improving risk assessment of color additives in medical device polymers. *J Biomed Mater Res.* (2018) 106:310–9. doi: 10.1002/jbm.b.33845
56. Ghanian Z, Pezeshk A, Petrick N, Sahiner B. Towards the use of computationally inserted lesions for mammographic CAD assessment. In medical imaging 2018: image perception, observer performance, and technology assessment. *Int Soc Opt Photonics* (2018) 10577:105770L. doi: 10.1117/12.2293800
57. Saylor D, Buehler P, Brown R, Malinauskas R. Predicting plasma free hemoglobin levels in patients due to medical device related hemolysis. *ASAIO J.* (2018). doi: 10.1097/MAT.0000000000000801. [Epub ahead of print].
58. Saylor DM, Craven BA, Chandrasekar V, Simon DD, Brown RP, Sussman EM. Predicting patient exposure to nickel released from cardiovascular devices using multi-scale modeling. *Acta Biomater.* (2018) 70:304–14. doi: 10.1016/j.actbio.2018.01.024
59. Myers MR, Hariharan P, Guha S, Yan J. A mathematical model for assessing the effectiveness of protective devices in reducing risk of infection by inhalable droplets. *Math Med Biol A J IMA* (2018) 35:1–23. doi: 10.1093/imammb/dqw018
60. Badano A, Badal A, Glick S, Graff CG, Samuelson F, Sharma D, et al. *In silico* imaging clinical trials for regulatory evaluation: initial considerations for VICTRE, a demonstration study. In: *Medical Imaging 2017: Physics of Medical Imaging*, Thomas GF, Joseph YL, Taly GS, editors. Vol. 10132. International Society for Optics and Photonics (2017). p. 1013220.
61. Gallas BD. One-shot estimate of MRMC variance: AUC. *Acad Radiol.* (2006) 13:353–62. doi: 10.1016/j.acra.2005.11.030
62. Gallas BD, Pennello GA, Myers KJ. Multireader multicase variance analysis for binary data. *J Opt Soc Am A Special Issue Image Qual.* (2007) 24:B70–80. doi: 10.1364/JOSAA.24.000B70
63. Gallas BD, Brown DG. Reader studies for validation of CAD systems. *Neural Netw Special Conf Issue* (2008) 21:387–97. doi: 10.1016/j.neunet.2007.12.013
64. Gallas BD, Bandos A, Samuelson F, Wagner RF. A framework for random-effects roc analysis: biases with the bootstrap and other variance estimators. *Commun Stat A Theory* (2009) 38:2586–603. doi: 10.1080/03610920802610084
65. Gallas BD, Hillis SL. Generalized Roe and Metz ROC Model: analytic link between simulated decision scores and empirical AUC variances and covariances. *J Med Img* (2014) 1:031006. doi: 10.1117/1.JMI.1.3.031006
66. Gallas BD. iROEMETZ v2.1: Application for Modeling and Simulating MRMC Reader Studies.In: *Division of Imaging and Applied Mathematics*. Silver Spring, MD: CDRH, FDA. Available onlin at: https://github.com/DIDSR/iMRMC/releases.Computational Fluid Dynamics at the National Cancer Institute (NCI), National Institutes of Health (NIH) (2013).
67. Gallas BD. iMRMC v4.0: Application for Analyzing and Sizing MRMC Reader Studies. In: *Division of Imaging, Diagnostics, and Software Reliability*, Silver Spring, MD: OSEL/CDRH/FDA. Available onlin at: https://github.com/DIDSR/iMRMC/releases, https://cran.r-project.org/web/packages/iMRMC/index.html (2017).
68. Gray RA, Pathmanathan P. Patient-specific cardiovascular computational modeling: diversity of personalization and challenges. *J Cardiovasc Trans Res.* 11:80–8. doi: 10.1007/s12265-018-9792-2
69. Morrison TM.. *FDA Final Guidance. Reporting on Computational Modeling Studies for Medical Device Submissions. Issued September 21, 2016.* Available online at: https://www.fda.gov/downloads/MedicalDevices/DeviceRegulationandGuidance/GuidanceDocuments/Ucomputational modeling381813.pdf (2016).
70. Morrison TM, Angelone LM, Bestelmeyer A, Bischoff JE. Innovations in modeling and simulation: patient-centered healthcare. *Ann Biomed Eng.* (2016) 44:3719–49. doi: 10.1007/s10439-016-1710-7
71. Morrison T, Angelone L, Myers M, Soneson J, Wang Q, Weaver J, et al. FDA seminar on computational modeling for medical devices. *Figshare* (2017). doi: 10.6084/m9.figshare.5018783.v3
72. Hariharan P, Paruchuri SS, Topoleski LDT, Rinaldi J, Casamento JP, Myers MR, et al. A test method to assess the contribution of fluid shear-stress to the cleaning of reusable device surfaces. *J Biomed Mat Res B.* (in press).
73. Regnier FE, Skates SJ, Mesri M, Rodriguez H, TeŽak Ž, Kondratovich MV, et al. Protein-based multiplex assays: mock presubmissions to the US Food and Drug Administration. *Clin Chem* (2010) 56:165–71. doi: 10.1373/clinchem.2009.140087
74. Haddad T, Himes A, Thompson L, Irony T, Nair R, MDIC Computer Modeling and Simulation Working Group Participants. Incorporation of stochastic engineering models as prior information in Bayesian medical device trials. *J Biopharma Stats* (2017) 6:1089–103. doi: 10.1080/10543406.2017.1300907

75. Campbell G. *FDA Final Guidance. Guidance for the Use of Bayesian Statistics in Medical Device Clinical Trials*. Available online at: https://www.fda.gov/downloads/MedicalDevices/DeviceRegulationandGuidance/GuidanceDocuments/ucm071121.pdf (2010).
76. Badano A. Open-source, *In-Silico* clinical trial evaluating digital breast tomosynthoesis as replacement for mammography, (2018).
77. Hamidian S, Sahiner B, Petrick N, Pezeshk A. 3D convolutional neural network for automatic detection of lung nodules in chest CT. *Proc SPIE Int Soc Opt Eng*. (2017) 10134:1013409. doi: 10.1117/12.2255795
78. Gulshan V, Peng L, Coram M, Stumpe MC, Wu D, Narayanaswamy A, et al. Development and validation of a deep learning algorithm for detection of diabetic retinopathy in retinal fundus photographs. *JAMA* (2016) 316:2402–10. doi: 10.1001/jama.2016.17216
79. Miller L. Product Innovation Through Computational Prototypes and Supercomputing. *Comput Sci Eng.* (2017) 19:9–17. doi: 10.1109/MCSE.2017.3301223
80. Ameri F, Dutta D. Product lifecycle management: closing the knowledge loops. *Comput Aided Design Appl* (2005) 2:577–90. doi: 10.1080/16864360.2005.10738322

Disclaimer: The mention of commercial products, their sources, or their use in connection with material reported herein is not to be constructed as either an actual or implied endorsement of such products by the Department of Health and Human Services or the Food and Drug Administration.

Conflict of Interest Statement: The authors declare that the research was conducted in the absence of any commercial or financial relationships that could be construed as a potential conflict of interest.

The reviewer AH declared a past co-authorship with one of the authors TM to the handling Editor.

The reviewer AH and handling Editor declared their shared affiliation.

frontiers in Medicine

ORIGINAL RESEARCH
published: 02 October 2018
doi: 10.3389/fmed.2018.00277

Retrospective Evaluation of Bayesian Risk Models of LVAD Mortality at a Single Implant Center

Lisa C. Lohmueller[1]*, *Manreet K. Kanwar*[2], *Stephen Bailey*[2], *Srinivas Murali*[2] and *James F. Antaki*[3]

[1] Computer Science, Carnegie Mellon University, Pittsburgh, PA, United States, [2] Cardiovascular Institute, Allegheny General Hospital, Pittsburgh, PA, United States, [3] Biomedical Engineering, Cornell University, Ithaca, NY, United States

Use of a left ventricular assist device (LVAD) can benefit patients with end stage heart failure, but only with careful patient selection. In this study, previously derived Bayesian network models for predicting LVAD patient mortality at 1, 3, and 12 months post-implant were evaluated on retrospective data from a single implant center. The models performed well at all three time points, with a receiver operating characteristic area under the curve (ROC AUC) of 78, 76, and 75%, respectively. This evaluation of model performance verifies the utility of these models in "real life" scenarios at an individual institution.

Keywords: left ventricular assist device, Bayesian, mortality prediction, patient selection, heart failure, INTERMACS

Edited by:
Christopher Basciano,
Becton Dickinson, United States

Reviewed by:
Harry Staines,
Sigma Statistical Services,
United Kingdom
Kurt Stromberg,
Medtronic, United States

***Correspondence:**
Lisa C. Lohmueller
lcarey@cmu.edu

Specialty section:
This article was submitted to
Translational Medicine,
a section of the journal
Frontiers in Medicine

Received: *16 April 2018*
Accepted: *10 September 2018*
Published: *02 October 2018*

Citation:
Lohmueller LC, Kanwar MK, Bailey S, Murali S and Antaki JF (2018) Retrospective Evaluation of Bayesian Risk Models of LVAD Mortality at a Single Implant Center. Front. Med. 5:277. doi: 10.3389/fmed.2018.00277

INTRODUCTION

Heart failure is a chronic, progressive condition that affects over 6 million Americans. It is characterized by a decline in function of the heart to pump enough blood to perfuse the body (1). As the condition progresses, treatments may escalate from risk factor modification and oral medications to intravenous inotropes and surgical interventions, such and mechanical heart-assist pumps and heart transplantation (2). Heart transplantation is the gold standard treatment for end stage heart failure; however, donor heart supply is limited and not all patients are eligible for transplant, due to their age, comorbid conditions, or lifestyle choices. As an alternative, advanced heart failure patients may receive a durable left ventricular assist device (LVAD) as a bridge to transplant (BTT) or as a destination therapy (DT) (3).

LVADs can improve quality of life and increase patient survival (4, 5), but also require changes in daily life, a significant investment of time and money, and are associated with risks of adverse events (6). These tradeoffs underscore the importance of careful patient selection, for which predictive models can serve as an important component of risk assessment.

We recently developed models to predict post-LVAD mortality at 1, 3, and 12 months after implant (7) using the data from the Interagency Registry for Mechanically Assisted Circulatory Support (INTERMACS), the largest registry of retrospective LVAD patient data in the United States (4). The models were developed using Bayesian analysis and validated with a subset of registry data that was withheld from the model derivation. While use of the large registry dataset provides a robust model, it obscures institution-dependent differences in patient selection, care, and outcomes. Use of a personalized decision support tool in a "real world" clinical setting is necessary to understand its applicability at individual institutions.

Additionally, the INTERMACS registry has missing data and entry errors. The extent to which missing data affects the performance of the Bayesian predictive models is unknown; therefore, a carefully checked and evaluated dataset from a single clinical site was used to measure model performance.

This study was undertaken to establish the performance of our Bayesian models for LVAD mortality at a single institution with a complete, retrospective patient data set. The goal of this work was to prove the utility of the models for eventual use in prospective patient risk assessment.

METHODS

Data Acquisition and Cleaning

We acquired site-specific INTERMACS data for 100 consecutive patients who received a CF-LVAD at Allegheny General Hospital (AGH) between 2014 and 2015. Patients signed consent forms for their data to be collected in INTERMACS at the time of LVAD implant. A data sharing agreement was established between Carnegie Mellon University (CMU) and AGH to assure the security of protected health information in this study. This study was approved by CMU and AGH's review boards for biomedical research (IRBs).

The time-period was selected to include records with at least 1 year of follow up data. The data was organized into three categories: Pre-Implant, Post-Implant, and Events. Missing or illogical data (outside of feasible range or conflicting with other entries) was manually identified and checked by a data coordinator. Data elements that were designated as "unknown" or "missing" were addressed by reviewing all available patient medical records. In cases where the data could not be found, the data field was denoted as "not recorded." All units for continuous variables were also checked. Once all 100 patients were verified by the coordinator at AGH, the data set was sent to CMU for analysis.

Data cleaning revealed 9% of all pre-implant information (2,704 out of 28,500 possible fields, 2,850 per patient) was missing or out of range in the patient records. After data cleaning, this was reduced to 4% (1,184) fields that were confirmed as not recorded. This cleaned data set was used for the validation analysis.

Data Pre-processing

Pre-implant continuous data were binned into groups, which were determined during the initial model derivation (7) and briefly described, below. Mortality outcomes were determined for each patient using the Event data for each of the three time points: 1, 3, and 12 months post-LVAD.

Original Model Derivation and Predictive Variables

The models used in this analysis were derived using pre-implant patient information from INTERMACS from January 2012 to December 2015, for adults (over 18 years of age) who received their first primary continuous flow LVAD or LVAD and right ventricular assist device (RVAD) in combination ($n = 10{,}277$). This time frame was chosen to include current generation continuous flow LVADs and contemporary approaches to patient management. Outcomes for mortality were chosen at 1, 3, and 12 months after primary LVAD implant, to capture early outcomes that may impact hospital performance and reimbursement (8) (1 and 3 months) and long-term outcomes (12 months).

Naïve Bayes (NB) models were derived for each time point using a training dataset consisting of 80% of the records selected at random ($n = 8{,}222$). The remaining 20% ($n = 2{,}055$) were held aside for model validation. Continuous variables were discretized using either expert binning, equal frequency, or equal width binning to achieve the maximum information gain for each variable with respect to the model time-point. Feature selection was performed using information gain on the training data. Models were learned using the NB method in GeNie 2.2 (BayesFusion, Pittsburgh, PA). Each model was optimized by running 10-fold cross validation and removing variables with low diagnostic value (as measured in GeNie) until the area under the receiver operator characteristics curve (ROC AUC) dropped precipitously. The final NB models had 28, 26, and 21 predictive variables for the 1, 3, and 12-months outcomes, respectively, with 36 total unique variables. The resulting Bayesian models are illustrated in **Supplemental Material**.

Variables with the highest diagnostic value for 1-month post-LVAD mortality were concomitant RVAD implant, total number of events during the implant hospitalization, platelet count, bilirubin, aspartate aminotransferase, and INTERMACS profile. For the 3-months mortality model, the highest diagnostic value variables were concomitant RVAD implant, age, blood urea nitrogen, hemoglobin and INTERMACS profile. For the long-term mortality prediction, the most associated variables were age, blood urea nitrogen, hemoglobin, device strategy (DT), and concomitant RVAD implant. The diagnostic value for each variable in the model is captured in **Supplemental Material**.

Analysis of Patient Population

The patient population from the AGH study cohort was compared to the LVAD patient population from INTERMACS that was used for original model derivation and validation. Fisher's exact test, Pearson's chi-square and student's *t*-test were used to compare the populations in SPSS (IBM).

Model Validation and Comparison

The complete AGH data sets were used to measure the Bayesian mortality model performance for each time point, using test validation in GeNie (BayesFusion, Pittsburgh, PA). The resulting ROC AUCs were compared to the original model validation performance using DeLong's test (9) with the pROC package in R.

RESULTS

The patient cohort at AGH was similar to the overall INTERMACs population in terms of patient age and gender (**Table 1**). The main difference between cohorts were the distribution of INTERMACS profiles (p-value < 0.001) and the distribution of device strategies (p-value < 0.001). The AGH population had a larger proportion of INTERMACS profiles 1

TABLE 1 | Comparison of AGH patient cohort with overall INTERMACS registry.

Characteristic		AGH patients (n = 100)		INTERMACS patients (n = 10,277)		*p*-value
		Mean (SD)		**Mean (SD)**		
Age		56.2 (12.7)		56.9 (13)		*0.592*
		n	**%**	***n***	**%**	
Gender	Male	73	73%	8,044	78%	*0.280*
Ischemic Etiology	Yes	52	52%	4,637	45%	*0.189*
INTERMACS	1	20	20%	1,671	16%	
	2	48	48%	3,548	35%	
	3	14	14%	3,318	32%	
	4–7	18	18%	1,740	17%	*<0.001*
Device Strategy	BTT likely	67	67%	5,261	51%	
	BTT unlikely	5	5%	267	3%	
	DT	25	25%	4,658	45%	
	Other	3	3%	91	1%	*<0.001*
Mortality	1-month	4	4%	540	5%	*0.820*
	3-months	8	8%	976	9%	*0.733*
	12-months	18	18%	1,849	18%	*1.000*

INTERMACS, Interagency Registry for Mechanically Assisted Circulatory Support; BTT, bridge to transplant; DT, destination therapy.

TABLE 2 | 1-Month mortality model performance.

	Mortality at 1 month	Survival at 1 month	Total
Actual outcome	4	96	100
Predicted*	3	87	90
Performance	75% Sensitivity (95% CI 0.22–0.99)	91% Specificity (95% CI 0.82–0.95)	90% Accuracy

**Based on predictive survival above 50%.*

and 2 and a larger proportion of likely bridge to transplant (BTT) patients. The rate of mortality events was similar to the INTERMACs population for all three end-points.

One month after implant, 4 (4%) of the 100 AGH patients had died. The 1-month mortality model correctly predicted 3 out of the 4 deaths (75%) and predicted 87 out of 96 alive patients (91%), using a threshold of 50% (**Table 2**). The ROC AUC was 78%, with a 95% confidence interval (CI) of 0.36–1.0. This is performance is comparable to the original model validation of 70% ROC AUC, with CI 0.65–0.74 (**Figure 1**). Comparison of the ROC AUCs with DeLong's test yielded *p*-value = 0.71, no statistical difference in performance.

At 3 months after implant, 8 (8%) of the 100 patients had died. The Bayesian mortality model correctly predicted 4 of the 8 deaths (50%) and 83 of the 92 living patients (90%), using a mortality risk threshold of 50% (**Table 3**). The ROC AUC for the model performance was 76% with 95% CI 0.56–0.96. This is comparable to the original model test validation of 71%, with 95% CI 0.67–0.75 (**Figure 2**). Comparison of the ROC AUCs with DeLong's test yielded *p*-value = 0.61, no statistical difference in performance.

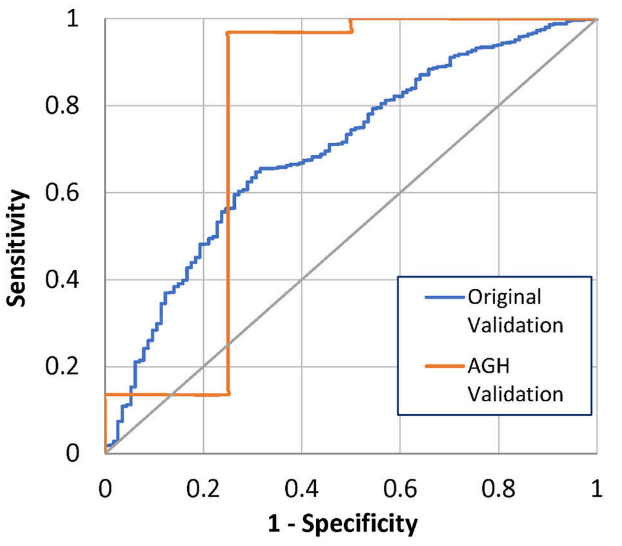

FIGURE 1 | ROC curves for 1-month mortality from original and AGH-specific validation.

By 12 months after implant, 18 (18%) of the 100 patients had died. The Bayesian mortality model correctly predicted 6 of the 18 deaths (33%) and 73 of the 82 living patients (89%), using a mortality risk threshold of 50% (**Table 4**). The ROC AUC for the model performance was 75%, 95% CI 0.65–0.87, which was comparable to the original model validation of 69%, 95% CI 0.66–0.72 (**Figure 3**). Comparison of the ROC AUCs with DeLong's test yielded *p*-value = 0.28, no statistical difference in performance.

TABLE 3 | 3-Months mortality model performance.

	Mortality at 3 months	Survival at 3 months	Total
Actual outcome	8	92	100
Predicted*	4	83	87
Performance	50% Sensitivity (95% CI 0.17–0.83)	90% Specificity (95% CI 0.82–0.95)	87% Accuracy

Based on predictive survival above 50%.

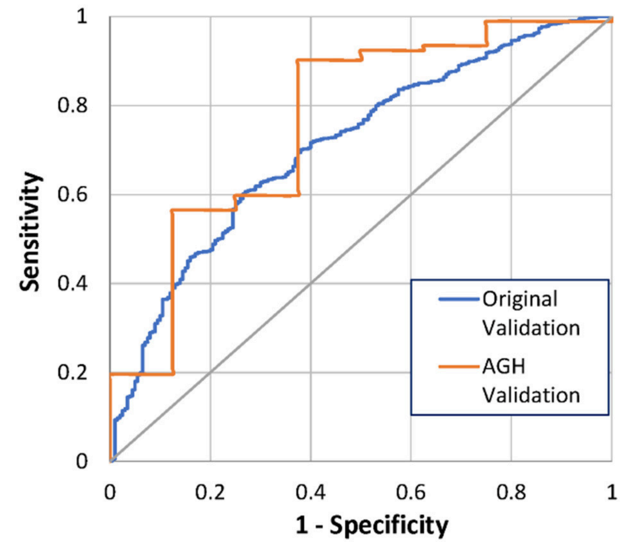

FIGURE 2 | ROC curves for 3-months mortality from original and AGH-specific validation.

TABLE 4 | 12-Months mortality model performance.

	Mortality at 12 months	Survival at 12 months	Total
Actual outcome	18	82	100
Predicted*	6	73	79
Performance	33% Sensitivity (95% CI 0.14–0.59)	75% Specificity (95% CI 0.80–0.94)	79% Accuracy

Based on predictive survival above 50%.

DISCUSSION

The Bayesian models for mortality derived on INTERMACS data performed with ROC AUCs of 78%, 76%, and 75% in a single center retrospective cohort for 1, 3, and 12 months post-LVAD implant, respectively. We had previously reported ROC AUCs of 70, 71, and 69% with a validation cohort from INTERMACS. All three mortality models performed comparably in the AGH patient dataset, indicating that these models have utility for prospective patient validation at this LVAD implant center.

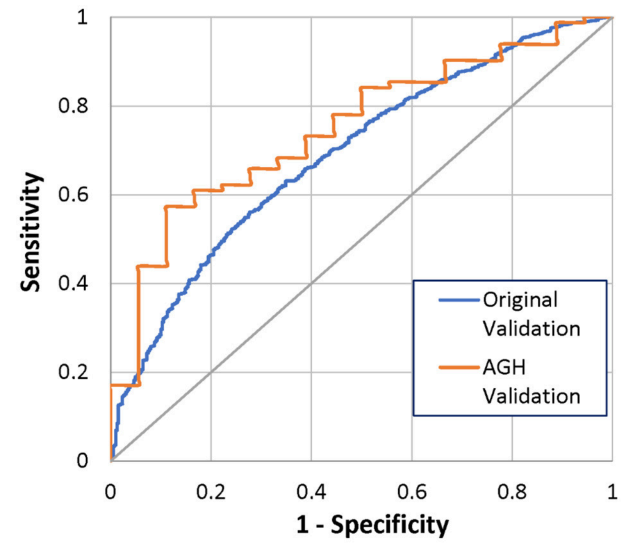

FIGURE 3 | ROC curves for 12-months mortality from original and AGH-specific validation.

Verifying model performance on a center's specific patient population is especially important given the influence of institutional experience on outcomes. This has been illustrated by the Heartmate II Risk Score, which includes institution implant volume as a statistically significant predictor for mortality outcomes (10). Additionally, an assessment of implant center volume on 1-year mortality of destination therapy (DT) patients found that low volume centers had a higher mortality rate (11). Similar relationships have been reported for transplant graft survival (12) and right heart failure-associated mortality (13). Since AGH is an experienced, high volume implant center, the models may perform better there than in a lower implant volume institution.

In addition to different in hospital experience, the mix of patient health status and strategy of patient management may impact model performance. There were significantly more patients with severe heart failure, as indicated by the percentage of patients with INTERMACS 1 and 2 profiles, at AGH. However, the mortality rates for AGH patients at each time point were comparable to the mortality rates in the INTERMACS population. Subjectivity in patient classification (14) or experience in patient management may contribute to the rate of patient survival. AGH also had significantly more patients who were BTT and fewer who were DT, compared to the INTERMACs population. However, this distribution of patients is in line with the INTERMACs cohort, where DT patients are more often INTERMACs profile 3 and 4 (15).

Despite the data cleaning step at AGH, there were 1,184 fields that were not recorded. A strength of using the Bayesian modeling for this risk tool is that it is robust to missing information when making predictions, as demonstrated by the resulting ROC AUCs. Whether having no missing data

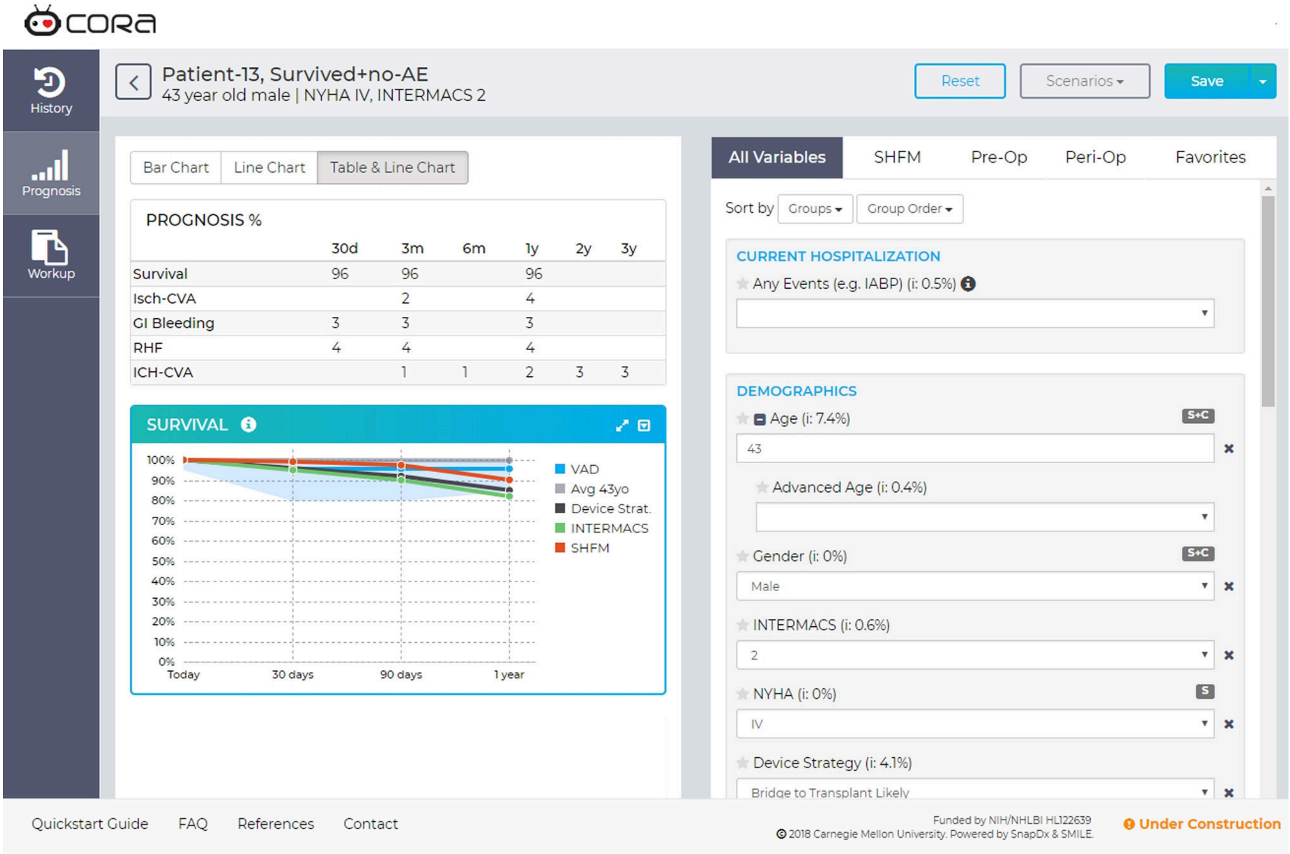

Patient-13, Survived+no-AE
43 year old male | NYHA IV, INTERMACS 2

PROGNOSIS %

	30d	3m	6m	1y	2y	3y
Survival	96	96		96		
Isch-CVA		2		4		
GI Bleeding	3	3		3		
RHF	4	4		4		
ICH-CVA		1	1	2	3	3

Sort by Groups Group Order

CURRENT HOSPITALIZATION

Any Events (e.g. IABP) (i: 0.5%)

DEMOGRAPHICS

Age (i: 7.4%): 43

Advanced Age (i: 0.4%)

Gender (i: 0%): Male

INTERMACS (i: 0.6%): 2

NYHA (i: 0%): IV

Device Strategy (i: 4.1%): Bridge to Transplant Likely

Funded by NIH/NHLBI HL122639
© 2018 Carnegie Mellon University. Powered by SnapDx & SMILE.

FIGURE 4 | Screen capture of the CORA decision support tool. The myCORA app shows risk predictions for survival, ischemic stroke (Isch-CVA), recurrent GI bleeding, right heart failure (RHF), and hemorrhagic stroke (ICH-CVA). Data are presented in the Prognosis table as percent probability at different time points. In the Survival line graph, the predicted survival for the patient on an LVAD is shown in the blue "VAD" line. The gray "Avg 43" presents the survival of a non-sick 43-years-old, derived from census data. The dark gray line "Device Strat" presents the survival prediction for all patients with the same device strategy (e.g., Bridge to Transplant). The green line "INTERMACS" presents the survival for all patients with the same INTERMACS Profile (e.g., profile 3). Finally, the orange line "SHFM" is the survival prediction for the patient calculated with the Seattle Heart Failure Model.

would improve the model performance remains unknown. However, it is unlikely that any institution can have a value for every possible patient variable, especially in cases where rapid patient deterioration requires an emergent decision. The use of Bayesian methods makes these models attractive for real world use.

The models assessed in this analysis are available at app.myCORA.org with an institutional login, as part of the Cardiac Outcomes Risk Assessment (CORA) decision support tool for physicians (**Figure 4**). This tool has begun to be prospectively evaluated by the multidisciplinary team at the weekly transplant meetings at AGH to assess its performance and impact on clinician decision making. At present, patient data will be entered manually into the tool by a VAD coordinator, but work is in progress to allow for integration with the electronic health record system. Predictive models for post-LVAD adverse events are being developed to add to the CORA tool (e.g., ischemic stroke, recurrent gastrointestinal bleeding, and right heart failure) and will be evaluated for performance with the same single center, retrospective validation methodology.

CONCLUSION

By validating the model set at a single clinical site, performance can be demonstrated for the patient population served at that particular site and for the unique surgical and medical management style of the clinicians. This exercise is imperative to confirm the utility of the mortality models for clinical decision making. Future work will be to prospectively test the model performance in the AGH multidisciplinary team meeting setting, to evaluate utility in real life decision making.

AUTHOR CONTRIBUTIONS

LL conceptualized the study, analyzed the data for this research, and wrote the manuscript. MK facilitated the data collection and provided input on study design, as well as provided substantial edits to the manuscript. SB edited the manuscript and provided insight for additional discussion. SM and JA provided input on study design, provided insight for discussion, and edited the manuscript.

ACKNOWLEDGMENTS

This work was supported by an R01 grant (R01HL086918) from the National Institutes of Health/National Heart, Lung, and Blood Institute.

This work made possible thanks to the Data Access, Analysis, and Publications Committee of INTERMACS for allowing us to use their registry for the study, with special thanks to Susan Meyers and Grant Studdard for administrative, database, and statistical assistance with INTERMACS. We are also grateful for contributions from Dr. Marek Druzdzel at the Decision Systems Laboratory, University of Pittsburgh and Ashley Wilfred, the data coordinator at AGH.

SUPPLEMENTARY MATERIAL

The Supplementary Material for this article can be found online at: https://www.frontiersin.org/articles/10.3389/fmed.2018.00277/full#supplementary-material

REFERENCES

1. *What is Heart Failure?* National Heart, Lung, and Blood Institute: U.S. Department of Health & Human Services (2015). Available online at: https://www.nhlbi.nih.gov/health/health-topics/topics/hf
2. *Classes of Heart Failure*. American Heart Association (2017). Available online at: http://www.heart.org/HEARTORG/Conditions/HeartFailure/AboutHeartFailure/Classes-of-Heart-Failure_UCM_306328_Article.jsp
3. Birati EYJ, Mariell. Left ventricular assist devices in the management of heart failure. *Card Fail Rev.* (2015) 1:25–30. doi: 10.15420/CFR.2015.01.01.25
4. Kirklin JK, Naftel DC, Pagani FD, Kormos RL, Stevenson LW, Blume ED, et al. Seventh INTERMACS annual report: 15,000 patients and counting. *J Heart Lung Transplant.* (2015) 34:1495–504. doi: 10.1016/j.healun.2015.10.003
5. Estep JD, Starling RC, Horstmanshof DA, Milano CA, Selzman CH, Shah KB, et al. Risk assessment and comparative effectiveness of left ventricular assist device and medical management in ambulatory heart failure patients: results from the ROADMAP study. *J Am Coll Cardiol.* (2015) 66:1747–61. doi: 10.1016/j.jacc.2015.07.075
6. Magid M, Jones J, Allen LA, McIlvennan CK, Magid K, Thompson JS, et al. The perceptions of important elements of caregiving for a left ventricular assist device patient: a qualitative meta-synthesis. *J Cardiovasc Nurs.* (2016) 31:215–25. doi: 10.1097/jcn.0000000000000242
7. Kanwar MK, Lohmueller LC, Kormos RL, Teuteberg JJ, Rogers JG, Lindenfeld J, et al. A Bayesian model to predict survival after left ventricular assist device implantation. *JACC Heart Fail.* (2018) 6:771–9. doi: 10.1016/j.jchf.2018.03.016
8. Chee TT, Ryan AM, Wasfy JH, Borden WB. Current state of value-based purchasing programs. *Circulation* (2016) 133:2197–205. doi: 10.1161/CIRCULATIONAHA.115.010268
9. DeLong ER, DeLong DM, Clarke-Pearson DL. Comparing the areas under two or more correlated receiver operating characteristic curves: a nonparametric approach. *Biometrics* (1988) 44:837–45.
10. Cowger JA, Castle L, Aaronson KD, Slaughter MS, Moainie S, Walsh M, et al. The HeartMate II risk score: an adjusted score for evaluation of all continuous-flow left ventricular assist devices. *ASAIO J.* (2016) 62:281–5. doi: 10.1097/mat.0000000000000362
11. Lietz K, Long JW, Kfoury AG, Slaughter MS, Silver MA, Milano CA, et al. Impact of center volume on outcomes of left ventricular assist device implantation as destination therapy: analysis of the Thoratec HeartMate Registry, 1998 to 2005. *Circ Heart Fail.* (2009) 2:3–10. doi: 10.1161/circheartfailure.108.796128
12. Haglund NA, Feurer ID, Ahmad RM, DiSalvo TG, Lenihan DJ, Keebler ME, et al. Institutional volume of heart transplantation with left ventricular assist device explantation influences graft survival. *J Heart Lung Transplant.* (2014) 33:931–6. doi: 10.1016/j.healun.2014.04.016
13. Krim SR, Vivo RP, Campbell P, Estep J, Fonarow GC, Naftel DC, et al. Regional differences in utilization and outcomes of left ventricular assist devices: insights from the intermacs registry. *J Heart Lung Transplant.* (2015) 34:912–20. doi: 10.1016/j.healun.2015.01.007
14. Cowger J, Shah P, Stulak J, Maltais S, Aaronson KD, Kirklin J, et al. Intermacs profiles and modifiers: heterogeneity of patient classification and the impact of modifiers on predicting patient outcome. *J Heart Lung Transplant.* (2016) 35:440–8. doi: 10.1016/j.healun.2015.10.037
15. Teuteberg JJ, Stewart GC, Jessup M, Kormos RL, Sun B, Frazier OH, et al. Implant strategies change over time and impact outcomes: insights from the INTERMACS (Interagency Registry for Mechanically Assisted Circulatory Support). *JACC Heart Fail.* (2013) 1:369–78. doi: 10.1016/j.jchf.2013.05.006

Conflict of Interest Statement: The authors declare that the research was conducted in the absence of any commercial or financial relationships that could be construed as a potential conflict of interest.

frontiers
in Physiology

ORIGINAL RESEARCH
published: 22 October 2018
doi: 10.3389/fphys.2018.01439

Radio-Frequency Safety Assessment of Stents in Blood Vessels During Magnetic Resonance Imaging

Kyoko Fujimoto, Leonardo M. Angelone, Elena Lucano, Sunder S. Rajan and Maria Ida Iacono*

Division of Biomedical Physics, Office of Science and Engineering Laboratory, Center for Devices and Radiological Health, U.S. Food and Drug Administration, Silver Spring, MD, United States

Purpose: The purpose of this study was to investigate the need for high-resolution detailed anatomical modeling to correctly estimate radio-frequency (RF) safety during magnetic resonance imaging (MRI). RF-induced heating near metallic implanted devices depends on the electric field tangential to the device (E_{tan}). E_{tan} and specific absorption rate (SAR) were analyzed in blood vessels of an anatomical model to understand if a standard gel phantom accurately represents the potential heating in tissues due to passive vascular implants such as stents.

Methods: A numerical model of an RF birdcage body coil and an anatomically realistic virtual patient with a native spatial resolution of 1 mm^3 were used to simulate the *in vivo* electric field at 64 MHz (1.5 T MRI system). Maximum values of SAR inside the blood vessels were calculated and compared with peaks in a numerical model of the ASTM gel phantom to see if the results from the simplified and homogeneous gel phantom were comparable to the results from the anatomical model. E_{tan} values were also calculated in selected stent trajectories inside blood vessels and compared with the ASTM result.

Results: Peak SAR values in blood vessels were up to ten times higher than those found in the ASTM standard gel phantom. Peaks were found in clinically significant anatomical locations, where stents are implanted as per intended use. Furthermore, E_{tan} results showed that volume-averaged SAR values might not be sufficient to assess RF safety.

Conclusion: Computational modeling with a high-resolution anatomical model indicated higher values of the incident electric field compared to the standard testing approach. Further investigation will help develop a robust safety testing method which reflects clinically significant realistic conditions.

Keywords: RF safety, SAR, blood vessels, small implantable device, tangential electric field

Edited by:
Markus Reiterer,
Medtronic (United States),
United States

Reviewed by:
Stephen Michael Moore,
IBM Research, Australia
Zhihui Wang,
Houston Methodist Research
Institute, United States

Correspondence:
Maria Ida Iacono
maria.iacono@fda.hhs.gov;
maria.iacono@gmail.com

Specialty section:
This article was submitted to
Computational Physiology
and Medicine,
a section of the journal
Frontiers in Physiology

Received: *17 April 2018*
Accepted: *21 September 2018*
Published: *22 October 2018*

Citation:
Fujimoto K, Angelone LM,
Lucano E, Rajan SS and Iacono MI
(2018) Radio-Frequency Safety
Assessment of Stents in Blood
Vessels During Magnetic Resonance
Imaging. Front. Physiol. 9:1439.
doi: 10.3389/fphys.2018.01439

INTRODUCTION

Magnetic resonance imaging (MRI) has become one of the most popular medical imaging modalities thanks to its noninvasive nature based on non-ionizing radiation. It is often used as the diagnostic tool of choice for various diseases and represents a safe imaging device, although some risks still exist and need to be mitigated. For example, the radio-frequency (RF) power used to elicit the magnetic resonance (MR) signal may induce a temperature increase inside the patient's body. Furthermore, implantable medical devices with electrically conductive components may act as RF antennas resulting in amplified energy absorption and temperature increase near the device, which may cause possible thermal tissue injury for the patient.

The ASTM F2182-11 standard proposes a testing method to assess MR RF heating safety of passive implantable devices such as stents (ASTM F2182-11a, 2011). The standard provides indication on how to evaluate the whole-body averaged specific absorption rate (SAR), the local SAR, and the temperature rise caused by the device using a rectangular box filled with a saline gel ("ASTM phantom").

The results of the ASTM testing are then used to generate the MR Conditional labeling of the device. Historically, ASTM testing has been considered to represent an upper limit for *in vivo* heating. Although the ASTM phantom allows heating assessment under well controlled conditions, one open question is how well an electrically homogeneous model can represent a whole human body with respect to RF-induced heating for implants. Anatomical structures in the human body are highly intricate and inhomogeneous. In addition, ASTM testing is performed with the phantom placed at the center of the RF coil whereas patients can be scanned in multiple positions depending on the anatomical area under clinical examination. Therefore, RF-induced heating measurements due to an implanted device performed using the ASTM phantom may not necessarily be the worst case and may not be directly translated into *in vivo* scenarios.

Choosing the right phantom to obtain a realistic assessment of *in vivo* heating in the human body is challenging. Adams et al. (2005) used an *ex vivo* superficial femoral artery to test 15 stents. It is difficult to perform such experiment for every possible stent because of the wide variety of shapes, materials (O'Brien and Carroll, 2009), and types, such as drug-eluting stents (Shellock and Forder, 2005; Garg and Serruys, 2010). Hug et al. (2000) tested 19 stents inside of yogurt, which has the MR relaxation time close to human myocardial tissue. Their choice of material successfully enabled them to observe safety of different stents including RF heating in the synthesized conditions. However, there remains an open question about the interactions of stents with the surrounding tissues such as muscle and fat. Creating an anthropomorphic phantom is difficult because tissue-mimicking medium and intricate structures of a human body are very challenging to fabricate.

Computational modeling is often used for medical device RF safety evaluation as a complementary approach to experimental measurements. The finite-difference time-domain (FDTD) method is one of the most popular techniques used to assess RF safety, as it allows calculating electromagnetic fields in anatomically detailed numerical whole-body human models. Currently available whole-body anatomical models have up to 77 anatomical structures (Ackerman, 1998; Nagaoka et al., 2003; Christ et al., 2009; Massey and Yilmaz, 2016). Some of these models have up to 1 mm spatial resolution and a fine segmentation of blood vessels, which are ideal for the MR RF safety analysis of a stent. Despite the availability of such high-resolution models, previous studies did not exploit the highest resolution of the models due to computational resource limitations.

For example, Homann et al. (2011) showed that a spatial resolution of 5 mm is sufficient to simulate the SAR of five volunteers. However, 5 mm spatial resolution does not allow the discernment and characterization of very thin structures such as blood vessels. With the advancement of computational hardware resources today, such as the amount of random-access memory (RAM) and the availability of a graphic processing unit (GPU), FDTD-based models up to 1 Giga cells – corresponding to a whole body spatial resolution of less than 2 mm – can now be handled. Such detailed simulations may provide more accurate predictions of the specific source of RF-induced heating and help us identify devices that are at higher risk for RF heating, due to their anatomical location.

In addition, using local SAR as the only parameter to assess RF-induced heating presents some significant limitations. Indeed, local SAR might not correlate directly with heating as it results from all the components of the electric field, while the tangential component of the electric field is exclusively responsible for the currents induced in the implant. As such, the local background SAR (tissue SAR without a device) may not be the best parameter to study RF-induced heating compared to tangential electric field.

In this study, we evaluated the local background voxel-averaged SAR (SAR_{raw}), 1 g-averaged SAR (SAR_{1g}), and 10 g-averaged SAR (SAR_{10g}) in the vascular territories of the 1 mm isotropic numerical whole-body AustinMan human model and in the ASTM phantom. The tangential electric field (E_{tan}) was also studied for selected trajectories typical of stents location within the vessels. Four imaging landmark positions of the human model within the RF coil were simulated with a local numerical resolution up to 0.98 mm.

MATERIALS AND METHODS

Computational Modeling Setup

Electromagnetic field simulations at 64 MHz (1.5 T MRI system) were performed using the commercially available FDTD platform, Sim4Life (Zurich Med Tech, Switzerland). The birdcage coil was modeled based on the MITS1.5 physical system (Zurich Med Tech, Zurich, Switzerland). As described by Lucano et al. (2016), the coil was 750 mm in length and 650 mm in diameter, included 16 legs and two rings. All the coil materials were modeled as perfect electric conductors (PEC). The coil was driven in quadrature mode with two sources of equal amplitude with a 90°phase shift. The electrical components (1 kΩ resistors and 69.5 pF capacitors) were distributed in parallel on the rings. The MRI RF exposure was modeled as a continuous wave, which is the typical approach used in literature. It is not directly scalable to the exposures at the clinical MRI scanners; however, it provides a worst-case exposure scenario as the clinical MR sequences never reach a 100% duty cycle.

The high-resolution AustinMan v2.4 model (Massey and Yilmaz, 2016) with 1 mm isotropic spatial resolution was chosen because the vascular territories were segmented in detail although some of the very thin vessels are not continuous. The model has 64 anatomical structures. Each structure was assigned to a material with a specific electrical conductivity, permittivity, and mass density based on Gabriel (1996).

Numerical Implementation

A multi-grid FDTD approach was used to discretize the simulation domain. In the multi-grid approach, a region with a main grid and another with a fine local grid were generated. The main grid with 2 mm isotropic resolution was used to discretize the anatomy of the patient. The fine local grid was used to discretize the fine components of the coil. As a result, some portions of the AustinMan model were discretized up to 0.98 mm in each dimension. A maximum isotropic resolution of 2 mm was used for the main grid as this was the highest achievable resolution utilizing all the available computational resources on our workstation (128 GB of RAM and NVIDIA Tesla K80 GPU).

SAR Values in ASTM vs. AustinMan

Four simulations were performed with the AustinMan model at four different imaging landmarks with the isocenter of the coil placed at the brain, the heart, the hip bone, and the knee. These body parts are scanned often with an MRI for diagnostic purposes. An additional simulation was run using the ASTM phantom model at the isocenter of the coil. The conductivity of the gel was 0.47 S/m. Each simulation with the AustinMan model took approximately 27 h. The simulation with the ASTM phantom took approximately 4 h.

The maximum $SARraw$, SAR_{1g}, and SAR_{10g} values were calculated over the entire ASTM phantom as well as within the 10 cm trajectory as recommended in the standard. The maximum SAR values were also calculated in the blood vessels of the AustinMan model at each landmark. 3D surface maps of the SAR distribution on the vessels were generated to observe the appearance of any localized high exposure. In addition, axial slices of SAR were compared with the anatomical segmentation to identify the vessels with high exposure.

Electric Field Tangential to Stents in Blood Vessels

Five stent locations were chosen and studied from Shellock (2014) as well as the archives of the premarket submissions on the U.S. Food and Drug Administration website (U.S. Food and Drug Administration, 2018). The location, orientation, and length of each stent trajectory in the AustinMan model was determined to calculate the tangential electric field.

Five case studies were analyzed for the ascending aorta, the brachial artery, the femoral artery, the iliac artery, and the popliteal artery. Stent trajectories were created based on the centerline of each blood vessel to model realistic scenarios. The centerlines were calculated in MATLAB (The MathWorks, Inc., Natick, MA, United States) by binarizing the label map of a specific vessel and determining the centroid of the consecutive axial slices. The centerline was then imported into Sim4Life to create a smooth trajectory. The E_{tan} value was calculated along each trajectory using the IMSAFE module in Sim4Life. The magnitudes of E_{tan} values were calculated offline.

E_{tan} values were also calculated in the gel of ASTM phantom. A straight 10 cm trajectory was placed in the gel where the electric field is high and homogeneous as recommended by ASTM standard (ASTM F2182-11a, 2011). The trajectory was placed along z-axis, 3.7 cm away from the wall of the container in x-axis, and the middle plane in y-axis. This satisfies the recommendation in the standard (at least 2 cm away from the gel surface, bottom, and walls of the container). Magnitudes of E_{tan} were calculated by following the same procedure as explained above for the stent trajectories.

Normalization

All the results were normalized to satisfy the limits of SAR defined for normal operating mode (IEC, 2015). Specifically, the normalization coefficient was calculated to ensure that the following three conditions were all satisfied: whole-body SAR $\leq$ 2 W/kg, head SAR $\leq$ 3.2 W/kg, and partial-body SAR $\leq$ 2–10 W/kg. The exact limit for partial-body SAR limit was determined based on the exposed mass covered under the RF coil at the landmark as follows.

$$\mathrm{SAR}_{\mathrm{exposed}} = 10\,\mathrm{W/kg} - \left(8\,\mathrm{W/kg} \times \frac{\text{exposed mass of AustinMan}}{\text{whole body mass of AustinMan}}\right)$$

In this study, the whole-body SAR of 2 W/kg was the limiting safety condition for all the simulations except for the simulation at the heart landmark, which was normalized using the partial-body SAR.

RESULTS

SAR Values in ASTM vs. AustinMan

The maximum SAR_{raw}, SAR_{1g}, and SAR_{10g} values in the ASTM phantom were compared against those in the AustinMan model at four landmarks. The results are summarized in **Figure 1**. The maximum SAR_{raw} value along the 10 cm trajectory was 4.9 W/kg. The ratio of the peak value at that location to the average SAR value of the phantom (2 W/kg) was 2.45.

The blood vessels of the AustinMan model showed much higher SAR values compared to the SAR values in gel regardless of volume averaging: the maximum values in the blood vessels were up to 63 times higher for SAR_{raw} (564.1 W/kg vs. 9.0 W/kg), up to 11 times higher for SAR_{1g} (92.2 W/kg vs. 8.7 W/kg), and up to nine times higher for SAR_{10g} (70 W/kg vs. 8.2 W/kg) compared to the entire ASTM phantom results. The maximum values in the blood vessels were up to 115 times higher for SAR_{raw} (564.1 W/kg vs. 4.9 W/kg), up to 19 times higher for SAR_{1g} (92.2 W/kg vs. 4.9 W/kg), and up to 14 times higher for SAR_{10g} (70 W/kg vs. 4.9 W/kg) compared to the reference point in the ASTM phantom as the standard suggests.

For the brain landmark, all the maximum SAR values were found in the heart region where various coronal stents can be implanted. For the heart landmark, the maximum SAR values

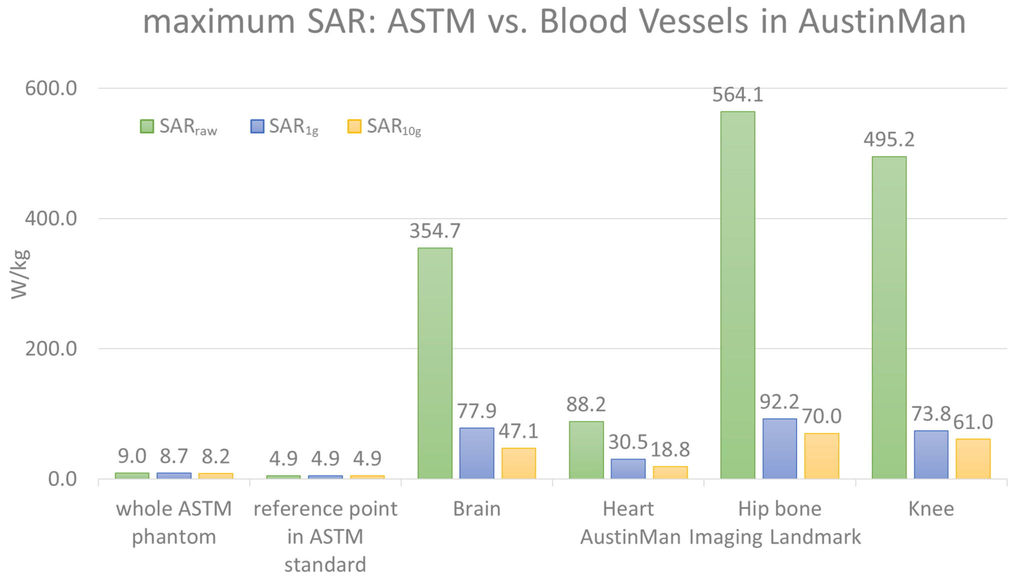

FIGURE 1 | The maximum values of SAR_{raw}, SAR_{1g}, and SAR_{10g} values are shown for the ASTM phantom model and the blood vessels at four different landmarks in the AustinMan model. The maximum SAR values in the ASTM phantom were identified in the whole ASTM phantom and within the 10 cm trajectory placed in the reference location suggested by the ASTM standard. The maximum SAR values in ASTM regardless of locations were much lower than that in the AustinMan model at any image landmarks. The maximum SAR_{10g} value in the blood vessels at the hip bone landmark was 70 W/kg, which was also the highest SAR_{10g} value among all the anatomical structures in the same simulation.

were found at the different locations. The maximum SAR_{raw} was located close to the skin where the AustinMan's left elbow is rested on the oblique abdominal region. The maximum SAR_{1g} was found in the AustinMan's right oblique abdominal region. The maximum SAR_{10g} was located in the lower spine where inferior and superior mesenteric stents can be implanted. At the hip bone landmark, all the maximum SAR values were found at the groin region where the brachytherapy devices can be inserted. These devices require MRI scans to calculate the dosage after the device is inserted in the body. For the knee landmark, the maximum SAR_{raw} was at the left ankle where bypass grafts can be implanted. The maximum SAR_{1g} and SAR_{10g} were at the location where popliteal stents can be implanted.

SAR Values in the Blood Vessels of AustinMan

The SAR maps from the AustinMan simulations were masked to evaluate the results exclusively in the blood vessels as shown in **Figure 2**. We performed masking after calculating volume-averaged SAR values. Thus, the SAR values of surrounding structures of blood vessels were considered in calculating over 1 and 10 g volumes. Clusters of high SAR values exceeding the ASTM peak were found for all SAR_{raw}, SAR_{1g}, and SAR_{10g} results. In addition, there were some high SAR regions being washed out by volume averaging. For example, the brachial artery showed high SAR_{raw}, but low SAR_{1g} and SAR_{10g} at the heart landmark (pink arrows in **Figure 2**). The SAR maps of the blood vessels at all the imaging landmarks (brain, heart, hip bone, and knee) are shown in **Supplementary Figure S1**.

All the SAR results were compared with the anatomical map of the AustinMan model. The blood vessels showed higher SAR compared to the surrounding tissues. Examples of such cases are shown in the axial slices in **Figure 3** along with the corresponding anatomical maps. Blood vessels are shown in cyan and the pink arrows indicate those with high SAR_{1g}. Maximum SAR_{1g} in the blood vessels shown in these axial slices are 32, 20, 23, and 40 W/kg, for the brain, heart, hip bone, and knee landmarks, respectively.

Electric Field Tangential to Stents in Blood Vessels

Five stent locations were identified in the AustinMan model (**Figure 4**). Stents for these selected locations can have a range of 10.0–300.0 mm in length and 2.5–46.0 mm in diameter. The lengths of the trajectories were 70.9 mm for the ascending aorta, 83.9 mm for the brachial artery, 179.7 mm for the femoral artery, 111.4 mm for the iliac artery, and 91.6 mm for the popliteal artery. Each length was determined based on the commercially available stents identified in **Figure 4** as well as the vessel continuity of the AustinMan model.

The E_{tan} profile in each location is shown in **Figure 5**. The landmark highly affected the E_{tan} values for all five different stent trajectories. High E_{tan} values were found in the brachial artery (194.1 V/m) at the heart landmark, the iliac artery (153.2 V/m) at the hip bone landmark, and the popliteal artery (231.3 V/m) at the knee landmark. The E_{tan} values were consistently high in the popliteal and iliac arteries at the hip bone landmark. The mean E_{tan} value in the popliteal artery was 59.6 V/m and the mean E_{tan} value at in the iliac artery was 111.5 V/m.

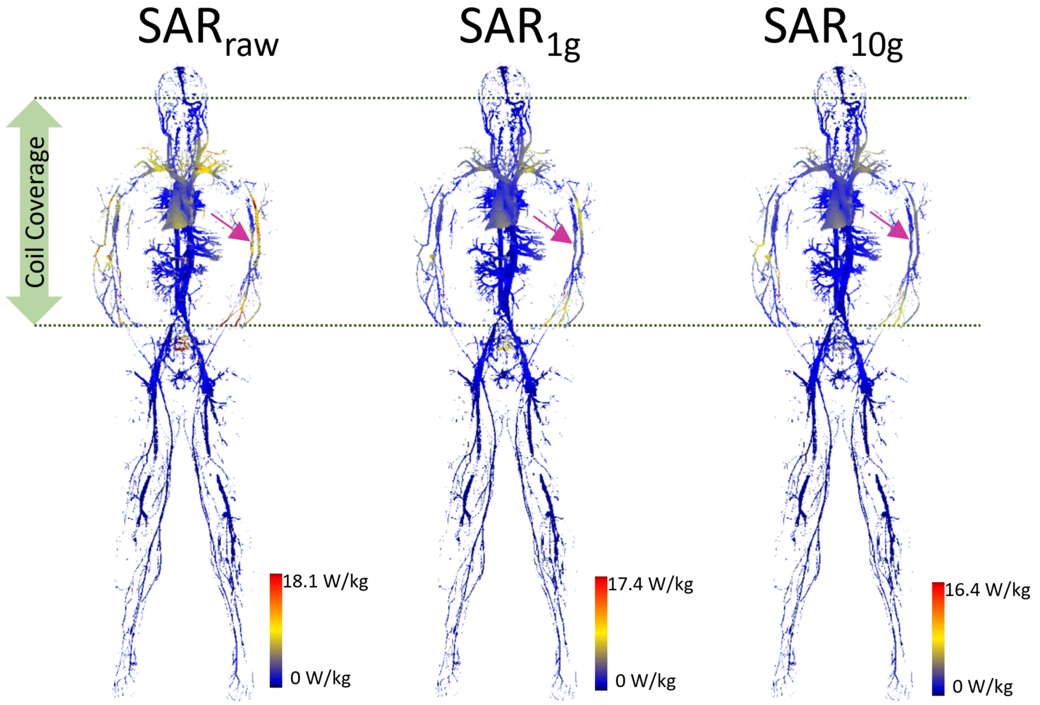

FIGURE 2 | The blood vessel 3D SAR maps at the heart landmark are shown. The color scale was set such that the maximum was twice the peak SAR calculated in the whole ASTM phantom model (9.0, 8.7, and 8.2 W/kg for SAR_{raw}, SAR_{1g}, and SAR_{10g}, respectively) to optimize the visualization of the peaks across all the models. The pink arrows pointing to the brachial artery show the example of high SAR values in SAR_{raw} which were washed away in the SAR_{1g} and SAR_{10g} maps due to volume averaging.

The maximum E_{tan} values in five blood vessel locations and in the ASTM phantom were compared (**Figure 6**). The following three stent locations exceeded the maximum E_{tan} in the gel of the ASTM phantom (146.2 V/m): the brachial artery at the heart landmark (194.1 V/m), the iliac artery at the hip bone landmark (153.2 V/m), and the popliteal artery at the knee landmark (231.3 V/m). The highest E_{tan} value which was found in the popliteal artery at the knee landmark was approximately 58% higher than that in the gel of the ASTM phantom.

DISCUSSION

In this study, we compared SAR and E_{tan} in the ASTM phantom with those in the AustinMan model at four landmarks and evaluated whether the RF exposure in a simplified geometry with a homogeneous medium is representative of the exposure in the human body in a clinical setting. The ratio of the peak SAR value in the 10 cm trajectory to the averaged SAR value in the ASTM phantom (2.45) was comparable to that of previous studies. Amjad et al. (2005) quantified the SAR distribution at 64 MHz with two different conductivities: 0.27 and 0.6 S/m. The ratio of their local to whole-phantom SAR values were 2.5 and 2, respectively. Additionally, this ratio is in line with values reported by MR testing companies when performing RF-safety testing in ASTM phantom (Song et al., 2018).

Some parts of the human model were subject to high SAR across different landmarks. For example, simulations at both the brain and the heart landmarks showed high SAR values in the common carotid arteries, the subclavian arteries, and the innominate artery. This is likely due to the length of the coil which covered those three arteries at both the brain and the heart landmarks. A shorter coil may result in a smaller exposed body volume, and the SAR_{raw} and E_{tan} values in those tissues may be lower. Nevertheless, tissues outside of the coil can still have high SAR due to eddy currents induced in the body as shown in the heart, hip bone, and knee landmarks (**Figure 3**). Thus, it is important to consider the possible effect of different coil geometrical and electrical characteristics when evaluating medical device safety.

This study focused on the safety assessment at 64 MHz (1.5 T MRI system). The scanners used in a clinical setting can have a static field up to 7 T. Therefore, further analysis may be needed to evaluate RF safety in the 3 and 7 T environments.

The SAR_{raw} values were proportional to the E_{tan} values in all the blood vessel trajectories that we evaluated. The popliteal artery at the knee landmark showed high SAR_{raw} values up to 76.2 W/kg and its averaged E_{tan} value was 154 V/m. The iliac artery at the hip bone landmark also showed high SAR values up to 68.9 W/kg and its averaged E_{tan} value was 112 V/m. The ascending aorta and the femoral artery had mean SAR_{raw} less than 2 W/kg and their averaged E_{tan} values were less than 50 V/m.

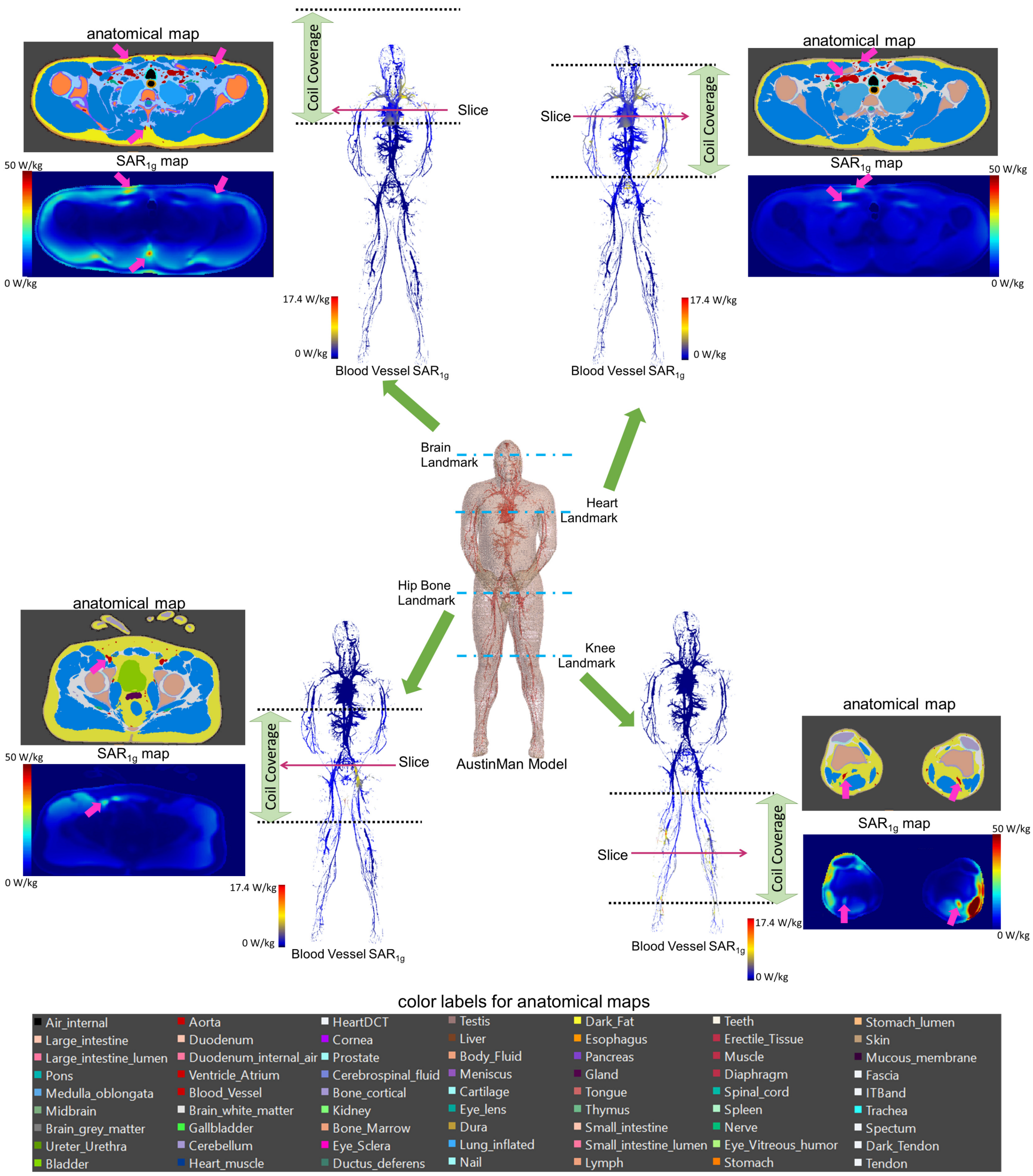

FIGURE 3 | 3D SAR_{1g} maps in blood vessels are shown for all four landmarks. High SAR_{1g} was reported in some of the blood vessels compared to surrounding tissues. Examples of high SAR_{1g} in vessels are provided in axial views along with the corresponding anatomical maps.

However, the volume-averaged SAR in the patient-left brachial artery at the heart landmark was not in agreement with E_{tan} because the high SAR_{raw} was washed out by averaging over the surrounding tissues. This example shows that volume averaging is not always a proper surrogate for E_{tan} and substantiates the need for SAR_{raw} or E_{tan} as metrics for safety assessment.

The length of the device also plays a key role in the quantification of heating. For electrically short devices (Volakis, 2007) with a length shorter than $\frac{\lambda}{4\pi}$ of the RF wavelength in tissues, the local background SAR at the tip of the implant can be used as surrogate metric for worst-case heating. Thus, in this scenario, *in vivo* heating may be estimated by simply scaling the background SAR with respect to *in vivo* local SAR without the need for performing a full thermal simulation with a stent. On the other hand, for a longer stent such as those used for peripheral arteries, this approach may not be valid since E_{tan} magnitude and phase contributions along the path of the device become more significant. In these cases, both the amplitude and phase of E_{tan} may need to be taken into account (Park et al., 2007), and full electromagnetic and thermal simulations may be needed with the device in place as per intended use.

We have shown the SAR and E_{tan} results of the ASTM model. The phantom has a homogeneous medium with a

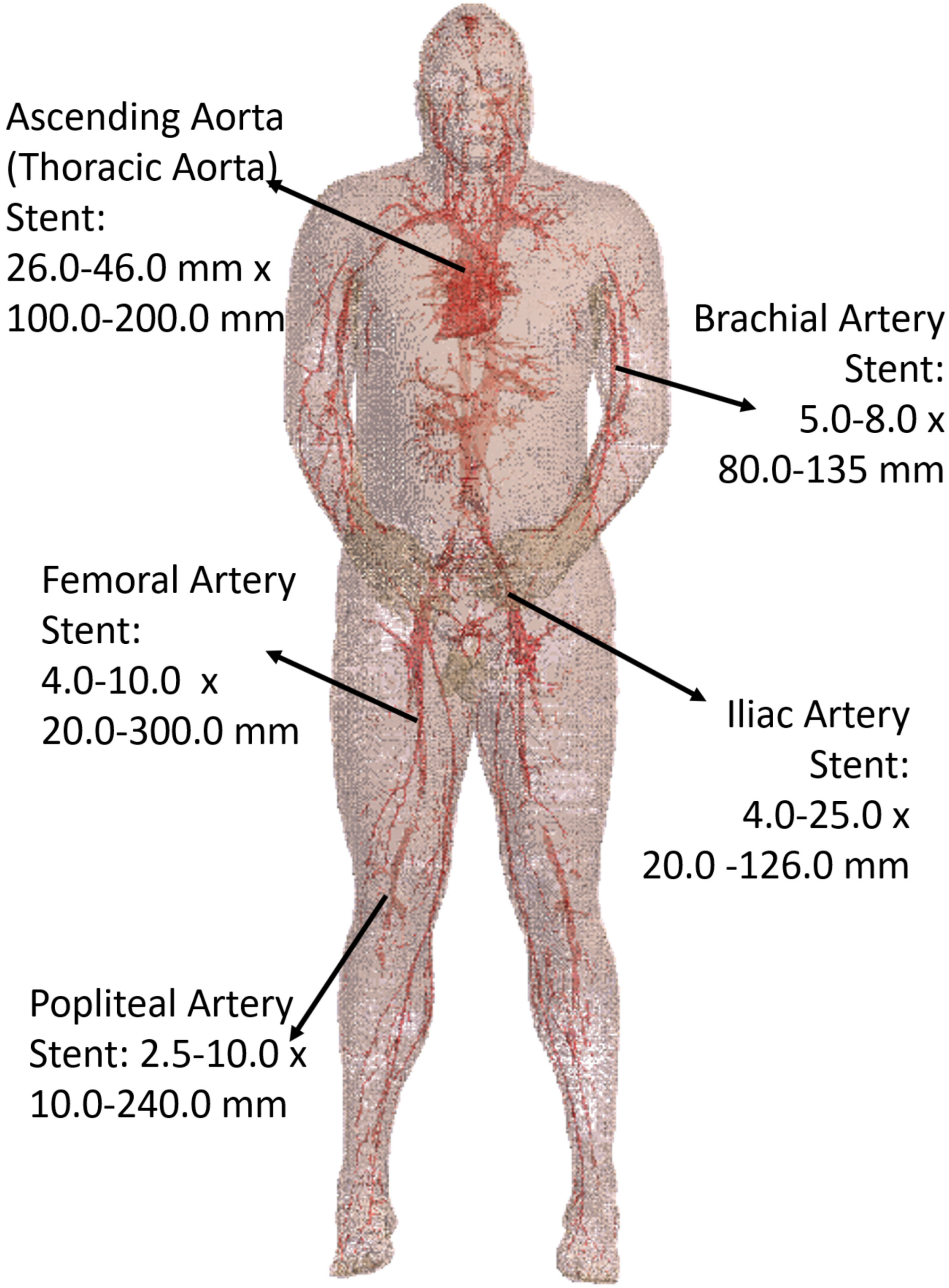

FIGURE 4 | The blood vessels of the AustinMan model and its skin are shown. The black arrows indicate the five stent locations investigated. The lengths and diameters of commercially available stents are summarized. The blood vessels are modeled in detail although some discontinuities exist.

simple rectangular structure whereas the human body consists of complex structures and various dielectric properties. The underestimation of SAR and E_{tan} values of the ASTM phantom may be due to the simple and homogenous structure.

This study highlighted the need of detailed anatomical modeling. We have not performed a detailed modeling of the stent structure which is one of the limitations of this study. Santoro et al. (2012) have modeled the geometry of a coronary stent at a 7.0 T MRI with finite element method (FEM) in a homogeneous phantom. Modeling an actual stent with the intricate whole-body anatomical human model is a hurdle with approaches based on FDTD due to the current limitations of computational

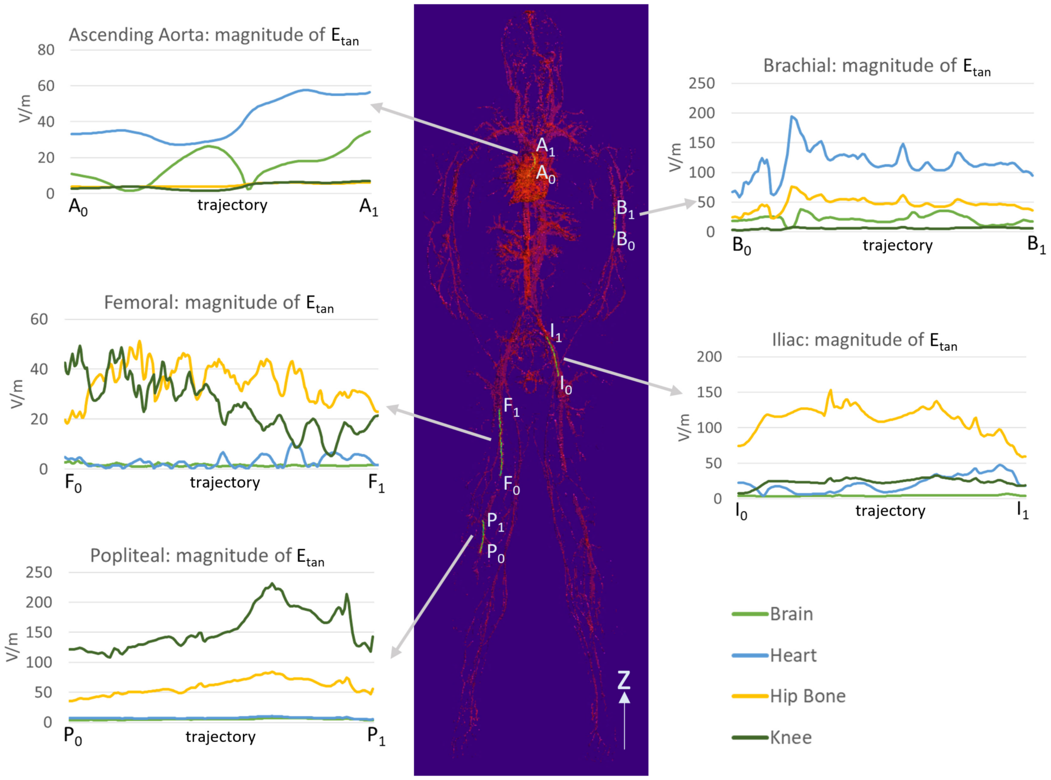

FIGURE 5 | The magnitudes of E_{tan} were calculated along five trajectories in the ascending aorta, the brachial artery, the femoral artery, the iliac artery, and the popliteal artery. The lengths of the trajectories were 70.9, 83.9, 179.7, 111.4, and 91.6 mm for the ascending aorta, the brachial artery, the femoral artery, the iliac artery, and the popliteal artery, respectively.

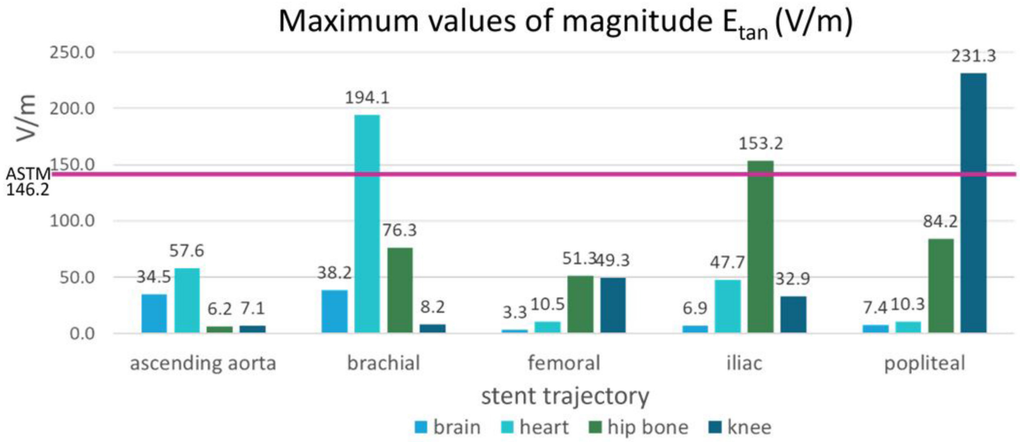

FIGURE 6 | The maximum magnitudes of E_{tan} calculated in the blood vessels of the five stent locations were compared with the maximum magnitude of E_{tan} calculated in the ASTM phantom (shown by the pink horizontal line).

resources. On the other hand, detailed anatomical models such as AustinMan are currently not available in FEM-based platforms. We envision that an improvement of computational resources and a development of FEM-based anatomical models may enable to overcome our current limitations.

In this study, the tissue properties of blood vessels modeled were limited to electrical conductivity, permittivity, and mass density. The *in vivo* blood vessels have blood perfusion and flow which have significant effect on reducing the RF induced heating. Moore et al. (2014) have incorporated heat sink due to both blood perfusion and skin blood perfusion in their models. Gross (2016) have shown that the flow reduces the temperature rise of a stent along with the surrounding medium significantly. Scandling (2016) reported the flow rate similar to the one of the iliac artery reduced the temperature by 4°C compared to the model without the flow. Elder (2013) also showed temperature reduction with different flow rates. Incorporating the blood perfusion and the different blood flow rate will enable more robust assessment in RF safety.

There is another possible scenario where SAR alone might not be sufficient to measure heating. The vascular tree spreads out all over the body as shown in **Figure 4**. Stents can be implanted in multiple orientations depending on the intended use. In these cases, E_{tan} may be more appropriate to use as a metric for safety assessment as SAR does not incorporate information on the angle of the electric field. Thus, further investigation with implantable devices placed at different angles in different tissues may be needed to assure the accuracy of the current safety assessment method.

This study focused on SAR and E_{tan} results in the ASTM phantom and the AustinMan model. Thermal simulations were not included and it is another limitation of the study. It is expected that investigating the translation to temperature rise will provide better understanding in SAR and E_{tan} values in each model.

Superficial tissues have higher exposure compared to deep tissues. For example, at the knee landmark, high SAR values were observed in the vessels in the ankle area. The vascular territories in this area tend to be close to the surface of the body (skin). The ankle area is one common placement for cosmetic tattoos where skin burns can occur during MRI (Ross and Matava, 2011). The detailed surrounding tissue conditions must be considered when modeling for safety evaluation.

For fine structures like skin, sub-millimeter modeling might be necessary to accurately estimate the electric field and potential heating. Currently, only the head has been modeled using a sub-millimeter spatial resolution (Iacono et al., 2015). In addition to a fine resolution, physiological responses of tissues may need to be included in the model to increase the accuracy of the prediction. Continued advancement of realistic computational modeling is necessary to assure the safety of performing MRI scans on patients with medical devices.

CONCLUSION

The simulation results in this study suggest that ASTM-based testing may underestimate *in vivo* values for the vascular regions in the human body. Computational modeling with high-resolution whole-body numerical models, when properly validated, represents an important tool to evaluate accurate RF exposure in blood vessels. Also, safety assessment may need to be tailored to the physical characteristic of the medical device and its position in the human body to ensure patient safety during an MRI scan.

AUTHOR CONTRIBUTIONS

LA, SR, and MI conceived the project and provided overall direction. KF designed the study, performed the computational modeling, and analyzed the data. EL designed the RF coil model. EL and MI assisted computational modeling setup. KF wrote the manuscript under the supervision of MI. All authors reviewed the manuscript.

FUNDING

This work was supported by the U.S. Food and Drug Administration Office of Women's Health and the Research Participation Program at the Center for Devices and Radiological Health administered by the Oak Ridge Institute for Science and Education through an inter-agency agreement between the United States Department of Energy and the U.S. Food and Drug Administration.

ACKNOWLEDGMENTS

The authors would like to thank Amir M. Razjouyan and Josh W. Guag for the helpful discussion on experimental measurement, Peter Serano, Amir M. Razjouyan, and Dr. Anant Agrawal for computer hardware assistance, Jake McCright for his help in identifying the locations of stents, and Trent Robertson, Drs. David Soltysik, and Brian B. Beard for helpful comments and discussion.

SUPPLEMENTARY MATERIAL

The Supplementary Material for this article can be found online at: https://www.frontiersin.org/articles/10.3389/fphys.2018.01439/full#supplementary-material

FIGURE S1 | The blood vessel 3D SAR maps at the brain, heart, hip bone, and knee landmarks are shown. The color scale was set such that the maximum was twice the peak SAR calculated in the whole ASTM phantom model (9.0, 8.7, and 8.2 W/kg for SAR_{raw}, SAR_{1g}, and SAR_{10g}, respectively) to optimize the visualization of the peaks across all the models.

REFERENCES

Ackerman, M. J. (1998). The visible human project. *Proc. IEEE* 86, 504–511. doi: 10.1109/5.662875

Adams, G. J., Baltazar, U., Karmonik, C., Bordelon, C., Lin, P. H., Bush, R. L., et al. (2005). Comparison of 15 different stents in superficial femoral arteries by high resolution mri ex vivo and *in vivo*. *J. Magn. Reson. Imaging* 22, 125–135. doi: 10.1002/jmri.20359

Amjad, A., Kamondetdacha, R., Kildishev, A., Park, S., and Nyenhuis, J. (2005). Power deposition inside a phantom for testing of MRI heating. *IEEE Trans. Magn.* 41, 4185–4187. doi: 10.1109/TMAG.2005.854840

ASTM F2182-11a (2011). *Standard Test Method for Measurement of Radio Frequency Induced Heating On or Near Passive Implants During Magnetic Resonance Imaging*. West Conshohocken, PA: Standard, American Society for Testing and Materials (ASTM) International.

Christ, A., Kainz, W., Hahn, E. G., Honegger, K., Zefferer, M., Neufeld, E., et al. (2009). The virtual family—development of surface-based anatomical models of two adults and two children for dosimetric simulations. *Phys. Med. Biol.* 55, N23–N38. doi: 10.1088/0031-9155/55/2/N01

Elder, N. (2013). *Effects of Blood Flow on the Heating of Cardiac Stents Due to Radio Frequency Fields*. Ph.D. thesis, Purdue University, West Lafayette, IN.

Gabriel, C. (1996). "Compilation of the dielectric properties of body tissues at rf and microwave frequencies," in *Tech Rep*, King's Coll London: Dept of Physics. doi: 10.21236/ADA303903

Garg, S., and Serruys, P. W. (2010). Coronary stents: looking forward. *J. Am. Coll. Cardiol.* 56, S43–S78. doi: 10.1016/j.jacc.2010.06.008

Gross, D. C. (2016). *Improving Patient Safety by Quantifying Vascular Tissue Damage from Radio Frequency Induced Heating of Implanted Medical Devices During Magnetic Resonance Imaging* Ph.D. thesis, The Ohio State University, Columbus, OH.

Homann, H., Bornert, P., Eggers, H., Nehrke, K., Dossel, O., and Graesslin, I. (2011). Toward individualized sar models and *in vivo* validation. *Magn. Reson. Med.* 66, 1767–1776. doi: 10.1002/mrm.22948

Hug, J., Nagel, E., Bornstedt, A., Schnackenburg, B., Oswald, H., and Fleck, E. (2000). Coronary arterial stents: safety and artifacts during mr imaging. *Radiology* 216, 781–787. doi: 10.1148/radiology.216.3.r00se03781

Iacono, M. I., Neufeld, E., Akinnagbe, E., Bower, K., Wolf, J., Oikonomidis, I. V., et al. (2015). Mida: a multimodal imaging-based detailed anatomical model of the human head and neck. *PLoS One* 10:e0124126. doi: 10.1371/journal.pone.0124126

IEC (2015). *Medical Electrical Equipment - Part 2-33: Particular Requirements for the Basic Safety and Essential Performance of Magnetic Resonance Equipment for Medical Diagnosis*. Geneva: IEC.

Lucano, E., Liberti, M., Mendoza, G. G., Lloyd, T., Iacono, M. I., Apollonio, F., et al. (2016). Assessing the electromagnetic fields generated by a radiofrequency mri body coil at 64 mhz: defeaturing versus accuracy. *IEEE Trans. Biomed. Eng.* 63, 1591–1601. doi: 10.1109/TBME.2015.2506680

Massey, J. W., and Yilmaz, A. E. (2016). "Austinman and austinwoman: high-fidelity, anatomical voxel models developed from the vhp color images," in *Proceedings of the Engineering in Medicine and Biology Society (EMBC) 2016 IEEE 38th Annual International Conference of the (IEEE)* (Orlando, FL: EEE), 3346–3349.

Moore, S. M., McIntosh, R. L., Iskra, S., and Wood, A. W. (2014). Effect of adverse environmental conditions and clothing on temperature rise in a human body exposed to radiofrequency electromagnetic fields. *IEEE Trans. Biomed. Eng.* 62, 627–637. doi: 10.1002/bem.22048

Nagaoka, T., Watanabe, S., Sakurai, K., Kunieda, E., Watanabe, S., Taki, M., et al. (2003). Development of realistic high-resolution whole-body voxel models of japanese adult males and females of average height and weight, and application of models to radio-frequency electromagnetic-field dosimetry. *Phys. Med. Biol.* 49, 1–15. doi: 10.1088/0031-9155/49/1/001

O'Brien, B., and Carroll, W. (2009). The evolution of cardiovascular stent materials and surfaces in response to clinical drivers: a review. *Acta Biomater.* 5, 945–958. doi: 10.1016/j.actbio.2008.11.012

Park, S.-M., Kamondetdacha, R., and Nyenhuis, J. A. (2007). Calculation of mri-induced heating of an implanted medical lead wire with an electric field transfer function. *J. Magn. Reson. Imaging* 26, 1278–1285. doi: 10.1002/jmri.21159

Ross, J. R., and Matava, M. J. (2011). Tattoo-induced skin "burn" during magnetic resonance imaging in a professional football player: a case report. *Sports Health* 3, 431–434. doi: 10.1177/1941738111411698

Santoro, D., Winter, L., Müller, A., Vogt, J., Renz, W., Özerdem, C., et al. (2012). Detailing radio frequency heating induced by coronary stents: a 7.0 tesla magnetic resonance study. *PLoS One* 7:e49963. doi: 10.1371/journal.pone.0049963

Scandling, B. (2016). *Radio Frequency Induced Heating of a Medical Device with Vascular Flow Conditions*. Undergraduate thesis, The Ohio State University, Columbus, OH.

Shellock, F. G. (2014). *Reference Manual for Magnetic Resonance Safety*. Los Angeles: Biomedical Research Publishing Group.

Shellock, F. G., and Forder, J. R. (2005). Drug eluting coronary stent: in vitro evaluation of magnet resonance safety at 3 tesla. *J. Cardiovasc. Magn. Reson.* 7, 415–419. doi: 10.1081/JCMR-200053588

Song, T., Xu, Z., Iacono, M. I., Angelone, L. M., and Rajan, S. (2018). Retrospective analysis of RF heating measurements of passive medical implants. *Magn. Reson. Med.* doi: 10.1002/mrm.27346 [Epub ahead of print].

U.S. Food and Drug Administration (2018). *Devices@FDA*. Available at: https://www.accessdata.fda.gov/scripts/cdrh/devicesatfda/index.cfm

Volakis, J. L. (2007). *Antenna Engineering Handbook*. 4th Edn. New York, NY: McGraw-Hill Professional.

Disclaimer: The mention of commercial products, their sources, or their use in connection with material reported herein is not to be construed as either an actual or implied endorsement of such products by the Department of Health and Human Services.

Conflict of Interest Statement: The authors declare that the research was conducted in the absence of any commercial or financial relationships that could be construed as a potential conflict of interest.

frontiers
in Physiology

ORIGINAL RESEARCH
published: 16 November 2018
doi: 10.3389/fphys.2018.01594

Functionalized Anatomical Models for Computational Life Sciences

Esra Neufeld[1*], *Bryn Lloyd*[1], *Beatrice Schneider*[2], *Wolfgang Kainz*[3] *and Niels Kuster*[1,4]

[1] IT'IS Foundation for Research on Information Technologies in Society, Zurich, Switzerland, [2] Ärzteteam 51, Arbeitsmedizin Brugg, Brugg, Switzerland, [3] Division of Biomedical Physics, OSEL, CDRH, Food and Drug Administration, Silver Spring, MD, United States, [4] Swiss Federal Institute of Technology (ETHZ), Zurich, Switzerland

The advent of detailed computational anatomical models has opened new avenues for computational life sciences (CLS). To date, static models representing the anatomical environment have been used in many applications but are insufficient when the dynamics of the body prevents separation of anatomical geometrical variability from physics and physiology. Obvious examples include the assessment of thermal risks in magnetic resonance imaging and planning for radiofrequency and acoustic cancer treatment, where posture and physiology-related changes in shape (e.g., breathing) or tissue behavior (e.g., thermoregulation) affect the impact. Advanced functionalized anatomical models can overcome these limitations and dramatically broaden the applicability of CLS in basic research, the development of novel devices/therapies, and the assessment of their safety and efficacy. Various forms of functionalization are discussed in this paper: (i) shape parametrization (e.g., heartbeat, population variability), (ii) physical property distributions (e.g., image-based inhomogeneity), (iii) physiological dynamics (e.g., tissue and organ behavior), and (iv) integration of simulation/measurement data (e.g., exposure conditions, "validation evidence" supporting model tuning and validation). Although current model functionalization may only represent a small part of the physiology, it already facilitates the next level of realism by (i) driving consistency among anatomy and different functionalization layers and highlighting dependencies, (ii) enabling third-party use of validated functionalization layers as established simulation tools, and (iii) therefore facilitating their application as building blocks in network or multi-scale computational models. Integration in functionalized anatomical models thus leverages and potentiates the value of sub-models and simulation/measurement data toward ever-increasing simulation realism. In our o^{2}S^{2}PARC platform, we propose to expand the concept of functionalized anatomical models to establish an integration and sharing service for heterogeneous computational models, ranging from the molecular to the organ level. The objective of o^{2}S^{2}PARC is to integrate all models developed within the National Institutes of Health SPARC initiative in a unified anatomical and computational environment, to study the role of the peripheral nervous system in controlling organ physiology. The functionalization concept, as outlined for the o^{2}S^{2}PARC platform, could form the basis for many other application areas of CLS. The relationship to other ongoing initiatives, such as the Physiome Project, is also presented.

Keywords: computational life sciences, computational phantom, anatomical model, functionalization, simulation, modeling

Edited by:
Melissa Knothe Tate,
University of New South Wales,
Australia

Reviewed by:
William W. Lytton,
SUNY Downstate Medical Center,
United States
Steve McKeever,
Uppsala University, Sweden

****Correspondence:***
Esra Neufeld
neufeld@itis.swiss

Specialty section:
This article was submitted to
Computational Physiology and
Medicine,
a section of the journal
Frontiers in Physiology

Received: *12 April 2018*
Accepted: *24 October 2018*
Published: *16 November 2018*

Citation:
Neufeld E, Lloyd B, Schneider B,
Kainz W and Kuster N (2018)
Functionalized Anatomical Models for
Computational Life Sciences.
Front. Physiol. 9:1594.
doi: 10.3389/fphys.2018.01594

1. INTRODUCTION

Human and animal anatomical models, highly detailed geometric representations of the distribution of different tissues in the body, have established themselves as crucial components not only for the dosimetric assessment of ionizing/non-ionizing radiation exposure, but also, more recently, in computational life sciences (CLS)—e.g., to gain mechanistic understanding, to develop novel therapeutic approaches and medical devices, or to demonstrate the safety of implants in magnetic resonance environments. The greater vision is that they can be routinely applied for treatment personalization and optimization, and to complement or replace classical animal or human clinical trials by *in silico* clinical trials for the assessment of safety and/or efficacy. The first ever created, highly detailed anatomical models for dosimetric simulation purposes were based on the cryosection data from the Visible Human project (Spitzer et al., 1996). Thanks to advances in imaging technologies, such models are now mainly based on non-invasive imaging, thus enabling the creation of representations of broader sections of the population and of personalized anatomical models. One example is our Virtual Population (ViP), a set of highly detailed anatomical models (Christ et al., 2009; Gosselin et al., 2014) generated from magnetic resonance imaging (MRI) data of male and female adults and children across a wide range of ages, including models of an elderly and an obese male. To date, the ViP has been used in over 1000 publications and over 200 regulatory submissions worldwide. Another widely employed set of models are the XCAT phantoms (Segars et al., 2018). These are NURBS-based models (whereas the ViP employs triangle meshes) that are particularly popular in ionizing radiation dosimetry research.

The rise of computational modeling, involving complex anatomical models, has been fueled by progress in simulation methodology, available computational power, and the existence of a larger number of suitable anatomical models (Xu, 2014). The latest generation of anatomical models, such as VIP 3.0, provides the necessary detailed 3D tissue (and tissue properties) distributions to determine whole-body and local physical exposure and interactions. However, the anatomical representation of the body cannot be entirely separated from the modeling of living tissue and (organ) physiology within it. Physical exposure from medical devices/therapies is the source of tissue interactions that affect (with therapeutic benefit or adversely) physiology, while physiology affects exposure. For example, dielectric tissue properties affect electromagnetic (EM) exposure in neurostimulation applications, resulting in modulation of electrophysiological function. In turn, physiological activity, such as breathing, can result in changes to the anatomical geometry, which then affects the medical device function (e.g., a radiotherapy treatment). Local energy absorption results in a thermoregulatory response that determines the final tissue temperature distribution. Hence, there is the need to bring anatomical and physiology representation closer together. Support in this endeavor is offered by recent rapid advances in medical imaging, which provide access to detailed information about the anatomy, physiological dynamics, and tissue properties and behavior, as well as by an increased understanding of the physiology and its computational representation.

In this paper, we present our vision of functionalized anatomical models as a paradigm for CLS (a more limited neuro-functionalized anatomical model concept has been formulated in Neufeld et al., 2016a). The goal is to discuss different forms that model functionalization can take, as well as how they can converge in a comprehensively functionalized general model, and to illustrate them with practical examples drawn from our efforts toward generating such models. Furthermore, we introduce and argue the concept of using functionalized anatomical models as integration centers for heterogeneous models at various scales and data in larger CLS initiatives, using the o^{2}S^{2}PARC platform as example (section 2.3).

It should be noted that there is a partial overlap between the functionalized anatomical model concept presented here and Physiome initiatives such as the International Union of Physiological Sciences (IUPS) and the Virtual Physiological Human (VPH) Physiome Projects (Bassingthwaighte, 2000; Hunter and Borg, 2003; Hunter and Viceconti, 2009). These initiatives aim at characterizing an individual's or species' physiological state (i.e., the physiome) through "databasing" and integrated modeling (Bassingthwaighte, 2000). While part of the functionalized anatomical model concept can be seen as a realization of the physiome vision in that it involves integration of physiological data and computational models, the functionalization concept is distinct in several ways as it (i) finds its primary application in the context of physical interactions between the environment or medical devices with the human body and physiology, (ii) focuses on the strong link between (whole body) anatomy and physiological dynamics, and (iii) pursues a more heterogeneous and flexible integration – even though this is typically associated with looser integration and weaker coupling – compared to the strict multi-scale model integration promoted in the Physiome Project (through common markup language descriptions and imposition of conservation laws across model components; Hunter, 2016). The differences between the Physiome initiatives and our vision for functionalized anatomical models (e.g., the advantages and disadvantages of heterogeneous coupling) are discussed in more detail in section 3.1. In addition, the relationship to precision medicine visions, such as the digital patient "Avatar," is discussed in view of the potential and benefit of creating personalized functionalized anatomical models.

The employed technologies presented here, such as performing simulations with the help of anatomical models and co-registered data or computational models, are *per se* not novel. However, the goal of this paper is to argue (i) for the systematic creation of functionalized anatomical models that are based on sufficiently standardized building blocks to facilitate the coupling and linking of a range of computational/anatomical models and simulation/measurement data, as well as (ii) the concept that they can serve as integration services for unified computational frameworks or platforms.

2. METHODS AND RESULTS

This section consists of two parts: First (section 2.2), different forms of functionalization are described and illustrated with concrete application examples from the literature. These examples are mostly taken from our own work with the anatomical models summarized in section 2.1. Based on the lessons learned about the value of integrating functionalization layers within anatomical models and on the related concepts that have been established, we put functionalized anatomical models at the center of the o^{2}S^{2}PARC platform, a CLS platform initially developed in the context of investigating peripheral nervous system (PNS) control of organ physiology, as described in section 2.3.

2.1. Anatomical Models

Most of the examples discussed in this paper involve one of the following anatomical models:

- Virtual Population (Christ et al., 2009; Gosselin et al., 2014): The ViP includes a range of 11 detailed models (s. section 1). It is unique in that it provides wide population coverage based on painstakingly segmented image data from healthy volunteers, rather than relying solely on morphing of a single underlying model. The image data has been segmented using a range of automatic and manual methods. Subsequently, triangular surfaces have been extracted, smoothed, and simplified, with methods that ascertain conformality of adjoining regions (no gaps or overlaps) and absence of (self-)intersections.
- MIDA (Iacono et al., 2015): MIDA is a detailed anatomical human head and neck model with over 160 distinguished structures. The full version includes a detailed segmentation of thalamic and subthalamic nuclei, which had to be removed from the freely available version for IP reasons. The distinguishing feature of the MIDA model (in addition to the high resolution and detailedness) is that it is based on a broad, multi-modal set of MRI images acquired in a single session from one volunteer. That set includes differently weighted (T1, T2, high nerve contrast) structural images, diffusion tensor imaging (DTI), as well as phase-contrast and time-of-flight angiography. The multimodal image data facilitates detailed segmentation (e.g., the two blood flow imaging modalities facilitated separation of arteries and veins), but also provides valuable information for functionalization (s. section 2.2.2). The anatomical model generation approach is similar to that used for the ViP models.
- NEUROMAN (Lloyd et al., 2018): NEUROMAN (**Figure 1**) are two evolving anatomical models based on high resolution cryosection image data from a Korean female and male (Park et al., 2006; Yeom et al., 2014). In addition to the unique quality of the underlying color-image data and the large number of identified tissues, the distinguishing feature of NEUROMAN is the effort toward adding an extensive tracing of the PNS to the model. The aim is to functionalize the PNS trajectories with electrophysiological neuron models, a concept developed in recent pilot studies (Neufeld et al., 2016b; Cassara et al., 2017b). Foreseen applications are manifold and include, e.g., risk assessment of low-frequency exposures from high-power wireless power transfer systems (Reilly and Hirata, 2016) or the development of safe MRI sequences with improved contrast and resolution.

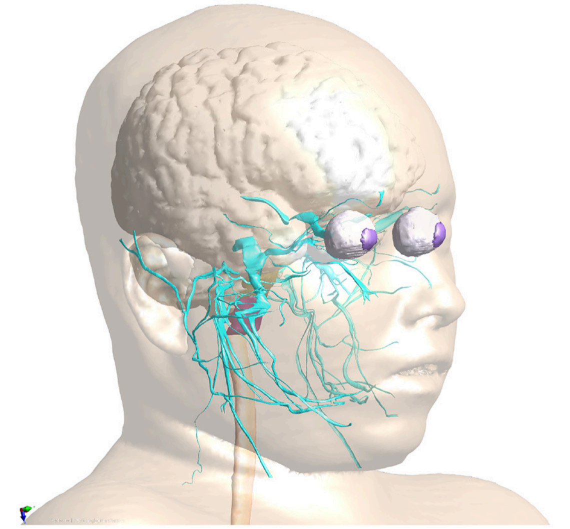

FIGURE 1 | PNS functionalization of NEUROMAN: The cranial nerve traced for the basic version of NEUROMAN are shown. They have been obtained by segmentation of color cryosection images. These trajectories are complemented with dynamic electrophysiology models. Within the SPARC initiative, additional nerve trajectories and electrophysiology models elaborated by SPARC teams will be successively integrated.

2.2. Functionalization Forms

Functionalization describes the integration of additional model layers into the static, geometrical anatomical models. There are different forms of functionalization—depending on the kind of dynamics, computational model, or data to be integrated—which are discussed below.

2.2.1. Geometry Functionalization

The initial anatomical model is a static geometric representation of the different tissues, organs, and regions. There can be different reasons, why the geometry should be rendered dynamic or parameterized:

- The anatomy of the patient/subject undergoes rapid changes on the time-scale of treatments (e.g., related to breathing, heartbeat, bowel movement, organ sliding after changing from standing to resting position). The deformed anatomy can affect exposure, e.g., during proton-beam therapy. Similar considerations apply to posture changes.
- The anatomy of the patient/subject undergoes slow changes on the time-scale of treatments (e.g., due to tumor shrinkage during radiotherapy).
- The population coverage needs to be increased (e.g., in the context of *in silico* clinical trials) to better account for anatomical variability. This can be achieved by parameterizing

anatomical models with gross anatomical measures such as height or body-mass-index (BMI).

- Personalized models need to be created, e.g., by registering an existing anatomical model to (image) data of a person.

The following techniques were developed to advance the ViP models beyond static geometries:

- Image registration: Registration of the anatomical model to image data can be used to personalize models, or to reflect motion and anatomical change. It is possible to either (i) register the original image data, used to generate the anatomical model, to specific image data (e.g., of that of a patient) or (ii) to directly register the anatomical model surfaces to the specific image data. When performing image-to-image registration, the imaging modalities do not necessarily need to agree. In some cases, it can be helpful to identify landmarks as registration constraints.
  For example, Kyriakou et al. (2014) functionalized a ViP model with a transient deformation field extracted from 4D MRI images to realistically model breathing motion and related organ deformation and displacement (**Figure 2**). The dynamic anatomical model was used to simulate the strong impact of breathing motion on focused ultrasound liver ablation therapies. It was concluded that breathing motion can lead to defocusing, collateral damaging near ribs, and the inability to reach therapeutic temperatures. However, considering breathing motion in the treatment planning and administration can mostly avoid these issues and can even be employed to achieve better coverage of large treatment areas.
- Biomechanical morphing: The muscle- or fat-content of anatomical models can be parameterized by performing biomechanical simulations in which shrinking or growing forces are associated with specific tissues, while other soft tissues are treated as passively deforming and bones as hard boundary conditions (Lloyd et al., 2016). A similar biomechanical approach can be applied to change the posture. A virtual skeleton consisting of "bones" and articulations is defined that can be posed, determining the displacement of some regions (mostly bones), while soft tissue again passively deforms, following the laws of biomechanics. Such an approach, while computationally demanding, produces more realistic posture changes, than, e.g., an influence region-based computation of deformation fields (Cherubini et al., 2009).
  Murbach et al. (2017b) investigated the dependency of local radiofrequency (RF) exposure during MRI on patient posture and obesity levels. Physics-based morphing was used to morph the obese male "Fats" ViP model to a similar BMI as the normal-weight "Duke" model. Combined morphing and posing allowed the testing of different hypotheses, identifying posture and BMI as key parameters for assessing RF exposure.
- Surface registration: Full-body anatomical models can be personalized to match gross anatomical characteristics of individuals by a three-step registration process (Lloyd et al., 2017; Alaia et al., 2018): first (i) the body surface of the template or reference model is registered to a target body shape (e.g., obtained from 3D laser scanner data), then (ii) various heuristics are used to reconstruct the estimated thickness distribution of the subcutaneous adipose tissue (SAT), and finally (iii) all internal tissues are registered based on a Poisson extension of the deformation field on the interior skin (i.e., the surface below the skin and SAT). The method is able to morph a complete model to a target body shape while ensuring anatomical correctness.
  Although organ sizes and shapes cannot be predicted solely based on the body shape, various tissues (e.g., muscle, SAT) and bones are reconstructed remarkably well, as evidenced in another MRI exposure safety study. Murbach et al. (2017a) used models with different body shapes, obtained by registering the ViP model "Ella" to female body shapes from the CAESAR project (Robinette et al., 1999). Based on the surface registration technique, various ViP models were registered to different body shapes. In order to analyze the predictive power and accuracy of the registered model, the Duke model was registered to Fats and the differences between the real Fats and the Duke-based Fats were analyzed (Alaia et al., 2017). Results revealed a remarkably good overlap of the overall body shape, bones and many other tissues. The internal structures of the template model agree with the internal structures of the target with relative surface area deviations of 1–15% between corresponding tissues and relative volume errors of 5–20%. A large difference was seen in the volume of the lungs, which is considerably below population average in Fats.
- Control-point (free-form) morphing: By overlaying a grid of control-points that can be freely shifted, a deformation field can be defined and applied to the model mesh. For example, a sequence of deformation fields mimicking breathing motion can be defined, or the shape of an organ parameterized (e.g., variable heart volume) (Neufeld et al., 2011).

With the exception of biomechanical morphing and posing, the described techniques must be considered as "tools" – providing them in combination with anatomical models does not yet constitute functionalization (there is no inherent connection between the transformed anatomical model and the transforming tool, as the use of the tool does not rely on the integration of information within the anatomical model). However, storing deformation fields (obtained through biomechanical morphing, image-registration, or principal component analysis of shape variability) along with the anatomical model is a form of functionalization that enhances the model's value in applications where motion or population coverage is relevant. The biomechanical morphing and the poser tool require model-specific information (e.g., "bone" and pivot system) and the combination of that information and the tool with the anatomical model is a form of functionalization.

Image- and surface-based registrations are important and powerful tools frequently employed in the context of functionalization. Beyond the use of registration tools to adapt general anatomical models to subject specific information, co-registration is crucial when merging information originating from different modalities into a synchronized functionalized model, as illustrated below. A wide range of techniques exist

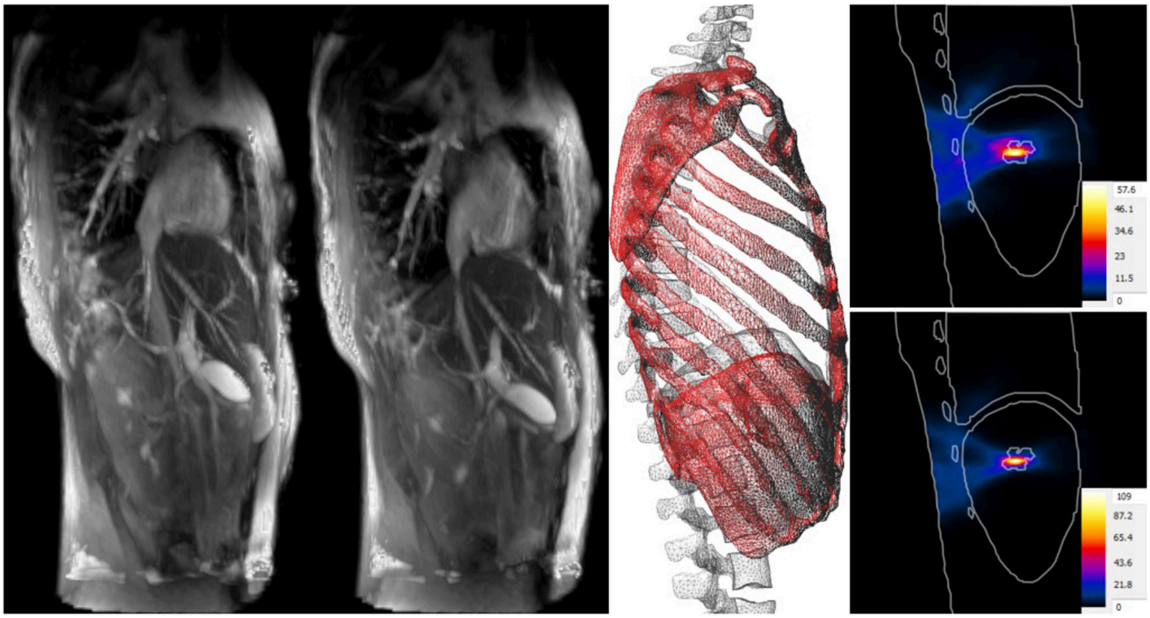

FIGURE 2 | Impact of breathing motion on focused ultrasound liver ablation. 4D MRI data (**A** at maximal exhalation, **B** at maximal inhalation) is used to create deformation fields that are registered to the anatomical model, thus functionalizing it with breathing motion **(C)**. Compared to the temperature increase when neglecting motion **(D)**, tracking compensation **(E)** can double the theoretical temperature increase, result in better focusing, and reduce collateral damage.

that can (co-)register image-data, segmentations, and surfaces to each other. Many of these have been applied in the context of the ViP and MIDA. However, discussing registration techniques further in more detail is outside the scope of this paper.

2.2.2. Physics Functionalization

Physical modeling is important, as physical interactions with tissues and/or physiology (e.g., from device-related exposure) is at the origin of most life sciences applications. Accurate determination of tissue exposure is therefore fundamental and requires proper specification of the physical characteristics and conditions present in the body. Anatomical model functionalization with regard to physical modeling can take various forms, which are described below.

2.2.2.1. Tissue properties

Anatomical models provide discretization into distinct tissues that are associated with distinct physical properties. Linking an anatomical region to a set of tissue properties, such as density or dielectric properties, is a basic form of functionalization. Properties can be parameter-dependent, such as the frequency-dependence of acoustic properties, and that dependence can be derived from physical insights or from measurements. In some cases, it can be valuable to parameterize properties with regard to tissue composition – for example, age affects water content in many tissues and, therefore, also tissue properties. Through a tagging mechanism, the different regions in the ViP models are directly functionalized with material properties from the IT'IS tissue database (Hasgall et al., 2015). The database contains information about density, thermal properties, perfusion, dielectric properties (low-frequency conductivity and conductivity/permittivity dispersion relationships across a wide range of frequencies), frequency dependent acoustic properties, MRI relaxation times, element composition, and viscosity. It has been assembled through an extensive literature review and provides not only guidance on the most representative values for a wide range of tissues, but also on the variability of the reported values, which is an indicator of inter/intra-person variability and measurement uncertainty and thus required as part of modeling-uncertainty quantification.

A form of tissue property functionalization that illustrates the functionalized anatomical model philosophy better, concerns tissue heterogeneity: The segmentation process involved in anatomical model creation reflects the simplifying approach of identifying regions that can be treated as somehow homogeneous. However, this can in some cases be overly simplistic. For example, bone has a highly heterogenous density. Imaging techniques can be used to collect information about such heterogeneity, such as MRI perfusion maps or computed tomography (CT) density maps. Co-registering such property maps along with anatomical models is a form of functionalization that makes this valuable information available for modeling purposes. The MIDA model provides functionalization with anisotropic (tensorial) low frequency conductivity maps, based on the co-registered DTI data. EM simulations of transcranial direct current stimulation (Iacono et al., 2015) demonstrate that consideration of the (inhomogeneous) anisotropy of neural tissue conductivity in a suitably functionalized head model results in a decrease of predicted field strength and penetration depth. The DTI information can also be used to trace neuron trajectories that can then be funtionalized with dynamic electrophysiological models. Similar to the use of DTI-derived electrical conductivity anisotropy maps in transcranial electric stimulation modeling is the use of anatomical head models functionalized with CT-based bone-property maps for the simulation of transcranial focused ultrasound (**Figure 3**). Simulations considering bone heterogeneity predict reduced sonication intensities, but improved focality (less side-foci), as confirmed by experimental measurements (Montanaro et al., 2018).

2.2.2.2. Boundary conditions

Imaging-based information worth adding to anatomical models is not restricted to property distributions. Another case is the use of image data to impose boundary conditions on physics simulations. For example, various forms of imaging techniques are capable of determining (transient) blood flow rates in a vascular cross-section. Functionalization of anatomical models with such data adds additional realism when performing hemodynamics simulations within the anatomical vasculature model, as illustrated by Kyriakou et al. (2012). An anatomical model was functionalized with data from MRI flow velocimetry in 2D cross sections, which was then used as a transient boundary condition for blood flow simulations in the aorta and vena cava compartments. Subsequently, the ECG signal distortion due to the magneto-hemodynamic effect (present during high magnetic field exposure) was modeled using coupled EM simulations (Kainz et al., 2010), in order to assess its suitability as non-invasive biomarker for blood-flow features. The co-registered flow velocimetry data was used in the same study to validate the computational fluid-dynamics predictions, while co-registered surface potential measurement data served to validate the electric potential modeling predictions.

2.2.3. Physiology Functionalization

The next level of functionalization is concerned with adding tissue or organ physiology layers. The inclusion of physiology modulated tissue properties is conceptually situated between physics- and physiology-functionalization. For illustration purposes, we consider perfusion, which is an important parameter of the Bioheat Equation (Pennes, 1948) frequently employed to study heating or cooling of living tissue. Local vasodilation strongly depends on local temperature and, therefore, it can be necessary to associate tissues with tissue-specific, temperature-dependent perfusion models. While this is still readily viewed as a classic, non-constant material law, the situation changes, when the physiological complexity of thermoregulation is increasingly considered. In these cases, non-local variables (such as the median skin temperature or the temperature of the hypothalamus) come into play and depending on the situation, physiological models, e.g., for sweating or shivering, need to be included. Functionalizing anatomical models with physiological models, such as thermoregulation models, prepares them for applications beyond the classical exposure modeling.

Physiological functionalization is clearly not limited to tissue properties. For example, neuron trajectory/morphology models, complemented with models of their electrophysiology, can be included in anatomical models to study the impact of physical exposure within anatomical environments on physiological response. Going to the level of modeling physiology, instead of stopping at physical exposure characterization, is important, as it is rarely the exposure that matters, but rather the resulting therapeutic or adverse physiological effect. Even exposure safety guidelines, which are by their nature formulated in terms of physical exposure quantities (such as energy deposition or field strength) aim at preventing adverse physiological effects (such as thermal collapse or blood clot formation). Hence, there is value in directly modeling the ultimate, physiological quantity of interest, even if it comes at the cost of additional complexity and uncertainty. Providing physiologically functionalized anatomical models can reduce that effort and increase access to such modeling.

For example, functionalization of anatomical models with nerve trajectories (**Figure 1**) and with neuron electrophysiology models has proven valuable in questioning the assumptions behind current low-frequency exposure safety standards (Neufeld et al., 2016a,b; Reilly and Hirata, 2016) and gaining insights into relevant factors. Only by combining anatomical models that provide the physical environment in which exposure occurs with realistic neuron trajectories and electrophysiologically accurate neuron models it could be shown that (i) the inhomogeneous *in vivo* field conditions connect with the non-linearity of neural response to elicit action potentials and (ii) the discontinuity of these fields at tissue interfaces can give rise to neurostimulation in passing nerves. These forms of stimulation together produce safety concerns related to field inhomogeneity at relevant exposure strengths, which contradicts the mechanistic view underlying current safety standards. Current standards and safety limits are solely based on stimulation of nerve endings, which depends on field strength rather than field inhomogeneity. A new research agenda aimed at establishing the basis for revision of safety guidelines has been formulated to clarify these concerns (Reilly and Hirata, 2016). The agenda also includes a call for the development of new induction and electrostimulation models to update human exposure limits. Another illustration of neurofunctionalized anatomical models is the work presented in Cassara et al. (2017a), where a large number of electrophysiologically and morphologically detailed layer V pyramidal neuron models has been placed at anatomically realistic locations within a high resolution head model to investigate different forms of transcranial electric and magnetic stimulation (**Figure 4**). While the normal component of the electric field at the brain surface was found to correlate well with subthreshold neuron polarization (believed to be relevant for transcranial electric stimulation therapies), suprathreshold spiking excitability maps (relevant for transcranial magnetic stimulation) were found to poorly correlate with field exposure metrics. This demonstrates the value of using functionalized anatomical models to study the physiological impact, rather than stopping at physical exposure computation.

Functionalizing an anatomical model with a physiological network model of transient blood flow in major vessels (either 4D flow fields or reduced order models such as presented in Reymond et al., 2009) could support a wide range of modeling

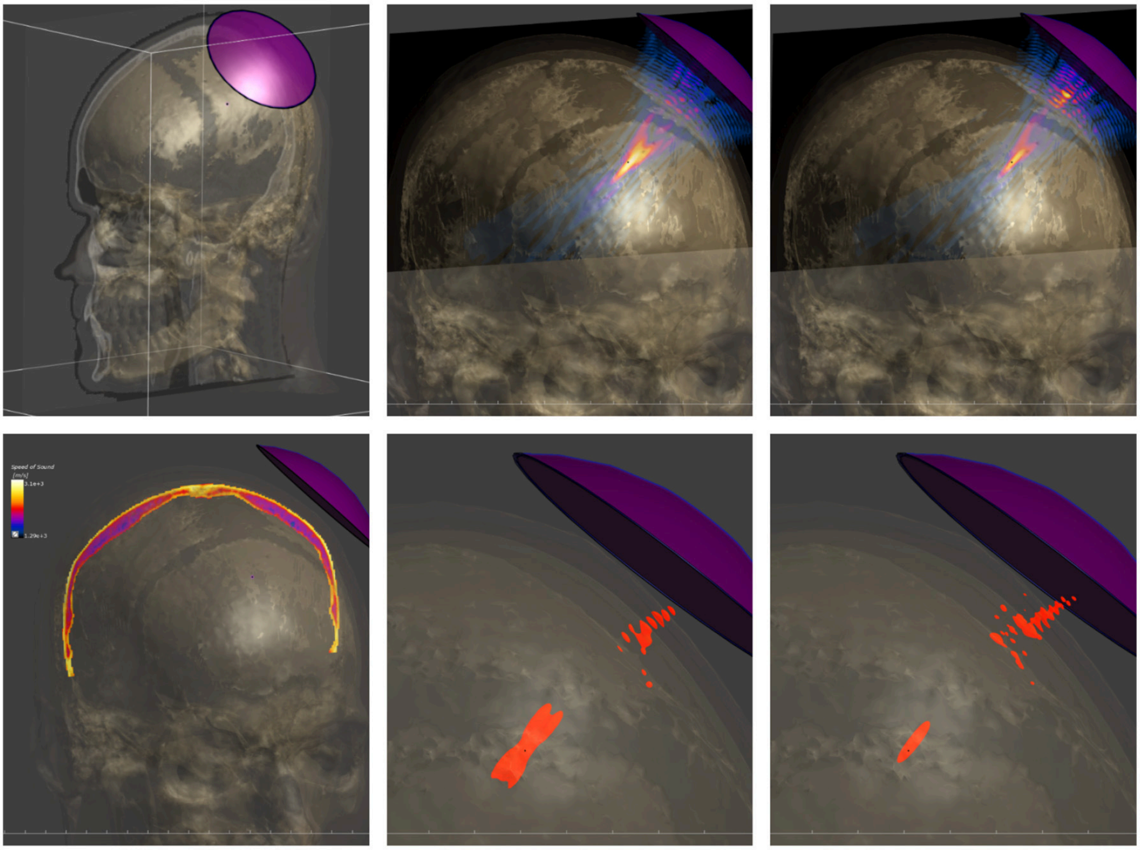

FIGURE 3 | Modeling of transcranial focused ultrasound using a detailed head model functionalized with CT-based tissue property maps. **(Top)** Setup involving the head model and a single-element, curved acoustic transducer (left), simulated pressure distribution when neglecting skull heterogeneity (center) and when employing the functionalized head model (right). **(Bottom)** CT-based acoustic velocity map in skull (left) and half-peak pressure isosurfaces when neglecting skull heterogeneity (center) and when considering it (right). The latter model predicts lower pressure amplitudes, but a sharper focus with reduced interference side-lobes, as confirmed experimentally.

types: For example, it could provide realistic in- and out-flow boundary conditions for fluid-dynamics studies in anatomical vessel segments, or be used to simulate the thermal impact of discrete blood vessels during hyperthermic oncology therapies, or for pharmacokinetic modeling.

2.2.4. Simulation and Measurement Results Functionalization

An extension of the concept of anatomical model functionalization with image data is the functionalization with (physics) simulation results. There are many instances where simulation results are a generic first step to a more specific physics or physiology modeling step. In such cases, it can be valuable to precompute these results and provide them as a functionalization layer along with the individual anatomical models.

For example, computationally determined EM exposure conditions (e.g., from far-field exposure) are frequently fed into subsequent modeling of, e.g., implant safety. This is the motivation behind the library of MRI RF coil exposure induced *in vivo* electric fields conditions (Cabot et al., 2016). Active implants exposed to MRI RF fields can pick up energy along the lead and deposit it at critical implant locations (e.g., the tip of a pacemaker or of an implantable neurostimulator), resulting in tissue heating and potential damage. According to ISO/TS 10974 standard (ISO, 2018), MRI implant safety can be ascertained by (i) determining the potential *in vivo* incident field conditions along lead trajectories, (ii) deriving the implant RF-heating characteristics (by measurement or simulation) as a transfer function from the tangential incident field to the resulting field/energy deposition at critical implant locations, and (iii) combining these two components to obtain the *in vivo* estimate of the energy deposition at critical locations. In a final step, (iv) the energy deposition is related to tissue heating. While the transfer function and potential implant trajectories are implant specific, the range of incident field conditions is determined by large permutations of coils, patient anatomies, and scanning positions. By precomputing a large set of *in vivo* field conditions, resulting from different coils, patient anatomies, and scanning positions, and storing them as functionalization layers of the anatomical models, it becomes possible to rapidly obtain statistical and worst-case information about a specific

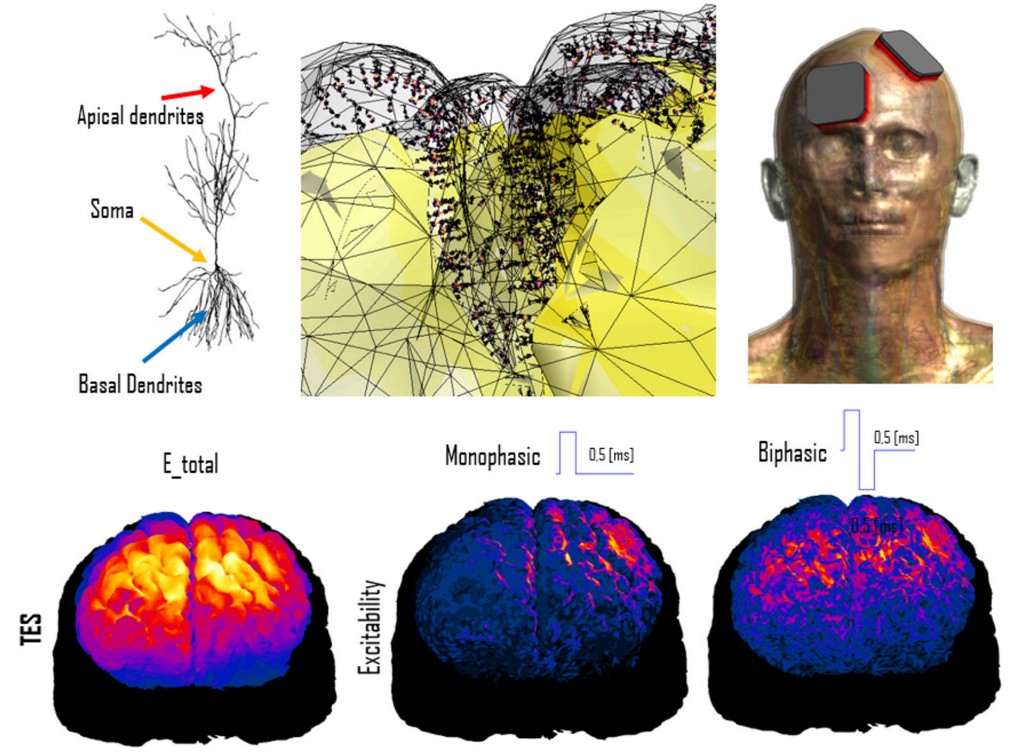

FIGURE 4 | Simulation of transcranial electric stimulation. **(Top)** A detailed anatomical head model (right) has been functionalized with dynamic electrophysiological layer V pyramidal neurons (left) by integrating them at the correct anatomical depth within the folded cortical structure (center; the neuron coloring represents transmembrane potential). **(Bottom)** When exposed to modeled electric fields (left), the functionalized model can be used to computed neural excitability maps (shown for monophasic (center) and biphasic (right) pulse-shapes).

implant. One only has to identify possible trajectories in the anatomical models (which are used to extract incident field conditions from the field-functionalized anatomical models) and to provide a transfer function (Zastrow et al., 2016; Córcoles et al., 2017). This approach has given rise to some of the first successful regulatory submission based on *in silico* clinical trials (Brown et al., 2017). Libraries of field-functionalized anatomical models for 1.5 T MRI coils (**Figure 5**) have been made available to the ISO/TS 10974 (Annex P) for the derivation of conservative implant exposure.

Other examples of functionalization with simulation result layers include blood-flow velocity distributions or biomechanical motion displacement fields, which can be required information for implant effectivity assessment.

Similarly, it can make sense to store measured information as far as it can be localized or spatially associated with the anatomy in a functionalization layer. In addition to the use-case of providing input for simulations, measurement data can also serve the purpose of validation. For example, the ASME V&V40 standardization committee (ASME-V&V40-Subcommittee, 2016) employs the concept of validation evidence (Pathmanathan et al., 2017), which is the association of models with a collection of potential validation data, a selection of which can then be applicable to validate the model within a specific context of use. Illustrating examples of validation evidence functionalization include surface potential measurements (to validate electrocardiogram (ECG) modeling), flow velocimetry (to validate hemodynamics modeling), and compound action potential recordings (to validate neural dynamics modeling).

2.3. o^{2}S^{2}PARC

Based on the lessons learned during our extensive research over the last 15 years (see section 2.2), where specific functionalized anatomical models repeatedly offered the key to increased modeling realism, model reuse, and model potentiation, we put functionalized models at the core of our vision, design, and implementation of the o^{2}S^{2}PARC platform—the simulation platform and computational model integration center of the National Institutes of Health (NIH) SPARC initiative. Opting for functionalized anatomical models as integration centers offers a range of benefits:

- it integrates the computational models within their natural anatomical environment,
- it permits integration and coupling of initially disconnected, heterogeneous sub-models and advances interoperability,
- it permits the assessment of physical exposure by devices—the first step toward modulating physiology—which is frequently dependent on the local and sometimes large-scale anatomy with its tissue and physical properties distribution,

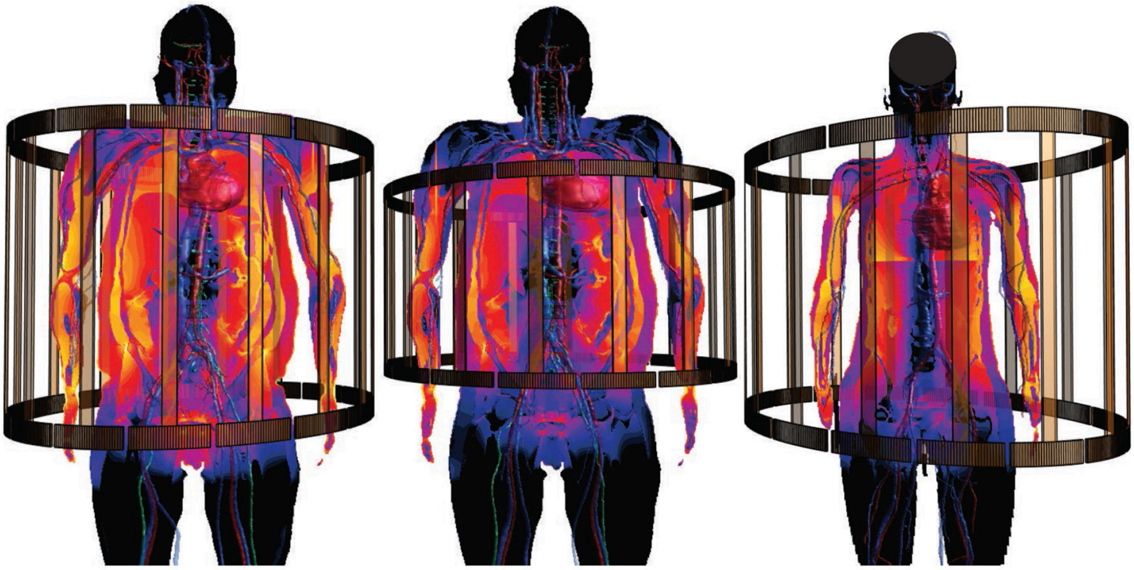

FIGURE 5 | Anatomical models functionalized with incident *in vivo* field conditions from MRI RF-coil exposure, for use in MRI implant safety assessment (s. section 2.2.4). Different coils and anatomical models are shown.

- it provides a framework to localize data and models according to their corresponding location within the body,
- it facilitates the identification of components for network or multi-scale computational models,
- it associates computational models with data, potentially originating from other users, that can be valuable to feed, tune, or validate the computational models.

The goal of this section is to provide a short description of the o^{2}S^{2}PARC platform as a specific example that highlights the value of centering unified computational frameworks or platforms on functionalized anatomical models.

The NIH SPARC initiative is an ambitious program to study the PNS and its role in controlling organ physiology toward the goal of being able to modulate the PNS to influence organ function and precisely treat diseases. In order to achieve sustainability and broad usage of the results of this research initiative, the SPARC data resource center (DRC) was established. One arm of the DRC supports the development, installation, and maintenance of a freely accessible online platform to host, run, couple, and study all computational models developed across the SPARC community. Our (funded) proposal for the design and implementation of this platform is based on our belief that this ambitious goal can be only achieved by the presented paradigm of functionalized models. At the center of the o^{2}S^{2}PARC platform will be the so-called "NEUROCOUPLE" and the "NEUROFAUNA" (**Figure 6**), detailed anatomical representations based on segmented image data (initially a male and female human model, as well as a rat model) that include an extensive tracing of PNS trajectories. These models are complemented by a more abstract body representation established by the SPARC MAP-CORE team, which is primarily used to represent dependencies, coupling, and multi-scale models, and to map information between models. The anatomical models will increasingly be functionalized with data and models elaborated within SPARC and, as such, serve as integration centers for the knowledge generated by that initiative.

Functionalization of the anatomical models in o^{2}S^{2}PARC started by including electrophysiological models of PNS neurodynamics. Further functionalization with anatomical microstructure, e.g., of the different nerve tissues (fascicles, epineurium, perineurium), statistical neuron distributions, and functional sub-units, will enable the investigation and design of different neuromodulation devices, by allowing modeling of the stimulator physics (e.g., EM or ultrasound exposure) and the induced electrophysiological response. Different SPARC teams are developing, often multi-scale, models of organ physiology, which typically accept PNS activity descriptors as input and output. Those physiological models will also be added as part of the model functionalization to simulate organ electrophysiology and the impact of PNS neuromodulation on organ function. o^{2}S^{2}PARC allows to execute computational models locally, or in the cloud, as microservices (see below), and to couple multiple such models, with a primarily electrophysiologically driven coupling concept—meaning that the data exchange between computational physiology models will typically be in terms of neural activity quantities (spiking frequency, transmembrane potential traces, network activity, etc.). Much of the SPARC activity currently focuses on establishing enervation maps, neural tracing, and connectivity information, which will be integrated with other data and models by mapping to the whole-body anatomy. Other data being collected within SPARC and valuable for model functionalization includes image data (e.g., enabling the creation of high-resolution

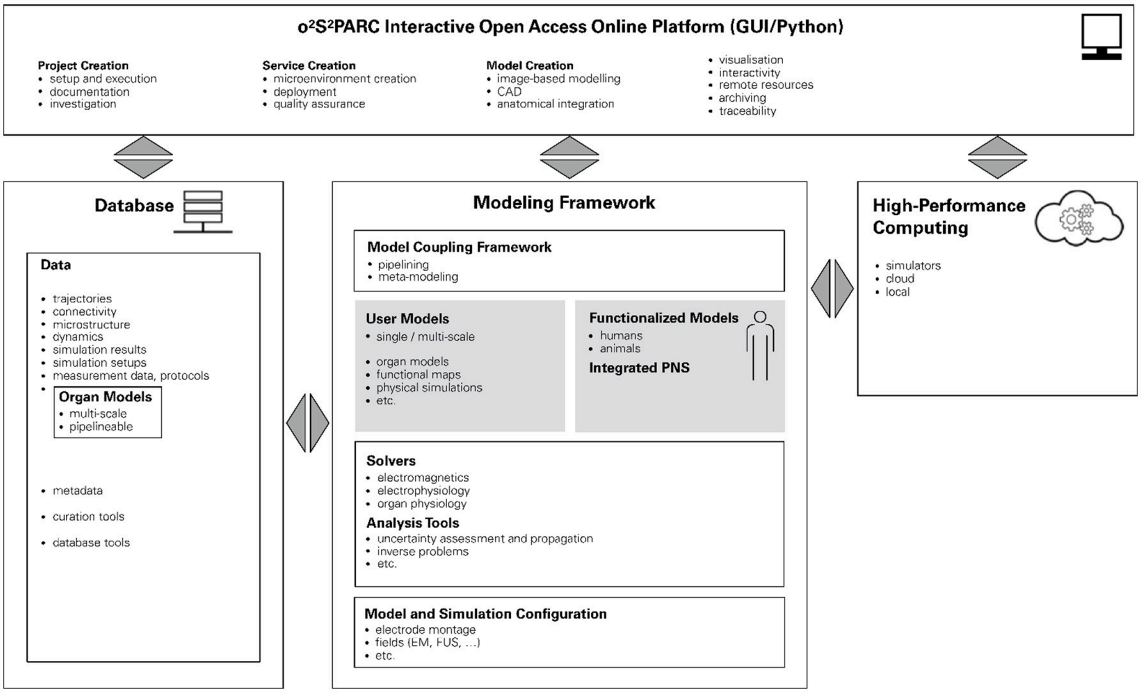

FIGURE 6 | Schematic illustration of the o^{2}S^{2}PARC platform. At its center are functionalized human and animal anatomical models which serve as integrators for computational models (and data) from SPARC. The modeling framework is complemented by physics and physiology solvers and analysis tools. In combination with configuration information, studies can be composed that are then evaluated locally or in the cloud. All underlying data (including versions of the employed solvers and computational models) are routed through a database to ascertain full chain-of-custody and support quality assurance. The platform is accessible through a user-friendly online GUI.

sub-region anatomical models), organ motion data (e.g., to phenomenologically describe activity of the gastric system), and electrophysiological measurements (e.g., large-scale neural activity recording, sometimes synchronized with related organ physiology recording).

o^{2}S^{2}PARC is not limited to the integration of data and models within functionalized reference anatomical models, the creation and execution of computational models, and their coupling, but also foresees a range of meta-modeling (e.g., optimization, inverse problem solving, uncertainty assessment), versioning (e.g., derivation of updated/modified models), and quality assurance (e.g., reproducibility, verification and validation, quality certification, chain-of-custody, referencability) functionalities. o^{2}S^{2}PARC will also offer a range of physics simulators (e.g., EM solvers).

o^{2}S^{2}PARC is an open-source (MIT License) project hosted at https://github.com/ITISFoundation/osparc-simcore, (see also for further technical information). The o^{2}S^{2}PARC platform is realized (**Figure 7**) as a web-browser-based graphical user interface (GUI) front-end implemented in Qooxdoo that communicates through RESTful and web-socket APIs with the Python-based web-server back-end. The web-server, in turn, communicates with a Python-based director that orchestrates a scalable network of computational service modules. Inter-service communication between computational services is restricted to file sharing. Each service module is encapsulated within a Docker microservice (a concept similar to virtual machines, but with less computational overhead, that allows to execute programs within flexibly configurable environments) and paired with a "sidecar" that is responsible for the monitoring and command of the associated computational service (including communication with the director). Encapsulating the computational services within Docker containers ensures that (i) the services can run anywhere (locally, in the cloud, or on an in-house cluster) within a known and tested environment (libraries, operating system, compiler, etc.), (ii) the services and their environment can be archived together in a docker repository to ensure future reproducibility, and (iii) services can be implemented using a wealth of available docker environments (scripting languages, Octave, command-line executables, C/Java compilation and execution, Jupyter Notebooks, machine learning frameworks, etc.) while maintaining a standardized communication interface and protocol through the sidecar. This ensures that service providers can implement their computational models and services flexibly, using familiar technologies and environments, and do not need to convert them to imposed technologies and forms. Services are typically setup as pipelines (or more generally as graphs) which can include, e.g., geometric or image-based model creation, data-sources, physics and physiology solvers, visualization and analysis modules. The functionalized anatomical models themselves will be provided as service module, providing visualization and searchability (e.g., through ontologies and knowledge-graphs elaborated by the SPARC MAP-CORE team), and offering geometry and functionalization layers as selectable outputs that are then further processed/employed throughout a project's graph.

3. DISCUSSION

The results obtained using functionalized anatomical models presented in section 2.2 illustrate the value and importance of bringing anatomical representation, information supporting modeling and model validation, as well as physiological dynamics closer together and synchronizing them. Combining these factors not only helps to ensure consistency, but is also a way of leveraging the value of individual contributions to modeling and of integrating parts into a bigger total. Once validated, functionalization layers can become established model components for third party users, just like anatomical models currently are. An important benefit of the functionalized anatomical model paradigm is that it can also facilitate interoperability for heterogeneous models developed by research group from different modeling backgrounds and fields.

The functionalized anatomical model concept presented here does not stand alone. It is related to other initiatives, such as the IUPS and VPH Physiome Projects mentioned before (see also section 3.1) and—when coupled with model personalization—to the concept of the digital patient 'avatar' and precision medicine in general (section 3.3).

3.1. Physiome Projects and the Functionalized Anatomical Models Concept

The Physiome Project was initiated by the IUPS in 1997 to bring multi-scale engineering modeling approaches to the physiological interpretation of the vast data, from the molecular to the organism level, that was becoming increasingly available (Hunter and Borg, 2003; Hunter, 2016). It aims at providing a quantitative, multi-scale description of physiological dynamics and functional behavior of the intact organism. The Physiome idea has produced a range of initiatives, such as the VPH Physiome Project, which emerged from the European Commission VPH Project, in combination with the US Interagency Modeling and Analysis Group (IMAG) initiative and others (for more background on different Physiome Projects and related initiatives, see http://tutorial-on-cellml-opencor-and-pmr.readthedocs.io/en/latest/background.html). Particularly the VPH Physiome Project pursues a vision where models and sub-models are reproducible, reusable, and discoverable (Nickerson and Hunter, 2017), e.g., by elaborating standardized markup-language descriptions of computational models, data, and measurement protocols. The project aims to describe the Physiome through ordinary and partial differential equations (ODEs and PDEs) that are made compatible, e.g., by enforcing energy and mass fluxes through Bond-graph theory (Paynter, 1961; Safaei et al., 2018), and by employing standardized naming conventions/ontologies and formats (e.g., CellML, SBML Chaouiya et al., 2013, FieldML) that are in turn compatible with general purpose solvers such as OpenCOR and OpenCMISS (Hunter, 2016).

The functionalized anatomical model concept is, in parts, a realization of the Physiome vision in that it also pursues the integration of computational physiology models, with the goal of achieving model reuse and potentiation, as well as a more comprehensive description of the organism. However, it is also distinct on several levels:

- The functionalized anatomical model concept emerged from the need to consider the human anatomy and body as an environment that is subject to physical exposure or within which physical exposure occurs that interacts with physiological activity. The interaction with physiology can be intended (e.g., therapeutic) or unintended, in which case human safety is the motivation. Hence, the anatomical geometry, the tissue and external environments, and the modeling of physical exposure and physical processes in and around the body are central. In contrast, the Physiome Projects have a holistic approach: they aim to explain how each and every component in the body works as part of the integrated whole by establishing a multi-scale model of the physiology.
- The multi-scale physiology models in Physiome Projects can in some cases be related to the spatial distribution of molecules, cells, tissues etc. and therefore can also involve anatomy. However, anatomy is only a potential contributor to the computational physiology model, while the interconnection between anatomy, physical interaction, and physiological response or dynamics is at the center of the functionalized anatomical model concept. Whereas conservation of mass and energy fluxes serves as primary integration frame in the VPH Physiome Project (Hunter and Viceconti, 2009), it is the anatomical space that is central in functionalized anatomical models. The anatomical space not only allows one to integrate sub-models, but also serves as a coordinate system for locating and storing other information, such as measurement data.
- The Physiome vision (Hunter and Borg, 2003) pursues a strong integration of sub-models through standardized (markup language) formats, descriptions, and meta-data. Its ultimate goal is to accumulate mathematical descriptions of physiome components at all model scales resulting in an emerging organism physiome model that can be solved using dedicated software such as OpenCMISS and OpenCOR. It employs methods, such as Bond-graph theory, to ensure flux conservation and physico-chemical consistency.

  While we embrace these initiatives for unified descriptive or markup languages and model databases, wide adoption of such markup languages is still lacking. The process of a posteriori converting established models into Physiome Project-compatible models and descriptions is often a considerable burden for groups. In addition, models are often implemented using numerous custom or proprietary software tools, which do not (yet) support Physiome standards and formats, and which are difficult to replace with other tools for performance or robustness reasons. Furthermore, not all forms of modeling are amenable to mathematical descriptions

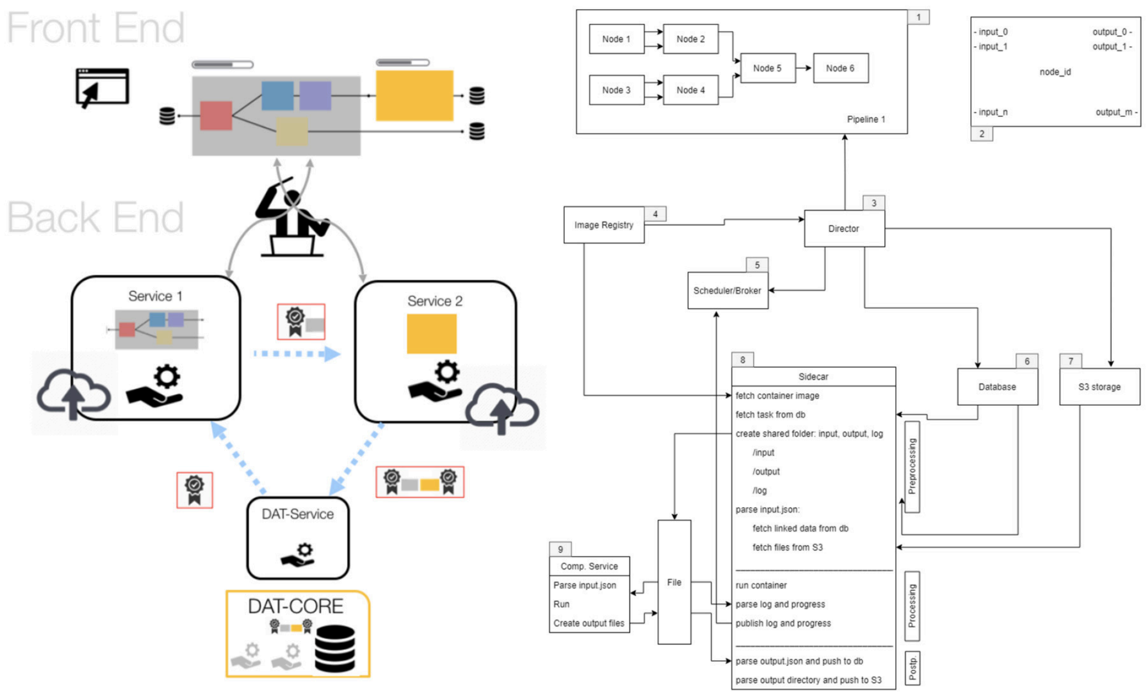

FIGURE 7 | Structure of the o^{2}S^{2}PARC implementation. The online GUI communicates with a director that orchestrates a scalable network of computational service modules (left). The components of the backend: 1. computational pipeline, 2. nodes, 3. director, 4. Docker image registry, 5. scheduler/broker, 6. database, 7. S3 storage, 8. sidecar, and 9. computational services. For more information, see https://github.com/ITISFoundation/osparc-simcore.

that can be used to ensure flux conservation—for example, machine learning produces models that frequently have no known mathematical description or guaranteed conservation. We believe that a more heterogeneous and flexible integration approach is needed to ensure a wide adoption and the emergence of a broad range of functionalized anatomical models, even though this comes with the expense of typically being limited to looser integration and weaker coupling.

Recent progress—in particular the emergence of Docker microservices, with the wealth of software tools becoming available in dockerized form and the simplicity of creating and deploying such services—enables the easy integration of heterogeneous models developed with widely differing technologies, as proposed in the o^{2}S^{2}PARC platform. The platform is designed to facilitate orchestration and communication between the services and only requires to provide translators between outputs of one service and inputs of another service.

3.2. o^{2}S^{2}PARC and Beyond

Realizing o^{2}S^{2}PARC permits to demonstrate the value of the functionalized anatomical model vision, as a means of reflecting the tight interconnectedness between anatomical geometry, physics, and physiology, and of providing users with leveraged benefits from data and computational models developed by others as stepping-stones and building blocks for their own models and studies. The open-source, online technology generated for o^{2}S^{2}PARC is sufficiently general to be of broad usability for a large variety of computational life sciences communities and applications.

To take this forward, the CLS community needs to agree, at least at the level of application-specific communities, on standardizing at the minimum (i) coordinate mapping between anatomical models and functionalization layers, (ii) descriptors of required input and provided output for computational models, to facilitate model coupling, as well as (iii) data descriptors, minimal data standards, and ontologies. Some standards and ontologies have already been developed, e.g., in the VPH Physiome Project, and remaining close to these standards will maximize compatibility. Additional valuable meta-data include information about the degree of verification, validation, and certification, corresponding experimental data, unique identifiers (also to facilitate referenceability), documentation (for example: How was a model/data generated? What are the associated uncertainties? How is it correctly used?), version log, related publications, usage history, access- and copyrights, to name a few. As already mentioned, the right balance between facilitating compatibility and avoiding high integration are significant challenges for model and sub-model creators. Means to incentivise this additional effort must be found. Apart from offering model integrators the benefit of increasing the use and usefulness of their own models and giving them access to third party integrated models, platforms such as o^{2}S^{2}PARC serve as powerful integration motivators, as they afford model creators with a complete platform infrastructure that enhances the model—with minimal effort—with features such as an attractive GUI and support for cloud execution.

3.3. Personalized Functionalized Anatomical Models

Another level in the value of functionalized anatomical models can be achieved through model personalization, which supports and enables a wide range of additional applications, e.g., in precision medicine or *in silico* clinical trials.

As repeatedly illustrated in section 2.2, image-data offers a way to personalize functionalized anatomical models. At the scale of the whole body, organs, and tissues, personalization is achieved by registration of a reference anatomical model to patient- or subject-specific image-data. For functionalized anatomical models, the functionalization layers can be transformed along with the anatomy. Once the anatomy is co-registered to the subject-specific image-data, further-going use of subject-specific image-data can be made, to personalize tissue property distributions, boundary conditions, organ motion, and more.

Personalized functionalized anatomical models can be valuable for personalized safety assessment (e.g., dosimetric evaluation of MRI exposure based on patient-specific anatomical geometries to relax restrictions of scan sequences Murbach et al., 2017b) or for patient-specific treatment planning (e.g., personalization of hyperthermic oncology treatments through optimization of the energy deposition considering thermoregulatory response Paulides et al., 2013). The latter can be seen as an implementation of the “Precision Medicine” concept, where healthcare is customized and tailored to the individual patient through patient-specific data obtained, e.g., from molecular diagnostics, imaging, and analytics. An extension of the use of patient-specific anatomical models is the concept of digital patient “avatars” (Maniadi et al., 2013; Brown, 2015), “a vision for the digital representation of personal health status in body centric views. It is designed as an integrated facility that allows collection of, access to, and sharing to life-long and consistent data.” (Maniadi et al., 2013). The digital avatars concept envisions comprehensive digital models which allow to integrate patient-specific information, such as diagnostic measurements and computational models, in order to provide a comprehensive and accessible patient picture, tailored predictions of disease progression and therapy outcome, and to facilitate precision medicine. Large scale, ideally automatized, creation of personalized functionalized anatomical models will support the digital avatar vision and will also result in patient functionalized anatomical model populations. Such functionalized anatomical model populations are valuable for the assessment of variability, e.g., of dosimetric exposure or therapeutic impact. They are fundamental for the realization of *in silico* clinical trials, where sufficient coverage of the target population is required.

4. CONCLUSIONS

In the last 20 years, the use of computational anatomical models has driven the field of CLS to new heights and as such they have become an indispensable staple. More recently, the possibility of model functionalization with geometry parametrization, physical and physiological dynamics, and simulated/measured data has empowered researchers to take another major step forward (i) by increasing model dynamism and realism through consideration of the coupled nature of anatomy and physiology, and (ii) by supporting reuse of established models/data. The development of functionalized models and the related techniques has already started to broaden the application range of CLS dramatically, e.g., in *in silico* treatment optimization and personalization, medical device research and development, as well as safety and efficacy assessment. In the near future, it is expected that this approach will bring CLS even closer to the goal of replacing clinical human trials with *in silico* human trials.

Functionalization properly accounts for the interconnection between anatomical geometry and bodily dynamics—both the impact of physiology and motion on the anatomical geometry and the impact of changes in anatomical geometry on the environment within which physical exposure occurs, which in turn affects physiology. It leverages the value of individual model components, especially if care has been taken to ensure consistency between the underlying anatomical model and the functionalization layers. Functionalized anatomical models can serve as natural integration approach in collaborative efforts, as illustrated by the introduction of the paradigm for the o^{2}S^{2}PARC platform. Furthermore, functionalization with measurement information can help realize the vision of validation evidence, as formulated, e.g., by the ASME V&V 40 committee, toward scientifically sound validation. The value of functionalized anatomical models has already been demonstrated in a wide range of application, but it is a very general concept, suitable as one of the fundamental components of CLS.

The integration of models and sub-models within functionalized anatomical models can be both facilitated and advanced by reducing the model integration effort through the support of heterogeneous model functionalization—one of the main aspects of the o^{2}S^{2}PARC platform—and by offering the motivation of benefiting the model with the functionality of a comprehensive computational platform, including an attractive GUI and cloud computing.

AUTHOR CONTRIBUTIONS

All authors contributed to the formulation of the functionalized anatomical model vision and provided input affecting all of the paper content. The first manuscript version has been drafted by EN. The manuscript has been extensively reviewed and revised by NK. WK has been fundamental in driving the development of the Virtual Population and in first formulating the vision of o^{2}S^{2}PARC. BL has contributed particularly to sections related to model shape parametrization (morphing, position, etc.), and to specific anatomical models. BS helped with literature review and interpretations of the contribution of the paper and revised the manuscript accordingly.

FUNDING

Research reported in this paper was supported by Common Fund's Stimulating Peripheral Activity to Relieve Conditions (SPARC) of the National Institutes of Health under other transaction award number 1OT3OD025348-01, by the Swiss Commission for Technology and Innovation (NEUROMAN 25290.1 PFLS-LS), and by funds received under the FDA Critical Path Initiative (FDA Solicitation Number: FDA-SOL-13-1119644 and FDA-SOL-12-11 05179).

ACKNOWLEDGMENTS

The authors gratefully acknowledge the above-mentioned funding, as well as all the colleagues that contributed to the research from which application examples were drawn and that provided associated input.

REFERENCES

Alaia, A., Lloyd, B., and Kuster, N. (2017). "Personalization of human computational anatomical models," in *Proceedings of the XXXII International Union of Radio Science General Assembly and Scientific Symposium (URSI GASS)*. Montreal, QC.

Alaia, A., Lloyd, B., and Kuster, N. (2018). "Mapping computational phantoms to subject specific body shapes," in *Proceedings of the Annual Meeting of the Bioelectromagnetics Society 2018 (BioEM)*. Piran; Portorož.

ASME-V&V40-Subcommittee (2016). "Verification and validation in computational modeling and simulation–a community effort," in *2016 Summer Biomechanics, Biotransport and Bioengineering Conference* (National Harbor, MD).

Bassingthwaighte, J. B. (2000). Strategies for the physiome project. *Ann. Biomed. Eng.* 28, 1043–1058. doi: 10.1114/1.1313771

Brown, J. E., Qiang, R., Stadnik, P. J., Stotts, L. J., and Von Arx, J. A. (2017). Virtual humans for implantable device safety assessment in MRI: mitigating magnetic resonance imaging hazards for implanted medical devices. *IEEE Pulse* 8, 50–53. doi: 10.1109/MPUL.2017.2701258

Brown, S. A. (2015). Building supermodels: emerging patient avatars for use in precision and systems medicine. *Front. Physiol.* 6:318. doi: 10.3389/fphys.2015.00318

Cabot, E., Zastrow, E., and Kuster, N. (2016). "Development of a set of generic numerical birdcages for comprehensive evaluations of induced RF fields for implant safety," in *Proceedings of the 24th International Society for Magnetic Resonance in Medicine (ISMRM)*. Singapore.

Cassara, A. M., Neufeld, E., Guidon, M., Kainz, W., and Kuster, N. (2017a). "Pulse-shape-related effects in transcranial sub- and suprathreshold stimulation of cortical neurons using anatomically, morphologically, and electrophysiologically detailed coupled electromagnetic and neuronal modeling," in *Proceedings of the 8th International IEEE EMBS Neural Engineering Conference*. Shanghai.

Cassara, A. M., Neufeld, E., Hagberg, G., Guidon, M., Scheffler, K., and Kuster, N. (2017b). "Peripheral nerve stimulation in MRI: insights from a three level analysis and coupled EM-electrophysiological simulations in neuro-functionalized human models," in *Proceedings of the 25th International Society for Magnetic Resonance in Medicine (ISMRM)*.

Chaouiya, C., Bérenguier, D., Keating, S. M., Naldi, A., van Iersel, M. P., Rodriguez, N., et al. (2013). SBML qualitative models: a model representation format and infrastructure to foster interactions between qualitative modelling formalisms and tools. *BMC Syst. Biol.* 7:135. doi: 10.1186/1752-0509-7-135

Cherubini, E., Chavannes, N., and Kuster, N. (2009). "Realistic skeleton based deformation of high-resolution anatomical human models for electromagnetic simulations," in *The 31st Annual Meeting of the Bioelectromagnetics Society* (Davos), 88.

Christ, A., Kainz, W., Hahn, E. G., Honegger, K., Zefferer, M., Neufeld, E., et al. (2009). The virtual family—development of surface-based anatomical models of two adults and two children for dosimetric simulations. *Phys Med Biol.* 55:N23. doi: 10.1088/0031-9155/55/2/N01

Córcoles, J., Zastrow, E., and Kuster, N. (2017). On the estimation of the worst-case implant-induced RF-heating in multi-channel MRI. *Phys. Med. Biol.* 62:4711. doi: 10.1088/1361-6560/aa641b

Gosselin, M. C., Neufeld, E., Moser, H., Huber, E., Farcito, S., Gerber, L., et al. (2014). Development of a new generation of high-resolution anatomical models for medical device evaluation: the virtual population 3.0. *Phys. Med. Biol.* 59:5287. doi: 10.1088/0031-9155/59/18/5287

Hasgall, P., Neufeld, E., Gosselin, M., Klingenböck, A., and Kuster, N. (2015). *IT'IS Database for Thermal and Electromagnetic Parameters of Biological Tissues.* Version 2.6.

Hunter, P. (2016). The virtual physiological human: the physiome project aims to develop reproducible, multiscale models for clinical practice. *IEEE Pulse* 7, 36–42. doi: 10.1109/MPUL.2016.2563841

Hunter, P. J., and Borg, T. K. (2003). Integration from proteins to organs: the physiome project. *Nature Rev. Mol. Cell Biol.* 4:237. doi: 10.1038/nrm1054

Hunter, P. J., and Viceconti, M. (2009). The VPH-physiome project: Standards and tools for multiscale modeling in clinical applications. *IEEE Rev. Biomed. Eng.* 2, 40–53. doi: 10.1109/RBME.2009.2036204

Iacono, M. I., Neufeld, E., Akinnagbe, E., Bower, K., Wolf, J., Oikonomidis, I. V., et al. (2015). MIDA: a multimodal imaging-based detailed anatomical model of the human head and neck. *PLoS ONE* 10:e0124126. doi: 10.1371/journal.pone.0124126

ISO, T. (2018). *10974: Assessment of the safety of Magnetic Resonance Imaging for Patients With an Active Implantable Medical Device.* Geneva : International Organization for Standardization.

Kainz, W., Guag, J., Benkler, S., Szczerba, D., Neufeld, E., Krauthamer, V., et al. (2010). Development and validation of a magneto-hydrodynamic solver for blood flow analysis. *Phys. Med. Biol.* 55:7253. doi: 10.1088/0031-9155/55/23/005

Kyriakou, A., Neufeld, E., Preiswerk, F., Lloyd, B., Cattin, P., Szekely, G., et al. (2014). "Modeling of motion tracking and focusing strategies in HIFU ablation of hepatic tumors," in *Proceedings of the 14th International Symposium on Therapeutic Ultrasound (ISTU 2014)*. Las Vegas, NV.

Kyriakou, A., Neufeld, E., Szczerba, D., Kainz, W., Luechinger, R., Kozerke, S., et al. (2012). Patient-specific simulations and measurements of the magneto-hemodynamic effect in human primary vessels. *Physiol. Measur.* 33:117. doi: 10.1088/0967-3334/33/2/117

Lloyd, B., Alaia, A., Liorni, I., and Kuster, N. (2017). "Model registration: a tool for studying anatomical variability and personalizing phantoms. in *Proceedings of the 6th International Workshop on Computational Human Phantoms*. Annapolis, MD.

Lloyd, B., Cassara, A., Farcito, S., Neufeld, E., Chung, B. S., Park, J. S., et al. (2018). "Neuroman: reference computational human phantoms for evaluation of safety thresholds for peripheral nerve stimulation," in *Proceedings of the 26th International Society for Magnetic Resonance in Medicine (ISMRM)*. Paris.

Lloyd, B., Cherubini, E., Farcito, S., Neufeld, E., Baumgartner, C., and Kuster, N. (2016). " Covering population variability: morphing of computation anatomical models," in *International Workshop on Simulation and Synthesis in Medical Imaging* (Athens: Springer), 13–22.

Maniadi, E., Kondylakis, H., Spanakis, E. G., Spanakis, M., Tsiknakis, M., Marias, K., et al. (2013). "Designing a digital patient avatar in the context of the myhealthavatar project initiative," in *2013 IEEE 13th International Conference on Bioinformatics and Bioengineering (BIBE)* (Chania: IEEE), 1–4.

Montanaro, H., Pasquinelli, C., Neufeld, E., Hansen, L., Kuster, N., and Thielscher, A. (2018). "Investigation of fallacies in focused ultrasound transducer acoustic modeling," in *Proceedings of the International Symposium for Therapeutic Ultrasound 2018 (ISTU)*. Nashville, TN.

Murbach, M., Lloyd, B., Alaia, A., Neufeld, E., Kainz, W., Fraser, R., et al. (2017a). "Posing, morphing and image registration of anatomical models for MRI RF safety assessments," in *BMES/FDA Frontiers in Medical Devices Conference*. Washington, DC.

Murbach, M., Neufeld, E., Lloyd, B., and Kuster, N. (2017b). "Enhanced numerical per-patient MRI RF exposure prediction via morphing and posing of anatomical models," in *Proceedings of the 25th International Society for Magnetic Resonance in Medicine (ISMRM)*. Honolulu, HI.

Neufeld, E., Cassará, A. M., Montanaro, H., Kuster, N., and Kainz, W. (2016a). Functionalized anatomical models for EM-neuron interaction modeling. *Phys. Med. Biol.* 61:4390. doi: 10.1088/0031-9155/61/12/4390

Neufeld, E., Oikonomidis, I. V., Iacono, M. I., Angelone, L. M., Kainz, W., and Kuster, N. (2016b). Investigation of assumptions underlying current safety guidelines on EM-induced nerve stimulation. *Phys. Med. Biol.* 61:4466. doi: 10.1088/0031-9155/61/12/4466

Neufeld, E., Szczerba, D., Bühlmann, B., Zefferer, M., and Kuster, N. (2011). "Fast interpolation based morphing of whole body human models," in *General Assembly and Scientific Symposium, 2011 XXXth URSI* (Istanbul: IEEE), 1–3.

Nickerson, D. P., and Hunter, P. J. (2017). "Introducing the physiome journal: improving reproducibility, reuse, and discovery of computational models," in *2017 IEEE 13th International Conference on e-Science (e-Science)* (Auckland: IEEE), 448–449.

Park, J. S., Chung, M. S., Hwang, S. B., Shin, B. S., and Park, H. S. (2006). Visible korean human: its techniques and applications. *Clin. Anat.* 19, 216–224. doi: 10.1002/ca.20275

Pathmanathan, P., Gray, R. A., Romero, V. J., and Morrison, T. M. (2017). Applicability analysis of validation evidence for biomedical computational models. *J. Verific. Valid. Uncert. Quantific.* 2:021005. doi: 10.1115/1.4037671

Paulides, M. M., Stauffer, P. R., Neufeld, E., Maccarini, P. F., Kyriakou, A., Canters, R. A., et al. (2013). Simulation techniques in hyperthermia treatment planning. *Int. J. Hypertherm.* 29, 346–357. doi: 10.3109/02656736.2013.790092

Paynter, H. M. (1961). *Analysis and Design of Engineering Systems: Class Notes for M.I.T. Course 2.751*. Cambridge, MA: MIT Press.

Pennes, H. H. (1948). Analysis of tissue and arterial blood temperatures in the resting human forearm. *J. Appl. Physiol.* 1, 93–122. doi: 10.1152/jappl.1948.1.2.93

Reilly, J. P., and Hirata, A. (2016). Low-frequency electrical dosimetry: research agenda of the IEEE international committee on electromagnetic safety. *Phys. Med. Biol.* 61:R138. doi: 10.1088/0031-9155/61/12/R138

Reymond, P., Merenda, F., Perren, F., Rüfenacht, D., and Stergiopulos, N. (2009). Validation of a one-dimensional model of the systemic arterial tree. *Am. J. Physiol. Heart Circulat. Physiol.* 297, H208–H222. doi: 10.1152/ajpheart.00037.2009

Robinette, K. M., Daanen, H., and Paquet, E. (1999). "The CEASAR project: a 3-d surface anthropometry survey," in *Proceedings of Second International Conference on 3-D Digital Imaging and Modeling, 1999* (Ottawa: IEEE), 380–386.

Safaei, S., Blanco, P. J., Müller, L. O., Hellevik, L. R., and Hunter, P. J. (2018). Bond graph model of cerebral circulation: toward clinically feasible systemic blood flow simulations. *Front. Physiol.* 9:148. doi: 10.3389/fphys.2018.00148

Segars, W. P., Tsui, B. M., Cai, J., Yin, F. F., Fung, G. S., and Samei, E. (2018). Application of the 4-D XCAT phantoms in biomedical imaging and beyond. *IEEE Transac. Med. Imaging* 37, 680–692. doi: 10.1109/TMI.2017.2738448

Spitzer, V., Ackerman, M. J., Scherzinger, A. L., and Whitlock, D. (1996). The visible human male: a technical report. *J. Am. Med. Informat. Assoc.* 3, 118–130. doi: 10.1136/jamia.1996.96236280

Xu, X. G. (2014). An exponential growth of computational phantom research in radiation protection, imaging, and radiotherapy: a review of the fifty-year history. *Phys. Med. Biol.* 59:R233. doi: 10.1088/0031-9155/59/18/R233

Yeom, Y. S., Jeong, J. H., Kim, C. H., Han, M. C., Ham, B. K., Cho, K. W., et al. (2014). HDRK-woman: whole-body voxel model based on high-resolution color slice images of korean adult female cadaver. *Phys. Med. Biol.* 59:3969. doi: 10.1088/0031-9155/59/14/3969

Zastrow, E., Corcoles, J., and Kuster, N. (2016). "Convex optimization of MRI exposure for RF-heating mitigation of leaded implants: extended coverage of clinical scenarios at 128 MHz," in *Proceedings of the 24th International Society for Magnetic Resonance in Medicine (ISMRM)*. Singapore.

Disclaimer: The mention of commercial products, their sources, or their use in connection with material reported herein is not to be construed as either an actual or suggested endorsement of such products by the Department of Health and Human Service. The content is solely the responsibility of the authors and does not necessarily represent the official views of the National Institutes of Health.

Conflict of Interest Statement: The authors declare that the research was conducted in the absence of any commercial or financial relationships that could be construed as a potential conflict of interest.

frontiers in Medicine

TECHNOLOGY REPORT
published: 13 December 2018
doi: 10.3389/fmed.2018.00348

Prospective Design, Rapid Prototyping, and Testing of Smart Dressings, Drug Delivery Patches, and Replacement Body Parts Using Microscopy Aided Design and ManufacturE (MADAME)

*Hans Jörg Sidler[1,2,3], Jacob Duvenage[2], Eric J. Anderson[3,4], Joanna Ng[2], Daniel J. Hageman[2] and Melissa L. Knothe Tate[1,2,3]**

[1] Institute of Biomedical Engineering and Medical Informatics, Swiss Federal Institute of Technology, Zurich, Switzerland, [2] MechBio Team, Graduate School of Biomedical Engineering, University of New South Wales, Sydney, NSW, Australia, [3] Departments of Mechanical & Aerospace Engineering and Biomedical Engineering, Case Western Reserve University, Cleveland, OH, United States, [4] National Oceanic and Atmospheric Administration, Great Lakes Environmental Research Laboratory, Ann Arbor, MI, United States

Edited by:
*Enrico Capobianco,
University of Miami, United States
Marco Aiello,
IRCCS SDN, Italy
Marco Diego Dominietto,
Paul Scherrer Institut (PSI),
Switzerland*

***Correspondence:**
*Melissa L. Knothe Tate
m.knothetate@unsw.edu.au*

Specialty section:
*This article was submitted to
Translational Medicine,
a section of the journal
Frontiers in Medicine*

Received: *06 May 2018*
Accepted: *27 November 2018*
Published: *13 December 2018*

Citation:
Sidler HJ, Duvenage J, Anderson EJ, Ng J, Hageman DJ and Knothe Tate ML (2018) Prospective Design, Rapid Prototyping, and Testing of Smart Dressings, Drug Delivery Patches, and Replacement Body Parts Using Microscopy Aided Design and ManufacturE (MADAME). Front. Med. 5:348. doi: 10.3389/fmed.2018.00348

Natural materials exhibit smart properties including gradients in biophysical properties that engender higher order functions, as well as stimuli-responsive properties which integrate sensor and/or actuator capacities. Elucidation of mechanisms underpinning such smart material properties (i), and translation of that understanding (ii), represent two of the biggest challenges in emulating natural design paradigms for design and manufacture of disruptive materials, parts, and products. Microscopy Aided Design And ManufacturE (MADAME) stands for a computer-aided additive manufacturing platform that incorporates multidimensional (multi-D) printing and computer-controlled weaving. MADAME enables the creation of composite design motifs emulating e.g., patterns of woven protein fibers as well as gradients in different caliber porosities, mechanical, and molecular properties, found in natural tissues, from the skin on bones (periosteum) to tree bark. Insodoing, MADAME provides a means to manufacture a new genre of smart materials, products and replacement body parts that exhibit advantageous properties both under the influence of as well as harnessing dynamic mechanical loads to activate material properties (mechanoactive properties). This Technical Report introduces the MADAME technology platform and its associated machine-based workflow (pipeline), provides basic technical background of the novel technology and its applications, and discusses advantages and disadvantages of the approach in context of current 3 and 4D printing platforms.

Keywords: microscopy-aided design and manufacture, advanced materials, imaging, computational modeling, medical devices, smart materials and systems, translational medicine

INTRODUCTION

With the increasing mean age of the population and pressures on the health care system to increase accessibility to while also decreasing cost of care, there is an acute imperative to develop smarter materials enabling the creation and manufacture of products, devices, replacement tissue body parts, and associated therapeutic approaches. Such products, devices, and approaches will obviate the need for allo- and xeno-grafts (i.e., tissue graft from same species but not the same subject, and respectively from a different species) and their inherent limitations. At the same time, as the regulatory processes regarding combination products and devices become more streamlined, there is a great opportunity to use computational modeling for prospective design as well as rapid manufacture of such materials, products, devices, therapies, materials, and parts. This technology report lays out the process for the novel Microscopy Aided Design and ManufacturE (MADAME) technology platform (1), spanning ideation through to manufacture of such smart materials, products and parts. *Smart* in this context refers to materials that respond to stimuli in their environment, adapting their own structure to their prevailing environment, in short and/or long time periods with respect to design life, and thereby augment function through their entire lifecycle.

The impetus for MADAME's development lies in the acute need to engineer and manufacture materials, products, and devices that emulate the smart mechanical and transport properties of nature's own (**Figure 1**). Nature abounds with advanced, stimuli responsive materials, that if emulated, provide new solutions to currently untenable design problems. Such problems include the discrepancy between the human life span and the design life of the human hip and its contemporary implant replacement. Human joints offer complex geometrical solutions to increase range of motion and stability during daily activities, e.g., ball and socket for the hip or complex composite bone and composite bone and ligamentous structure of the plane synovial acromioclaviular joint. Yet, novel design solutions may emulate emergent properties of natural joints and springs. For example, the eucalyptus tree exhibits a gradient in mechanical properties, enabling it to bend like a blade of grass under gale force winds while transporting nutrients upwards of 100 meters from the roots to the tip. At a different length scale, the grasshopper knee also exhibits gradients enabling "jointedness" and an intrinsic leaf spring. While 3D printing offers advantages with regard to rapid manufacturing materials and parts with mechanical gradients, it shows distinct disadvantages in particular for parts exposed to bending and tension (1, 3, 4). Recent advances in 4D printing incorporate actuator and sensor functions intrinsic to i.a. piezoelectric properties of 3D printed pieces (5–9), engineering of residual stresses into parts that can transform their geometry reversibly via folding (10–12). One such disruptive 4D printing modality harnesses natural movements, e.g., of the wearer or attributable to nature's cycles (tidal, weather, seasons, etc.), to design novel wearables and smart systems. MADAME uses computer-aided additive manufacturing incorporating three dimensional (4D) printing and computer-controlled weaving to create composite design motifs that emulate tissue patterns of woven protein fibers (3, 4), gradients in different caliber porosities, and mechanical and molecular properties intrinsic to tissues (13, 14). In so doing, MADAME enables a new genre of smart materials, products and replacement body parts that exhibit advantageous properties in bending and tension as well as in compression and materials that harness forces linked to physiological activity to activate material properties.

This Technical Report introduces the MADAME technology platform and the technical background of the new technology and its applications. Advantages and disadvantages of the approach are discussed in context of future directions.

Recursive Logic and Weaving of Textiles With Biophysical and Spatiotemporal Patterns

MADAME describes the novel process of mapping spatial and temporal properties intrinsic to nature's smart materials, using imaging, and advanced computational methods (**Figures 1**, **2**) (1, 3). The patterns intrinsic to such materials are then recreated using recursive logic. Remarkably, the loom was the earliest computer–prior to the first punch card driven computers, the Jacquard loom wove patterns using loops of paper with holes to guide when hooks fell through the paper loop (hook down) or stayed above the loop (hook up), thereby encoding binary patterns of e.g., tapestry weaves (1, 3). Recursive logic provides a basis for computer coding algorithms (15) and computer-controlled Jacquard looms enable creation of physical embodiments (textiles) of mechanical and other biophysical and spatiotemporal patterns intrinsically encoded in natural materials.

The MADAME technology was developed to emulate the intrinsic weaves of natural tissues, from tree bark to grasshopper joints to human skin and bones. As an example, the patterns of structural proteins including elastin and collagen which imbue tissues with their respective elastic and toughness properties can be recursively mapped out and then imported into computer aided design files to weave textiles with scaled up mechanical property patterns mimicking those of the natural tissue (**Figure 3**) (1, 3, 4). In this way, the Jacquard loom technology provides a platform to create patterns of a variety of biophysical properties instead of its traditional use for the creation of color patterns in fabric and/or tapestries. Modern computer-controlled looms provide a rapid manufacturing method enabling control over 5,000 individual fibers, which themselves have different physical properties such as elasticity, respectively, stiffness. Composite materials are thus created in combination with 3D printing.

Mapping of Hierarchical Porosities in Natural Tissues

A critical aspect of MADAME is the quantification and visualization of several orders of magnitude different length scale features within the same natural sample, which is often studied in the form of a histological section. The process from which patterns are derived from biological samples can involve

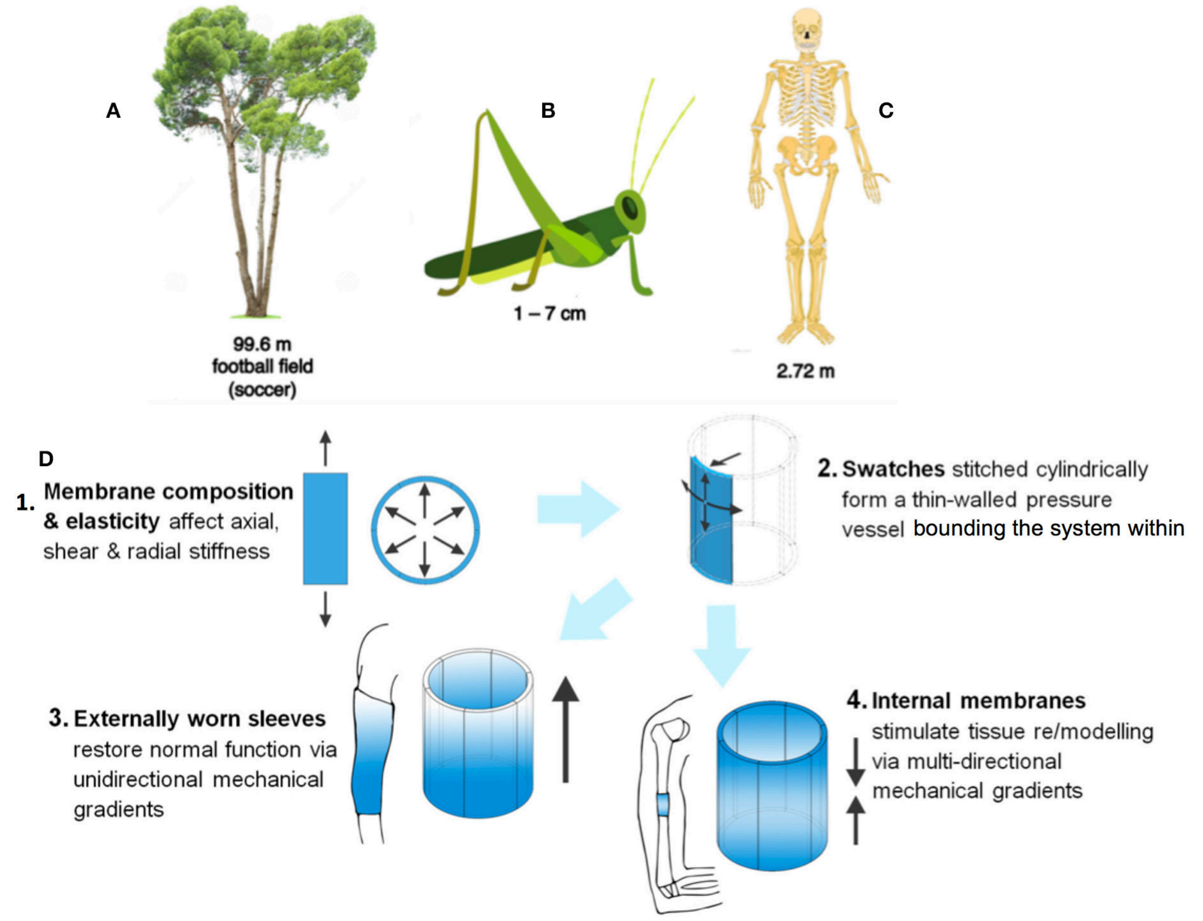

FIGURE 1 | MADAME describes a design and manufacturing process that is applicable for the creation of diverse materials exhibiting unique gradients in mechanical structure. These gradients underpin the remarkable higher order function of such structures. For example, **(A)** the towering eucalyptus tree that bends like a blade of grass in high winds, **(B)** the mechanical gradients intrinsic to joint function in insect exoskeletons, and **(C)** the internal musculoskeletal system of vertebrates are all enabled through prescient distribution of mechanical properties in space and time. Nature provides infinite patterns that provide inspiration for ideation of smart materials. **(D)** Such mechanical gradient properties can be implemented to harness natural movements (**D1, D2**) for external (wearables, **D3**) and internal (implants, **D4**) applications that harness the movement of the local system e.g., to deliver directional pressure gradients and/or gradients in strain at interfaces. Figure adapted and used with permission (2).

recursive logic, as previously described, or clever image analysis approaches to identify and separate out (segment) different sized features, after which gradients can be described spatially, e.g., as heat maps, to better visualize their distribution in space and in relationship to each other.

In addition to the importance of mechanical property gradients in natural materials, porosity gradients provide transport pathways while also modulating mechanical properties of natural materials. As an exemplary case study, bone exhibits at least three levels of hierarchical porosity and gradients thereof (14, 19) which are characteristic to the tissue and which imbue the tissue with remarkable smart properties, such as counterintuitive flow properties (exuding fluid under compression and imbibing fluid under tension) (13, 14, 20–22), and flow directing transport areas of the tissue that are poorly vascularized, as well as providing direct conduits (resorption cavities created by osteoclasts) for osteoblasts to penetrate and lay down new bone in an oriented fashion, achieving anisotropic structural stability similar to reinforced concrete (21).

Automated segmentation and mapping of different calibers of porosity within the sample sample is a non-trivial problem. In the following case study we address the problem in detail for clarity and to allow for reduction to practice using different imaging modalities. To analyze porosity of whole bone cross-sections and multiple length scales, enabling spatial mapping and analysis of vascular porosity and pericellular porosity, a computer algorithm was developed in MATLAB (MathWorks, Inc., Natick, MA, United States) (14, 19). First, the vascular porosity of bone was mapped. High resolution confocal microscopy collages were acquired for the entire cross section of a histological sample containing a rat ulna and radius which had been injected intravitally with a 300 Da fluorescent tracer (**Figure 4**) (9). Vessels were identified automatically using the MATLAB algorithm and a mask of bone devoid of vessels was created to

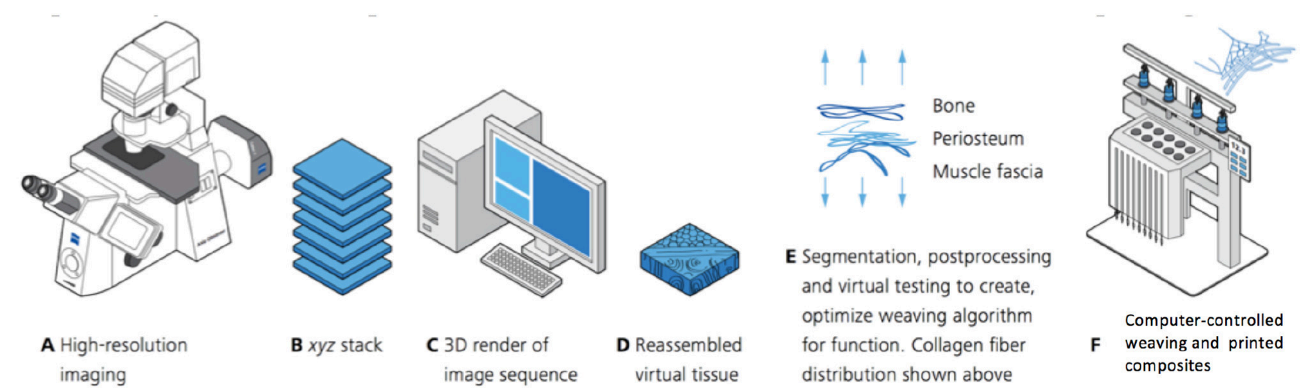

FIGURE 2 | "Pipeline" for microscopy-enabled, scaled-up computer-aided design, and manufacture of composite multifunctional textiles and 3D prints emulating the body's own tissues, on hand from an example mapping, and weaving patterns emulating those of structural proteins, collagen, and elastin, in tissues. "Pipeline" describes the process of acquisition, filtering, and transformation of data, taking the raw data as input, processing it, and producing a final result as the end process in the pipeline. **(A–D)** Second harmonic generation and two photon microscopy of tissues reveals a spatial map of elastin and collagen, e.g., in the periosteum, a soft, and elastic tissue sheath that bounds all non-articular surfaces of bone. In this example, microscopy is used to map the precise pattern of elastin and collagen in native tissue. As the initial step in the pipeline, the raw microscopy data is thus transformed to patterns of representing material properties, e.g., stiffness. **(E)** These tissue maps are then rendered using computer-aided design software, where the patterns can be optimized for desired design specifications. This step in the pipeline creates stl files that are input into rapid manufacturing processes including e.g., integrated weaving and/or multi-dimensional printing. **(F)** Optimized designs thus provide inputs for computer controlled weaving of textiles and combined printing of composites that emulate the tissue studied under the microscope. This end process in the pipeline results in novel composite textiles that can be implemented in multiple fields of use. Figure adapted from (1) and used with permission.

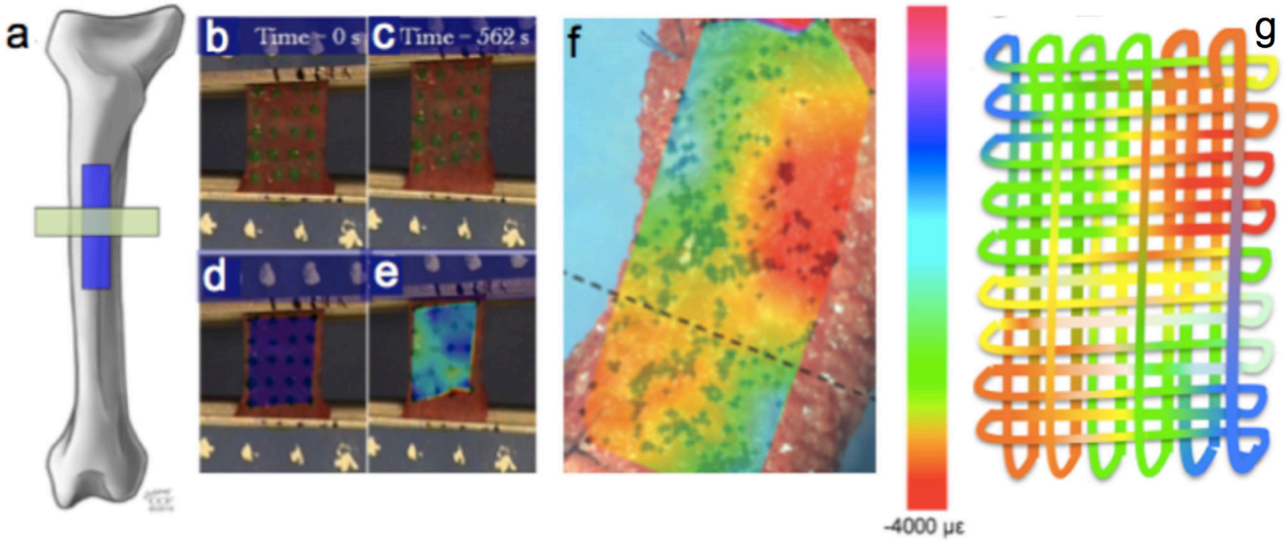

FIGURE 3 | Recursive weaving of advanced materials that emulate Nature's own. **(a–e)** Example depicting anisotropic mechanical properties of periosteum, the hyperelastic sheath covering all bony surfaces in vertebrates. In the sheep femur **(a)** strain maps are created during loading in tension using digital image correlation, on sections of periosteum **(a–e)** cut in either the longitudinal or circumferential direction **(a)**. High resolution strain maps of the entire periosteum of the femur, *in situ* during stance shift loading, show heterogeneity of mechanical properties in space and time over the course of the loading cycle [**(f)**, still image taken from single frame of digital video over the loading cycle]. **(g)** Conceptually, a singular solution to recursively weave the tissue fabric of the periosteum tested would be to "unravel" a single strand's mechanical properties that would vary along the entire length of the strand. Many more solutions exist through creation of fiber patterns comprised of elastic and tough fibers such as elastin and collagen using computer-controlled weaving (1, 3, 4). Figure adapted from (1, 16–18) and used with permission.

segment bone and calculate internal porosity. In this particular sample, the vascular porosity made up 2.46% of the cross sectional area of bone (**Figure 4**).

To calculate the cell-length scale lacunar porosity (the lacunae are the voids in which the cells reside), transmitted light images were used similar to the way that the confocal images were used to calculate vascular porosity in the previous example. A mask was created, first without porosity, and then the lacunar porosity was calculated in 100 micron thick samples. The different caliber pores were identified as vessels and lacunae,

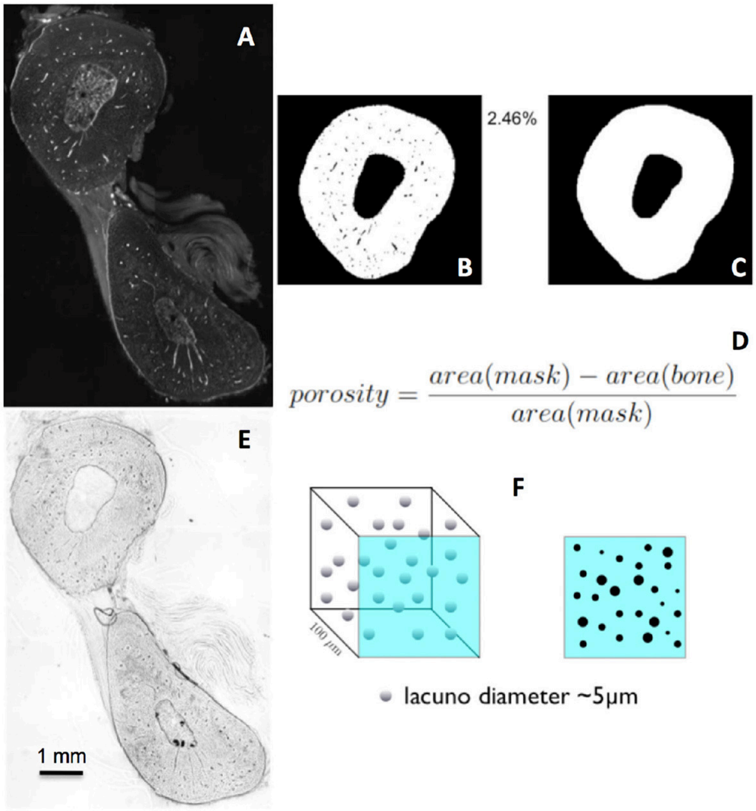

$$porosity = \frac{area(mask) - area(bone)}{area(mask)}$$

FIGURE 4 | (A–C). Mapping of the vascular porosity in bone. **(A)** Fluorescent confocal image. **(B)** Mask depicting area with vascular pores, *area*(*bone*) in the equation **(D)**. **(C)** Mask depicting area without vascular pores or *area*(*mask*) in the equation **(D)**. **(D)** Equation to calculate vascular porosity. **(E,F)** Calculation of lacunar porosity in bone, using **(E)** transmitted light images.

while also accounting for the volume (**Figures 4E,F**). The lacunar porosity was calculated by generating a mask without porosity, and calculating the number of lacunae (**Figures 5A,B**), resulting in a lacunar porosity of 1.1% for the example. This process was then carried out for specific areas around the cross section to determine the site specific lacunar porosity (**Figures 5C1–5**).

Then the site specific distribution of the vascular and lacunar porosities that make up the transport pathways were mapped using collages of high resolution confocal images (**Figures 6A–C**), which are depicted as "heatmaps" (warm colors represent high densities of particular features and cool colors reresent respective low densities, **Figure 7**). The logic underpinning the "heatmaps" forms the basis of a MatLab algorithm. In short, the measured porosity values are displayed in the form of color contour plots. These plots resemble the false color images obtained from imaging. MATLAB stores most images as two-dimensional arrays (i.e., matrices), in which each element of the matrix corresponds to a single pixel in the displayed image. A matrix with exactly the same dimension as the input image comprises all zero values. Next a randomly chosen region in the image is analyzed and two outputs are calculated including number of lacunae per area and vascular pores per area. These two parameters are then linked to the region in a way that the values are assigned to every matrix element representing the randomly selected area. Repeating this procedure several times causes regions to overlap (**Figure 6D**). Overlapping regions are averaged (**Figure 7A**), which leads to a good representation of the output-data over the cross-section if enough iterations are performed. In this way, a heat map of density of pores of two different calibers is created for the entire cross section, with warm colors depicting areas of high density and cool colors depicting areas of low density of e.g., lacunar and vascular porosity (**Figures 7C,D**).

This algorithm can be used to co-register images and their collages from imaging modalities as diverse as confocal laser imaging (yielding e.g., porosity gradients) (22, 23), second harmonic imaging (yielding e.g., collagen and elastin fiber gradients) (4), atomic force and electron microscopy (24, 25), multibeam scanning electron microscopy (26), computed tomography, magnetic resonance imaging (27), etc. These data sets, when encoded in computer aided design and computer aided manufacture file formats, serve as inputs for combined weaving of fiber patterns and multidimensional advanced manufacture (e.g., 3D printing or laser sintering) of porous structures. This enables creation of composite materials with strength in tension and bending and with smart, poroelastic

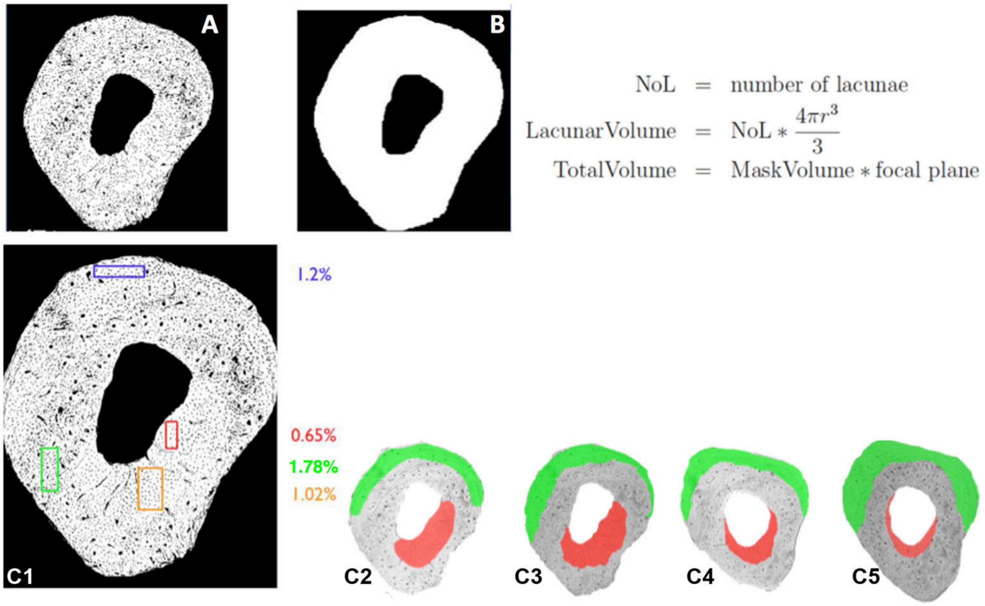

$$\begin{aligned} \text{NoL} &= \text{number of lacunae} \\ \text{LacunarVolume} &= \text{NoL} * \frac{4\pi r^3}{3} \\ \text{TotalVolume} &= \text{MaskVolume} * \text{focal plane} \end{aligned}$$

FIGURE 5 | Mapping of the lacunar porosity in bone using transmitted light images **(A,B)** and mapping of site specific lacunar porosity in bone **(C1–5)**. **(A)** Mask of bone with lacunae. **(B)** MaskVolume of bone without lacunae. Based on the calculations, the lacunar porosity is 1.1% for the example shown. **(C1)** Different colors represent different lacunar porosities in specific sites of the cross section. **(C2-5)** Color plots depicting regions on different cross sections exhibiting characteristic porosities, e.g., **1.78** and **0.65%**.

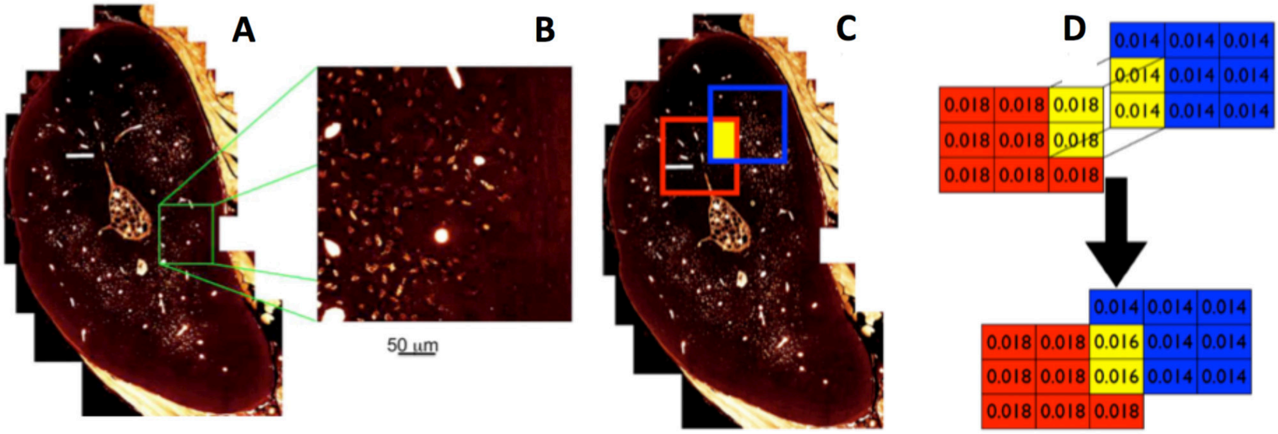

FIGURE 6 | From high resolution maps of different caliber porosities [vascular, lacunar–**(A,B)**] to generation of matrices representing imaging data **(C,D)**.

properties such as flow directing materials. Hence, MADAME can be used to create novel materials and parts with gradients in poroelastic properties emulating those found in smart, natural materials.

Additive Manufacturing of Scaled Up Natural Properties, Including Pore Gradients

Encoded in computer aided design and computer aided manufacture file formats, i.a. stereolithography (stl) or 3D Manufacturing Format (3MF) files, spatial plots of features provide inputs for additive manufacturing of materials, products, and parts that exhibit gradients and/or distributions in properties of natural materials. Additive manufacturing can take place via either computer-controlled weaving and/or additive manufacturing processes including i.a. stereolithography, powder sintering, 3D printing, etc. and/or electrospinning, weaving, and knitting.

The order and/or combined processes of weaving, knitting and spinning with 3D printing can be tuned to achieve the desired final properties of the materials, products and parts. For example, a weave can be placed within a stereolithography bath, enabling polymerization of polymeric matrix in gradients defined

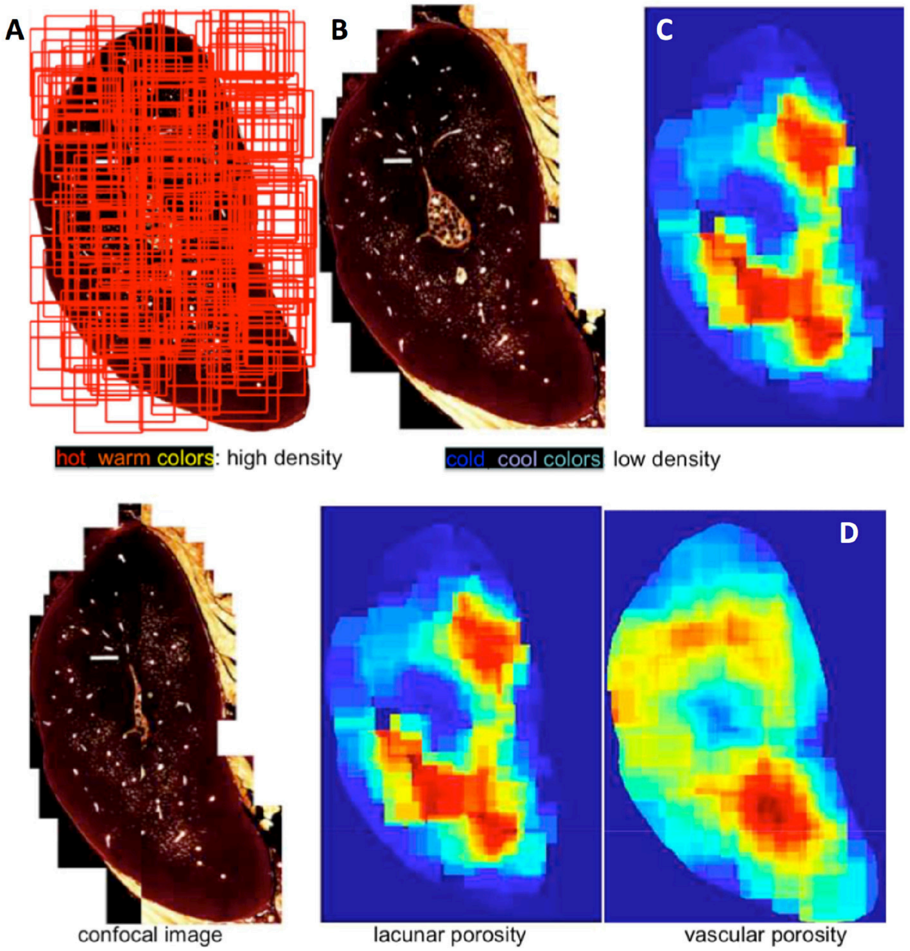

FIGURE 7 | Heat maps are generated from random assessment of areas **(A)**, for lacunar and vascular porosity **(B)** in this case, and depicted as density gradients **(C,D)**, using hot-warm colors (red, orange, yellow) and low density using cool colors (blue, green). Images adapted from Knothe Tate et al. (14) and used with permission.

by scaled microscopy data around the weave. Similarly, with laser sintering, apatite and other mineral or metal based powders can be sintered around the weave. Integrated weaving and 3D systems will enable the weaving of textiles within the monomer baths using jets instead of hook-based weaving looms that are completely integrated with 3D printing modalities (18).

Thus, we have described a pipeline or machine-based workflow (**Figure 2**) to design and manufacture smart dressings, drug deivery patches, and replacement body parts using MADAME. While "pipeline" refers to data driven processes that execute on the order of minutes and hours, "workflows" have more human interaction and periods of execution can be extend to days and years. MADAME shows great promise for the realization of new classes of materials, products and devices that will benefit patients, allowing for incorporation of unprecedented spatial and temporal patterns. One example is a new class of "designer" wound dressings *cum* delivery devices that are tuned to the spatial and temporal wound healing and drug release kinetics of individual patients, that harness the patient's movements to facilitate delivery, and that signal the wearer or the carer when the active ingredients are spent (**Figure 8**). This application can be further expanded as a disruptive platform for development of new classes of wearable materials and devices as well as internal applications, such as implants and medical devices.

The pipeline has been tested on scaled up, three dimensional confocal microscopy datasets of the pericellular space in cortical bone (**Figure 9**). In this case, volumetric microscopy data was inverted to represent the fluorescent-dye infused cellular features as voids, and approximated in stl file format. The stl files contain no scale information, i.e., can be scaled up or down and used as inputs to create physical renderings at any desired scale and using any compatible rapid manufacturing modality. The physical renderings thus created, e.g., via 3D printing, enable unprecedented measurements using similitude theory, where measures at actual length scale are scaled up and down from the physical rendering. Similitude is a powerful, classical tool in mechanical engineering, applied by Da Vinci through to the

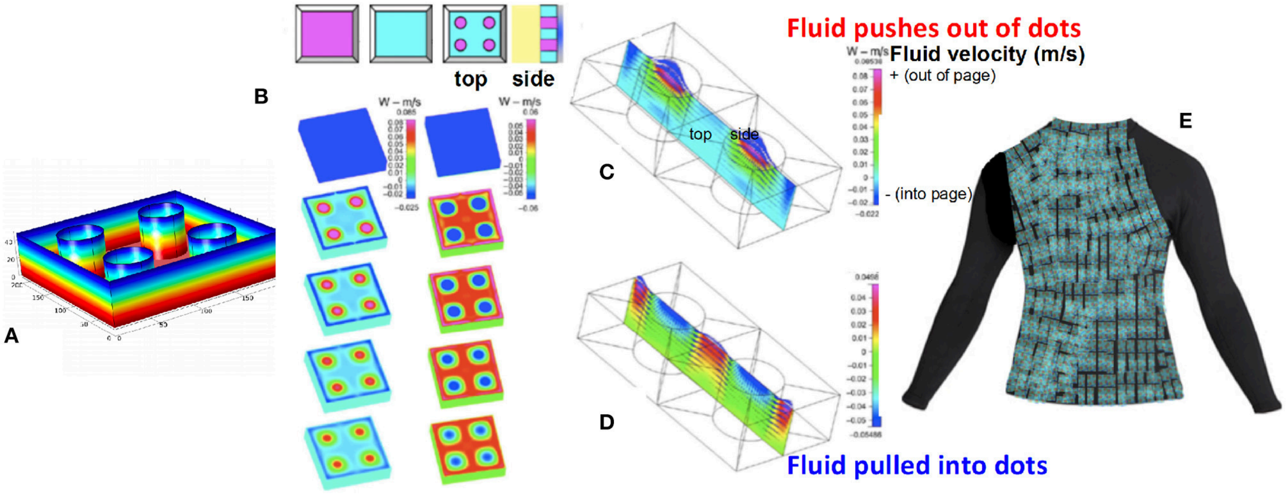

FIGURE 8 | Application of MADAME to designer dressings and wearables. Modular designs **(A)** can be scaled up and tuned e.g., for bespoke bandages with spatial and temporal control of drug delivery. **(B–D)** Directionality of delivery dots and surrounding areas can be controlled by the architecture of the module. Scale bars depict fluid velocity, with warm colors indicating flow outwards and cool colors, flow inwards; e.g., pushing on the patch **(B,C)** results in flow out of the delivery dots. **(E)** Example of large scale, wearable wound dressing for e.g., burn treatment. Images recreated with permission from (14, 17).

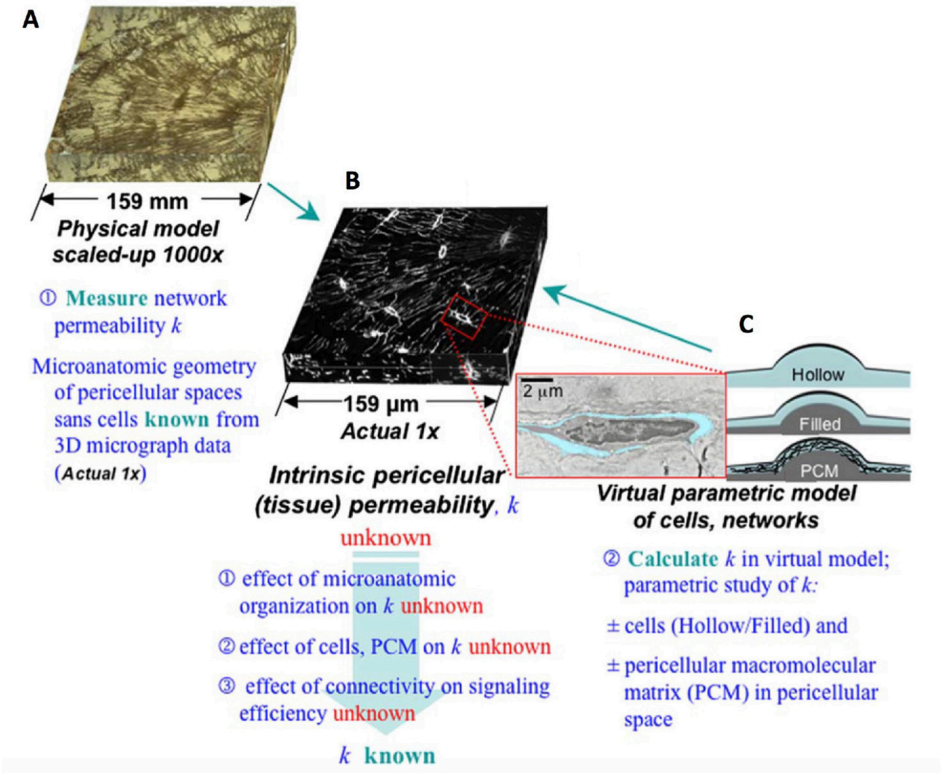

FIGURE 9 | Early example of scale up and rapid prototyping of micron scale systems to emulate smart permeability properties in 1,000x scaled up (cm length scale) system. The intrinsic tissue permeability cannot be measured based on microscopy alone **(B)**. 1,000x scaled up physical renderings of the microscopic data are depicted as inverse microscopy data to encode flow around cells and their networks **(A)**. Virtual renderings of single cells enable analysis of the effect of pericellular matrix permeability on bulk pericellular tissue permeability **(C)**. Only through parallel study of virtual, scaled up physical renderings, and virtual *in silico* modeling based renderings of the system at different length scales, can the interactions between the elements and bulk properties of the tissue be estimated and validated. These studies were the first of their kind and they paved the way for organ to nano scale maps of human tissues and organs using other imaging modalities. Images used with permission after (28).

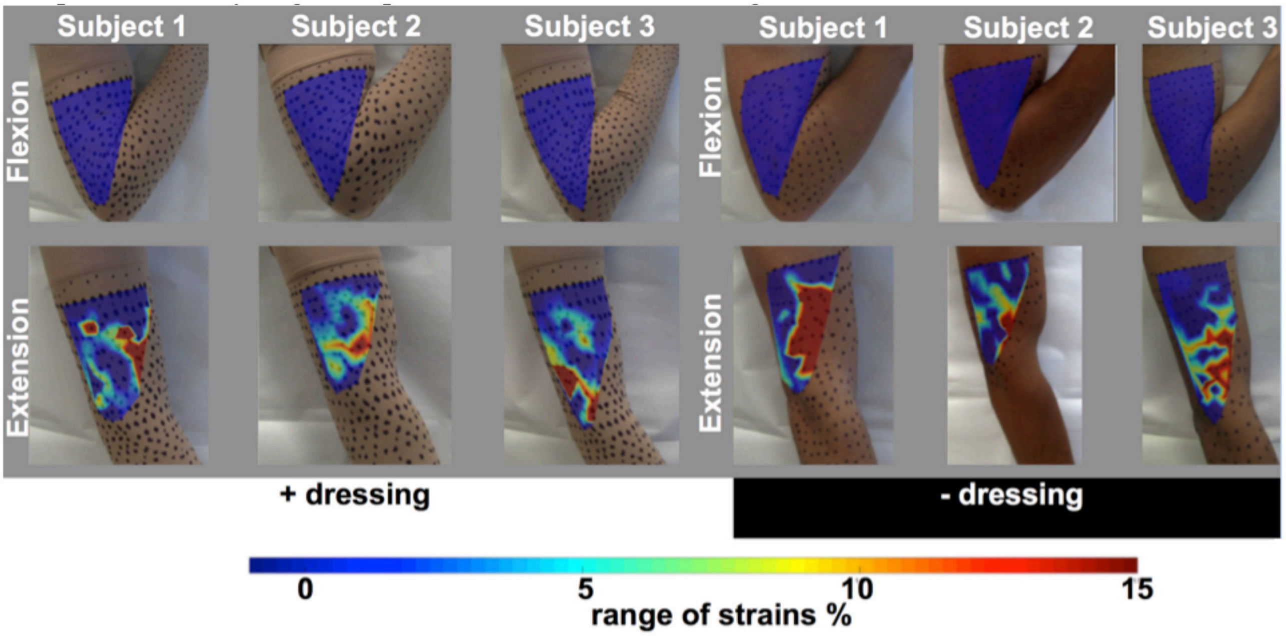

FIGURE 10 | Coupled experimental mechanics and modeling studies enable determination of the range of strains on the surface of the human arm typical for daily activities. Digital imaging correlation methods and custom computer code developed for mapping strains *in situ* on the surface of the periosteum (*cf.* **Figure 3**) were used to measures strain on the surface of the arms of three subjects, with and without the presence of a compressive dressing. Strains are mapped at one point in time (one frame of digital video) during flexion and compression of the arm. Figure after (33) and used with permission.

modern day (14, 22). In the current example of the pericellular fluid space in cortical bone, for the first time pericellular tissue permeability could be measured on scaled up physical renderings of actual tissues. Pericellular permeability measures are of particular relevance for predicting of pharmaceutical delivery kinetics at local and global length scales.

Similarly, the pipeline was tested and validated in scaled up patterns of structural proteins mapped in ovine periosteum, an elastic and soft tissue sheath covering all bone surfaces and providing a niche for stem cells (1, 3, 4, 29–32). For the first time, using MADAME it was possible to create textiles that emulate the smart mechanical properties of the periosteum. The value proposition of MADAME is to scale up gradients in i.a. mechanical properties, porosities, and protein patterns to rapid prototype new materials that emulate patterns in natural materials. This provides an unprecedented means by which smart properties of natural tissues and systems can be mapped precisely using high resolution microscopy and used as a basis for manufacturing of scaled up materials that emulate nature systems.

The pipeline can be further tailored to best harness the wearer's natural movements and thereby to e.g., augment transport to and from the wound surface via material design that directs convective flow by harnessing displacements at the interface with the skin (**Figures 8**, **10**). Thus, MADAME integrates inputs encoding material properties in context of the physiological mechanical environment in which the thus designed and manufactured products will be used, which provides independent and synergistic optimization of materials design and manufacture.

The inherent advantages and disadvantages of the enabling and disruptive MADAME technology align with those of current 3D- and 4D-printing technology platforms (**Table 1**). The major advantage of MADAME over current 3D- and 4D-printing modalities is that provides a means to manufacture novel composites with biophysical and spatiotemporal gradients and associated sensor and actuator functions that harness natural movements or transformations. The major disadvantages of MADAME include the need for high resolution imaging that crosses length scales, as well as cutting edge testing and validation, both of which requires operators with multidisciplinary, technical, and soft skillsets. With increasing sophistication of manufacturing and design capabilities, the need for creation of a future workforce with multivalent skillsets as well as creative ideation capacity will increase in importance, which in turn will drive the need for an educational curricula and training opportunities to gain those skillsets. At the same time, opportunities for integration of clean manufacturing methods and for employment of a highly educated workforce presents new opportunities for economic growth in geographical regions with lagging traditional manufacturing sectors.

DISCUSSION AND CONCLUSIONS

Using rapid prototyping, we expect the next generation of external and internal wearables including garments and implants, designer dressings, and drug delivery devices to be customizable and 3D printable in the General Practitioner's or nurse's office, and/or at the drug store/chemists. In the future, such devices

TABLE 1 | Comparison of the relative advantages and disadvantages of MADAME, 3D- and 4D-printing.

	Advantages	Disadvantages
3D printing	Off the shelf technology widely available and implementable	Limitations with regard to practical achievement of seamless, high resolution gradients in properties Lack of actuation and sensing in its simplest form Need for enabling technologies to prepare materials so they can be implemented using additive manufacturing processes such as stereolithography, laser sintering, etc. and limitation to combining materials in a single system
4D printing	Adds "smart" functionality to 3D printed materials, including actuation and sensing functions Disruptive platform - can be used to invent novel products and devices with wide range of applications in different industry sectors	Disadvantages of 3D printing may apply but may be overcome if functionality is added independent of 3D printing logistics, *e.g.* engineering in residual strains Implementation is initially specific to functionality added
MADAME	Can be implemented using 3D and 4D printing Enables creation of novel composites with biophysical and spatiotemporal gradients intrinsic to fibers and printing medium making up the materials Novel composites with biophysical stimuli activation depending on choice of fibers and surrounding matrix and their respective integration	Disadvantages of 3D and 4D printing may apply but may be overcome if functionality is added independent of 3D/4D printing logistics, e.g., using composite manufacturing methods Requires high resolution imaging platforms that enable cross scale imaging Requires state-of-the-art/cutting edge testing and validation Requires multidisciplinary skillsets

will exhibit novel functionality, from delivery of drugs and biologics including stem cells, to active collection and monitoring of wound exudate, to modulation of the wound healing cascade through spatial and temporal presentation of factors that modulate cell behavior (migration, adhesion, proliferation, differentiation). Through clever implementation of e.g., click chemistry, they will signal the patient when it is time to return to the medical provider for follow up care (or, alternatively they will signal the wound care team when it is time for dressing change).

Aging is associated with impairment to healing and repair processes. Mobility decreases with increasing age and, in conjunction with incidence of diabetes or other comorbidities, the incidence and challenges intrinsic to treatment of chronic wounds increases. Concomitant to the increasing incidence of difficult to treat wounds, providing care to the ever-increasing aged population presents significant societal and economic challenges. Ultimately this approach will facilitate repair and healing processes that promote longevity through the described pipeline to rapid prototype bespoke external (wearables) and internal (implants, medical devices) wound dressings that deliver drugs and take up wound exudate.

MADAME is paradigm shifting and its significance can be demonstrated by the fact that it addresses an important problem as well as a critical barrier to progress in the field. Applied to medical products, materials and replacement parts, MADAME will provide caregivers a new means by which to treat wounds and physical impairments in a manner that is doubly efficient in that it will facilitate and thereby speed wound healing while also reducing the burden to caregivers.

ETHICS STATEMENT

The digital image correlation study of strains on the surfaces of human subjects' arms was carried out in accordance with the recommendations and with approval of the UNSW human ethics committee, University of New South Wales, Sydney, Australia (HC 14077). All subjects gave written informed consent in accordance with the Declaration of Helsinki.

The studies quantifying and creating spatiotemporal maps of mechanical and porosity properties across cross sections in tissues of sheep and rats was carried out in accordance with the recommendations of the Animal Care and Use Committee of the Canton of Grisons Switzerland, who approved the protocols.

AUTHOR CONTRIBUTIONS

HS and MKT carried out the coupled imaging and computational modeling porosity analyses. JD carried out the coupled digital image correlation and computational analysis of surface based strains of the arm under flexion and extension, in collaboration with JN, DH, and MKT. MKT conceived of the collagen and elastin mapping studies and JN carried them out to create the first MADAME based textiles emulating periosteum. EA and MKT carried out experimental and computational modeling research and development of the flow directing foams technology platform. MKT conceived of the flow directing foam technology, the recursive weaving and the MADAME platforms. MKT wrote the manuscript, which was read and approved by all co-authors.

FUNDING

This work has been supported by grants from the Wallace H. Coulter Foundation, the Paul Trainor Foundation, and the National Health and Medical Research Council (Development Grant, APP1119636).

REFERENCES

1. Knothe Tate ML. "Navigation of bee brains to human hips - microscopy and the modern Magellans," in *A New Age in Scanning Electron Microscopy: Applications in the Life Sciences.* Washington, DC: Science/AAAS (2017) p. 19–23.
2. Ng JL, Collins CE, Knothe Tate ML. Engineering mechanical gradients in next generation biomaterials – lessons learned from medical textile design, *Acta Biomater*. (2017) 56:14–24. doi: 10.1016/j.actbio.2017.03.004
3. Knothe Tate ML *Biotextilogy - The Cellular Catwalk*, ISBN: 978-0-646-97861-1, Sydney. (2017).

4. Ng J, Knothe L, Whan R, Knothe U, Knothe Tate ML. Scale-up of Nature's Tissue Weaving Algorithms to Engineer Advanced Functional Materials. *Sci Rep.* (2017) 7:40396. doi: 10.1038/srep40396
5. Lewis JA. Direct ink writing of 3D functional materials. *Adv Funct Mater*. (2006) 16:2193–204. doi: 10.1002/adfm.200600434
6. Duoss EB. Three-dimensional printing of elastomeric, cellular architectures with negative stiffness. *Adv Func Mater*. (2014) 24:4905–13. doi: 10.1002/adfm.201400451
7. Khoo ZX, Teoh JEM, Liu Y, Chua CK, Yang S, An J, et al. 3D printing of smart materials: A review on recent progresses in 4D printing. *Virtual Phys Prototyping* (2015) 10:103–22. doi: 10.1080/17452759.2015.1097054
8. Lee J, Kim HC, Choi JW, Lee IH. A review on 3D printed smart devices for 4D printing. *Int J Precis Eng Manuf-Green Tech*. (2017) 4:373–83. doi: 10.1007/s40684-017-0042-x
9. Lantada AD. Systematic development strategy for smart devices based on shape-memory polymers. *Polymers* (2017) 496:1–19. doi: 10.3390/polym9100496
10. Maiti A, Small W, Lewicki JP, Weisgraber TH, Duoss EB, Chinn SC, et al. 3D printed cellular solid outperforms traditional stochastic foam in long-term mechanical response. *Sci Rep.* (2016) 6:24871. doi: 10.1038/srep24871
11. Sundaram S, Kim DS, Baldo MA, Hayward RC, Matusik W. 3D-Printed, Self-folding Electronics. *ACS Appl Mater Interfaces* (2017) 9:32290–8. doi: 10.1021/acsami.7b10443
12. Fu H, Nan K, Froeter P, Huang W, Liu Y, Wang Y, et al. Mechanically-guided deterministic assembly of 3D mesostructures assisted by residual stresses. *Small* (2017) 13:1700151. doi: 10.1002/smll.201700151
13. Knothe Tate ML, Anderson E. *Flow Directing Materials and Systems*. U.S. patent 12/106,748 (priority date 20 April 2007) (2013)
14. Knothe Tate ML, Steck R, Anderson EJ. Bone as an inspiration for a novel class of biomaterials. *Biomaterials* (2009) 30:133–40. doi: 10.1016/j.biomaterials.2008.09.028
15. Roberts ES. *Thinking Recursively*. ISBN13: 9780471816522, Boston: Wiley. (1986).
16. McBride SH, Dolejs S, Brianza S, Knothe U, Knothe Tate ML. Net change in periosteal strain correlates to rapid *de novo* bone generation in critical sized defects. *Ann Biomed Eng.* (2011) 39:1570–81. doi: 10.1007/s10439-010-0242-9
17. Knothe Tate ML. Smart body armor inspired by flow in bone. *Smart Struct Syst.* (2011) 7:223–8. doi: 10.12989/sss.2011.7.3.223
18. Knothe Tate ML. *A substrate*. European Patent No. 14836910.1 (priority date 15 August 2014). (2018).
19. Sidler HJ. *Site-Specific Porosity in Cortical Bone*. Master's thesis of the Swiss Federal Institute of Technology Zürich, carried out at the Case Western Reserve University in Cleveland, USA (2005).
20. Knothe Tate ML. Top down and bottom up engineering of bone. *J Biomech.* (2011) 44:304–12. doi: 10.1016/j.jbiomech.2010.10.019
21. Knothe Tate ML, Knothe U. *Composition and Method for Inducing Bone Growth and Healing* (priority date 20 February 2003). U.S. Patent No. US 7,879,107 B2. (2011)
22. Knothe Tate ML, Niederer P, Knothe U. *In vivo* tracer transport through the lacunocanalicular system of rat bone in an environment devoid of mechanical loading. *Bone* (1998) 22:107–17.
23. Knothe Tate M.L. (2003) "Whither flows the fluid in bone?": an Osteocyte's Perspective. *J Biomech.* 36:1409–24. doi: 10.1016/S0021-9290(03)00123-4
24. Knapp HF, Reilly GC, Stemmer A, Niederer P, Knothe Tate ML. Development of preparation methods for and insights obtained from atomic force microscopy of fluid spaces in cortical bone. *Scanning* (2002) 24:25–33. doi: 10.1002/sca.4950240104
25. Reilly G, Knapp H, Stemmer A, Niederer P, Knothe Tate ML. Investigation of the lacunocanalicular system of cortical bone using atomic force microscopy. *Ann Biomed Eng.* (2001) 29:1074–81. doi: 10.1114/1.1424910
26. Pereira A, Hageman D, Knothe U, Zeidler D, Knothe Tate ML. Creating high-resolution multiscale maps of human tissue using multi-beam SEM. *PLoS Comp Biol.* (2016) 12:e1005217. doi: 10.1371/journal.pcbi.1005217
27. Freutel M, Seitz AM, Galbusera F, Bornstedt A, Rasche V, Knothe Tate M.L, et al. Medial meniscal displacement and strain in three dimensions under compressive loads: MR assessment. *J Magn Reson Imaging* (2014) 40:1181–8. doi: 10.1002/jmri.24461
28. Anderson EJ, Kreuzer SM, Small O, Knothe Tate ML. Pairing computational and scaled physical models to determine permeability as a measure of cellular communication in micro- and nano-scale pericellular spaces. *Microfluid Nanofluid.* (2008) 4:193–204. doi: 10.1007/s10404-007-0156-5
29. Knothe Tate ML, Yu NYC, Jalilian I, Pereira A, Knothe UR. Periosteum mechanobiology and mechanistic insights for regenerative medicine. *BoneKey Rep.* (2016) 5:857. doi: 10.1038/bonekey.2016.70
30. Knothe Tate ML, Detamore M, Capadona J, Wooley A, Knothe U. Engineering and Commercialization of Human-Device Interfaces, from Bone to Brain. *Biomaterials* (2016) 95:35–46. doi: 10.1016/j.biomaterials.2016.03.038
31. Evans S, Chang H, Knothe Tate ML. Elucidating multiscale periosteal mechanobiology: A key to unlocking the regenerative capacity of the periosteum? *Tissue Engineering Part B* (2013) 19:147–59. doi: 10.1089/ten.TEB.2012.0216
32. Evans S, Parent J, Lasko C, Zheng X, Knothe U, Lemaire T, Knothe Tate ML Periosteum, Bone's "Smart" Bounding Membrane, Exhibits Direction Dependent Permeability. *J Bone Miner Res*. (2013) 28:608–17. doi: 10.1002/jbmr.1777
33. Hageman D, Duvenage J, Knothe Tate ML. Quantitative strain mapping as a technology platform to test efficacy of compression sleeves. *Adv Mater Tech* (in press).

Conflict of Interest Statement: Several patent applications have been issued and/or are pending in relation to the work described in this technical report. While these technologies have the potential to generate revenues for the inventors, they are still in the preclinical R&D phase of the translational cycle. The intent of the technical report is to disseminate findings among the R&D community and to share the novel approach to med tech ideation, development, and translation.

The authors declare that the research was conducted in the absence of any commercial or financial relationships that could be construed as a potential conflict of interest.

frontiers
in Physiology

ORIGINAL RESEARCH
published: 04 January 2019
doi: 10.3389/fphys.2018.01788

A Study on the Feasibility of the Deep Brain Stimulation (DBS) Electrode Localization Based on Scalp Electric Potential Recordings

Maria Ida Iacono[1,2†], *Seyed Reza Atefi*[1†], *Luca Mainardi*[3], *Harrison C. Walker*[4,5], *Leonardo M. Angelone*[2] and *Giorgio Bonmassar*[1*]

[1] Athinoula A. Martinos Center for Biomedical Imaging, Department of Radiology, Massachusetts General Hospital, Harvard Medical School, Charlestown, MA, United States, [2] Division of Biomedical Physics, Office of Science and Engineering Laboratories, Center for Devices and Radiological Health, U.S. Food and Drug Administration, Silver Spring, MD, United States, [3] Bioengineering Department, Politecnico di Milano, Milan, Italy, [4] Department of Neurology, University of Alabama at Birmingham, Birmingham, AL, United States, [5] Division of Movement Disorders, University of Alabama at Birmingham, Birmingham, AL, United States

OPEN ACCESS

Edited by:
Markus Reiterer,
Medtronic, United States

Reviewed by:
Bradley John Roth,
Oakland University, United States
Diego Ghezzi,
École Polytechnique Fédérale de Lausanne, Switzerland

***Correspondence:**
Giorgio Bonmassar
Giorgio.bonmassar@mgh.harvard.edu

† These authors have contributed equally to this work

Specialty section:
This article was submitted to Computational Physiology and Medicine, a section of the journal Frontiers in Physiology

Received: *16 April 2018*
Accepted: *28 November 2018*
Published: *04 January 2019*

Citation:
Iacono MI, Atefi SR, Mainardi L, Walker HC, Angelone LM and Bonmassar G (2019) A Study on the Feasibility of the Deep Brain Stimulation (DBS) Electrode Localization Based on Scalp Electric Potential Recordings. Front. Physiol. 9:1788. doi: 10.3389/fphys.2018.01788

Deep Brain Stimulation (DBS) is an effective therapy for patients disabling motor symptoms from Parkinson's disease, essential tremor, and other motor disorders. Precise, individualized placement of DBS electrodes is a key contributor to clinical outcomes following surgery. Electroencephalography (EEG) is widely used to identify the sources of intracerebral signals from the potential on the scalp. EEG is portable, non-invasive, low-cost, and it could be easily integrated into the intraoperative or ambulatory environment for localization of either the DBS electrode or evoked potentials triggered by stimulation itself. In this work, we studied with numerical simulations the principle of extracting the DBS electrical pulse from the patient's EEG – which normally constitutes an artifact – and localizing the source of the artifact (i.e., the DBS electrodes) using EEG localization methods. A high-resolution electromagnetic head model was used to simulate the EEG potential at the scalp generated by the DBS pulse artifact. The potential distribution on the scalp was then sampled at the 256 electrode locations of a high-density EEG Net. The electric potential was modeled by a dipole source created by a given pair of active DBS electrodes. The dynamic Statistical Parametric Maps (dSPM) algorithm was used to solve the EEG inverse problem, and it allowed localization of the position of the stimulus dipole in three DBS electrode bipolar configurations with a maximum error of 1.5 cm. To assess the accuracy of the computational model, the results of the simulation were compared with the electric artifact amplitudes over 16 EEG electrodes measured in five patients. EEG artifacts measured in patients confirmed that simulated data are commensurate to patients' data ($0 \pm 6.6\ \mu V$). While we acknowledge that further work is necessary to achieve a higher accuracy needed for surgical navigation, the results presented in this study are proposed as the first step toward a validated computational framework that could be used for non-invasive localization not only of the DBS system but also brain rhythms triggered by stimulation at both proximal and distal sites in the human central nervous system.

Keywords: electroencephalography (EEG), source localization, DBS placement, surgical navigation, finite difference time domain, computational electromagnetic modeling, forward and inverse problem

INTRODUCTION

Deep brain stimulation (DBS) of globus pallidus internus (GPi), subthalamic nucleus (STN), and ventral intermediate nucleus (Vim) significantly improves symptoms from patients affected by Parkinson's disease (PD), essential tremor, dystonia, and obsessive-compulsive disorder that no longer respond to drug therapy. Furthermore, recent evidence suggests that DBS may provide therapeutic benefit to patients with other neurological disorders, including Tourette syndrome, epilepsy, and psychiatric disorders such as depression (Vercueil et al., 2001; Hodaie et al., 2002; Gabriels et al., 2003; Hemm et al., 2005).

Despite the therapeutic success of DBS and its increasing adoption in clinical practice, outcomes are not uniform among different studies (Kleiner Fisman et al., 2006). Significant effort has been dedicated to investigating the wide range of factors that can influence outcomes including stimulation parameters [i.e., contact configurations, frequency, pulse width and voltage (Holsheimer et al., 2000; Moro et al., 2002; O'Suilleabhain et al., 2003; Kuncel and Grill, 2004; McIntyre et al., 2004b; Volkmann et al., 2006)], electrode geometry (Kuncel and Grill, 2004; Butson and McIntyre, 2005; Butson and McIntyre, 2006; Butson et al., 2006), electrode location (Maks et al., 2009), and the electrical properties of the tissues surrounding the implant (Grill and Mortimer, 1994; Grill, 1999; Butson et al., 2007; Yousif et al., 2007). Furthermore, evidence suggests that precise placement of DBS electrodes is key for the optimal clinical outcome of the DBS treatment. A misplaced DBS electrode not only results in decreased effectiveness but could also increase the risk for motor side-effects, such as increased muscular contractions, difficult articulation of speech, oculomotor disturbances or altered sensory phenomena, such as somatosensory paresthesia, diplopia or visual field phosphenes (Montgomery, 2010).

Deep Brain Stimulation is conventionally placed through stereotaxic guidance and microelectrode recording (MER) of single neuron activity. Preoperative images are usually co-registered into the stereotactic coordinate system, and MER is used to confirm the location of the DBS targets by recording and identifying characteristic neuronal discharge patterns that have been associated specifically with GPi, STN, and Vim, as well as other adjacent nuclei. Retrospective analysis of microelectrode track error between the planned trajectory and the microelectrode tip was performed in (Brahimaj et al., 2018), and a total radial error of 1.2 mm was reported. However, MER is time-consuming and requires the patient to be awake due to effects of the anesthesia on neuronal firing. On the other hand, localizing the exact DBS position by visual inspection using conventional imaging techniques such as magnetic resonance imaging (MRI) and computed tomography (CT) during surgery is still a great challenge as they are both affected by metal artifacts (Barrett and Keat, 2004). MRI artifacts induced by DBS have been reported in (Pollo et al., 2004) to be up to 10.4 mm and significant discrepancy between the centers of electrodes estimated by CT and MRI have also been reported. Furthermore, there are also concerns associated with the safety of MRI in patients with DBS electrodes (Gleason et al., 1992; Rezai et al., 2001, 2002, 2004; Bhavaraju et al., 2002).

Several numerical models with varying levels of complexity have been proposed in the literature for low-frequency electromagnetic analysis of the effectiveness of DBS (McIntyre et al., 2004a; Astrom et al., 2009; Grant and Lowery, 2009). Most of these studies model only the electrodes and a few surrounding structures, not the entire human head. Furthermore, available DBS numerical models (McIntyre et al., 2004a, 2007; Astrom et al., 2009; Grant and Lowery, 2009; Miocinovic et al., 2009; Vasques et al., 2009; Yousif and Liu, 2009) are limited by two sequential challenges: 1) prediction of stimulation-induced electromagnetic (EM) field and potential ("forward problem"), and 2) detection/interpretation of EM fields noninvasively from outside the skull ("inverse problem"). We propose a model aimed to bridge the pathway from DBS to noninvasive EEG readout.

To address the first point, we have built an MRI-based anatomical model of the human head previously proposed for RF dosimetry studies (Makris et al., 2008), which has also been adopted for studies with DBS implants in MRI (Angelone et al., 2010; Iacono et al., 2013). We have performed whole-head bioelectromagnetic simulations based on Finite Differences Time Domain (FDTD) method and predicted the DBS signal propagation throughout the head and on the scalp (simulated DBS voltage artifact).

To address the second point, we predicted potential on the scalp to solve the inverse problem and localize the source of the stimulation, i.e., the dipole that generates the DBS stimulation and the large artifact on the EEG. Filtering is commonly used to remove this artifact while preserving the spectral and temporal fidelity of the underlying brain signal. In our methodology, however, we propose to exploit such an artifact present on the EEG recordings of DBS patients and noninvasively "decode" its source with the aim of locating or guiding the DBS electrode implantation during DBS surgery. Dipole source localization – commonly performed to localize the source of brain electrical activity, such as the epileptogenic foci – is proposed in this case to localize the device. In this proof of concept study, we have addressed the technical challenges to achieving a robust DBS localization that could be used in the future for electrode navigation guidance during surgery or spatial localization of stimulus evoked electrical potential to better understand stimulation dose, spatial propagation, or time-dependent effects on distal components in the central nervous system motor network.

MATERIALS AND METHODS

Electromagnetic Simulations

The simulations were based on a head model described in (Makris et al., 2008), based on 1 mm^3 resolution T1-weighted MRI of a healthy adult human subject. 28 non-brain and 21 brain structural entities were distinguished and segmented on the dataset. Each anatomical structure was converted into its corresponding electrical structural entity as described in (Makris et al., 2008). The result was a heterogeneous model with uniform electrical properties within each anatomical structure. Since the

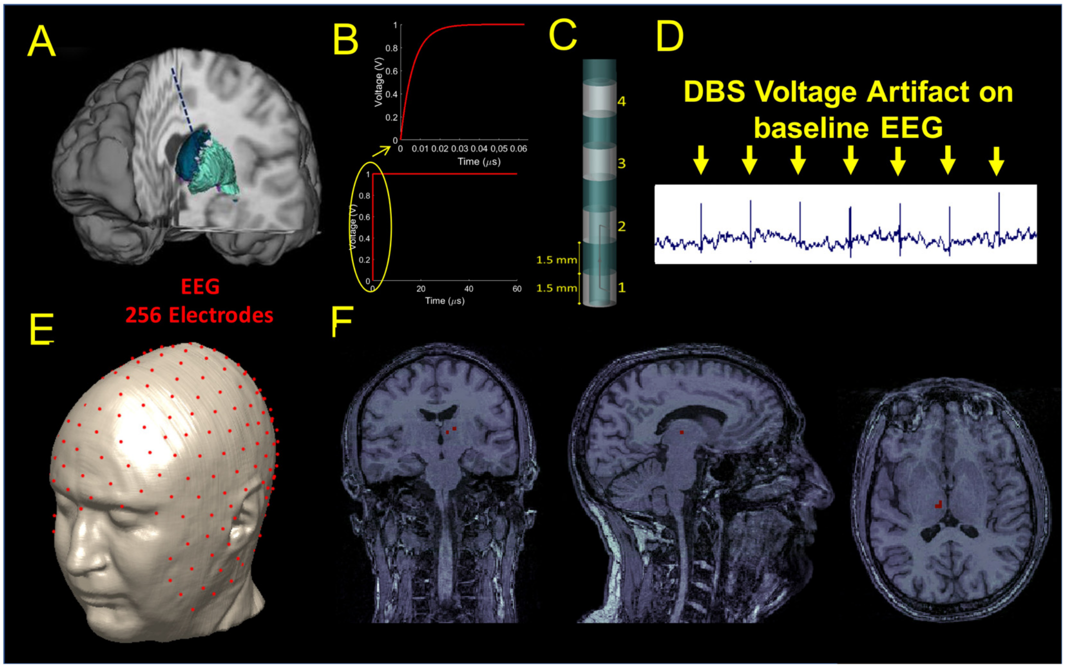

FIGURE 1 | **(A)** Illustration of the DBS placed in the STN. **(B)** waveform used as input for stimulation. **(C)** DBS electrode geometry. **(D)** DBS voltage artifact present on the clinical EEG recordings extracted from **Figure 3**. **(E)** Source localization of the DBS based on the 256 scalp potential samples. **(F)** Estimated source location on the coronal (let), sagittal (middle), and axial (right) original MRIs.

electrical properties of human tissues are frequency-dependent, each electrical structural entity was modeled using the one-pole Debye approximation (Gabriel et al., 1996).

One left unilateral DBS implant was modeled for the study. The lead was placed along a unique sagittal plane in the subcutaneous structure between the epidermis and the outer table, and then in a coronal plane through the outer table along the brain down to the basal ganglia (**Figure 1A**). The proximal end of the lead was placed in the neck of the head model and the distal end placed in the white matter region below the thalamus where the subthalamic nucleus is located. The implant was modeled as an insulated lead with an array of four perfect electric conductor cylindrical electrode contacts (Elwassif et al., 2012) at the distal end of the lead (**Figure 1C**). The length of each electrode was 1.5 mm. A bipolar configuration was considered for the stimulation, and the two electrodes were modeled as a cathode and anode and connected by a conducting wire, as shown in **Figure 1C**.

A smoothed voltage waveform, resembling the anodic pulse from an implantable pulse generator (IPG) from our clinical data, with an equivalent amplitude of 1 V and 60 μs pulse width was used for stimulation through the DBS electrode. The smoothed voltage step was computed by filtering the 60 μs pulse with a Butterworth low-pass filter of the first order and with a cut-off frequency of 100 MHz (**Figure 1B**).

Electromagnetic simulations were performed using commercially available software (XFDTD, Remcom, Inc., State College, PA) and each of the electric fields generated by the DBS for three bipolar configurations (1-2, 1-3, 1-4) was transferred into Multiphysics (COMSOL, Burlington MA) for post-processing to calculate the electric potential distribution on the scalp and generate a simulated signal mimicking the magnitude of the DBS voltage artifact present on the EEG recordings of patients with DBS. An example of such an artifact can be seen in **Figure 1D** and (Frysinger et al., 2006). We called this signal "simulated DBS voltage artifact," and we used it as input to solve the inverse EEG problem to localize the electric dipole generated by two active DBS electrodes. The three bipolar configurations were chosen as they matched those used in the clinical setting and they produced fields that ranged from narrow (1-2) to wide (1-4) stimulation. Each simulation took 10 days on a workstation that used four NVIDIA Tesla Dual GPU Kepler K80 Graphics Cards with 24 GB of memory each, installed on a 14-core system with 768 GB of RAM. The remaining possible configurations (2-3, 3-4, and 2-4) were not analyzed because they were expected to generate similar results with a shift of 3 mm (1.5 mm length of the electrode + 1.5 mm length of the insulation in between).

The electric scalar potential V was calculated by solving Gauss's law: $-\nabla\cdot(\varepsilon_z \nabla V) = \nabla\cdot(\varepsilon_z \mathbf{E})$, where V is the unknown electric potential, **E** is the electric field computed by XFDTD, and ε_z is the complex permittivity of tissues. A ground boundary condition ($V = 0$) was set on the side underneath the neck of the bounding box, which encloses the entire head geometrical model. On the remaining sides of the bounding box, an electric insulation boundary condition was used: $\varepsilon_z\ \mathbf{n}\cdot\mathbf{E} = 0$, where **n** is a vector perpendicular to the bounding box.

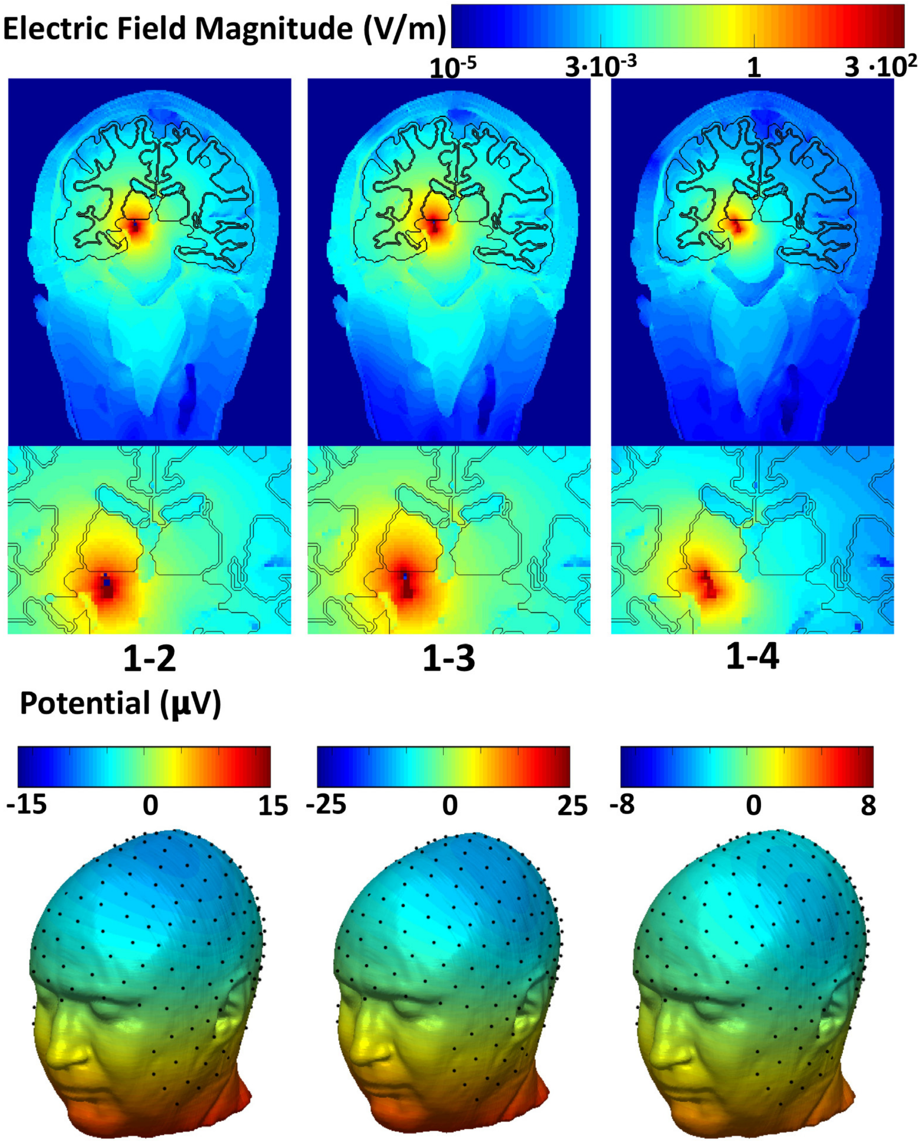

FIGURE 2 | Global and zoomed local spatial distribution of the electric field magnitude overlaid with the precise anatomy of the area surrounding the DBS implant (top row) and the electric potential on the scalp (bottom row).

Source Localization

Source localization was performed with Brainstorm (Tadel et al., 2011) in MATLAB (Mathworks, Natick, MA, United States). The original MRI data used to build the numerical head model (Makris et al., 2008) was used to build a three-shell forward head model including scalp, skull, and brain for localization. Once the forward model was built, a 256 channels EEG electrodes net was co-registered onto the head model (**Figure 1E**). The simulated potentials were then sampled at the 256 channels electrodes positions of the EEG net and imported into Brainstorm. The built-in source localization module of Brainstorm was then used to solve the inverse problem using the unconstrained dynamic Statistical Parametric Maps (dSPM) method with the following default parameters: depth weighting order of 0.5, regularization noise covariance of 0.1 and SNR of 3. Once the inverse problem was solved, full results were exported into MATLAB to find the center of mass of the largest dipole source(s) and its location (**Figure 1F**). The estimated source location (Sloc) for the three bipolar configurations (Sloc 1-2, Sloc 1-3, and Sloc 1-4, respectively) were compared with the physical center of mass (Mc) of the three pairs of electrodes (Mc 1-2, Mc 1-3, and Mc 1-4, respectively) and the localization error was calculated as the Euclidean distance between the estimated location (Sloc) and the physical one (Mc).

Clinical Data

All clinical data were acquired according to the IRB (Institutional Review Board) for the protection of human subjects and

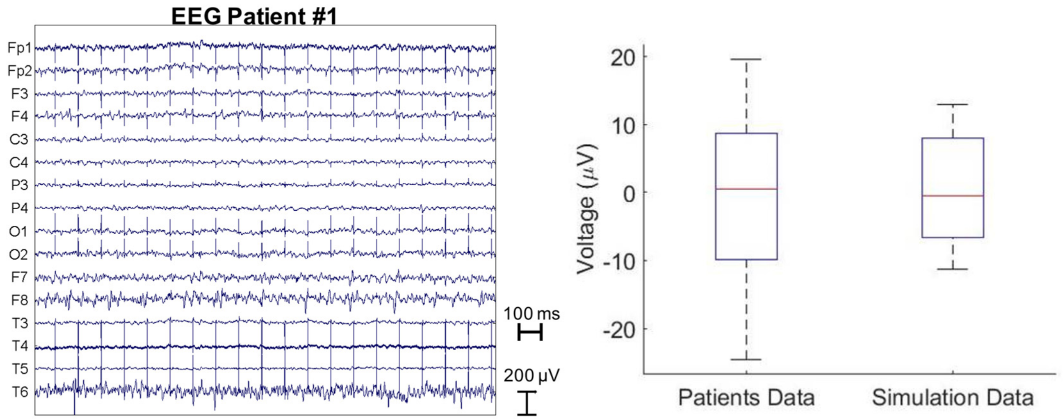

FIGURE 3 | Raw EEG traces of a patient stimulated with 10 Hz and 60 µs DBS pulses (left). The average electric artifact amplitudes over 16 EEG electrodes estimated from five patients vs. those predicted by the electromagnetic simulation with bipolar electrode configuration 1-2 (right).

consist of a cross-sectional sample of resting 10-20 clinical EEG of five PD patients with chronically (>6 weeks) implanted DBS electrodes in the STN. Standard EEG was acquired during delivery of biphasic and bipolar DBS stimulation pulses (amplitude of 3.5 V or 4.5V, width of 60 µs, 10 pulses per second, and two adjacent contacts activated). To assess the accuracy of the FDTD model, the results of the simulation with adjacent contact bipolar activation (i.e., 1–2) were compared with the electric artifact measured in this population. The EEG data were reformatted using a common average reference, linearly scaled to adjust them to the same voltage input (1 V) of the simulated data, and filtered using a high-pass filter with a cut-off frequency of 300 Hz to extract the electrical artifact.

RESULTS

Figure 2 shows the spatial distribution of the electric field amplitude (top) overlaid with the precise anatomy of the area surrounding the DBS implant and the potential (bottom) on the scalp. The maximum intensity of the electric field produced for the narrow (1-2) and the wide bipolar stimulation configurations (1-3) was 713 V/m and 993 V/m, respectively. The electric field increased up to twofold (1472 V/m) when the widest bipolar configuration (1-4) was used. The peak of the potential was found in proximity to the DBS electrodes and was 5.3 mV, −6 mV, −7.4 mV for the pair 1–2, 1–3, and 1–4, respectively.

The electric potential on the scalp followed a dipole pattern oriented according to the DBS electrodes axis in the head. The 256 sampled scalp potentials (**Figure 1E**), allowed localization of the DBS electrode pair center of mass (**Table 1**) with an error of 1.5 cm, 1.4 cm, and 1.2 cm for the three cases, respectively.

Furthermore, we compared the results obtained with the FDTD model to a cross-sectional sample of clinical EEG of PD patients with DBS. The amplitude of electrical artifact measured from the EEG clinical data averaged over all the patients and the EEG electrodes was 0 ± 6.6 µV. All EEG potentials are zero mean averaged as a common average reference was used. **Figure 3** (left) shows the raw EEG traces of a patient with the DBS on at 10Hz. The average electric artifact amplitudes over 16 EEG electrodes estimated from five patients were compared with those predicted by the electromagnetic simulation with bipolar electrode configuration 1-2 (right).

DISCUSSION

Intraoperative brain imaging would be the optimal approach for guiding DBS surgery. However, one of the main concerns regarding the use of imaging systems such as MRI for DBS patients is related to possible induced heating. There is an example of a patient reporting edema near the tip of one of the electrodes with the consequent paralysis after undergoing MRI (Henderson et al., 2005) (notably, the FDA-approved manufacturer's guidelines were not followed). Additionally, MRI acquisition considerably lengthens the duration of the surgery and requires the use of general anesthesia for targeting, without the ability to adjust the electrode position in real time based on MER and/or assessment of stimulation effectiveness and side effects during surgery. EEG has the potential for being a high impact and disruptive technology compared to the intra-operative imaging for non-invasive guidance of DBS surgery procedures because of the low cost of the device, installation, operation, ease of use and safety. When performing EEG on a patient with an active DBS, the DBS pulse typically constitutes an artifact on the EEG signal. In this paper, we have instead

TABLE 1 | The estimated source location (Sloc) for the three bipolar configurations (Sloc 1-2, Sloc 1-3, and Sloc 1-4, respectively) compared with the corresponding physical centers of mass (Mc) of the same three pairs of electrodes (Mc 1-2, Mc 1-3, and Mc 1-4, respectively).

	Mc 1-2	Sloc 1-2	Mc 1-3	Sloc 1-3	Mc 1-4	Sloc 1-4
x (mm)	111.5	124.3	111	123.5	110.5	121.7
y (mm)	121.5	125.6	122	124.6	122.5	125.5
z (mm)	150.5	157.1	152	156.6	153.5	156.9

studied such pulse and shown that it is possible to non-invasively localize a DBS electrode analyzing the distribution of electric potential on the scalp generated by this DBS pulse.

Notably, the method is still in its infancy and significant limitations still exist with EEG, most important of which is the accuracy of the localization of the brain sources from the recorded EEG due to the ill-posed nature of the methodology which leads to multiple solutions (Bonmassar, 2016). An error of 1-3 cm has been reported by studies investigating source localization using simplified spherical models (Acar and Makeig, 2013). In line with these studies, we report a maximum localization error of 1.5 cm.

In this study we describe a set of technical strategies that can be adapted to improve localization accuracy further. To the best of our knowledge, the proposed model is the first of its kind and is provided as a proof-of-concept methodology for device localization. Further methods are under development for minimizing/eliminating the stimulus artifact from electrophysiological recordings (Walker et al., 2012a,b). Future studies could conceivably expand on these methods, in order to better understand how DBS interacts with local and distant neuronal elements as a function of time after the stimulus pulse. For these explorations, confirmation of the known location of the DBS electrode with the stimulus transient could be used to constrain other investigations of brain activation as a function of time after the stimulus pulse.

These methods have some potential limitations. The most critical source of error is the forward head model employed in the source localization algorithm. Herein we used a forward head model that was automatically segmented into three tissue types: skin, skull, and brain. Errors due to automatic segmentation can jeopardize the localization accuracy. Furthermore, taking into account the anisotropic conductivity of tissues can improve volume conduction modeling.

Additionally, uncertainties in electrical parameters should be taken into account as a dominant source of localization error in the simulation results. For example, EEG models are sensitive to the skull conductivity and anisotropy. In addition, electrical properties may vary between individuals (Atefi, 2015; Atefi et al., 2016).

Another possible source of errors is due to the co-registration of the EEG cap onto the head model. Co-registration was performed by visually adjusting the position of the electrodes on the scalp of the virtual patient. More accurate co-registration strategies, e.g., non-linear co-registration methods, could be performed to fit the EEG electrode cap on the head.

The performance of the proposed source localization method should be assessed in the presence of noise (i.e., which is in our case better than standard EEG given that the DBS artifact is usually greater than any physiological EEG signal), using reduced electrode numbers (16, 32, 64, and 128 electrodes) and different localization algorithms such as the Minimum Norm Estimate (MNE) and LORETA (Pascual-Marqui, 1999). A new type of source localization, namely Direct Electromagnetic Source Tomographic Imaging Neurotechnology (DESTIN), may allow us to study DBS patients during DBS surgery not using a traditional source localization approach but rather a time of flight localization as it is similarly done in PET (Bonmassar, 2016). This could result in improved results as well as in decreased computational load.

Additional error mitigation – independent from the source localization method – could be achieved by improving the prediction of the simulated EEG potential on the scalp used to feed the inverse problem. A uniform 1 mm^3 electric grid was used to discretize the head and the DBS model in the FDTD EM simulations due to available computational resources. However, a multi-scale discretization with both millimetric and micrometric resolution, as used in (Iacono et al., 2013) may be needed to calculate a more accurate solution of the electric field generated by the DBS. Micro-resolution is crucial in order to precisely sample objects like DBS electrodes and to avoid errors such as staircasing (Railton and Schneider, 1999; Gajsek et al., 2002). The millimetric resolution is also crucial because performing simulations using a uniform submillimetric resolution for the entire head (Iacono et al., 2015) would require an extremely long processing time with the available computational resources. The uniform milli-resolution modeling alone – that was used in our simulations – may have resulted in a loss of accuracy in the mimicked scalp electric potential which in turn can confound the source localization.

Finally, the electrical properties of the head model used in the FDTD simulations were considered isotropic (i.e., the Debye model is isotropic). The inclusion of anisotropic electrical properties may enhance the accuracy of the simulated electric potential on the scalp. However, due to limitations in memory of the GPU cards, the inclusion of the anisotropic material was not feasible. Furthermore, the dielectric properties of the electrode/tissue interface did not include a capacitive component to model the drop in voltage that occurs in the transition from the polarization of the DBS electrode contact to the ionic medium because of convergence issues with the FDTD algorithm (Yousif and Liu, 2007).

Nevertheless, an improved EEG localization method tailored specifically to DBS, like the one proposed in this paper, could one day revolutionize DBS implantation resulting in a more uniform procedure across centers, using the EEG as a non-invasive image-guided tool. Pre-operative MRI data of the patients could be segmented in advance to generate the forward model. Real-time EEG recording with the implantable pulse generator of the DBS turned ON could be filtered to isolate the DBS artifact (Allen et al., 2010) and used to localize the electrode in the brain during surgical navigation similarly to how a Global Positioning System (GPS) is used in terrestrial navigation. Sterilization of the EEG system could be one obstacle to put in practice such a procedure while performing a stereotaxic surgery. However, safe use of disposable sterilized high-density EEG net has been previously reported (Yamazaki et al., 2013; Ahmadi et al., 2016).

Other applications may stem from this methodology: for example, the DBS artifact present on EEG recording can be used during the post-operative reprogramming of the IPG and provide the clinician with information about the composition and electrical changes of the tissues that surround the electrode, which may be important in patients with reduced stimulation efficacy to establish whether glial scar or changes in electrode impedance may play a role in changing clinical state after surgery. Furthermore, closed-loop smart DBS devices have already been proposed to dynamically and automatically adjust the stimulation to suppress pathological synchronization in patients with PD (Eusebio et al., 2011; Rosin et al., 2011). In these devices, the EEG electrical artifact may represent a simple yet widely available means of obtaining DBS pulse amplitude information in order to adjust the stimulation automatically during IPG programming/calibration. Finally, automatic calibration based on EEG artifact may become even more significant when applied to psychiatric disorders like obsessive-compulsive disorder and depression where the symptoms and the effects of the therapy are more difficult to observe and quantify.

CONCLUSION

We presented a computational modeling framework proposed as a proof-of-concept for non-invasive localization of DBS by means of EEG recording on the scalp. Numerical results were comparable with EEG clinical data recorded from PD patients with implanted DBS. Our findings showed that the subcortical DBS sources were localized using EEG data on the scalp with a ~1 cm accuracy. While we acknowledge that further work is necessary to achieve a higher accuracy needed for surgical navigation, the results presented in this study are proposed as the first step toward a validated computational framework that could be used for non-invasive localization not only of the DBS system but also for other types of medical implants.

AUTHOR CONTRIBUTIONS

GB conceived the project. MII, SRA, and GB designed the study, performed the numerical modeling, and analyzed the data. HCW acquired the data. LMA, HCW, and LM provided scientific feedback. MII wrote the manuscript. All authors reviewed the manuscript.

FUNDING

Preparation of this paper was supported by the grants National Institutes of Health, National Institute of Biomedical Imaging and Bioengineering; Grant number: R01EB024343. This work was supported in part by the Research Participation Program at the Center for Devices and Radiological Health (CDRH) administered by the Oak Ridge Institute for Science and Education through an interagency agreement between U.S. Department of Energy and the U.S. Food and Drug Administration (FDA).

ACKNOWLEDGMENTS

The authors would like to thank Nikos Makris (MGH), Emad Eskandar (MGH), John Gale (Emory University), Erwin B. Montgomery (Greenville Neuromodulation Center), Sheraz Khan (MGH), and A. Van der Kouwe (MGH) for their scientific input and support.

REFERENCES

Acar, Z. A., and Makeig, S. (2013). Effects of forward model errors on EEG source localization. *Brain Topogr.* 26, 378–396. doi: 10.1007/s10548-012-0274-6

Ahmadi, E., Katnani, H. A., Daftari Besheli, L., Gu, Q., Atefi, R., Villeneuve, M. Y., et al. (2016). An electrocorticography grid with conductive nanoparticles in a polymer thick film on an organic substrate improves CT and MR imaging. *Radiology* 280, 595–601. doi: 10.1148/radiol.2016142529

Allen, D. P., Stegemöller, E. L., Zadikoff, C., Rosenow, J. M., and MacKinnon, C. D. (2010). Suppression of deep brain stimulation artifacts from the electroencephalogram by frequency-domain Hampel filtering. *Clin. Neurophysiol.* 121, 1227–1232. doi: 10.1016/j.clinph.2010.02.156

Angelone, L., Ahveninen, J., Belliveau, J., and Bonmassar, G. (2010). Analysis of the role of lead resistivity in specific absorption rate for deep brain stimulator leads at 3 T MRI. *IEEE Trans. Med. Imaging* 29, 1029–1038. doi: 10.1109/TMI.2010.2040624

Astrom, M., Zrinzo, L. U., Tisch, S., Tripoliti, E., Hariz, M. I., and Wardell, K. (2009). Method for patient-specific finite element modeling and simulation of deep brain stimulation. *Med. Biol. Eng. Comput.* 47, 21–28. doi: 10.1007/s11517-008-0411-2

Atefi, S. R. (2015). *Electrical Bioimpedance Cerebral Monitoring: From Hypothesis and Simulation to First Experimental Evidence in Stroke Patients*. Doctoral dissertation, KTH Royal Institute of Technology, Stockholm.

Atefi, S. R., Seoane, F., Kamalian, S., Rosenthal, E. S., Lev, M. H., and Bonmassar, G. (2016). Intracranial hemorrhage alters scalp potential distribution in bioimpedance cerebral monitoring: preliminary results from FEM simulation on a realistic head model and human subjects. *Med. Phys.* 43, 675–686. doi: 10.1118/1.4939256

Barrett, J. F., and Keat, N. (2004). Artifacts in CT: recognition and avoidance. *Radiographies* 2, 1679–1691. doi: 10.1148/rg.246045065

Bhavaraju, N. C., Nagaraddi, V., Chetlapalli, S. R., and Osorio, I. (2002). Electrical and thermal behavior of non-ferrous noble metal electrodes exposed to MRI fields. *Magn. Reson. Imaging* 20, 351–357. doi: 10.1016/S0730-725X(02)00506-4

Bonmassar, G. (2016). Direct electromagnetic source tomographic imaging neurotechnology (DESTIN). *Int. J. Bioelectromagn.* 18, 79–98.

Brahimaj, B., Kochanski, R. B., and Sani, S. (2018). Microelectrode accuracy in deep brain stimulation surgery. *J. Clin. Neurosci.* 50, 58–61. doi: 10.1016/j.jocn.2018.01.020

Butson, C. R., Cooper, S. E., Henderson, J. M., and McIntyre, C. C. (2007). Patient-specific analysis of the volume of tissue activated during deep brain stimulation. *Neuroimage* 34, 661–670. doi: 10.1016/j.neuroimage.2006.09.034

Butson, C. R., Maks, C. B., and McIntyre, C. C. (2006). Sources and effects of electrode impedance during deep brain stimulation. *Clin. Neurophysiol.* 117, 447–454. doi: 10.1016/j.clinph.2005.10.007

Butson, C. R., and McIntyre, C. C. (2005). Tissue and electrode capacitance reduce neural activation volumes during deep brain stimulation.

Clin. Neurophysiol. 116, 2490–2500. doi: 10.1016/j.clinph.2005.06.023

Butson, C. R., and McIntyre, C. C. (2006). Role of electrode design on the volume of tissue activated during deep brain stimulation. *J. Neural Eng.* 3, 1–8. doi: 10.1088/1741-2560/3/1/001

Elwassif, M. M., Datta, A., Rahman, A., and Bikson, M. (2012). Temperature control at DBS electrodes using a heat sink: experimentally validated FEM model of DBS lead architecture. *J. Neural Eng.* 9:046009. doi: 10.1088/1741-2560/9/4/046009

Eusebio, A., Thevathasan, W., Doyle Gaynor, L., Pogosyan, A., Bye, E., Foltynie, T., et al. (2011). Deep brain stimulation can suppress pathological synchronisation in parkinsonian patients. *J. Neurol. Neurosurg. Psychiatry* 82, 569–573. doi: 10.1136/jnnp.2010.217489

Frysinger, R. C., Quigg, M., and Elias, W. J. (2006). Bipolar deep brain stimulation permits routine EKG, EEG, and polysomnography. *Neurology* 66, 268–270. doi: 10.1212/01.wnl.0000194272.79084.7e

Gabriel, C., Gabriel, S., and Corthout, E. (1996). The dielectric properties of biological tissues: III. Parametric models for the dielectric spectrum of tissues. *Phys. Med. Biol.* 41, 2271–2293. doi: 10.1088/0031-9155/41/11/003

Gabriels, L., Cosyns, P., Nuttin, B., Demeulemeester, H., and Gybels, J. (2003). Deep brain stimulation for treatment-refractory obsessive-compulsive disorder: psychopathological and neuropsychological outcome in three cases. *Acta Psychiatr. Scand.* 107, 275–282. doi: 10.1034/j.1600-0447.2003.00066.x

Gajsek, P., Walters, T. J., Hurt, W. D., Ziriax, J. M., Nelson, D. A., and Mason, P. A. (2002). Empirical validation of SAR values predicted by FDTD modeling. *Bioelectromagnetics* 23, 37–48. doi: 10.1002/bem.96

Gleason, C. A., Kaula, N. F., Hricak, H., Schmidt, R. A., and Tanagho, E. A. (1992). The effect of magnetic resonance imagers on implanted stimulators. *Pacing Clin. Electrophysiol.* 15, 81–94. doi: 10.1111/j.1540-8159.1992.tb02904.x

Grant, P. F., and Lowery, M. M. (2009). Electric field distribution in a finite-volume head model of deep brain stimulation. *Med. Eng. Phys.* 31, 1095–1103. doi: 10.1016/j.medengphy.2009.07.006

Grill, W. M. Jr. (1999). Modeling the effects of electric fields on nerve fibers: influence of tissue electrical properties. *IEEE Trans. Biomed. Eng.* 46, 918–928. doi: 10.1109/10.775401

Grill, W. M., and Mortimer, J. T. (1994). Electrical properties of implant encapsulation tissue. *Ann. Biomed. Eng.* 22, 23–33. doi: 10.1007/BF02368219

Hemm, S., Mennessier, G., Vayssiere, N., Cif, L., El Fertit, H., and Coubes, P. (2005). Deep brain stimulation in movement disorders: stereotactic coregistration of two-dimensional electrical field modeling and magnetic resonance imaging. *J. Neurosurg.* 103, 949–955. doi: 10.3171/jns.2005.103.6.0949

Henderson, J. M., Tkach, J., Phillips, M., Baker, K., Shellock, F. G., and Rezai, A. R. (2005). Permanent neurological deficit related to magnetic resonance imaging in a patient with implanted deep brain stimulation electrodes for Parkinson's disease: case report. *Neurosurgery* 57, E1063–E1063. doi: 10.1227/01.NEU.0000180810.16964.3E

Hodaie, M., Wennberg, R. A., Dostrovsky, J. O., and Lozano, A. M. (2002). Chronic anterior thalamus stimulation for intractable epilepsy. *Epilepsia* 43, 603–608. doi: 10.1046/j.1528-1157.2002.26001.x

Holsheimer, J., Dijkstra, E. A., Demeulemeester, H., and Nuttin, B. (2000). Chronaxie calculated from current-duration and voltage-duration data. *J. Neurosci. Methods* 97, 45–50. doi: 10.1016/S0165-0270(00)00163-1

Iacono, M. I., Makris, N., Mainardi, L., Angelone, L. M., and Bonmassar, G. (2013). MRI-based multiscale model for electromagnetic analysis in the human head with implanted DBS. *Comput. Math. Methods Med.* 2013:694171. doi: 10.1155/2013/694171

Iacono, M. I., Neufeld, E., Akinnagbe, E., Bower, K., Wolf, J., Vogiatzis Oikonomidis, I., et al. (2015). MIDA: a multimodal imaging-based detailed anatomical model of the human head and neck. *PLoS ONE* 10:e0124126. doi: 10.1371/journal.pone.0124126

Kleiner Fisman, G., Herzog, J., Fisman, D. N., Tamma, F., Lyons, K. E., Pahwa, R., et al. (2006). Subthalamic nucleus deep brain stimulation: summary and meta-analysis of outcomes. *Mov. Disord.* 21, S290–S304.

Kuncel, A. M., and Grill, W. M. (2004). Selection of stimulus parameters for deep brain stimulation. *Clin. Neurophysiol.* 115, 2431–2441. doi: 10.1016/j.clinph.2004.05.031

Makris, N., Angelone, L., Tulloch, S., Sorg, S., Kaiser, J., Kennedy, D., et al. (2008). MRI-based anatomical model of the human head for specific absorption rate mapping. *Med. Biol. Eng. Comput.* 46, 1239–1251. doi: 10.1007/s11517-008-0414-z

Maks, C. B., Butson, C. R., Walter, B. L., Vitek, J. L., and McIntyre, C. C. (2009). Deep brain stimulation activation volumes and their association with neurophysiological mapping and therapeutic outcomes. *J. Neurol. Neurosurg. Psychiatry* 80, 659–666. doi: 10.1136/jnnp.2007.126219

McIntyre, C. C., Grill, W. M., Sherman, D. L., and Thakor, N. V. (2004a). Cellular effects of deep brain stimulation: model-based analysis of activation and inhibition. *J. Neurophysiol.* 91, 1457–1469.

McIntyre, C. C., Mori, S., Sherman, D. L., Thakor, N. V., and Vitek, J. L. (2004b). Electric field and stimulating influence generated by deep brain stimulation of the subthalamic nucleus. *Clin. Neurophysiol.* 115, 589–595.

McIntyre, C. C., Miocinovic, S., and Butson, C. R. (2007). Computational analysis of deep brain stimulation. *Expert Rev. Med. Devices* 4, 615–622. doi: 10.1586/17434440.4.5.615

Miocinovic, S., Lempka, S. F., Russo, G. S., Maks, C. B., Butson, C. R., Sakaie, K. E., et al. (2009). Experimental and theoretical characterization of the voltage distribution generated by deep brain stimulation. *Exp. Neurol.* 216, 166–176. doi: 10.1016/j.expneurol.2008.11.024

Montgomery, E. B. Jr. (2010). *Deep Brain Stimulation Programming: Principles and Practice*. Oxford: Oxford University Press.

Moro, E., Esselink, R. J., Xie, J., Hommel, M., Benabid, A. L., and Pollak, P. (2002). The impact on Parkinson's disease of electrical parameter settings in STN stimulation. *Neurology* 59, 706–713. doi: 10.1212/WNL.59.5.706

O'Suilleabhain, P. E., Frawley, W., Giller, C., and Dewey, R. B. Jr. (2003). Tremor response to polarity, voltage, pulsewidth and frequency of thalamic stimulation. *Neurology* 60, 786–790. doi: 10.1212/01.WNL.0000044156.56643.74

Pascual-Marqui, R. D. (1999). Review of methods for solving the EEG inverse problem. *Int. J. Bioelectromagn.* 1, 75–86.

Pollo, C., Villemure, J. G., Vingerhoets, F., Ghika, J., Maeder, P., and Meuli, R. (2004). Magnetic resonance artifact induced by the electrode Activa 3389: an in vitro and in vivo study. *Acta Neurochir.* 146, 161–164. doi: 10.1007/s00701-003-0181-4

Railton, C. J., and Schneider, J. B. (1999). An analytical and numerical analysis of several locally conformal FDTD schemes. *IEEE Trans. Microw. Theory Tech.* 47, 56–66. doi: 10.1109/22.740077

Rezai, A. R., Finelli, D., Nyenhuis, J. A., Hrdlicka, G., Tkach, J., Sharan, A., et al. (2002). Neurostimulation systems for deep brain stimulation: in vitro evaluation of magnetic resonance imaging-related heating at 1.5T. *J. Magn. Reson. Imaging* 15, 241–250. doi: 10.1002/jmri.10069

Rezai, A. R., Finelli, D., Rugieri, P., Tkach, J., Nyenhuis, J. A., and Shellock, F. G. (2001). Neurostimulators: potential for excessive heating of deep brain stimulation electrodes during magnetic resonance image. *J. Magn. Reson. Imaging* 14, 488–489. doi: 10.1002/jmri.1212

Rezai, A. R., Phillips, M., Baker, K. B., Sharan, A. D., Nyenhuis, J., Tkach, J., et al. (2004). Neurostimulation system used for deep brain stimulation (DBS): MR safety and implications of failing to follow safety recommendations. *Invest. Radiol.* 39, 300–303. doi: 10.1097/01.rli.0000124940.02340.ab

Rosin, B., Slovik, M., Mitelman, R., Rivlin-Etzion, M., Haber, S. N., Israel, Z., et al. (2011). Closed-loop deep brain stimulation is superior in ameliorating parkinsonism. *Neuron* 72, 370–384. doi: 10.1016/j.neuron.2011.08.023

Tadel, F., Baillet, S., Mosher, J. C., Pantazis, D., and Leahy, R. M. (2011). Brainstorm: a user-friendly application for MEG/EEG analysis. *Comput. Intell. Neurosci.* 2011:879716. doi: 10.1155/2011/879716

Vasques, X., Cif, L., Hess, O., Gavarini, S., Mennessier, G., and Coubes, P. (2009). Stereotactic model of the electrical distribution within the internal globus pallidus during deep brain stimulation. *J. Comput. Neurosci.* 26, 109–118. doi: 10.1007/s10827-008-0101-y

Vercueil, L., Pollak, P., Fraix, V., Caputo, E., Moro, E., Benazzouz, A., et al. (2001). Deep brain stimulation in the treatment of severe dystonia. *J. Neurol.* 248, 695–700. doi: 10.1007/s004150170116

Volkmann, J., Moro, E., and Pahwa, R. (2006). Basic algorithms for the programming of deep brain stimulation in Parkinson's disease. *Mov. Disord.* 14, S284–S289. doi: 10.1002/mds.20961

Walker, H. C., Huang, H., Gonzalez, C. L., Bryant, J. E., Killen, J., Cutter, G. R., et al. (2012a). Short latency activation of cortex during clinically effective subthalamic deep brain stimulation for Parkinson's disease. *Mov. Disord.* 27, 864–873. doi: 10.1002/mds.25025

Walker, H. C., Huang, H., Gonzalez, C. L., Bryant, J. E., Killen, J., and Knowlton, R. C. (2012b). Short latency activation of cortex by clinically effective thalamic brain stimulation for tremor. *Mov. Disord.* 27, 1404–1412. doi: 10.1002/mds.25137

Yamazaki, M., Tucker, D. M., Terrill, M., Fujimoto, A., and Yamamoto, T. (2013). Dense array EEG source estimation in neocortical epilepsy. *Front. Neurol.* 4:42. doi: 10.3389/fneur.2013.00042

Yousif, N., Bayford, R., Bain, P. G., and Liu, X. (2007). The peri-electrode space is a significant element of the electrode-brain interface in deep brain stimulation: a computational study. *Brain Res. Bull.* 74, 361–368. doi: 10.1016/j.brainresbull.2007.07.007

Yousif, N., and Liu, X. (2007). Modeling the current distribution across the depth electrode-brain interface in deep brain stimulation. *Expert Rev. Med. Devices* 4, 623–631. doi: 10.1586/17434440.4.5.623

Yousif, N., and Liu, X. (2009). Investigating the depth electrode-brain interface in deep brain stimulation using finite element models with graded complexity in structure and solution. *J. Neurosci. Methods* 184, 142–151. doi: 10.1016/j.jneumeth.2009.07.005

Disclaimer: The mention of commercial products, their sources, or their use in connection with material reported herein is not to be construed as either an actual or implied endorsement of such products by the Department of Health and Human Services.

Conflict of Interest Statement: HCW receives funding for fellowship training from Medtronic. HCW also serves as a consultant for Medtronic and Boston Scientific.

The remaining authors declare that the research was conducted in the absence of any commercial or financial relationships that could be construed as a potential conflict of interest.

The handling Editor is currently co-organizing a Research Topic with one of the authors LMA, and confirms the absence of any other collaboration.

frontiers in Medicine

PERSPECTIVE
published: 26 March 2019
doi: 10.3389/fmed.2019.00056

Improving the Quality of Life of Patients With Medical Devices by a Timely Analysis of Adverse Events

Urs P. Wyss[1,2]*

[1] Department of Mechanical Engineering, University of Manitoba, Winnipeg, MB, Canada, [2] Department of Mechanical Engineering, Queen's University, Kingston, ON, Canada

Implanted and non-implanted medical devices, including artificial joints, are widely accepted to improve the quality of life of patients. While implant survival rates of over 80% can be accepted for artificial joints, there is still a large need to achieve higher survival rates at 15 years or longer to reduce the need for revisions due to implant failure before the end of the patient's life. Therefore, artificial joints are constantly improved with design changes and new designs, including modified or new materials. Most of these improvements perform as expected, but there are still cases where previously unknown failures occur, requiring premature revisions. A few examples of such unsuccessful improvements in the last 20 years are mentioned in this technical case report. The main focus of this paper is on an acetabular cup that was recalled due to unexpected revisions after a few weeks to a few months *in vivo*. The main reason for the revisions were small amounts of an oily residue containing endotoxins trapped inside the porous coating applied to the cup to facilitate bone ingrowth. The cup was recalled within 4 months after the company become aware of the problem, and prior to knowing exactly why the cups were failing early. The root cause analysis took several more months to complete. The lessons learned during the analysis are discussed so that similar events in other implantable medical devices can be avoided. The acetabular cup case aims to highlight that a timely root cause analysis, triggered by very few unexplained revisions, will benefit patients and improve the quality of life.

Keywords: medical devices, implants, adverse events, root cause analysis, joint replacements

OPEN ACCESS

Edited by:
Melissa Knothe Tate,
University of New South Wales,
Australia

Reviewed by:
Peter Felix Niederer,
ETH Zürich, Switzerland
Marian Klinger,
Opole University, Poland

***Correspondence:**
Urs P. Wyss
urs.wyss@queensu.ca

Specialty section:
This article was submitted to
Translational Medicine,
a section of the journal
Frontiers in Medicine

Received: 23 November 2018
Accepted: 05 March 2019
Published: 26 March 2019

Citation:
Wyss UP (2019) Improving the Quality of Life of Patients With Medical Devices by a Timely Analysis of Adverse Events. Front. Med. 6:56.
doi: 10.3389/fmed.2019.00056

INTRODUCTION

Implanted and non-implanted medical devices such as pacemakers, artificial joints, fracture fixation devices, dental implants, catheters, syringes, artificial limbs, braces, wheelchairs, *etc.*, have become widely accepted to improve the quality of life for patients. These devices perform very well, depending on the application, for hours, days, months, or many years.

The focus of this paper is on artificial joints, where patient survival rates of 80% or higher after 15 years of use can be expected. An 80% implant survival rate means that up to 20% of today's implants must be replaced after <15 years of use, and implant revisions (replacement of the original, so-called primary implant) are often not as functional as primary implants. Therefore, a great need exists for survival rates much higher than 80% and for artificial joints that last twenty, 30 or more years, so that no revision is required before the end of the patient's life. While some revisions are necessary for reasons that are not related to the implant *per se*, those that are caused by the implant must be reduced.

Artificial joints have continuously been improved by more realistic modeling and simulation work, and improved *in vitro* testing. Pre-operative techniques are based on the understanding of the anatomy and physiology of normal and pathological structures that the artificial joints are replacing, and how these structures are being modified under the influence of the implant. Earlier analysis and understanding of adverse events has significantly contributed to the improvement of pre-operative evaluation methods. Often it would take months or even years, before adverse events leading to premature revisions were understood well enough to develop better modeling and simulation work, and more accurate *in vitro* testing protocols. The time it takes to fully understand adverse events means that tens of thousands of artificial joints that put patients at a higher risk for revision than necessary are still implanted.

Recent adverse events with artificial joints will be briefly described. The recall of the Inter-Op cup in December 2000 will be described in more detail. Legal issues were the main reason why not much was published about that event. The lessons learned from the Inter-Op cup event are still not well-known today, and the possibility of similar problems occurring with other artificial joints cannot be excluded.

RECENT ADVERSE EVENTS

The DePuy ASR artificial metal-on-metal hip joint (Articular Surface Replacement) was sold since 2005 to more than 90,000 persons worldwide, and the device was voluntarily recalled by the company in August of 2010 (1, 2). There were reports of higher than normal revision rates for over 1 year before the recall. The reasons for the higher than normal revisions were not obvious, but it appeared that they were related to the metal-on-metal articulation of the device. The multi-billion dollar settlements with the patients after the recall were costly for the company, but the real cost was to the patients who required a premature revision with all the associated risks of an additional surgical intervention. An earlier recognition of the cause could have saved thousands of patients from suffering from a potentially faulty implant.

Another recent adverse event was the Zimmer Durom hip replacement where the cementless acetabular cup did not grow in properly in all cases, and eventually came loose, requiring revision surgery (3). There have also been reports of a higher ion release with the large diameter Durom hip (LDH). The company took the device from the market in 2012 and offered to settle outstanding lawsuits.

It has been known since at least 1992 (4) that corrosion can occur in modular hip implants, in particular between the implant head and the neck. The corrosion was noticed at revision surgery, but it was not believed to be a major concern. More corrosion in a larger number of revised implants was observed in larger heads that were introduced by several manufacturers since 2000. Higher corrosion at the head-neck taper connection appears to lead to an adverse tissue reaction due to the released corrosion substances. Several factors, such as material properties, surface structure, tolerances, the toggling moment, and others are responsible for the problems (5, 6). Much has been learned about head-neck corrosion in the meantime by a detailed retrieval analysis, simulation and modeling work, as well as *in vitro* tests. Nevertheless, there is still a need for better understanding why the corrosion occurs, and how it can be prevented, to eliminate corrosion at modular connections as a problem requiring revisions.

In addition to adverse events related to hip implants, other recent adverse issues also occurred with e.g., the Zimmer Persona trabecular metal tibia plate that was voluntarily recalled in 2015 (7). The reason was an increase in complaints of radiolucent lines and loosening. Another recent recall was the Zimmer Biomet Comprehensive Reverse Shoulder (8).

It is important to remember that the majority of artificial joints and other implants function well and remain in the body for a very long time. Frequent technical and/or manufacturing modifications and new implant designs aim to improve function and longevity. Some, however, do not work as expected and require early revision surgery, while others must be recalled and taken off the market immediately. Therefore, it is crucial to detect and understand adverse events as early as possible, so that as few as possible additional devices are implanted. Understanding adverse events in a timely manner will aid in the development of better modeling and simulation work and more realistic *in vitro* testing, ultimately improving *in vivo* success and patient outcomes.

INTER-OP RECALL ON DECEMBER 5, 2000

The Inter-op cup

The Inter-Op cup was manufactured by Sulzer Orthopedics, Inc. in Austin, Texas. The Ti-alloy cup was hemispherical and coated with cancellous-structured Titanium (CSTi) on the bone side, allowing for bone ingrowth. The bone was reamed slightly smaller than the cup, so that a press-fit seating for primary fixation could be achieved during surgery. Screws could be used for additional initial primary fixation. The inside of the cup allowed for the insertion of a metal-on-metal or polyethylene articulation.

Disclaimer

The description of the Inter-Op cup recall, how it happened and what was learned, is based solely on the knowledge of the author, who was Vice President of Research at Sulzer Orthopedics when it happened, and who coordinated the internal company investigation that followed the recall. The author feels strongly that the company dealt with this adverse event in a very timely manner, making the voluntary recall only a few months after it first became aware of a potentially higher failure rate of this particular cup. Of course, in hindsight, it is easy to argue that an even earlier recall would have saved many patients from receiving a faulty device.

Investigations Before the Recall

In the summer of 2000, the product manager of the Inter-Op acetabular cup was informed by a surgeon from Los Angeles that a few unexpected early revisions had to be made in hip implants with a metal-on-metal articulation. The patients complained within weeks after surgery about pain. Some patients already showed reddening and swelling near the hip joint, which appeared to be a localized inflammatory reaction near the implant, and no positive bacterial culture could be detected. The surgeon was aware that in Europe between ten and twenty metal-on-metal articulation revisions were made, and that there was concern the metal-on-metal articulation was responsible. This was one reason why he contacted the company soon after he had to perform the first few unexpected revisions. As soon as the president of the company was made aware of higher than expected revisions, a task force consisting of project management, development, research, clinical studies, manufacturing, biology and legal was formed. The surgeon who made the company aware of the adverse events sent the retrieved cups to Dr. Pat Campbell, an international retrieval analysis specialist, for neutral analysis (**Figure 1**). Within a few weeks it was possible to rule out tolerance issues in the cup and/or the instruments as the possible cause of the problems, either on the articulation side and on the bone side. Adverse reactions due to the metal-on-metal articulation, first thought to be a possible cause, could be ruled out as a number of the same cups with a polyethylene articulation also had to be revised due to similar symptoms.

The time between the end of September and the recall on December 5, 2000 was very difficult, as the number of revisions started to increase and the company was at a loss about what was causing the problems. Recalling the Inter-Op cup, with all the consequences that a recall triggers, was discussed as the right thing to do, however, recalling an otherwise successful device without understanding the root cause of the problem would have been problematic. In November of 2000 extraction studies looking at residues on some off-the-shelf stored cups showed small amounts of oily residue. The oily residue of a few milligrams was trapped in the CSTi surface that has about 50% porosity. Dr. Campbell (retrieval analysis specialist) and Dr. Mirra (pathologist) from Los Angeles, who received many of the revised cups, suggested to the company that a biological problem was the most likely cause for the adverse reaction leading to pain and early revision. The absence of finding any other possible causes, and the fact that the revisions started to increase, led the company to make a voluntary recall of the Inter-Op cup on December 5, 2000. The reason for the recall was communicated as unacceptable levels of oily residues. Of the 25,000 cups that were recalled 17,000 were already implanted.

FIGURE 1 | Revised Inter-Op cup after 11 months *in vivo* showing no bone ingrowth and a few areas with a red and gray gel-like residue.

Investigations After the Recall

Oily Residue in Porous CSTi Structure

The analysis of the residue was continued after the recall, on hundreds of not yet implanted cups in the company laboratory, and in two independent laboratories. The data was put into groups based on lot number and manufacturing and cleaning processes. The lot numbers of the revised devices were compared with the data from the off-the-shelf devices. This resulted in the following observations:

- Oily residue levels between a few mg and occasionally as high as 50 mg were found in manufacturing lots going back to 1997
- Most revisions were in one manufacturing group, where nitric acid passivation had been eliminated, as it was determined that nitric passivation did not enhance the existing self-passivation of Ti-alloy
- There were fewer revisions in cups manufactured within the first few weeks after the summer holiday shut down of manufacturing

The source of the oily residue was in the machine used to finish the parts after porous coating (**Figure 2**). The CSTi porous coating requires very high temperatures under vacuum to eliminate all non-metallic residues. Ideally, machining should not be necessary after porous coating in order to avoid contamination of the porous bone ingrowth structure. Oily residue can be cleaned from smooth surfaces during the final cleaning process, but it is not possible to completely clean a porous structure once it has been contaminated. The cooling fluid used during machining can contain small amounts of oil from the way bed of the machine, as well as the machine's gearbox and hydraulics. All manufacturing groups of the Inter-Op cup required some machining after porous coating, leaving various amounts of oily residue in the porous structure, even after the final cleaning process (9).

Very few revisions were observed in the groups where nitric acid passivation was applied after porous coating, as the nitric acid largely eliminated the oily residue within the porous structure. The holiday shut down was used to clean all machines and was also the time the cooling fluid was replaced. This meant that after the holiday break, the cooling fluid used contained very little oily residue. The different oily residues were identified and assessed for toxicity. Very small amounts of toxic additives could be detected, but in such small amounts that it could not explain the adverse tissue reaction observed in the retrieved devices. The pathologist Dr. Mirra from Los Angeles also did not feel that the oily residue alone could explain the inflammatory response requiring a revision of the cup. Endotoxins, sterile residues from

FIGURE 2 | Coolant applied during machining finishing of the cup after porous coating.

bacteria, were already considered before the recall as a possible cause for the adverse tissue reaction. Endotoxin tests on finished off-the-shelf cups, however, were all negative.

Endotoxins

Endotoxins are a toxin associated with the outer membranes of certain gram-negative bacteria. They are released upon disruption of intact bacteria (death, cell lysis). Their presence in the blood stream may cause septic reactions, and high concentrations can, amongst other reactions, lead to very serious intravascular coagulation or blood clotting (10). Therefore, standards exist for testing of cardiovascular medical devices, which dictate acceptable lower limits of endotoxins. Tests for endotoxins use the limulus amoebocyte lysate (LAL), which tests the fluid extract after immersing the medical device in the water, usually using ultrasonic cleaners. No standards or acceptable limits exist for endotoxin tests for orthopedic devices. Nevertheless, the Inter-Op cups were tested before and after the recall for endotoxins, but none could be detected.

An oily residue within the CSTi porous coating was given as the cause for the adverse tissue reactions in patients requiring cup revisions at the time of the recall. Only in the months after the recall was it possible to investigate the oily residue further, in order to understand the failure mechanism. It was already known by the assessment of Drs. Mirra and Campbell that the failure was likely be caused by an inflammatory process.

Coolant fluid was tested for endotoxins from a number of tool machines used for machining after porous coating. Various levels of live and dead bacteria (endotoxins) were found, depending on how much time had elapsed since the last coolant replacement. Several dozens of different bacteria were found when the air and many surfaces in the plant were tested. This explains how the bacteria were able to get into the coolant of the tool machines.

The coolant is a water-based, warm solution, *i.e.,* an ideal environment for bacteria growth. These bacteria also mixed with the oil, leading to an endotoxin-loaded oily residue left in the porous coating of the cup. The subsequent washing was unable to remove all residues from the porous structure. The sterilization process took care of the live bacteria, but did nothing to the endotoxins. No endotoxin could be detected with the LAL test, as no oily residue could be extracted during the ultrasonic cleaning. Once the cup was implanted, it appears that when the body fluid came into contact with the endotoxin contaminated oily residue in the cup, it started an inflammatory reaction, preventing the bone from growing into the CSTi porous structure. This led to the loosening of the cup within a few weeks to a few months.

About a third of the 17,000 patients that had received an Inter-Op cup required a revision. Not all cups had the same amount of oily residue and endotoxins. This explains why fewer revisions were observed after the coolant replacement during the summer holiday shut down. Furthermore, some patients might have already had antibodies against some of the bacteria, leading to a lower or no inflammatory reaction. It was also learned during the investigation of the root cause that mineral oil acts as an adjuvant when mixed with endotoxin leading to a much stronger inflammatory response than endotoxin alone.

Vitality of Bone After Revision

The annual meeting of the American Academy of Orthopedic Surgeons took place, almost 3 months after the recall, in February of 2001. A few hundred revisions had already been made at that time, and the surgeons were wondering how deep into the bone the adverse tissue reaction had spread. Therefore, a tetracycline double labeling bone study was initiated in January of 2001 (11). Patients scheduled for revision surgery that had consented to the study were injected with tetracycline 2 weeks before surgery, and a second time again immediately before surgery. A thin layer of bone was removed after the cup had been taken out until fresh bleeding bone appeared. The bone chips were then analyzed for chips showing two bands, indicating that the bone was alive and growing (**Figure 3**). The results showed that only a thin layer of bone below the contaminated cup was compromised, and it was possible to ream it out without problems. This was very important for surgeons, who were faced with having to revise patients who developed pain and implant loosening due to the affected cup. The author, an engineer, was not aware that the revisions were abnormally difficult.

Lessons Learned

The recall of the Inter-Op cup was an adverse event that took about 4 months from first reports about problems to the voluntary recall of the cup. While this was, in the opinion of the author, a timely process, one might question why the company did not act even earlier, preventing many patients from receiving a faulty device. Much was learned during the analysis of the root

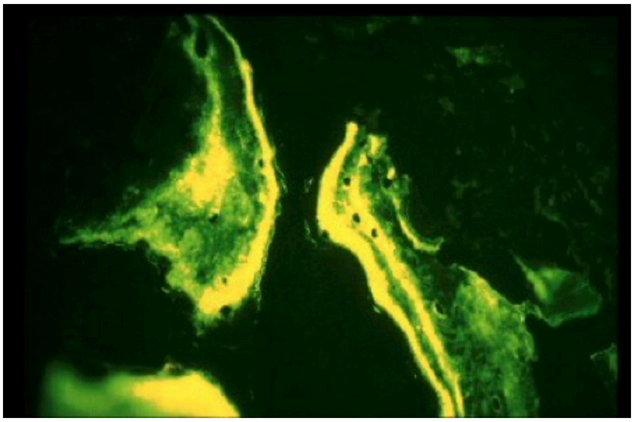

FIGURE 3 | Tetracycline labeled bone chips showing the dual band of live bone.

cause of the problem, but it could not be published for legal reasons. Here are a few of the lessons learned:

- It was important to recall the product once it appeared obvious that the Inter-Op cup was the reason for the majority of the premature revisions, even without fully understanding the failure mechanism
- It was crucial to send the retrieved cups to a specialized laboratory for independent analysis. This gave the surgeons confidence, as some did not trust the company to be completely open about the findings
- The adverse reactions endotoxins can cause when they get into porous structures of implantable medical devices is much better understood as a result of the implant failure and subsequent root cause analysis.

  Recommendation:

  - Any possibility of endotoxin contamination of rough or porous coating must be avoided, as it is extremely difficult to remove endotoxins from such surfaces. Endotoxins can enter porous surfaces during machining, through final cleaning in the case that the industrial water contains endotoxins, or through the air if the otherwise finished implants are not handled in a sterile environment before packaging
  - The industrial water upgraded from regular city water must be routinely tested for endotoxins

- Small changes in the manufacturing process should not be underestimated, and a thorough risk analysis is very important when any changes are made
- Relying on existing standards and tests is not sufficient, as with every change or potential improvement, previously unknown adverse events can occur. Standards and published *in vitro* tests are typically years behind the current knowledge, as it takes time to incorporate new knowledge into a standardized test.
- It is crucial to review the literature thoroughly about any aspect that could lead to an adverse event of a medical device. An article by Hollingsworth and Atkins published in (12) describes a synovial inflammatory response to bacterial endotoxin. The company was not aware of this article; knowledge of the article might have helped to understand the failure mechanism at an earlier time point.
- It is essential to take one or only a few adverse events with a medical device seriously and quickly analyze the cause of the problem. In many cases, there might not be a problem with the device, but missing a problem can put many patients unnecessarily at risk for a premature revision. If there appears to be a problem with the device, action should start without delay.

CONCLUSIONS

It is important to remember that hundreds of thousands of patients experience a long lasting improvement in their quality of life after joint replacement. Nevertheless, there are routinely changes in existing and new devices to further improve the survival rate of artificial joints. Every change, however, bears the risk of unexpected consequences, which is why it is so important to perform excellent clinical studies, and to do a timely analysis of even the smallest number of adverse events. The Inter-Op example shows how important it was to quickly start the analysis of only a few initial unexpected revisions. The recall with all the severe consequences for the company, and more importantly the patients, was made only months after first hearing about problems with the cup. Of course it can always be argued that the recall should have been made earlier. The root cause analysis involved assessing a large number of retrieved and off-the-shelf devices. It showed the potential problems with endotoxins, especially on rough or porous surfaces. Once there endotoxins can hardly be detected or removed. Doing everything possible to prevent endotoxins from attaching themselves to such surfaces is crucial. It would be useful if companies would be required to publish what was learned in the root cause analysis of every recall, as other companies would be prevented from marketing devices with similar problems. Ultimately, patients would benefit from getting fewer faulty artificial joints.

DATA AVAILABILITY

All datasets generated for this study are included in the manuscript and/or the supplementary files.

ETHICS STATEMENT

The article is a commentary on an adverse event scenario and associated root cause analysis in real human patients, i.e., not as part of a clinical or other study. No identifying information is included in the manuscript.

AUTHOR CONTRIBUTIONS

The author confirms being the sole contributor of this work and has approved it for publication.

REFERENCES

1. Tibrewal S, Sabah S, Henckel J, Hart A. The effect of a manufacturer recall on the threshold to revise a metal-on-metal hip. *Int Orthop.* (2014) 38:2017–20. doi: 10.1007/s00264-014-2369-z
2. Maurer-Ertl W, Friesenbichler J, Holzer LA, Leitner L, Ogris K, Maier M, et al. Recall of the ASR XL head and hip resurfacing systems. *Orthopaedics*. (2017) 40:e340–7. doi: 10.3928/01477447-20161213-04
3. Naal FD, Pilz R, Munzinger U, Hersche O, Leunig M. High revision rate at 5 years after hip resurfacing with the durom implant. *Clin Orthop Relat Res.* (2011) 469:2598–604. doi: 10.1007/s11999-011-1792-3
4. Collier JP, Surprenant VA, Jensen RE, Mayor MB, Surprenant HP. Corrosion between the components of modular femoral hip prostheses. *J Bone Joint Surg Br*. (1992). 74B:511–17.
5. Dyrkacz RMR, Brandt JM, Ojo OA, Turgeon TR, Wyss UP. The influence of head size on corrosion and fretting behaviour at the head-neck interface of artificial hip joints. *J Arthroplasty.* (2013) 28:1036–40. doi: 10.1016/j.arth.2012.10.017
6. Dyrkacz RMR, O'Brien ST, Brandt JM, Morrison JB, Brien STO, Ojo OA, et al. Finite element analysis at the head-neck taper interface of modular hip prostheses. *Tribol Int*. (2015) 91:206–13. doi: 10.1016/j.triboint.2015.01.016
7. FDA Announces a Class II Recall of Zimmer Inc.'s Persona[R] Trabecular Metal$^{\mathrm{TM}}$ Tibial Plate, according to Seeger Weiss LLP. *Pharma Business Week*, 41 (2015).
8. *Zimmer Biomet Recalls Comprehensive Reverse Shoulder Due to a High Fracture Rate*. Rockaway, NJ: Medical Design Technology (2017).
9. Deluzio KJ, Spiegelberg SH, Muratoglu OK. *The Affected Lot Range and the Residual Mass Data for the Inter-Op Shell*. Halifax, NS; Somerville, MA; Boston, MA: School of Biomedical Engineering, Dalhousie University, Cambridge Polymer Group, Massachusetts General Hospital (2000).
10. Bonsignore LA, Anderson JA, Lee Z, Goldberg VM, Greenfield EM. Adherent lipopolysaccharide inhibits the osseointegration of orthopedic implants by impairing osteoblast differentiation. *Bone.* (2013) 52:93–101. doi: 10.1016/j.bone.2012.09.011
11. Bloebaum RD, Ferguson RP, Neff CM, Van Gorp C, Woolley DL, Hofmann AA. Bone viability determination in human cancellous bone from patients undergoing revision hip arthroplasty. *J Arthroplasty* 19:745–50.
12. Hollingsworth JW, Atkins E. Synovial inflammatory response to bacterial endotoxins. *Yale J Biol Med*. (1965) 38:242–56.

Conflict of Interest Statement: UW was Vice President of Research at Sulzer Orthopedics during the recall and root cause analysis events described in the manuscript.

METHODS
published: 27 March 2019
doi: 10.3389/fphys.2019.00203

Meta-Analytic Methodology for Basic Research: A Practical Guide

Nicholas Mikolajewicz[1,2] *and Svetlana V. Komarova*[1,2*]

[1] *Faculty of Dentistry, McGill University, Montreal, QC, Canada,* [2] *Shriners Hospital for Children-Canada, Montreal, QC, Canada*

Basic life science literature is rich with information, however methodically quantitative attempts to organize this information are rare. Unlike clinical research, where consolidation efforts are facilitated by systematic review and meta-analysis, the basic sciences seldom use such rigorous quantitative methods. The goal of this study is to present a brief theoretical foundation, computational resources and workflow outline along with a working example for performing systematic or rapid reviews of basic research followed by meta-analysis. Conventional meta-analytic techniques are extended to accommodate methods and practices found in basic research. Emphasis is placed on handling heterogeneity that is inherently prevalent in studies that use diverse experimental designs and models. We introduce *MetaLab*, a meta-analytic toolbox developed in MATLAB R2016b which implements the methods described in this methodology and is provided for researchers and statisticians at Git repository (https://github.com/NMikolajewicz/MetaLab). Through the course of the manuscript, a rapid review of intracellular ATP concentrations in osteoblasts is used as an example to demonstrate workflow, intermediate and final outcomes of basic research meta-analyses. In addition, the features pertaining to larger datasets are illustrated with a systematic review of mechanically-stimulated ATP release kinetics in mammalian cells. We discuss the criteria required to ensure outcome validity, as well as exploratory methods to identify influential experimental and biological factors. Thus, meta-analyses provide informed estimates for biological outcomes and the range of their variability, which are critical for the hypothesis generation and evidence-driven design of translational studies, as well as development of computational models.

Keywords: meta-analysis, basic research, rapid review, systematic review, MATLAB, methodology

INTRODUCTION

Evidence-based medical practice aims to consolidate best research evidence with clinical and patient expertise. Systematic reviews and meta-analyses are essential tools for synthesizing evidence needed to inform clinical decision making and policy. Systematic reviews summarize available literature using specific search parameters followed by critical appraisal and logical synthesis of multiple primary studies (Gopalakrishnan and Ganeshkumar, 2013). Meta-analysis refers to the statistical analysis of the data from independent primary studies focused on the same question, which aims to generate a quantitative estimate of the studied phenomenon, for example, the effectiveness of the intervention (Gopalakrishnan and Ganeshkumar, 2013). In clinical research,

Edited by:
Christopher Basciano,
Becton Dickinson, United States

Reviewed by:
Tomas Drgon,
United States Food and Drug Administration, United States
Ulf Knothe,
TissuTex Pty Ltd., Wentworth Falls, NSW, Australia

****Correspondence:***
Svetlana V. Komarova
svetlana.komarova@mcgill.ca

Specialty section:
This article was submitted to Computational Physiology and Medicine,
a section of the journal Frontiers in Physiology

Received: *22 December 2017*
Accepted: *15 February 2019*
Published: *27 March 2019*

Citation:
Mikolajewicz N and Komarova SV (2019) Meta-Analytic Methodology for Basic Research: A Practical Guide. Front. Physiol. 10:203. doi: 10.3389/fphys.2019.00203

systematic reviews and meta-analyses are a critical part of evidence-based medicine. However, in basic science, attempts to evaluate prior literature in such rigorous and quantitative manner are rare, and narrative reviews are prevalent. The goal of this manuscript is to provide a brief theoretical foundation, computational resources and workflow outline for performing a systematic or rapid review followed by a meta-analysis of basic research studies.

Meta-analyses can be a challenging undertaking, requiring tedious screening and statistical understanding. There are several guides available that outline how to undertake a meta-analysis in clinical research (Higgins and Green, 2011). Software packages supporting clinical meta-analyses include the Excel plugins MetaXL (Barendregt and Doi, 2009) and Mix 2.0 (Bax, 2016), Revman (Cochrane Collaboration, 2011), Comprehensive Meta-Analysis Software [CMA (Borenstein et al., 2005)], JASP (JASP Team, 2018) and MetaFOR library for R (Viechtbauer, 2010). While these packages can be adapted to basic science projects, difficulties may arise due to specific features of basic science studies, such as large and complex datasets and heterogeneity in experimental methodology. To address these limitations, we developed a software package aimed to facilitate meta-analyses of basic research, *MetaLab* in MATLAB R2016b, with an intuitive graphical interface that permits users with limited statistical and coding background to proceed with a meta-analytic project. We organized *MetaLab* into six modules (**Figure 1**), each focused on different stages of the meta-analytic process, including graphical-data extraction, model parameter estimation, quantification and exploration of heterogeneity, data-synthesis, and meta-regression.

In the present manuscript, we describe each step of the meta-analytic process with emphasis on specific considerations made when conducting a review of basic research. The complete workflow of parameter estimation using *MetaLab* is demonstrated for evaluation of intracellular ATP content in osteoblasts (OB $[ATP]_{ic}$ dataset) based on a rapid literature review. In addition, the features pertaining to larger datasets are explored with the ATP release kinetics from mechanically-stimulated mammalian cells (ATP release dataset) obtained as a result of a systematic review in our prior work (Mikolajewicz et al., 2018).

MetaLab can be freely accessed at Git repository (https://github.com/NMikolajewicz/MetaLab), and a detailed documentation of how to use MetaLab together with a working example is available in the **Supporting materials**.

VALIDITY OF EVIDENCE IN THE BASIC SCIENCES

To evaluate the translational potential of basic research, the validity of evidence must first be assessed, usually by examining the approach taken to collect and evaluate the data. Studies in the basic sciences are broadly grouped as hypothesis-generating and hypothesis-driven. The former tend to be small-sampled proof-of-principle studies and are typically exploratory and less valid than the latter. An argument can even be made that studies that report novel findings fall into this group as well, since their findings remain subject to external validation prior to being accepted by the broader scientific community. Alternatively, hypothesis-driven studies build upon what is known or strongly suggested by earlier work. These studies can also validate prior experimental findings with incremental contributions. Although such studies are often overlooked and even dismissed due to a lack of substantial novelty, their role in external validation of prior work is critical for establishing the translational potential of findings.

Another dimension to the validity of evidence in the basic sciences is the selection of experimental model. The human condition is near-impossible to recapitulate in a laboratory setting, therefore experimental models (e.g., cell lines, primary cells, animal models) are used to mimic the phenomenon of interest, albeit imperfectly. For these reasons, the best quality evidence comes from evaluating the performance of several independent experimental models. This is accomplished through systematic approaches that consolidate evidence from multiple studies, thereby filtering the signal from the noise and allowing for side-by-side comparison. While systematic reviews can be conducted to accomplish a qualitative comparison, meta-analytic approaches employ statistical methods which enable hypothesis generation and testing. When a meta-analysis in the basic sciences is hypothesis-driven, it can be used to evaluate the translational potential of a given outcome and provide recommendations for subsequent translational- and clinical-studies. Alternatively, if meta-analytic hypothesis testing is inconclusive, or exploratory analyses are conducted to examine sources of inconsistency between studies, novel hypotheses can be generated, and subsequently tested experimentally. **Figure 2** summarizes this proposed framework.

STEPS IN QUANTITATIVE LITERATURE REVIEW

All meta-analytic efforts prescribe to a similar workflow, outlined as follows:

1) **Formulate research question**
    - Define primary and secondary objectives
    - Determine breadth of question
2) **Identify relevant literature**
    - Construct search strategy: rapid or systematic search
    - Screen studies and determine eligibility
3) **Extract and consolidate study-level data**
    - Extract data from relevant studies
    - Collect relevant study-level characteristics and experimental covariates
    - Evaluate quality of studies
    - Estimate model parameters for complex relationships (optional)
4) **Data appraisal and preparation**
    - Compute appropriate outcome measure

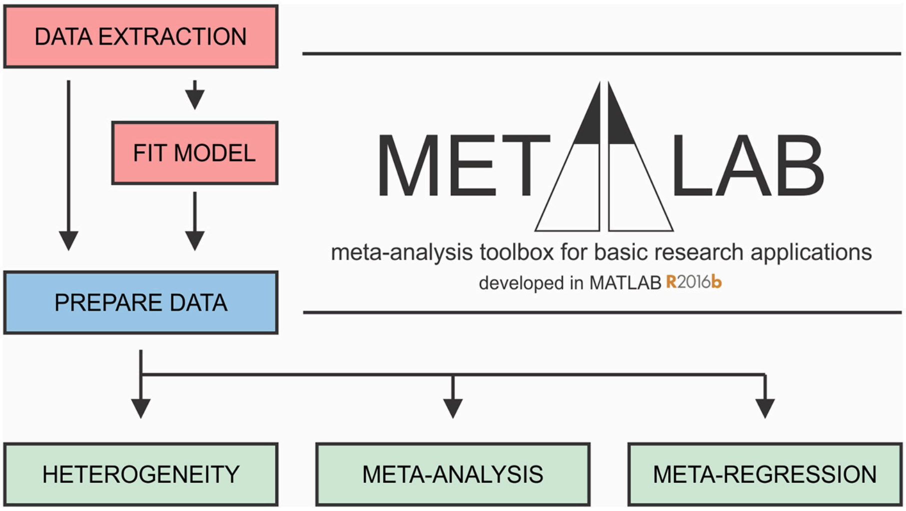

FIGURE 1 | General framework of *MetaLab*. The *Data Extraction* module assists with graphical data extraction from study figures. *Fit Model* module applies Monte-Carlo error propagation approach to fit complex datasets to model of interest. Prior to further analysis, reviewers have opportunity to manually curate and consolidate data from all sources. *Prepare Data* module imports datasets from a spreadsheet into MATLAB in a standardized format. *Heterogeneity*, *Meta-analysis* and *Meta-regression* modules facilitate meta-analytic synthesis of data.

- Evaluate extent of between-study inconsistency (heterogeneity)
- Perform relevant data transformations
- Select meta-analytic model

5) **Synthesize study-level data into summary measure**
   - Pool data and calculate summary measure and confidence interval

6) **Exploratory analyses**
   - Explore potential sources of heterogeneity (ex. biological or experimental)
   - Subgroup and meta-regression analyses

7) **Knowledge synthesis**
   - Interpret findings
   - Provide recommendations for future work

META-ANALYSIS METHODOLOGY

Search and Selection Strategies

The first stage of any review involves formulating a primary objective in the form of a research question or hypothesis. Reviewers must explicitly define the objective of the review before starting the project, which serves to reduce the risk of data dredging, where reviewers later assign meaning to significant findings. Secondary objectives may also be defined; however, precaution must be taken as the search strategies formulated for the primary objective may not entirely encompass the body of work required to address the secondary objective. Depending on the purpose of a review, reviewers may choose to undertake a rapid or systematic review. While the meta-analytic methodology is similar for systematic and rapid reviews, the scope of literature assessed tends to be significantly narrower for rapid reviews permitting the project to proceed faster.

Systematic Review and Meta-Analysis

Systematic reviews involve comprehensive search strategies that enable reviewers to identify all relevant studies on a defined topic (DeLuca et al., 2008). Meta-analytic methods then permit reviewers to quantitatively appraise and synthesize outcomes across studies to obtain information on statistical significance and relevance. Systematic reviews of basic research data have the potential of producing information-rich databases which allow extensive secondary analysis. To comprehensively examine the pool of available information, search criteria must be sensitive enough not to miss relevant studies. Key terms and concepts that are expressed as synonymous keywords and index terms, such as Medical Subject Headings (MeSH), must be combined using Boolean operators AND, OR and NOT (Ecker and Skelly, 2010). Truncations, wildcards, and proximity operators can also help refine a search strategy by including spelling variations and different wordings of the same concept (Ecker and Skelly, 2010). Search strategies can be validated using a selection of expected relevant studies. If the search strategy fails to retrieve even one of the selected studies, the search strategy requires further optimization. This process is iterated, updating the search strategy in each iterative step until the search strategy performs at a satisfactory level (Finfgeld-Connett and Johnson, 2013). A comprehensive search is expected to return a large number of studies, many of which are not relevant to the topic, commonly resulting in a specificity of <10% (McGowan and Sampson, 2005). Therefore, the initial stage of sifting through the library to select relevant studies is time-consuming (may take 6 months to 2 years) and prone to human error. At this stage, it is recommended to include at least two independent reviewers to minimize

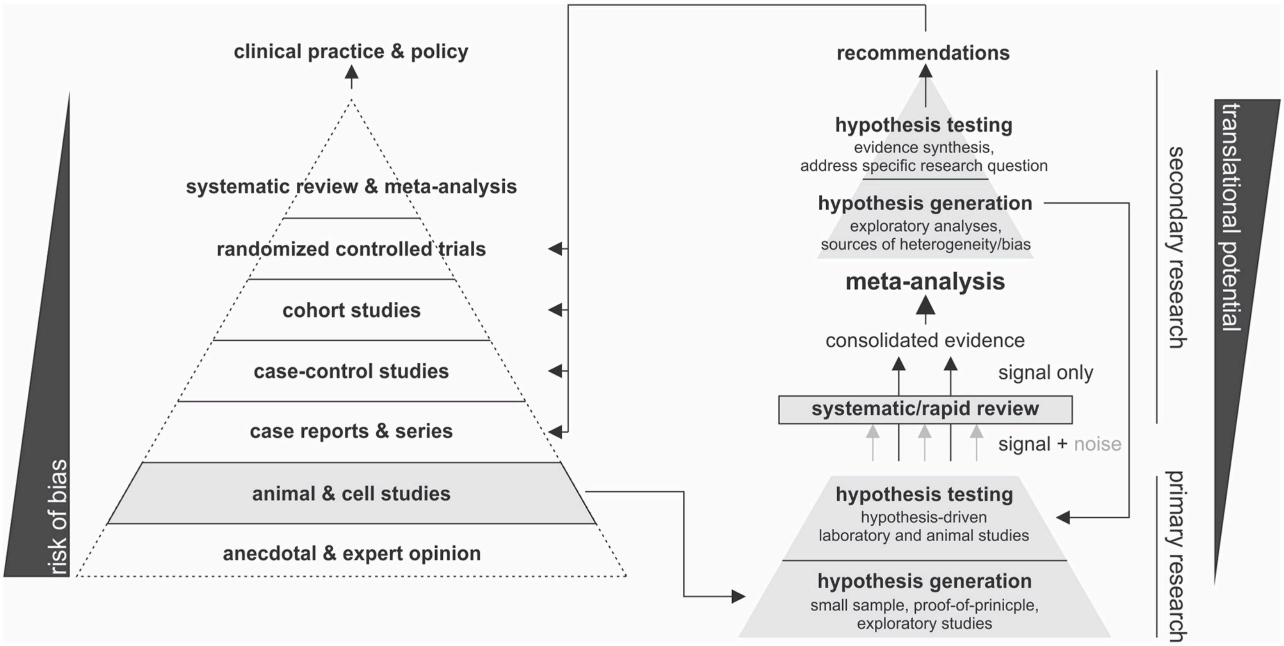

FIGURE 2 | Schematic of proposed hierarchy of translational potential in basic research.

selection bias and related errors. Nevertheless, systematic reviews have a potential to provide the highest quality quantitative evidence synthesis to directly inform the experimental and computational basic, preclinical and translational studies.

Rapid Review and Meta-Analysis

The goal of the rapid review, as the name implies, is to decrease the time needed to synthesize information. Rapid reviews are a suitable alternative to systematic approaches if reviewers prefer to get a general idea of the state of the field without an extensive time investment. Search strategies are constructed by increasing search specificity, thus reducing the number of irrelevant studies identified by the search at the expense of search comprehensiveness (Haby et al., 2016). The strength of a rapid review is in its flexibility to adapt to the needs of the reviewer, resulting in a lack of standardized methodology (Mattivi and Buchberger, 2016). Common shortcuts made in rapid reviews are: (i) narrowing search criteria, (ii) imposing date restrictions, (iii) conducting the review with a single reviewer, (iv) omitting expert consultation (i.e., librarian for search strategy development), (v) narrowing language criteria (ex. English only), (vi) foregoing the iterative process of searching and search term selection, (vii) omitting quality checklist criteria and (viii) limiting number of databases searched (Ganann et al., 2010). These shortcuts will limit the initial pool of studies returned from the search, thus expediting the selection process, but also potentially resulting in the exclusion of relevant studies and introduction of selection bias. While there is a consensus that rapid reviews do not sacrifice quality, or synthesize misrepresentative results (Haby et al., 2016), it is recommended that critical outcomes be later verified by systematic review (Ganann et al., 2010). Nevertheless, rapid reviews are a viable alternative when parameters for computational modeling need to be estimated. While systematic and rapid reviews rely on different strategies to select the relevant studies, the statistical methods used to synthesize data from the systematic and rapid review are identical.

Screening and Selection

When the literature search is complete (the date articles were retrieved from the databases needs to be recorded), articles are extracted and stored in a reference manager for screening. Before study screening, the inclusion and exclusion criteria must be defined to ensure consistency in study identification and retrieval, especially when multiple reviewers are involved. The critical steps in screening and selection are (1) removing duplicates, (2) screening for relevant studies by title and abstract, and (3) inspecting full texts to ensure they fulfill the eligibility criteria. There are several reference managers available including Mendeley and Rayyan, specifically developed to assist with screening systematic reviews. However, 98% of authors report using Endnote, Reference Manager or RefWorks to prepare their reviews (Lorenzetti and Ghali, 2013). Reference managers often have deduplication functions; however, these can be tedious and error-prone (Kwon et al., 2015). A protocol for faster and more reliable de-duplication in Endnote has been recently proposed (Bramer et al., 2016). The selection of articles should be sufficiently broad not to be dominated by a single lab or author. In basic research articles, it is common to find data sets that are reused by the same group in multiple studies. Therefore, additional precautions should be taken when deciding

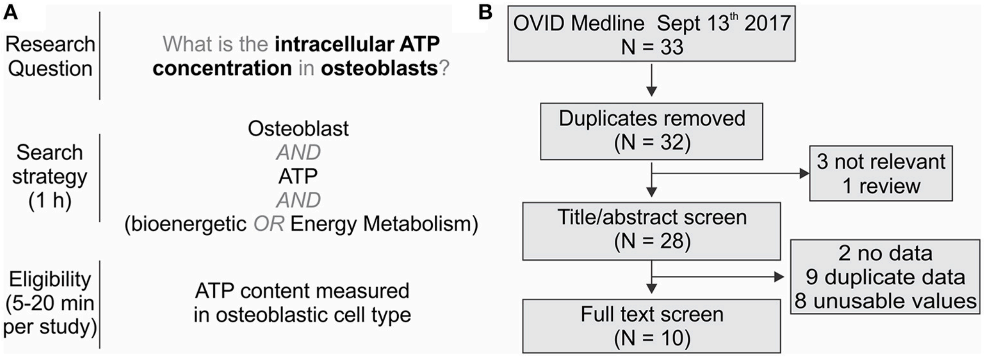

FIGURE 3 | Example of the rapid review literature search. **(A)** Development of the search parameters to find literature on the intracellular ATP content in osteoblasts. **(B)** PRISMA diagram for the information flow.

to include multiple studies published by a single group. At the end of the search, screening and selection process, the reviewer obtains a complete list of eligible full-text manuscripts. The entire screening and selection process should be reported in a PRISMA diagram, which maps the flow of information throughout the review according to prescribed guidelines published elsewhere (Moher et al., 2009). **Figure 3** provides a summary of the workflow of search and selection strategies using the OB $[ATP]_{ic}$ rapid review and meta-analysis as an example.

Data Extraction, Initial Appraisal, and Preparation

Identification of Parameters to be Extracted

It is advised to predefine analytic strategies before data extraction and analysis. However, the availability of reported effect measures and study designs will often influence this decision. When reviewers aim to estimate the absolute mean difference (absolute effect), normalized mean difference, response ratio or standardized mean difference (ex. Hedges' g), they need to extract study-level means (θ_i), standard deviations $\left(sd\left(\theta_i\right)\right)$, and sample sizes ($n_i$), for control (denoted θ_i^c, $sd\left(\theta_i^c\right)$, and n_i^c) and intervention (denoted θ_i^r, $sd\left(\theta_i^r\right)$, and n_i^r) groups, for studies i. To estimate absolute mean effect, only the mean (θ_i^r), standard deviation $\left(sd\left(\theta_i^r\right)\right)$, and sample size ($n_i^r$) are required. In basic research, it is common for a single study to present variations of the same observation (ex. measurements of the same entity using different techniques). In such cases, each point may be treated as an individual observation, or common outcomes within a study can be pooled by taking the mean weighted by the sample size. Another consideration is inconsistency between effect size units reported on the absolute scale, for example, protein concentrations can be reported as g/cell, mol/cell, g/g wet tissue or g/g dry tissue. In such cases, conversion to a common representation is required for comparison across studies, for which appropriate experimental parameters and calibrations need to be extracted from the studies. While some parameters can be approximated by reviewers, such as cell-related parameters found in BioNumbers database (Milo et al., 2010) and equipment-related parameters presumed from manufacturer manuals, reviewers should exercise caution when making such approximations as they can introduce systematic errors that manifest throughout the analysis. When data conversion is judged to be difficult but negative/basal controls are available, scale-free measures (i.e., normalized, standardized, or ratio effects) can still be used in the meta-analysis without the need to convert effects to common units on the absolute scale. In many cases, reviewers may only be able to decide on a suitable effect size measure after data extraction is complete.

It is regrettably common to encounter unclear or incomplete reporting, especially for the sample sizes and uncertainties. Reviewers may choose to reject studies with such problems due to quality concerns or to employ conservative assumptions to estimate missing data. For example, if it is unclear if a study reports the standard deviation or standard error of the mean, it can be assumed to be a standard error, which provides a more conservative estimate. If a study does not report uncertainties but is deemed important because it focuses on a rare phenomenon, imputation methods have been proposed to estimate uncertainty terms (Chowdhry et al., 2016). If a study reports a range of sample sizes, reviewers should extract the lowest value. Strategies to handle missing data should be pre-defined and thoroughly documented.

In addition to identifying relevant primary parameters, *a priori* defined study-level characteristics that have a potential to influence the outcome, such as species, cell type, specific methodology, should be identified and collected in parallel to data extraction. This information is valuable in subsequent exploratory analyses and can provide insight into influential factors through between-study comparison.

Quality Assessment

Formal quality assessment allows the reviewer to appraise the quality of identified studies and to make informed and methodical decision regarding exclusion of poorly conducted studies. In general, based on initial evaluation of full texts, each study is scored to reflect the study's overall quality and scientific rigor. Several quality-related characteristics have been described (Sena et al., 2007), such as: (i) published in peer-reviewed journal, (ii) complete statistical reporting, (iii) randomization of treatment or control, (iv) blinded analysis, (v) sample size calculation prior to the experiment, (vi) investigation of a dose-response relationship, and (vii) statement of compliance with regulatory requirements. We also suggest that the reviewers of basic research studies assess (viii) objective alignment between the study in question and the meta-analytic project. This involves noting if the outcome of interest was the primary study objective or was reported as a supporting or secondary outcome, which may not receive the same experimental rigor and is subject to expectation bias (Sheldrake, 1997). Additional quality criteria specific to experimental design may be included at the discretion of the reviewer. Once study scores have been assembled, study-level aggregate quality scores are determined by summing the number of satisfied criteria, and then evaluating how outcome estimates and heterogeneity vary with study quality. Significant variation arising from poorer quality studies may justify study omission in subsequent analysis.

Extraction of Tabular and Graphical Data

The next step is to compile the meta-analytic data set, which reviewers will use in subsequent analysis. For each study, the complete dataset which includes parameters required to estimate the target outcome, study characteristics, as well as data necessary for unit conversion needs to be extracted. Data reporting in basic research are commonly tabular or graphical. Reviewers can accurately extract tabular data from the text or tables. However, graphical data often must be extracted from the graph directly using time consuming and error prone methods. The Data Extraction Module in *MetaLab* was developed to facilitate systematic and unbiased data extraction; Reviewers provide study figures as inputs, then specify the reference points that are used to calibrate the axes and extract the data (**Figures 4A,B**).

To validate the performance of the *MetaLab* Data Extraction Module, we generated figures using 319 synthetic data points plotted with varying markers sizes (**Figure 4C**). Extracted and actual values were correlated ($R^2 = 0.99$) with the relationship slope estimated as 1.00 (95% CI: 0.99 to 1.01) (**Figure 4D**). Bias was absent, with a mean percent error of 0.00% (95% CI: −0.02 to 0.02%) (**Figure 4E**). The narrow range of errors between −2.00 and 1.37%, and consistency between the median and mean error indicated no skewness. Data marker size did not contribute to the extraction error, as 0.00% of the variation in absolute error was explained by marker size, and the slope of the relationship between marker size and extraction error was 0.000 (95% CI: −0.001, 0.002) (**Figure 4F**). There data demonstrate that graphical data can be reliably extracted using *MetaLab*.

Extracting Data From Complex Relationships

Basic science often focuses on natural processes and phenomena characterized by complex relationships between a series of inputs (e.g., exposures) and outputs (e.g., response). The results are commonly explained by an accepted model of the relationship, such as Michaelis-Menten model of enzyme kinetics which involves two parameters–V_{max} for the maximum rate and K_m for the substrate concentration half of V_{max}. For meta-analysis, model parameters characterizing complex relationships are of interest as they allow direct comparison of different multi-observational datasets. However, study-level outcomes for complex relationships often (i) lack consistency in reporting, and (ii) lack estimates of uncertainties for model parameters. Therefore, reviewers wishing to perform a meta-analysis of complex relationships may need to fit study-level data to a unified model $y = f(x, \beta)$ to estimate parameter set β characterizing the relationship (**Table 1**), and assess the uncertainty in β.

TABLE 1 | Commonly used models of complex relationships in basic sciences.

Model	Equation	Parameter meaning	Applications
Linear model	$y = \beta_1 x + \beta_2$	β_1: slope, magnitude of relationship β_2: intercept, response at x = 0	Reaction rates
Quadratic model (vertex form)	$y = \beta_1 \left(x - \beta_2\right)^2 + \beta_3$	β_1: curvature factor β_2: x at global max/min β_3: global maxima/minimal	Trajectory modeling
Exponential model	$y = \beta_1 e^{\beta_2 x}$	β_1: intercept, response at x = 0 β_2: decay/growth constant	Population decay/growth
Michaelis-Menten, hyperbolic curve	$y = \frac{\beta_1 x}{\beta_2 + x}$	β_1: max response β_2: x at half max response	Enzyme kinetics, reaction rates, infection rates, drug clearance
Sigmoidal E_{max} Model, Hill Function	$y = \frac{\beta_1 x^{\beta_3}}{(\beta_2)^{\beta_3} + x^{\beta_3}}$	β_1: max response β_2: x at half max response β_3: slope-related term	Dose-response relationships, pharmaco dynamics

The study-level data can be fitted to a model using conventional fitting methods, in which the model parameter error terms depend on the goodness of fit and number of available observations. Alternatively, a Monte Carlo simulation approach (Cox et al., 2003) allows for the propagation of study-level variances (uncertainty in the model inputs) to the uncertainty in the model parameter estimates (**Figure 5**). Suppose that study i reported a set of k predictor variables $x = \{x_j | 1 \le j \le k\}$ for a set of outcomes $\theta = \{\theta_j | 1 \le j \le k\}$, and that there is a corresponding set of standard deviations $sd(\theta) = \{sd(\theta_j) | 1 \le j \le k\}$ and sample sizes $n = \{n_j | 1 \le j \le k\}$ (**Figure 5A**). The Monte Carlo error propagation method assumes that outcomes are normally distributed, enabling pseudo random observations to be sampled from a distribution approximated by $\mathcal{N}(\theta_j, sd(\theta_j)^2)$. The pseudo random observations are then averaged to obtain a Monte-Carlo estimate θ_j^* for each observation such that

$$\theta_j^* = \frac{1}{n_j} \sum_{m=1}^{n_j} (\theta_{j,m}^*) \tag{1}$$

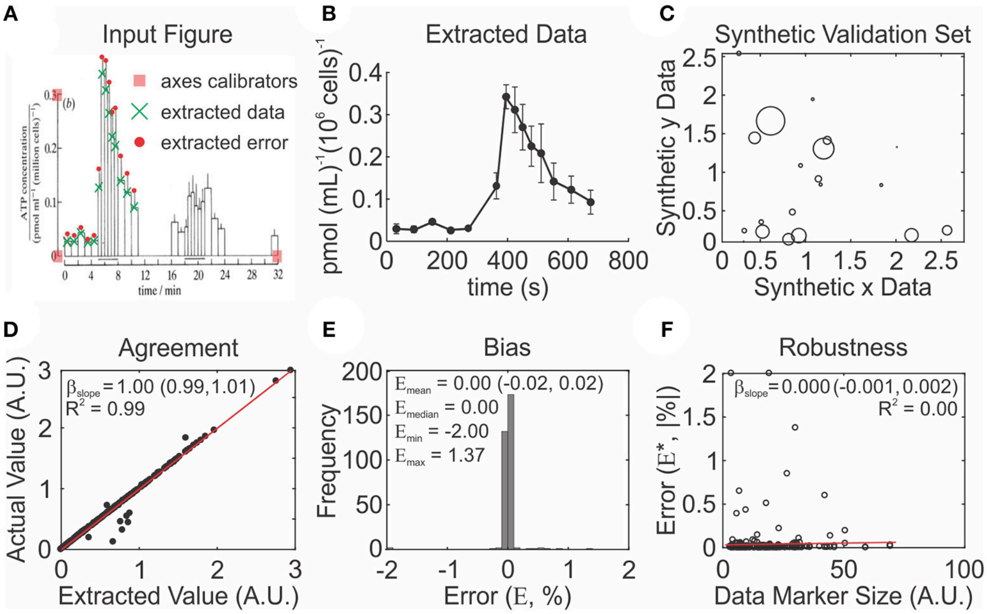

FIGURE 4 | MetaLab data extraction procedure is accurate, unbiased and robust to quality of data presentation. **(A,B)** Example of graphical data extraction using MetaLab. **(A)** Original figure (Bodin et al., 1992) with axes, data points and corresponding errors marked by reviewer. **(B)** Extracted data with error terms. **(C–F)** Validation of MetaLab data-extraction module. **(C)** Synthetic datasets were constructed using randomly generated data coordinates and marker sizes. **(D)** Extracted values were consistent with true values evaluated by linear regression with the slope β_{slope}, red line: line of equality. **(E)** Data extraction was unbiased, evaluated with distribution of percent errors between true and extracted values. E_{mean}, E_{median}, E_{min}, and E_{max} are mean, median, minimum, and maximum % error respectively. **(F)** The absolute errors of extracted data were independent of data marker size, red line: line regression with the slope β_{slope}.

where $\theta(j,m)^*$ represents a pseudo-random variable sampled n_j times from $\mathcal{N}(\theta_j, sd(\theta_j)^2)$. The relationship between x and $\theta^* = \{\theta_j^* | 1 \leq j \leq k\}$ is then fitted with the model of interest using the least-squares method to obtain an estimate of model parameters β (**Figure 5B**). After many iterations of resampling and fitting, a distribution of parameter estimates $\mathcal{N}(\overline{\beta},\ sd\left(\overline{\beta}\right)^2)$ is obtained, from which the parameter means $\overline{\beta}$ and variances $sd\left(\overline{\beta}\right)^2$ can be estimated (**Figures 5C,D**). As the number of iterations M tend to infinity, the parameter estimate converges to the expected value $E(\beta)$.

$$\lim_{M\to\infty} \frac{1}{M}\left(\beta_1 + \beta_2 + \ldots + \beta_M\right) = E(\beta) \tag{2}$$

It is critical for reviewers to ensure the data is consistent with the model such that the estimated parameters sufficiently capture the information conveyed in the underlying study-level data. In general, reliable model fittings are characterized by normal parameter distributions (**Figure 5D**) and have a high goodness of fit as quantified by R^2. The advantage of using the Monte-Carlo approach is that it works as a black box procedure that does not require complex error propagation formulas, thus allowing handling of correlated and independent parameters without additional consideration.

Study-Level Effect Sizes

Depending on the purpose of the review product, study-level outcomes θ_i can be expressed as one of several effect size measures. The absolute effect size, computed as a mean outcome or absolute difference from baseline, is the simplest, is independent of variance, and retains information about the context of the data (Baguley, 2009). However, the use of absolute effect size requires authors to report on a common scale or provide conversion parameters. In cases where a common scale is difficult to establish, a scale-free measure, such as standardized, normalized or relative measures can be used. Standardized mean differences, such Hedges' g or Cohen d, report the outcome as the size of the effect (difference between the means of experimental and control groups) relative to the overall variance (pooled and weighted standard deviation of combined experimental and control groups). The standardized mean difference, in addition to odds or risk ratios, is widely used in meta-analysis of clinical studies (Vesterinen et al., 2014), since it allows to summarize metrics that do not have unified meaning (e.g., a pain score), and takes into account the variability in the samples. However, the standardized measure is rarely used in basic science since study outcomes are commonly a defined measure, sample sizes are small, and variances are highly influenced by experimental and biological factors. Other measures that are more suited for basic science are the normalized mean difference, which expresses the difference between the outcome and baseline as a proportion of the baseline (alternatively called the percentage difference), and response ratio, which reports the outcome as a proportion of the baseline. All discussed measures have been included in *MetaLab* (**Table 2**).

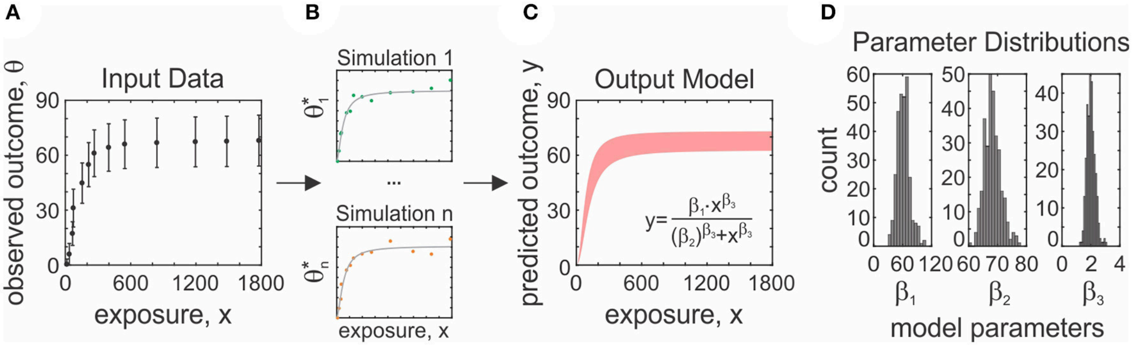

FIGURE 5 | Model parameter estimation with Monte-Carlo error propagation method. **(A)** Study-level data taken from ATP release meta-analysis. **(B)** Assuming sigmoidal model, parameters were estimated using *Fit Model MetaLab* module by randomly sampling data from distributions defined by study level data. Model parameters were estimated for each set of sampled data. **(C)** Final model using parameters estimated from 400 simulations. **(D)** Distributions of parameters estimated for given dataset are unimodal and symmetrical.

Data Synthesis

The goal of any meta-analysis is to provide an outcome estimate that is representative of all study-level findings. One important feature of the meta-analysis is its ability to incorporate information about the quality and reliability of the primary studies by weighing larger, better reported studies more heavily. The two quantities of interest are the overall estimate and the measure of the variability in this estimate. Study-level outcomes θ_i are synthesized as a weighted mean $\hat{\theta}$ according to the study-level weights w_i:

$$\hat{\theta} = \frac{\sum_i^N (\theta_i \cdot w_i)}{\sum_i (w_i)} \tag{3}$$

where N is number of studies or datasets. The choice of a weighting scheme dictates how study-level variances are pooled to estimate the variance of the weighted mean. The weighting scheme thus significantly influences the outcome of meta-analysis, and if poorly chosen, potentially risks over-weighing less precise studies and generating a less valid, non-generalizable outcome. Thus, the notion of defining an *a priori* analysis protocol has to be balanced with the need to assure that the dataset is compatible with the chosen analytic strategy, which may be uncertain prior to data extraction. We provide strategies to compute and compare different study-level and global outcomes and their variances.

Weighting Schemes

To generate valid estimates of cumulative knowledge, studies are weighed according to their reliability. This conceptual framework, however, deteriorates if reported measures of precision are themselves flawed. The most commonly used measure of precision is the inverse variance which is a composite measure of total variance and sample size, such that studies with larger sample sizes and lower experimental errors are more reliable and more heavily weighed. Inverse variance weighting schemes are valid when (i) sampling error is random, (ii) the reported effects are homoscedastic, i.e., have equal variance and (iii) the sample size reflects the number of independent experimental observations. When assumptions (i) or (ii) are violated, sample size weighing can be used as an alternative. Despite sample size and sample variance being such critical parameters in the estimation of the global outcome, they are often prone to deficient reporting practices.

Potential problems with sample variance and sample size

The standard error $se(\theta_i)$ is required to compute inverse variance weights, however, primary literature as well as meta-analysis reviewers often confuse standard errors with standard deviations $sd\,(\theta_i)$ (Altman and Bland, 2005). Additionally, many assays used in basic research often have uneven error distributions, such that the variance component arising from experimental error depends on the magnitude of the effect (Bittker and Ross, 2016). Such uneven error distributions will lead to biased weighing that does not reflect true precision in measurement. Fortunately, the standard error and standard deviation have characteristic properties that can be assessed by the reviewer to determine whether inverse variance weights are appropriate for a given dataset. The study-level standard error $se(\theta_i)$ is a measure of precision and is estimated as the product of the sample standard deviation $sd(\theta_i)$ and margin of error $\frac{1}{\sqrt{n_i}}$ for study i. Therefore, the standard error is expected to be approximately inversely proportionate to the root of the study-level sample size n_i

$$se(\theta_i) \sim \frac{1}{\sqrt{n_i}} \tag{4}$$

Unlike the standard error, the standard deviation–a measure of the variance of a random variable $sd\,(\theta)^2$-is assumed to be independent of the sample size because it is a descriptive statistic rather than a precision statistic. Since the total observed study-level sample variance is the sum of natural variability (assumed to be constant for a phenomenon) and random error, no relationship is expected between reported standard deviations and sample sizes. These assumptions can be tested by correlation analysis and can be used to inform the reviewer about the reliability of the study-level uncertainty measures. For example,

TABLE 2 | Types of effect sizes.

Measure	Mean	Standard error
Absolute	$\theta_i = \begin{cases} \theta_i^r - \theta_i^c, \textit{if } \theta_i^c \textit{ reported} \\ \theta_i^r, \textit{else} \end{cases}$	$se(\theta_i) = \begin{cases} \sqrt{\frac{n_i^c+n_i^r}{n_i^c n_i^r} sd(\theta_i)^2}, \textit{if } \theta_i^c \textit{ reported} \\ \frac{sd(\theta_i^r)}{\sqrt{n_i^r}}, \textit{else} \end{cases}$ Where $sd(\theta_i) = \sqrt{\frac{(n_i^c-1)sd(\theta_i^c)+(n_i^r-1)sd(\theta_i^r)}{n_i^c+n_i^r-2}}$
Standardized (Hedges' g)	$\theta_i = \frac{\theta_i^r-\theta_i^c}{sd(\theta_i)} \cdot \left(1 - \frac{3}{4(n_i^c+n_i^r)-9}\right)$ Where $sd(\theta_i) = \sqrt{\frac{(n_i^c-1)sd(\theta_i^c)+(n_i^r-1)sd(\theta_i^r)}{n_i^c+n_i^r-2}}$	$se(\theta_i) = \sqrt{\frac{n_i^c+n_i^r}{n_i^c n_i^r} + \frac{\theta_i^2}{2((n_i^c+n_i^r)-3.94)}}$
Normalized	$\theta_i = \frac{\theta_i^r-\theta_i^c}{\theta_i^c}$	$se(\theta_i) = \sqrt{\frac{\left(\frac{sd(\theta_i^c)}{\theta_i^c}\right)^2}{n_i^c} + \frac{\left(\frac{sd(\theta_i^r)}{\theta_i^r}\right)^2}{n_i^r}}$
Ratio	$\theta_i = \frac{\theta_i^r}{\theta_i^c}$	$se(\theta_i) = \sqrt{\frac{(\theta_i^r)^2}{(\theta_i^c)^2}\left(\frac{sd(\theta_i^r)^2}{n_i^r(\theta_i^r)^2} + \frac{sd(\theta_i^c)^2}{n_i^c(\theta_i^c)^2}\right)}$

Provided are formulas to calculate the mean and standard error for the specified effect sizes.

a relationship between sample size and sample variance was observed for the OB $[\text{ATP}]_{\text{ic}}$ dataset (**Figure 6A**), but not for the ATP release data (**Figure 6B**). Therefore, in the case of the OB $[\text{ATP}]_{\text{ic}}$ data set, lower variances are not associated with higher precision and inverse variance weighting is not appropriate. Sample sizes are also frequently misrepresented in the basic sciences, as experimental replicates and repeated experiments are often reported interchangeably (incorrectly) as sample sizes (Vaux et al., 2012). Repeated (independent) experiments refer to number of randomly sampled observations, while replicates refer to the repeated measurement of a sample from one experiment to improve measurement precision. Statistical inference theory assumes random sampling, which is satisfied by independent experiments but not by replicate measurements. Misrepresentative reporting of replicates as the sample size may artificially inflate the reliability of results. While this is difficult to identify, poor reporting may be reflected in the overall quality score of a study.

Inverse variance weighting

The inverse variance is the most common measure of precision, representing a composite measure of total variance and sample size. Widely used weighting schemes based on the inverse variance are fixed effect or random effects meta-analytic models. The fixed effect model assumes that all the studies sample one true effect γ. The observed outcome θ_i for study i is then a function of a within-study error ε_i, $\theta_i = \gamma + \varepsilon_i$, where ε_i is normally distributed $\varepsilon_i \sim \mathcal{N}\left(0, se(\theta_i)^2\right)$. The standard error $se(\theta_i)$ is calculated from the sample standard deviation $sd(\theta_i)$ and sample size n_i as:

$$se(\theta_i) = \frac{sd(\theta_i)}{\sqrt{n_i}} \tag{5}$$

Alternatively, the random effects model supposes that each study samples a different true outcome μ_i, such that the combined effect μ is the mean of a population of true effects. The observed effect θ_i for study i is then influenced by the intrastudy error ε_i and interstudy error ξ_i, $\theta_i = \mu_i + \varepsilon_i + \xi_i$, where ξ_i is also assumed to be normally distributed $\xi_i \sim \mathcal{N}\left(0, \tau^2\right)$, with τ^2 representing the extent of heterogeneity, or between-study (interstudy) variance.

Study-level estimates for a fixed effect or random effects model are weighted using the inverse variance:

$$w_i = \begin{cases} \frac{1}{se(\theta_i)^2}, & \text{fixed effect} \\ \frac{1}{se(\theta_i)^2+\tau^2}, & \text{random effects} \end{cases} \tag{6}$$

These weights are used to calculate the global outcome $\hat{\theta}$ (Equation 3) and the corresponding standard error $se(\hat{\theta})$:

$$se(\hat{\theta}) = \frac{1}{\sqrt{\sum_i^N w_i}} \tag{7}$$

where N = number of datasets/studies. In practice, random effects models are favored over the fixed effect model, due to the prevalence of heterogeneity in experimental methods and biological outcomes. However, when there is no between-study variability ($\tau^2 = 0$), the random effects model reduces to a fixed effect model. In contrast, when τ^2 is exceedingly large and interstudy variance dominates the weighting term $[\tau^2 \gg se(\theta_i)^2]$, random effects estimates will tend to an unweighted mean.

Interstudy variance $\boldsymbol{\tau^2}$ *estimators.* Under the assumptions of a random effects model, the total variance is the sum of the intrastudy variance (experimental sampling error) and interstudy variance τ^2 (variability of true effects). Since the distribution of true effects is unknown, we must estimate the value of τ^2 based on study-level outcomes (Borenstein, 2009). The DerSimonian

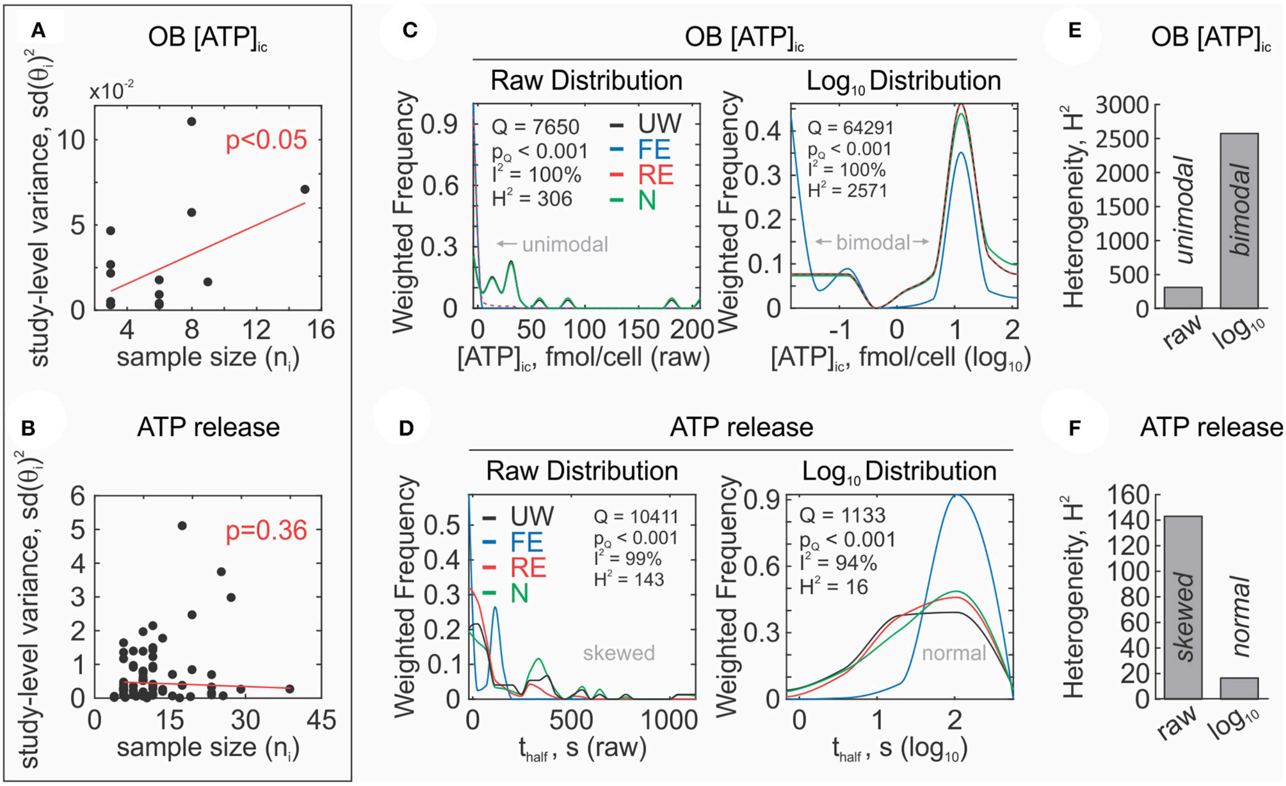

FIGURE 6 | Assessment of study-level outcomes. **(A,B)** Reliability of study-level error measures. Relationship between study-level squared standard deviation $sd(\theta_i)^2$ and sample sizes n_i are assumed to be independent when reliably reported. Association between $sd(\theta_i)^2$ and n_i was present in OB $[\text{ATP}]_{\text{ic}}$ data set **(A)** and absent in ATP release data set **(B)**, *red line*: linear regression. **(C,D)** Distributions of study-level outcomes. Assessment of unweighted (UW–*black*) and weighted (fixed effect; FE–*blue*, random effects; RE–*red*, sample-size weighting; N–*green*) study-level distributions of data from OB $[\text{ATP}]_{\text{ic}}$ (**C**) and ATP release (**D**) data sets, before (*left*) and after $\log_{10}$ transformation (*right*). Heterogeneity was quantified by Q, I^2, and H^2 heterogeneity statistics. **(E,F)** After $\log_{10}$ transformation, H^2 heterogeneity statistics increased for OB $[\text{ATP}]_{\text{ic}}$ data set (**E**) and decreased for ATP release (**F**) data set.

and Laird (DL) method is the most commonly used in meta-analyses (DerSimonian and Laird, 1986). Other estimators such as the Hunter and Schmidt (Hunter and Schmidt, 2004), Hedges (Hedges and Olkin, 1985), Hartung-Makambi (Hartung and Makambi, 2002), Sidik-Jonkman (Sidik and Jonkman, 2005), and Paule-Mandel (Paule and Mandel, 1982) estimators have been proposed as either alternatives or improvements over the DL estimator (Sanchez-Meca and Marin-Martinez, 2008) and have been implemented in *MetaLab* (**Table 3**). Negative values of τ^2 are truncated at zero. An overview of the various τ^2 estimators along with recommendations on their use can be found elsewhere (Veroniki et al., 2016).

Sample-size weighting

Sample-size weighting is preferred in cases where variance estimates are unavailable or unreliable. Under this weighting scheme, study-level sample sizes are used in place of inverse variances as weights. The sampling error is then unaccounted for; however, since sampling error is random, larger sample sizes will effectively average out the error and produce more dependable results. This is contingent on reliable reporting of sample sizes which is difficult to assess and can be erroneous as detailed above. For a sample size weighted estimate, study-level sample sizes n_i replace weights that are used to calculate the global effect size $\hat{\theta}$, such that

$$w_i = n_i \tag{8}$$

The pooled standard error $se(\hat{\theta})$ for the global effect is then:

$$se(\hat{\theta}) = \sqrt{\frac{\sum_i^N \left(se(\theta_i)^2 \cdot (n_i - 1)\right)}{\sum_i^N (n_i - 1)}} \tag{9}$$

While sample size weighting is less affected by sampling variance, the performance of this estimator depends on the availability of studies (Marin-Martinez and Sanchez-Meca, 2010). When variances are reliably reported, sample-size weights should roughly correlate to inverse variance weights under the fixed effect model.

Meta-Analytic Data Distributions

One important consideration the reviewer should attend to is the normality of the study-level effects distributions assumed by most meta-analytic methods. Non-parametric methods that do not assume normality are available but are more computationally intensive and inaccessible to non-statisticians (Karabatsos et al.,

TABLE 3 | Interstudy variance estimators.

Estimator	τ^2 estimate
DerSimonian-Laird (DL)*†	$\tau_{DL}^2 = \frac{Q-(N-1)}{c}$
Hunter-Schmidt (HS)*	$\tau_{HS}^2 = \frac{Q-N}{\sum_i se(\theta_i)^{-2}}$
Hedges (H)	$\tau_H^2 = \frac{\sum_i \left(\theta_i - \left(\frac{\sum_i \theta_i}{N}\right)\right)^2}{N-1} - \frac{\sum_i se(\theta_i)^2}{N}$
Hartung-Makambi (HM)*†	$\tau_{HM}^2 = \frac{Q^2}{(2(N-1)+Q)\cdot c}$
Sidik-Jonkman (SJ)	$\tau_{SJ}^2 = \frac{\sum_i \upsilon_i^{-1}\left(\theta_i - \left(\frac{\sum_i \upsilon_i^{-1}\theta_i}{\sum_i \upsilon_i^{-1}}\right)\right)^2}{N-1}$, Where $\upsilon_i = \left(\frac{se(\theta_i)^2}{\left(\frac{\sum_i (\theta_i - \overline{\theta})^2}{N}\right)} + 1\right)$ and $\overline{\theta} = \frac{1}{N}\sum_i \theta_i$
Paule-Mandel (PM)#	$\tau_{PM}^2 = \frac{\sum_i w_i\left(\theta_i - \hat{\theta}_{PM}\right)^2 - \left(\sum_i w_i^2 se(\theta_i)^2 - \left(\frac{\sum_i w_i^2 se(\theta_i)^2}{\sum_i w_i}\right)\right)}{\sum_i w_i - \left(\frac{\sum_i w_i^2}{\sum_i w_i}\right)}$ Where $\hat{\theta}_{PM} = \frac{\sum_i (\theta_i \cdot w_i)}{\sum_i (w_i\ )}$

*$Q = \sum_i \left(se(\theta_i)^{-2}\left(\theta_i - \frac{\sum_i se(\theta_i)^{-2}\theta_i}{\sum_i se(\theta_i)^{-2}}\right)^2\right)$. †$c = \sum_i se(\theta_i)^{-2} - \frac{\sum_i \left(se(\theta_i)^{-2}\right)^2}{\sum_i se(\theta_i)^{-2}}$. #*iterative estimator.*
N = number of datasets/studies.

2015). The performance of parametric meta-analytic methods has been shown to be robust to non-normally distributed effects (Kontopantelis and Reeves, 2012). However, this robustness is achieved by deriving artificially high estimates of heterogeneity for non-normally distributed data, resulting in conservatively wide confidence intervals and severely underpowered results (Jackson and Turner, 2017). Therefore, it is prudent to characterize the underlying distribution of study-level effects and perform transformations to normalize distributions to preserve the inferential integrity of the meta-analysis.

Assessing data distributions

Graphical approaches, such as the histogram, are commonly used to assess the distribution of data; however, in a meta-analysis, they can misrepresent the true distribution of effect sizes that may be different due to unequal weights assigned to each study. To address this, we can use a weighted histogram to evaluate effect size distributions (**Figure 6**). A weighted histogram can be constructed by first binning studies according to their effect sizes. Each bin is then assigned weighted frequencies, calculated as the sum of study-level weights within the given bin. The sum of weights in each bin are then normalized by the sum of all weights across all bins

$$P_j = \frac{\sum_i w_{ij}}{\sum_j^{nBins} \sum_i w_{ij}} \tag{10}$$

where P_j is the weighted frequency for bin j, w_{ij} is the weight for the effect size in bin j from study i, and *nBins* is the total number of bins. If the distribution is found deviate from normality, the most common explanations are that (i) the distribution is skewed due to inconsistencies between studies, (ii) subpopulations exist within the dataset giving rise to multimodal distributions or (iii) the studied phenomenon is not normally distributed. The source of inconsistencies and multimodality can be explored during the analysis of heterogeneity (i.e., to determine whether study-level characteristics can explain observed discrepancies). Skewness may however be inherent to the data when values are small, variances are large, and values cannot be negative (Limpert et al., 2001) and has been credited to be characteristic of natural processes (Grönholm and Annila, 2007). For sufficiently large sample sizes the central limit theorem holds that the means of a skewed data are approximately normally distributed. However, due to common limitation in the number of studies available for meta-analyses, meta-analytic global estimates of skewed distributions are often sensitive to extreme values. In these cases, data transformation can be used to achieve a normal distribution on the logarithmic scale (i.e., lognormal distribution).

Lognormal distributions

Since meta-analytic methods typically assume normality, the log transformation is a useful tool used to normalize skewed distributions (**Figures 6C–F**). In the ATP release dataset, we found that log transformation normalized the data distribution. However, in the case of the OB $[ATP]_{ic}$ dataset, log transformation revealed a bimodal distribution that was otherwise not obvious on the raw scale.

Data normalization by log transformation allows meta-analytic techniques to maintain their inferential properties. The outcomes synthesized on the logarithmic scale can then be transformed to the original raw scale to obtain asymmetrical confidence intervals which further accommodate the skew in the data. Study-level effect sizes θ_i can be related to the logarithmic mean Θ_i through the forward log transformation, meta-analyzed on the logarithmic scale, and back-transformed to the original scale using one of the back-transformation methods (**Table 4**). We have implemented three different back-transformation methods into MetaLab, including geometric approximation (anti-log), naïve approximation (rearrangement of forward-transformation method) and tailor series approximation (Higgins et al., 2008). The geometric back-transformation will yield an estimate of $\hat{\theta}$ that is approximately equal to the median of the study-level effects. The naïve or tailor series approximation differ in how the standard errors are approximated, which is used to obtain a point estimate on the original raw scale. The naïve and tailor series approximations were shown to maintain adequate inferential properties in the meta-analytic context (Higgins et al., 2008).

Confidence Intervals

Once the meta-analysis global estimate and standard error has been computed, reviewers may proceed to construct the confidence intervals (CI). The CI represents the range of values within which the true mean outcome is contained with the probability of 1-α. In meta-analyses, the CI conveys information about the significance, magnitude and direction of an effect, and is used for inference and generalization of an outcome. Values that do not fall in the range of the CI may be interpreted as significantly different. In general, the CI is computed as the product of the standard error $se(\hat{\theta})$ and the critical value $v_{1-\alpha/2}$:

$$\pm CI = \pm v_{1-\alpha/2} \cdot se(\hat{\theta}) \tag{11}$$

CI estimators

The critical value $v_{1-\alpha/2}$ is derived from a theoretical distribution and represents the significance threshold for level α. A theoretical distribution describes the probability of any given possible outcome occurrence for a phenomenon. Extreme outcomes that lie furthest from the mean are known as the tails. The most commonly used theoretical distributions are the z-distribution and *t*-distribution, which are both symmetrical and bell-shaped, but differ in how far reaching or "heavy" the tails are. Heavier tails will result in larger critical values which translate to wider confidence intervals, and vice versa. Critical values drawn from a z-distribution, known as z-scores (z), are used when data are normal, and a sufficiently large number of studies are available (>30). The tails of a z-distribution are independent of the sample size and reflect those expected for a normal distribution. Critical values drawn from a t-distribution, known as t-scores (t), also assume data are normally-distributed, however, are used when there are fewer available studies (<30) because the t-distribution tails are heavier. This produces more conservative (wider) CIs, which help ensure that the data are not misleading or misrepresentative when there is limited evidence available. The heaviness of the t-distribution tails is dictated by the degree of freedom *df*, which is related to the number of available studies N ($df = N-1$) such that fewer studies will result in heavier t-distribution tails and therefore larger critical values. Importantly, the t-distribution is asymptotically normal and will thus converge to a z-distribution for a sufficiently large number of studies, resulting in similar critical values. For example, for a significance level $\alpha = 0.05$ (5% false positive rate), the z-distribution will always yield a critical value $v = 1.96$,

TABLE 4 | Logarithmic Transformation Methods.

Forward-Transformation (raw to log$_{10}$)		
	Mean	**Standard error**
	$\Theta_i = \log_{10}(\theta_i) - \left(\frac{se(\Theta_i)^2}{2}\right)$	$se(\Theta_i) = \sqrt{\log_{10}\left(\frac{se(\theta_i)^2}{\theta_i^2} + 1\right)}$
Back-Transformation (log$_{10}$ to raw)		
Method	**Mean**	**Standard error**
Geometric	$\hat{\theta} = 10^{\hat{\Theta}}$	$\pm CI_{1-\alpha/2}\left(\hat{\theta}\right) = 10^{\hat{\Theta} \pm v_{1-\alpha/2} \cdot se(\hat{\Theta})}$ $se\left(\hat{\theta}\right) = \frac{\left(+CI_{1-\alpha/2}\left(\hat{\theta}\right)\right) - \left(-CI_{1-\alpha/2}\left(\hat{\theta}\right)\right)}{2v_{1-\alpha/2}}$ Where $v_{1-\alpha/2}$ corresponds to critical value
Naïve approximately	$\hat{\theta} = 10^{\left(\hat{\Theta} + \frac{se\left(\hat{\Theta}\right)^2}{2}\right)}$	$se\left(\hat{\theta}\right) = \frac{1}{\sqrt{n_i}}\left(10^{sd(\hat{\Theta})^2} - 1\right)10^{2\hat{\Theta} + sd(\hat{\Theta})^2}$
Tailor Series approximately	$\hat{\theta} = 10^{\left(\hat{\Theta} + \frac{se\left(\hat{\Theta}\right)^2}{2}\right)}$	$se\left(\hat{\theta}\right) = \sqrt{\frac{1}{n_i}10^{\left(2\hat{\Theta} + sd(\hat{\Theta})^2\right)} sd(\hat{\Theta})^2 \left(1 + \left(\frac{sd\left(\hat{\Theta}\right)^2}{2}\right)\right)}$

Forward-transformation of study-level estimates θ_i to corresponding log-transformed estimates Θ_i, and back-transformation of meta-analysis outcome $\hat{\Theta}$ to the corresponding outcome $\hat{\theta}$ on the raw scale (Higgins et al., 2008). $v_{1-\alpha/2}$: confidence interval critical value at significance level α.

regardless of how many studies are available. The t-distribution will however yield $\nu = 2.78$ for 5 studies, $\nu = 2.26$ for 10 studies, $\nu = 2.05$ for 30 studies and $\nu = 1.98$ for 100 studies, gradually converging to 1.96 as the number of studies increases. We have implemented the z-distribution and t-distribution CI estimators into MetaLab.

Evaluating Meta-Analysis Performance

In general, 95% of study-level outcomes are expected to fall within the range of the 95% global CI. To determine whether the global 95% CI is consistent with the underlying study-level outcomes, the coverage of the CI can be computed as the proportion of study-level 95% CIs that overlap with the global 95% CI:

$$\begin{aligned} \left|\hat{\theta} - \theta_i\right| &\leq \nu_{1-\frac{\alpha}{2}} \cdot se\left(\hat{\theta}\right) + \nu_{1-\frac{\alpha}{2}} \cdot se\left(\theta_i\right), \qquad \text{covered} \\ \left|\hat{\theta} - \theta_i\right| &> \nu_{1-\alpha/2} \cdot se(\hat{\theta}) + \nu_{1-\frac{\alpha}{2}} \cdot se\left(\theta_i\right), \text{not covered} \quad (12) \end{aligned}$$

The coverage is a performance measure used to determine whether inference made on the study-level is consistent with inference made on the meta-analytic level. Coverage that is less than expected for a specified significance level (i.e., <95% coverage for $\alpha = 0.05$) may be indicative of inaccurate estimators, excessive heterogeneity or inadequate choice of meta-analytic model, while coverage exceeding 95% may indicate an inefficient estimator that results in insufficient statistical power.

Overall, the performance of a meta-analysis is heavily influenced by the choice of weighting scheme and data transformation (**Figure 7**). This is especially evident in the smaller datasets, such as our OB $[\text{ATP}]_i$ example, where both the global estimates and the confidence intervals are dramatically different under different weighting schemes (**Figure 7A**). Working with larger datasets, such as ATP release kinetics, allows to somewhat reduce the influence of the assumed model (**Figure 7B**). However, normalizing data distribution (by log transformation) produces much more consistent outcomes under different weighting schemes for both datasets, regardless of the number of available studies (**Figures 7A,B**, *log_{10} synthesis*).

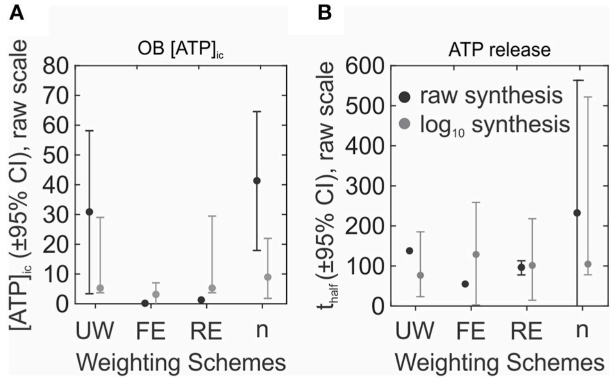

FIGURE 7 | Comparison of global effect estimates using different weighting schemes. **(A,B)** Global effect estimates for OB $[\text{ATP}]_{\text{ic}}$ **(A)** and ATP release **(B)** following synthesis of original data (raw, *black*) or of $\log_{10}$-transformed data followed by back-transformation to original scale ($\log_{10}$, *gray*). Global effects ± 95% CI were obtained with unweighted data (UW), or using fixed effect (FE), random effects (RE), and sample-size (*n*) weighting schemes.

Analysis of Heterogeneity

Heterogeneity refers to inconsistency between studies. A large part of conducting a meta-analysis involves quantifying and accounting for sources of heterogeneity that may compromise the validity of meta-analysis. Basic research meta-analytic datasets are expected to be heterogeneous because (*i*) basic research literature searches tend to retrieve more studies than clinical literature searches and (*ii*) experimental methodologies used in basic research are more diverse and less standardized compared to clinical research. The presence of heterogeneity may limit the generalizability of an outcome due to the lack of study-level consensus. Nonetheless, exploration of heterogeneity sources can be insightful for the field in general, as it can identify biological or methodological factors that influence the outcome.

Quantifying of Heterogeneity

Higgins and Thompson emphasized that a heterogeneity metric should be (i) dependent on magnitude of heterogeneity, (ii) independent of measurement scale, (iii) independent of sample size and (iv) easily interpretable (Higgins and Thompson, 2002). Regrettably, the most commonly used test of heterogeneity is the Cochrane's Q test (Borenstein, 2009), which has been repeatedly shown to have undesirable statistical properties (Higgins et al., 2003). Nonetheless, we will introduce it here, not because of its widespread use, but because it is an intermediary statistic used to obtain more useful measures of heterogeneity, H^2 and I^2. The measure of total variation Q_{total} statistic is calculated as the sum of the weighted squared differences between the study-level means θ_i and the fixed effect estimate $\hat{\theta}_{FE}$:

$$\begin{aligned} Q_{total} &= \sum_{i=1}^{N} \left(w_i \cdot \left(\theta_i - \hat{\theta}_{FE} \right)^2 \right) \\ \text{where } \hat{\theta}_{FE} &= \frac{\sum_i se(\theta_i)^{-2} \theta_i}{\sum_i se(\theta_i)^{-2}} \text{ and } w_i = se(\theta_i)^{-2} \end{aligned} \quad (13)$$

The Q_{total} statistic is compared to a chi-square (χ^2) distribution (*df* = *N-1*) to obtain a *p*-value, which, if significant, supports the presence of heterogeneity. However, the Q-test has been shown to be inadequately powered when the number of studies is too low ($N < 10$) and excessively powered when study number is too high ($N > 50$) (Gavaghan et al., 2000; Higgins et al., 2003). Additionally, the Q_{total} statistic is not a measure of the magnitude of heterogeneity due to its inherent dependence on the number of studies. To address this limitation, H^2 heterogeneity statistics was developed as the relative excess in Q_{total} over degrees of freedom df:

$$H^2 = \frac{Q_{total}}{df} \quad (14)$$

H^2 is independent of the number of studies in the meta-analysis and is indicative of the magnitude of heterogeneity (Higgins and Thompson, 2002). For values <1, H^2 is truncated at 1, therefore values of H^2 can range from one to infinity, where $H^2 = 1$ indicates homogeneity. The corresponding confidence intervals for H^2 are

$$H^2 \pm 95\%\ \mathrm{CI} = \left(e^{\ln(H) \pm 1.96 \cdot \sqrt{\frac{1}{2(df-1)}\left(1 - \frac{1}{3(df)^2}\right)}} \right)^2 \tag{15}$$

Intervals that do not overlap with 1 indicate significant heterogeneity. A more easily interpretable measure of heterogeneity is the I^2 statistic, which is a transformation of H^2:

$$I^2 = \frac{H^2 - 1}{H^2} \cdot 100\% \tag{16}$$

The corresponding 95% CI for I^2 is derived from the 95% CI for H^2

$$I^2 \pm 95\%\ CI = \frac{(H^2 \pm 95\%\ CI) - 1}{(H^2 \pm 95\%\ CI)} \cdot 100\% \tag{17}$$

Values of I^2 range between 0 and 100% and describe the percentage of total variation that is attributed to heterogeneity. Like H^2, I^2 provides a measure of the magnitude of heterogeneity. Values of I^2 at 25, 50, and 75% are generally graded as low, moderate and high heterogeneity, respectively (Higgins and Thompson, 2002; Pathak et al., 2017). However, several limitations have been noted for the I^2 statistic. I^2 has a non-linear dependence on τ^2, thus I^2 will appear to saturate as it approaches 100% (Huedo-Medina et al., 2006). In cases of excessive heterogeneity, if heterogeneity is partially explained through subgroup analysis or meta-regression, residual unexplained heterogeneity may still be sufficient to maintain I^2 near saturation. Therefore, I^2 will fail to convey the decline in overall heterogeneity, while H^2 statistic that has no upper limit will allow to track changes in heterogeneity more meaningfully. In addition, a small number of studies (<10) will bias I^2 estimates, contributing to uncertainties inevitable associated with small meta-analyses (von Hippel, 2015). Of the three heterogeneity statistics Q_{total}, H^2 and I^2 described, we recommend that H^2 is used as it best satisfies the criteria for a heterogeneity statistic defined by Higgins and Thompson (2002).

Identifying bias

Bias refers to distortions in the data that may result in misleading meta-analytic outcomes. In the presence of bias, meta-analysis outcomes are often contradicted by higher quality large sample-sized studies (Egger et al., 1997), thereby compromising the validity of the meta-analytic study. Sources of observed bias include publication bias, methodological inconsistencies and quality, data irregularities due to poor quality design, inadequate analysis or fraud, and availability or selection bias (Egger et al., 1997; Ahmed et al., 2012). At the level of study identification and inclusion for meta-analysis, systematic searches are preferred over rapid review search strategies, as narrow search strategies may omit relevant studies. Withholding negative results is also a common source of publication bias, which is further exacerbated by the small-study effect (the phenomenon by which smaller studies produce results with larger effect sizes than larger studies) (Schwarzer et al., 2015). By extension, smaller studies that produce negative results are more likely to not be published compared to larger studies that produce negative results. Identifying all sources of bias is unfeasible, however, tools are available to estimate the extent of bias present.

Funnel plots. Funnel plots have been widely used to assess the risk of bias and examine meta-analysis validity (Light and Pillemer, 1984; Borenstein, 2009). The logic underlying the funnel plot is that in the absence of bias, studies are symmetrically distributed around the fixed effect size estimate, due to sampling error being random. Moreover, precise study-level estimates are expected to be more consistent with the global effect size than less precise studies, where precision is inversely related to the study-level standard error. Thus, for an unbiased set of studies, study-level effects θ_i plotted in relation to the inverse standard error $1/se(\theta_i)$ will produce a funnel shaped plot. Theoretical 95% CIs for the range of plotted standard errors are included as reference to visualize the expected distribution of studies in the absence of bias (Sterne and Harbord, 2004). When bias is present, study-level effects will be asymmetrically distributed around the global fixed-effect estimate. In the past, funnel plot asymmetries have been attributed solely to publication bias, however they should be interpreted more broadly as a general presence of bias or heterogeneity (Sterne et al., 2011). It should be noted that rapid reviews (**Figure 8A**, *left*) are far more subject to bias than systematic reviews (**Figure 8A**, *right*), due to the increased likelihood of relevant study omission.

Heterogeneity sensitivity analyses

Inconsistencies between studies can arise for a number of reasons, including methodological or biological heterogeneity (Patsopoulos et al., 2008). Since accounting for heterogeneity is an essential part of any meta-analysis, it is of interest to identify influential studies that may contribute to the observed heterogeneity.

Baujat plot. The Baujat Plot was proposed as a diagnostic tool to identify the studies that contribute most to heterogeneity and influence the global outcome (Baujat, 2002). The graph illustrates the contribution $Q_i^{\inf}$ of each study to heterogeneity on the x-axis

$$Q_i^{\inf} = \frac{\theta_i - \hat{\theta}_{FE}}{se(\theta_i)^2} \tag{18}$$

and contribution $\theta_i^{\inf}$ to global effect on the y-axis

$$\theta_i^{\inf} = \frac{\hat{\theta}_{-i} - \hat{\theta}_{FE}}{se\left(\hat{\theta}_{-i}\right)^2} \tag{19}$$

Studies that strongly influence the global outcome and contribute to heterogeneity are visualized in the upper right corner of the plot (**Figure 8B**). This approach has been used to identify outlying studies in the past (Anzures-Cabrera and Higgins, 2010).

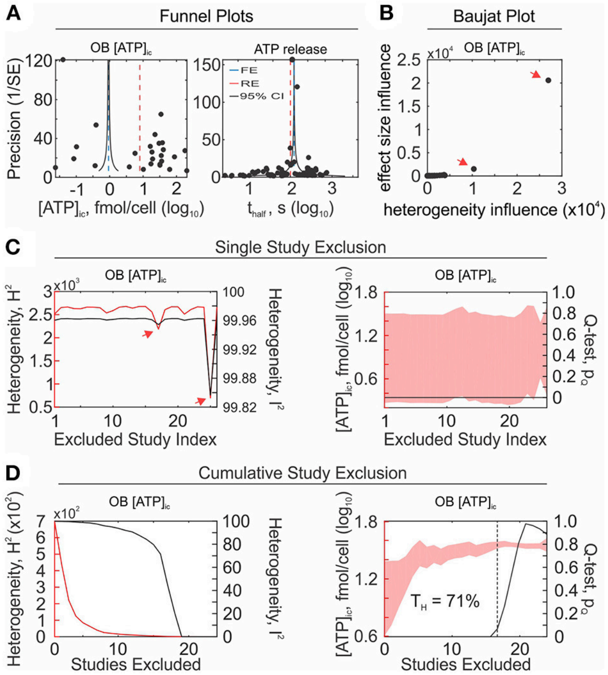

FIGURE 8 | Analysis of heterogeneity and identification of influential studies. **(A)** Bias and heterogeneity in OB $[ATP]_{ic}$ (*left*) and ATP release (*right*) data sets were assessed with funnel plots. Log_{10}-transformed study-level effect sizes (black markers) were plotted in relation to their precision assessed as inverse of standard error (1/SE). *Blue dashed line*: fixed effect estimate, *red dashed line*: random effects estimate, *gray lines*: Expected 95% confidence interval (95% CI) in the absence of bias/heterogeneity. **(B)** OB $[ATP]_{IC}$ were evaluated using Baujat plot and inconsistent and influential studies were identified in top right corner of plot (*arrows*). **(C,D)** Effect of the single study exclusion **(C)** and cumulative sequential exclusion of the most inconsistent studies **(D)**. *Left*: heterogeneity statistics, H^2 (*red line*) and I^2 (*black line*). *Right*: 95% CI (*red band*) and Q-test *p*-value (*black line*). *Arrows*: influential studies contributing to heterogeneity (same as those identified on Baujat Plot). *Dashed Black line*: homogeneity threshold T_H where *Q*-test $p = 0.05$.

Single-study exclusion sensitivity. Single-study exclusion analysis assesses the sensitivity of the global outcome and heterogeneity to exclusion of single studies. The global outcomes and heterogeneity statistics are computed for a dataset with a single omitted study; single study exclusion is iterated for all studies; and influential outlying studies are identified by observing substantial declines in observed heterogeneity, as determined by Q_{total}, H^2, or I^2, and by significant differences in the global outcome (**Figure 8C**). Influential studies should not be blindly discarded, but rather carefully examined to determine the reason for inconsistency. If a cause for heterogeneity can be identified, such as experimental design flaw, it is appropriate to omit the study from the analysis. All reasons for omission must be justified and made transparent by reviewers.

Cumulative-study exclusion sensitivity. Cumulative study exclusion sequentially removes studies to maximize the decrease in total variance Q_{total}, such that a more homogenous set of studies with updated heterogeneity statistics is achieved with each iteration of exclusion (**Figure 8D**).

$$\hat{\theta}_{-j} \pm 95\%\ CI_{-j}$$
$$\text{where } j = \arg\max_{i} (Q - Q_{-i})^2 \tag{20}$$

This method was proposed by Patsopoulos et al. to achieve desired levels of homogeneity (Patsopoulos et al., 2008), however, Higgins argued that its application should remain limited to (i) quantifying the extent to which heterogeneity permeates the set of studies and (ii) identifying sources of heterogeneity (Higgins, 2008). We propose the homogeneity threshold T_H as a measure of heterogeneity that can be derived from cumulative-study exclusion sensitivity analysis. The homogeneity threshold describes the percentage of studies that need to be removed (by the maximal Q-reduction criteria) before a homogenous set of studies is achieved. For example, in the OB $[ATP]_{ic}$ dataset, the homogeneity threshold was 71%, since removal of 71% of the most inconsistent studies resulted in a homogeneous dataset (**Figure 8D**, *right*). After homogeneity is attained by cumulative exclusion, the global effect generally stabilizes with respect to subsequent study removal. This metric provides information about the extent of inconsistency present in the set of studies that is scale invariant (independent of the number of studies), and is easily interpretable.

Exploratory Analyses

The purpose of an exploratory analysis is to understand the data in ways that may not be represented by a pooled global estimate. This involves identifying sources of observed heterogeneity related to biological and experimental factors. Subgroup and meta-regression analyses are techniques used to explore known data groupings define by study-level characteristics (i.e., covariates). Additionally, we introduce the cluster-covariate dependence analysis, which is an unsupervised exploratory technique used to identify covariates that coincide well will natural groupings within the data, and the intrastudy regression analysis, which is used to validate meta-regression outcomes.

Cluster-covariate dependence analysis

Natural groupings within the data can be informative and serve as a basis to guide further analysis. Using an unsupervised k-means clustering approach (Lloyd, 1982), we can identify natural groupings within the study-level data and assign cluster memberships to these data (**Figure 9A**). Reviewers then have two choices: either proceed directly to subgroup analysis (**Figure 9B**) or look for covariates that co-cluster with cluster memberships (**Figure 9C**) In the latter case, dependencies between cluster memberships and known data covariates can be tested using Pearson's Chi-Squared test for independence. Covariates that coincide with clusters can be verified by subgroup analysis (**Figure 9D**). The dependence test is limited by the availability of studies and requires that at least 80% of covariate-cluster pairs are represented by at least 5 studies (McHugh, 2013). Clustering results should be considered exploratory and warrant further investigation due to several limitations. If the subpopulations were identified through clustering, however they do not depend on extracted covariates, reviewers risk assigning misrepresentative meaning to these clusters. Moreover,

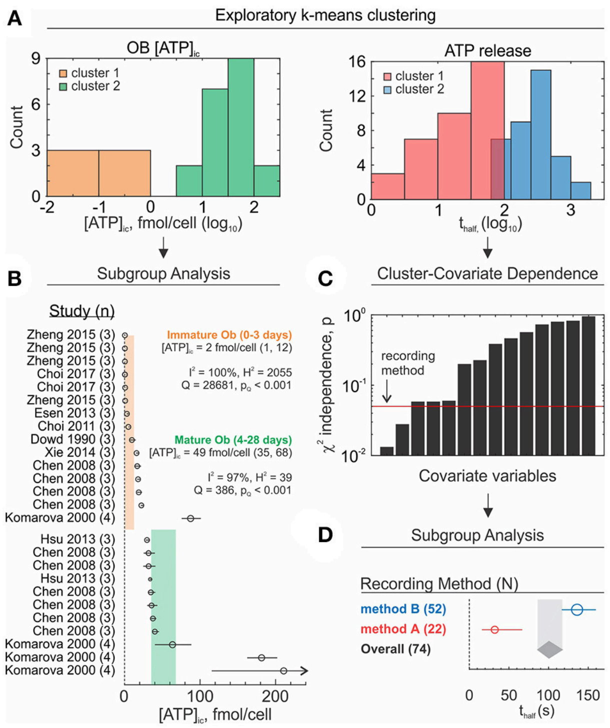

FIGURE 9 | Exploratory subgroup analysis. **(A)** Exploratory k-means clustering was used to partition OB $[\mathrm{ATP}]_{\mathrm{ic}}$ (*left*) and ATP release (*right*) data into potential clusters/subpopulations of interest. **(B)** Subgroup analysis of OB $[\mathrm{ATP}]_{\mathrm{ic}}$ data by differentiation status (immature – 0 to 3 day osteoblasts vs. mature – 4 to 28 day osteoblasts). Subgroup outcomes (fmol ATP/cell) estimated using sample-size weighting-scheme; *black markers*: Study-level outcomes ± 95% CI, marker sizes are proportional to sample size *n*. *Orange and green bands*: 95% CI for immature and mature osteoblast subgroups, respectively. **(C)** Dependence between ATP release cluster membership and known covariates/characteristics was assessed using Pearson's χ^2 independence test. *Black bars*: χ^2 test *p*-values for each covariate-cluster dependence test. *Red line*: $\alpha = 0.05$ significance threshold. *Arrow*: most influential covariate (ex. recording method). **(D)** Subgroup analysis of ATP release by recording method. Subgroup outcomes (t_{half}) estimated using random effects weighting, τ^2 computed using DerSimonian-Laird estimator. *Round markers*: subgroup estimates ± 95% CI, marker sizes are proportional to number of studies per subgroup *N*. *Gray band/diamond*: global effect ± 95% CI.

conventional clustering methods always converge to a result, therefore the data will still be partitioned even in the absence of natural data groupings. Future adaptations of this method might involve using different clustering algorithms (hierarchical clustering) or independence tests (G-test for independence) as well as introducing weighting terms to bias clustering to reflect study-level precisions.

Subgroup analysis

Subgroup analyses attempt to explain heterogeneity and explore differences in effects by partitioning studies into characteristic groups defined by study-level categorical covariates (**Figures 9B,D**; **Table 5**). Subgroup effects are estimated along with corresponding heterogeneity statistics. To evaluate the extent to which subgroup covariates contribute to observed inconsistencies, the explained heterogeneity $Q_{between}$ and unexplained heterogeneity Q_{within} can be calculated.

$$Q_{within} = \sum_{j=1}^{S} \left(\sum_{i=1}^{N_j} \left(se(\theta_i)^{-2} \cdot \left(\theta_i - \hat{\theta}_{(FE)j} \right)^2 \right) \right) \tag{21}$$

where S is the total number of subgroups per given covariate and each subgroup j contains N_j studies. The explained heterogeneity $Q_{between}$ is then the difference between total and subgroup heterogeneity:

$$Q_{between} = Q_{total} - Q_{within} \tag{22}$$

If the *p*-value for the χ^2 distributed statistic $Q_{between}$ is significant, the subgrouping can be assumed to explain a significant amount of heterogeneity (Borenstein, 2009). Similarly, Q_{within} statistic can be used to test whether there is any residual heterogeneity present within the subgroups.

The $R^2_{explained}$ is a related statistic that can be used to describe the percent of total heterogeneity that was explained by the covariate and is estimated as

$$R^2_{explained} = \left(1 - \frac{\tau^2_{within}}{\tau^2_{total}} \right) \cdot 100\% \tag{23}$$

Where pooled heterogeneity within subgroups τ^2_{within} represents the remaining unexplained variation (Borenstein, 2009):

$$\tau^2_{within} = \frac{\sum_{j=1}^{s} Q_{(within)j} - \sum_{j=1}^{s} df_j}{\sum_{j=1}^{s} c_j}$$

$$\text{where } c_j = \sum_{i=1}^{N_j} se(\theta_i)^{-2} - \frac{\sum_i \left(se(\theta_i)^{-2} \right)^2}{\sum_i se(\theta_i)^{-2}} \tag{24}$$

Subgroup analysis of the ATP release dataset revealed that recording method had a major influence on ATP release outcome, such that method A produced significantly lower outcomes than method B (**Figure 9D**; **Table 5**, significance determined by non-overlapping 95% CIs). Additionally, recording method accounted for a significant amount of heterogeneity ($Q_{between}$, $p < 0.001$), however it represented only 4% ($R^2_{explained}$) of the total observed heterogeneity. Needless to say, the remaining 96% of heterogeneity is significant (Q_{within}, $p < 0.001$). To explore the remaining heterogeneity, additional subgroup analysis can be conducted by further stratifying method A and method B subgroups by other covariates. However, in many meta-analyses multi-level data stratification may be unfeasible if covariates are unavailable or if the number of studies within subgroups are low.

Multiple comparisons. When multiple subgroups are present for a given covariate, and the reviewer wishes to investigate the statistical differences between the subgroups, the problem of multiple comparisons should be addressed. Error rates are multiplicative and increase substantially as the number of subgroup comparisons increases. The Bonferroni correction has

TABLE 5 | Exploratory subgroup analysis.

Subgroup summary statistics

Group (N)	$\hat{\theta}$± 95% CI	I^2 (%)	H^2	Q
Total (74)	101 (86, 117)	94	16	1133
Method A (22)	32 (16, 66)	94	17	358
Method B (52)	136 (117, 159)	92	13	669

Accounting for heterogeneity with subgroup analysis

	Q	df	p-value	Interpretation
Total	1,133	73	<0.001	Data are heterogeneous
Method A	358	21	<0.001	Data are heterogeneous
Method B	669	51	<0.001	Data are heterogeneous
Between	106	1	<0.001	Subgrouping explained significant heterogeneity
Within	1,027	72	<0.001	Significant heterogeneity remains

Effect and heterogeneity estimates of ATP release by recording method.

been advocated to control for false positive findings in meta-analyses (Hedges and Olkin, 1985) which involves adjusting the significance threshold:

$$\alpha^* = \frac{\alpha}{m} \tag{25}$$

α^* is the adjusted significance threshold to attain intended error rates α for m subgroup comparisons. Confidence intervals can then be computed using α^* in place of α:

$$\pm\, CI = \pm v_{1-\alpha^*/2} \cdot se(\hat{\theta}) \tag{26}$$

Meta-regression

Meta-regression attempts to explain heterogeneity by examining the relationship between study-level outcomes and continuous covariates while incorporating the influence of categorical covariates (**Figure 10A**). The main differences between conventional linear regression and meta-regression are (i) the incorporation of weights and (ii) covariates are at the level of the study rather than the individual sample. The magnitude of the relationship β_n between the covariates $x_{n,i}$ and outcome y_i for study i and covariate n are of interest when conducting a meta-regression analysis. It should be noted that the intercept β_0 of a meta-regression with negligible effect of covariates is equivalent to the estimate approximated by a weighted mean (Equation 3). The generalized meta-regression model is specified as

$$y_i = \beta_0 + \beta_1 x_{1,i} + \ldots + \beta_n x_{n,i} + \eta_i + \varepsilon_i \tag{27}$$

where intrastudy variance ε_i is

$$\varepsilon_i \sim \mathcal{N}\left(0, se(\theta_i)^2\right) \tag{28}$$

and the deviation from the distribution of effects η_i depends on the chosen meta-analytic model:

$$\eta_i \sim \begin{cases} 0, & \textit{fixed effect} \\ \mathcal{N}(0, \tau^2), & \textit{random effets} \end{cases} \tag{29}$$

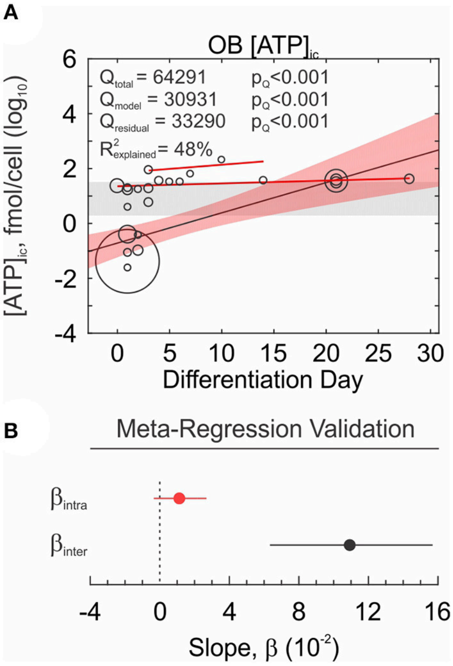

FIGURE 10 | Meta-regression analysis and validation. **(A)** Relationship between osteoblast differentiation day (covariate) and intracellular ATP content (outcome) investigated by meta-regression analysis. Outcomes are on $\log_{10}$ scale, meta-regression markers sizes are proportional to weights. *Red bands*: 95% CI. *Gray bands*: 95% CI of intercept only model. *Solid red lines*: intrastudy regression. **(B)** Meta-regression coefficient β_{inter} (*black*) compared to intrastudy regression coefficient β_{intra} (*red*). Shown are regression coefficients ± 95% CI.

The residual Q statistic that explains the dispersion of the studies from the regression line is calculated as follows

$$Q_{residual} = \sum_{i=1}^{N} \left(w_i \cdot (\theta_i - y_i)^2 \right) \tag{30}$$

Where y_i is the predicted value at x_i according to the meta-regression model. $Q_{residual}$ is analogous to $Q_{between}$ computed during subgroup analysis and is used to test the degree of remaining unaccounted heterogeneity. $Q_{residual}$ is also used to approximate the unexplained interstudy variance $\tau^2_{residual}$

$$\tau^2_{residual} = \frac{Q_{residual} - df}{c_{total}}$$

$$\text{where } c_{total} = \sum_i se(\theta_i)^{-2} - \frac{\sum_i \left(se(\theta_i)^{-2}\right)^2}{\sum_i se(\theta_i)^{-2}} \qquad (31)$$

Which can be used to calculate $R^2_{explained}$ estimated as

$$R^2_{explained} = \left(1 - \frac{\tau^2_{residual}}{\tau^2_{total}}\right) \cdot 100\% \qquad (32)$$

Q_{model} quantifies the amount of heterogeneity explained by the regression model and is analogous to Q_{within} computed during subgroup analysis.

$$Q_{model} = Q_{total} - Q_{residual} \qquad (33)$$

Intrastudy regression analysis The challenge of interpreting results from a meta-regression is that relationships that exist within studies may not necessarily exist across studies, and vice versa. Such inconsistencies are known as aggregation bias and in the context of meta-analyses can arise from excess heterogeneity or from confounding factors at the level of the study. This problem has been acknowledged in clinical meta-analyses (Thompson and Higgins, 2002), however cannot be corrected without access to individual patient data. Fortunately, basic research studies often report outcomes at varying predictor levels (ex. dose-response curves), permitting for intrastudy (within-study) relationships to be evaluated by the reviewer. If study-level regression coefficients can be computed for several studies (**Figure 10A,** *red lines*), they can be pooled to estimate an overall effect β_{intra}. The meta-regression interstudy coefficient β_{inter} and the overall intrastudy-regression coefficient β_{intra} can then be compared in terms of magnitude and sign. Similarity in the magnitude and sign validates the existence of the relationship and characterizes its strength, while similarity in sign but not the magnitude, still supports the presence of the relationship, but calls for additional experiments to further characterize it. For the Ob $[ATP]_i$ dataset, the magnitude of the relationship between osteoblast differentiation day and intracellular ATP concentration was inconsistent between intrastudy and interstudy estimates, however the estimates were of consistent sign (**Figure 10B**).

Limitations of exploratory analyses

When performed with knowledge and care, exploratory analysis of meta-analytic data has an enormous potential for hypothesis generation, cataloging current practices and trends, and identifying gaps in the literature. Thus, we emphasize the inherent limitations of exploratory analyses:

Data dredging. A major pitfall in meta-analyses is data dredging (also known as p-hacking), which refers to searching for significant outcomes only to assign meaning later. While exploring the dataset for potential patterns can identify outcomes of interest, reviewers must be wary of random patterns that can arise in any dataset. Therefore, if a relationship is observed it should be used to generate hypotheses, which can then be tested on new datasets. Steps to avoid data dredging involve defining an *a priori* analysis plan for study-level covariates, limiting exploratory analysis of rapid review meta-analyses and correcting for multiple comparisons.

Statistical power. The statistical power reflects the probability of rejecting the null hypothesis when the alternative is true. Meta-analyses are believed to have higher statistical power than the underlying primary studies, however this is not always true (Hedges and Pigott, 2001; Jackson and Turner, 2017). Random effects meta-analyses handle data heterogeneity by accounting for between-study variance, however this weakens the inference properties of the model. To maintain statistical powers that exceed those of the contributing studies in a random effects meta-analysis, at least five studies are required (Jackson and Turner, 2017). This consequently limits subgroup analyses that partition studies into smaller groups to isolate covariate-dependent effects. Thus, reviewers should ensure that group are not under-represented to maintain statistical power. Another determinant of statistical power is the expected effect size, which if small, will be much more difficult to support with existing evidence than if it is large. Thus, if reviewers find that there is insufficient evidence to conclude that a small effect exists, this should not be interpreted as evidence of no effect.

Causal inference. Meta-analyses are not a tool for establishing causal inference. However, there are several criteria for causality that can be investigated through exploratory analyses that include consistency, strength of association, dose-dependence and plausibility (Weed, 2000, 2010). For example, consistency, the strength of association, and dose-dependence can help establish that the outcome is dependent on exposure. However, reviewers are still posed with the challenge of accounting for confounding factors and bias. Therefore, while meta-analyses can explore various criteria for causality, causal claims are inappropriate, and outcomes should remain associative.

CONCLUSIONS

Meta-analyses of basic research can offer critical insights into the current state of knowledge. In this manuscript, we have adapted meta-analytic methods to basic science applications and provided a theoretical foundation, using OB $[ATP]_i$ and ATP release datasets, to illustrate the workflow. Since the generalizability of any meta-analysis relies on the transparent, unbiased and accurate methodology, the implications of deficient reporting practices and the limitations of the meta-analytic methods were discussed. Emphasis was placed on the analysis and exploration of heterogeneity. Additionally, several alternative and supporting methods have been proposed, including a method for validating meta-regression outcomes—intrastudy regression analysis, and a novel measure of heterogeneity—the homogeneity threshold. All analyses were conducted using *MetaLab*, a meta-analysis toolbox that we have developed in MATLAB R2016b. *MetaLab* has been provided for free to promote meta-analyses in basic research (https://github.com/NMikolajewicz/MetaLab).

In its current state, the translational pipeline from benchtop to bedside is an inefficient process, in one case estimated to produce ∼1 clinically favorable clinical outcome for ∼1,000 basic research studies (O'Collins et al., 2006). The methods we have described here serve as a general framework for comprehensive data consolidation, knowledge gap-identification, evidence-driven hypothesis generation and informed parameter estimation in computation modeling, which we hope will contribute to meta-analytic outcomes that better inform translation studies, thereby minimizing current failures in translational research.

AUTHOR CONTRIBUTIONS

Both authors contributed to the study conception and design, data acquisition and interpretation and drafting and critical revision of the manuscript. NM developed MetaLab. Both authors approved the final version to be published.

ACKNOWLEDGMENTS

This work was supported by Natural Sciences and Engineering Research Council (NSERC, RGPIN-288253) and Canadian Institutes for Health Research (CIHR MOP-77643). NM was supported by the Faculty of Dentistry, McGill University and le Réseau de Recherche en Santé Buccodentaire et Osseuse (RSBO). Special thanks to Ali Mohammed (McGill University) for help with validation of MetaLab data extraction module.

SUPPLEMENTARY MATERIAL

The Supplementary Material for this article can be found online at: https://www.frontiersin.org/articles/10.3389/fphys.2019.00203/full#supplementary-material

REFERENCES

Ahmed, I., Sutton, A. J., and Riley, R. D. (2012). Assessment of publication bias, selection bias, and unavailable data in meta-analyses using individual participant data: a database survey. *Br. Med. J.* 344:d7762 doi: 10.1136/bmj.d7762

Altman, D. G., and Bland, J. M. (2005). Standard deviations and standard errors. *Br. Med. J.* 331, 903–903. doi: 10.1136/bmj.331.7521.903

Anzures-Cabrera, J., and Higgins, J. P. T. (2010). Graphical displays for meta-analysis: an overview with suggestions for practice. *Res. Synth. Methods* 1, 66–80. doi: 10.1002/jrsm.6

Baguley, T. (2009). Standardized or simple effect size: what should be reported? *Br. J. Soc. Psychol.* 100, 603–617. doi: 10.1348/000712608X377117

Barendregt, J., and Doi, S. (2009). *MetaXL User Guide: Version 1.0*. Wilston, QLD: EpiGear International Pty Ltd.

Baujat, B. (2002). A graphical method for exploring heterogeneity in meta-analyses: application to a meta-analysis of 65 trials. *Stat. Med.* 21:18. doi: 10.1002/sim.1221

Bax, L. (2016). *MIX 2.0 – Professional Software for Meta-analysis in Excel. Version 2.0.1.5. BiostatXL*. Available online at: https://www.meta-analysis-made-easy.com

Bittker, J. A., and Ross, N. T. (2016). *High Throughput Screening Methods: Evolution and Refinement*. Cambridge: Royal Society of Chemistry. doi: 10.1039/9781782626770

Bodin, P., Milner, P., Winter, R., and Burnstock, G. (1992). Chronic hypoxia changes the ratio of endothelin to ATP release from rat aortic endothelial cells exposed to high flow. *Proc. Biol. Sci.* 247, 131–135. doi: 10.1098/rspb.1992.0019

Borenstein, M. (2009). *Introduction to Meta-Analysis*. Chichester: John Wiley & Sons. doi: 10.1002/9780470743386

Borenstein, M., Hedges, L., Higgins, J. P. T., and Rothstein, H. R. (2005). *Comprehensive meta-analysis (Version 2.2.027) [Computer software]*. Englewood, CO.

Bramer, W. M., Giustini, D., de Jonge, G. B., Holland, L., and Bekhuis, T. (2016). De-duplication of database search results for systematic reviews in EndNote. *J. Med. Libr. Assoc.* 104, 240–243. doi: 10.3163/1536-5050.104.3.014

Chowdhry, A. K., Dworkin, R. H., and McDermott, M. P. (2016). Meta-analysis with missing study-level sample variance data. *Stat. Med.* 35, 3021–3032. doi: 10.1002/sim.6908

Cochrane Collaboration (2011). *Review Manager (RevMan) [Computer Program]*. Copenhagen.

Cox, M., Harris, P., and Siebert, B. R.-L. (2003). Evaluation of measurement uncertainty based on the propagation of distributions using monte carlo simulation. *Measure. Techniq.* 46, 824–833. doi: 10.1023/B:METE.0000008439.82231.ad

DeLuca, J. B., Mullins, M. M., Lyles, C. M., Crepaz, N., Kay, L., and Thadiparthi, S. (2008). Developing a comprehensive search strategy for evidence based systematic reviews. *Evid. Based Libr. Inf. Pract.* 3, 3–32. doi: 10.18438/B8KP66

DerSimonian, R., and Laird, N. (1986). Meta-analysis in clinical trials. *Control. Clin. Trials* 7, 177–188. doi: 10.1016/0197-2456(86)90046-2

Ecker, E. D., and Skelly, A. C. (2010). Conducting a winning literature search. *Evid. Based Spine Care J.* 1, 9–14. doi: 10.1055/s-0028-1100887

Egger, M., Smith, G. D., Schneider, M., and Minder, C. (1997). Bias in meta-analysis detected by a simple, graphical test. *Br. Med. J.* 315, 629–634. doi: 10.1136/bmj.315.7109.629

Finfgeld-Connett, D., and Johnson, E. D. (2013). Literature search strategies for conducting knowledge-building and theory-generating qualitative systematic reviews. *J. Adv. Nurs.* 69, 194–204. doi: 10.1111/j.1365-2648.2012.06037.x

Ganann, R., Ciliska, D., and Thomas, H. (2010). Expediting systematic reviews: methods and implications of rapid reviews. *Implementation Sci.* 5, 56–56. doi: 10.1186/1748-5908-5-56

Gavaghan, D. J., Moore, R. A., and McQuay, H. J. (2000). An evaluation of homogeneity tests in meta-analyses in pain using simulations of individual patient data. *Pain* 85, 415–424. doi: 10.1016/S0304-3959(99)00302-4

Gopalakrishnan, S., and Ganeshkumar, P. (2013). Systematic reviews and meta-analysis: understanding the best evidence in primary healthcare. *J Fam. Med. Prim. Care* 2, 9–14. doi: 10.4103/2249-4863.109934

Grönholm, T., and Annila, A. (2007). Natural distribution. *Math. Biosci.* 210, 659–667. doi: 10.1016/j.mbs.2007.07.004

Haby, M. M., Chapman, E., Clark, R., Barreto, J., Reveiz, L., and Lavis, J. N. (2016). What are the best methodologies for rapid reviews of the research evidence for evidence-informed decision making in health policy and practice: a rapid review. *Health Res. Policy Syst.* 14:83. doi: 10.1186/s12961-016-0155-7

Hartung, J., and Makambi, K. H. (2002). Positive estimation of the between-study variance in meta-analysis: theory and methods. *S. Afr. Stat. J.* 36, 55–76.

Hedges, L. V., and Olkin, I. (1985). *Statistical Methods for Meta-Analysis*. New York, NY: Academic Press.

Hedges, L. V., and Pigott, T. D. (2001). The power of statistical tests in meta-analysis. *Psychol. Methods* 6, 203–217. doi: 10.1037/1082-989X.6.3.203

Higgins, J. P. (2008). Commentary: heterogeneity in meta-analysis should be expected and appropriately quantified. *Int. J. Epidemiol.* 37, 1158–1160. doi: 10.1093/ije/dyn204

Higgins, J. P., and Green, S. (Eds.) (2011). *Cochrane Handbook for Systematic Reviews of Interventions*, Vol. 4. Oxford: John Wiley & Sons.

Higgins, J. P., and Thompson, S. G. (2002). Quantifying heterogeneity in a meta-analysis. *Stat. Med.* 21, 1539–1558. doi: 10.1002/sim.1186

Higgins, J. P., Thompson, S. G., Deeks, J. J., and Altman, D. G. (2003). Measuring inconsistency in meta-analyses. *Br. Med. J.* 327, 557–560. doi: 10.1136/bmj.327.7414.557

Higgins, J. P., White, I. R., and Anzures-Cabrera, J. (2008). Meta-analysis of skewed data: combining results reported on log-transformed or raw scales. *Stat. Med.* 27, 6072–6092. doi: 10.1002/sim.3427

Huedo-Medina, T. B., Sanchez-Meca, J., Marin-Martinez, F., and Botella, J. (2006). Assessing heterogeneity in meta-analysis: Q statistic or I^2 index? *Psychol. Methods* 11, 193–206. doi: 10.1037/1082-989X.11.2.193

Hunter, J. E., and Schmidt, F. L. (2004). *Methods of Meta-analysis: Correcting Error and Bias in Research Findings*. Thousand Oaks, CA: Sage.

Jackson, D., and Turner, R. (2017). Power analysis for random-effects meta-analysis. *Res. Synth. Methods* 8, 290–302. doi: 10.1002/jrsm.1240

JASP Team (2018). *JASP (Verision 0.9) [Computer Software]*. Amsterdam.

Karabatsos, G., Talbott, E., and Walker, S. G. (2015). A Bayesian nonparametric meta-analysis model. *Res. Synth. Methods* 6, 28–44. doi: 10.1002/jrsm.1117

Kontopantelis, E., and Reeves, D. (2012). Performance of statistical methods for meta-analysis when true study effects are non-normally distributed: a simulation study. *Stat. Methods Med. Res.* 21, 409–426. doi: 10.1177/0962280210392008

Kwon, Y., Lemieux, M., McTavish, J., and Wathen, N. (2015). Identifying and removing duplicate records from systematic review searches. *J. Med. Libr. Assoc.* 103, 184–188. doi: 10.3163/1536-5050.103.4.004

Light, R. J., and Pillemer, D. B. (1984). *Summing Up: The Science of Reviewing Research*. Cambridge, MA: Harvard University Press.

Limpert, E., Stahel, W. A., and Abbt, M. (2001). Log-normal Distributions across the sciences: keys and clues: on the charms of statistics, and how mechanical models resembling gambling machines offer a link to a handy way to characterize log-normal distributions, which can provide deeper insight into variability and probability—normal or log-normal: That is the question. *AIBS Bull.* 51, 341–352.

Lloyd, S. (1982). Least squares quantization in PCM. *IEEE Trans. Inf. Theory* 28, 129–137. doi: 10.1109/TIT.1982.1056489

Lorenzetti, D. L., and Ghali, W. A. (2013). Reference management software for systematic reviews and meta-analyses: an exploration of usage and usability. *BMC Med. Res. Methodol.* 13, 141–141. doi: 10.1186/1471-2288-13-141

Marin-Martinez, F., and Sanchez-Meca, J. (2010). Weighting by inverse variance or by sample size in random-effects meta-analysis. *Educ. Psychol. Meas.* 70, 56–73. doi: 10.1177/0013164409344534

Mattivi, J. T., and Buchberger, B. (2016). Using the amstar checklist for rapid reviews: is it feasible? *Int. J. Technol. Assess. Health Care* 32, 276–283. doi: 10.1017/S0266462316000465

McGowan, J., and Sampson, M. (2005). Systematic reviews need systematic searchers. *J. Med. Libr. Assoc.* 93, 74–80.

McHugh, M. L. (2013). The Chi-square test of independence. *Biochem. Med.* 23, 143–149. doi: 10.11613/BM.2013.018

Mikolajewicz, N., Mohammed, A., Morris, M., and Komarova, S. V. (2018). Mechanically-stimulated ATP release from mammalian cells: systematic review and meta-analysis. *J. Cell Sci.* 131:22. doi: 10.1242/jcs.223354.

Milo, R., Jorgensen, P., Moran, U., Weber, G., and Springer, M. (2010). BioNumbers—the database of key numbers in molecular and cell biology. *Nucleic Acids Res.* 38:D750–3. doi: 10.1093/nar/gkp889

Moher, D., Liberati, A., Tetzlaff, J., and Altman, D. G. (2009). Preferred reporting items for systematic reviews and meta-analyses: the PRISMA statement. *PLoS Med.* 6:e1000097. doi: 10.1371/journal.pmed.1000097

O'Collins, V. E., Macleod, M. R., Donnan, G. A., Horky, L. L., van der Worp, B. H., and Howells, D. W. (2006). 1,026 experimental treatments in acute stroke. *Ann. Neurol.* 59, 467–477. doi: 10.1002/ana.20741

Pathak, M., Dwivedi, S. N., Deo, S. V. S., Sreenivas, V., and Thakur, B. (2017). Which is the preferred measure of heterogeneity in meta-analysis and why? a revisit. *Biostat Biometrics Open Acc.* 1, 1–7. doi: 10.19080/BBOAJ.2017.01.555555

Patsopoulos, N. A., Evangelou, E., and Ioannidis, J. P. A. (2008). Sensitivity of between-study heterogeneity in meta-analysis: proposed metrics and empirical evaluation. *Int. J. Epidemiol.* 37, 1148–1157. doi: 10.1093/ije/dyn065

Paule, R. C., and Mandel, J. (1982). Consensus values and weighting factors. *J. Res. Natl. Bur. Stand.* 87, 377–385. doi: 10.6028/jres.087.022

Sanchez-Meca, J., and Marin-Martinez, F. (2008). Confidence intervals for the overall effect size in random-effects meta-analysis. *Psychol. Methods* 13, 31–48. doi: 10.1037/1082-989X.13.1.31

Schwarzer, G., Carpenter, J. R., and Rücker, G. (2015). "Small-study effects in meta-analysis," in *Meta-Analysis with R,* eds G. Schwarzer, J. R. Carpenter, and G. Rücker (Cham: Springer International Publishing), 107–141.

Sena, E., van der Worp, H. B., Howells, D., and Macleod, M. (2007). How can we improve the pre-clinical development of drugs for stroke? *Trends Neurosci.* 30, 433–439. doi: 10.1016/j.tins.2007.06.009

Sheldrake, R. (1997). Experimental effects in scientific research: how widely are they neglected? *Bull. Sci. Technol. Soc.* 17, 171–174. doi: 10.1177/027046769701700405

Sidik, K., and Jonkman, J. N. (2005). Simple heterogeneity variance estimation for meta-analysis. *J. R. Stat. Soc. Ser. C Appl. Stat.* 54, 367–384. doi: 10.1111/j.1467-9876.2005.00489.x

Sterne, J. A., Sutton, A. J., Ioannidis, J. P., Terrin, N., Jones, D. R., Lau, J., et al. (2011). Recommendations for examining and interpreting funnel plot asymmetry in meta-analyses of randomised controlled trials. *Br. Med. J.* 343:d4002. doi: 10.1136/bmj.d4002

Sterne, J. A. C., and Harbord, R. (2004). Funnel plots in meta-analysis. *Stata J.* 4, 127–141. doi: 10.1177/1536867X0400400204

Thompson, S. G., and Higgins, J. P. (2002). How should meta-regression analyses be undertaken and interpreted? *Stat. Med.* 21, 1559–1573. doi: 10.1002/sim.1187

Vaux, D. L., Fidler, F., and Cumming, G. (2012). Replicates and repeats—what is the difference and is it significant?: a brief discussion of statistics and experimental design. *EMBO Rep.* 13, 291–296. doi: 10.1038/embor.2012.36

Veroniki, A. A., Jackson, D., Viechtbauer, W., Bender, R., Bowden, J., Knapp, G., et al. (2016). Methods to estimate the between-study variance and its uncertainty in meta-analysis. *Res. Synth. Methods* 7, 55–79. doi: 10.1002/jrsm.1164

Vesterinen, H. M., Sena, E. S., Egan, K. J., Hirst, T. C., Churolov, L., Currie, G. L., et al. (2014). Meta-analysis of data from animal studies: a practical guide. *J. Neurosci. Methods* 221, 92–102. doi: 10.1016/j.jneumeth.2013.09.010

Viechtbauer, W. (2010). Conducting meta-analyses in R with the metafor package. *J. Stat. Softw.* 36, 1–48. doi: 10.18637/jss.v036.i03

von Hippel, P. T. (2015). The heterogeneity statistic I^2 can be biased in small meta-analyses. *BMC Med. Res. Methodol.* 15:35. doi: 10.1186/s12874-015-0024-z

Weed, D. L. (2000). Interpreting epidemiological evidence: how meta-analysis and causal inference methods are related. *Int. J. Epidemiol.* 29, 387–390. doi: 10.1093/intjepid/29.3.387

Weed, D. L. (2010). Meta-analysis and causal inference: a case study of benzene and non-hodgkin lymphoma. *Ann. Epidemiol.* 20, 347–355. doi: 10.1016/j.annepidem.2010.02.001

Conflict of Interest Statement: The authors declare that the research was conducted in the absence of any commercial or financial relationships that could be construed as a potential conflict of interest.

Advantages of publishing in Frontiers

OPEN ACCESS
Articles are free to read
for greatest visibility
and readership

FAST PUBLICATION
Around 90 days
from submission
to decision

HIGH QUALITY PEER-REVIEW
Rigorous, collaborative,
and constructive
peer-review

TRANSPARENT PEER-REVIEW
Editors and reviewers
acknowledged by name
on published articles

Frontiers
Avenue du Tribunal-Fédéral 34
1005 Lausanne | Switzerland

Visit us: www.frontiersin.org
Contact us: info@frontiersin.org | +41 21 510 17 00

REPRODUCIBILITY OF RESEARCH
Support open data
and methods to enhance
research reproducibility

DIGITAL PUBLISHING
Articles designed
for optimal readership
across devices

FOLLOW US
@frontiersin

IMPACT METRICS
Advanced article metrics
track visibility across
digital media

EXTENSIVE PROMOTION
Marketing
and promotion
of impactful research

LOOP RESEARCH NETWORK
Our network
increases your
article's readership